PROCEEDINGS BOOK SERIES
-PBS-

IBEM-2023

4th International Conference on Innovation in Business, Economics & Marketing Research

ISSN : 2961-6611
-PBS- Vol. 07

Proceedings Book Series (PBS)

4th International Conference on Innovation in Business, Economics & Marketing Research (IBEM - 2023)

Editors:
Dr. Ahmed Rhif (Tunisia)
Dr. Hiroko Kawamorita (Turkey)

Summary

Design Solar Cell Patch Antenna for 5GHz WLAN Application

Sara A. Rashed [1] [(1)], *Fathi Hareb* [(2)], *Said Elkhetali*[(3)]

School of Engineering and Applied Sciences, Department of Electrical & Electronic Engineering.
Libyan Academy of Graduate Studies. **Tripoli, Libya**
sararashedeng@gmail.com , fathi.hareb@academy.edu.ly

***Abstract*—In this paper, Design Microstrip antenna integrated with solar cell which used for transmitted and received the RF signal and generate DC voltage *at same time,* The antenna was printed using Perpex substrate material with dielectric constant of εr = 2.6 and thickness of h = 1.6 mm as insulation layer and use solar cell as substrate layer with εr = 3.9 and thickness 2.3 mm. The overall dimension of the antenna is *85 mm* x *55 mm* x *3.9 mm* with 50 Ω impedance. This antenna operates between 4.9106 GHz and 5.1219 GHz for return loss of less than -10 dB. The simulation results present that the antenna gain ranges between 3.479 dBi and dBi with Directivity ranges between 4.833 and 6.574.**

Keywords*— *Microstrip antenna, solar cell antenna, CST Microwave studio Simulation

I. INTRODUCTION

The electrical energy is very important to use as source to operation of wireless communication system. The photovoltaic systems of power generation when combined with communications systems can provide compact and reliable autonomous communication systems for many applications [1]. Both the solar cell generator and antenna are integrating them into a single system produces more advantages as reducing the space, cost and acting as standalone system [2]. This has become a significant challenge when it comes to powering communication systems in remote places where the electricity grid is not available [3]. Simultaneously both solar cell and patch antenna used as transmitted and received RF signal beside produce the electrical energy which utilize PV cell as back-up power source used in many application such as disaster alert system, moving vehicles, remote sensing, and meteorological surveillance[4].

II. ANTENNA DESIGN

A. Equivalent Circuit of Microstrip Patch and Solarcell Antenna:

Compare with Microstrip antenna and solar cell, ground plate, coaxial port, subtract are similar. In upper part of the solar cell, silicon wafer is used for light reception and in microstrip antenna metallic plate is used for receiving EM waves as shown in "figure 1" [5].

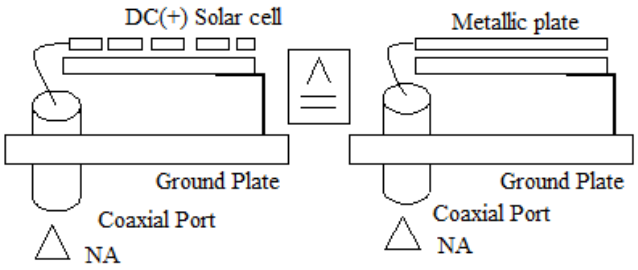

Figure1:Equavalint circuit of solar cell and Microstrip antenna

To know whether the dielectric layer (insulator) of
In order to provide high gain and a good efficiency the materials used in planar antenna designs should be as lossless as possible. Numerous measurements have shown, that from a RF point of view the solar cell acts nearly like a metallic patch [6].

B. Design for Microstrip Patch Antenna:

In this paper was a designed solar cell patch antenna that utilizes solar cell as substrate with thickness 2.3 mm. Add insulation layer between patch antenna and solar cell it is perpex with dielectric constant 2.6 and thickness 1.6 mm.The overall dimensions show in table 1:

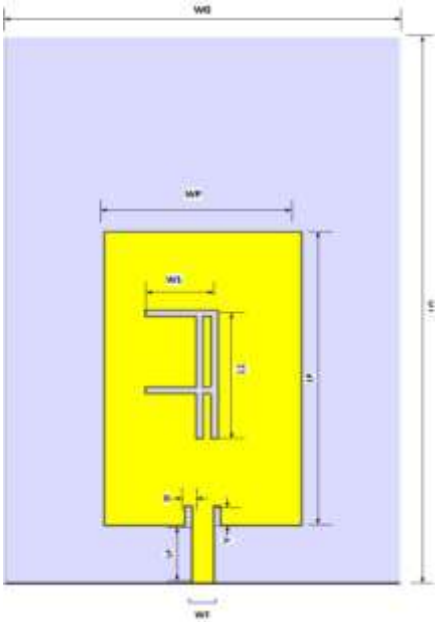

Figure 2: Rectangular solar cell patch antenna

ISSN: 2961-6611

Tabe1:Antenna parameter's size

PARAMETER	SIZE(mm)
LG	55
WG	85
LP	24
WP	27.4
W1	6
WF	3
LF	9
L1	20
X	1
Y	3

The fabrication of microstrip antenna was managed based on the simulation results utilizing the above mentioned software. Antenna fabrication was very easy to do and inexpensive.

III. SIMULATION RESULTS

The software that be used to simulate the antenna has the ability to display several antenna parameters such as return loss, VSWR, impedance, gain and radiation pattern. This section illustrates several simulation results of the designed antenna.

A. Return loss and Bandwidth

Figure 2 demonstrates the return loss (S-Parameter) value, The antenna operates between 4.9106 GHz and 5.1219 GHz. Bandwidth is obtained from the difference between the upper and the lower frequencies. Bandwidth obtained from the simulation was quite large, 210.4 MHz as a result of antenna simulation

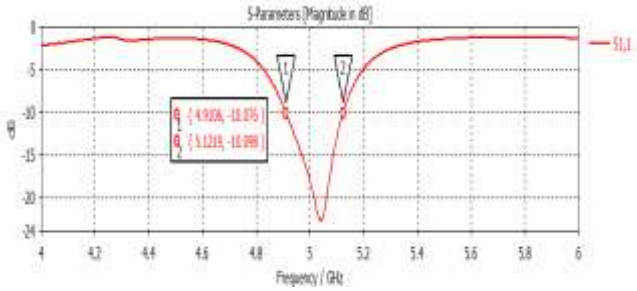

Figure 3. Return loss (S-Parameter) of simulation result

B. VSWR

- Figure 3 illustrates the VSWR simulation result value.

  The VSWR value obtained from simulation at 4.9106 GHz was1.91372. This VSWR value achieve the criteria of less than 2.

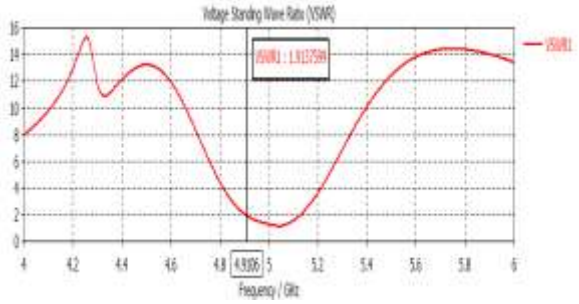

Figure 4. VSWR at frequency 4.9106 GHz

- The designed antenna operates very well at frequency 5.04 GHz, with the value of VSWR is 1.15656. As shown in Figure 4 shows

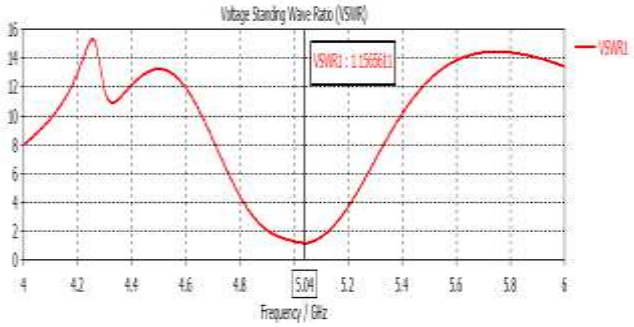

Figure 5. VSWR at frequency 5.04 GHz

- At frequency 5.1219 GHz, a reduce in antenna's quality performance was observed. This is due to high VSWR value of 1.911. However, this would not be an issue, as the VSWR value was still below the requirement of < 2. Figure 5 shows the VSWR value at 5.1219 GHz.

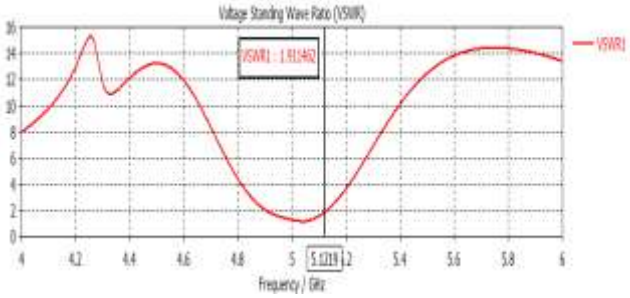

Figure 6. VSWR at frequency 5.1219 GHz

C. Gain

The antenna has varied gains at frequency range between 4.9106 GHz and 5.1219 GHz. At 4.9106 GHz, the antenna gain was 3.429 dBi as shown in Figure 7. The antenna gain at 5.04 GHz was 4.409 dBi, which is observed in Figure 6. At 5.1219 GHz, the antenna gain was 5.014 dBi as shown in Figure 8. From the results, it can be observed that at the operating frequency, the highest antenna gain occurs at 5.1219 GHz In addition, the antenna at 5.04 GHz is where at this frequency, the VSWR antenna reaches the lowest value.

ISSN: 2961-6611

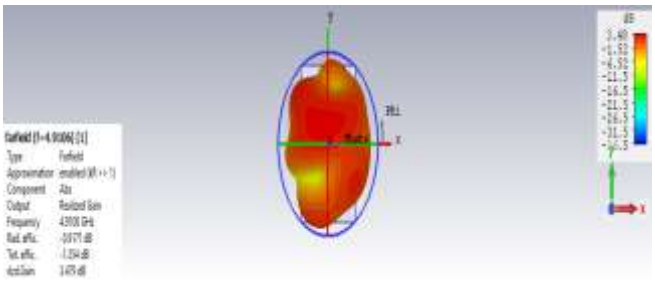

Figure 7.3D Radiation pattern of Gain at 4.9106 GHz

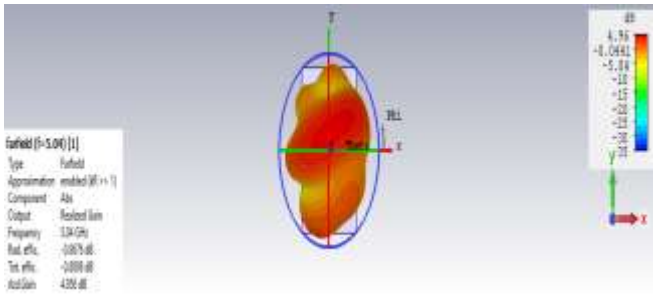

Figure 8. 3D Radiation pattern of Gain at 5.04 GHz

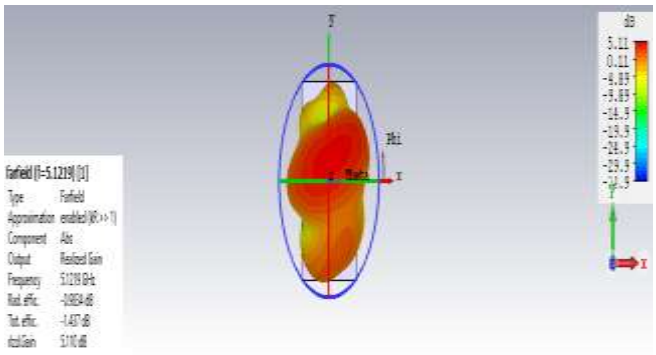

Figure 9. 3D Radiation pattern of Gain at 5.1219 GHz

Table 2 shows VSWR value, Directivity and antenna gain simulation results. The antenna operates very well at 5.1219 GHz frequency and exerts larger gain of 5.110 dB, which is larger than that of other frequencies. In addition at 5.04 GHz

Frequency	VSWR	Gain	Directivity
4.9106	1.91372	3.479	4.833
5.04	1.157	4.956	5.846
5.1219	1.911	5.110	6.547

IV. CONCLUSION

From the design and simulation of microstrip antenna with the help of software utilizing FIT method, it can be concluded that the antenna operating frequency ranges from 4.9106 GHz to 5.1219 GHz for less than -10 dB return loss or almost equivalent to VSWR less than 2. The antenna gain ranges between 3.479 dBi and 5.110 dBi. The highest gain occurs at 5.1219 GHz where the VSWR value reaches 1.91. This antenna has directivity 6.547 dBi which is highest value occur at 5.1219 GHzqqq. The antenna dimension is 85 mm x 55 mm x 3.9 mm. Due its 211.3 MHz operating frequency, this antenna can be implemented in WLAN (*Wireless Local Area Network*) 200 MHz applications

REFERENCES

[1] E. Praveen Kumar, S. Sundaravadivelu "Design and Performance Analysis of Solar Cell Antenna," in IEEE WiSPNET 2017 conference.

[2] Chokri Baccouch, Dhaou Bouchouicha, Hedi Sakli and Taoufik Aguili" Patch Antenna based on a Photovoltaic Cell with a Dual resonance Frequency," in ADVANCED ELECTROMAGNETICS, VOL. 5, NO. 3, NOVEMBER 2016.

[3] F. Nashad, S. Foti, D. Smith, M. Elsdon, and O. Yurduseven " Ku-Band Suspended Meshed Patch Antenna Integrated with SolarCells for Remote Area Applications," in Progress In Electromagnetics Research C, Vol. 83, 245–254, 2018.

[4] Chokri Baccouch, Hedi Sakli, Dhaou Bouchouicha, Taoufik Aguili," Leaf-shaped solar cell antenna for Energy Harvesting and RF Transmission in ku-band," in Advances in Science, Technology and Engineering Systems Journal Vol. 2, No. 6, 130-135 (2017).

[5] A.Suresh Kumar, S.Sundaravadivelu" Design of solar cell antenna (SOLAN) in different AgHT-8 patch shape for reflection co-efficient, gain, power and directivity compared with existing AgHT-4 and ITO",International Journal of Engineering and Technical Research (IJETR) ISSN: 2321-0869, Volume-2, Issue-6, June 2014.

[6] A. Suresh Kumar S.Sundaravadivelu, " An Efficient Design of Solar Cell Antenna for Mobile and Vehicular Applications," 2011 IEEE Global Humanitarian Technology Conference.

ISSN: 2961-6611

Comparison an axisymmetric between pure lattice Boltzmann method and hybrid lattice Boltzmann and finite volume methods for simulation of Taylor-Couette flows

[1]Insaf Mehrez [1#]Ramla Gheith [2]Fethi Aloui [1]Sassi Ben Nasrallah

1 Université de Monastir, École Nationale d'Ingénieurs de Monastir, Laboratoire LESTE, Avenue Ibn El Jazzar 5019, Monastir Tunisie
ramla.gheith@enim.u-monstir.tn

[2a]Univ. Valenciennes, UMR 8201 - LAMIH - Laboratoire d'Automatique de Mécanique et d'Informatique Industrielles et Humaines, F-59313 Valenciennes, France
[2b]CNRS, UMR 8201, F-59313 Valenciennes, France
fethi.aloui@univ-valenciennes.fr

ABSTRACT

Taylor- Couette is the most important flow problems in practice exist for which there is axial symmetry and the unique outcome of a centrifugal instability. In this study, the problem was simulated by two methods: a pure Lattice Boltzmann model [21] for axisymmetric flow (LBM-LBM) and a hybrid scheme with lattice Boltzmann method for the axial and radial velocities and finite volume method for the azimuthal velocity (LBM-FVM). Later, the Taylor Couette with axial flow is added to the validation of the method. The present work involves the flow of water between two coaxial cylinders. Taylor-Couette system characterized by a radius ratio η=0.5 and an aspect ratio Γ=3.8. The inner cylinder rotates while the outer one is fixed. The Reynolds number is fixed to 100. Numerical results showed that the efficiency of the model of Zhou [21] in Taylor-Couette flows. In this article, we demonstrate also that the pure lattice Boltzmann method is much more efficient than the hybrid scheme for an axisymmetric flow problem.

I. INTRODUCTION

The lattice Boltzmann method (LBM) and finite volume method (FVM) are widely used methods in computational fluid dynamics (CFD) and each has their own advantages. The LBM is based on microscopic models and mesoscopic kinetic equations. NcMamara and Zanetti [1] were the first to propose the Lattice Boltzmann equation. Higuera and al. [2] introduced a linearized collision operator to simplify the macroscopic flow equation. The Bhatnagar–Gross–Krook collision operator is the simplest linearized version [3], which uses a single relaxation time to accelerate the computation process. The obtained formulation is referred to the Lattice Boltzmann BGK model which is the most popular version of the Lattice Boltzmann model [4]. The formulation of the standard lattice Boltzmann model is based on the Cartesian coordinate system (x,y) but more important flow problems in practice exist for which there is axial symmetry e.g., flow between two cylindrical coaxial [13, 25,26,27]. The computational demand required for three-dimensional (3D) Lattice Boltzmann (LB) models is considerably greater than for the 2D case. The additional terms in the cylindrical coordinate system (x,r) are considered as external forcing terms in the axisymmetric Lattice Boltzmann model [11-27]. Halliday et al., [11] first proposed an axisymmetric D2Q9 model by sources terms into the Lattice Boltzmann Equation (LBE) so that it could recover the axisymmetric Navier Stokes equations at the macroscopic level. Until 2009, their method has successfully been applied [12-16] to solve many axisymmetric flow problems. Sheng Chen et al. [18] simplified the source terms by involving the vorticity-stream formulation but the source terms used by Zhou [17] are simpler relatively, but they still contain a velocity gradient. Later, Q. Li.,[18] proposed an improved lattice Boltzmann scheme for incompressible axisymmetric flows with the source term is simple and contains no velocity gradient terms and the calculations of macroscopic variables are simplified. Lin Zheng [19-20] proposed a simple lattice Boltzmann equation model for axisymmetric thermal flow. The flow field is solved by a two-dimensional nine-speed (D2Q9) LBE, while the temperature field is solved by another four-speed (D2Q4) LBE. The terms source were simple and contains no velocity gradient terms. In 2011, Zhou [21] comes back to further more than simplify the force terms. Their model is

ISSN: 2961-6611

efficient without calculation of a derivative of velocity and is suitable for studying complex axisymmetric flows with or without swirling effect. In 2013 Like Li et al [22] proposed for simulating the axisymmetric equation, a multiple-relaxation-time (MRT) LB model with five discrete velocities in two dimensions (D2Q5). Sudhir Srivastava et al [23] presented and validated a lattice Boltzmann method for axisymmetric multiphase flows. They quantitatively validated the mass conservation and the dynamics of an axially symmetric oscillating droplet. In 2015, Wei Wang and Zhou [24] come back to present a LB model for axisymmetric turbulent flows in pipe flow, in separated and reattached flow and pulsatile flows in a stenotic vessel. The FVM is successful because it can be adopted easily and its discrete schemes always satisfy conservation laws. The algorithm in FVM is widely used to solve fluid flow and heat-transfer problems. Combination of the LBM and FVM will allow us to combine the advantages of both of them [7-10]. They used the hybrid lattice Boltzmann with finite volume method for conduction–radiation problems and natural convection problems where the velocity is coupled with the temperature field.

For several years, the Taylor-Couette flow has been an important research topic. Recently, X.D.Niu et al [13] presented a developed Taylor-series-expansion and least-square-based lattice Boltzmann method for the transformed Lattice Boltzmann equation and a second order explicit finite difference method for the azimuthal moment equation. To show the performance of the proposed model, they simulated by the three-dimensional LBM. Their study showed that the axisymmetric model is much more efficient than the 3D model for an axisymmetric flow problem. Khalil et al [27] presented the instability of the Taylor-Couette flow for Newtonian and non-Newtonian fluids of finite aspect ratios. This study is conducted numerically using the lattice Boltzmann method two-dimensional nine-velocity (D2Q9) developed from the Bhatnagar-Gross-Krook approximation. The azimuthal velocity is obtained through the following equation by using first-order forward difference scheme in time and a second-order central difference scheme in space. Huang et al [26] proposed of a hybrid scheme *(*LBM + FD*)* and compared with explicit finite volume method (FVM). The time taken by LBM+FD solver and explicit FVM solver are of same order.

The objective of this paper was to solve a Couette-Taylor problem for the first time with the model of Zhou (LBM-LBM) [21] and hybrid LBM–FVM for Re=100. The results are compared with those obtained for validation.

II. Numerical methods

A. Incompressible axisymmetric LBGK model

This study simulates at the Couette-Taylor flow using the Lattice Boltzmann D2Q9 model with a 2D square lattice through the Chapman-Enskog expansion (for more details see [21]). Since the LBGK model [5] is the simplest model among the LBE models.

$$\frac{\partial f_\alpha}{\partial t} + c_\alpha . \nabla f_\alpha = \frac{1}{\tau_f}(f_\alpha{}^{eq} - f_\alpha) + F \quad (1)$$

$$\frac{\partial g_\alpha}{\partial t} + c_\alpha . \nabla g_\alpha = \frac{1}{\tau_g}(g_\alpha{}^{eq} - g_\alpha) + G \quad (2)$$

Where $f_\alpha$and g_α were the distribution function of particles; τ_v and τ_g characterizes the relaxation time of the density istribution function. In this model, the discrete velocities ($c_\alpha = (c_{\alpha x}, c_{\alpha r})$ with $i = 0..8$) for the D2Q9 model are defined as: $c_0 = (0,0), c_1 = -c_3 = (c,0), c_2 = -c_4 = (0,c), c_5 = -c_7 = (c,c), c_6 = -c_8 = (-c,c)$ with $c = \frac{\Delta x}{\Delta t}$ and in our studies c=1 (Δx is the lattice size and Δt is the time step.

The equilibrium distribution functions $f_\alpha{}^{eq}$ and $g_\alpha{}^{eq}$ are written as [21]:

$$f_\alpha^{eq} = \rho w_\alpha \left(1 + \frac{c_\alpha . u}{c_s^2} + \frac{1}{2}\left(\frac{c_\alpha . u}{c_s^2}\right)^2 - \frac{u^2}{2c_s^2}\right) \quad (3)$$

$$g_\alpha^{eq} = \left(1 + \frac{2c_{\alpha j}u_j}{c^2}\right)\frac{\rho u_\theta}{9} \quad (4)$$

The weighting factor w_i are given by $w_0 = 4/9, w_{1\sim4} = 1/9$ and $w_{5\sim8} = 1/36$.

The discrete forcing terms are given by:

$$F_i = -w_\alpha \Delta t \frac{\rho u_r}{r} + \frac{\Delta t}{6c^2}\, c_{\alpha i}\left(-\frac{\rho u_r u_i}{r} - \frac{2\rho\vartheta u_i}{r^2}\delta_{ir} + \frac{u_\theta^2}{r}\delta_{ir}\right) \quad (5)$$

$$G = -\frac{2\rho u_r u_\theta}{r} - \frac{\rho u_\theta \vartheta}{r^2} \quad (10)$$

The macroscopic fluid density and velocity are determined as follows:

$$\rho = \sum_\alpha f_\alpha , \qquad u_i = \frac{1}{\rho}\sum_\alpha e_{\alpha i} f_\alpha , \qquad u_\theta = \frac{1}{\rho}\sum_\alpha g_\alpha \quad (6)$$

B. Hybrid scheme

In this following part, the momentum equation of azimuthal velocity is solved to test the volumes finis method. The momentum equation of azimuthal velocity can be solved implicitly by using upwind scheme.

$$a_P(u_\theta^{n+1})_P = a_E(u_\theta^{n+1})_E + a_W(u_\theta^{n+1})_W + a_S(u_\theta^{n+1})_S + a_N(u_\theta^{n+1})_N + a_P^0(u_\theta^n)_P + S \quad (7)$$

$$a_P = a_P^0 + a_E + a_W + a_S + a_N \quad (8)$$

With $a_P^0 = \rho c\left(\frac{\Delta V}{\Delta t}\right)$, $a_E = \frac{k_e A_e}{\delta x_{PE}}$, $a_W = \frac{k_w A_w}{\delta x_{WP}}$, $a_E = \frac{k_s A_s}{\delta y_{SP}}$, $a_N = \frac{k_n A_n}{\delta y_{PN}}$.

$$\Delta V = \Delta x \Delta y,\ A_e = A_w = \Delta y \text{ and } A_n = A_s = \Delta x$$

C. Description and geometries

The geometry is a concentric cylinder which the outer cylinder is stationary while the inner cylinder is rotating with the velocity W. The fluid between the cylinders is water. The diameters of these internal and external cylinders are respectively R_1 and R_2. The boundary conditions used in our simulation are also illustrated in fig.1.

ISSN: 2961-6611

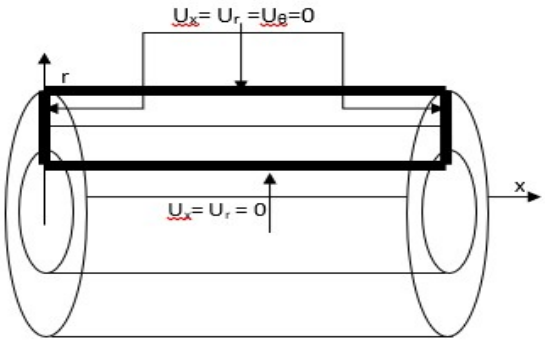

Fig.1: schematic of Taylor Couette system

The flow is assumed to be two-dimensional, isothermal and Newtonian fluid with constant properties. In our simulation, the space is divided in the x direction (Nx) and in the r direction (Nr). The Reynolds number is defined Re=Wd/ν. The aspect ratio is set as Γ=3.8. The radius ratio of inner and out cylinder is set as η=0.5.

$$d = R_2 - R_1 \quad \text{is the gap of the annulus}$$

$$\eta = \frac{R_1}{R_2} \quad \text{is the radius of inner and out cylinder}$$

$$\Gamma = \frac{h}{d} \quad \text{is the aspect ration}$$

Boundary condition is an important issue when using hybrid scheme (LBM-FVM) or (LBM-LBM) to simulate Couette-Taylor flows. The bounce-back boundary conditions are applied on both moving and stationary walls in present study. The Reynolds number is fixed to 100 for the Taylor-Couette flow is tested to validate the present work. When using the finite volume method to solve the equation for azimuthal velocity, we may boundary condition when velocity zero in stationary walls and know velocity in moving wall. The results are compared with either available analytical solutions or other numerical results.

III. RESULTS

Figure 2 show the flow patterns in the x-r plane obtained by the present axisymmetric LBM for the Taylor-Couette flow at Re= 100, respectively.

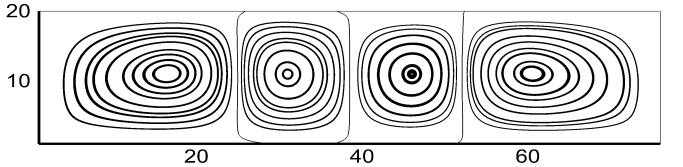

Streamlines

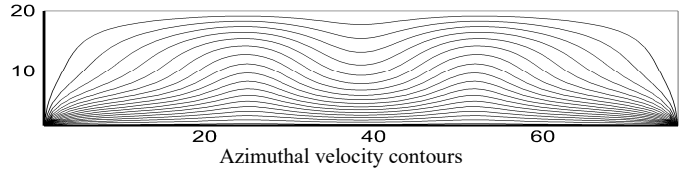

Azimuthal velocity contours

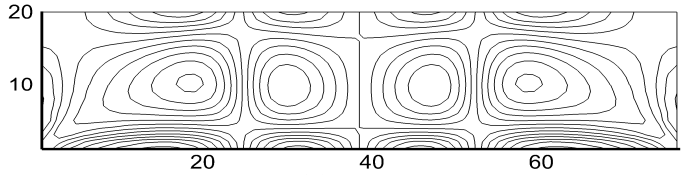

Vorticity contours

Fig.2: Flow patterns of Re=100

These observation agree well with the resuts in litterature. The streamline, azimuthal velocity contours and Vorticity contours were presented the same characteristic. As Reynolds number is equal to 100, the cell is gradually evolved in size and the coutours of the azimuthal velocity becomes tighter. This can alse be found in the vorticty contours.

In view of importance of the azimuthal velocity of the inner cylinder, the comparison of this velocity has been noted in fig.3. For infinite Couette-Taylor systems, analytical solution for the azimuthal U_θ velocity component with the corresponding boundary conditions. It is briefly recalled below (see [] for more details):

$$u_\theta(r) = \frac{a}{r} + br$$

With $a = -\frac{r_e^2 R_1^2}{(R_2^2 - R_1^2)} w^2$ and $b = \frac{-WR_1^2}{(R_2^2 - R_1^2)}$

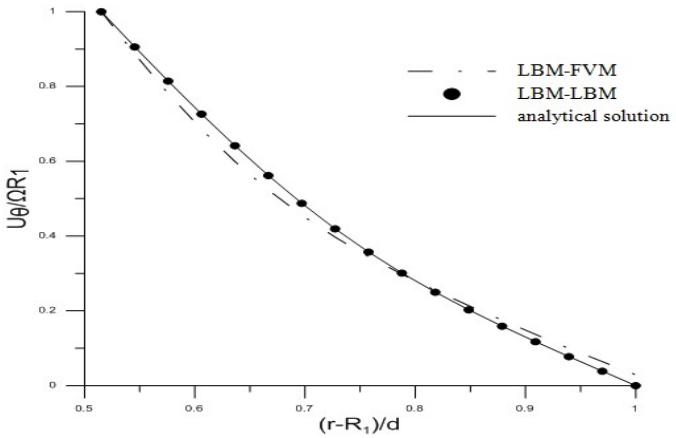

Fig.3. Comparison of the azimuthal velocity with analytical solution for η =0.5 and Γ =3.8

It is shown that the velocity profile decreases gradually along the radial position. However, it can be seen that the model LBM-LBM is more accurate that the model LBM-FVM. The obtained results are compared with the other model and validated with the literature. The convergence for the both models is displayed in Fig.4 in terms of relative error. The convergence trend of the model LBM-LBM is faster to the model LBM-FVM.

ISSN: 2961-6611

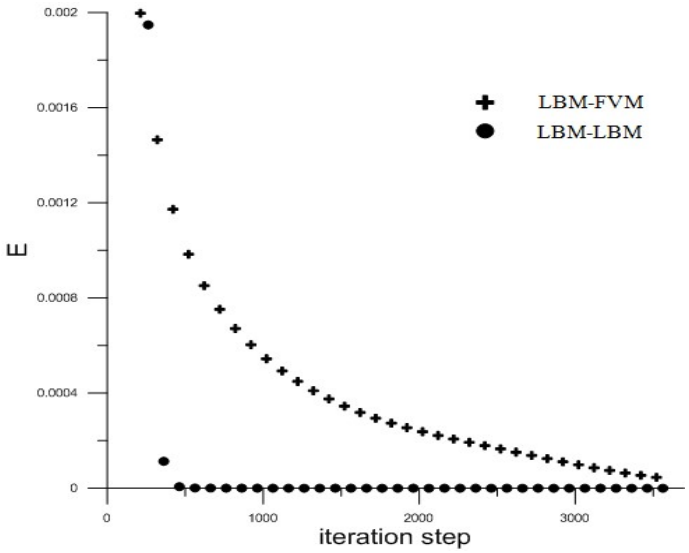

Fig.4. Convergent history of axisymmetric LBM-LBM simulation for Taylor Couette flow for the model B and model C

In the following parts, the mesh size 33×57, 33×65and 33×73 were chosen. The reference data of Niu [13] was included in table 2 for comparison. It can be observed that the iteration number required by hybrid scheme (LBM-FVM) solver is less than that required by the LBM-LBM solver. Clearly, for the same proprieties of fluids, in addition, as compared with reference data of Niu [13], it was found that LBM-LBM results are better than LBM-FVM.

TABLE 2: COMPARISON OF THE MAXIMUM STREAM FUNCTION AD NUMBER OF ITERATION BETWEEN LBM-LBM AND LBM-FVM FOR THE TAYLOR-COUETTE FLOW AT RE=100

mesh	**33×57**	**33×65**	**33×73**
Niu [13]	**0.05619**	**0.05580**	**0.05580**
LBM-LBM	0.05740	0.05570	0.05563
error	2.15%	0.17%	0.3%
Iteration	34543	28751	39188
CPU	11274	10669	14274
LBM-FVM	0.05018	0.04997	0.04975
error	10.69%	10.4%	10.84%
Iteration	17397	22464	20320
CPU	4056	10031	5898

IV. CONCLUSION

The developed hybrid scheme was successfully applied to simulate the laminar Taylor Couette flow in an annulus with two end plates and a rotating inner cylinder when the outer is stationary. It was found in this article that the pure LBM gives a better result than the hybrid scheme but it is much efficient that the pure LBM in terms of computational time.

REFERENCES

[1] NcNamara.G, Zanetti.G., use of the Boltzmann equation to simulate Lattice –Gas automata, Journal of Phys.Rev.Lett.61, 2332-2335 (1988).
[2] F.Higuera, S.Jimenez, Boltzmann approach to lattice gas simulations, Journal of Europhys. Lett, 9, 663-668, (1989).
[3] P.L. Bhatnagar, E.P. Gross, M. Krook, A model for collision process in gases. I. Small amplitude processes in charged and neutral one-component system, journal of Phys. Rev. 94 511–521, (1954).
[4] H. Chen, S. Chen, W.H. Matthaeus, Recovery of the Navier–Stokes equation using a lattice Boltzmann method, Journal of Phys. Rev. 45, 5339–5342 (1992).
[5] Z.L.Guo, B.C.Shi and N.CWang, lattice BGK model for incompressible Navier Stokes equation, J.Comput.Phys.,288-306 (2000)
[6] Pablo S. Rojas Fredini, Alejandro C. Limache: Evaluation of weakly compressible SPH variants using derived analytical solutions of Taylor–Couette flows, 304-317 (2013)
[7] Zheng Li, Mo Yang, Yuwen Zhang, Hybrid Lattice Boltzmann and Finite Volume Method for Natural Convection, Journal of thermophysics and heat transfer.(2014)
[8]: Zheng Li, Mo Yang, Yuwen Zhang, hybrid lattice Boltzmann and finite volume methods for fluid flow problems, *Journal for Multiscale Computational Engineering*. 177–192 (2014)
[9] Subhash C. Mishra, Hillol K. Roy, Solving transient conduction and radiation heat transfer problems using the lattice Boltzmann method and the finite volume method. *Journal of Computational Physics.* 89–107 (2007)
[11] I. Halliday, L.A.Hammond, C.M.Care, K.Good, A.Stevens: Lattice Boltzmann equation hydrodynamics. PHYSICAL REVIEW E. (2001)
[12] T S.Lee, Haibo Huang, Chang Shu, an axisymmetric incompressible lattice BGK model for simulation of the pulsatile flow in a circular pipe. *International journal for numerical methods in fluids.*99-116(2005)
[13]: X D.Niu C. SHU, Y. T. CHEW an axisymmetric lattice Boltzmann model for simulation of Taylor Couette flows between two concentric cylinders *International Journal of Modern Physics C* 785-796 (2003)
[14] T. Reis and T. N. Phillips Modified lattice Boltzmann model for axisymmetric flows. *PHYSICAL REVIEW E 75* (2007)
[15] Sheng Chen, Jonas Tölke, Sebastian Geller, Manfred Krafczyk Lattice Boltzmann model for incompressible axisymmetric flows *PHYSICAL REVIEW E 78* (2008)
[16] Haibo Huang, Xi-Yun Lu, Theoretical and numerical study of axisymmetric lattice Boltzmann models *PHYSICAL REVIEW E 80,*(2009)
[17] Jian Guo Zhou Axisymmetric lattice Boltzmann method *PHYSICAL REVIEW E* 78 (2008)
[18] Q.Li, Y.L.He, G.H.Tang, W.Q.Tao: Improved axisymmetric lattice Boltzmann scheme. (2010)
[19] Lin.Z, Zhaoli.G, Baochang.S, Chuguang.Z: Kinestic theory based lattice Boltzmann equation with viscous dissipation and pressure work for axisymmetric thermal flows. Journal of Computational Physics. (2010)
[20]: Lin.Z, Baochang.S, Zhaoli.G, Chuguang.Z: Lattice Boltzmann equation for axisymmetric thermal flow. Computers & Fluids (2010)
[21] Jian Guo Zhou: Axisymmetric lattice Boltzmann method revised. Phys. Rev. (2011)
[22] Like.L, Renwei.M, James.F.K: Multiple-relaxation-time lattice Boltzmann model for the axisymmetric convection diffusion equation. International Journal of Heat and Mass Transfer. (2013)
[23]: Sudhir.S, Prasad.P, Jan.H.M.ten.T.B, Nishith.V, Federico.T : Axisymmetric multiphase lattice Boltzmann method. PHYSICAL REVIEW. (2013)
[24]: Wei.W, Jian Guo Zhou: Lattice Boltzmann method for axisymmetric turbulent flows. International Journal of Modern Physics C. (2015)
[25]: Y.Wang, C.Shu, C.J.Teo, a fractional step axisymmetric lattice Boltzmann flux solver for incompressibke swirling and rotating flows, computers & fluids (2014)
[26] Haibo Huang, T. S. Lee, C. Shu, Hybrid lattice Boltzmann finite-difference simulation of axisymmetric swirling and rotating flows, International journal for numerical methods in fluids (2007)
[27] S. Khali, R. Nebbali, D. E. Ameziani, K. Bouhadef, Numerical investigation of non-Newtonian fluids in annular ducts with finite aspect ratio using lattice Boltzmann method (2013)

ISSN: 2961-6611

CFD Simulation of heat transfer and flow inside 1kW Double-acting Stirling Engine

Ramla Gheith[#1], Houda Hachem [*2], Ramla Gheith [#3]

 # Université de Monastir, École Nationale d'Ingénieurs de Monastir, Laboratoire LESTE, Avenue Ibn El Jazzar 5019, Monastir Tunisie

ramla.gheith@enim.u-monstir.tn

houdahachem@yahoo.fr

[2a]Univ. Valenciennes, UMR 8201 - LAMIH - Laboratoire d'Automatique de Mécanique et d'Informatique Industrielles et Humaines, F-59313 Valenciennes, France

[2b]CNRS, UMR 8201, F-59313 Valenciennes, France

fethi.aloui@univ-valenciennes.fr

***Abstract*— In this paper a CFD numerical simulation of 1 kW double acting Stirling engine is proposed. A very particular configuration of the Stirling engine, characterized by a single-cylinder arrangement, is simulated numerically based on the turbulence model k- SST, to study heat transfer and flow to optimize the output power of the Stirling engine. Firstly, a specific mesh motion strategy was developed using the software STARCCM+, to describe the motion of the power piston and the displacer. Heat-transfer models were implemented for considering the presence of two heat sources and the regenerator porous structure. Results are compared with experimental data. The cyclical evolution of pressure, temperature and velocity has been discussed and interpreted. The effect of the regenerator porosity as well as the effect of the engine load pressure on the mechanical power produced were studied. Results show that there is optimal porosity about 0.775 to maximize power.**

***Keywords*—CFD modelling, Stirling engine, Regenerator, Cooler, Heater**

I. INTRODUCTION

This document is a template. An electronic copy can be downloaded from the conference website. For questions on paper guidelines, please contact the conference publications committee as indicated on the conference website. Information about final paper submission is available from the conference website.

Nowadays, digital simulation has become a key tool for pre-analysis of industrial facilities and systems. CFD deals with numerical solutions of differential equations governing mass transport, momentum and energy. In this work, CFD is used to study the flow and heat transfer inside a double-acting Stirling engine.

Recently, many studies (CFDs) have treated the performance of the Stirling engine [1-7]. Zhigang Li et al. [4] simulated the flow and heat transfer in a compact porous-leaf heat exchanger. Its results showed that the viscous friction loss in such a regenerator is low and it is equal to 800 Pa under operating conditions of 1atm and 2600 rpm. The porous sheet regenerator has excellent heat transfer characteristics and its compact design significantly reduces dead volume. Compared to the conventional wire mesh regenerator, they found that the porous leaf regenerator has a total entropy generation rate of 38 to 51%, resulting in less loss and thus results in greater power and thermal efficiency.

In this study, the double-effect Stirling engine geometry of the Whispergen boiler was considered to simulate the flow and heat transfer inside the Stirling engine. Results show pressure, temperature and velocity variations, the PV diagram and the effect of the regenerator porosity and the initial charge pressure on the mechanical power produced.

II. CFD MODELLING

A. *Double-acting Stirling engine description*

The double-acting Stirling engine is made up of 4 cylinders interconnected between them in which oscillate four ascending and descending pistons according to the cycle of expansion and compression of the working fluid (Fig.1). Between 2 consecutive pistons is inserted a regenerator. The pistons are double-acting, ie they work on their 2 faces: there are thus 8 different volumes of coolant. This engine is of the kinematic type (Wobble-yoke type drive system). It is a compact and powerful engine, reliable and robust. And it is installed in the Whispergen micro-CHP unit. This engine uses nitrogen as a compressed working fluid at a pressure of 20 bar. Its rotation speed is about 1500 rpm. It is connected to a generator (4-pole single-phase induction motor) to produce electricity such that its nominal electrical output power reaches up to 1kW.

B. *Geometry description*

The studied geometry consists of five workspaces as shown in Fig.1: the relaxation space in contact with the hot heat exchanger, the connection tubes between hot and regenerative space, the porous annular regenerator, the connection tubes between regenerator and cold space and the compression space in contact with the cold heat exchanger.

ISSN: 2961-6611

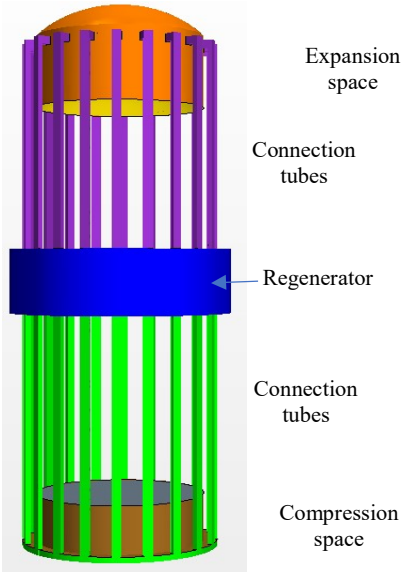

Fig. 1: Geometry of the double acting Stirling engine

C. *Boundary conditions and numerical calculation assumptions*

The assumptions considered are as follows:
-A constant temperature of 1100K is fixed on the walls of the expansion space in contact with the hot heat exchanger.
-A constant temperature of 313K is fixed on the walls of the compression space in contact with the cold heat exchanger.
-The working fluid (nitrogen) is considered perfect gas.
-The flow through the singularities of the engine is turbulent and the equations are solved using the turbulence model k-ω SST.
-Piston displacement follow a periodic sinusoidal evolution and described as follows:

$$y_1(t) = \bar{y}_1 sin(2\pi ft) \quad (1)$$

$$y_2(t) = \bar{y}_2 sin(2\pi ft + \varphi) \quad (2)$$

Where f is the frequency and φ is the Expansion space phase angle advance

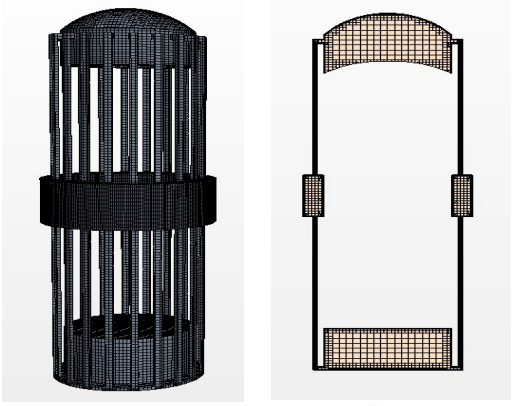

(a) 3D (b) 2D

Figure 2: Meshing of geometry

III. Results and Discussions

A. Cyclical evolution of temperature, pressure and speed

The temperature distribution is represented in figure 3. This distribution is non-uniform. The highest temperature of the working fluid is observed on the expansion space about 1200K. The temperature increases from 785K to almost 900 K between the regenerator and the expansion chamber. The fluid leaves the regenerator with a temperature of 670K to cool in the compression space in contact with the cold heat exchanger up to 320K (Fig. 3 (b)). The regenerator thus plays the role of a thermal barrier between the two chambers not only to avoid thermal shocks but also to keep the expansion space warmer and the compression space colder. This will eventually increase the efficiency of the engine. The temperature inside the regenerator increase linearly as we are closer to the hot space. Temperature distribution inside the Stirling engine has not a symmetric distribution due to turbulence.

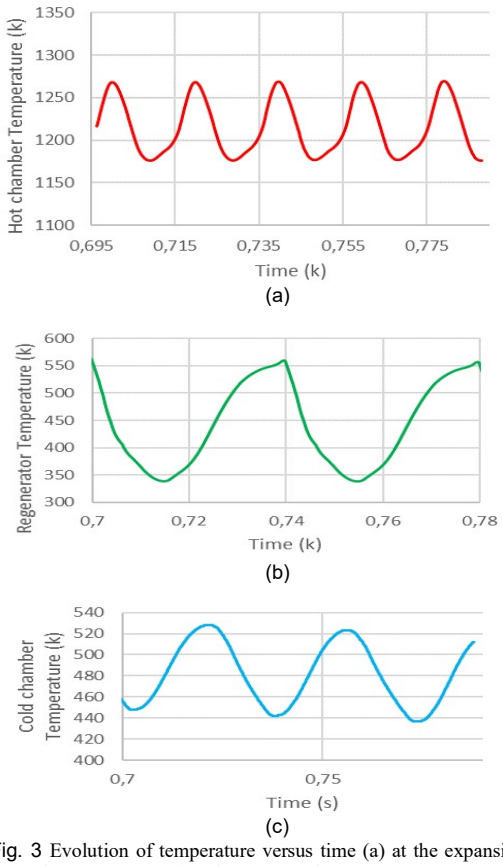

Fig. 3 Evolution of temperature versus time (a) at the expansion space (b) at the regenerator (c) at the compression space

Pressure

Fig. 4 represents the pressure at a time t of the expansion compression process. The maximum pressure appears in the cold chamber. it varies from 25 to 42 bar (Fig. 4 (a)). The minimum pressure appears in the hot chamber. it varies from 22 to 38 bar (Fig. 4 (b)). However, the pressure in the regenerator is an intermittent pressure between the two hot and cold spaces.

ISSN: 2961-6611

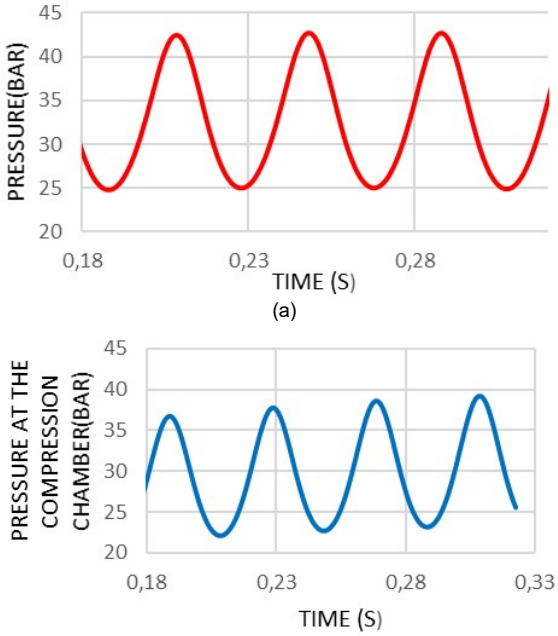

Fig. 4. Evolution of pressure versus time (a) at the expansion space (b) at the compression space

Velocity

According to the evolution of the velocity as a function of the crank shaft angle at the expansion space (Fig.5 (a)), we record the highest velocity value corresponds to the angle 250° and the lowest value corresponds to 150°. The maximum velocity is observed during the expansion phase between 170 and 350 °

The flow velocity in the compression space is high (Fig. 5 (c)). As it passed through the regenerator, the flow velocity slowed due to its porous structure (Fig. 5 (b)). The velocity varies from 12 m/s to 1m/s between the compression space and the regenerator. Four swirls are formed in the hot expansion space due to the change in surface area between the channels and the expansion space. At the compression space, there are two vortices only. Turbidity improves the heat transfer between the walls of the heat exchangers and the working fluid (Fig.5 (d)).

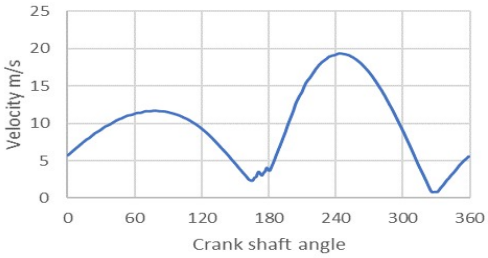

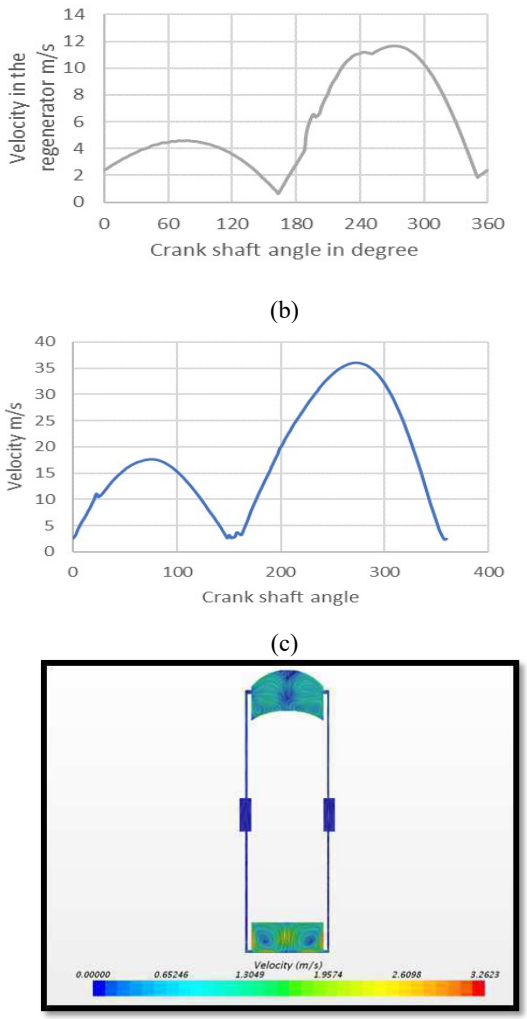

Fig. 5: Evolution of velocity versus crank angle during a cycle (a) at the expansion space (b) at the regenerator (c) at the compression space

B. Evolution of the operating parameters in the regenerator region

Fig.6 (a) shows the evolution of the regenerator temperature as a function of crank angle. This evolution is sinusoidal and varies between 560 K and 340 K. The maximum temperature of the regenerator is reached when the pressure drop in the regenerator is minimal (Fig. 6 (a)). In fact, the pressure drop is strongly related to the dissipation of energy. During the expansion phase (between 0 ° and 180 °) the pressure increases, and the volume decreases in the hot chamber. Thus, the regenerator stores heat from the fluid flowing from the hot chamber to the cold room. During the expansion phase (between 180 ° and 360 °), the regenerator transfers this stored heat to the working fluid flowing from the cold room to the hot chamber. This phenomenon is similar to the behavior of an electric capacitor that charges and discharges due to the presence of an electrical resistance in the circuit.

ISSN: 2961-6611

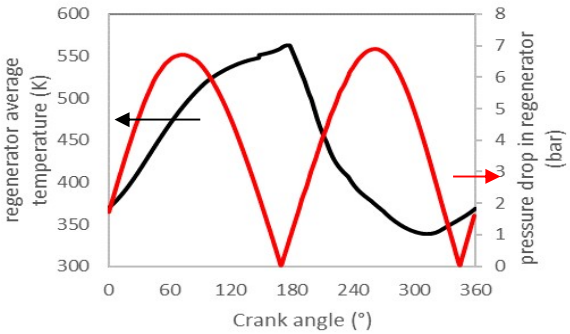

(a) Temperature and pressure drop

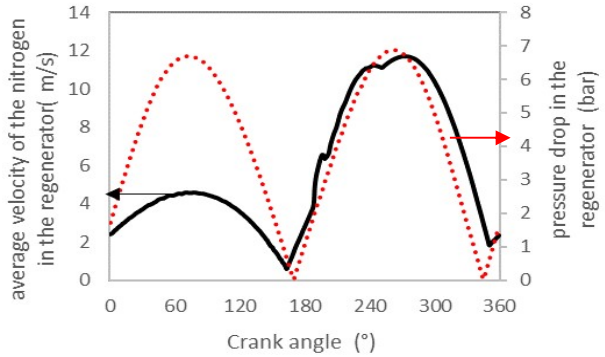

(b) Velocity and pressure drop

Fig. 6: Evolution of the operating parameters according to the angle of the crank during a cycle in the regenerator [8]

C. Effect of regenerator porosity on Stirling engine power

For the regenerator part equations related to porous media based on ERGUN Equation were used.

$$\frac{\Delta P}{L} = \frac{150\mu V_0}{D_p^2}\frac{(1-\varepsilon)^2}{\varepsilon^3} + \frac{1.75\rho_g V_0^2}{D_p}\frac{1-\varepsilon}{\varepsilon^3}$$

- ΔP is the pressure drop
- L is the height of the bed
- D_p is the particle diameter
- ε is the porosity of the bed
- μ is the gas viscosity
- V_0 is the superficial velocity (the volumetric gas flow rate divided by the cross-sectional area of the bed)
- ρ_g is the gas density

The two principal's parameter for the Porous Media simulation are introduced which are the viscous Resistance $\mathbf{R_v}$ and inertial Resistance $\mathbf{R_i}$ as follow and calculated for different porosity values as shown in table 2 :

$$\frac{dP}{dl} = \mathbf{R_v}\mu V_0 + \left(\frac{\mathbf{R_i}}{2}\right)\rho V_0^2$$

TABLE I

VISCOUS RESISTANCE R_V AND INERTIAL RESISTANCE R_I

Porosity	R_v	R_i
0.65	1.8586e+10	7.4344e+04
0.725	8.2688e+09	4.2095e+04
0.85	1.5266e+09	1.4248e+04
0.95	1.2149e+08	3.4019e+03

The porosity of the regenerator is a critical parameter. The curve of the mechanical power as a function of the porosity of the regenerator admits an optimum when the porosity is equal to 0.775 (Table 2). High porosity values lead to high regenerator efficiency but low Stirling engine performance.

IV. CONCLUSIONS

A CFD simulation of a double-acting Stirling engine has been successfully developed. The following results are deduced:

• The temperature distribution is non-uniform in different motor spaces during a cycle.

• The evolution of the temperature is in advance of phase with respect to the pressure. This time shift is called response time.

• Optimum porosity of the regenerator (equal to 0.775) ensures maximum mechanical power.

• The mechanical power of the Stirling engine increases with its initial charging pressure.

REFERENCES

[1] Cun-quan Zhang, Cheng Zhong, Theoretical modeling of a gas clearance phase regulation mechanism for a pneumatically-driven split-Stirling-cycle cryocooler, Cryogenics 66, 13-23, 2015.

[2] Cun-quan Zhang, Cheng Zhong, Experimental study of a gas clearance phase regulation mechanism for a pneumatically-driven split-Stirling-cycle cryocooler, Cryogenics 66, 24-33, 2015.

[3] Jose Leon Salazar, Wen-Lih Chen, A computational fluid dynamics study on the heat transfer characteristics of the working cycle of a β-type Stirling engine, Energy Conversion and Management, 88 , 177-188, 2014.

[4] Zhigang L., Yoshihiko H., Yohei K., Dawei T., Analysis of a high performance model Stirling engine with compact porous-sheets heat exchangers, Energy, 64, 31-43, 2014.

[5] Hachem H., Gheith R., Aloui F., Ben Nasrallah S., A CFD Analysis of the Air Flow through the Stirling Engine's Singularities. 7th international Exergy,Energy and Environment Symposium , 2015.

[6] Wen-Lih*Chen*,King-Leung Wong, Li-Wen Po. A numerical analysis on the performance of a pressurized twin power piston gamma-type *Stirling*engine. Energy Conversion and Management. Volume 62, 84-92, 2012.

[7] Wen-LihChen,Yu-Ching Yang,Jose Leon Salazar.A CFD parametric study on the performance of a low-temperature-differential γ-type *Stirling*engine. Energy Conversion and Management, Volume 106, 635-643, 2015.

[8] R. Gheith, H. Hachem, F. Aloui, Ben Nasrallah S. "Comprehensive Energy Systems", Volume 4, pp. 169-2008, doi:10.1016/B978-0-12-809597-3.00409-0.

ISSN: 2961-6611

Performance Enhancement Of Microstrip Patch Antenna Using Metamaterial Structure For WLAN Applications

Abdelhadi M. Aburgiga
Departement of Communication Engineering
Faculty of Electronic Technology
Tripoli - Libya
TheFateMan88@gmail.com

Adel S. Emhemmed
EE Eng. Deprt, Faculty of Engineering
University of Tripoli
Tripoli - Libya
dr.adel.elec@gmail.com

Amer R. Zerek
EE Eng. Deprt, Faculty of Engineering
Zawia University
Zawia – Libya
anas_az94@yahoo.co.uk

Abstract **– The degradation of microstrip patch antenna performance is due to the excitation of surface wave modes, since it difficult to control and are not radiated in the main beam direction of the radiation pattern. This distorts the main beam radiation pattern and increases the level of the side and back lobes. This paper presents effect of metamaterail on the performance of microstrip patch antenna at 2.4GHz band. The antenna structures combine the advantages of microstrip patch antenna with the advantages of metamaterail technology and it simplifies the structure of the antenna to make the patch antenna easier to integrate with MMICs. The results show that the bandwidth and the gain of the antenna radiation pattern with metamaterial is increased compared with conventional patch antenna without the metamaterial without distorting the antenna resonance frequency. CST Microwave Studio Software was used to simulate and analysis the antenna configurations**

Keywords - Rectangular microstrip patch antenna RMPA , Left handed metamaterial LHM , Bandwidth , Return loss , Gain , Half power beam width HPBW .

I. INTRODUCTION

Microstrip antenna has many advantages over the conventional antennas such as thin surface area , easy to fabricate , small size , light weight , and easy to integrate to existing communication devices . Due to these advantages they are getting much importance in various fields , On the other hand microstrip antennas also features some disadvantages compared to conventional antennas like narrow bandwidth , low gain , high loss . There are various techniques that can be used to overcome these weaknesses , One of the proposed techniques is by using metamaterial [1 - 4] .

Recently, there has been growing interest in the study of Metamaterials both theoretically and experimentally. Metamaterials MTM are artificial materials engineered to have properties that may not be found in nature. Although Metamaterial does not present in nature, interesting properties were theoretically predicted for these substances, such as the reversal of the Snell Law, Doppler Effects, and Cherenkov radiation etc.

The basic properties of conventional materials available in nature are Positive dielectric permittivity ε and magnetic permeability μ called as Double Positive materials ($\varepsilon_r > 0$ and $\mu_r > 0$) positive and they follow the right hand thumb rule for the direction of propagation of wave k (except the cases of noble metals like gold silver etc. where permitivitty is negative for certain range of frequency) . Metamaterial is material structure that has negative dielectric permittivity ε and magnetic permeability μ which is not found in nature . Metamaterial can be classified on the basis of (ε) and (μ) in three types , as double negative material ($\varepsilon_r < 0$ and $\mu_r < 0$) called as left-handed metamaterial LHM also termed as negative index material NIM , mu-negative material ($\varepsilon_r > 0$ and $\mu_r < 0$) , and epsilon negative material ($\varepsilon_r < 0$ and $\mu_r > 0$) [1] . The first theoritical study of NIM was performed by V.G VESELAGO [5] and it took nearly 30 years for experimental verification . Different structures used for designing NIM , The famous SRR (split ring resonator suggested by Sir Pendry) and first Realized by D.R Smith group in 2000 [6] .

Metamaterial structure that are applied in microstrip antennas such as a split ring resonator SRR [2] , a complementary split ring resonator CSRR [3] and the left-handed metamaterial LHM [4].

A composite medium of conducting , non-magnetic elements can form a Left-Handed Metamaterial , as the electric field E, magnetic intensity H and propagation vector k are related by a left-hand rule [7] because propagation of wave takes place in backward direction in this medium . Several shapes can be considered to make the metamaterial structure in order to operate in different frequencies . Framed Square rings, different C patterns, square and circular patterns, etc. are considered to make metamaterial antenna structure . All these shapes are designed with the intention to ameliorate the bandwidth , return loss and gain along with size reduction . Metamaterial has several applications such as engineered textured surfaces, artificial impedance surfaces, artificial magnetic conductors, double negative materials, frequency selective surfaces,

ISSN: 2961-6611

Photonic Band-Gap (PBG) surfaces, Electromagnetic Band-Gap (EBG) surfaces/structures , and even fractals or chirals . Broad band antenna design is one of the major applications of metamaterials .

This paper observes the use of the left-handed metamaterial usage for rectangular microstrip patch antenna working on the wireless local area network WLAN at operating frequency of 2.4 GHz to improve antenna performance such as bandwidth , return loss and gain . The results obtained from CST MWS design software are very good for wirelessly access network resources at home and elsewhere with up to 2.4 GHz performance like IEEE 802.11b/g/n .

II. Antenna Design And Simulation Without Metamaterial

To design a microstrip patch antenna , the operating frequency and the insulating material must be selected for the designed antenna.The parameters to be determined are as the following.

The following equation determines the width of the patch[8].

$$W = \frac{C_0}{2f_r}\sqrt{\frac{2}{\varepsilon_r + 1}} \tag{1}$$

Where f_r is an operating frequency, W is the patch Width , C_0 is a light speed, and ε_r is a dielectric constant of a substrate. The effective value of an insulating constant for the antenna substrate in the design process of a microstrip patch antenna is an important parameter . The radiation crosses from the ground plane to the patch through the air and some through the substrate is called fringing . Both the substrate and the air have not the same values of dielectric constant, so we need to calculate the value of effective insulating constant . The following equation is used to determine the value of the effective dielectric constant [8] :

$$\varepsilon_{reff} = \frac{\varepsilon_r + 1}{2} + \frac{\varepsilon_r - 1}{2}[1 + 12(\frac{h}{W})]^{-1/2} \tag{2}$$

Where h is the height of the substrate.

Because of fringing , electrically the antenna size increases by a value of ΔL . So the actual increase in length ΔL of the patch is determined by the following equation [8] :

$$\Delta L = 0.412h\frac{(\varepsilon_{reff} + 0.3)(\frac{W}{h} + 0.264)}{(\varepsilon_{reff} + 0.258)(\frac{W}{h} + 0.8)} \tag{3}$$

The effective length L_{reff} is determined using the following equation :

$$L_{reff} = \frac{C_0}{2f_r\sqrt{\varepsilon_{reff}}} \tag{4}$$

The actual length L of the patch can be determined now by the following equation [9,10,11] :

$$L = L_{reff} - 2\Delta L \tag{5}$$

The patch dimensions now are determined. The width and length of the ground plane is the same for the substrate. The width W_s and the length L_s of the substrate are determined by the following equations [12] :

$$W_s = 6h + W \tag{6}$$

$$L_s = 6h + L \tag{7}$$

The geometry of the conventional rectangular microstrip patch antenna with inset fed and operating at 2.4 GHz is illustrated in Figure 1. The dimensions of RMPA are listed in Table 1 .

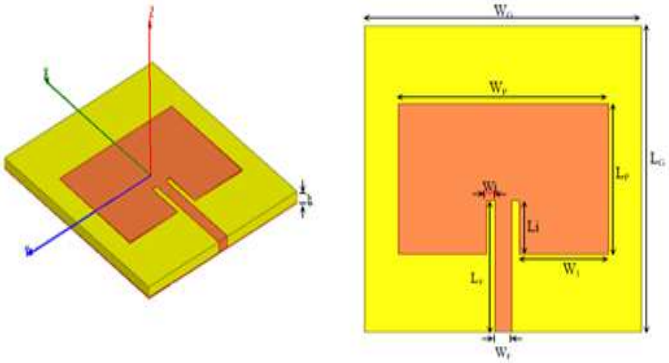

(a) (b)

Fig .1. Conventional RMPA (a) 3D view (b) top view

TABLE 1 Dimensions Of RMPA

Parameter	(mm)
W_G	1.5*W
L_G	1.5*L
W_P	38.393
L_P	29.786
W_F	3
W_i	2
L_i	5
h	1.2

Now the antenna is ready to simulate using CST Microwave Studio Suite software . The varying of the return loss with frequency for RMPA is shown in figure 2 . From the figure, it can be observed that the return loss of -12.836 dB at 2.4 GHz . Depending on -10 dB return loss , the designed Antenna has a band width of 59.8 MHz , with 2.49% impedance bandwidth is found, in the range of 2.37 to 2.4298 GHz .

ISSN: 2961-6611

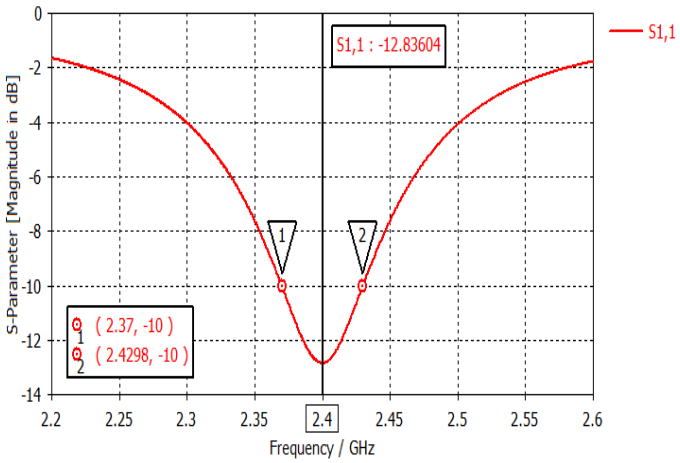

Fig .2. Return loss versus the frequency of (RMPA).

Figure 3 shows the three dimensionls radiation pattern of the designed antenna in the farfield . The direction of the highest gain value of the antenna is in the direction of theta , and the back lobe is on the bottom side . The highest gain value of the antenna is 1.83 dB .

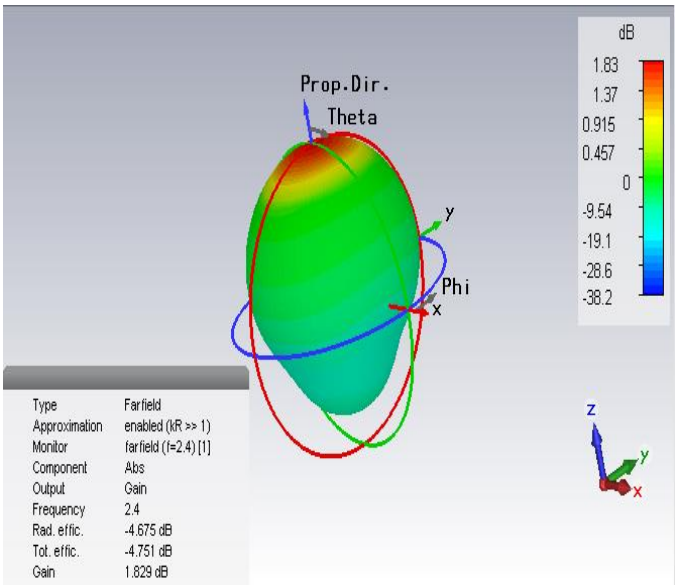

Fig. 3. Three dimensionals radiation pattern of the antenna in the farfield .

Figure 4 shows tow dimensionals radiation pattern which achieves a highest gain value of 1.83 dB and half power beamwidth of 95.9^0 .

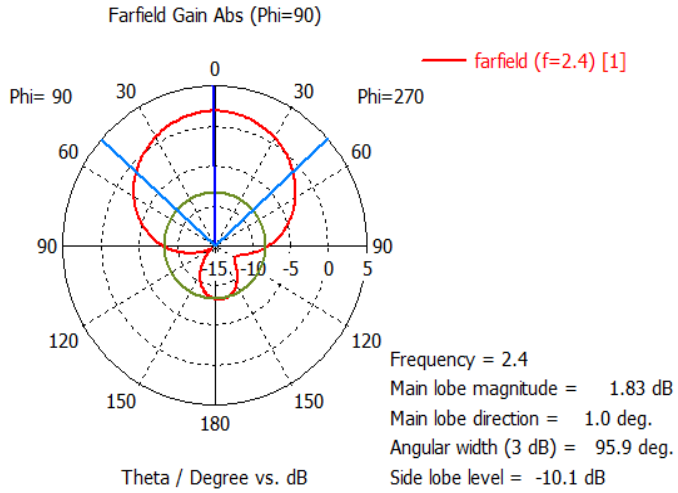

Fig. 4. Tow dimensionals Radiation pattern of RMPA .

III. Antenna Design And Simulation With Metamaterial

The Left-handed Metamaterial LHM effect is possible to generate by modifying the ground plane dimension . The RMPA by using LHM structure [13] is shown in Figure 5. The dimension is taken in millimeters mm and simulated by the CST Microwave Studio Suite Software .

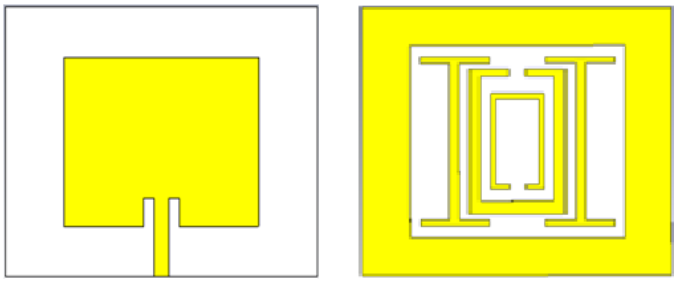

(a) (b)

Fig. 5. The RMPA design with LHM structure (a) Front view (b) Back view

The optimization is performed by applying LHM structure to increase the bandwidth and improve the other parameters of the antenna . Figure 6 shows the changing of the return loss with frequency after employed LHM . It can be noted that the return loss of -37.16 dB at 2.4 GHz.

ISSN: 2961-6611

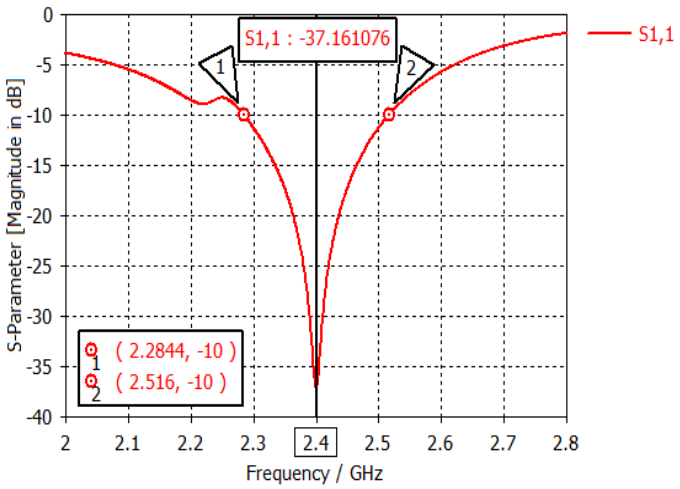

Fig. 6. Return loss versus the frequency of the antenna with LHM .

Based on -10 dB return loss , the antenna with LHM has a bandwidth of 231.6 MHz , with 9.65% impedance bandwidth is found, in the range of 2.2844 to 2.516 GHz for 2.4 GHz band.

The three dimensionals representation of the radiation pattern of the antenna with LHM is presented in Figure 7 .

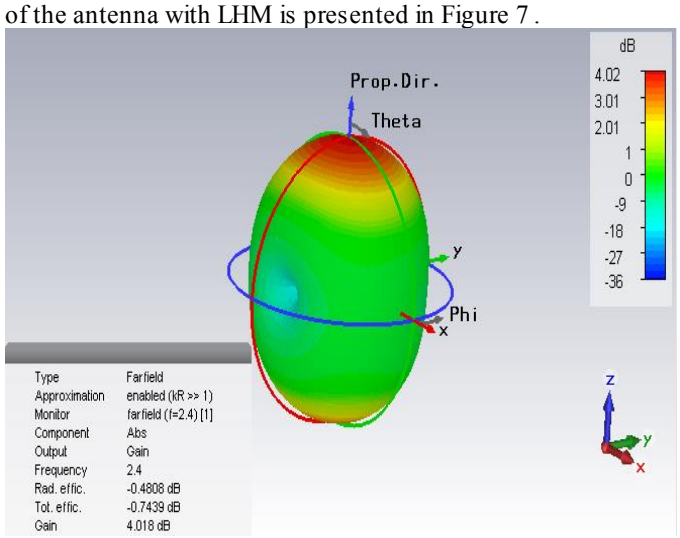

Fig. 7. Three dimensionals radiation pattern of the antenna with LHM in the farfield .

Figure 8 shows tow dimensionals radiation pattern of the antenna with LHM which achieves a highest gain value of 4.02 dB and half power beamwidth of 81.3^0 .

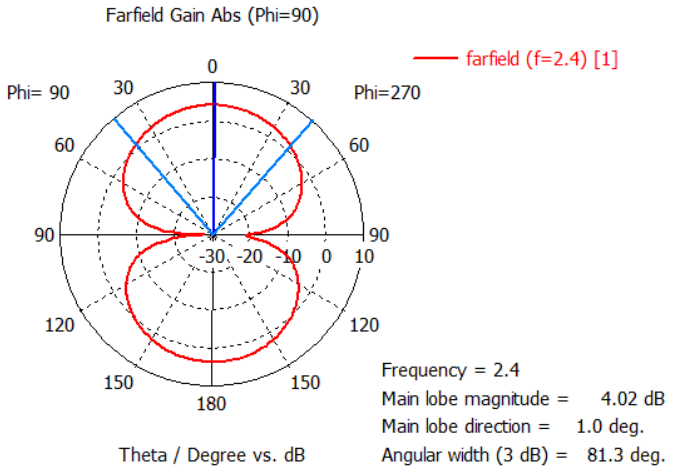

Fig. 8. Tow dimensionals Radiation pattern of the antenna with LHM .

IV. Simulation Results Compartion

Depending on the found results , the radiation parameters comparison between rectangular microstrip patch antenna that operating at 2.4 GHz without and with LHM structure is displayed in Table 2 .

TABLE 2 Comparison Between RMPA Without And With LHM Structure Working On 2.4 GHz .

Parameters	RMPA without LHM	RMPA with LHM
Return Loss (dB)	-12.83	-37.16
VSWR	1.59	1.02
Impedance BW (%)	2.49%	9.65%
Peak gain (dB)	1.83	4.02
HPBW (degree)	95.9^0	81.3^0

V. Conclusion

A rectangular microstrip patch antenna with Left-handed Metamaterial structure has been designed for better results to increase the bandwidth and gain and decrease the return loss by using CST Microwave Studio Suite Software at operating frequency of 2.4 GHz for WLAN applications . Depending on the simulation results , it can be concluded that , the conventional RMPA without LHM has a resonant frequency of 2.4 GHz , which covers the frequency range of (2.37 to 2.4298 GHz) with bandwidth of 59.8 MHz, and good level of impedance matching where its return loss is better than -10 dB . The radiation parameters of RMPA with LHM have improvements over conventional RMPA , where the peak gain , impedance bandwidth are increased and return loss is decreased . Therefore , RMPA with LHM structure can be operated with high performance at the desired band of 231.6 MHz which covers the frequency range of (2.2844 to 2.516

ISSN: 2961-6611

GHz) , and it can be used properly for WLAN applications at 2.4 GHz.

REFERENCES

[1] Nakano. H . Low-Profile Natural and Metamaterial Antennas Analysis Methods and Applications. Canada: John Wiley and Sons , 2016 .

[2] Kulkarni, G., & Lohiya, G. B.. A Compact Microstrip Patch Antenna using Metamaterial. International Journal of Engineering Trends and Technology (IJETT) , 42(7), 365–369 , 2016 .

[3] Ali, T., Saadh, M., & Biradar, R. C.. A Novel metamaterial rectangular CSRR with pass band characteristics at 2.95 and 5.23 GHz. In IEEE International Conference On Recent Trends in Electronics Information & Communication Technology (pp. 256 – 260). India , 2017.

[4] Majid, H. A., Rahim, M. K. A., & Masri, T.. Left Handed Metamaterial Design for Microstrip Antenna Application. In IEEE International RF and Microwave (pp. 218 – 221). Kuala Lumpur , 2008 .

[5] V. G. Veselago . 'The electrodynamics of substances with simultaneously negative values of ε and μ' . P. N. Lebedev Physics Institute, Academy of Sciences , U.S.S.R , Usp .Fiz. Nauk 92, pp. 517-526 , July. 1964 .

[6] D. R. Smith , Willie J. Padilla , D. C. Vier , S. C. Nemat-Nasser , S. Schultz . 'Composite Medium with Simultaneously Negative pemeability and permeittivity' . Department of Physics , University of California , San Diego , 9500 Gilman Drive , La Jolla , California 92093-0319 ,1- May 2000 .

[7] Zani MZM, Jusoh MH, Sulaiman AA, et al. Circular Patch Antenna On Metamaterial. IEEE International Conference on Electronic Devices, Systems and Applications (ICEDSA). pp.313–316 .2010 .

[8] C. Balanis, "Antenna Theory Analysis And Design", Third Edition, A John Wiley & Sons, Inc., Publication, 2005.

[9] V. Niranjan, A. Saxena, and K. Srivastava, "CPW-fed Slot Patch Antenna for 5.2/5.8GHz WLAN Application", PIERS Proceedings, Kuala Lumpur, Malaysia, March 27–30, 2012.

[10] A. Kumar, N. Gupta, and P. Gautam, "Gain and Bandwidth Enhancement Techniques in Microstrip Patch Antennas-A Review", International Journal of Computer Applications, Vol. 148–No. 7, 2016.

[11] Sotyohadi*, Riken Afandi, and Dony Rachmad Hadi, "Design and Bandwidth Optimization on Triangle Patch Microstrip Antenna for WLAN 2.4 GHz", International Conference on Electrical Systems, Technology and Information, , Indonesia, 26-29 Sep 2017.

[12] S. Kumar, and H. Gupta, "Design and Study of Compact and Wideband Microstrip U-Slot Patch Antenna for Wi-Max Application", Journal of Electronics and Communication Engineering (IOSR-JECE), Vol. 5, Issue 2, pp. 45-48, Mar. - Apr. 2013 .

[13] Ali H. Rambe , Mutiara W. Sitopu , Suherman Suherman. 'Bandwidth enhancement of rectangular patch microstrip antenna using left handed metamaterial at 2.4 GHz'.(IOP) Conference Series ,Materials Science and Engineering ,pp. 4 , 2018 .

ISSN: 2961-6611

Evaluation of SAR Distribution in Realistic Human Head Model

Feras A. Osman[1], Adel S. Emhemmed[2], Amer R. Zerek[3]
[1] Department of Communication Engineering, College of electronic technology, Tripoli, Libya
[2]Electrical and Electronic Engineering Department, University of Tripoli, Tripoli, Libya
[2]Electrical and Electronic Engineering Department, University of Zawia, Zawia, Libya
Feras.Osman750@gmail.com

***Abstract*- The rapid evolution of the wireless communication technology and the widespread use of mobile phone lead to the increase of public concerns of the influence of the electromagnetic (EM) radiation on the human body. The amount of this energy absorbed by the human head is measured by the specific absorption rate (SAR). There are standard limits, according to which phones sold should be below certain SAR. The amount of SAR depends on type of the antenna, the distance between the antenna and the user, and the extent and type of use.**

In this paper the interaction between human head model and electromagnetic field sources is studied. The Realistic Human Head model is composed of 20 different tissue types. A Planar Inverted F Antenna PIFA antenna as a source of exposure is designed and simulated within UMTS / LTE (1920-2170MHz). The analysis is performed using a mobile phone model in speech mode tilt modes. CST Microwave Studio simulation software is used to analysis SAR at 1 gram and 10 grams at 5-10 mm distance between head and antenna with 0.5w radiated power.

Keywords – PIFA antenna, Specific Absorption Rate (SAR), Human head Modelling, CST.

I. INTRODUCTION

In recent years, human beings live completely surrounded by many wireless devices. Modern society lives and works with wireless applications such as mobile phones, GPS devices or other wireless devices that make our life easier. It means that humankind are constantly interacting with electromagnetic fields and non-ionizing radiation. This radiation has various effects on human health. Due to their heating effects, they can cause biological damage to cells. The fundamental absorption mechanism of electromagnetic radiation is essentially based on the induction of eddy currents on the skin and in the tissue due to the electromagnetic fields caused by the RF currents on the antenna and device. The basic parameter in the electromagnetic absorption is defined in terms of the Specific Absorption Rate (SAR), or the absorbed power in unit mass of tissue [1-7].

SAR is a measure of the rate at which energy is absorbed by the body when exposed to a RF electromagnetic field. SAR is usually averaged either over the whole body, or over a small sample volume (typically 1 g or 10 g of tissue). The value cited is then the maximum level measured in the body part studied over the stated volume or mass. It can be calculated from the electric field within the tissue as:

$$SAR = \frac{\sigma E^2}{2\rho} \quad w/kg \ldots\ldots\ldots\ldots\ldots\ldots\ldots\ldots (1)$$

The SAR value will also depend on the mathematical shape of the part of the body which is exposed to the RF energy [3, 4].

$$SAR = \frac{1}{V}\int \frac{\sigma(r)E(r)^2}{\rho(r)}\, dr \ldots\ldots\ldots\ldots\ldots (2)$$

Where E refers to the electric field strength (V/m), σ the conductivity (S/m) and ρ the density (kg/m^3) of human Head tissues. SAR is the standard for determining safe levels of operation for cell phones.

To avoid effects of mobile phone radiation on human health, various governments have defined maximum SAR levels for RF energy emitted by mobile phones [6, 7]. To ensure public safety with respect to exposure to electromagnetic radiation, the International Commission on Protection from Non-Ionizing Radiation (ICNIRP) and the Institute of Electrical and Electronics Engineers (IEEE) have developed guidelines and standards for the reduction of electromagnetic exposure zones. These guidelines and standards set out the basic limitations that define SAR limits that should not be exceeded. (IEEE) has set a standard the limit for exposure to electromagnetic fields that does not exceed value of Maximum SAR distribution about *1.6w/kg* in a 30 minute period by 1 gram of tissue mass,(ICNIRP) has set a standard that does not exceed the value of Maximum SAR distribution *2w/kg* for 6 minutes in 10 grams of the tissue mass. The electrical property of the human head is changed like conductivity and permeability when humans are affected by the electromagnetic field [8-11].

II. SIMULATION MODEL

In this paper, the SAR distribution is calculated on a human head exposed to an electromagnetic field emitted from a cellular telephone using the Planar Inverted F Antenna (PIFA) designed to operate within UMTS / LTE (1920-2170MHz) as shown in Fig. 1 (a) & (b). In the model, a realistic human head model. Measurement of power absorbed gives the description of the measurement of SAR and heat-induced when mobile is nearer to the human head model is used to investigate SAR at 1 g and 10 g tissue exposed to EM waves radiated from an antenna by using software CST microwave Studio.

ISSN: 2961-6611

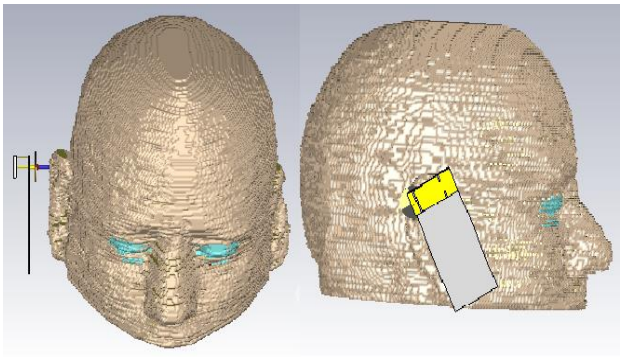

Fig.1 PIFA with realistic human head model

A. Antenna model

In this paper, the Planar Inverted F Antenna (PIFA) is designed, which is used in mobile phones as shown in Fig. 2 (a) & (b) The antenna is designed and optimized to operate at 2.1GHz (UMTS/LTE-Band 1). This antenna is used in mobile phones due to its small size and high gain. The proposed antenna is emulated using CST Microwave Studio.

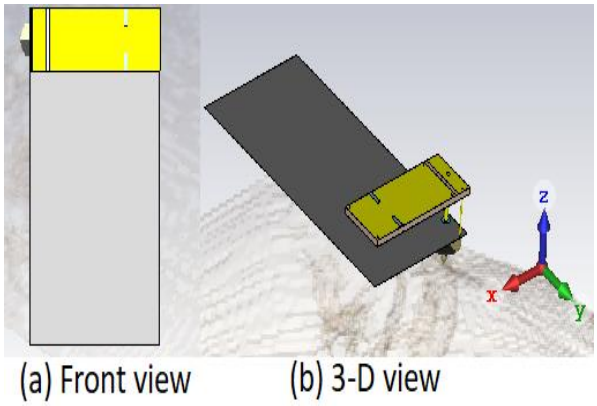

Fig.2 Planar Inverted F Antenna

The dimension of proposed PIFA structure with dimension of ground plane (Lg×Wg) *80mm x 35mm* as Shown in Fig. 3 (a) & (b). The rectangular radiating patch is placed above the substrate with a separate vacuum gap with a height (H) *10mm*. The top radiating patch is printed on a copper plate with thickness *0.035mm*. The antenna substrate is FR4 with εr= 4.3 with thickness of *h=1.6 mm* and dielectric loss tangent, tan δ = 0.025. The antenna is packed with a vacuum substrate (εr= 1.0). The vertical sub-strip made from copper is used as the shorting plate and connect between the top radiating patch and the ground plane.

The 50Ω coaxial connector is used to feed antenna with *0.5w* power at the (LTE 2100) band. The position of feeding points and shorting plates is varied to get the optimum results.

The return loss of the PIFA antenna was simulated at two different positions (5mm and 10mm) as shown in Fig. 4 a and b. The resonant frequency of the antenna is about 2.1GHz with 120MHz bandwidth from 2.04GHz to 2.16GHz, which the same for two positions. The return loss is about -23 dB at 5mm position and -28.9dB at 10mm position, since the matching of the antenna increase by increasing the distance from the head

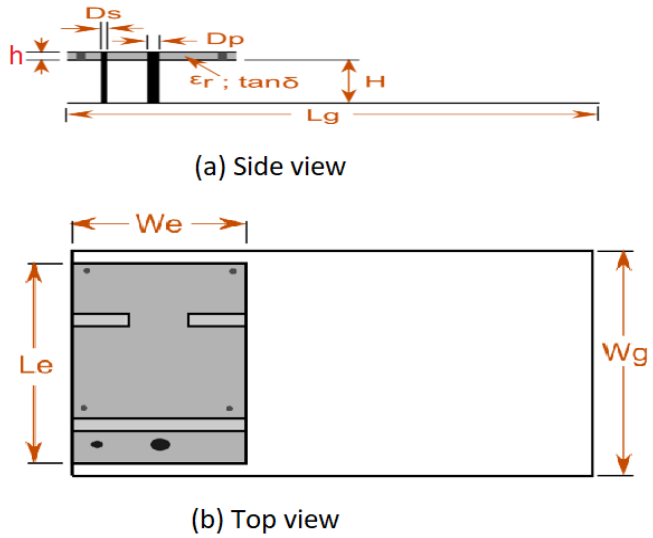

Fiq.3 The dimension of proposed PIFA structure.

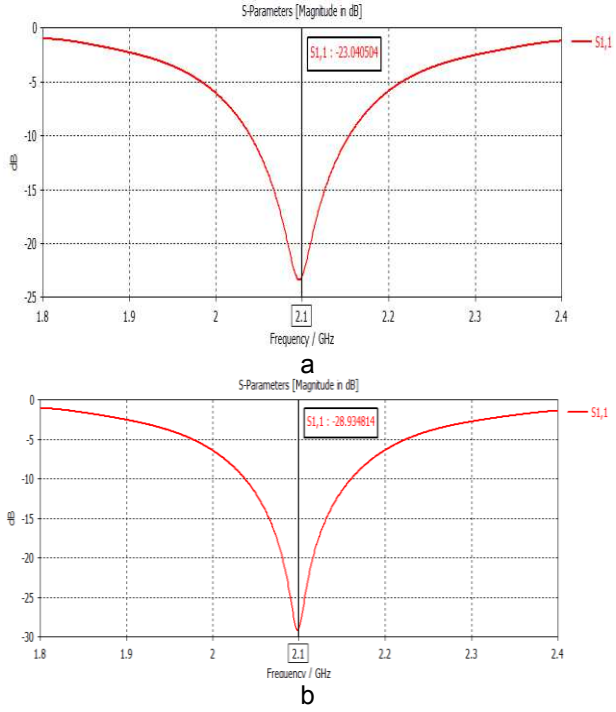

Fig. 4 the return loss of PIFA antenna at *5mm (a)* and *10mm (b) from human head.*

The PIFA antenna demonstrates also a nearly broadside radiation pattern over its resonant frequencies as shown in Fig. 5 (a) and (b). The maximum antenna directivity is 5.8dBi when the head at 5mm distance and 5.77dBi at 10mm distance. The change of directivity due to the head work as reflector for the antenna and directivity increase by reduces the distance of the antenna from the head.

ISSN: 2961-6611

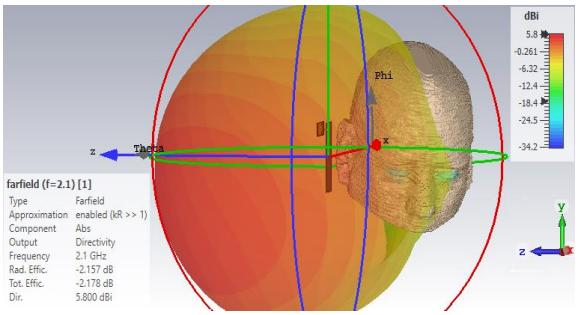

a

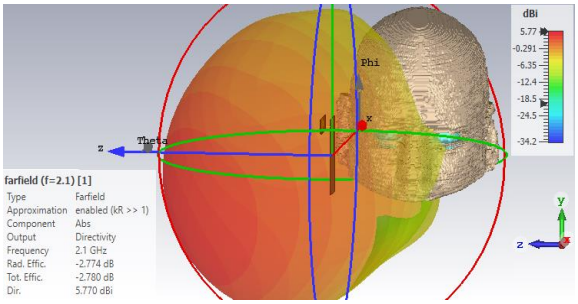

b

Fig. 5 Simulated 3-D radiation pattern for the antenna directivity at *5mm (a)* and *10mm (b) from human head.*

B. Human head model

Human body tissues have different values of dielectric properties, that is, permittivity and conductivity. These properties are functions of several variables, such as frequency, geometry and size of tissue, and water contents. The realistic human head model (Zubal Model's) [3] was used in this paper. It component of 20 different tissues such as skin, skull, bone, gray matter, white matter, fat, humor, CSF. Etc. The sectional view of realistic human head model is shown in Fig.6.

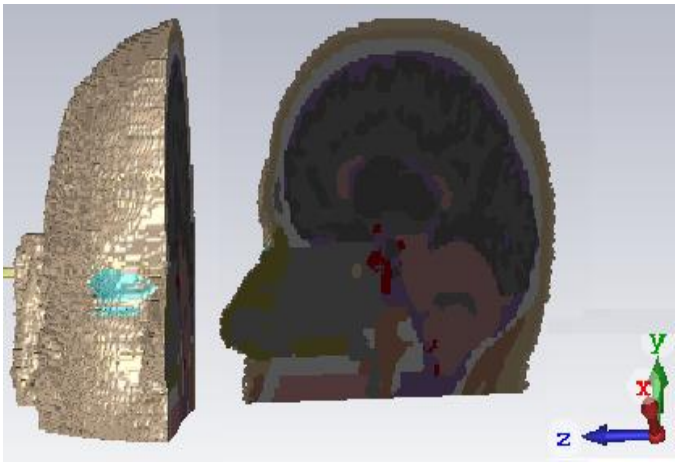

Fig.6 different tissue layers of human head

The proposed voxel model contains *256x256x128* voxels elements with dimensions of *1.1x1.1x1.4 mm*. In addition, the insulating properties of head tissue, as well as density and conductivity, the properties of all tissues used in this paper were obtained from IT'IS's tissues [4, 5], according to the user frequency of 2.1GHz. as showing in Table 1.

Table 1 property of the head tissues at 2.1GHz

Tissue	Mass density ρ (kg/m^3)	permittivity ε_r	Conductivity σ (S/m)
Skin	1109	38.4	1.310
Muscle	1090	53.2	1.519
Bone	1908	11.6	0.328
Blood	1050	58.9	2.260
Fat	0911	5.32	0.089
Cartilage	1100	39.5	1.490
Gray Matter	1045	49.5	1.570
White Matter	1041	36.6	1.050
Eye (Humor)	1005	68.4	2.220
Eye (Sclera)	1005	53.1	1.790
Eye (Lens)	1076	34.3	0.918
Air	0001	01.0	0.000
Cerebellum	1045	45.5	1.880
Dura	1174	42.5	1.470
CSF	1007	66.8	3.150
Nerve	1850	30.5	0.951
Tongue	1090	53.1	1.560
Pituitary Gland	1050	57.7	1.700
Lacrimal Gland	1028	58.3	1.000
Parotid Gland	1048	74.4	1.020

III. RESULTS & DISCUSSIONS

A. Influences of Distance Between Human Head and Handset Antenna

In this part, it is aimed to analyze the impacts of the distances between the user's head and the mobile phone model at 2100 MHz the distance is changed from 5 mm to 10 mm. The maximum SAR is clearly identifiable from the results, since the change in the distance between the mobile phone and the user header may increase or decrease the SAR value. As shown in Fig.7,8, 9.and 10.

B. Influences of Angle Between Head and Antenna

While people talking on cell phones, the human head can be exposed to radiation at various angles. Therefore, it is crucial to analyze the effect of various angles between the antenna and the human head on the SAR values. The simulations are starting from 25degrees to 30 degrees for the main angles (θ variation, φ variation) at 2100 MHz SAR distributions on the head are shown in Fig.7 & Fig.8 when the angle between the user head and the antenna at 25 degrees(θ , φ) and SAR distributions on the head are shown in Fig.8 & Fig.9 When the angle between the human head and the PIFA antenna is 30 ° (θ, φ) according to simulations. We can note the value of SAR decrease by increasing the angel.

ISSN: 2961-6611

C. SAR results of PIFA near to the Human head model

SAR is calculated at 1 g and 10 g tissue of the human head when placing the mobile phone near the human head. The level of energy absorption of each layer varies due to its thickness, water content, conductivity and permittivity. 3D thermal distribution in head from the results of SAR values obtained using CST Microwave Studio. SAR is concentrated at limited area around the human head as shown in Fig.5(a) &(b). The SAR rate is about 2.96 W/kg at 2.1 GHz for 1 g with a distance of 5 mm and a 25 ° (θ, φ) angle between the human head and the antenna. Fig.7 (a) & (b) shows PIFA antenna and its SAR distribution around the human head the SAR about 1.538 W/kg at 2.1 GHz for 10g with a distance of 10 mm and a 30 ° (θ, φ) angle between the human head and the antenna.

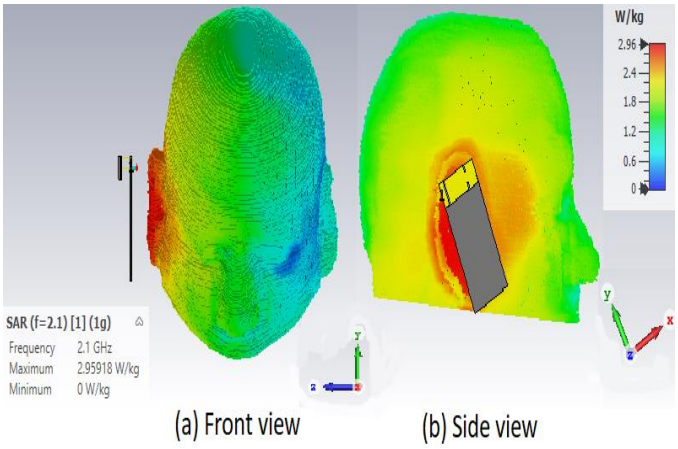

Fig.7 The maximum SAR of 2.96 W / kg in 1 g is obtained for 5 mm distance, the angles (θ 25 °, φ 25°) between head and antenna at 2.1GHz.

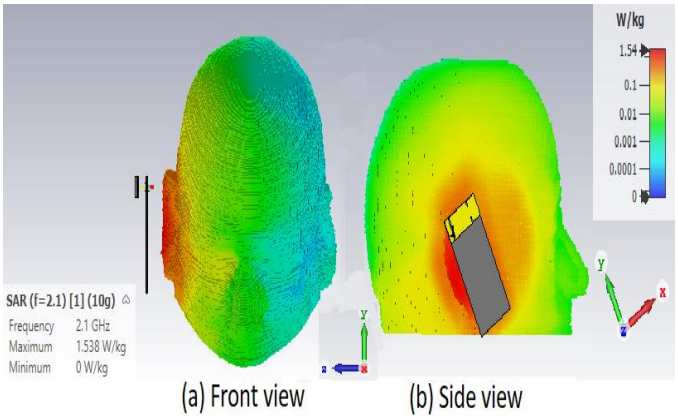

Fig.8 The maximum SAR of 1.538 W / kg in 10 g is obtained for 5 mm distance, the angles (θ 25 °, φ 25°) between head and antenna at 2.1GHz.

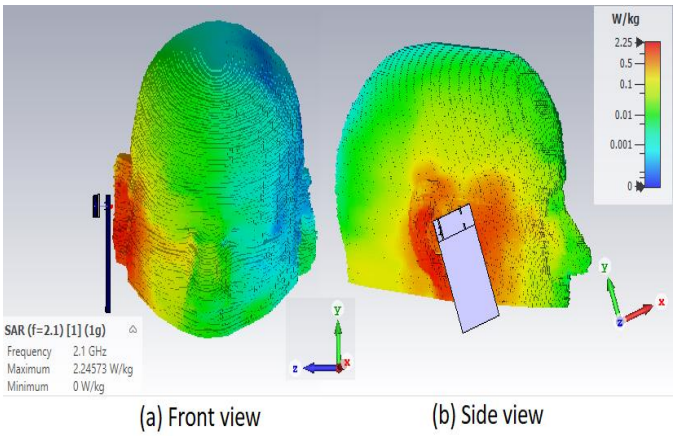

Fig.9 The maximum SAR of 2.25 W / kg in 10 g is obtained for 10 mm distance, the angles (θ 30 °, φ 30°) between head and antenna at 2.1GHz.

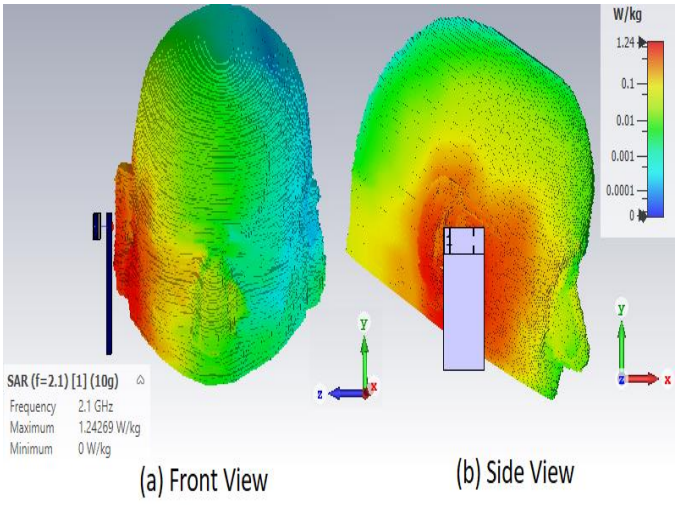

Fig.10 The maximum SAR of 1.24 W / kg in 10 g is obtained for 10 mm distance, the angles (θ 30 °, φ 30°) between head and antenna at 2.1GHz.

Fig. 11 shows the comparison between SAR values at 5mm and 10mm distance for 2.1GHz and 500mW peak power. Except for cartilage tissue, all other tissues SAR value is lower than the FCC regulated SAR safety limit (1.6W/Kg). Maximum SAR value at cartilage tissue is 1.69W/Kg.

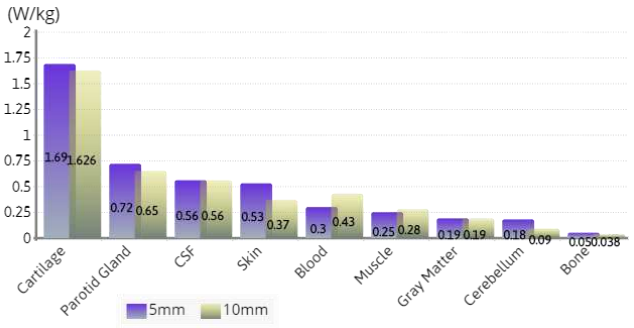

Fig 11: Comparison between 5mm and 10mm distance of SAR value at 2.1GHz

ISSN: 2961-6611

Table.2: calculated SAR Value for each tissue and distance between head and antenna (5&10 mm).

Tissue	SAR (w/kg) 5mm	SAR (w/kg) 10mm
Skin	0.5316	0.369
Muscle	0.278716	0.25
Bone	0.05	0.038
Blood	0.3	0.4304
Fat	0.0411	0.028
Cartilage	1.69	1.626
Gray Matter	0.1923	0.1923
White Matter	0.12116	0.127
Eye (Humor)	0.1104	0.070686
Eye (Sclera)	0.08905	0.05699
Eye (Lens)	0.04266	0.02730
Air	0	0
Cerebellum	0.1763	0.0899
Dura	0.00563	0.0056
CSF	0.5646	0.5646
Nerve	0.0504	0.0503
Tongue	0.00286	0.0005
Pituitary G	0.052	0.020238
Lacrimal G	0.1756	0.1245
Parotid Gland	0,72	0.6662

IV. CONCLUSION

Applying a model that determines the distribution of absorbed energy into human head structures would improve our understanding of the harmful effects of mobile phones.

In this paper, the SAR distribution is calculated on a human head exposed to an electromagnetic field emitted from a cellular telephone using the Planar Inverted F Antenna (PIFA) designed to operate within UMTS / LTE (1920-2170MHz)

This model enabled us to investigate the SAR for different head tissues. This results from the fact that the dielectric properties are frequency dependent.

Results obtained from the simulation show that maximum local SAR increases significantly for smaller mass average. The maximum SAR rate is about 2.96 W / kg at 2.1 GHz for 1g. SAR is distributed around 1.538 W / kg at the same frequency for 10 g for 5 mm between head and antenna and at 25 ° (θ, φ) angle with 0.5(watt) radius power .The distance between the human head and the antenna was increased to 10 mm and the angular change was increased by 30 °(θ, φ) , with better results obtained for human health. The maximum specific absorption rate of 2.25 W/kg was obtained in 1 g and 1.25 w/kg in 10 g. These values can be changed by increasing the distance and angle between the phone and the human head.

Lastly, we can conclude, the SAR deposition depends on tissue material properties (conductivity, permittivity, and permeability) and by increasing the conductivity, SAR increases too.

REFERENCES

[1] J. B. Van de Kamer and J. J. W. Lagendijk, "Computation of high resolution SAR distributions in a head due to a radiating dipole antenna representing a hand-held mobile phone," Phys. Med. Biol., vol. 47, pp. 1827-1835, 2002.

[2] P. J. Dimbylow and S. M. Mann, "SAR calculations in an anatomically realistic model of the head for mobile communications transceivers at 900 MHz and 1.8 GHz," Phys. Med. Biol., vol. 39, pp. 1537-1553, 1994.

[3] A.Arayeshnia, A.Keshtkar and S. Amiri,"Realistic human head voxel model for brain microwave imaging,"2017 Iranian Conference on Electrical Engineering (ICEE),pp.1660-1663, 2017.

[4] C. Gabriel. Compilation of the Dielectric properties of body tissues at RF and microwave frequencies. Report N.AL/OE-TE-1996-0004, Brooks Air Force Base, 1996.

[5] C. Gabriel, A. Peyman, and E.H. Grant. Electrical conductivity of tissue at frequencies below 1 MHz. Physics in Medicine and Biology, 54(16), pp. 4863-4878, 2009.

[6]IEEE Standard for Safety Levels with Respect to Human Exposure to Radio Frequency Electromagnetic Fields, 3 kHz to 300 GHz, IEEE C95.1-1991, Institute of Electrical and Electronics Engineers, Inc., New York, 1992.

[7] Takashi Nakamura, Kazuyoshi Uchida, and Shinobu Tokumaru, "SAR of Multiple Cylindrical Human Models", Electronics and Communications in Japan, Part 1, Vol. 81, No. 10, pp. 899.905, 1998.

[8] O. P. Gandhi, Gianluca Lazzi and Cynthia M. Furse, "Electromagnetic Absorption in the Human Head and Neck for Mobile Telephones at 835 and 1900 MHz," IEEE Trans. Microwave Theory Tech., vol. MTT – 44. No.10, pp.1884-1897, October-1996.

[9] M.Okoniewski, E.Okoniewski and M.A.Stuchly, "A Study of the Handset Antenna and Human Body Interaction," IEEE Trans. Microwave Theory Tech., vol. MTT – 44. No.10, pp.1855-1864, October-1996.

[10] L. Asmae and O. Homayoon, "Simulation and evaluation of specific absorption rate in human body in high frequency electromagnetic fields," in Advanced Materials Research, vol. 433–440, pp. 5489–5493, Trans Tech Publications, Zurich, Switzerland, 2012.

[11] M. R. I. Faruque, M. T. Islam, and N. Misran, "Analysis of SAR levels in human head tissues for four types of antennas with portable telephones," Australian Journal of Basic and Applied Sciences, vol. 5, no. 3, pp. 96–107, 2011.

ISSN: 2961-6611

Studying and Investigation Ardunio of Landmines Detection Robotic

MoeidMElsokah[1] and Amer R. Zerek[2]

[1] *College of Electronic Technology, Communication Engineering Department*
Tripoli, Libya
E- mail moayedmohamedm@gmail.com
[2]*ZawiaUniversity, Faculty of Engineering/ EE Department,*
Zawia, – Libya,
E-mail anas_94az@yahoo.co.uk

Abstract ***The United Nations estimates that the number of mines in Libya is estimated at three million, most of which were planted between 1940 and 1943 by Italians, Germans and English during World War II in Libya. In the wake of the war, the presence of buried landmines poses particular threats to local populations and minefields. Since human life is always precious, these robots are an alternative to mine detection in war zones. Recently the hub of many research projects for military and civilian applications such as military, surveillance, security service, riot, police, hostage situation, riots, law enforcement, border patrols, border control. We take into account the challenges involved in the demining of humanitarian landmines and the techniques currently used in this area. This paper presents some basic ideas about the formation of a mobile robot system to detect and locate antipersonnel landmines at the lowest cost, effective, effective, fast and quality.***

Keywords- Humanitarian Demining, Landmines Detection, Metal detector, GPS, Arduino microcontroller, ultrasonic, Remote Experimentation.

I. IINTRODUCTION

A landmine is an explosive device hidden underground or designed to destroy or disable enemy targets, from combatants to vehicles and tanks as they pass or near them. This device is usually automatically detonated by pressing when the target moves on it or moves over it, despite the use of other detonation mechanisms. A landmine may cause damage as a result of the direct explosion, fragments caused by the explosion or both. The name derives from the old practice of military mining, where the tunnels were dug under enemy fortifications or formations of forces. The war in North Africa began on June 10, 1940, when Italy declared war on Britain and France in the wake of the Second World War. After a slight advance of the Italian forces in the Egyptian territories, the British launched a counterattack that resulted in the defeat of the Italians in the Battle of Bedim, prompting the Italians to seek help from their allies The Germans sent a small force called the African Legion, which held the military situation of the British, who could defeat the Germans and the Italians only a final defeat in the Battle of Alamein, which enabled them to end the battle of North Africa for them (with the help of the Americans) on 13 May 1943. But the suffering of the people of North Africa did not end with the end of the fighting. In order to prevent the warring States from advancing their enemies, the warring countries were laying mines of all kinds, but they did not mine mines after the end of the war, which makes it worse that mines do not diminish over time, On the peoples of that region. No one knows exactly how many mines left by this conflict in North Africa, but we can take an idea from the memoirs of the commander of German-Italian forces in North Africa, Eron Rommel, who said that 80,000 mines, mostly antipersonnel, were planted in the Boerat line (In Libya). It should be said here that the battle of the Boerat (or the Zamzam Valley) was not one of the major battles in the war, such as the battles of Alamein, Tobruk and the Libyan-Egyptian border battles. Although North African countries have the same problem, they have never united their diplomatic efforts to demand from the warring countries of Germany, Italy and Britain demining, and compensation for war damage. While Egypt and Libya are separate, Tunisia signed in December 1997 the Ottawa Convention on the Prohibition of the Use of Landmines, but this signature will not only save the Tunisian people from the threat of mines.[1]
In post-conflict operations, demining is necessary to secure the resettlement of civilians and the recovery of war-ravaged

ISSN: 2961-6611

communities. However, ensuring that all land areas are mine-free is a major challenge. The detection and removal of anti-personnel landmines at present is a serious political issue, economic, environmental and humanitarian. There is a common interest in solving this problem, and solutions are being sought in many engineering fields.[2]But look for landmines and Detection of explosives can be classified into Follow the instructions:

1. Landmines, information, species, facts, findings;
2. Vehicle detection and loading system.
3. Detectors (sensors for detection of mines);
4. Identification of detected mine sites;
5. Data (signal / image) processing techniquesAlgorithms.
6. Data transfer techniques.
7. Mine clearance techniques;
8. Landmine detection performance.

This paper focuses on the proposed solutionrobot car and transfer data toVisualization and data monitoring for Improved detection.Manual on Landmine Detection and Removal Hand held human hand detector, Mechanical methods And / or biological (using trained dogs and rodents) Ways are still out for reasonsReliability, but it is a very slow way Including risk consumption and time. So need Synthetic systems using automated systems In this area is necessary and paves the way for Researchers work to improve Performance of automated landmines reveal. The research area includes many challenges and gaps. To work on such as:

1 - Automatic control of the gap and position The heads of the sensor and the surface of the earth.
2 - The location of the detected mine operation.
3 - Speed detection during detection.

Operation to avoid mine loss. Few robots detect mines that have the capability To recognize the earth's surface and can control the gap The position of the sensor heads is reported in (Armada, MA et al., 2005) (Chesney, R. et al., 2002) (Nonami, K. et al., 2003). Through the review Literature is obviously the use of one of mine Detection techniques (a growing area of Search) along with unmanned vehicles or robots It is the most appropriate technique to minimize Human interaction near the hazardous area Increase detection speed.

II. OTTAWA TREATY

The Convention on the Prohibition of the Use, Stockpiling, Production and Transfer of Anti-Personnel Mines and on their Destruction, known informally as the Ottawa Treaty, the Anti-Personnel Mine Ban Convention, or often simply the Mine Ban Treaty, aims at eliminating anti-personnel landmines (AP-mines) around the world. To date, there are 164 state parties to the treaty. One state (the Marshall Islands) has signed but not ratified the treaty, while 32 UN states, including the United States, Russia, China, and India are non-signatories, making a total of 33 United Nations states not a party. The Ottawa Treaty is a success in progress with a huge amount of land cleared of landmines, a significant decrease in the number of casualties, millions of stockpiled mines destroyed and 80% of the world belonging to the treaty. However, there is still work to do – 64 states and other areas are contaminated by landmines and other explosive remnants of war and there were over 6,400 casualties in 2015. [3].

III. UNITED NATIONS GENERAL ASSEMBLY ANNUAL RESOLUTIONS

A recurrent opportunity for States to indicate their support for the ban on antipersonnel mines is their vote on the annual UN General Assembly (UNGA) resolution calling for universalization and full implementation of the Mine Ban Treaty. UNGA Resolution 66/29, for example, was adopted on 2 December 2011 by a vote of 162 in favor, none opposed, and 18 abstentions. Since the first UNGA resolution supporting the Mine Ban Treaty in 1997, the number of states voting in favour has ranged from a low of 139 in 1999 to a high of 165 in 2010. The number of states abstaining has ranged from a high of 23 in 2002 and 2003 to a low of 17 in 2005 and 2006. Of the 19 states not party that voted in support of Resolution 66/29 on 2 December 2011, nine have voted in favour of every Mine Ban Treaty resolution since 1997 (Armenia, Bahrain, Finland, Georgia, Oman, Poland, Singapore, Sri Lanka, and the United Arab Emirates); 10 that consistently abstained or were absent previously now vote in favour (Azerbaijan, China, Kazakhstan, Kyrgyzstan, Lao PDR, Marshall Islands, Micronesia FS, Mongolia, Morocco, and Tonga). Somalia, now a State Party, was absent from the 2011 resolution, but has voted in favour in previous years. The number of states abstaining from supporting the resolution has ranged from a high of 23 in 2002 and 2003 to a low of 17 in 2010, 2005 and 2006. The group of states that could be described as most concerned about the security implications of the Mine Ban Treaty are the 15 states not party that have voted against consecutive resolutions since 1997: Cuba, Egypt, India, Iran, Israel, Libya (since 1998), Myanmar, North Korea (since 2007), Pakistan, Russia, South Korea, Syria, Uzbekistan (since 1999), the United States, and Vietnam (since 1998) .[7]

IV. HUMANITARIAN MINE ACTION

Non-governmental organizations and the United Nations have been involved in mine clearance since the late 1980s, emerging over the last decade as key actors in efforts to reduce the threat landmines pose to innocent civilians throughout the word. This has led to a new concept: humanitarian mine action, which is an integrated approach to removing landmines from the ground and reducing their disastrous impact on mine-affected communities. Nobody knows how many mines there are in the ground, and that number is not very relevant, despite the attention given to the issue.What is relevant is how many people are affected by the presence of mines, which are obstacles to post-conflict reconstruction and socio-economic re-development.

ISSN: 2961-6611

V. PROPOSED METHOD

A robot is needed to detect landmines to be used to support peace, operations and clearing contaminated areas. The robot has an ultrasonic sensor installed in order to identify and avoid the obstacle. The mine can be found with the help of longitude and latitude of the GPS sensor. [8] We strive to develop the material structure of the robot from materials that can resist eruptions up to a certain point. The robot issues a warning to the next person with the help of a robot-based bell. The engine is powered by a high-power DC motor powered by the h-bridge circuit that allows the robot to move in any direction. The objective of the proposed system is to develop a mobile robot on the ground to apply detection and assistance to humanitarian demining, as well as solutions to the detection of detected mines and monitoring of the area passed, the remote monitoring was introduced for online operation. The system consists of an atmega controller with an Arduino platform to control the movement of the vehicle and steering the motors. A bomb was discovered using metal detection technology. GPS is connected to the vehicle for tracking. GPS signals are obtained using NImyRIO (National Data Acquisition Unit) and Labview. Figures 1 below shows the block diagram proposed method.

. Fig 1 : Block Diagram Proposed Method.

IV. HARDWARE

Arduino Uno microcontrollerH-Bridge, GPS, relay, ADC adapter, GSM module, PIR Sensor .

Ardunio Microcontroller Arduino Uno is a microcontroller board based on the ATmega328P .It has 14 digital input/output pins of which 6 can be used as PWM outputs, 6 analogue inputs, a 16 MHz quartz crystal, a USB connection**,** a power jack, an ICSP header and a reset button. Atmega328p is the microcontroller we are using because, it is more efficient, less cost and easily programmable.Figures 2 below shows the Arduino Uno Microcontroller Board.

Fig 2 :Arduino Uno Microcontroller Board

GPS is used for positioning, localization anddetermining time. The civil signal SPS (StandardPositioning Service) can be used freely by the generalpublic, while the Military signal PPS (PrecisePositioning Service) can be used only by authorizedgovernment agencies. The GPS data can be retrievedfrom the GPS receiver in various formats. GPRMC data format is used in the proposed system. The RMCdata Set (Recommended Minimum Specific GNSS) contains information on time, latitude, longitude andheight, system status, speed, course and date [3].Wiring of the GPS used with the NImyRio is shown in Fig.5.; GPS receiver requires five connections toNI myRIO, as follows; MXP Connector A:

1. +3.3-volt supply (VCC3V3)/+3.3V.
2. Ground (GND)/GND.
3. UART transmit data (TXD)/UART.RX.
4. UART receive data (RXD)/UART.TX.
5. One-pulse-per-second (1PPS)/DIO0.Figures 3 below shows the NEO-6M GPS module And Figures 4 below shows the Setup for GPS connected to NImyRIO.

ISSN: 2961-6611

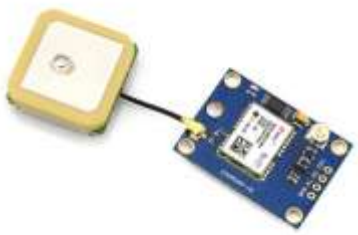

Fig 3 :NEO-6M GPS module

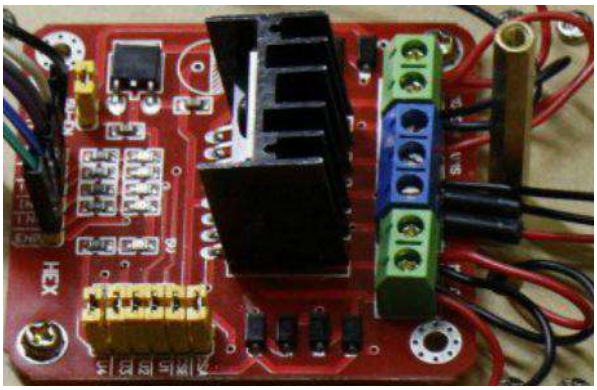

Fig.5 : H-Bridge Circuit used in the robot

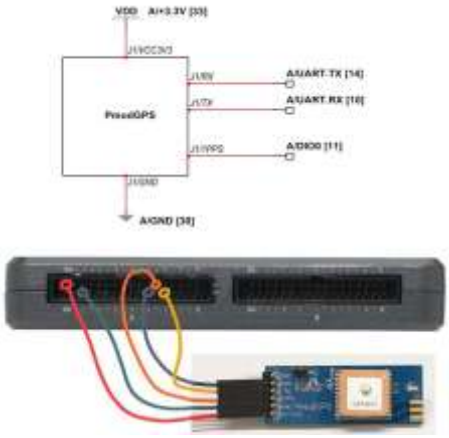

Fig.4 :Setup for GPS connected to NImyRIO

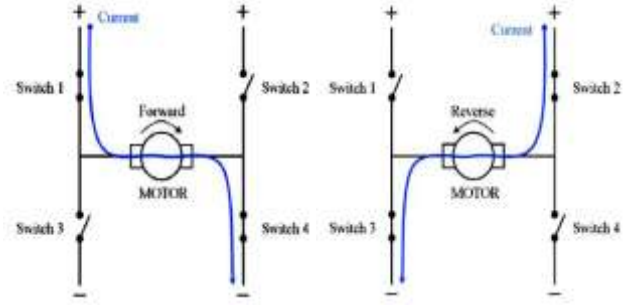

Fig6 : Forward direction& Reverse direction

H-BridgeDC Motors rotate in two directions depending on howapplied voltages are connected to the motor terminals.In order to run the motor in the forward direction, thepositive terminal of the motor is connected to thepositive terminal of the battery and negative to negative. However, to run the motor in reverse direction, simply switch the connections; connect thepositive terminal of the battery to the negativeterminal of the motor and the negative terminal of the battery to the positive terminal of the motor. An H Bridge circuit allows a large DC motor to be run inboth directions with a low level input logic signal.The H-Bridge electronic structure is explicit in thename of the circuit - H-Bridge. Input signals to the H Bridge are being provided from the Arduino boardaccording to the control program, Figures 4 below shows the H-Bridge Circuit used in the robot And Figures 6 below shows Forward direction& Reverse direction.

Ultrasonic Sensor are transducers that convert ultra-sound waves to electrical signals or vice versa. These devices work on a principle similar to that of transducers usedInternational Journal of Engineering Science and Computing, in radar and sonar systems, which evaluate attributes of a target by interpreting the echoes from radio or sound waves, respectively. The HC-SR04 Ultrasonic Sensor is the perfect solution for any distance detection application in robotics. Figure 7 shows HC-SR04 Ultrasonic Sensor.

ISSN: 2961-6611

Fig 7 : HC-SR04 Ultrasonic Sensor

V. METAL DETECTION DEVICE USING HARMONIC LEVEL DETECTION

A metal detection device includes a metal detection coil arranged in a metal detection area, wherein the metal detection coil is excited, and an electromagnetic wave radiated from the metal detection coil detects whether metal exists in the metal detection area. An oscillation circuit generates a sinusoidal oscillating current having a single fundamental frequency and supplies the oscillating current to the metal detection coil to excite the coil. A harmonic level detection circuit detects a harmonic component of the fundamental frequency component of the oscillating current and generates a detection signal. A comparison circuit compares a signal level of the detection signal and a pre-set reference value. A processing circuit determines whether metal exists in the metal detection area based on a comparison result. When determining that metal exists in the metal detection area, the processing circuit drives a notification unit to issue a notification indicating detection of metal.Figures 8 below shows the metal detection circuit.

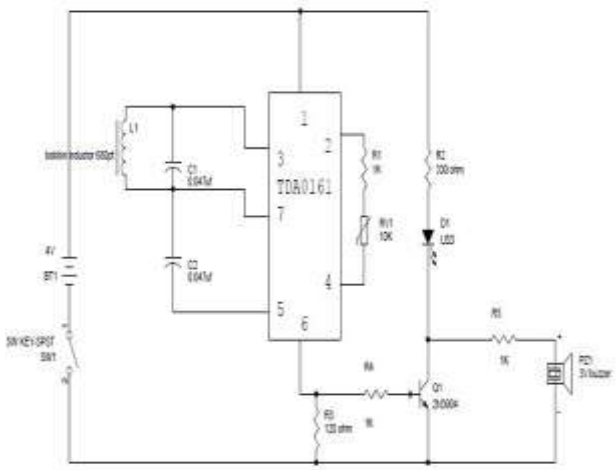

Fig 8 : Metal Detection Circuit

VI. TESTS AND RESULTS

The performance of the mine sensor is evaluated on a pilot basis by measuring the output voltage of the detection circuit in different target states. The experimental results of the standard mine detector and the robot show that the designer robot is capable of detecting and extracting personal mines. The whole system can follow the designer path and terrain violations. Tests are performed using the prototype to ensure the success of the robot design. However, in order to make the roller wheel capable of extracting mines of different sizes, it is necessary to introduce an adaptive capacity to change the size of the rotary wheel according to the size of the buried mines. The study of the case of some materials, including iron copper and aluminum, gold and silver and the following form shows the efficiency of the system in the detection of metal detection and come with acceptable results in practice and helps in the process of mine detection and location with acceptable accuracy. Figures 9 below shows the demonstrates the detection efficiency of different metals.

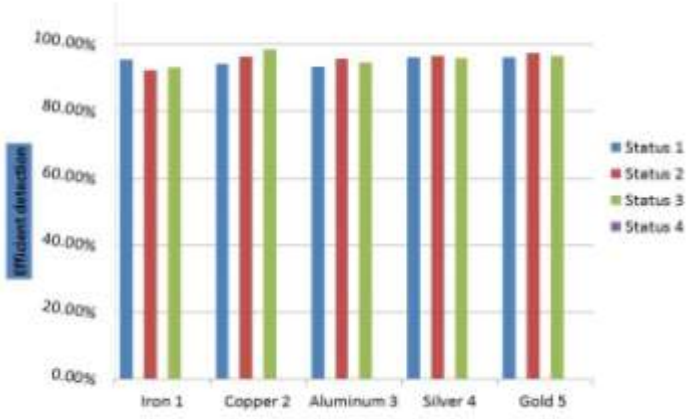

Fig 9 : Detection Efficiency OfDifferent Metals

VII. PROJECT SNAPSHOTS

The snapshots of the final robot with all the components attached are shown below in the following figures in all the views. Figures 10 below shows the robot prototype

.

ISSN: 2961-6611

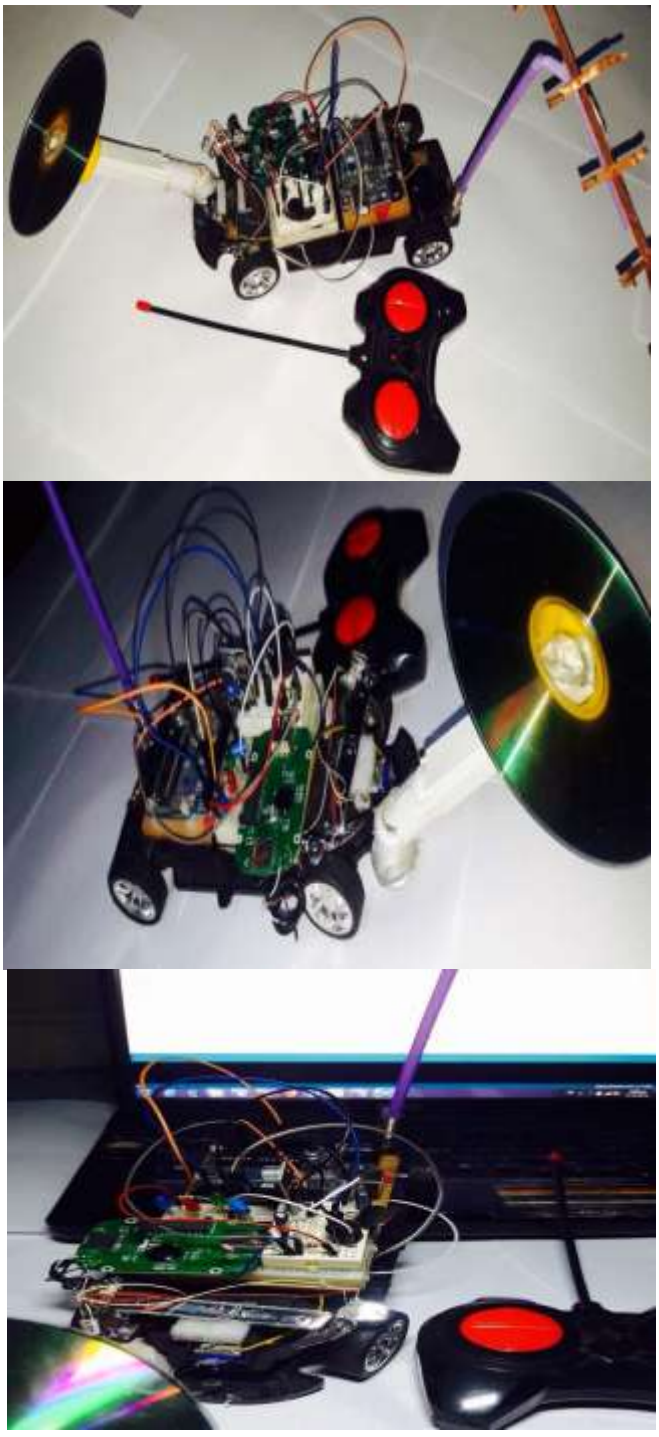

Fig 10 : Robot Prototype

XI. RESULTS AND DISCUSSION

The test is carried out with the prototype assures us of the success of the robot, except for some minor problems. Detectors are made of cheap components and thus the reliability is uncertain with low range of detection. Sometimes, false alarms are generated due to the detection of robot's own metal component. However, this problem is solved by separating the detection coil from the circuit with the use of plastic plates. The second problem occurs in the DC motors. These motors don't generate precise displacements. They are made to provide speed and torque closest to their specifications, but not the exact amount. However, these minor problems won't occur in the actual robot since they are caused by the poor quality of the equipment not due to the proposed concept. Hardware Atmega-328P with the Arduino Board controller; Robot chassis and four 9v Dc , (the structure mainly of a commercial off-the-shelf parts, which are available at low costs :

- H-Bridge is implemented by L293d driver IC, to drive the motors :
- NImy RIO and GPS are attached to the NImyRIO data acquisition :
- Metal detector; Ultrasonic Sensor, IR sensor, batteries and connectors.

Software :

- Arduino IDE 1.6.3,LabVIEW software.
- NImyRIO software and drivers.

XI. CONCLUSION AND FUTURE WORK

This paper describes the general design of the wheeled robot for landmine detection and implementation in Libya. The wheeled robot is less expensive, more powerful and simpler than programming, design, maintenance, modification and development. It is a useful tool for the Army for surveying and monitoring as well as organizations that support mine surveying. Future work is focused on improving body designs by placing a suspension system for more than a shock from uneven surfaces using gear wheels instead. The robot is equipped with a camera to monitor the Android case. The energy system was developed by replacing the battery with solar panels to produce continuous energy. The robot is equipped with a robotic arm for the purpose of using it to catch, pick up and cut wires. The extraction process begins once satisfaction with mine discrimination is assured. The robot combines the flexibility of manual and automatic operation with speed and safety Automated survey and extraction. The introduced robot offers features such as reduced cost and size, reduced system complexity and ease of use. The experimental results show a high resolution of mine detection, as experimental results show that detection and discrimination provide acceptable sensitivity at a range of less than one meter.

REFERENCES

[1] Habib M.K., "Mine detection and sensing technologies-new development potentials in the context of humanitarian demining," in Industrial Electronics Society, Vol. 30, No. 9, 10 May 2009, 2399–2410.

ISSN: 2961-6611

[2] L. Kasprzyczak, S. Trenczek, Z. Borkowicz, M. Cader, “Functional assumptions and concepts of technical solutions of mobile inspective robot for working in explosive hazardous environments”. In: Proc. of EMTECH 2009 Conf. ”Supply, computer science and automatics in excavation industry”, Poland, 2009, pp.99-105.
[3] Kenneth R. Rutherford, (2000) "Internet activism: NGOs and the Mine Ban Treaty", International Journal on Grey Literature, Vol. 1 Issue: 3, pp.99-106.
[4] "Nairobi Summit on a Mine Free World". Nairobisummit.org. Archived from the original on 21 November 2008. Retrieved 15 November 2013.
[5] "Cartagena Summit on a Mine-Free World". Icrc.org. 14 June 2010. Archived from the original on 19 October 2009.Retrieved 15 November 2013.
[6] "Maputo Summit: 3rd Review Conference". Maputoreviewconference.org. Archived from the original on 17 July 2017. Retrieved 19 November 2017.
[7] *"Where global solutions are shaped for you | Disarmament | UNGA resolution on APLC". Unog.ch. 2 December 2011. Archived from the original on 24 February 2013.Retrieved 29 September 2013.*
[8] A. Mokhtar, Choi SeongJoo, G Mikhaell “A Survey onRemote Laboratories for E-Learning and RemoteExperimentation,” vol. 7, no. 29, pp. 1617–1624, 2014.

ISSN: 2961-6611

Financial control by the state over public institutions and companies

Author: Kaoutar MOUDDEN

Under direction of: Dr. TAOUAB Omar

Function: PhD Student

Topic: Corporate finance and governance

Institution: ENCGK – Université Ibn Tofaïl Kenitra Morocco

Contact: kaoutar.moudden@gmail.com

Abstract:

The moderate state is no longer able on its own, to insure the enormous tasks which assign to in the satisfaction of the common interest of the national community.

That is why it is multiplying to a variety of organizations with moral personality and financial autonomy, this shows that the power of public finances is more widespread today, and the thing that explains the broad meaning of the expression: public finances.

Financial control by the state over public institutions and companies is a crucial step, which allows the state to ensure that the allocated budgets are used effectively and efficiently, so that public institutions can achieve performance.

This is not limited to the control practiced by the minister of economy and finance especially state controller and paying treasurer, but, on the respect of good governance practices, transparency and the application of the new reform of public expenditure.

Key words: Corporate governance, Public institutions and companies, Control, Financial performance

I. INTRODUCTION

The modern State alone is no longer able to ensure the enormous stains which assign to it the satisfaction of the common interest of the national collectivity of which it is the representative, for this reason it is multiplying to a variety of bodies having the moral personality and the financial autonomy, to which it entrusts certain tasks of general interest this shows that the power of public finances is today more widespread, the thing that explains the broad meaning of the expression: public finance.

The responsibility of the public authorities for the tasks of general interest does not only meet economic and social objectives, but also to a political concern of the State, that of ensuring its authority and justifying its longevity and legitimacy.

The budget is par excellence the instrument that can be put at the service of its multiple purposes.

The current government cannot function without finances, since they must make revenues and expenditures in order to achieve the objectives they have set for themselves.

This taking over of large sectors of economic and social activity by public bodies, and in particular by the State, requires the mobilization of significant financial resources. These means, which are partly constituted by taxes levied on taxpayers, must be used to finance the programs to be carried out, without being wasted, thus justifying the existence of careful regulation of revenue and expenditure transactions (general tax code, code of recovery of public debts). That is why legislators have adopted public accounting regulations and texts to guide budgetary and financial action.

Similarly, the concern to preserve so-called public funds prompted legislators to put in the hands of the public institutions that use them (public funds) the means to control their jobs. This explains why control will take place not only within the public body, but also within private bodies receiving public financial assistance.

There is a variety of public finance supervisory bodies: the first encompasses bodies external to the administration having some independence, the second category consists of supervisory bodies integrated into the administration in particular public institutions. At this point questions should be asked:

II. WHAT ARE THE BODIES OF THE STATE'S FINANCIAL CONTROL?

III. HOW DOES THIS CONTROL WORK?

The organs of internal control in the administration depend on the Ministry of Economy and Finance, which is responsible for major budgetary and financial matters, it is through this

ISSN: 2961-6611

ministry that the finance bills are prepared, it ensures their execution and control and it must give its approval for all measures that have a direct or indirect financial impact.

The Moroccan Ministry of Economy and Finance, as it stands today, controls in addition to the revenue and expenditure of the State, the operations carried out by the decentralized authorities or by anybody benefiting from the financial assistance of the State or another public authority.

The financial power of the Ministry of Finance is also measured by the development of the means of control between which the general inspection of the finances and the financial control. It also holds under its authority the body of public accountants who play a significant role in the implementation and control of the budget through its various means, the Ministry of Finance can intervene at any stage of the implementation of the budget and thus plays a major role in the control of public finances.

Traditional budgetary controls are classified either according to their nature (political, jurisdictional or administrative) or according to their position in relation to the audited bodies: internal, external.

In general, however, budgetary controls are one or other of the instruments available to the State and public bodies to help them clarify their financial management by submitting them to some regularity.

IV. EXTERNAL CONTROL

The organs of state control in the administration enjoy a relative independence, the latter must not be apprehended in the absolute because they are part of a political-administrative system where a limitation is imposed on the exercise of power.

Despite these institutional limitations, external controls can still play a role in budgetary and financial matters if their actions exploit all the opportunities available to them. Two main reasons for the existence of state control are:

- They capture all public operations performed not transaction functions such as internal control.
- They have the opportunity to put into play the responsibilities of the budget enforcement officers.

External controls are exercised either in political or jurisdictional form, the former are the work of the parliament or the deliberative bodies and the latter are the responsibility of the financial judge.

V. INTERNAL CONTROL

Inter-administrative checks on the implementation of the budget must meet a number of objectives, including remedying the imbalance in favor of external controls in the administration and, above all, preventing irregularities and mistakes before they happen.

Thus different bodies of control exist within the administration some have general tasks encompassing the financial aspect this is the case of the general inspection of the administration, others are specialized in the control of the budget, it is the general inspection of the finances, the control of commitment and the expenditure and the body of the public accountants (accounting control by the general treasury of the kingdom).

The inter-administrative budget control process links authorities which are an integral part of the Ministry of Economy and Finances and which keep under its authority the internal administrative controls which are three in number: CCS the Control of commitment and spending(expense) which is the financial control, FGK The Finance general of the kingdom which is the accounting control and control of the general financial inspection and all these controls constituted by the administrative means to control the budget implementation process, each means of control put at the disposal of the administration intervenes at a certain stage of the budget implementation procedure which reflects the concern to ensure that the fate of public finances and public funds is monitored within the administrations, public services by means of laws and doctrines for the performance of an effective and efficient management of the state finances.

Similarly, the functioning of public bodies is characterized by a division of tasks between authorizing officers who have the power to carry out all the transactions of entry or exit of public funds. The two functions mentioned above are carried out by means of the legislation in force. This segregation of the two functions is one of the rules of public accounting which aims at delimiting each action of each party within the framework of a division of work.

Inter-administrative control was established in Morocco before the colonial era, during the time when the country had instituted a body of “Oumanas”, public control was governed by Muslim rules governing the organization of public funds. These rested on the body of the Oumanas (amine plural). The latter are recruited from among the noble merchants who applied to the state finances the accounting rules in use in their profession (commerce) and answer by their own fortune for the sincerity of their management. The Oumanas were placed under the direct authority of the Amine El Oumanas, which acts as finance minister.

- The Amine Eddakhl: (Amine of revenues) responsible for the recovery of state revenues.
- The Amine Elkharaj: (Expenditure Amine) responsible for the payment of state expenditure

ISSN: 2961-6611

- Amine Elhassab: Who was in charge of the accounts and controlled the accounting transmitted by the oumanas.

In the absence of precise budgetary rules the oumanas applied rules of revenue and expenditure often disparate.

Moreover, the traditional Moroccan public ethic derives its origins from the Muslim administrative organization when the Sultan of the Amir surrendered several Wali assisting him to exercise his duties as protector of believers against abuse. In this respect we find the Wali of Alkadae (Minister of Justice) the Wali of the Hisba (Financial Control Authority) and the Wali of Al Madhalim (Ombudsman).

This previous organization modernized under the influence of the colonial passage through Morocco, the latter instituted control bodies that operate according to procedures, subject to legal texts.

Internal administrative control takes two forms:

- The hierarchical control is the work of any head of the Executive Administration in particular the Secretary General and the Directors.
- The General Inspectorate is directly attached to the Minister and informs him regularly about the operation of the services.

It is also responsible for examining any request entrusted to it, for carrying out any inspection, investigation or study.

The control by means of inspection may relate to the operating conditions of the services. It may also be a check of regularity.

The control of Public Finance takes several forms. It is prioritized and posteriori, and covers the various categories of public services. The concern for good management of public's funds led especially the ministry of finance to extend control along the circuits of expenditure and revenue of public services

The GIF is now active to get out of control, mainly tax collectors. It organizes its work in a wider and more balanced field, which includes more and more administrations and public institutions.

Priority control is exercised by accounting officers and financial controllers placed with public administrations and institutions.

The control of Finance is also exercised quite strongly by the Budget Directorate and by the Control of Expenditure Commitments.

The reform of the Directorate of Public companies and privatization in 1978 and the 2003 project were aimed at reducing the burden of financial control on commercial and industrial public companies.

These laws organizing the operation and implementation of the budget and those relating to its controls have undergone several reforms that have affected the substance and the form of each State function and the control of public finances and that in particular is involved and is also the subject of several reforms aimed at modernizing it.

Internal control in the administration of consists of three authorities which are internal administrations in the Ministry of Economy and Finance in particular the CCE and financial control, the FGK which ensures the control of the body of public accountants and which practices accounting control and general financial inspections. Being organized from the following achievement:

Commitment and expenditure control should control the initiation of the authorizing officers' expenses and should give its approval so that the scheduling can take place, once the order of expenditure or revenue is received by the public accountant, the latter should in turn check the legality and regularity of this order before committing or making any money or generating revenue, on behalf of the public treasury, these public accountants are in turn controlled by the FGK with which they must make an accounting report.

The general financial inspection carries out a control that succeeded the two controls that were initially applied to public funds.

In a context of international administrative modernization, public authorities have been forced to follow a pace of development of administrative management, in a constantly evolving international context, the thing that has pushed administrative and political powers to make changes in the system of management of public affairs as a whole by introducing decrees and legislation as part of an administrative reform aimed in particular at the modernization and adoption of public management at an international rate of modernization, this is due to the gradual implementation of results-based management within the various departmental departments and also within the public institutions in order to make available to them a new management tool aimed in particular at achieving effectiveness and efficiency in the management of public funds.

As a result of the reforms that have made Morocco and its administrations a vast project of modernization of its services and its operating tools (scheduling, accounting and control).

Inter-administrative control has undergone some changes which have affected the position of the control against the supervised bodies. This is due to the very remarkable merging of commitment control and expenditure and the general treasury of the kingdom in the old structure, this form applies

ISSN: 2961-6611

the will of the public authorities to give more flexibility but also a huge accountability, to the authorizing officers and who must carry out their functions as part of a results-based management with the help of new management systems, which will allow through a program contract the central services and those deconcentrated and has action plans, to achieve more effectiveness and efficiency in public management.

VI. CONCLUSION

The control of public finances as it currently exists is a powerful tool to help the public authorities and to ensure the proper functioning of public funds.

To answer this concern that various controls are involved in the development and implementation of budget decisions through legislation and new management approaches to promote public management and modernize administration, while ensuring the audit and regularity of budget decisions.

References

1) A.BENBRIK :'' l'IGF ... au cœur de la transparence''. la nouvelle tribune. n°03.09 janvier 2000.
2) André Barilari : le contrôle financier comptable, administratif et juridictionnel des finances publiques, 2003.
3) BENNANI : « L'agent comptable » revue marocaine d'administration locale et de développement n° 3 Rabat
4) GUAY Marie-Michèle, Performance et secteur public: Réalités, enjeux et paradoxes, 2e édition, Presses de l'Université du Québec, 2002.
5) Jacques Magnet, « Eléments de comptabilité » publique », LGDJ, 1991.
6) Michel power, la société de l'audit : l'obsession du contrôle, la découverte, paris, 2005.
7) Mohammed Harakat, les finances publiques, édition 2010.
8) Stéphane flizot, « les relations entre les institutions supérieures de contrôle financier et les pouvoirs publics de l'union européenne ».LGDJ 2003 panorama des finances publique dans le monde » in RFFP, n°101, mars 2008.
9) « La réforme du contrôle de la dépense publique ». Revue ALMALIYA février 2007.
10) « la mission de contrôle du département de l'économie et des finances ». Revue ALMALIYA n°26. avril 2001.
11) Décret royal 21/04/1967 portant règlement général de la comptabilité publique
12) Loi 69-00 relative au contrôle financier de l'Etat sur les entreprises publiques et autre organismes.
13) La loi organique relatif a la loi de finance
14) Arrêté du ministère d'économie et des finances.
15) Note de présentation du projet de loi relative à la gouvernance et au contrôle financier de l'Etat sur les EEP et autres organismes.

ISSN: 2961-6611

The Relationship between Socially Responsible Human Resource Management and Employees Organizational Commitment: an integrative model of social exchange in the organization

MAKATI Safaa[#1], BENABDELHADI Abdelhay[*2]
[#1 *2] *Economy and management department,* [#1 *2] *Ibn Tofeil University*
[#1 *2] *Campus universitaire Maamora BP:2010, Av. de L'Université, Kenitra, Morocco*
[#]1safaa_makati@hotmail.fr
*2 benabdelhadi.abdelhay@yahoo.fr

Abstract: ***This article explores the different mechanisms by which the implementation of a socially responsible system of human resources management is likely to positively influence the organizational commitment of employees. Our goal is to fill the theoretical gap by proposing a research model synthesizing the different relationships between the main concepts through two mechanisms of social exchange namely: perceived organizational support and organizational trust***

Keywords**—Ssocially responsible human resource management, Organizational Commitment, Social Exchange, Organizational support, trust.**

I. INTRODUCTION

In order to meet the new requirements of competitiveness and flexibility, companies and organizations are increasingly in the process of orienting their policy and management style towards responsible management through the implementation of socially responsible practices and policies[3]. Corporate Social Responsibility (CSR) which appears to be a voluntary commitment of the company in the social and environmental fields, beyond the economic and legal aspects of its activity [4], takes the social company's relation with its stakeholders, mainly employees, towards new concerns in order to be a Socially Responsible Company. In the case of internal management, authors and researchers introduce the concept of "Socially Responsible Human Resource Management (SR-HRM)" [5]; [6]; [7];[8];[9]; [10]. Reflecting the internal aspect of CSR [2]; [11] SR-HRM refers to all CSR practices that are directly aimed to employees and that influence their behaviours and attitudes like motivation, commitment and implication etc.

Interested in studying the Organizational Commitment (OC) of employees[2];[12];and [13] research's classify employee-related CSR practices into seven categories and highlight their direct influence on employee involvement.

Considering employees as social capital and based on the social exchange theory [14],we propose a theoretical model to explain the relationship between the SR-HRM and the three OC dimensions[15] through two exchange mechanisms namely "perceived organizational support "and" trust in the organization. The significant contribution of this article also lies in the fact that no study has, to our knowledge, proposed a theoretical model integrating mediating and moderating variables of the influence of socially responsible HRM on the organizational commitment of employees. To do this we will first we will review the main concepts related to human resources' management (HRM) and its links with CSR and OC. And finally, we will determine all the links characterizing our research model.

II. LITERATURE REVIEW : CSR, SR-HRM, OC

Through this work, we hope to better identify the CSR-HRM relationship before proposing a definition of the "socially responsible HRM" and "organizational commitment" concept. The linking of two major conceptual frameworks such as "SR-HRM" and "OC" will undoubtedly enrich the existing academic literature on the subject.

A. CSR definitions

Corporate Social Responsibility (CSR) is a concept that differs across societies, cultures and ideologies. Generally speaking, Corporate Social Responsibility (CSR) reflects all of society's social, environmental and economic concerns and their interactions with stakeholders on a voluntary basis.

The term of CSR has been used in different contexts over the last 40 years[3]. The original concept of CSR came into being in the 1950s and generally regarded the social aspect of CSR as referring directly to its responsibilities beyond economic and legal obligations [16]; [17]; [18]. Since the definition of the social responsibility of the company known as CSR is not unanimous neither at the level of its theoretical

ISSN: 2961-6611

bases nor of its societal and organizational implications [8]. According to [19], there are 37 academic definitions of CSR that highlight its main categories and objectives, as well as its results and influence on the company's performance. In all of its definitions there are authors who do not want CSR in business [20], others who are only interested in the economic and legal dimensions of CSR, a third group that adds the responsibility towards society and finally those who supplement it with a discretionary responsibility [17]; [21].

Starting from the fact that CSR is built with the stakeholders of the company; we have adopted the only definition of ISO 26 000 that considers CSR as "the responsibility of an organization for the impacts of its decisions and activities on society and the environment resulting in ethical behaviour and transparent which: 1) contributes to sustainable development, including the health and well-being of society; 2) takes into account the expectations of stakeholders; 3) respect the laws in force while being consistent with international standards of behaviour; 4) is integrated throughout the organization and implemented in its relationships ".

Reading this definition, we limited ourselves to showing the influence of CSR on one of these stakeholders, namely employees. In fact, human resources seem to be a key player in developing and deploying the approach within companies as they are the first player to be influenced by CSR practices. Health and safety, the well-being, development of the collaborators, the evolution of behaviours and attitudes constitute the DNA of the function in the company [8]. Thus, we wish in the following point to better identify and think about the CSR / HRM relationship.

B. SR-HRM: Definitions and practices

To define the socially responsible HRM, we refer to the concept of Personnel-Mix developed by [22] which seems appropriate to our research. In this context, SR-HRM is perceived as a social steering instrument that makes it possible to assess the degree of alignment of HRM practices and policies with the principles of CSR [6].

Considered as a coherent set of human resource practices that promote employee involvement and commitment, SR-HRM is a set of important dimensions during a sustainable employment relationship with the organization [6];[23]. Moreover, sustainable HRM aims to reconcile efficiency and economic efficiency with the environmental and social principles of CSR. To do this, human resources managers must integrate and preserve the interests of each stakeholder in the long term. It is therefore a question of integrating the principles of social responsibility into the multiple HRM practices with the help of several actions that act on the different dimensions of the well-being of individuals, all of which are experienced by the organization.

A human resources management aligned to the principles of CSR (SR-HRM) leads to taking into account various stakeholders interests, the establishment of a space of mutual dialogue and exchanges and involving, in particular, employees in decisions, beyond the traditional processes of employee representation [24]. This gives them the opportunity to express their expectations and their points of view on the company's project, therefore to have the feeling of control over the decisions of the company [24].

HRM in a CSR perspective realizes the traditional mission of the company through training, recruitment, skills development and other policies, yet these approaches are more humane by offering more autonomy to employees in work, and social support illustrated by reasonable charges and recognition practices [6]. Social Responsible-HRM practices identified in the literature [25]; [26]; [27]; [6]; [28]; [23]; [29];[30] mainly concern prevention in health and safety at work; work / family balance; training and development; diversity management etc. From these clarifications we present in the following table the internal CSR practices of the literature on *Socially Responsible Human Resources Management.*

TABLE I
INTERNAL CSR PRACTICES

SR-HRM practices	Characteristics	Authors
Forward planning of jobs and skills development	- The employee is seen as a potential and an opportunity in terms of skills and abilities - Anticipatory risk taking in the management of career paths - Development of internal promotion - Employability development of employees	[31] [32]
Recruitment and social integration	- Diversity Recruitment Policy - The inclusion of disabled workers - Workplace Diversity - Fight against discrimination - Equal opportunities - Men and women equality	[27] [31] [28]
Work conditions	- Health and safety at work, - Well-being and satisfaction of the workers, - Quality of work. - Implementation of a plan to improve working conditions	[26] [6] [11]
Working time	- Development of work-life balance programs - Proposals for childcare solutions within the company - Taking into account long commutes - Optimization of maternity and parental leave	[31]
Human rights.	- Justice and equity - respect for the economic, social, cultural, and political	[33] [30]

ISSN: 2961-6611

	rights of employees	
Training and Education	- Development of Validation of Acquired Experience (VAE) - Introduction of the individual right to training - Training of employees in New Technologies	[6] [30] [30]
Internal communication and social relations	- Conducting staff satisfaction surveys - Realization of social climate surveys - Set up of ideas box. - Development of social and intranet networks dedicated to CSR communication within the company.	[22] [31]
Workers compensation	- Equal pay attribution - Set up a company savings maney plan linked to solidarity sites - Promote internal equity of remuneration	[27] [34] [34]

Personal elaboration

B. *Organizational Commitment: Definitions and dimensions*

Organizational Commitment is a concept that, because of its positive consequences for both individuals and the organization, has attracted significant interest from researchers. Indeed, it is one of the most studied concepts in management sciences and especially in human resources. A first definition of Organizational Commitment illustrates the "*degree of attachment of an individual to his or her organization*"[35] . Commitment as a term only translates and explains the relationship between the person and the company, but it has many definitions.[36] has identified thirty notions related to Commitment its objective is to build a taxonomy of the different Commitment forms based on collecting and the analysing of these thirty concepts. Grouped into five broad categories, Organizational Commitment occupies an important place in this ranking.

Based on Social Exchange theory [37] make the distinction between the motivation of individuals to participate in the organization (to join the organization and stay there) and the motivation to produce, which concerns their propensity to be effective in the tasks they perform. This distinction can be spotted in the conceptualization of the organizational Commitment of [37] which includes three characteristics: 1) a high degree of belief and adherence to the values and goals of the organization; 2) willingness to exert considerable effort on behalf of the organization and 3) a determined desire to remain a member of the organization.

Since the mid-eighties, a reconceptualization of commitment has gradually emerged. Based on the remarks of [38] whose work currently serves as the basis for the majority of research, we retain the affective, calculated and normative Commitment dimensions.

- *Affective Commitment*

Affective Commitment is defined on the basis of three dimensions: 1) identification with the organization values, 2) engagement to the achievement of its objectives and 3) emotional attachment to it. So we talk about affective commitment when the employee wants to stay in the organization [15] . From this perspective,[39] proposes the following definition of OC *"... (a) a strong belief in, and acceptance of, the organization's goals and values, (b) a willingness to exert considerable effort on behalf of the organization, and (c) definite desire to maintain organizational membership* ". It follows that the employee's connection to his organization is at a level of abstraction that has the effect of evading any form of personal interest other than those relating to the field of public interest [38].

- *Continuance Commitment*

Continuance Commitment refers to an individual's knowledge of the costs associated with leaving the organization: from a reasoned choice, individuals judging it more appropriate to remain loyal to the network than to leave it, a disadvantageous tangible and intangible investments. This type of commitment is only realized when the person feels the sense of developing costs that may be lost by leaving the organization [38].

- *Normative Commitment*

Normative Commitment refers to the feeling of obligation to remain working in the organization by moral duty, loyalty or to complete a project in which the person is engaged (duty to stay in the network given what the network has brought them). For [40] Normative Commitment is defined as "*the set of internalized normative pressures that push an individual to act in the direction of the objectives and interests of the latter, to do, not to profit from it, but because it is good and moral to do so* ".

C. *SR-HRM influence on Organizational Commitment: Social Exchange Theory : analytical framework*

The association between CSR and Human Resources can contribute to three uses: 1) Social responsible Human Resource Management in the sense of sustainability; 2) better integration of financial and environmental concerns in HR management and 3) optimization of the contribution of HRM to better overall performance of the organization [23]. In [41] model, all determinants of the internal environment are directly related to job satisfaction and organizational commitment [8]. In questioning the effects of perceived socially responsible practices on the attitudes and behaviours of employees at work. [42] confirm that the perception of these practices is positively related to organizational commitment and job satisfaction .

The influence of SR-HRM on employees, their perceptions and commitment can be explained by social exchange theory [3]. This theory explicitly recognizes the different interests of the exchange parties and their influence on the relationships, and recommend the importance of

ISSN: 2961-6611

considering that the contributions of one party are based on the previous contributions of the other party following compliance with the standard of reciprocity [43].

The social exchange theory is a century-old theory whose premises go back mainly to the work of ethnographers and anthropologists. Interest in this theory has been increased with the rise of the social sciences in the second half of the twentieth century. According to the theory, the more or less tangible and expressive exchanges of resources between two parties, such as sense of belonging, pride or prestige, are at the very foundation of the processes of social interaction and reveal predictive structural regularities of individual and collective behaviour. The theory of social exchange, by its ability to consider a wide variety of human behaviours beyond the classical framework of economic theories, such as altruism or spontaneous cooperation, has been developed theoretical and an unprecedented empirical examination in the social sciences as it has been widely adopted by researchers in management sciences [44]. The theory has notably established itself as the dominant theoretical framework in the study of relationships at work [45]; [46]; [47].

From a CSR perspective, social exchange theory suggests that any attitude and / or behaviour of employees is linked to their perception of the values and benefits they receive from belonging to the organization [3]. In this respect, [1] argue that a strong involvement of the company towards its employees, embodied in the practices of social responsibility, as well as the trust that these place in the top management have an important impact on the construction of organizational commitment. According to this theory, social exchange relationships are characterized by a long-term orientation, the exchange of tangible and intangible resources such as perception of justice and organizational support, as well as trust, commitment, involvement and attachment [46]. On the basis of the above, we retain the mediating effect of trust and organizational support as key elements reflecting the employee-organization exchange relationship.

III. Integrative Model of SR-HRM influence on Organizational Commitment

The influence of socially responsible HRM on organizational commitment is a topic of research that has been little discussed by researchers. This attention is focused on global CSR practices in its external and internal dimensions simultaneously. The lack of studies in this subject can be attributed to many different causes, such as the lack of a clear and precise definition of socially responsible HR practices , for a clear measure of these as well as a mediator explaining the intensity of the relationship.

A. Organizational Support and Trust as Intermediate variables

We will try essentially in this paragraph to explain the theoretical framework in which these variables of social exchange fit.

1) Perceived Organizational Support

In the literature there is a general consensus on the importance that the perception of organizational support can play in business-employee relationships. Developed by [48] this concept makes it possible to study the employee's perception of the extent to which the organization values its contribution and is concerned about its well-being. In this perspective, perceived organizational support is defined as "*the belief of an employee about the degree of care and attention that the company gives to it and how it values its contributions*" [48].

Organizational support theory [49];[48] suggests that employees develop a perception of how important the organization is to their contributions and well-being. This theory also states that the development of the SOP is encouraged by the tendency of employees to attribute human characteristics to the organization [48]. In fact, employees respond to their perceived treatment by the organization by modifying their efforts to achieve organizational objectives and by remaining committed to achieving the company's objectives [50]. This is perfectly in line with[43] principle of reciprocity, which is the basis of the majority of social exchange constructs within the firm, and which states that "*the employee who receives organizational support develops a sense of self-esteem. The obligation to be concerned about the well-being of one's organization, and tends to want to help it in achieving its objectives* "[46].

Numerous studies and meta-analyses have shown that perceived organizational support was positively and significantly associated with performance, emotional involvement, job satisfaction, good mood and well-being at work, the desire to stay in the workplace organization and citizenship behaviours [50][55]. Conversely, perceived organizational support is negatively related to absenteeism, anxiety and burnout [50].

2) Organisational Trust

Trust is a concept strongly debated by researchers for thirty years, as it is discussed in several fields of research: in social psychology [14], in sociology [51] , in human Resource management [52] , economics [53] , and marketing [54]. Thus trust is defined as "*the willingness of one party to make itself vulnerable to the actions of the other party, based on the expectation that the other party will perform actions that are important to oneself, without any form of control or monitoring is necessary* " [55]. Moreover, trust could be approached from many theoretical frameworks such as the theory of social exchanges [14], the theory of attributions [56], the theory of transaction costs [57], the theory of the system [51], [64]or resource theory [58].

ISSN: 2961-6611

As part of a social exchange perspective, trust is presented as a major component that is built in a process of lasting and reciprocal exchange [14]. Thus trust has been recognized as an essential component in maintaining a successful long-term relationship [54]. Indeed, without some degree of trust it is almost impossible to establish concerted action within an organization [59].

Research on the role of organizational trust in the development of organizational commitment has established that it is related to antecedents and attitudes that are centred on social exchange with the organization[60]. It also appears that trust as a psychological state consists of two major components [3]. At this level [61] distinguishes affective trust from cognitive trust. Confidence based on cognition describes a rational assessment of an individual's ability to fulfil his obligations and, therefore, reflects beliefs about the reliability, consistency and competence of that individual. In contrast, trust based on the affects reflects an emotional attachment that stems from the mutual care and concerns that exist between individuals. It reflects the beliefs of availability, caring and openness. Our conceptualization reflect that trust positively influence employee organizational commitment.

B. Overview of the Integrative Model

The understanding and conception of employees 'perception of socially responsible practices has led us to question the impact of socially responsible HRM on employees' organizational commitment. Based on the precept that employees act in exchange for benefits received and their perception of the organizational environment [46]. We support the hypothesis that an adoption of CSR practices in HRM and a strong involvement in the field reinforces their commitment through social exchange mechanisms: the perception of organizational support and organizational trust. Our research model thus reflects two major types of relationships. A part validated and tested empirically by the literature and another part that we propose for the first time as part of this research.

As a mechanism for social exchange [14] the mediating role of organizational trust exists when an employee feels that his company is concerned about his interests. Therefore he assesses the reliability of the various events and actions held at work. It will stimulate organizational involvement in return [46]. While expressing organizational trust as employees' beliefs about the likelihood that their company's future actions will be beneficial to them [44], we suggest that the expectations and beliefs of employees that their organization will carefully, equitably and precisely invoke an attachment and an organizational commitment among them.

The main idea that emerges from our conceptual model, retracing the provisional answers to the research problem, is that the voluntary adoption of socially responsible HR practices by companies attests to the ability of these companies to earn the trust of its employees and subsequently generate a sense of mutual obligation. This sense of obligation is materialized in our case in the form of organizational implication. To the same extent [62] refers to the theory of attachment to highlight the fact that trust as a direct result of corporate citizenship and CSR initiatives inculcates employees' commitment to their organization.

The link between the SOP and the affective organizational commitment dimension has been widely demonstrated in previous research [50]; [66]. [67] Even established that affective organizational commitment plays a mediating role between the SOP and the intention to leave the organization. Since the direct effect of the SOP on affective commitment has been widely documented, organizational trust plays a mediating role between these variables in a number of works. [49] and [68] specifically invoke organizational trust to explain the effects of the SOP. They note that the SOP creates the trust that the organization is able to fulfil its obligations and reward individuals' efforts. The motivational foundations of trust lie in the fact that the employment relationship cannot be sustainable without the prior existence of trust [68].

According to the social exchange theory, it is the trust created by the favourable social exchange that encourages the employee to develop favourable reactions to the organization [3]. In the absence of trust, social exchange cannot exist and only a more economic and transactional exchange can exist between the employee and his or her organization. The mediating role of trust between human resource management practices and retention variables has been found in previous work. [69] established a partial mediation of organizational trust between organizational justice and, on the one hand, affective organizational commitment, on the other hand, the intention to leave. However, we can think that this type of result will be transposable to the case of the SOP.

ISSN: 2961-6611

Figure 1: Internal CSR influence on employee's Commitment Research Model

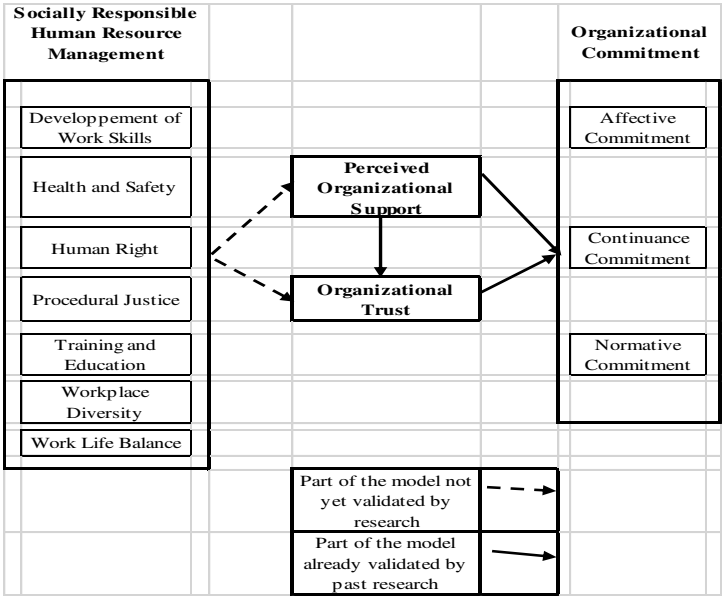

All in all, our arguments are supported by abundant research that reveals that perceived organizational support and organizational trust are strong antecedents of organizational commitment.

IV. CONCLUSION

This research confirms the importance of concepts such as perceived organizational support and trust for a better understanding of the process by which internal CSR is able to influence the organizational commitment of employees. Applying the theoretical foundations of relational psychology, the social exchange theory allowed us to propose a conceptual model reflecting all the mechanisms of this influence. The analysis of the literature in this area highlights the existence of direct and positive links between the two variables (dependent and independent) and explain the proposed model.

In addition, through the model thus designed, the current study also has important implications for managers. More specifically, managers should be concerned with integrating CSR practices into their HRM strategies so that they bring real added value to the company. In fact the company that wants to adopt a socially responsible behaviour attributes an important role to the human dimension and to the management of the human resources. This amounts to involve all employees in the overall strategic decisions of the company. CSR then becomes, in its operational dimension, inseparable from HRM.

It remains to be mentioned that this CSR-HRM relationship will incur additional costs for the company, but in return, it would prevent significant risks both internally and externally and have serious direct or indirect repercussions on its performance. For a CSR approach to be truly beneficial for both the company and its employees, it must be built coherently, and be part of a win-win exchange while aiming for a longer horizon, wider than the short term or that of a marketing vision.

Finally, we are aware that the variables of the conceptual model proposed in this article are quite numerous, and the relations between them are very complex. This article paves the way for new and very important research perspectives for researchers and doctoral students who wish to study and understand the behaviours and attitudes of employees of socially responsible enterprises.

REFERENCES

[1] J. Collier et R. Esteban, « Corporate social responsibility and employee commitment », *Bus. Ethics Eur. Rev.*, vol. 16, nº 1, p. 19-33, janv. 2007.
[2] S. Brammer, A. Millington, et B. Rayton, « The contribution of corporate social responsibility to organizational commitment », *Int. J. Hum. Resour. Manag.*, vol. 18, nº 10, p. 1701-1719, oct. 2007.
[3] A. Benabdelhadi et S. Makati, « INFLUENCE DES PRATIQUES SOCIALEMENT RESPONSABLES SUR LA PERFORMANCE ORGANIS », *CCA*, nº 5, p. 171-195, 2018.
[4] J.-P. Gond et F. Dejean, « HAL-SHS - Sciences de l'Homme et de la Société - Responsabilité sociétale de l'entreprise : enjeux stratégiques et méthodologies de recherche », 2005. [En ligne]. Disponible sur: https://halshs.archives-ouvertes.fr/halshs-00005763. [Consulté le: 09-janv-2019].
[5] M. Orlitzky et J. Shen, « Corporate Social Responsibility, Industry, and Strategy », *Ind. Organ. Psychol.*, vol. 6, déc. 2013.
[6] D. Beaupré, J. Cloutier, C. Gendron, A. Jiménez, et D. Morin, « Gestion des ressources humaines, développement durable et responsabilité sociale », *Rev. Int. Psychosociologie*, vol. XIV, nº 33, p. 77, 2008.
[7] J. Shen et C. Jiuhua Zhu, « Effects of socially responsible human resource management on employee organizational commitment », *Int. J. Hum. Resour. Manag.*, vol. 22, nº 15, p. 3020-3035, sept. 2011.
[8] N. Barthe et K. Belabbes, « La « GRH socialement responsable » : un défi pour les entreprises engagées dans une démarche RSE », *Manag. Avenir*, vol. 83, nº 1, p. 95, 2016.
[9] A. BOUCHIKHI, Y. KHATORI, et H. BADDIH, « GESTION RESPONSABLE DES RESSOURCES HUMAINES (2) : ANALYSE BI-SECTORIELLE | BOUCHIKHI | Revue d'Etudes en Management et Finance d'Organisation », 2016. [En ligne]. Disponible sur: https://revues.imist.ma/index.php?journal=REMFO&page=article&op=view&path%5B%5D=6464. [Consulté le: 09-janv-2019].
[10] A. Benabdelhadi et S. Makati, « Application of corporate social responsibility approaches in human resources management: a qualitative study in the Moroccan context », vol. 2, p. 12, 2017.
[11] V. Skudiene et V. Auruskeviciene, « The contribution of corporate social responsibility to internal employee motivation », *Balt. J. Manag.*, vol. 7, nº 1, p. 49-67, janv. 2012.
[12] A. Ali, E. Nasruddin, et S. K. Lin, « The Relationship between Internal Corporate Social Responsibility and Organizational Commitment within the Banking Sector in Jordan », *Int. J. Econ. Manag. Eng.*, vol. 4, nº 7, p. 20, 2010.
[13] I. L. Santoso, « The Impact of Internal CSR towards Employee Engagement and Affective Commitment in XYZ Hotel Surabaya », vol. 2, nº 2, p. 10, 2014.
[14] P. M. Blau, *Exchange and Power in Social Life*. Transaction Publishers, 1964.
[15] J. P. Meyer et N. J. Allen, « A three-component conceptualization of organizational commitment », *Hum. Resour. Manag. Rev.*, vol. 1, nº 1, p. 61-89, mars 1991.
[16] H. R. Bowen, *Social Responsibilities of the Businessman*, [1st ed.]. New York: Harper & Brothers, 1953.
[17] A. B. Carroll, « A Three-Dimensional Conceptual Model of Corporate Performance », *Acad. Manage. Rev.*, vol. 4, nº 4, p. 497, oct. 1979.
[18] A. Crane, A. McWilliams, D. Matten, J. Moon, et D. S. Siegel, *The Oxford Handbook of Corporate Social Responsibility*. Oxford, New York: Oxford University Press, 2008.
[19] A. Dahlsrud, « How corporate social responsibility is defined: an analysis of 37 definitions », *Corp. Soc. Responsib. Environ. Manag.*, vol. 15, nº 1, p. 1-13, janv. 2008.
[20] M. Friedman, « The Social Responsibility of Business Is to Increase Its Profits », in *Corporate Ethics and Corporate Governance*, W. C. Zimmerli, M. Holzinger, et K. Richter, Éd. Berlin, Heidelberg: Springer Berlin Heidelberg, 2007, p. 173-178.

ISSN: 2961-6611

[21] A. B. Carroll, « The pyramid of corporate social responsibility: Toward the moral management of organizational stakeholders », *Bus. Horiz.*, vol. 34, nº 4, p. 39-48, juill. 1991.
[22] D. Crozet et B. Martory, *Gestion des ressources humaines*. 2016.
[23] N. S. Bchara, N. Dubruc, et S. Berger-Douce, « Le discours de la GRH dans les outils RSE », p. 26, 2016.
[24] L. Mazari, S. Berger-Douce, et B. Deschamps, « L'impact des pratiques RSE sur la relation entre repreneur et salariés : une analyse par la légitimité du repreneur », p. 31, 2016.
[25] R. Coulon, « Responsabilité sociale de l'entreprise et pratiques de gestion des ressources humaines », *Rev. L'organisation Responsab.*, vol. 1, nº 1, p. 48, 2006.
[26] M. El Abboubi et A. Cornet, « La PME et les processus de certification sociale SA 8000: Le cas de WebTel », *Rev. Int. PME Économie Gest. Petite Moy. Entrep.*, vol. 20, nº 3-4, p. 95, 2007.
[27] M. E. Abboubi et F. E. Kandoussi, « Le virage de la responsabilité sociale au Maroc. Le cas du secteur agroalimentaire », *Reflets Perspect. Vie Econ.*, vol. Tome XLVIII, nº 4, p. 69-77, 2009.
[28] M. Thévenet, « Crise et GRH », *Rev. Francaise Gest.*, vol. n° 193, nº 3, p. 37-41, mai 2009.
[29] S. Borter, F. Gonin, et T. Bornand, « VERS UN MODELE DE GRH DURABLE », p. 26, 2011.
[30] R. Giuliano, « L'influence sur la productivité du travail d'une gestion socialement responsable des ressources humaines : l'analyse du cas de la formation par genre », *Humanisme Entrep.*, vol. n° 309, nº 4, p. 37-60, 2012.
[31] C. Vermeulin et F. Vermeulin, *Comprendre et entreprendre une démarche RSE la responsabilité sociétale pour tous les entrepreneurs*. La Plaine Saint-Denis: Afnor éd., 2012.
[32] A. Dietrich, « L'employabilité à l'épreuve de la RSE ou la RSE à l'épreuve de l'emploi ? », *Rev. Lorganisation Responsab.*, vol. Vol. 5, nº 1, p. 30-38, 2010.
[33] J.-P. Gond et Igalens, *Manager la responsabilité sociale de l'entreprise*, Darios et Pearson. France, 2012.
[34] H. Poissonnier et D. Drillon, « Le développement de la gestion durable des ressources humaines : un éclairage par les outils de pilotage des performances », *Vie Sci. Entrep.*, vol. 179-180, nº 2, p. 22, 2008.
[35] J. E. Mathieu, « A causal model of organizational commitment in a military training environment », *J. Vocat. Behav.*, vol. 32, nº 3, p. 321-335, juin 1988.
[36] P. C. Morrow, « Concept Redundancy in Organizational Research: The Case of Work Commitment^ », p. 16, 1983.
[37] L. W. Porter, R. M. Steers, R. T. Mowday, et P. V. Boulian, « Organizational commitment, job satisfaction, and turnover among psychiatric technicians », *J. Appl. Psychol.*, vol. 59, nº 5, p. 603-609, 1974.
[38] J. Meyer et N. Allen, *Commitment in the Workplace: Theory, Research, and Application*. Thousand Oaks, California, 1997.
[39] R. T. Mowday, L. W. Porter, et R. M. Steers, *Employee-organization linkages the psychology of commitment, absenteeism, and turnover*. New York Academic Press, 1982.
[40] Y. Wiener et Y. Vardi, « Relationships between job, organization, and career commitments and work outcomes—An integrative approach », *Organ. Behav. Hum. Perform.*, vol. 26, nº 1, p. 81-96, août 1980.
[41] J. L. Price, « Reflections on the determinants of voluntary turnover », *Int. J. Manpow.*, vol. 22, nº 7, p. 600-624, nov. 2001.
[42] C. Closon, « La perception de la responsabilité sociale des Entreprises : adaptation et validation française de l'échelle de Maignan et Ferrell, 1999 », *Psychol. Trav. Organ.*, vol. 17, nº 1, p. 43-56, 2011.
[43] A. W. Gouldner, « The Norm of Reciprocity: A Preliminary Statement », *Am. Sociol. Rev.*, vol. 25, nº 2, p. 161, avr. 1960.
[44] R. Cropanzano et M. S. Mitchell, « Social Exchange Theory: An Interdisciplinary Review », *J. Manag.*, vol. 31, nº 6, p. 874-900, déc. 2005.
[45] J. A.-M. Coyle-Shapiro et L. M. Shore, « The employee–organization relationship: Where do we go from here? », *Hum. Resour. Manag. Rev.*, vol. 17, nº 2, p. 166-179, juin 2007.
[46] N. Tahri, *Responsabilité sociale des entreprises et comportements citoyens: application au cas de la mutuelle ; thèse de doctorat*. Cormelles-le-Royal: Éd. EMS, Management & société, 2014.
[47] O. Farooq, M. Payaud, D. Merunka, et P. Valette-Florence, « The Impact of Corporate Social Responsibility on Organizational Commitment: Exploring Multiple Mediation Mechanisms », *J. Bus. Ethics*, vol. 125, nº 4, p. 563-580, déc. 2014.
[48] R. Eisenberger, R. Huntington, S. Hutchison, et D. Sowa, « Perceived organizational support », *J. Appl. Psychol.*, vol. 71, nº 3, p. 500-507, 1986.
[49] R. Eisenberger, P. Fasolo, et V. Davis-LaMastro, « Perceived organizational support and employee diligence, commitment, and innovation », *J. Appl. Psychol.*, vol. 75, nº 1, p. 51-59, 1990.
[50] R. Eisenberger, S. Armeli, B. Rexwinkel, P. D. Lynch, et L. Rhoades, « Reciprocation of perceived organizational support », *J. Appl. Psychol.*, vol. 86, nº 1, p. 42-51, févr. 2001.
[51] N. Luhman, *Trust ; And, Power: Two Works - Niklas Luhmann - Google Livres*. 1979.
[52] J. Cook et T. Wall, « New work attitude measures of trust, organizational commitment and personal need non-fulfilment », *J. Occup. Psychol.*, vol. 53, nº 1, p. 39-52, mars 1980.
[53] M. Sako, « Price, Quality and Trust: Inter-firm Relations in Britain and Japan - Mari Sako, Professor of International Business Mari Sako - Google Livres », 1992.
[54] S. D. Hunt et R. M. Morgan, « ORGANIZATIONAL COMMITMENT: ONE OF MANY COMMITMENTS OR KEY MEDIATING CONSTRUCT? », *Acad. Manage. J.*, vol. 37, nº 6, p. 1568-1587, déc. 1994.
[55] R. C. Mayer, J. H. Davis, et F. D. Schoorman, « An Integrative Model of Organizational Trust », *Acad. Manage. Rev.*, vol. 20, nº 3, p. 709, juill. 1995.
[56] B. Hesketh, « Attribution theory and unemployment: Kelley's covariation model, self-esteem, and locus of control », *J. Vocat. Behav.*, vol. 24, nº 1, p. 94-109, févr. 1984.
[57] O. E. Williamson, « Markets and hierarchies : analysis and antitrust implications : a study in the economics of internal organization. », 1975. .
[58] J. Barney, « Firm Resources and Sustained Competitive Advantage », 1991. [En ligne]. Disponible sur: https://journals.sagepub.com/doi/10.1177/014920639101700108. [Consulté le: 09-janv-2019].
[59] R. Kramer et T. Tyler, *Trust in Organizations: Frontiers of Theory and Research - Google Livres*. 1996.
[60] R. C. Mayer et M. B. Gavin, « Trust in Management and Performance: Who Minds the Shop While the Employees Watch the Boss? », *Acad. Manage. J.*, vol. 48, nº 5, p. 874-888, oct. 2005.
[61] D. J. McAllister, « Affect- and Cognition-Based Trust as Foundations for Interpersonal Cooperation in Organizations », *Acad. Manage. J.*, vol. 38, nº 1, p. 24-59, 1995.
[62] C.-P. Lin, « Modeling Corporate Citizenship, Organizational Trust, and Work Engagement Based on Attachment Theory », *J. Bus. Ethics*, vol. 94, nº 4, p. 517-531, juill. 2010.
[63] H.-R. Kim, M. Lee, H.-T. Lee, et N.-M. Kim, « Corporate Social Responsibility and Employee–Company Identification », *J. Bus. Ethics*, vol. 95, nº 4, p. 557-569, sept. 2010.
[64] M. Gupta et O. Sayeed, « Social Responsibility and Commitment in Management Institutes: Mediation by Engagement », *Verslas Teor. Ir Prakt.*, vol. 17, nº 3, p. 280-287, sept. 2016.
[65] Ž. Prutina, « THE EFFECT OF CORPORATE SOCIAL RESPONSIBILITY ON ORGANIZATIONAL COMMITMENT », vol. 21, p. 22, 2016.
[66] L. M. Shore, J. A.-M. Coyle-Shapiro, X.-P. Chen, et L. E. Tetrick, « Social Exchange in Work Settings: Content, Process, and Mixed Models », *Manag. Organ. Rev.*, vol. 5, nº 03, p. 289-302, nov. 2009.
[67] D. G. Allen, L. M. Shore, et R. W. Griffeth, « The Role of Perceived Organizational Support and Supportive Human Resource Practices in the Turnover Process », *J. Manag.*, vol. 29, nº 1, p. 99-118, févr. 2003.
[68] S. Guerrero et O. Herrbach, « La confiance organisationnelle au coeur de l'échange social: Et si bien traiter ses employés était payant ? », *Relat. Ind.*, vol. 64, nº 1, p. 6, 2009.
[69] S. Aryee, P. S. Budhwar, et Z. X. Chen, « Trust as a mediator of the relationship between organizational justice and work outcomes: test of a social exchange model », *J. Organ. Behav.*, vol. 23, nº 3, p. 267-285, mai 2002.

ISSN: 2961-6611

Study of Fouling in Tubular Heat Exchanger of Phosphoric Acid Concentration Process

Rania Jradi[#1], Ali Fguiri[#], Christophe Marvillet[*], Mohamed Razak Jeday[#]

[#]*Energy and Environment Research Unit, National Engineering School of Gabes, University of Gabes Road Omar Ibn-Elkhattab, 6029 Gabes, Tunisia*

[1] Corresponding author: Email: raniajradi@yahoo.fr

[*]*CMGPCE Laboratory, French Institute of Refrigeration, National Conservatory of Arts and Crafts of Paris 292 Road Saint-Martin, 75003 Paris, France*

***Abstract*— Phosphoric acid fouling in concentration process of preheat exchangers is a chronic operational problem that compromises energy recovery in these systems. Progress is hindered by the lack of quantitative knowledge of the dynamic effects of fouling on heat exchanger transfer.**

In subject of this work is an experimental determination of the thermal fouling resistance in the tubular heat exchanger of the phosphoric acid preheats installed in a concentration process. By measuring the inlet and outlet temperatures and mass flows of the two fluids, the overall heat transfer coefficient has been determined. Determining the overall heat transfer coefficient for the heat exchanger with clean and fouled surfaces, the fouling resistance was calculated. The results obtained from the heat exchanger studies, showed that the fouling resistance increased with time presented an exponential evolution in agreement with the model suggested by Kern and Seaton, with the existence of fluctuation caused by the instability of the flow rate and the temperature. Bad cleaning of the heat exchangers involved the absence of the induction period and consequently, caused high values of the fouling resistance and the deposit fouling during a relatively short period of time.

***Keywords*—Fouling, Tubular Heat Exchanger, Heat Transfer Coefficient, Fouling Resistance, Phosphoric Acid Concentration Unit.**

I. INTRODUCTION

The most severe and complex problem faced by various industries is the accumulation, on the heat transfer surfaces, of organic compounds or various particles dissolved or present as a suspension in the fluid [1],[2]. This phenomenon which called fouling affects the device functioning by reducing their thermal efficiency and by engendering a considerable pressure loss. This causes a significant economic loss due to the pumping and the frequent cleaning of facilities [3], [4]. Fouling in heat transfer systems is often inevitable and reduces energy efficiency and the functionality of the facility. Mitigation of fouling, and effective cleaning strategies, require both understanding of the mechanisms involved in deposition and cleaning [5].

Numerous heat transfer systems are subject to fouling, reduces the efficiency of heat transfer and limiting productivity [6]. Phosphoric acid fouling in heat exchangers in the concentration process is a persistent operational problem that compromises energy recovery in these systems. Progress is impeded by the lack of quantitative knowledge of the dynamic effects of fouling on heat transfer exchanger [7]. Typically the phosphoric acid flows through the tube side while the steam flows through the shell side of the heat exchangers [8].

There are a wide variety of deposit problems and facility types susceptible to fouling. In this study, we present a description of the deposit phenomenon for its modeling [9]. Tools to understand fouling should be developed so as to provide quantified information for the validation of the fouling models. Several studies have been devoted to the parameters influencing the fouling deposit by scaling. For instance, number of studies have shown that the fouling rate rise by the reduction in the fluid temperature [10].

They are explained by the fact that the velocity and temperature constant, the increase of the thermal transfer involves rise of fouling rates. Others have gone to the increase of fouling rates with the fluid temperature [11], [12]. Radhakrishman et al. [8] developed a predictive model using statistical methods allows the prediction of the fouling rate and the efficiency decrease of the heat exchanger. Mohanty and Singru [6] used the C-factor for fouling monitoring in shell and tube heat exchanger. Ishiyama et al. [13] address in their work the problem of the inlet temperature monitoring in the event of a disaster using hot flow, within a PHT fouling mitigation strategy based on heat exchanger cleaning. Wang et al. [14], in their results of heat transfer experiments, show that the shell-side heat transfer coefficient of the improved heat exchanger raised by 18.2– 25.5 %, the overall heat transfer coefficient increased by 15.6–19.7 %, and the energy efficiency increased by 12.9–14.1 %. Sanaye and Hajabdollahi [15] used a first thermal model which is the ε-NTU method which is applicable to optimal conception of tubular heat exchanger.

Most engineering calculations in heat transfer use the experimental heat transfer coefficients [16]. Heat exchanger fouling used in concentration process is a barrier to their development.

ISSN: 2961-6611

In this study, we will examine the fouling phenomenon of the heat exchanger tubes for the preheat circuit of phosphoric acid in the concentration process. The heat exchangers which are used for the heating of the phosphoric acid are exposed to the fouling problem at the tube side of heat exchangers. Within this framework, an experimental determination of the thermal fouling resistance, by measuring the inlet and outlet temperatures and mass flows of the two fluids, allowed to determine the overall heat transfer coefficient. Determining the overall heat transfer coefficient for the heat exchanger with clean and fouled surfaces, the fouling resistance was calculated for the heat exchanger studied.

II. Process Description

The study was done on the level of heat exchanger of the concentration phosphoric acid process. The mixture of phosphoric acid (the dilute and the circulating phosphoric acid) leaves the basket filter; the centrifugal pump drives it back towards the heat exchanger, which is the tube-and shell type [17].

The phosphoric acid crosses the heat exchanger where it is heated from 70 °C to about 80 °C using the steam flow which undergoes a condensation at the heat exchanger at a temperature of 120 ° C. The superheated mixture of phosphoric acid passes them by the boiler where a quantity of water evaporates and the concentrated acid is produced by overflowing in a piping system inside the boiler. The remaining quantity of phosphoric acid is recycled. The condenser also ensures incurring un-condensable gases outgoing of the boiler by the effect of water cheated created as water falls (Fig. 1).

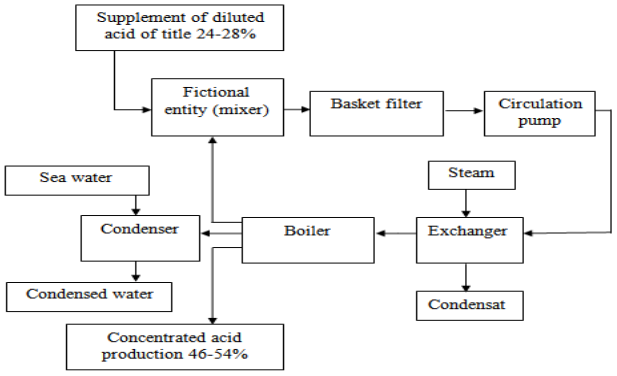

Fig. 1 Simplified Diagram of the Phosphoric Acid Concentration Process

Our experimental study is based on the following assumptions.

1. The flow of two fluids (Phosphoric acid and steam) is at counter-current.
2. Values of the thermo-physical properties of the fluids were considered constant.
3. The thermal losses were neglected.
4. The inlet and outlet temperatures of the two fluids are determined at the ends of the heat exchanger.
5. Pump suction and discharge pressure measurements are perform at the ends of the circulation pump.

III. Calculation Method

The experimental data was collected out during one year. The method that we used to monitor the fouling evolution consists of carrying out a heat balance at the boundaries of the heat exchanger through the measurements of inlet and outlet temperatures (Fig. 2), pump suction and discharge pressure and acid density. The latter were taken every 2 h throughout all the day.

This method, although indirect, allow to detect the necessary moment to shut down the installation for cleaning. In the present study, the temporal evolution of the fouling resistance of the phosphoric acid was studied.

The calculation of the fouling resistance was carried out using the following relation:

$$Rf(t) = \left(\frac{1}{U_s}\right) - \left(\frac{1}{U_p}\right)$$

The overall heat transfer coefficient at the dirty state was given in the time course, via the expression:

$$U_s = U(t) = \frac{\dot{m}_{ac,cir} * Cp_{ac} * (t_{out,ac} - t_{in,ac})}{A * F * \Delta T_{lm}}$$

This relation is drawn from the evaluation of energy on the heat exchanger assuming the isolated system and the physical properties of the two fluids remain constant along the exchanger.

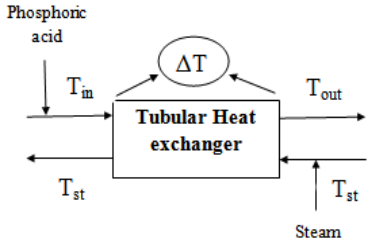

Fig. 2 The Measurement Method at the Boundaries of the Heat Exchanger

In the phosphoric acid concentration process, the operating conditions at the boundary of the heat exchanger are unstable, it is necessary to disclosure the heat exchanger coefficients in proper conditions Up corresponding to the new operating conditions. Assuming that the cleaning between operational runs is perfect and that the heat exchangers are totally free of fouling at the outset of a new cycle. The initial value of the overall heat transfer coefficient at the beginning of every cycle is considered as the value of the overall heat transfer coefficient in the clean state.

$$U_p = U(t=0) = \frac{\dot{m}_{ac,cir} * Cp_{ac} * (t_{out,ac} - t_{in,ac})}{A * F * \Delta T_{lm}}$$

ISSN: 2961-6611

IV. RESULTS AND DISCUSSION

TEMPORAL EVOLUTION OF FOULING RESISTANCE

The evolution of the fouling resistance in the phosphoric acid concentration process of the heat exchanger was followed for a study period quoted previously. All the results of the fouling resistance are presented in the curve form on Fig. 3.

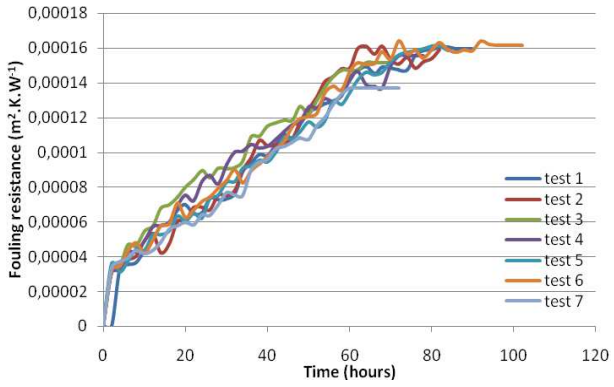

Fig. 3 Variation of the fouling resistance as a function of time.

From the values of these resistances, which are the higher than zero, the heat exchanger contains in his surface fouling. The curves presented show that the temporal evolution of the fouling resistance, appears to follow an asymptotic evolution, which conforms to the model of Kern and Seaton [18], with the lack of the induction period. This is explained by the fact that there are a time offset between the last cleaning, which corresponds to t = 0, and the beginning of this experiments. As it appears clearly as the fouling resistance increases with time until reaching a maximum value, ranging from $6.99 * 10^{-5}$ to $1.65 * 10^{-4}$ $m^2.K.W^{-1}$. As can be seen from Fig. 3, the time required to reach a fouling deposit is 70 h for the tubular heat exchanger. As of that moment, the asymptotic zone begins and the fouling thickness does not vary any more overtime.

At that time, it is necessary to stop the heat exchanger for an emergency cleaning.

The fluctuations observed on these curves are caused by the variation of flow rate, which, acting on the shear stress on the wall, causes re-entrainment of deposit particles or their deposition depending on the flow rate sent.

So, it is necessary to know the operational parameters which promote the formation of fouling in the concentration process, such as:

• The decrease of the phosphoric acid flow rates, whence the decrease the fluid speed (phosphoric acid);
• The good quality of the phosphoric acid: a very low content of impurity;
• The washing water of the heat exchanger is well treated and does not pose the tartar and corrosion problem.

TEMPORAL EVOLUTION OF VOLUME FLOW RATES

Fig. 4 and 5 shows a temporal evolution of the volume flow rates at the tube side (phosphoric acid) and the shell side (steam) in heat exchanger. The values for the flow rates are picked up directly from the concentration process. We therefore note, according to these Figures, that the volume flow rates of phosphoric acid is higher than the volume flow rates of steam, elsewhere, the flow rates of the two fluids decreases in the time. As shown previously according to Fig. 3, which represent the increase of the fouling resistance as a function of time in the heat exchanger, we have noticed that this increase caused the decrease of the volume flow rates of fluids (tube side and shell side), as of Fig. 4 and 5.

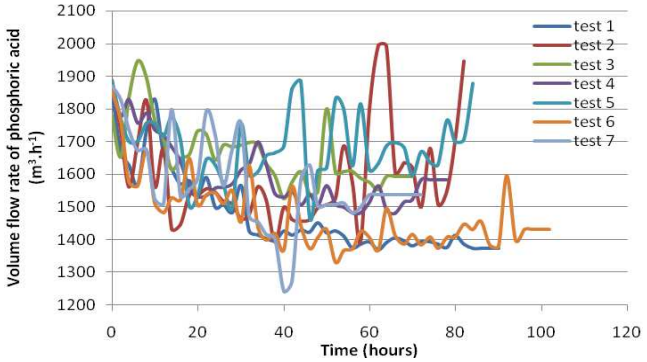

Fig. 4 Variation of volume flow rates of phosphoric acid as a function of time.

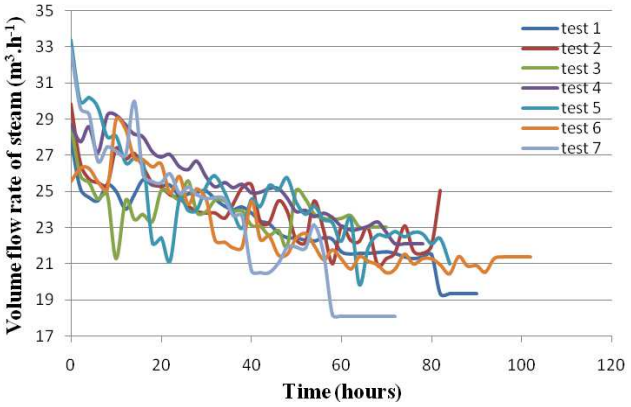

Fig. 5 Variation of volume flow rates of steam as a function of time.

TEMPORAL EVOLUTION OF THE DIFFERENCE PHOSPHORIC ACID TEMPERATURE

Nonetheless, the curve giving the variation of the temperature difference of the phosphoric acid according to time illustrated on Fig. 6. Fig. 1 and 6, show that when the fouling resistance grow, the phsphoric acid difference temperature decreases.

ISSN: 2961-6611

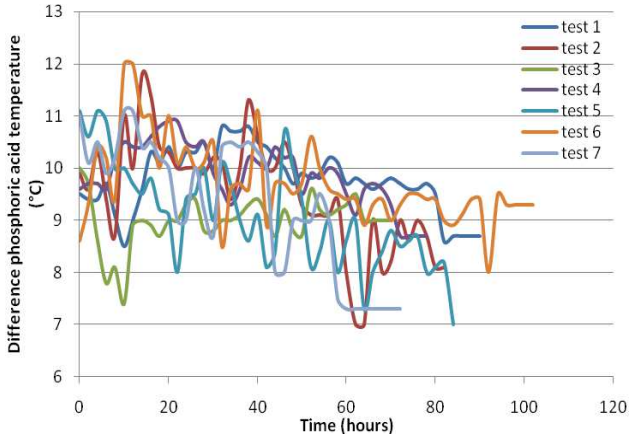

Fig. 6 Variation of temperature difference of phosphoric acid as a function of time.

TEMPORAL EVOLUTION OF THE STEAM TEMPERATURE

Fig. 7 shows a temporal evolution of the steam temperature. We therefore note, according to this Figure, that the steam temperature increases in the time. As shown previously according to Fig. 3, which represents the increase of the fouling resistance as a function of time in the heat exchanger, we have noticed that this increase caused the increase of the steam temperature as of Fig. 7.

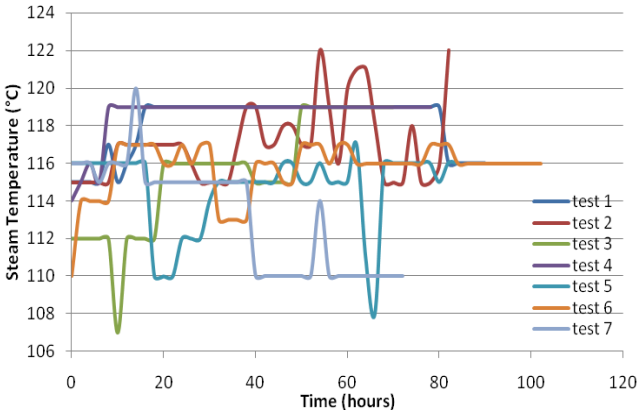

Fig. 7 Variation of steam temperature as a function of time.

TEMPORAL EVOLUTION OF THE PHOSPHORIC ACID DENSITY

The results obtained of phosphoric acid density are grouped in the Fig. 8, where notice that the density vary with the time.

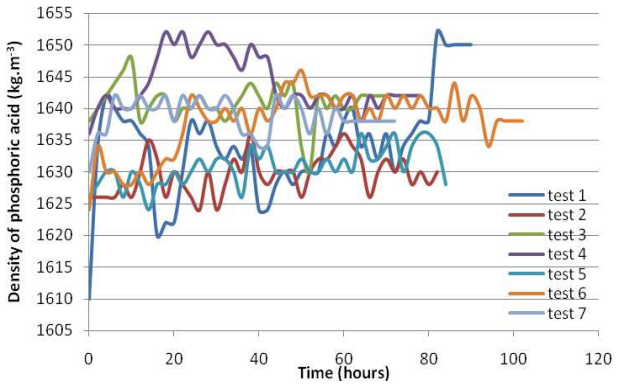

Fig. 8 Variation of phosphoric acid density as a function of time.

V. CONCLUSIONS

The monitoring of heat exchangers allows to fully knowing the fouling evolution under specific conditions of the process. The deposit formation is a thermal resistance that causes significant economic and ecological penalties [19].

The objective of this work was the study of the heat exchanger fouling phenomenon in the concentration process. The study focused on the temporal evolution of the fouling resistance, the volume flow rates, the temperature difference of phosphoric acid, the steam temperature and the effect of the phosphoric acid density.

Results indicated that the fouling resistance follows an exponential evolution in conformity with the model of Kern and Seaton with the absence of the induction period, which is explained by a poor cleaning, or a deviation between the present study and the beginning of the functioning of the heat exchanger after the last stop.

In the concentration process, the phosphoric acid flow rates is not maintained constant, they decrease as a function of time, this is explained by the important production demand as well as the problems which appear when the unit function.

Concerning the influence of parameters on the fouling resistance, we found an analogy between our experimental results and the theoretical prediction. Indeed, the increase of the fouling resistance causes the decreases of volume flow rates of both the phosphoric acid and the steam, the decrease of temperature difference of phosphoric acid and the increase of steam temperature and phosphoric acid density.

The instability of the operating conditions (flow rates, input and output fluids temperatures, density…) is favorable factors for the deposits formation in the heat exchanger.

REFERENCES

[1] Demasles H, Mercier P, Tochon P et Thonon B, 2007, Guide de l'encrassement des échangeurs de chaleur. Editions GREThTh.France.

[2] Gu T, Albert F, Augustin W, Chew Y.M.J, Mayer M, Paterson W.R, Scholl S, Sheikh I, Wang K, Wilson D.I, 2011, Application of fluid dynamic gauging to annular test apparatuses for studying fouling and cleaning. Experimental Thermal and Fluid Science, 35, pp.509–520.

[3] Farajollahi B, Etemad S. Gh, Hojjat M, 2010, Heat transfer of nanofluids in a shell and tube heat exchanger. International Journal of Heat and Mass Transfer, 53, pp.12–17.

ISSN: 2961-6611

[4] Lalot S, Pálsson H, 2010, Detection of fouling in a cross-flow heat exchanger using a neural network based technique. International Journal of Thermal Science, 49, pp.675–679.
[5] Pogiatzis T, Ishiyama E.M, Paterson W.R, Vassiliadis V.S, Wilson D.I, 2011, Identifying optimal cleaning cycles for heat exchangers subject to fouling and ageing. Applied Energy, 89, pp.60–67.
[6] Mohanty D.K, Singru P.M, 2011, Use of C-factor for monitoring of fouling in a shell and tube heat exchanger. International Journal of Energy, 36, pp. 2899- 2904.
[7] Yeap B.L, Wilson D.I, Polley G.T, Pugh S.J, 2004, Mitigation of crude oil refinery heat exchanger fouling through retrofits based on thermo-hydraulic fouling models. International Journal of Chemical Engineering Research and Design, 82, pp.53–71.
[8] Radhakrishnan V.R, Ramasamy M, Zabiri H, Thanh V.Do, Tahir N.M, Mukhtar H, Hamdi M.R, Ramli N ,2007, Heat exchanger fouling model and preventive maintenance scheduling tool. Applied Thermal Engineering, 27, pp. 2791–2802.
[9] Vessakosol P, Charoensuk J, 2010, Numerical analysis of heat transfer and flow field around cross-flow heat exchanger tube with fouling. Applied Thermal Engineering, 30, pp.1170–1178.
[10] Srinivasan M, Watkinson A.P, 2005, Fouling of some Canadian crude oils. Heat Transfer Engineering, 26, pp. 7–14.
[11] Asomaning S, 1997, Heat exchanger fouling by petroleum asphaltenes. Ph.D. Thesis, University of British Columbia.
[12] Saleh Z.S, Sheikholeslami R, Watkinson A.P, 2005, Fouling characteristics of a light Australian crude oil. Heat Transfer Engineering, 26, pp. 15–22.
[13] Ishiyama E.M, Heins A.V, Paterson W.R, Spinelli L, WilsonD.I, 2010, Scheduling cleaning in a crude oil preheats train subject to fouling: incorporating desalter control. Applied Thermal Engineering, 30, pp.1852–1862.
[14] Wang S, Wen J, Yanzhong Li, 2009, An experimental investigation of heat transfer enhancement for a shell-and-tube heat exchanger. Applied Thermal Engineering, 29, pp.2433–2438.
[15] Sanaye S, Hajabdollahi H, 2010, Multi-objective optimization of shell and tube heat exchangers. Applied Thermal Engineering,30, pp.1937–1945.
[16] Taler D, 2013, Experimental determination of correlations for average heat transfer coefficients in heat exchangers on both fluid sides. Heat and Mass Transfer, 49, pp. 1125–1139.
[17] Becker P, 1989, Phosphates and Phosphoric Acid: raw materials, technology and economics of the wet process, second edition.
[18] Kern D.Q, Seaton R.E, 1959, A theoretical analysis of thermal surface fouling. British Chemical.Engeineering, 5, pp. 258-262.
[19] Salehi H, Zeinali Heris S, Esfandyari M, Koolivand M, 2015, Erratum to: neuro-fuzzy modeling of the convection heat transfer coefficient for the nanofluid. Heat and Mass Transfer, 51, pp.575–583.

NOMENCLATURE

A	Area, m^2
Cp	Specific heat capacity, $J.Kg^{-1}.K^{-1}$
F	Correction Factor (=1 for a steam condenser)
$\dot{m}$	Mass flow rate, $kg.s^{-1}$
Q	Thermal power, W
Rf	Fouling resistance, $m^2.K.W^{-1}$
T	Temperature, K
t	Time, h
U	Global heat transfer coefficient, $W.m^{-2}.K^{-1}$
$\dot{v}$	Volume flow rate, $m^3.h^{-1}$

Greek letters

Δ	Difference of greatness between two points

Subscripts

ac	Acid
cir	Circulation
in	Input
ml	Logarithmic average
0	Clean
out	Output
s	dirty state
st	Steam
p	proper state

ISSN: 2961-6611

Conjugate non-Gray Gas Radiation Combined with Natural Convection inside a Square Cavity with Internal Heat Source: Entropy Generation

A. Mazgar[#1], F. Hajji[*2], K. Jarray[*3], F. Ben Nejma[*4]

[#]*Department of Energy Engineering, The Higher Institute of Applied Sciences and Technology of Sousse, University of Sousse*
Ibn Khaldun Street, Taffala City, 4003, Sousse, Tunisia
[1]mazgarakram@yahoo.fr

[*] *The Preparatory Institute for Engineering Studies of Monastir, University of Monastir*
Ibn Al-Jazzar Street, 5019, Monastir, Tunisia
[2]fadhila_hajji@yahoo.fr
[3]jarraykhouloud89@gmail.com
[4]faycal.bennejma@ipeim.rnu.tn

***Abstract*—This analysis aims to investigate the effect of gas radiation on laminar free convection flow within a square cavity having an internal heat source, with special attention being paid to entropy generation. The cavity walls are isothermally cooled whereas the inner body is kept constant at a higher temperature. An association between the discrete-ordinate method through FT_{40} directions and the statistical narrow-band correlated-k method (SNBcK) is applied in the objective of solving equation of radiative transport. Influence of the heater size has been determined and discussed. An important finding from this analysis is that radiative contribution plays a major role in the acceleration of the vortexes and providing either a homogenizing effect on temperature fields. It is also shown that the heater size has a significant effect on flow structure, heat transfer and entropy generation.**

***Keywords*— Thermal radiation; free convection; heat source; square cavity; entropy generation**

I. INTRODUCTION

Combined convective-radiative in closed cavities has become the main concern in many fields. In particular, enclosures with a heater inner body have been subjects of interest due to its importance in most industrial thermal processes in which free convection and thermal radiation play significant roles in controlling fluid flow and heat transfer. To deepen understanding of such subjects, several numerical computations have been done for modelling gas contribution in flow structure and heat transfer. Liu and Phan-Thien [1] simulated radiation heat transfer-interaction with convection and conduction in a square enclosure with a heat generating body. They concluded that the heated block provides resistance to wall-to-wall heat transfer. Mazgar and Ben Nejma [2] studied partial heating effect on combined free convection and thermal radiation in a participating media confined between vertical plates. They indicated that there is no major influence of two-dimensional radiation to reduce the difference between the reported top and bottom heating for the chosen gas. Hajji et al. [3] presented a numerical analysis for the modelling of combined natural convection and thermal radiation in a rectangular enclosure. They showed that thermal radiation improved heat transfer at walls and contributed to the acceleration of eddies.

The analyses of thermodynamic irreversibility and exergy efficiency were considered as interesting technics in designing thermal systems and became the primary concern in the majority of industrial applications such as heat exchangers, solar collectors, nuclear reactors cooling and microelectronics. Bejan [4] was among the first to formulate the concept of entropy production number and irreversibility distribution ratio. Since then, entropy generation minimization is often used as an effective approach of thermodynamic optimization of real systems. It is against this background that many investigations dealing with irreversibility due to heat transfer were set. Mahmud and Fraser [5] conducted a comprehensive analytical study of entropy generation due to interaction between thermal radiation and mixed convection in a vertical duct. Mun et al. [6] and Doo et al. [7] analyzed irreversibility induced by free convection in a square enclosure with cold isothermal surfaces, heated from the interior by cylindrical heat source. They find that entropy generation rates due to viscous dissipation and heat transfer increase significantly with Rayleigh number. Jarray et al. [8] investigated the second law analysis through gas radiation heat transfer in a cylindrical annulus. They indicated that entropy generation is greatly affected by gas and wall temperatures.

An overview of the above studies clearly shows that there are many other physical setups of industrial interest for which the information of radiation effect on convection and entropy generation is still lacking. The main purpose of the present work is to evaluate entropy generation due to laminar natural

ISSN: 2961-6611

convection and radiation heat transfer in a square cavity with isothermal walls and an internal heat source.

II. GENERAL FORMULATION

The flow domain is the interior of a 2D square cavity in the presence of internal heat source with grey diffusive walls. The working fluid is overheated steam which can be considered as non-grey, emitting-absorbing and non-scattering medium. The flow is assumed to be stationary, laminar and compressible. The enclosure walls are maintained isothermal at low temperature T_c whereas the internal heating element is at high temperature T_h, as shown in Fig.1

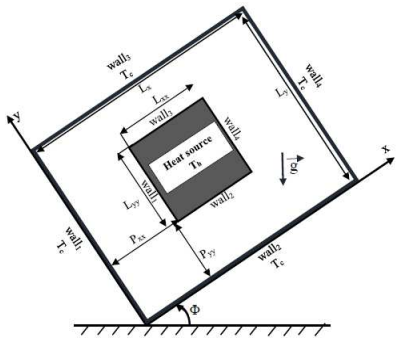

Fig.1 Geometry and boundary conditions of the physical problem

A computational fluid dynamics (CFD) code using COMSOL Multiphysics software is adopted to examine characteristics of heat transfer and fluid flow whereas the iterative coupling computation is achieved by Matlab software.

Based on stated assumptions mentioned in the previous paragraph, the governing equations corresponding to the present study are given as:

$$\nabla.\left(\rho\vec{u}\right)=0 \tag{1}$$

$$\rho\left(\vec{u}.\nabla\right).\vec{u}=\nabla.\left[-P\overline{\overline{I}}+\mu\left(\nabla\vec{u}+\left(\nabla\vec{u}\right)^{T}\right)-\frac{2}{3}\mu\left(\nabla\vec{u}\right)\overline{\overline{I}}\right]+\vec{F}_{B} \tag{2}$$

Under the assumption that $\vec{F}_B$ symbolizes the buoyant forces

$$F_{Bx}=-\rho g\sin\Phi \tag{3}$$

$$F_{By}=-\rho g\cos\Phi \tag{4}$$

$$\rho C_p\vec{u}.\nabla T=\nabla.\left(\lambda\nabla T\right)-div\left(\vec{q}_r\right) \tag{5}$$

The radiative source term in Eq. (5) characterizes the radiative participation of the medium. Resolving the radiative transfer equation given in Eq. (6) leads to compute this term.

$$\frac{dI_\nu^i(l,\vec{\Omega})}{dl}=-\kappa_\nu^i(l)I_\nu^i(l,\vec{\Omega})+\kappa_\nu^i(l)I_\nu^b(T) \tag{6}$$

The relevant boundary conditions corresponding to the convection governing equations are:

on cavity walls: $T = T_c$

on heat source walls: $T = T_h$

on all walls: $u_x = u_y = 0$

The radiation boundary conditions are expressed as follows:

$$I_\nu^i\left(\vec{\Omega}\right)=\varepsilon_w I_\nu^b\left(T_w\right)+\frac{1-\varepsilon_w}{\pi}\int_{\vec{\Omega}'/\vec{\Omega}'.\vec{n}<0} I_\nu^i\left(\vec{\Omega}'\right)\vec{\Omega}'.\vec{n}_w d\Omega' \tag{7}$$

The expression of average temperature is given in Eq. (8)

$$T_a=\frac{1}{L_xL_y}\int_0^{L_x}\int_0^{L_y}T\left(x,y\right)dy.dx \tag{8}$$

III. NUMERICAL PROCEDURE AND VALIDATION

The simulations of heat transfer and fluid flow are performed with the software Comsol Multiphysics® and Matlab. Generally speaking, COMSOL solves the governing equations using the finite element method while Matlab is used to initialize and to store the different variables. The finite element mesh is made up of an automatic adaptive mesh refinement in order to accelerate the resolution and to improve the physical solution, as seen in Fig. 2.

The radiative transfer equation given in equation (5) is resolved using the discrete-ordinate method through FT40 directions, whereas the radiative properties of the gas are computed by means of the SNBcK model.

To ensure that the results are grid size independent, repeated numerical runs were made by varying the number of elements in our grid. This is achieved if the mean radiative Nusselt numbers computed along the walls attain a grid independent solution. As can be seen in Table 1, the use of 40*40 spaced grid reflects a reasonable compromise to ensure accuracy numerical computing.

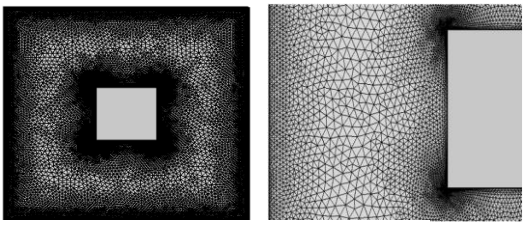

(a) (b)

Fig.2: COMSOL grid resolution; (a) within the cavity; (b) close to walls T_c=400K; T_h=800K; Φ=0; L_x=L_y=0.1m; L_{xx}= L_{yy} =0.025m; ε_c=ε_h=1; P=1atm, P_{xx}=P_{yy}= 0.0375m

Table 1. Grid sensitivity test (case of pure thermal radiation) T_c=400K; T_h=800K; P=1atm; L_x=L_y=0.1m; L_{xx}=L_{yy}=0.025m; P_{xx} =P_{yy}=0.0375m; Φ= 0; ε_c= ε_h=1

Grid (x*y)	Average radiative Nusselt numbers at cavity walls			Average radiative Nusselt numbers at heat source walls		
	$Nur_{1,4}$	Nur_2	Nur_3	$Nur_{1,4}$	Nur_2	Nur_3
(24*24)	36.254	33.042	38.915	66.080	66.639	63.734
(32*32)	36.159	33.076	38.995	65.999	66.591	63.712
(40*40)	36.102	33.080	39.014	66.006	66.724	63.773

IV. RESULTS AND DISCUSSION

The main characteristics of radiation effect on natural convection flow, energy transport and entropy generation in a square enclosure including a located isothermal heat source

ISSN: 2961-6611

are shown in Figures 3-7. Notice that local evolutions of velocity and thermal fields, displayed in Fig.3 and Fig.4, show that the flow pattern generates two symmetrical counter-rotating cells which are spread over the entire domain. Kindly note that the buoyancy driven thermal plume is extended towards the upper horizontal surface of the cavity, alternating between the left and the right corner of the local heat source. The maximum flow velocity through the cavity is reached in the vicinities of the upper surface of the enclosure and close to the top corners of the heat source. In fact, the fluid particles are heated on contact with the vertical walls of the heat source, causing important motion of the gas close to these areas. Moreover, the gas layer induced below the internal heating element is destabilized by vortexes which are generated above this heat source, inducing thermal stratification in the area between the bottom wall of the cavity and the local heat source. This specific zone is characterized by low fluid velocities.

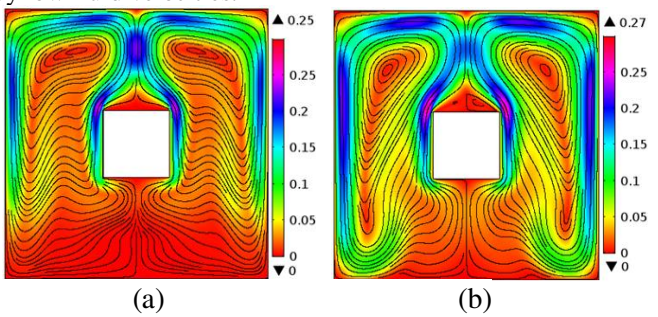

(a) (b)

Fig.3: Local velocity fields (m/s); (a) without radiation; (b) with radiation T_c=400K; T_h=800K; Φ=0; L_x=L_y=0.1m; L_{xx}= L_{yy} =0.025m; ε_c=ε_h=1; P=1atm; P_{xx}=P_{yy}= 0.0375m

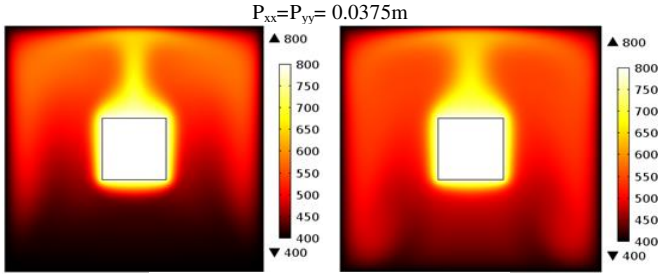

(a) (b)

Fig.4: Local temperature fields (K); (a) without radiation; (b) with radiation T_c=400K; T_h=800K; Φ=0; L_x=L_y=0.1m; L_{xx}= L_{yy} =0.025m; ε_c=ε_h=1; P=1atm; P_{xx}=P_{yy}= 0.0375m

It is worth noting that thermal radiation is having an important contribution on flow structure and heat transfer. In fact, when the radiation is taken into consideration, the temperature trends are much more important and the cells are deformed and become more developed, taking up more cavity space. Against this background, the fluid particles are clearly accelerated at the centre of the cells and in the vicinities of the upper wall of the enclosure. We point out also the presence of the heat source causes local entropy generation due to heat conduction in the vicinities of walls. This generates high temperature gradients, particularly at the movement of plumes due to the formation of a hot gas field with plumes corresponding to the climbing up of the hot gas due to the buoyant force. Quite the contrary, entropy generation is practically absent at the central region of the enclosure, reporting very low temperature gradients. It should also be noted that thermal radiation has a significant impact on local entropy generation due to heat conduction, particularly close to walls. Moreover, the volumetric entropy generation due to thermal radiation, even though it is less developed compared to that generated due to thermal conduction, it still remains non-negligible. Furthermore, it is omnipresent and practically uniform due to the fact that medium is optically thin. In addition, the radiative contribution promotes entropy generation, not only because it enhanced heat transfer through walls, but also it generates direct heat exchanges between the control volumes. On the other hand, note that entropy generation due thermal radiation at walls are due mainly to surface to surface radiation heat transfer, giving a status of a not too thick medium.

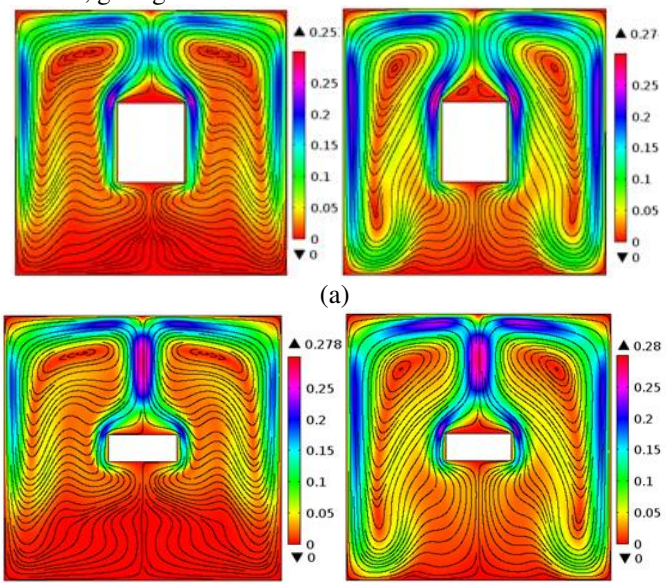

(a)

(b)

Fig.5: Effect of the heater size on local velocity (m/s)
(a) AR=1.2; (b) AR=0.4
T_c=400K; T_h=800K; Φ=0; L_x=L_y=0.1m; L_{yy} =0.025m; ε_c=ε_h=1; P=1atm;

Fig. 5(a) and (b) show local velocity computed without radiation (left column) and with radiation (right column) for AR=1.2 and 0.4, respectively. Note that the heater size which is represented by the aspect ratio value is varied in combination with different heat source length (Lxx), while keeping the same corresponding width (Lyy). As can be seen, a decrease in the heating element size leads to increasing the flow rate inside the plume, all while maintaining its aspect. As regards to temperature fields given in Fig. 6(a) and (b) in the absence of radiation (left column) and when radiation is considered (right column), it is important to point out that the plume becomes thinner and more confined above the heat source, with a marked rise in cold areas below the heating element. Also notable is the decrease in the gas average temperature above the heat source which is due to the reduction in heat-exchange surface by decreasing the size of the heating element. In addition, we should note that plume increases in width under the impact of thermal

ISSN: 2961-6611

radiation where cold areas below the heating element are concerned by heat exchange. This is a logical outcome if we consider downwards extension of cells. In these circumstances, more fluid particles are trapped by the cells below the heat source.

The influences of the heater size on average values of gas temperature and entropy generation are presented in Fig. 7(a) and (b), respectively. It must be noted that the average temperature and entropy generation display increasing and quasi-linear profiles. Further, it is important to report that entropy generation is practically not affected by the heater size when radiation is not considered. On the contrary, radiation contribution leads to significantly higher temperature and entropy generation according to the heater size. Another important thing to note is the constancy of the difference between the average temperature when taking into consideration the radiative effect and that computed in absence of thermal radiation.

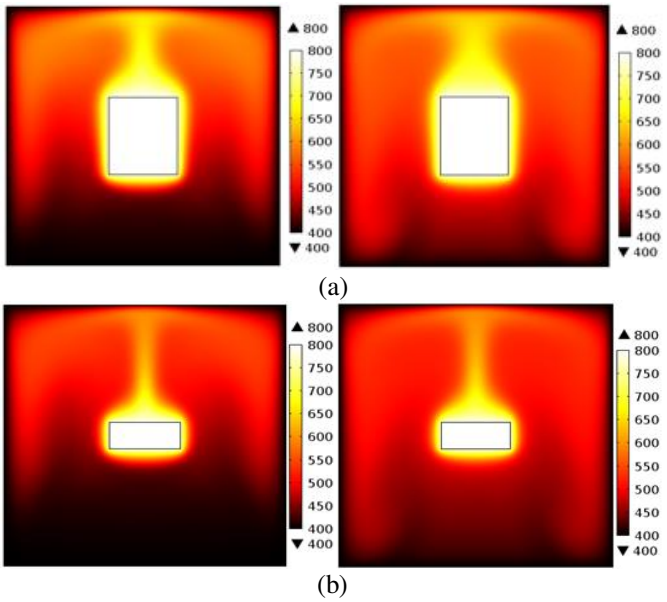

Fig.6: Effect of the heater size on local temperature (K)
(a) AR=1.2; (b) AR=0.4
T_c=400K; T_h=800K; Φ=0; L_x=L_y=0.1m; L_{yy} =0.025m; ε_c=ε_h=1; P=1atm;

V. Conclusions

Effects of internal heat source on combined laminar free convection and non-gray gas radiation in a square cavity is examined. The discrete-ordinates method through FT40 directions is used to evaluate thermal radiation heat transfer whereas the SNBcK4 model is applied to compute the radiative properties of the non-gray medium. What follow represents the main results obtained from the present study:

- The maximum flow velocity is reached close to the upper surface of the enclosure and in the vicinities of the top corners of the heat source.
- Radiative contribution may play a significant effect in controlling the flow structure and heat transfer by accelerating the vortexes and homogenizing the fluid temperature.
- Entropy generation due to gas radiation, even though it is less developed compared to that generated due to thermal conduction, it still remains non-negligible.
- Increasing aspect ratio of the heating element improves the average temperature of the gas and enhances entropy generation.

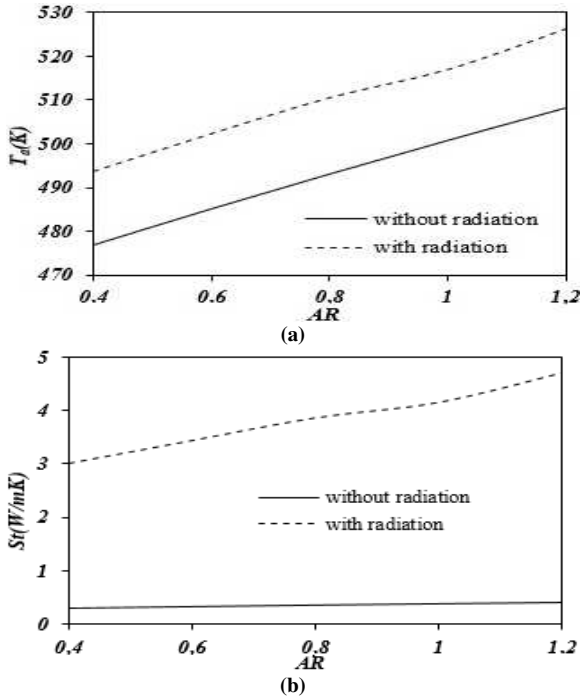

Fig.7: Heater size effect; (a) average temperature (K); (b) entropy generation
T_c=400K; T_h=800K; Φ=0; L_x=L_y=0.1m; L_{yy} =0.025m; ε_c=ε_h=1; P=1atm;

References

[1] Y. Liu and N. Phan-Thien, "A complete conjugate conduction convection and radiation problem for a heated block in a vertical differentially heated square enclosure," *Computational Mechanic,* vol. 24, no. 3, pp. 175–186, 1999.

[2] A. Mazgar A and F. Ben Nejma, "Combined effect of natural convection and non-gray gas radiation with partial heating," *Sādhanā,* vol. 41, no. 7, pp. 805–815, 2016.

[3] F. Hajji, A. Mazgar, A. Sakly, and F. Ben Nejma, "Natural convection analysis through a radiatively participating media within a rectangular enclosure," *Progress in Computational Fluid Dynamics,* vol. 18, no. 2, pp. 108–126, 2018.

[4] A. Bejan, "A study of entropy generation in fundamental convective heat transfer," *Journal of Heat Transfer,* vol. 101, no. 4, pp. 718–725, 1979.

[5] S. Mahmud and R.A. Fraser, "Analysis of mixed convection-radiation interaction in a vertical channel: entropy generation," *Exergy*, vol. 2, no. 4, pp. 330-339, 2002.

[6] G.S. Mun, J.H. Doo, and M.Y. Ha, "Thermo-dynamic irreversibility induced by natural convection in square enclosure with inner cylinder. Part-I: Effect of tilted angle of enclosure," *International Journal of Heat and Mass Transfer,* vol. 97, pp. 1102–1119, 2016.

[7] J.H. Doo, G.S. Mun, M.Y. Ha, and S.Y. Seong, "Thermo-dynamic irreversibility induced by natural convection in square enclosure with inner cylinder. Part-II: Effect of vertical position of inner cylinder," *International Journal of Heat and Mass Transfer,* vol. 97, pp. 1120–1139, 2016.

[8] K. Jarray, A. Mazgar, and F. Ben Nejma, "Numerical analysis of entropy generation through non-grey gas radiation in a cylindrical annulus," *International Journal of Hydrogen Energy*, vol. 42, no. 13, pp. 8795-8803, 2016.

ISSN: 2961-6611

Numerical simulation of a planar solid oxide fuel cell using Lattice Boltzmann method

Wael alimi[1], Amen allah Guizani[2]

Centre de Recherche et Technologies de l'Energie, Laboratoire des procédés thermiques,
BP 95, Hammam LIF, 2050, Tunisia

[1]alimi_wael@yahoo.com
[2] amenallah.guizani@crten.rnrt.tn

***Abstract*— In this study we present a comprehensive two dimensional Lattice Boltzmann method to numerically explore heat and mass transfer inside a planar SOFC. The results show that porosity and operating current density have a significant effect on the SOFC performances.**

***Keywords*— SOFC, Lattice Boltzmann Method, porous media, heat and mass transfer, Brinkman-Forchheimer equation**

I. INTRODUCTION

Solid oxide fuel cells (SOFCs), which are the subject of this study, offer a number of advantages for sustainable and efficient electricity generation, such as high conversion efficiency, high-quality exhaust heat and flexible fuel input. If the performance is improved and the cost is decreased, SOFC can stand as a viable sustainable power-generating device for a broad range of applications from mobile phones to power stations. SOFCs are interesting for two main reasons as a power-generating device. Firstly, they can convert fuel to electricity directly without any mechanically moving parts and are therefore highly efficient as power generating devices. Secondly, they can function with a variety of different fuels due to their high operating temperature (600–1100 °C).

Actually, it exists two main technology for the SOFC, tubular and planar geometry. The first one is in form of tubes pilled together, developed by the manufacturer Westinghouse, the ionic current (O2-) passes from inside the tube where the air flows to outside where fuel, Hydrogen or methane is circulating. The planar technology, developed by manufacturer such as Siemens and Sulzer, is relatively recent is consisting of sandwich of ceramic layers (anode, electrolyte and cathode) with interconnector separating fuel and oxidant and offer better performance compared to tubular technology.

A typical planar SOFC is composed by a Nickel/Zirconia (Ni-YSZ) anode, Strontium-doped Lanthanum Ferrite (LSF) or doped Lanthanum Strontium Manganite (LSM) cathode and Yttria Stabilized Zirconia (YSZ) electrolyte. The performance of SOFC depends on the heat, mass and charge transport occurring inside it simultaneously, in addition to electrochemical and fluids process, which affect strongly its efficiency and power.

These phenomenon needs to be explored and clarified by means of experiments or physically and mathematically modelling. The heat transfer occurs in form of conduction in solid parts, convection in the channel flow and porous electrodes and radiation in both solid and porous media. Moreover, since SOFC operates at high temperature the radiation heat cannot be neglected and needs to be investigated when modelling thermal process.

In the last few years, significant numerical models were developed to simulate the mass and heat transport, and electrochemical reactions inside planar SOFC [1-3]. The lattice Boltzmann method (LBM) is a powerful numerical technique based on kinetic theory for simulating fluid flows and modeling the physics in fluids. The LBM is second-order accurate in time and space, which is sufficient for most engineering applications and, provided that boundaries are appropriately treated, makes LBM competitive for complex domain geometries. The lattice Boltzmann method is an efficient and effective numerical scheme to analyze the flow in a complicated geometry such as the porous medium. In comparison with the conventional CFD methods, the advantages of LBM include simple calculation procedure, simple and efficient implementation for parallel computation, easy and robust handling of complex geometries, and others. In the last decade lattice kinetic theory, and most notably the lattice Boltzmann method has evolved as a significant success alternative numerical approach for the solution of a large class of problems.

In this work, a two-dimensional LB model of non-isothermal planar SOFC was developed to study the multicomponent gases transport in the channels and porous electrodes. The results are compared with those from the literature and a good agreement is found. After model validation, a parametric analysis is conducted to examine the effect of operating parameters on the SOFC performance. It is found that the SOFC performance is improved with the increase of operating temperature.

II. MODEL DESCRIPTION

As it is shown in Fig 1, the physical problem considered is a two dimensional planar SOFC fed with humidified hydrogen and air divided in the following components: anodic flow (fuel) and cathodic flow (air) channels, anodic and cathodic electrodes and ion-conducting electrolyte. The phenomena involved are: gas transport in the gas channels

ISSN: 2961-6611

and porous electrodes; electrochemical reactions taking place at electrode/electrolyte interface; oxygen ion through the electrolyte and electrons through the electrodes and current collectors and energy transport. Under operating conditions, these phenomena occur instantaneously and simultaneously and are strongly coupled.

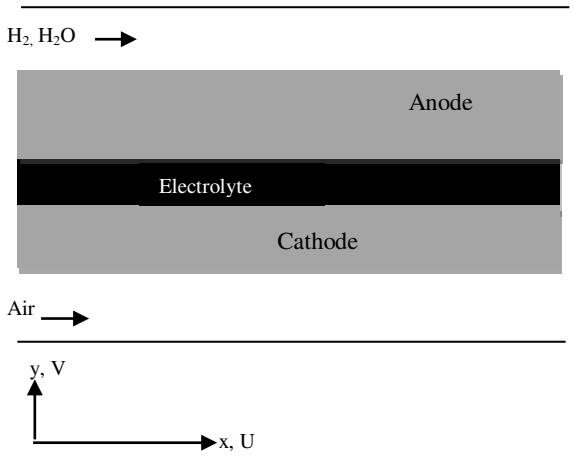

Fig. 1 2-D Model Of planar SOFC

A. Governing Equations

Y The gas flow in the SOFC is modelled by the Brinkman-Forchheimer equation:

$$\nabla.\mathbf{u} \tag{1}$$

$$\frac{\partial \mathbf{u}}{\partial t} + (\mathbf{u}.\nabla)(\frac{\mathbf{u}}{\varepsilon}) = -\frac{1}{\rho}\nabla(\varepsilon p) + \upsilon_e \nabla^2 \mathbf{u} + \mathbf{F} \tag{2}$$

ρ is the fluid density, $\mathbf{u}$ and p the volume-averaged velocity and pressure of the gas mixture, respectively, and υ_e is the effective viscosity. $\mathbf{F}$ represents the total body force due to the presence of a porous medium and other external force fields, expressed by:

$$\mathbf{F} = -\frac{\varepsilon \upsilon}{K}\mathbf{u} - \frac{\varepsilon F_\varepsilon}{\sqrt{K}}|\mathbf{u}|\,\mathbf{u} \tag{3}$$

Where K is permeability of the porous media and F_ε is the geometric function related to the porosity ε by:

$$F_\varepsilon = \frac{1.75}{\sqrt{150\varepsilon^3}} \tag{4}$$

We can see that in the absence of porous media $\varepsilon \to 0$ (channels flow) the generalized momentum equation reduces to Navier-Stockes equation. The flow is characterized by the porosity and two nondimensional parameters: the Reynolds number Re, the Darcy number Da expressed by:

$$\mathrm{Re} = \frac{LU}{\upsilon} \;;\; \mathrm{Da} = \frac{K}{L^2} \tag{5}$$

The conservation laws stated below govern mass and heat transfer:

$$\frac{\partial\left(\varepsilon \rho X_\beta\right)}{\partial t} + \nabla.(\rho X_\beta \mathbf{u}) = \nabla.(\rho D^{eff}_{\beta,mix}\nabla X_\beta) + S_{m,\beta} \tag{6}$$

$$\sigma\frac{\partial T}{\partial t} + \mathbf{u}.\nabla T = \nabla.(\alpha^{eff}\nabla T) + S_T \tag{7}$$

T and X_β are the temperature and mass fraction of the spices β. The coefficient $\sigma = \frac{\varepsilon(\rho\, c_p)_f + (1-\varepsilon)(\rho\, c_p)_s}{(\rho\, c_p)_f}$ is the ratio between the heat capacities of the solid and fluid phases, $\alpha^{eff} = \frac{\lambda^{eff}}{(\rho\, c_p)_f}$ and $D^{eff}_{\beta,mix} = \left(\frac{\varepsilon}{\tau}\right)D_{\beta,mix}$ are the effective thermal diffusivity and the effective diffusivity of spices i in the gas mixture respectively, where : the effective thermal conductivity is and τ being the tortuosity of the porous medium.

The Right Hand Side (RHS) of Equations (6) and (7) includes the source/sink terms $S_{m,\beta}$ and S_T in the species and energy conservation equations respectively. $S_{m,\beta}$ accounts for the generation or consumption of species β due to the electrochemical reactions at the active surface (electrode–electrolyte interface) given as follows:

$$S_{H_2} = -\frac{M_{H_2}}{2F}I \;;\; S_{H_2O} = \frac{M_{H_2O}}{2F}I \;;\; S_{O_2} = -\frac{M_{O_2}}{2F}I \tag{8}$$

With I being the current density. The heat term S_T is based on heat generation by the electrochemical reactions, radiative transfer within the electrodes and the electrolyte and on the losses through the activation, the concentration and the ohmic polarizations.

- Joule effect heating due to electronic resistance in the electrodes and ionic resistance in the solid electrolyte and is calculated as follows:

$$S_{joule} = \frac{\eta_{ohm}}{\delta}I \quad \text{with} \quad \eta_{ohm} = \frac{e_k}{\sigma_k}I \tag{9}$$

Where η_{ohm} represents the Ohmic polarisation, e_k is the thickness, σ_k is the electrical conductivity given by [4]:

$$\sigma_k = \begin{cases} \frac{9{,}5.10^7}{T}exp\left(-\frac{1150}{T}\right) \text{; anode} \\ \frac{4{,}2.10^7}{T}exp\left(-\frac{1300}{T}\right) \text{; cathode} \\ 3{,}34.10^4 exp\left(-\frac{1300}{T}\right) \text{; electrolyte} \end{cases} \tag{10}$$

δ represents the thickness of the region where heat is produced.

- Heat produced by the activation overpotentials at the the active surface (electrode-electrolyte interface) calculated by:

$$S_{act,k} = \frac{\eta_{act,k}}{\delta}I \text{, with: } \eta_{act,k} = \frac{RT}{F}\sinh^{-1}\left(\frac{I}{2I_{o,i}}\right) \tag{11}$$

Where $\eta_{act,k}$ is the activation overpotential, $i_{0,k}$ is the exchange current density defined by:

$$\begin{aligned} i_{0,an} &= \gamma_a\left(\frac{P_{H_2}}{P_0}\right)\left(\frac{P_{H_2O}}{P_0}\right)\exp\left(-\frac{E_{act,an}}{RT}\right) \\ i_{0,ca} &= \gamma_c\left(\frac{P_{O_2}}{P_0}\right)^{0.25}\exp\left(-\frac{E_{act,ca}}{RT}\right) \end{aligned} \tag{12}$$

ISSN: 2961-6611

γ_k is a factor depending on the reaction, $E_{act,k}$ is the activation energy. F stands for the Faraday number and R is the perfect gas constant.

● Heat produced by the concentration overpotentials in the electrodes, can be expressed by:

$$S_{con,k} = \frac{\eta_{con,k}}{\delta} I \tag{13}$$

With [14]

$$\eta_{con,an} = \frac{RT}{2F} ln\left(\frac{P^I_{H_2O} \cdot P^f_{H_2}}{P^f_{H_2O} \cdot P^I_{H_2}}\right) \text{ and } \eta_{con,ca} = \frac{RT}{4F} ln\left(\frac{P^a_{O_2}}{P^I_{O_2}}\right) \tag{14}$$

Representing the concentration overpotential in the cathode or anode assuming that the electrochemical reactions occur only at the electrode/electrolyte interface. P^I is the gas partial pressure at the interface and is calculated for each species as follows:

$$\begin{aligned} P^I_{H_2} &= P^f_{H_2} - \frac{RTe_{anode}}{2FD_{eff,anode}} I \\ P^I_{H_2O} &= P^f_{H_2O} + \frac{RTe_{anode}}{2FD_{eff,anode}} I \\ P^I_{O_2} &= P - (P - P^f_{O_2}) \exp\left(\frac{RTe_{cathode}}{4FPD_{eff,cathode}} I\right) \end{aligned} \tag{15}$$

● Heat generated by chemical reaction at the interface of anode/electrolyte and can be expressed in term of enthalpy [15]:

$$Q_{chem} = -\Delta H_{f,H_2O} - 2FV \ , \tag{16}$$

Where:

$$\Delta H_{f,H_2O} = -(240506 + 7.3835T) \tag{17}$$

Is the enthalpy formation of water, and

$$V = E_{ideal} - (\eta_{ohm} + \eta_{act} + \eta_{con}) \tag{18}$$

is the cell tension. E_{ideal} is the ideal potential calculated by:

$$E_{ideal} = E^0 - \frac{RT}{2F} \ln\left(\frac{X_{H_2O}}{X_{H_2} X^{1/2}_{O_2}}\right) \tag{19}$$

And

$$E^0 = 1.2723 - 2.764510^{-4}.T \tag{20}$$

Therefore the expression of the chemical heat source is:

$$S_{chem} = \frac{Q_{chem}}{2F\delta} I \tag{21}$$

● Heat resulting from radiative transfer within the electrodes and the electrolyte which have different radiative properties. The electrodes are supposed optically Thick ($\tau_{L=\beta L}$ >>1), the radiative heat flux is estimated through Rosseland approximation as:

$$q_{rad} = -k_r.\nabla T \tag{22}$$

where k_r is the radiative conductivity defined as:

$$k_r = \frac{16n^2\sigma T^3}{3\beta_r} \tag{23}$$

β_r refers to the Rosseland-mean extinction coefficient, σ the Stefan-Boltzmann constant, and n is the refractive index.

The electrolyte supposed gray non-scattering medium and optically thin ($\tau_{L=\beta L}$<<1). Thus we can use the two-flux model proposed by Schuster–Schwarzschild to evaluate the radiative heat as [5]:

$$q_{rad} = Ae^{2kL} + Be^{-2kx} \tag{24}$$

A, B are given by:

$$\begin{aligned} A &= -\sigma(T^4_{top} - T^4)e^{-2kx} \\ B &= \sigma(T^4_{bot} - T^4) \end{aligned} \tag{25}$$

Where T_{top} and T_{bot} are the two isothermal of the two sides of the medium separated by a distance L. The radiative source term is obtained from the radiative heat flux by:

$$S_{rad} = -\nabla.q_{rad} \tag{26}$$

B. Boundary conditions

At the inlet for both gas flow channels (y=0), constant gas compositions, temperature and flow velocity are specified, while the solid walls are assumed to be no slip (U = 0, V = 0) and adiabatic ($\frac{\partial X_\beta}{\partial y} = \frac{\partial T}{\partial y} = 0$). At the outlet of the gas channels, fully developed flow is considered ($\frac{\partial X_\beta}{\partial y} = \frac{\partial T}{\partial y} = \frac{\partial U}{\partial y} = 0$). The continuity of velocity and normal stress is prevailing at the interface between gas flow channels and porous electrode ($\mathbf{u}|_{porous} = \mathbf{u}|_{fluid}$; $\frac{1}{\varepsilon}\frac{\partial \mathbf{u}}{\partial y}\Big|_{porous} = \frac{\partial \mathbf{u}}{\partial y}\Big|_{fluid}$). Similarly, heat and species flux are continuous $T|_{porous} = T|_{fluid}$ and $\lambda^{eff}\frac{\partial T}{\partial y}\Big|_{porous} = \lambda\frac{\partial T}{\partial y}\Big|_{fluid}$; $X_\beta|_{porous} = X_\beta|_{fluid}$ and $D^{eff}_\beta \frac{\partial X_\beta}{\partial y}\Big|_{porous} = D_\beta \frac{\partial X_\beta}{\partial y}\Big|_{fluid}$

C. The Lattice Boltzmann method

The Lattice Boltzmann (LB) method is an efficient and powerful simulation method for a wide range of phenomena and processes , such as single-phase flows, multiphase flows, turbulence, heat transfer, and phase change. The LB method is a mesoscopic approach based on the kinetic theory expressed by the original Boltzmann equation. In the present work a D2Q9 model is used, and its lattice velocities $\{\mathbf{e}_\alpha\}$ are given by [6]:

$$\mathbf{e}_\alpha = \begin{cases} (0,0) & \alpha = 0 \\ c(\cos[(\alpha-1)\pi/2], \sin[(\alpha-1)\pi/2]) & \alpha = 1\text{-}4 \\ \sqrt{2}c(\cos[(2\alpha-9)\pi/4], \sin[(2\alpha-9)\pi/4]) & \alpha = 5\text{-}9 \end{cases} \tag{27}$$

Where $c = \delta x / \delta t$ is the lattice velocity and δx and δt are the lattice spacing and time step respectively. The dynamics of the flow is described by a distribution function f, (Guo *et al*., 2009):

$$f_\alpha(\mathbf{x} + e_\alpha \delta t, t + \delta t) = f_\alpha(\mathbf{x}, t) - \frac{1}{\tau_f}(f_\alpha(\mathbf{x}, t) - f^{eq}_\alpha(\mathbf{x}, t)) + \delta t \ F_\alpha \tag{28}$$

The non-dimensional relaxation time τ_f is related to the effective viscosity by $\upsilon_e = (\tau_f - 0.5)c_s{}^2\delta t$, where $c_s = c/\sqrt{3}$ is

ISSN: 2961-6611

the sound speed. $f_\alpha^{eq}(\mathbf{x},t)$ is the equilibrium distribution function at location x and time t along the α direction used to recover the macroscopic Brinkman-Forchheimer equation expressed by:

$$f_\alpha^{eq}(\mathbf{x},t) = w_\alpha \rho \, [\, 1 + \frac{\mathbf{e}_\alpha.\mathbf{u}}{c_s^2} + \frac{\mathbf{uu}:(\mathbf{e}_\alpha\mathbf{e}_\alpha - c_s^2\mathbf{I})}{2\varepsilon c_s^4} \,] \quad (29)$$

Where w_α is the weight coefficient, the term force F_α chosen for porous media flow is given by:

$$F_\alpha = w_\alpha \rho \, (1-\frac{1}{2\tau_f}) \, [\, \frac{\mathbf{e}_\alpha.\mathbf{F}}{c_s^2} + \frac{\mathbf{uF}:(\mathbf{e}_\alpha\mathbf{e}_\alpha - c_s^2\mathbf{I})}{\varepsilon c_s^4} \,] \quad (30)$$

The macroscopic fluid density is defined by $\rho = \sum_\alpha f_\alpha$ and the fuid velocity $\mathbf{u}$ is given explicity by:

$$\mathbf{u} = \frac{\mathbf{v}}{c_0 + \sqrt{c_0^2 + c_1|\mathbf{v}|}} \quad (31)$$

Where $\mathbf{v}$ is a temporal velocity and the two parameters c_0 and c_1 are defined as:

$$\rho\mathbf{v} = \sum_\alpha \mathbf{e}_\alpha f_\alpha \;;\; c_0 = \frac{1}{2}(1 + \varepsilon\frac{\delta t}{2}\frac{\upsilon}{K}) \;;\; c_1 = \varepsilon\frac{\delta t}{2}\frac{F_\varepsilon}{\sqrt{K}} \quad (32)$$

To have accurate simulation of flow, Reynolds number must be equal in both real and LB method/

$$\mathrm{Re} = \left(\frac{UH}{\upsilon}\right)_{real} = \left(\frac{UN}{\upsilon}\right)_{LB} \quad (33)$$

N is the number of grid used for meshing and H is the height of the channel flow in LBM simulation.

To recover the heat transfer equation, the corresponding evolution equation of distribution function in lattice Boltzmann model is defined as:

$$g_\alpha(\mathbf{x} + e_\alpha\delta t, t+\delta t) = g_\alpha(\mathbf{x},t) - \frac{1}{\tau_T}(g_\alpha(\mathbf{x},t) - g_\alpha^{eq}(\mathbf{x},t)) + \delta t \; G_\alpha \quad (34)$$

Where g_α is the distribution function for the temperature, τ_T is the non dimensional relaxation time related to the effective thermal diffusivity: $\alpha^{eff} = \sigma(\tau_T - 0.5)c_s^2\delta t$, g_α^{eq} is the equilibrium distribution function written as:

$$g_\alpha^{eq}(\mathbf{x},t) = w_\alpha T \, [\, 1 + \frac{\mathbf{e}_\alpha.\mathbf{u}}{\sigma c_s^2} + \frac{\mathbf{uu}:(\mathbf{e}_\alpha\mathbf{e}_\alpha - c_s^2\mathbf{I})}{2\sigma^2 c_s^4} \,] \quad (35)$$

The source term G_α can be expressed by [7] :

$$G_\alpha = w_\alpha(1 - \frac{1}{2\tau_T})\frac{S_T}{\rho C_P} \quad (36)$$

Then the macroscopic temperature T is calculated by:

$$T = \sum_\alpha g_\alpha + \frac{\delta t}{2}\frac{S_T}{\rho C_p} \quad (37)$$

To consider the species transport within the SOFC, we consider the distribution function for the *l*th species mass fraction as below:

$$h_{l,\alpha}(\mathbf{x} + e_\alpha\delta t, t+\delta t) = h_{l,\alpha}(\mathbf{x},t) - \frac{1}{\tau_l}(h_{l,\alpha}(\mathbf{x},t) - h_{l,\alpha}^{eq}(\mathbf{x},t)) + \delta t \; w_\alpha S_l \quad (38)$$

S_l is the source term appeared in the spices transport equation. the equilibrium distribution function for the *l*th species defined by:

$$g_{l,\alpha}^{eq}(\mathbf{x},t) = w_\alpha X_l \, [\, 1 + \frac{\mathbf{e}_\alpha.\mathbf{u}}{c_s^2} + \frac{\mathbf{uu}:(\mathbf{e}_\alpha\mathbf{e}_\alpha - c_s^2\mathbf{I})}{2\varepsilon c_s^4} \,] \quad (39)$$

The relaxation time σ_l is related to effective mass diffusivity: $D_l^{eff} = (\tau_l - 0.5)c_s^2\delta t$. Then the macroscopic mass fraction is calculated by:

$$X_l = \sum_\alpha h_{l,\alpha} \quad (40)$$

It is important to note that for each species modeling, the relevant Schmidt number must be calculated and hold fixed in real and LBM simulations:

$$Sc = \left(\frac{\upsilon}{D}\right)_{real} = \left(\frac{\upsilon}{D}\right)_{LB} \quad (41)$$

D. Model validation

The LB model described above was validated with experimental study [8] performed, by simulating under the same operating conditions, the current-voltage curve was generated by the model for different values of operating temperature as shown in Fig.3. It can be seen that simulated results coincide quite well with the experimental results. The minor discrepancies between the LB model and experimental measurements can be attributed to the measurements uncertainties and simulation accuracy.

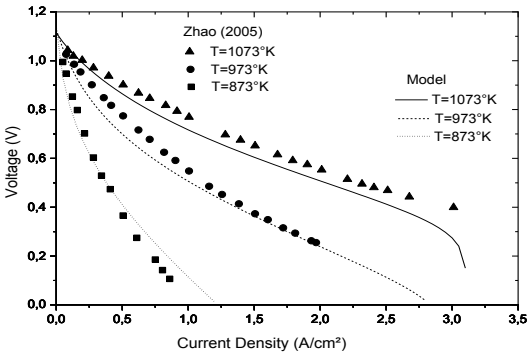

Fig. 1 Comparison between simulated and experimental cell voltages

III. RESULTS AND DISCUSSION

The input parameters used in the present study were obtained from literature and summarized in Table 1.

Fig 3.shows the molar fractions of H_2 and H_2O (anode) and O_2 (cathode) at a current density of 1.2 A/cm² and a porosity of electrode of 0.4. Due to the electrochemical reactions occurring in the SOFC, both H_2 and O_2 mass fraction decrease with increasing x. However for H2O the mass fraction increase slightly in the anode. Fig 4 shows the temperature distribution in the SOFC at the same conditions. The temperature of both the gas species and the solid structure increases with increasing x.

By increasing electrode porosity, the consumption of the reactive (H_2 and O_2) become more rapid, due to the high

ISSN: 2961-6611

effective diffusion coefficients as shown in Fig 5. While the temperature inside the SOFC (Fig 6.) decreases due to small ohmic loses at higher porosity (ε =0.6).

TABLE I

SOFC PROPERTIES AND OPERATING CONDITIONS [1-10]

parameters	anode	electrolyte	cathode
ε	0.4	/	0.4
τ	0.3		0.3
$D(m^2)$	$D_{eff} = \frac{\varepsilon}{\tau}.D_i$ i=(H_2O,O_2,H_2)		
κ (m^2)	10^{-12}		10^{-12}
λ ($wm^{-1}K^{-1}$)	6.2	2.7	9.6
ρ_s (kgm^{-3})	3030	5160	3310
Cp_s($Jkg^{-1}K^{-1}$)	595	606	573
γ (Am^{-2})	6.54 10^{11}	/	2.35 10^{11}
E (J)	140 10^3	/	130 10^3
e(μm)	300	100	200
ρ(kgm^{-3})	$\rho = \frac{P_i}{RT}.\sum_j M_j X_j$		
Cp($Jkg^{-1}K^{-1}$)	$Cp_{,i} = \sum_j Cp_{,j} X_j$ with $Cp_{,i} = a + bT + cT^2 + dT^3 + eT^4$		
μ (Pas)	$\mu_{,i} = \sum_j \mu_{,j} X_j$ with $\mu_{,i} = a + bT + cT^2 + dT^3 + eT^4$		
X_{O_2}	0	/	0.21
X_{H_2}	0.97	/	0
X_{H_2O}	0.03	/	0
P	1	/	1

At higher current density of 1.8 A/cm², the electrochemical reaction rates increases (Fig 7.) and the temperature increases also due to the high heat losses (Fig.8).

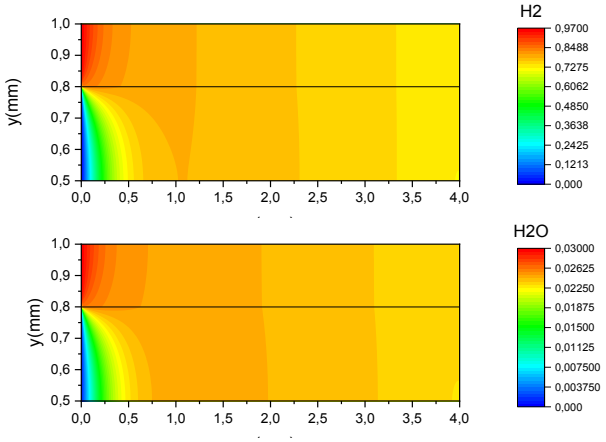

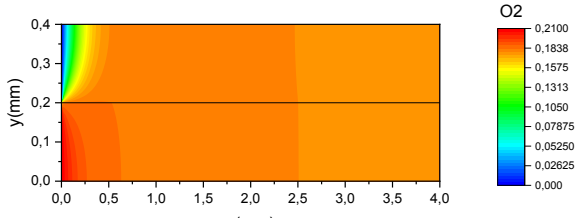

Fig. 3 Mass fractions of H_2, H_2O and O_2 in anodic and cathode side respectively at I=1.2A/cm² and ε =0.4

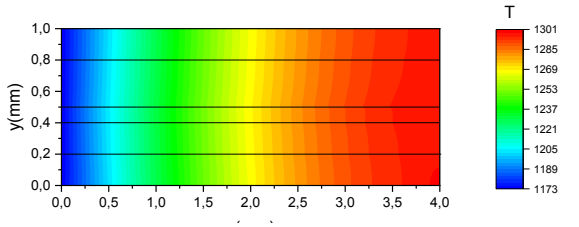

Fig. 4 Temperature distribution at I=1.2A/cm² and ε =0.4

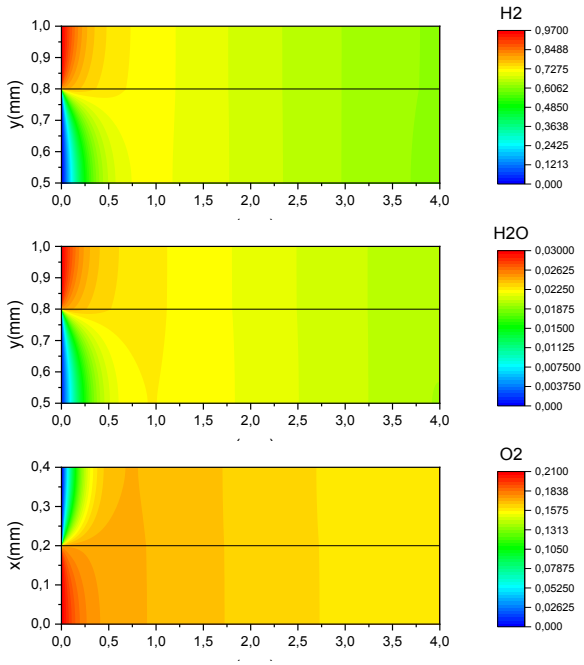

Fig. 5 Mass fractions of H_2, H_2O and O_2 in anodic and cathode side respectively at I=1.2A/cm² and ε =0.6

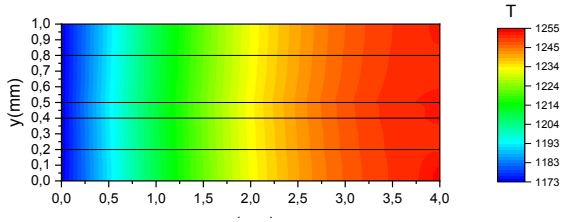

Fig. 6 Temperature distribution at I=1.2A/cm² and ε =0.6

ISSN: 2961-6611

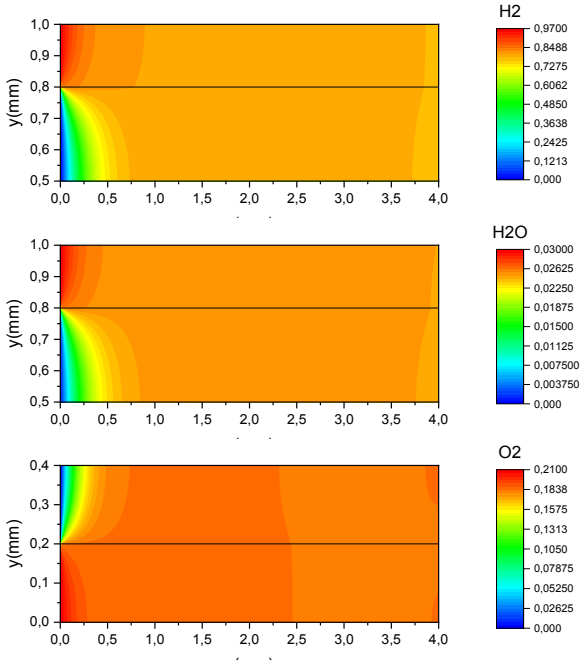

Fig. 7 Mass fractions of H_2, H_2O and O_2 in anodic and cathode side respectively at I=1.8A/cm² and ε =0.4

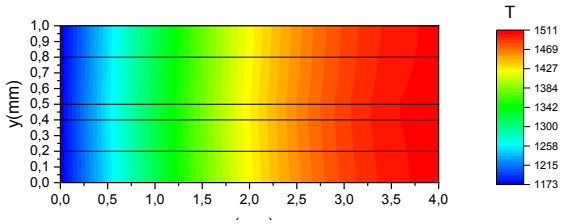

Fig. 8 Temperature distribution at I=1.8A/cm² and ε =0.4

IV. CONCLUSION

An accurate Lattice Boltzmann method has been presented to calculate two-dimensional heat and flow in a planar SOFC. The effect of electrode porosity and current density has been investigated. It is found that increasing porosity enhance heat and mass diffusion inside the cell while increasing operating current density increases cell overpotentials and thus heat losses.

REFERENCES

[1] J. Hartvigsen, S. Elangovan, A. Khandkar, "Modeling, design, and performance of solid oxide fuel cells", Proceedings, Science & Technology of Zirconia V 682-693, 1993

[2] S. Yixiang, Cai Ningsheng, Li Chen. "Numerical modelling of an anode-supported SOFC button cell considering anodic surface diffusion". J Power Sources ; 164:639–48 ,2007.

[3] N Meng., Michael K.H. Leung, Dennis Y.C. Leung "Parametric study of solid oxide fuel cell performance", Energy Conversion and Management 48 , 1525–1535,2007.

[4] MM Hussain, Li X, Dincer I. Mathematical modeling of planar solid oxide fuel cells. Journal of Power Sources;161(2):1012-22, 2006.

[5] K.J. Daun, S.B. Beale and F. Liu, "Radiation heat transfer in planar SOFC electrolytes" J.Power Sources, vol.157, pp.302–310, 2006.

[6] Z Guo., Zhao.TS. Lattice Boltzmann model for incompressible flows through porous media. Physical Review; 66: 036304.,2002

[7] W. Jinku, A lattice Boltzmann algorithm for fluid-solid conjugate heat transfer. Int. J. Ther. Sci. 228–234 ,2007.

[8] Zhao F, Anil V. Virkar, "Dependence of polarization in anode-supported solid oxide fuel cells on various cell parameters", Journal of Power Sources 141, 79–95, 2005

[9] CFD Fluent 6.2.16

[10] N Meng "2D thermal-fluid modeling and parametric analysis of a planar solid oxide fuel cell", Energy Conversion and Management 51 714–721, 2010

[11] *Wireless LAN Medium Access Control (MAC) and Physical Layer (PHY) Specification*, IEEE Std. 802.11, 1997.

ISSN: 2961-6611

Modeling, Analysis and Simulation of a D-STATCOM for Reactive Power Compensation in Electric Distribution Power System

F.Z.Messaoud[#*1], H.Tédjini[#2], O. Boughazi[#3], A. Hazzab[*4]
[#]*Smart Grids & Renewable Energies (SGRE), University Tahri Mohammed Bechar, Algeria*
[*] *Research Laboratory on Command, Analysis & Optimisation of Electro-Energetic Systems' university Tahri Mohammed ,Bechar,Algeria*
[1]fz.messaoud45@gmail.com
[2]tedjini_h@yahoo.fr
[3]othmaneboughazi@yahoo.fr
[4]A_hazzab@yahoo.fr

***Abstract*— The device analyzed in this paper is distribution static compensator (D-STATCOM) due to its capability to improve the power quality issues in distribution systems, in this paper the control of D-STATCOM is realized by proportional integral PI controllers to ensure perfect decoupling between the two active and reactive axes and to keep the DC-link voltage of D-STATCOM constant under linear-load variation. D-STATCOM is developed for the compensating reactive power demanded by unbalanced load. Moreover power factor of the source is improved, validation of models and control algorithms is carried out through simulations in MATLAB/Simulink**

.

Keywords— D-STATCOM; PI controller; DC-link voltage; Reactive power; unbalanced linear load .

I. INTRODUCTION

The Electrical Distribution System (EDS) is facing a number of power quality (PQ) issues such as low power factor, voltage fluctuation, voltage sag and voltage instability and many other problems due to non-linear loads, In fact in practical applications most of the loads are non-linear, Various custom power devices (CPD) are addressed in to enhance the quality of power, There are several types of CPDs such as DVR, D-STATCOM, UPQC etc, are used in the distribution system for specific purpose . The D-STATCOM is very attractive and it has a good cost-effective solution to minimize the PQ impact in EDS [1]–[3], The main advantage of D-STATCOM is that it can generates or absorb the reactive power required to distribution system[4],[5]. In this paper a detailed linear modeling of D-STATCOM, a conventional PI controller used to regulate the both voltage and current, direct current for active axe control, quadratic current for reactive axe control and voltage controller is designed for DC-link to reduce variations in case of sudden load changes which leads to high overshoot and undershoot[6] . The purpose is to ensure the decoupling between the direct and quadratic axes current that make it possible to control the reactive current flow between the D-STATCOM and the transmission power system used PI controller to regulate PCC voltage by dynamically absorbing or generating reactive power to the AC grid is fully studied in both capacitive and inductive modes across the reactance of coupling transformer, and improve the power factor in the side of the source, So conventional PI controller also feasible solution to show the better performance in driving D-STATCOM by maintaining the constant DC-link voltage under the change of linear inductive and capacitive loads have been demonstrated by some simulations results.

II. BASIC OPERATION OF D-STATCOM

The D-STATCOM is the SVC version consisting of a high-tech semiconductor-based voltage converter associated with a capacitor as a DC voltage source and the set connected in parallel to the distribution system network as shown in the "Fig.1", The D-STATCOM is connected through a filter circuit to the grid at the point of common coupling (PCC)[7]–[9] . In low power applications, low voltage power electronics technology can be used. Thus, higher switching frequencies and 2-level voltage converters based on conventional IGBTs can be used.

The instantaneous active power is defined by the scalar product between currents and voltages. On the other hand, the reactive power is defined by their vector product. The complex apparent power S_f at the output of D-STATCOM can be expressed by the following expression:

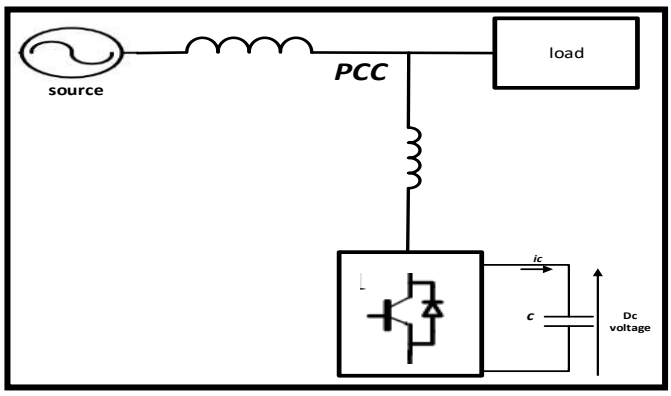

Fig. 1 basic diagram of D-STATCOM

ISSN: 2961-6611

$$S_f = P_f + jQ_f \quad (1)$$

The expressions of the powers in the reference of Park are given by:

$$P_f = V_{chd} i_{fd} \quad (2)$$

$$Q_f = -V_{chd} i_{fq} \quad (3)$$

We then notice that the component i_{fq} allows to control the reactive power and the component i_{fd} to control the active power [10]. If the current is late, as shown in the "Fig. 2" the sign of the quadratic component of the current is negative so the result is positive reactive power means the D-STATCOM absorbs reactive power (inductive mode).

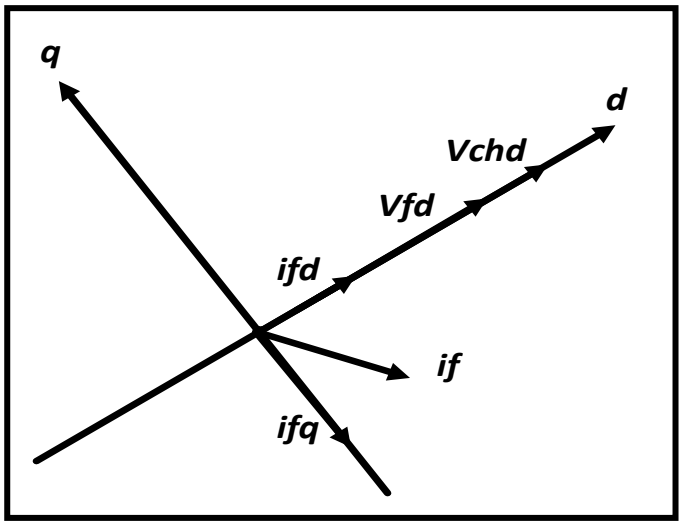

Fig. 2 Operation in inductive mode

When the sign of the quadratic component of the current is positive, the current is in advance, as shown in "Fig. 3", The result is a negative reactive power, which means the D-STATCOM provides reactive power to the network (capacitive mode).

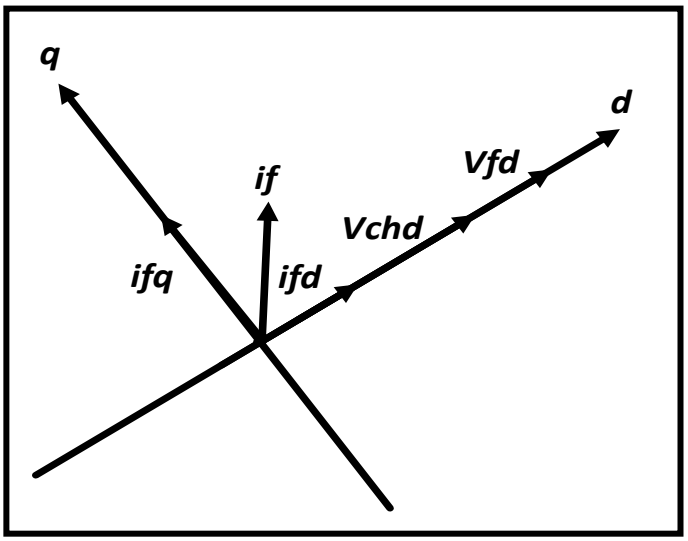

Fig. 3 Operation in capacitive mode

If the magnitude voltage (V_{fd}) of VSC is greater than (V_{chd}) of AC voltage $(V_{chd} < V_{fd})$, therefore D-STATCOM operated in capacitive mode and provides the reactive power to system. And If output voltage (V_{fd}) of VSC is smaller than (V_{chd}) of AC voltage $(V_{chd} > V_{fd})$,therefore D-STATCOM operated in inductive mode and absorbs the reactive power from the system, If the grid voltage V_{chd} and the DSTATCOM voltage V_{fd} are of the same magnitude $(V_{chd} = V_{fd})$, there is no exchange of reactive power between the grid and the D-STATCOM and is operating in the floating state.[11]

III. MODELLING OF D-STATCOM

The three-phase structure of D-STATCOM is given in "Fig. 4" the D-STATCOM is based on the topology of the voltage inverter. In low voltage distribution (BT) networks, two-level DSTATCOMs are usually coupled to the network by an RL filter. The electrical network is represented by three simple voltages $(V_{sa}, V_{sb}$ and $V_{sc})$ and its internal impedances. The load is a three-phase inductive load coupled in a star.

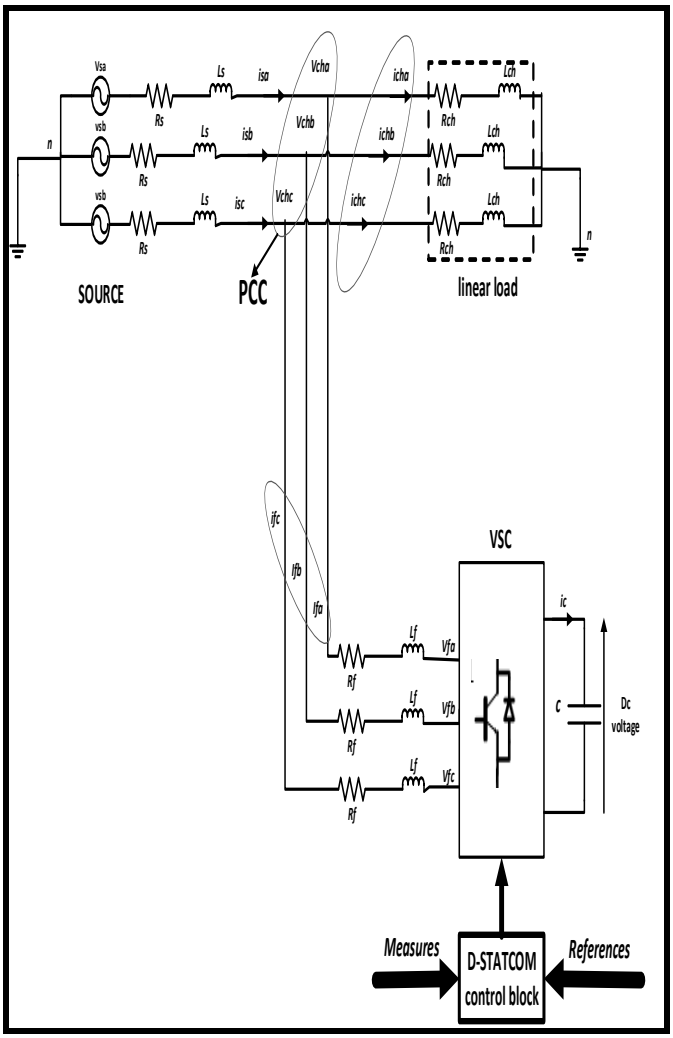

Fig. 4 Three-phase structure of the D-STATCOM coupled to the network

ISSN: 2961-6611

From the "Fig.4", the expressions of the load voltages are defined by:

$$\begin{cases} V_{cha=} - L_f \frac{di_{fa}}{dt} - R_f i_{fa} + V_{fa} \\ V_{chb} = -L_f \frac{di_{fb}}{dt} - R_f i_{fb} + V_{fb} \\ V_{chc} = -L_f \frac{di_{fc}}{dt} - R_f i_{fc} + V_{fc} \end{cases} \quad (4)$$

Which give:

$$\begin{cases} \frac{di_{fa}}{dt} = \frac{1}{L_f}(V_{fa} - V_{cha} - R_f i_{fa}) \\ \frac{di_{fb}}{dt} = \frac{1}{L_f}(V_{fb} - V_{chb} - R_f i_{fb}) \\ \frac{di_{fc}}{dt} = \frac{1}{L_f}(V_{fc} - V_{chc} - R_f i_{fc}) \end{cases} \quad (5)$$

On the other hand, we have:

$$\frac{d{V_{DC}}^2}{dt} = \frac{2V_{DC}i_c}{c} \quad (6)$$

The equation of the continuous side (6) can be related to the alternative side by the conservation of the active powers:

$$\frac{d{V_{DC}}^2}{dt} = \frac{2(V_{cha}i_{fa}+V_{chb}i_{fb}+V_{chc}i_{fc})}{C} \quad (7)$$

After transformation, the D-STATCOM model in the d-q frame is given by:

$$\begin{cases} \frac{di_{fd}}{dt} = \frac{1}{L_f}(V_{fd} - V_{chd} - R_f i_{fd} + \omega i_{fq}) \\ \frac{di_{fq}}{dt} = \frac{1}{L_f}(V_{fq} - V_{chq} - R_f i_{fq} - \omega i_{fd}) \\ \frac{d{V_{DC}}^2}{dt} = \frac{2\,V_{chd}\,i_{fd}}{C} \end{cases} \quad (8)$$

Equation (8) shows that the DSTATCOM model in the d-q frame shows coupling terms between the d and q axes.

IV. DESIGN OF PI CONTROLLER

In all practical applications, D-STATCOM is mainly used to compensate the reactive power at the PCC where is connected, The control structure of a DSTATCOM consists of a double nested control loop: An external current command generation loop and an internal current control loop "Fig.5". The active and reactive powers exchanged between the D-STATCOM and the network are controlled by the regulation of the direct and quadratic components of the current (i_{fd} , i_{fq}), the Components (V_{fd} , V_{fq}) are the command variables and (V_{chd},V_{chq}),are the disturbance variables so we have:

$$\begin{cases} \frac{di_{fd}}{dt} = \frac{1}{L_f}V_d - \frac{R_f}{L_f}i_{fd} \\ \frac{di_{fq}}{dt} = \frac{1}{L_f}V_q - \frac{R_f}{L_f}i_{fq} \end{cases} \quad (9)$$

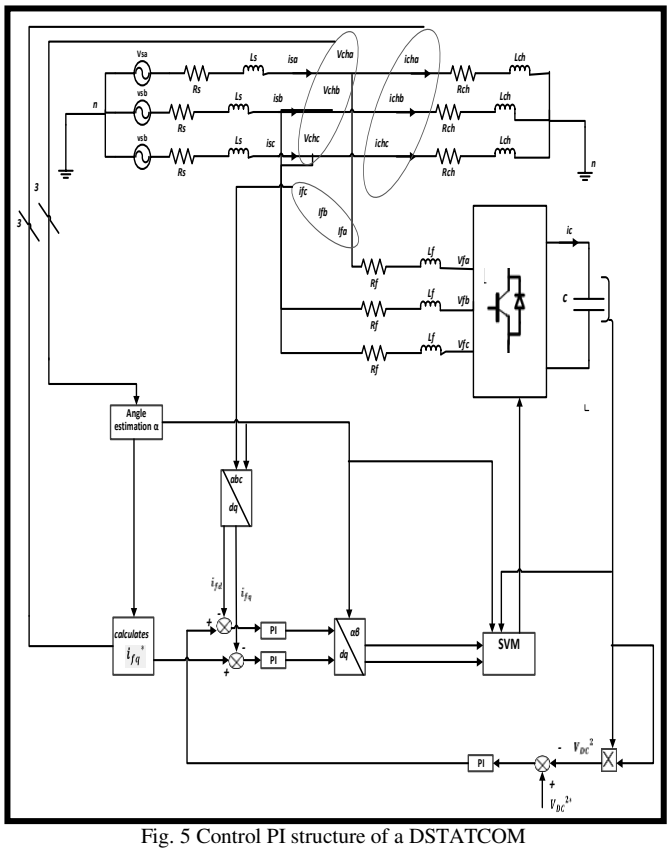

Fig. 5 Control PI structure of a DSTATCOM

A. *synthesis of current regulators*

The simplified diagram of the current regulation loop is illustrated by the "Fig.6".

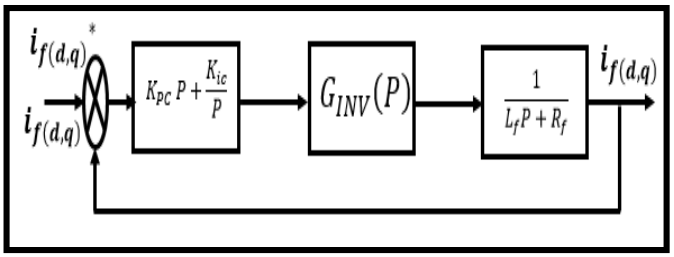

Fig. 6 Current regulation by PI regulators.

The open loop transfer function corresponding to this scheme is:

$$F(P) = K_{PC}\,P + \frac{K_{ic}}{P}\,\frac{1}{L_f P + R_f}\,G_{INV}(P) \quad (10)$$

the transfer function of the inverter is generally chosen equal to $G_{INV}(P) = 1$ in order to ensure that the value of the output voltage is equal to its reference. The closed loop transfer function will therefore be:

$$H(P) = \frac{K_{PC}\,P + K_{IC}}{L_f P^2 + (R_f + K_{PC})\,P + K_{ic}} \quad (11)$$

Finally we deduce the values of the regulator constants as follows:

ISSN: 2961-6611

$$K_{Pc} = 2\zeta_c \omega_{nc} L_f - R_f \quad (12)$$

$$K_{ic} = L_f {\omega_{nc}}^2 \quad (13)$$

B. synthesis of the DC voltage regulator

The role of the DC bus voltage regulation loop is to maintain this voltage at a constant reference value, controlling the active power transfer between the PCC and the DC bus, from the system (5),we have the following first order transfer function:

$$\frac{{V_{DC}}^2(P)}{i_{fd}(P)} = \frac{2V_{chd}}{C_P} \quad (14)$$

The following diagram shows the regulation of the DC voltage with a PI corrector:

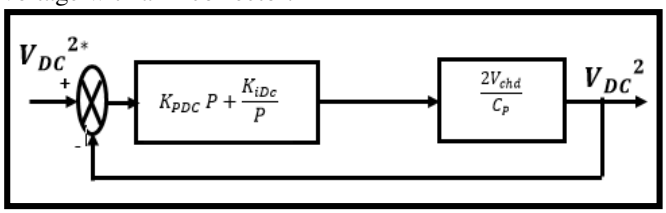

Fig. 7 Voltage regulating DC by a PI regulator

The closed loop transfer function will therefore be:

$$H(P) = \frac{2\,V_{chd}\,(K_{PDC}\,P + K_{iDC})}{C\,P^2 + 2\,V_{chd}\,K_{PDC}P + 2\,V_{chd}\,K_{iDC}} \quad (15)$$

Finally we deduce the values of the regulator constants as follows:

$$K_{PDC} = \frac{C\,\zeta_{DC}\,\omega_{nDC}}{V_{chd}} \quad (16)$$

$$K_{iDC} = \frac{C\,{\omega_{nDC}}^2}{2V_{chd}} \quad (17)$$

The reference of the reactive current ${i_{fq}}^*$ can be determined according to the operating mode of the DSTATCOM, either by the regulation of the voltage of the PCC, or by the regulation of the reactive power exchanged between the D-STATCOM and the network.

V. SYSTEM CONFIGURATIONS

The single-line diagram of the distribution network used to validate the operation of D-STATCOM is shown in "Fig.8"

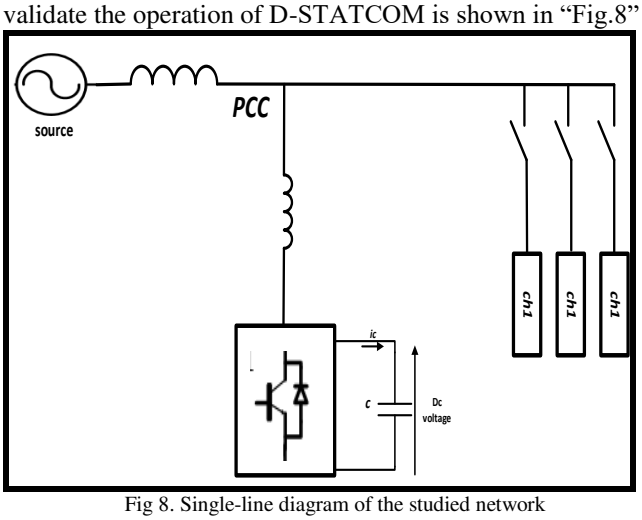

Fig 8. Single-line diagram of the studied network

Such as:

$ch1$ = Inductive load $(Lch1 + Rch1)$

$ch2$ = Inductive load $(Lch2 + Rch2)$

$ch3$ = Capacitive load $(Lch3 + Rch3 + Cch)$

The parameters of the system to be simulated are given by THE TABLE I AND II :

TABLE I

SYSTEM PARAMETERS TO SIMULATE

Parameters	Values	Parameters	Values
V_{Seff}	220 v	${V_{DC}}^*$	800V
L_s	0.001 H	R_{ch1}	50Ω
R_s	0.001Ω	R_{ch2}	50Ω
f_h	5 k Hz	R_{ch3}	15Ω
C_{Ch}	0.18 mH	L_{ch1}	65 mH
L_f	0.01 H	L_{ch2}	110 mH
R_f	0.001Ω	L_{ch3}	13 mH
f_S	50 Hz	C	5 mF

TABLE II

PARAMETERS OF THE PI REGULATORS

Regulators	ω_n	ξ_n
continuous voltage	100	0.707
currents	50 000	1

VI. RESULT AND DISCUSSION

The proposed D-STATCOM model is implemented in MATLAB/SIMULINK software using control algorithm for D-STATCOM with PI controller. The proposed model is verified under linear load condition and is used for power factor correction ,reactive power regulation and DC voltage regulation.

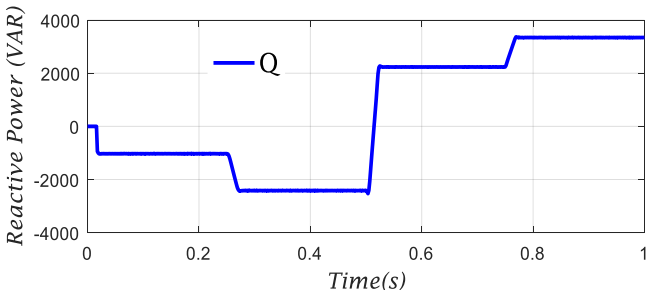

Fig. 9 Reactive Power of the D-STATCOM (injected and absorbed)

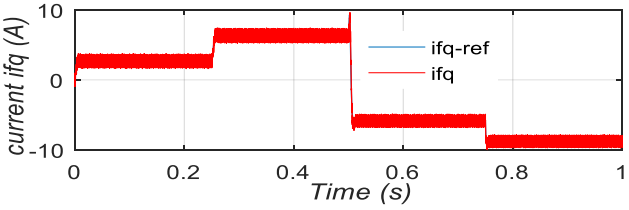

Fig. 10 Reactive current injected by the D-STATCOM into the network and its reference

ISSN: 2961-6611

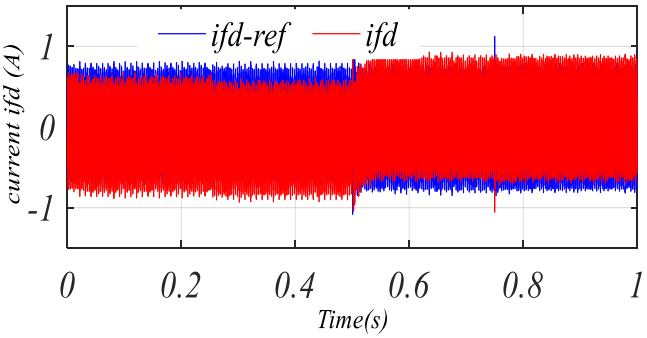

Fig. 11 Active current injected by the D-STATCOM into the network and its reference

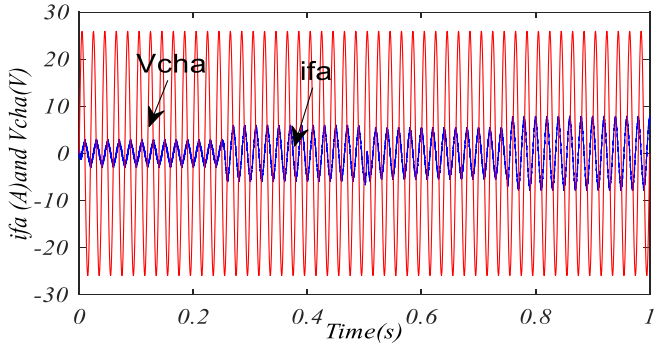

Fig. 12 Current of the first phase injected by the D-STATCOM and charging voltage

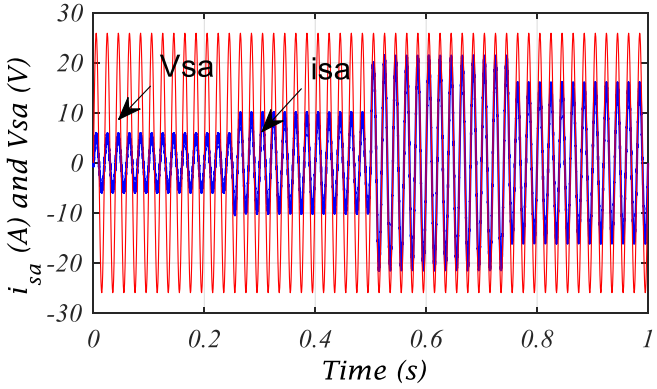

Fig. 13 Current and voltage of the first phase of the network

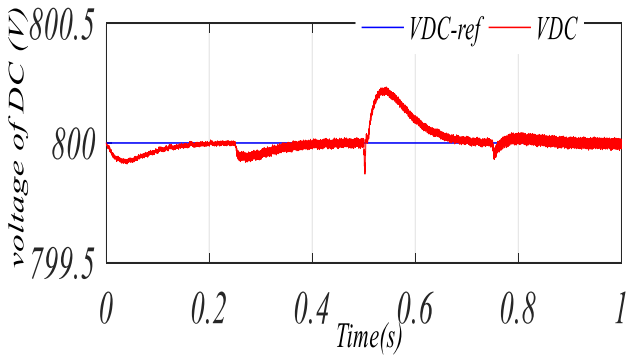

Fig. 14 DC bus voltage of the D-STATCOM and its reference with the PI regulator

Initially the capacitor of the DC bus is charged by a voltage equal to 800V. At the beginning of the simulation, the grid supplies the load ($Ch1$). A second load ($Ch2$) is connected to the network at the instant (t = 0.25 s), and at the instant (t = 0.5 s) we charge the line by the load($Ch3$), and finally (t = 0.75 s) the two loads ($Ch1$) and ($Ch2$) are disconnected. The D-STATCOM injects reactive power to the network from (0.1s to 0.5s) that means the operation of D-STATCOM which is in capacitive mode determines the sign of the reactive current i_{fq} injected by the D-STATCOM to the network. This current is positive "Fig.10", and as the reactive power is the inverse sign "Fig.9" of this current. After the instant (t = 0.5 s) D-STATCOM absorbs reactive power from the network when the inductive loads ($Ch1$ and $Ch2$) are disconnected , so the operation of D-STATCOM is in inductive mode and the reactive current is negative "Fig.9" . The form of this reactive current is shown in "Fig.10".

"Fig.11" shows the shape of the active current exchanged between the D-STATCOM and the network. This current is generally low since it represents only the active power required to maintain the voltage across the capacitor plus the switching losses of the semiconductor components. It is noted that the currents of the D-STATCOM, i_{fd} and i_{fq} follow their reference quantities calculated from the reactive and active powers necessary to compensate the reactive power in the line and to keep the DC voltage constant. These results prove the effectiveness of the regulators used.

In “Fig.12”, it is noted that the current is in advance with respect to the voltage of the point of common coupling PCC when the line is charged by the inductive load $Ch2$. It should be noted that at the instant (t = 0.5) the current of the first phase is backward relative to the voltage of the PCC because the D-STATCOM operates in inductive mode. Indeed, the capacitive load delivers a reactive power in the network, a part of this power compensates for the reactive need of the inductive loads ($Ch1$ and $Ch2$) and the remaining part is absorbed by the D-STATCOM. After the instant (t = 0.75) the two charges ($Ch1$ and $Ch2$) are disconnected and all of the reactive power delivered by the charge $Ch3$ is absorbed by the D-STATCOM. “Fig.13”, shows the source-side current and voltage and a unit power factor, such as the current to a sinusoidal form and in phase with the voltage of the source. From the curve of “Fig.14”, it seems very clear that the voltage regulator continues to prove its efficiency in maintaining a constant voltage across the global DC bus. The voltage goes through a transient period of less than 0.1s during the variation of the load before it returns to its reference with a zero static error.

VII. CONCLUSION

In this paper, the performance of the D-STATCOM has been analyzed effectively to improve the power quality (PQ) in the distribution network under the change of linear load, the simulation results shows the effectiveness and feasibility of proposed D-STATCOM with conventional PI controller for power factor correction and reactive power regulation, especially for DC voltage regulation.

ISSN: 2961-6611

REFERENCES

[1] K.-H. Tan, F.-J. Lin, C.-Y. Tsai, et Y.-R. Chang, " A Distribution Static Compensator Using a CFNN-AMF Controller for Power Quality Improvement and DC-Link Voltage Regulation ", *Energies*, vol. 11, nº 8, p. 1996, août 2018.

[2] S. S. SHIRDHONE, "A DSTATCOM Topology with Reduced DC-Link Voltage for Load compensating the using Non-stiff Source ", vol. 14, nº 2, p. 5.

[3] J. P. Busi et S. Yelavarthi, "A Fuzzy Logic based DSTATCOM for Diesel Generation System for Load Compensation ", *Indian J. Sci. Technol.*, vol. 8, nº 23, sept. 2015.

[4] C. Sumpavakup et T. Kulw, " Distribution Voltage Regulation Under Three- Phase Fault by Using D-STATCOM ", p. 5, 2008.

[5] *D. I. SATYANARAYANA, " Multilevel D-STATCOM for Linear and nonlinear loads to compensate reactive and active power during operation of distribution systems ", Appl. Sci., vol. 5, nº 8, p. 8, 2015.*

[6] D. S. Kumar, G. Pawanekar, et K. C. Reddy, " MMC based D-STATCOM for Different Loading Conditions ", vol. 02, nº 12, p. 6.

[7] G. Kumar A. et C. A. Babu, " A Zig-Zag Transformer and Three-leg VSC Based DSTATCOM for a Diesel Generator Based Microgrid ", *Procedia Technol.*, vol. 21, p. 310-316, janv. 2015.

[8] T. Yuvaraj, K. Ravi, et K. R. Devabalaji, " DSTATCOM allocation in distribution networks considering load variations using bat algorithm ", *Ain Shams Eng. J.*, vol. 8, nº 3, p. 391-403, sept. 2017.

[9] S. R. Reddy, P. V. Prasad, et G. N. Srinivas, " Design of PI and Fuzzy Logic Controllers for Distribution Static Compensator ", Int. J. Power Electron. Drive Syst. IJPEDS, vol. 9, no 2, p. 465-477, juin 2018.

[10] M. Kullan, R. Muthu, J. B. Mervin, et V. Subramanian, " Design of DSTATCOM Controller for Compensating Unbalances ", Circuits Syst., vol. 07, no 09, p. 2362-2372, 2016.

[11] O. P. Mahela et A. G. Shaik, " A review of distribution static compensator", Renew. Sustain. Energy Rev., vol. 50, p. 531-546, oct. 2015

ISSN: 2961-6611

Evolution of Crystal violet adsorption onto low cost adsorbent

Meriem Zamouche*[1], Asma Habib, Kenza Saaidia, Sihem Arris[1].

[1]*Laboratory of the engineering and the processes of environment (LIPE).Faculty of Processes Engineering, University of Constantine 3, 25000, Algeria.*
zamouche_meriem@yahoo.fr

***Abstract*—Cedar Cones (CC), an abundant forest waste in Algeria, was use as adsorbent for removal of basic Crystal Violet (CV) dye from aqueous solutions in a batch system. The adsorption process was examined as the functions of multiple variables affecting adsorption such as: stirring speed [100-600] rpm, solution pH [2-12], temperature [20-50]°C and initial dye concentration [10-200]mg/L. The adsorption uptake was found to increase with increase in initial dye concentration, but decreases with the amount of adsorbent and at very acidic pH. Maximum removal of dye was observed at stirring speed of 300rpm, pH 5.5 and temperature of 25°C. The equilibrium data were analyzed using the Langmuir, Freundlich and Temkin isotherm models. The equilibrium data were best described by the Freundlich isotherm model. The intra-particle diffusion was identified to be the rate-limiting step in addition to the film diffusion. Thermodynamic parameters such as Gibbs free energy, enthalpy and entropy were determined. It was found that the dye adsorption was spontaneous and endothermic.The results showed that CC sorbent was a promising for the removal of CV from aqueous solutions.**

***Keywords*— Adsorption; Cedar Cones; Crystal Violet; Kinetic.**

I. INTRODUCTION

In everyday life dyes are ubiquitous. These organic chemical compounds can be natural or synthetic. The manufacture and use of synthetic dyes for fabric dyeing has become a solid industry. It is estimated that around 700,000 tons of dyes are produced worldwide each year, about 20% of which is discharged as industrial waste into the environment without treatment [1].

Among the industries that use significant amounts of dye to color their products can include: textiles, ceramics, books and printing. Some dyes are absorbed in the product, and some of them are found in wastewater [2].

The increasing existence of dyes in aqueous bodies is one of the most important environmental issues. The dyes do not undergo natural degradation; hence the persistent color hinders the passage of light into the water and spoils the ecosystem [3].

Crystal Violet (CV) or Gentian Violet is a well-known cationic dye that penetrates the aquatic effluent systems of the textile industry, paint industry and also medicine and the biotechnology industry. CV is toxic and can be absorbed through skin causing irritation and is harmful by inhalation and ingestion and in extreme cases can lead to severe renal failure. So eliminating this dye from water and wastewater is of great importance.

Various methods of treatment have been used over the years by industries to remove dyes from their waste, whether physicochemical, chemical or biological treatment such as: flocculation-coagulation, precipitation, adsorption, membrane filtration, electrochemical techniques, ozonation. These dyes are generally of complex structures, is very difficult to treat using conventional methods. Adsorption is one of the most efficient advanced wastewater treatment process, which is used by industries to reduce hazardous pollutants present in effluents. This technique has been widely used for the removal of aqueous dyes worldwide because of the initial cost, operating conditions and simplicity of design [1].

In this work, we study the elimination of Crystal Violet (CV), a cationic dye from aqueous solutions by cedar cones (CC), a forest waste, chosen as a low-cost adsorbent material.

II. MATERIAL AND METHOD

A. *Adsorbat*

Crystal Violet (CV), also known as Gentian Violet, is a methyl violet, which is a group of basic dyes. It is a mixture of 5 and 6-methyl hydrochloride hydrides. (Penta methyl para rosaniline and hexa methyl violet). Its Rosanilines group, which is part of the Triphenylmethanes. It is soluble in water, and in alcohol [4, 5]. CV is extensively used as a purple dye in textile industry for dyeing of cotton, acrylic, nylon, wool, leather, paper, plastics and silk. [6] It also finds application in the manufacture of paints and printing inks. In the medical community, it is used as a biological stain and is the active ingredient in Gram's stain. In animal and veterinary medicine, it is employed as a bacteriostatic agent [7].

Further, it's a carcinogenic that has been classified among the recalcitrant molecules since it is poorly metabolized by microbial flora; it is not only biodegradable but it might persist in environmental medium as well. [6]. The dye is responsible for causing moderate eye irritation, causing painful sensitization to light. It can also cause permanent injury to the cornea and conjunctiva since the product contains a cationic dye. It is highly toxic to mammalian cells and if absorbed in harmful amounts through the skin, it can cause skin irritation and digestive tract irritation. [7]. The chemical structure of CV is shown in Fig.1 and the physicochemical characteristics of the dye are grouped in TABLE.1. All the chemicals used in this study were of analytical grade.

ISSN: 2961-6611

500mg/L CV stock solution was prepared and further diluted to achieve the desired mg/L levels for conducting experiments.

TABLE.1.

PHYSICOCHEMICAL PROPERTIES OF PURPLE CRYSTAL [5,6].

Brute formula	$C_{25}H_{30}ClN_3$
Molar mass	407.99 g/mol
Melting point	205°C- 215°C decompose
Colours	Yellow at acid pH / Blue-Violet at basic pH (>8)
pKa [8]	3.29 – 3.78 -4.26
Wavelength λ	590.5nm (measured value)

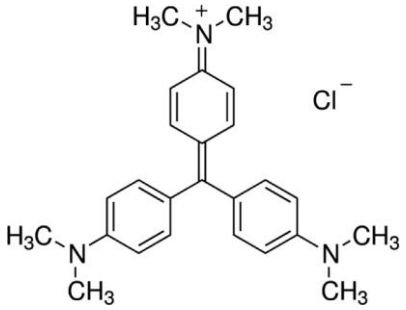

Fig. 1 Chemical structure of CV [5].

B. Adsorbent

The cedar cones were collected from the Chelia forest in Khenchla, Algeria. They were crushed and sieved to obtain a grain size between 1 and 1.25 mm. They are washed several times with distilled water until complete elimination of color and impurities. Then they are dried in an oven at a temperature of 105°C until constant weight.

C. Batch experimental study

The adsorption kinetics study of CV by CC was performed in batch reactor (250 mL) perfectly agitated and thermostated, the kinetic experiments were carried out by contacted 100mL of CV solution at concentration of 50 mg/L with a specified dose of CC to get an ratio of **20/0,1** (V/m). The mixture was stirring at 300 rpm at constant temperature of 25°C until equilibrium is reached. The amount of dye adsorbed is calculated from the residual concentration in solution according to the following equation:

$$q = \frac{C_0 - C_t}{m} * V \qquad (1)$$

Where

q: amount of pollutant per unit mass in mg/L

C_0 and C_t are the initial and residual concentration of dye in solution (mg/L);

V: volume of the adsorbent in L; m: mass of the adsorbent in g.

The percentage of dye removal can be calculated as follows:

$$E\% = \frac{C_0 - C_t}{C_0} * 100 \qquad (2)$$

With

E: The percent elimination of the dye considered.

Various operating parameters such as initial concentration of dye, contact time, pH, stirring were optimized to obtain maximum removal efficiency of CV by CC.

III. RESULTS AND DISCUSSION

A. Measure of pH_{PZC} and surface functional groups of CC

The pH of zero charge (pH_{PZC}) of the CC was determined by the so-called pH drift method as given by Nandi et al [9]. The technique consist to prepare solutions of NaCl at 0.01 $mol.L^{-1}$ at different initial pHs ranging from 2 to 12, the pH was adjusted by addition of HCl and/or NaOH at 0.1 mol/L. A volume of 50 mL of each solution was been contacts with (0.1 g) masses of CC with stirring for 48h and the final pHs were measured and plotted versus the initial pHs. The pH_{PZC} was determined by the value for which the pH_{final} is equal to the $pH_{initial}$ (The pH_{PZC} is the point where the pH_{final}=$pH_{initial}$). As shown in Fig.1, the pH_{PZC} determinate by the intersection of the two curves of the CC was equal to **5.8**.

The acidic and basic surface functional groups were determinate by the Bohem titration method [10]. The results obtained (TABLE.2) show that the acidic functional groups consist only of weak lactones and carboxylic acid (G II), the other two groups (GI) and (GIII) are zero. The quantity in basic functions is very low; the quantity of acid functions is greater than that of the basic ones. The total surface function of Cedar Cones is 0.19 m_{eq}/g.

TABLE.2.

CEDAR CONE SURFACE FUNCTION.

Concentration as a function of surface groups	**$m_{eq/g}$**
Concentration as a function of surface	0
Strong carboxylic acid (G I)	0.17
Lactone and weak carboxylic acid (G II)	0
Hydroxyl and phenol (G III)	0
Total of acidic surface functions	**0.17**
Total of basic surface functions	**0.02**

B. Effect of operating parameters

1) Effect of solution temperature

Temperature is a highly significant parameter in the adsorption process, to test its influence on the adsorption of CV by CC, the temperature were varied from 20, 25, 30, 40 and 50°C. Fig.2 presents the percent removal of CV as function as solution temperature. As depicted in Fig.2 the solution temperature have not a remarkable effect on the quantity of dye eliminated by Cedar Cone, the percent removal of CV is approximately equal to 99% for all the temperatures studied. A small exception has been observed at 30°C or the percentage is decreased to 96.52%.

A maximum of elimination was obtained at the temperature of 50°C, this is probably due to the destruction of the molecule Crystal Violet for high temperatures. This further contributes to increasing the percentage of dye removal by adsorption and destruction at elevated temperatures.

ISSN: 2961-6611

The value that was considered as optimum temperature for the rest of the adsorption tests of this work and which gave a maximum of dye removal is the ambient temperature of 25°C (99.62%).

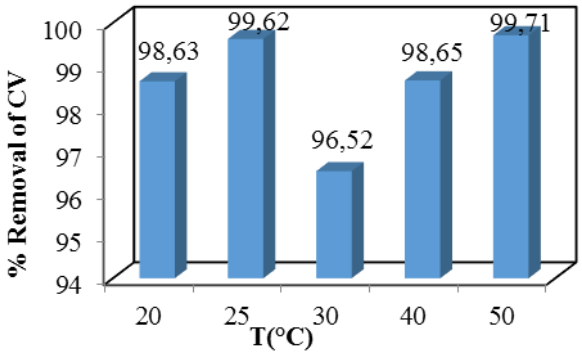

Fig.2 Percent removal of CV by CC as function as the solution temperature (C_0=50 mg/L, W = 300 tr/min, m=2.5 g and $pH_{naturel}$ = 5.5).

2) Effect of stirring speed

The search for optimal stirring speed is an essential step in any adoption study of a given pollutant. This is why we tested this effect on dye adsorption by CCs. Thus the stirring speed was varied as follows: 100, 250, 300, 400, 500 and 600 rpm.

Fig.3 show that the percent removal of dye increases with the increase in stirring speed from 100 to 250 rpm. With increasing the stirring speed, the rate of diffusion of dye molecules from bulk liquid to the liquid boundary layer surrounding the particle become higher because of an enhancement of turbulence and a decrease of thickness of the liquid boundary layer [11].

Above 250 rpm (between 300 and 600 rpm) the amount of dye removed remains almost constant. At the stirring speed of 100 rpm, there is a poor distribution of the adsorbate-adsorbent particles in the solution; the solution is not homogeneous, which does not ensure a preferable contact between them. The results obtained indicate that the optimal stirring speed chosen is 300 rpm; this speed ensures good stirring to promote the adsorption of the dye.

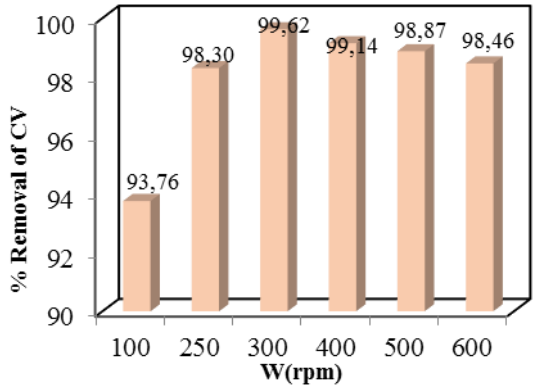

Fig. 3 The effect of the stirring speed on the removal of CV by CC (C_0= 50 mg/L, m = 2.5 g, T = 25°C and $pH_{naturel}$ =5.5).

3) Effect of pH solution

pH is one of the most important parameters which controls the adsorption process particularly the adsorption capacity. pH of the solution may change: the surface charge of the adsorbent, the degree of ionization of the adsorbate molecule and extent of dissociation of functional groups on the active sites of the adsorbent [12]. The effect of pH solution have been studied at the optimal speed of 300 rpm, the optimum temperature of 25°C and the optimum adsorbent dose of 2.5 g. While the concentration and volume of solution were kept constant (50 mg/L, 100 mL respectively). The pH was varied as follows: 2, 4, 6, 8, 10 and 12, the pH of the solution is adjusted by the addition of hydrochloric acid (0.1N) or sodium hydroxide (0.1N). The effect of pH is shown in Fig.4.

As can be seen in Fig.4 at pH 2, removal of CV was low (87.53%). At this pH, the surface of CC is positively charged ($pH<pH_{PZC}$=**5.8**), whereas the Crystal Violet is cationic which induces a repulsion between the surface of Adsorbent and the CV. Beyond pH equal to 2, at the pH range [4-10], it was observed an increase in the percent removal of CV by CC with the increase in pH solution. In this pH range [4-10], the surface of the CCs is positively charged when ($pH< pH_{PZC}$= 5.8) and became negative when ($pH>pH_{PZC}$= 5.8). At the first state [$pH>2$ to pH_{PZC}=5,8]), the percent removal increase gradually with the increase of the solution pH until reach a maximum value of 98.24% at pH equal to 5.5 (naturel pH without modification). At this pH, the surface of CC is positively charged ($pH <pH_{PZC}$) and the dye ion is positively charged, which normally gives rise to electrostatic repulsion, but unlike, a maximum of elimination has been obtained, which can be due to another phenomenon other than electrostatic forces like chemo-sorption.

At the second region [$pH>pH_{PZC}$=5.8 to 10], CV dye is positively charged (for CV dye, the pKa values of the N groups are 3.29, 3.78 and 4.26) and in parallel, the CC surface is negatively charged. Therefore, the positive CV dye molecule interacts with the negative surface of the CC, Similar trend was found by Brião and al [8]. In other hand in this second region [pH_{PZC}= 5.8 to 10] the concentration of H^+ decreases when pH increase which promotes the attraction between the dye ions and the adsorbent sites because the H^+ does not enter into competition with the CV to occupy active adsorption sites [13].

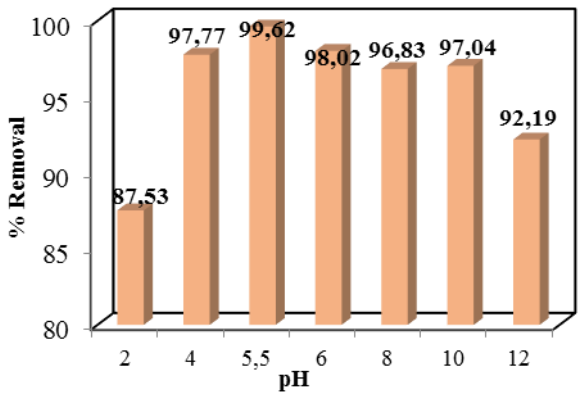

Fig. 4 The effect of pH on the removal of CV by CC (C_0=50 mg/L, m= 2.5 g, W = 300 rpm and T= 25°C).

4) Effect of sorbate concentration

The effect of initial CV concentration in the range of 10-200 mg/L on its percent removal of dye was studied at different temperature. The results are shown in Fig.5.(a, b and c).

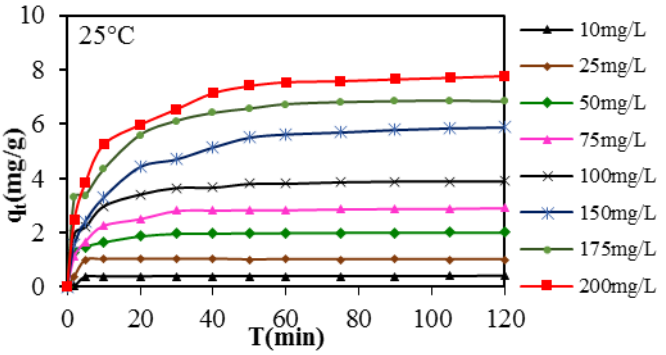

FIG. 5.a. The effect of initial concentration of dye on the removal of CV by CC (m = 2.5g, W = 300 rpm, T = 25°C and $PH_{NATUREL}$ =5.5).

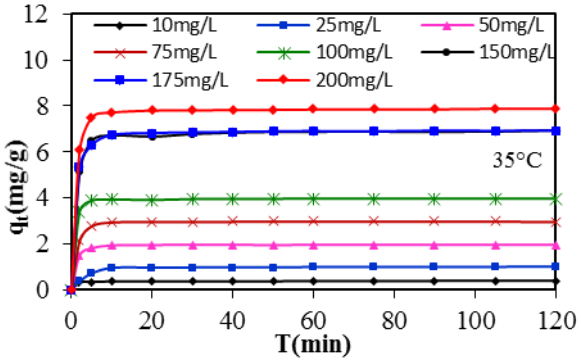

FIG. 5.b.The effect of initial concentration of dye on the removal of CV by CC (m = 2.5 g, W = 300 rpm, T = 35°C and $PH_{NATUREL}$ =5.5).

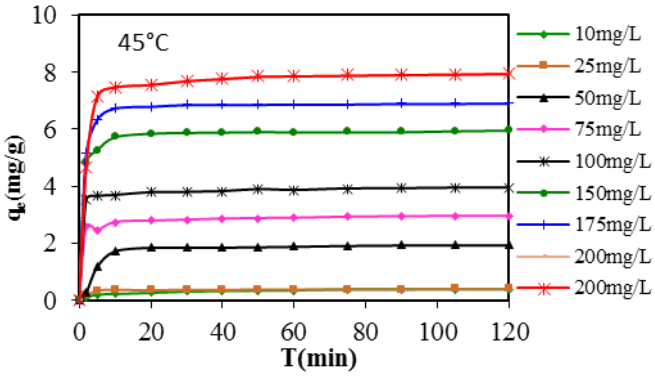

FIG. 5.c.The effect of initial concentration of dye on the removal of CV by CC (m = 2.5 g, W = 300 rpm, T = 45°C and $PH_{NATUREL}$ =5.5).

The result obtained shows that the increase in concentration of dye leads to an increase in the amount of dye adsorbed. It was clear that the elimination of CV was dependent on the initial concentration of dye. When the concentration of CV rise from 10 to 200 mg/L the amount of dye adsorbed increase from 0.39 to 7.7 mg/g, 0.39 to 7.79 mg/g and 0.37 to at 7.95 mg/g for the temperatures of 25, 35 and 45°C respectively. Concentration of adsorbate provides driving force to overcome mass transfer resistance between solid and solution phases [14].

C. Equilibrium isotherms

The isothermal adsorption models that have been used to fit and estimate the equilibrium data for CV adsorption on CC are Langmuir (four linear forms), Freundlich and Temkin. The Langmuir model assumes monolayer sorption on a surface with a finite number of identical sites [15]. The Freundlich model assumes heterogeneous adsorption surface and an exponential distribution of active sites [16]. The Temkin isotherm equation assumes that the fall in the heat of adsorption of all the molecules in the layer decreases linearly with coverage due to adsorbent–adsorbate interactions, and that the adsorption is characterized by a uniform distribution of the binding energies up to some maximum binding energy [17]. The linear form of the Langmuir, Freundlich and Temkin isotherm models are given in Table.3.

TABLE 3
ISOTHERM MODEL EQUATIONS

Isotherms	Non- linear forms	linear forms	Plot
Langmuir I [15]	$\frac{q_e}{q_m}=\frac{KC_e}{1+KC_e}$	$\frac{1}{q_e}=\frac{1}{q_m}+\frac{1}{Kq_m}\frac{1}{C_e}$	$1/q_e$ vs de $1/C_e$
Langmuir II [15]		$\frac{C_e}{q_e}=\frac{1}{Kq_m}+\frac{1}{q_m}C_e$	C_e/q_e vs de C_e
Langmuir III [15]		$q_e=-\frac{1}{KC_e}\frac{q_e}{}+q_m$	q_e vs de q_e/C_e
Langmuir IV [15]		$\frac{q_e}{C_e}=-Kq_e+Kq_m$	q_e/C_e vs de q_e
Langmuir V [15]		$\frac{1}{C_e}=K.q_m.\frac{1}{q_e}-K$	$1/C_e$ vs de $1/q_e$
Freundlich [16]	$q_e=K_F C_e^{1/n}$	$\ln q_e=\ln K_F+\frac{1}{n}\ln C_e$	$\ln q_e$ vs de $\ln C_e$
Temkin [17]	$\ln q_e=\frac{RT}{b}.\ln(K_T C_e)$	$q_e=B_1\ln K_T+B_1\ln C_e$ With $B_1=RT/b$	LnA vs $\ln C_e$

Where q_m(mg/g) and K(L/mg) are the Langmuir isotherm constants. K_F(mg/g)(L/mg)$^{1/n}$ and n are the Freundlich adsorption constant and n is the heterogeneity factor. T is the absolute temperature (K), R is the universal gas constant (8.314 J/mol.K), and b is the Temkin constant related to heat of adsorption (J/mol), B_1 is Temkin constant related to maximum binding energy (J/mol) and K_T is the equilibrium binding constant (L/mg).

The fitting curves of the adsorption isotherms based on a linear model of Langmuir (four linear forms), Freundlich and Temkin model are presented in Fig.6. The values of the constants of applied models are listed in Table.4.

TABLE 4
ISOTHERM PARAMETERS FOR ADSORPTION OF CV FROM AQUEOUS SOLUTION ON CC AT 25, 30, 45°C.

Type	Parameters	25°C	35°C	45°C
Langmuir I	q_m(mg/g)	-14.75	-17.03	-1.05
	K(L/mg)	-0.077	-0.12	-0.622

ISSN: 2961-6611

	r^2	0.845	0.603	0.920
Langmuir II	q_m(mg/g)	19.08	32.15	-2.365
	K(L/mg)	0.081	81.84	-2.354
	r^2	0.424	0.024	0.447
Langmuir III	q_m(mg/g)	8.23	5.355	-1.029
	K(L/mg)	0.298	0.323	-0.591
	r^2	0.2	0.079	0.687
Langmuir IV	q_m(mg/g)	24.38	91	-3.222
	K(L/mg)	0.064	0.045	-0.407
	r^2	0.216	0.001	0.687
Freundlich	K_F (mg/g) $(L/mg)^{1/n}$	1.38	1.19	2.45
	n	1.12	2.66	0.51
	r^2	0.93	0.69	0.91
Temkin	K_T (L/g)	2.39	5.11	2.24
	B_1(J/mol)	2.34	2.38	4.77
	b(J/mol)	1055.63	1072.90	553.9
	r^2	0.94	0.75	0.94

The isothermal data for CV adsorption by CC was incorrectly fitted with the Langmuir model, although the satisfactory coefficient of correlation obtained at T = 45°C (r^2=0.92) (Langmuir linear form I), since the maximum monolayer adsorption capacity (q_{max}) and the Langmuir constants (K) are negative for practically all linear forms of Langmuir tested. In addition, the maximum adsorption capacities and the positive equilibrium constants do not reflect the applicability of the model given the poor correlation coefficients obtained. Thus, the Langmuir model cannot adequately describe the experimental results of adsorption equilibria of CV by CC for all temperatures studied.

As reported in Table.4 and by comparing the coefficients correlation obtained for Freundlich and Langmuir, it can be seen that the Freundlich isotherm model could be the best model for the description of the adsorption behavior of CV on CC with higher coefficient of correlation (r^2= 0.91), with an exception at the temperature of 35°C (r^2 = 0.69). Similar result was reported in the literature for adsorption of CV on magnetic chitosan nanocomposite [18] and the adsorption of CV on waste materials [19].

The slope (1/n) value range of 0–1 is used to determine the surface heterogeneity and heterogeneity, it becomes more heterogeneous as its value gets closer to zero. The values n for temperature 25 and 35°C are higher than that of 45°C and higher than one indicates that the adsorption of CV by CC was favored by positive cooperativity binding and heterogeneous in nature [15, 20].

The value of 1/n in the range of 0.1-1 strongly supports the favorability of adsorption reaction [18,21]. From these findings, it is concluded that the Freundlich model gives a better fit of the experimental data with respect to the Langmuir equation.

The results obtained by the Temkin model show that the coefficients of determination obtained are very satisfactory ($r^2 \geq 0.94$) for the two temperatures of 25 and 45°C with an exception for the temperature of 35°C, signifying that adsorbate–adsorbate and adsorbate–adsorbent interactions both control the dye removal process isotherm [22]. The positive and higher value of (b_t) for all the temperatures studied which is an indication of the heat of adsorption signifying a chemical adsorption for CV uptake [22] and which shows also that the elementary adsorption process of CV by CC is exothermic [23].

D. Mechanism of sorption

1) Weber and Morris Model

The intra-particle diffusion model based on the theory proposed by Weber and Morris (1963) [24] was used to identify the diffusion mechanism. According to this theory, if the rate limiting step is intraparticle diffusion, a plot of solute sorbed against square root of contact time should yield a straight line passing through the origin [25]. However, if the data exhibit multi-linear plots, then two or more steps influence the sorption process [26]. The equation describing Weber and Morris model is given by:

$$q_t = c_i + K_i * \sqrt{t} \qquad (3)$$

Where c_i is the intercept and K_i (mg/gmin) is the intraparticle diffusion rate constant.

The slope of the linear plot of q_t versus $t^{1/2}$ is represented in the Fig.6. The obtained K_i and c_i values for different initial concentrations and shown in Table.5.

Given the multi-linear nature (Fig.6) of the plot for CV sorption on CC and very good correlation of coefficients obtained, it is proposed that sorption happened in three segments. The first region for all studied concentrations does not pass through the origin, suggesting that the diffusion in the pores does not control the overall rate of adsorption. Therefore, it is confirmed that the first linear segments represent external surface adsorption, the second linear segments represent the intraparticle diffusion, and the third segment is the equilibrium phase where low adsorbate concentration in solution results in the slowing down of the intraparticle diffusion [27]. Since the plot did not pass through the origin, intra-particle diffusion was not the only limiting step in the transfer of materials.

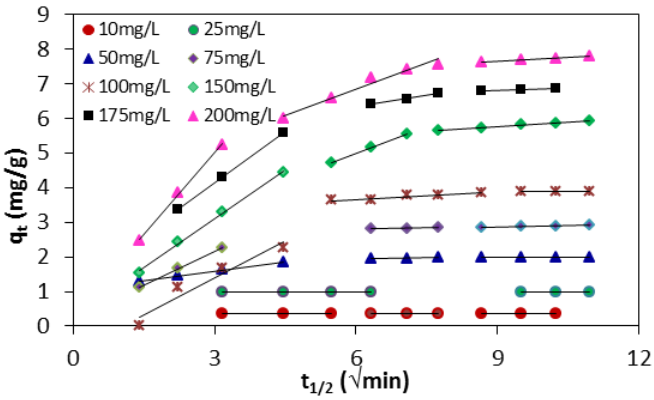

FIG.6. Evolution of the quantity adsorbed as function of square root of time for several initial concentrations at T = 25°C.

TABLE.5.

ISSN: 2961-6611

WEBER AND MORRIS MODEL PARAMETERS AND CORRELATION COEFFICIENTS FOR DIFFERENT INITIAL CONCENTRATION

	10	25	50	75
K_1(mg/gmin$^{1/2}$)	0.006	0.004	0.185	0.652
C_1(mg/g)	0.352	0.990	1.041	0.194
r_1^2	**0.994**	**0.899**	**0.995**	**0.998**
K_2(mg/gmin$^{1/2}$)	-0.002	/	0.010	0.006
C_2(mg/g)	0.405	/	1.895	2.785
r_2^2	**0.999**	**/**	**0.970**	**0.974**
K_3(mg/gmin$^{1/2}$)	0.004	0.005	0.004	0.018
C_3(mg/g)	0.342	1.027	1.953	2.705
r_3^2	**0.999**	**0.996**	**0.951**	**0.909**

TABLE.5.

WEBER AND MORRIS MODEL PARAMETERS AND CORRELATION COEFFICIENTS FOR DIFFERENT INITIAL CONCENTRATION

	100	150	175	200
K_1(mg/gmin$^{1/2}$)	0.504	0.938	0.990	1.586
C_1(mg/g)	1.200	0.267	1.163	0.24
r_1^2	**0.962**	**0.997**	**0.999**	**0.999**
K_2(mg/gmin$^{1/2}$)	0.071	0.504	0.224	-12.48
C_2(mg/g)	3.240	1.943	0.499	3.816
r_2^2	**0.895**	**0.999**	**0.959**	**0.967**
K_3(mg/gmin$^{1/2}$)	0.007	0.083	0.036	0.073
C_3(mg/g)	3.804	4.99	6.483	6.898
r_3^2	**0.956**	**0.980**	**0.959**	**0.983**

2) Boyd Model

The Boyd et al. [28] model was applied in order to investigate the diffusion mechanism. The equation of the model is as follows:

$$B_t = -0,4977 - \ln(1 - F) \quad (4)$$

B_t is a mathematical function of F, which F is equivalent to q_t/q_e that represents the fraction of adsorbate adsorbed at different times. Boyd's model suggests that if the linear representation of B_t versus t passes through the origin, particle diffusion is in control of the sorption process; otherwise film diffusion is considered as the rate limiting step of the process [28].

The plots obtained (Fig.7) do not pass through the origin, and it's linear up to 20 min, which suggests that external transport is the rate limiting only in the first stages.

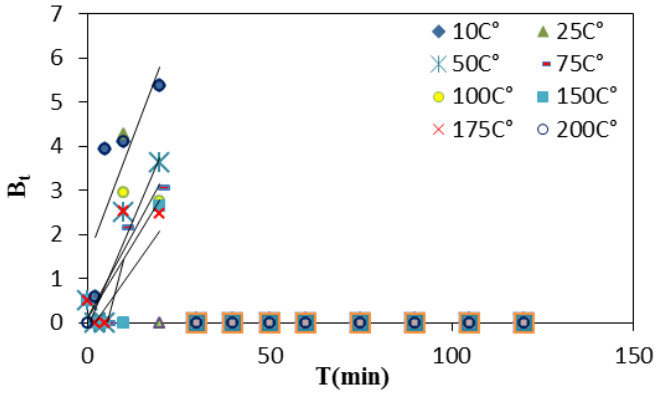

FIG.7. Evolution of Bt as a function of time for different initial CV concentration by CC at T = 25°C.

E. Thermodynamics studies

The adsorption studies was carried out at different temperatures from 298 to 318K with constant initial concentration, 50 mg/L, in order to calculate the thermodynamic parameters for the adsorption of CV onto CC.

The thermodynamic parameters that are determined are changes in standard enthalpy (ΔH), standard entropy (ΔS) and standard free energy (ΔG). The standard free energy ΔG is given by the Gibbs Helmholtz relation [29]:

$$\Delta G = -RT \ln K_d \quad (5)$$

Knowing that:

$$\Delta G = \Delta H - T\Delta S \quad (6) \text{ it comes}$$

$$\ln K_d = \frac{\Delta S}{R} - \frac{\Delta H}{RT} \quad (7)$$

With $$K_d = \frac{q_e}{C_e} \quad (8)$$

In which T is absolute temperature (K) and R is the gas constant. K_d is the distribution coefficient for adsorption, Where q_e and C_e are the equilibrium concentrations of dye ions on adsorbent (mg/L) and in the solution (mg/L), respectively.

The thermodynamic parameters were obtained from the linear plot of ln K_d vs 1/T and are shown in TABLE.6.

The positive value of ΔH° confirms the endothermic nature of CV adsorption by CC [30], [31].The low value of ΔS° may imply that no remarkable change in entropy has occurred during dye adsorption by cedar cone. In addition, the positive value of ΔS ° reflects the increased randomness at the solid-solution interface during adsorption [32] and also reflects the affinity of the adsorbent material for Crystal Violet [31]. The negative value of ΔG reveals that the CV adsorption process on CCs is spontaneous. As the temperature increases, the degree of spontaneity becomes more and more important [32].

ISSN: 2961-6611

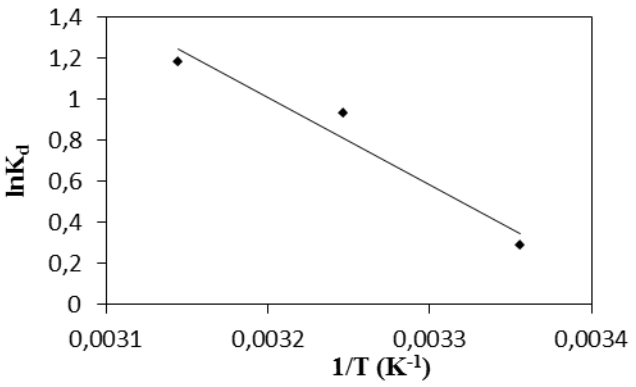

Fig.8. Plot of $\ln K_d$ against temperature for CV sorption onto CC.

TABLE.6.

THERMODYNAMIC PARAMETERS OF THE ADSORPTION OF CV ONTO CC.

T (K)	ΔG (KJ/mol)	ΔH (KJ/mol)	ΔS (KJ/mol.K)
298	-0.64	34.64	0.119
308	-22.43		
318	-26.31		

IV. CONCLUSIONS

Cedar Cone an available abundant forest waste, was effectively employed to remove of CV from aqueous solution. Batch adsorption studies informed that a maximum dye removal of 99,62% (almost a total elimination) at optimal level of pH 5,5, stirring speed of 300rpm, temperature of solution 25°C and initial dye concentration 50mg/L. Equilibrium adsorption data for CV is in good arrangement with Freundlich isotherm. The dye uptake process was found to be controlled by external transfer at the beginning of adsorption (the first 20 minutes) and by intraparticle diffusion at later times. Thermodynamic studies showed that adsorption system is spontaneous and endothermic. Cedar Cone as a forest waste is easily, abundantly available in north Algeria does not necessitate an additional pre-treatment step such as activation before its application, it's estimated to be economically viable for removal of basic dye from aqueous solution.

REFERENCES

[4] Marcel LECOMTE, fiche technique du crystal violet. http://www.pdffactory.com,

[5] Bertolini, T.C. R., Izidoro, J.C., Magdalena, C.P., Fungaro, D.A., Adsorption of Crystal Violet Dye from Aqueous Solution onto Zeolites from Coal Fly and Bottom Ashes. Electron. J. Chem. 5 (3):179-191, 2013.

[6] Miyah,Y and al. Assessment of adsorption kinetics for removal potential of Crystal Violet dye from aqueous solutions using Moroccan pyrophyllite, Journal of the Association of Arab Universities for Basic and Applied Sciences, 23, 20–28 (2017).

[7] Chakraborty,S., Chowdhury, S., Saha, P.D. Adsorption of Crystal Violet from aqueous solution onto NaOH-modified rice husk. Carbohydrate Polymers, 86, 1533–1541 (2011).

[8] Brião, G.V., Jahn, S.L., Foletto, E.L., Dotto, G.L. Adsorption of crystal violet dye onto a mesoporous ZSM-5 zeolite synthetized using chitin as template. Colloid and Interface Science. 508, 313–322 (2017).

[9] Nandi, B.K., Goswami, A., Purkait, M.K. Adsorption characteristics of brilliant green dye on kaolin. Journal of Hazardous Materials. 161, 387–395 (2009).

[10] Boehm, H.P. Chemical identification of surface groups. Advances in Catalysis 16, 179-274, 1966.

[11] Patil, S., Deshmukh, V., Renukdas, S., Patel, N. Kinetics of adsorption of crystal violet from aqueous solutions using different natural materials. Int. J of Environmental Sciences. 1.6, 2011.

[12] Nandi, B.K., Goswami, A., Das, A. K, Mondal, B., Purkait, M. K. Kinetic and Equilibrium Studies on the Adsorption of Crystal Violet Dye using Kaolin as an Adsorbent. Separation Science and Technology, 43: 1382–1403, 2008.

[13] Miyah, Y. and al. Removal of cationic dye "Crystal Violet" in aqueous solution by the local clay. JMES, 8 (10), pp. 3570-3582, 2017.

[14] Sidra Shoukat, Haq Nawaz Bhatti, Munawar Iqbal, Saima Noreen. Mango stone biocomposite preparation and application for crystal violet adsorption: A mechanistic study. j.micromeso.2016.10.004.

[15] El-Sayed, G.O. Removal of methylene blue and crystal violet from aqueous solutions by palm kernel fiber. Desalination, 272, 225–232 (2011).

[16] Sabna, V., Thampi, S.G., Chandrakaran, S. Adsorption of crystal violet onto functionalised multi-walled carbon nanotubes: Equilibrium and kinetic studies. Ecotoxicology and Environmental Safety, 134, 390-397 (2015).

[17] Sumanjit, Seema Rani, Mahajan, R.K. Equilibrium, kinetics and thermodynamic parameters for adsorptive removal of dye Basic Blue 9 by ground nut shells and Eichhornia. Arabian Journal of Chemistry, 9, S1464–S1477 (2016).

[18] Massoudinejad, M., Rasoulzadeh, H., Ghaderpoori, M. Magnetic chitosan nanocomposite: Fabrication, properties, and optimization for adsorptive removal of crystal violet from aqueous solutions. Carbohydrate Polymers (2018).

[19] Mittal, A., Mittal, J., Malviya, A., Kaur, D., Gupta, V.K. Adsorption of hazardous dye crystal violet from wastewater by waste materials. Journal of Colloid and Interface Science. 343, 463–473 (2010).

[20] Muthukumaran, C., Sivakumar, V.M., Thirumarimurugan, M. Adsorption isotherms and kinetic studies of crystal violet dye removal from aqueous solution using surfactant modified magnetic nanoadsorbent. Journal of the Taiwan Institute of Chemical Engineers, 63, 354–362 (2016).

[21] Hameed, B.H. Equilibrium and kinetic studies of methyl violet sorption by agricultural waste. Journal of Hazardous Materials. 154, 204–212 (2008).

[22] Ngulube, T., Gumbo, J.R., Masindi,V., Maity, A. Calcined magnesite as an adsorbent for cationic and anionic dyes: characterizationn, adsorption parameters, isotherms and kinetics study. Heliyon, 4, e00838 (2018).

[23] Hamdaoui, O., Naffrechoux, E.«Étude des equilibres et de la cinitique d'adsorption du cuivre cu (II) sur des particule reactives dans un reacteure ferme parfaitement agite et thermostat». Lebanese Science Journal, Vol. 6, No. 1 (2005).

[24] Weber, W.J., Morris, J.C., 1963. Kinetics of adsorption on carbon from solutions. J. Sanit. Eng. Div. 89, 31–60.

[25] V. J. P. Poots, G. McKay and J. J. Healy, Wat. Resour., 10, 1061 (1976).

[26] V. Fierro, V. Torne´-Ferna´ndez, D. Montane´, A. Celzard. Adsorption of phenol onto activated carbons having different textural and surface properties. Microporous and Mesoporous Materials 111 (2008) 276–284.

[27] Muhammad Khairud Dahri, Muhammad Raziq Rahimi Kooh, Linda B.L. Lim. Application of Casuarina equisetifolia needle for the removal of methylene blue and malachite green dyes from aqueous solution. Alexandria Engineering Journal . 54, 4, 2015, 1253-1263.

[28] G.E. Boyd, A.W. Adamson, L.S. Myers Jr., The exchange adsorption of ions from aqueous solutions by organic zeolites. II. Kinetics, J. Am. Chem. Soc. 69 (1947) 2836–2848.

[29] L. Zhu, X. Ren, S. Ku. Use of cethyltrimethylammonium bromide-bentonite to remove organic contaminants of varying polar character from water. Environ. Sc. Technol. 23 (1998), 3374-3378.

ISSN: 2961-6611

[30] Kezban Ada, Aysun Ergene, Sema Tan, Emine Yalcın: Adsorption of Remazol Brilliant Blue R using ZnO fine powder: Equilibrium, kinetic and thermodynamic modeling studies Journal of Hazardous Materials 165 (2009) 637–644.
[31] Hamdi M.H. Gad, Ashraf A. El-Sayed. « Activated carbon from agricultural by-products for the removal of Rhodamine-B from aqueous solution». Journal of Hazardous Materials 168 (2009) 1070–1081.
[32] Yu Liu, Ya-Juan Liu. «Biosorption isotherms, kinetics and thermodynamics». Separation and Purification Technology 61 (2008) 229–242.

ISSN: 2961-6611

The Impact of CT-density conversion curve for VMAT plans in Monaco Monte Carlo TPS: case of head and neck cancers

Said Elhaffari[#1], Yassine Herrassi[*2], Zineb Bouchbika[#3], Sofia Jebbari[*4], Ahmad Fathi[//5]

[#]*Centre Mohammed VI pour le traitement des cancers, CHU Ibn Rochd. Faculté de médicine et de pharmacie. Casablanca. Morocco*

[1]elhaffari@gmail.com

[3]bouchbika-zineb@yahoo.fr

[*]*PART consult Company Casablanca. Morocco*

[2]herassi.yassine@gmail.com

[4]jebbari.sofia@gmail.com

[//]*Laboratoire des sciences des matériaux, des milieux et de la modélisation. Faculté polydisciplinaire. Khouribga. Morocco*

[5]drfathi@hotmail.com

***Abstract*—**

Purpose: Inaccurate CT-to-density conversion curve (CDCC) information may introduce errors in dose calculation. The aim of this study is to investigate the sensitivity of volumetric modulated arc radiotherapy (VMAT) plans for head and neck cancer (HNC) with Monaco treatment planning system (TPS) to the CDCC. To obtain this goal, a comparison between dosimetric parameters obtained by VMAT plans using 3 different CDCCs was established.

Method: A CIRS phantom was scanned on 3 different CT-Scan. data from 10 previously treated patients were selected randomly from the list of patients with head and neck cancer that have received VMAT with Monaco planning system at our institution. Plans were evaluated using DVH for PTVs and OARs, the planning DVH objectives used to access plan quality for all plans included: minimum dose, D5%, D95%, V<95%, V>107% target, homogeneity index HI95% and conformity index CI95%. Paired t-test analysis was used to analyse the results. The number of UM of each arc, the total number of UM, the conformity and the heterogeneity indexes, were compared.

Results: A serious variation in the DVHs of the PTVs and the OARs were observed, a variation up to 6% for the OARs, and up to 6% for the PTVs were found. The number of UM of each arc and the total number of UM were found invariable. The conformity index (CI) and homogeneity index (HI) were acceptable.

Conclusion: It is important to consider the use of a specific (CDCC) for planning each VMAT treatment, A wrong (CDCC) will lead to a serious difference in delivering the wanted dose. The need to use the appropriate CT-to-density conversion curve through the treatment planning system is very clear.

***Keywords*— VMAT, MONACO MONTE CARLO, head and neck cancer, Ct-to-density conversion curve.**

I. INTRODUCTION

In radiotherapy, precise calculation of the dose is only possible when precise data are obtained from the patient. These data include body contour, shape and density of internal organs, location and spread of tumour volume, etc. The best way to obtain this data is to use three-dimensional imaging systems, including computed tomography (CT), magnetic resonance imaging (MRI), positron emission tomography (PET)

In radiotherapy treatment planning systems (TPS), dose calculations are performed on the CT image data. These images are imported into the treatment planning systems as input data in the planning process. CT images are used to contour different target treatment volumes and surrounding normal tissues or organs at risk (OAR). In addition, CT images contain quantitative data (CT values) that can be used to correct tissue heterogeneity in radiotherapy treatment plans. For accurate dose calculations, it is necessary to provide a correct relationship between CT numbers expressed in Hounsfield units (HU) and electron density in treatment planning systems. CT number values represent tissue electron densities and are directly related to the linear attenuation coefficients of tissues in the path length of the photon beam [1].

II. MATERIALS AND METHODS

In this study, we evaluate The Impact of CT-density conversion curve for VMAT plans using Monaco TPS

ISSN: 2961-6611

version 5.10 (Elekta CMS, Maryland Heights, MO, USA) on an Elekta Synergy linac (Elekta, Crawley, England).

A CIRS phantom (CIRS model 062 Tissue Simulation Technologie, Norfolk, VA) was scanned on 3 different CT-Scan using: NEUSOFT CT (Neusoft Medical System Co, China), OPTIMA CT 16 slice (GE Healthcare, Japan Corporation), OPTIMA CT 64 slice. After the scan, CT images of the CIRS phantom were downloaded into to the TPS, the HU values were used to establish the relationship between the different Physical Densities, electron densities and their corresponding CT number in Hounsfield units. Curves obtained from these 3 CT scanners are plotted in Fig 1.

Data from 10 previously treated patients were selected randomly from the list of patients with head and neck cancer that have received VMAT with Monaco TPS at our institution.

Two PTVs (PTV1 and PTV2) were defined from respective clinical target volumes (CTVs) by adding 3mm margin with 3D expansion. They were treated with two dose levels giving high dose to primary tumour (PTV1) and low dose to nodal disease (PTV2). Prescription to PTV1 were 66.6 in 30 fractions (#) and PTV2 WERE 54Gy in 30#. The PTVs were reduced to 3mm under skin surface to avoid optimization problem in the build-up region.

The VMAT plans consist of two full arcs (clockwise and counter clockwise) from 178° to 182°. Gantry spacing between two control points was 30° and optimization was made on cost functions parameters.

To identify the impact of changing a CDCC on the distribution of the dose, a recalculation of the treatment plan of the 10 patients was performed using each CDCC.

For each plan, a set of DVH parameters was analysed. For PTV, mean dose, D95%, D98% (near-minimum dose), and D2% (near-maximum dose) were taken into account, whereas, for OAR's, the maximum point and PTV2 were 54Gy in dose and the mean dose to the spinal cord (SC) and the mean dose to the left and right parotid (LP and RP) glands were considered.

To assess the homogeneity of dose distribution in the PTV, an homogeneity index was defined as HI = (D2% - D98%)/mean dose. The lower (closer to 0) the HI, the better is the dose homogeneity. Also, to facilitate the comparison of various treatment plans, the RTOG conformity index (CI) was calculated: CI = VRI/TV, where VRI = 95% − isodose volume and TV = target volume. A CI = 1 corresponds to ideal conformation. A CI > 1 indicates that the irradiated volume is greater than the target volume and includes healthy tissues. A CI < 1 indicates that the target volume is only partially irradiated.[2]

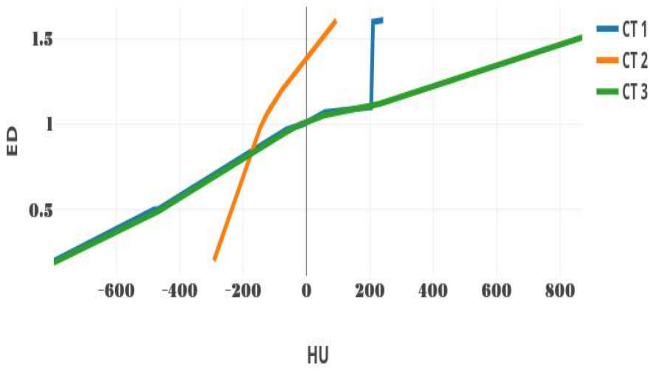

Figure 1 CT to ED conversion curves for the tree CTs

III. Results and Discussion

The overall results in terms of target dose homogeneity, Conformity Index and OARs statistics from DVH and plan analysis are displayed in Table 1. Figure 2 and 3 shows cumulative DVHs using the 3 CDCCs for one representative case. Paired t-test analysis was reported to determine the significance of the results (p<=0.05) for CDCC1 vs CDCC2 (P+) and CDCC1 VS CDCC3 (P-).

In terms of PTV1 homogeneity CDCC2 plans achieved best homogeneity followed by CDCC1.CDCC1 plans achieved very conformal plans with a mean of 0,312. However, difference was not statistically significant. D95% for CDCC1 plans that use a correct calibrated CDCC for TPS is significantly highest.

As shown in Table2. The number of UM of each arc and the total number of UM were found invariable.

As for the OAR's, CDCC2 plans allowed the largest sparing of spinal cord (SC), SC5mm in terms of maximum dose with statistical significance observed. Overall CDCC2 plans also allowed reduced parotid involvement compared to other CDCCs. CDCC1 plans spares SC5mm better then CDCC3 plans but difference is rather small. Mean dose to right parotid when using CDCC2 instead of CDCC1 resulted of a dose difference up to 5%, and 2% when using CDCC3. For left parotid the dose difference is 6% when using CDCC2 and 0.8% when using CDCC3.

Finally, difference dose for maximum doses to the spinal cord and SC5mm are 5% when using CDCC2 ,0.5% and 3 % respectively when using CDCC3.

	CDCC1	**CDCC2**	**P+**	**CDCC3**	**P+**
PTV1 H	1,093 (0,0035)	1,081	0,2216	1,098 (0,012)	6,79E-08
PTV1 CI	0,312 (0,084)	0,431	0,20	0,396 (0,05)	0,153
PTV95 %	65,48 (2,51)	61,92	0,0004	67,31(1,29)	0,0002
SC max dose	44,86 (1,63)	42,55	1,66E-10	44,62 (0,16)	5,98E-10
SC5mm max	50,77 (2,04)	47,88	1,15E-05	52,50 (1,22)	5,21E-06

ISSN: 2961-6611

dose					
Right parotid mean dose	25,58 (0,94)	24,24	2,53 E-08	26,09 (0,36)	1,05E-09
Left parotid mean dose	26 ,23 (1,02)	24,78	1,38E-08	26,45 (0,15)	1,28E-09

Table 1 CDCCS TARGET Homogeneity, Conformity Index, Coverage and OAR statistics

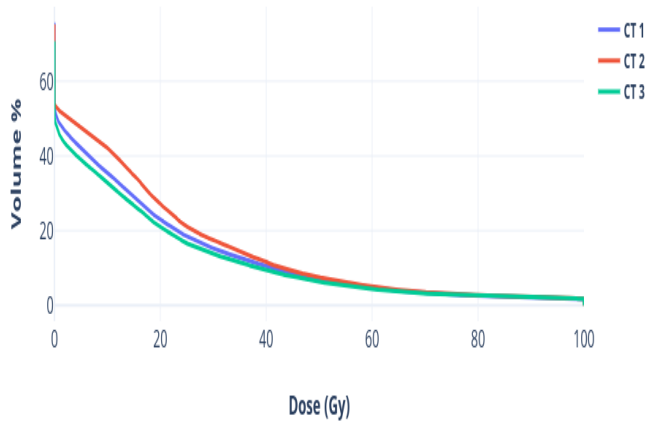

Figure 2 Right parotid DVH calculated with the 3 CDCC

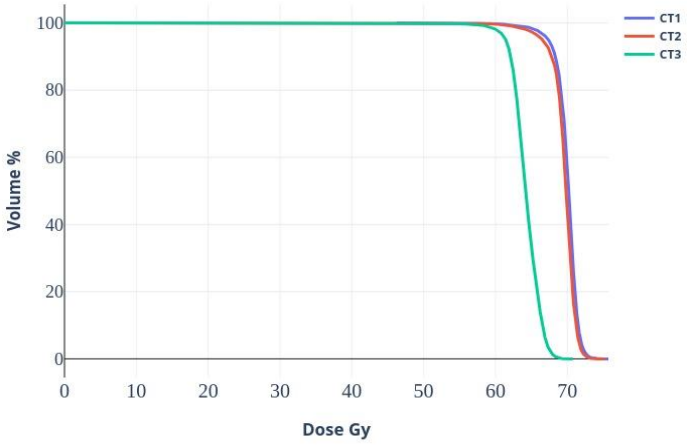

Figure 3 PTV1 DVH calculated with the 3 CDCC

Cases	CDCC	ARC1(UM)	ARC2(UM)	TOTAL(UM)
1	CDCC1	433,61	431,55	865,16
	CDCC2	464,9	378,83	843,73
	CDCC3	464,9	378,83	843,73
2	CDCC1	430,9	346,77	777,67
	CDCC2	430,9	346,77	777,67
	CDCC3	430,9	346,77	777,67
3	CDCC1	362,82	393,44	756,26
	CDCC2	362,82	393,44	756,26
	CDCC3	362,82	393,44	756,26
4	CDCC1	488,58	545,71	1034,29
	CDCC2	488,58	545,71	1034,29
	CDCC3	488,58	545,71	1034,29
5	CDCC1	547,63	387,3	934,93
	CDCC2	547,63	387,3	934,93
	CDCC3	547,63	387,3	934,93
6	CDCC1	407,2	389,92	797,12
	CDCC2	407,2	389,92	797,12
	CDCC3	407,2	389,92	797,12
7	CDCC1	623,9	566,77	1190,67
	CDCC2	623,9	566,77	1190,67
	CDCC3	623,9	566,77	1190,67
8	CDCC1	497,65	439,29	936,94
	CDCC2	497,65	439,29	936,94
	CDCC3	497,65	439,29	936,94
9	CDCC1	697,84	627,38	627,38
	CDCC2	697,84	627,38	627,38
	CDCC3	697,84	627,38	627,38
10	CDCC1	656,33	554,50	1210,83
	CDCC2	656,33	554,50	1210,83
	CDCC3	656,33	554,50	1210,83

Table 2 Monitor units for different CDCCs

IV. Conclusions

This study compared the dosimetric parameters obtained by VMAT plans for head and neck cancer using 3 different CDCCs and calculated by Monaco TPS, which to the best of our knowledge, has not been previously investigated.

the Monte Carlo method allows human tissues to be characterized by elemental composition and mass density, and hence allows the accurate consideration of all relevant electromagnetic and nuclear interactions [3].

The accuracy of Monte Carlo dose calculations is affected by the ability to precisely define materials based on the Hounsfield number information. Thus, in addition to electron or mass density, composing elements and their relative weights need to be known as well.

If there is a mismatch between the TPS calibration curve and Hounsfield unit values in the CT image for particular tissue types, it will lead to discrepancies in the dosimetric calculations performed by the TPS [4, 5].

In this study we present the impact of mismatching the CT images with the appropriate CDDCS for head and neck cancer. A serious variation in the DVHs of the PTVs and the OARs were observed, a variation up to 6% for the OARs, and the PTV were found.

ISSN: 2961-6611

Acknowledgment

We would like to acknowledge the Abdus Salam International Centre for Theoretical Physics (ICTP) in Trieste, Italy, for funding this research project.

We are also grateful to Prof. Renato Padovani for his continuous support and advice.

REFERENCES

[1] Schneider U, Pedroni E, Lomax A, *The calibration of CT Hounsfeild units for radiotherapy treatment planning*, Phys Med Biol. 1996 Jan;41(1):111-24.

[2] Mohamed Yassine Herrassi, Farida Benteyeb, Maria Rosa Malisan, *Comparative study of four advanced 3d-conformal radiation therapy treatment planning technique for head and neck cancer*, J Med Phys, 2013 Apr-Jun; 38(2):98-105.

[3] Hongyu Jiang, Joao Seco, Harald Paganetti, E*ffects of Hounsfeild number conversion on CT based proton Monte Carlo dose calculation,* Physmed.2007 apr;34(4):1439-1449.

[4] Inness EK, Moutrie V, Charles PH, *The dependence of computed tomography number to relative electron density conversion on phantom, geometry and its impact on planned dose*, Australas Phys Eng Sci Med. 2014 Jun;37(2):385-91.

[5] Cozzi L, Fogliata A, Buffa F, Bieri S. *Dosimitric impact of computed tomography calibration on a commercial treatment planning system for external radiation therapy*, Radiother Oncol.1998 Sep;48(3):335-8.

ISSN: 2961-6611

Lab-scale anaerobic digestion of cassava peels: A first step of energy recovery from cassava waste and water hyacinth

Sylvestre AHOU[1,2*], Lamine BABA-MOUSSA[2], Jean-Romain BAUTISTA ANGELI [1,3], Sary AWAD[1,]

Yves ANDRES[1]

[1] *IMT-Atlantique, GEPEA UMR CNRS 6144, Nantes, France*

[2] *Laboratory of Biology and Molecular Typing in Microbiology, LBTMM, UAC, Benin*

[3] *Scientific and Technical Center of the Building, Nantes, France*

[*]*Corresponding author. Tel: +33 6 10 04 04 78. E-mail: sylvestreahou@yahoo.fr*

Abstract

The cassava processing in Republic of Benin which is used to produce different food products generates a large amount of polluting organic matter into the environment in the form of peels and wastewater. Besides, the presence of water hyacinth on Beninese rivers poses a problem of water eutrophication and the aquatic ecosystem asphyxia. The waste come from cassava processing industry and the water hyacinth are both rich in biodegradable compounds which can be treated in anaerobic digester in order to produce methane. According to the literature, the main challenge in cassava waste anaerobic digestion is early inhibition caused by a rapid acidification due to low nitrogen and high biodegradable sugars content. In this paper, the complete physico-chemical characterization of cassava waste and water hyacinth was performed in order to evaluate their methanogenic potential. According to the theoretical estimates results, cassava peels and water hyacinth showed a high methanogenic potential. Experimentally, cassava waste has shown a high potential of methane production. However, it is important to emphasize that addition of *akanwu* potash and phosphate buffer pH 7.2 to cassava peels biochemical potential methane tests allowed biogas yield of 735±75 ml with 56 ± 2% of methane content (v/v of biogas) either the methane yield of 333 ± 58 ml CH_4 $g^{-1}VS_{added.}$ Therefore, co-digestion of cassava peels and water hyacinth has removed the chemicals products and improved cassava peels treatment. Furthermore, the methane yield of water hyacinth increased by 40 % when co-digested with cassava peels.

Keywords: Anaerobic digestion; methanogenic potential; Biogas; Cassava peels; Cassava wastewater; Water hyacinth.

1.Introduction

Population growth and food security result in discharging of different types of waste all over the world. Organic waste decomposes rapidly in the nature and cause large quantities of greenhouse gas emissions, just like the intensive consumption of fossil fuels. Cassava is a staple food for about 500 million people in the tropical countries. It widely grows in Africa, Latin America and Asia over a wide range of climates , altitudes and variety of soils [1]. In 2016, Benin produced about 4.32 million tons of cassava [2]. Out of this, 70% of the production was used in artisanal and semi-industrial methods to produce different food products [3] . The main problems of cassava processing are linked to high energy consumption and environmental pollution. For instance, processing of 1 kg of gari flour consumes about 1.30 to 2.40 kg of filao wood [4] . This fuelwood energy corresponds to 0.320-0.939 MJ of electrical energy and 1.141-2.749 MJ of thermal energy [5]. Cuzin et al.[6] demonstrated that 1200 kWh or 121 m^3 CH_4 is required to dry 1 ton of

ISSN: 2961-6611

cassava food derivatives . This intensive consumption of firewood affects considerably the forest resources and contributes to the global warming. Moreover one ton of starch processed requires about 20m^3 of washing water [7]. This also results in a discharge of a mass of cassava peels which accounts about 20-35% of the total wet weight of the cassava root [8] and 12 m^3 of effluent [7], [9], [10]. Due to the high content of cyanogenic glycoside compounds [11], cassava waste are uncomfortable for animal feed. Though efforts are generally made to add value to cassava peels by reducing the sugar content and enriching them with microbial protein, unfortunately the success of the study is limited [12]. Thus an accumulation of cassava peels and cassava wastewater is observed in industrial processing sites leading in nauseous odours and contaminated air, a source of diseases for humans and toxic for the surrounding ecosystems. At present, the disposal of cassava waste is a serious environmental problem and will become more in the future as a result of the growth of cassava processing industries. In fact, the efficient treatment of cassava waste through the anaerobic digestion technology could efficiency manage the cassava waste and generate back renewable energy at the same time. Okudoh et al.[13] showed that biogas production from an energy crop such as cassava can really add value to the whole bioenergy chain in Africa especially in South Africa. Moreover, the mean calorific value of cassava peels generated in Nigeria has been estimated to 10.61 MJ/kg [14]. However, these studies did not point out the acidification problem that occurs during the biogas production of cassava peels. Earlier Okafor et al.[11], conducted preliminaries studies on biogas production of cassava peels by the anaerobic digestion technology then showed their low biogas potential probably as a result of their content of toxic cyanogenic glycosides. These compounds degrade during fermentation of cassava waste and lead to hydrogen cyanide and acetone which are toxic to methanogenic bacteria.Some solutions have been identified to overcome the observed inhibition. For instance alkali pre-treatment such as addition of lime, sodium hydroxide (NaOH) and potassium hydroxide (KOH) removes the acetate groups from hemicellulose and makes them more accessible to hydrolytic enzymes which in turn enhances the digestibility[15]. Although the use of chemicals improved biogas production, attention should be paid to the investment cost related to the chemical products and environmental problem caused by the industrial scale of the process. Cassava waste, being rich in carbohydrates with a negligible amount of proteins, which lead the formation of fatty volatile acid and inhibit the methanogenic bacteria, as result of the low level of methane production in the digesters could be adjust by addition of nitrogen rich substrates. Manilal et al. [16] has showed the mixing of higher proportions of 20% (w/w) cow dung (C:N ratio 20:1) increased the nitrogen content of the materials in digesters and therefore increased the methane content of biogas. Water hyacinth (*Eichhornia crassipes*) which is an invasive plant widely spread on West African rivers, especially in Benin contents nitrogen in range of 12-35% [17]. Given to its high nitrogen content water hyacinth could adjust the high C:N ration of cassava peels to the optimum C:N of [20-30] for anaerobic digestion. Studies on the energy recovery from cassava waste and water hyacinth in the Republic of Benin are scarce or have not documented. The current study focused on cassava waste and water hyacinth methanogenic potential evaluation as an essential step in anaerobic treatment on a large scale. A small scale of anaerobic co-digestion of cassava peels with water hyacinth was experimented which is one step ahead of solving the environmental pollution caused by the proliferation of both cassava industries and

ISSN: 2961-6611

the water hyacinth. The biogas generated by the anaerobic digestion technology on large scale could provide to rural communities and cassava industries cost-effective energy and electricity in the Republic of Benin.

2.Materials and Methods

2.1. Biomass evaluation

2.1.1. Laboratory scale cassava processing

A mass of 3.6 kg of cassava root taken from exotic products markets in Nantes (France) were manually peeled wi and grated using a mixer in the GEPEA Laboratory of IMT-Atlantique of Nantes. The grated pulp was transferred into a basket, then fermented at room temperature for three days. The fermented pulp was manually pressed to extract the starch juice. The peels were dried-ground at 105 °C and stored at room temperature in sealed containers. Starchy water was stored at -20 °C for later use.

2.1.2. Evaluation of the biomass and sample collection in Benin

Cassava waste and water hyacinth evaluation was respectively carried out in several cassava processing units and rivers in Benin during the period of March 2018 to April 2018. The cassava processing industries visited, consist of small groups of women who process cassava manually throughout the year. The production averages 16 tons of cassava per week during the rainy season and 8 tons in the dry season. The collected cassava peels and water hyacinth were dried at 75°C and packaged at the Laboratory of Biology and Molecular Typing in Microbiology of the University of Abomey-Calavi in Benin Republic before being transported to the laboratory GEPEA in France for further analysis.

2.2. Characterization of samples

2.2.1. Gravimetric analysis

The elemental analysis (CHNS/O) were performed using a CHNS-O Analyzer ThermoFinnigan Flash EA 1112 Series. The total solids (TS), the volatile solids (VS) and the ash content were determined according to AFNOR standard [18], [19]. The dry matter was milled using an IKA MF 10 model knife mill to obtain a fine powder for carbohydrates assay. The thermogravimetric analysis (TGA) was carried out using the Setsys Evolution device in order to determine the fraction of complex sugars and the lignin content of the samples. According to the literature, the hemicellulose compounds degrade from 250 °C followed by the cellulosic compounds from 300 °C. Finally, the degradation of lignocellulosic compounds is achieved from 500°C.

2.2.2. Determination of protein content.

Protein content was calculated by multiplying the total nitrogen obtained from CHNS-O analysis by 6.25 (extracted from Zhong et al. [20]).

2.2.3. Determination of total carbohydrates.

The total sugars were determined according to the phenol-sulfuric acid method [21]. Briefly, 50 mg of the powder (dry matter) of the sample was hydrolyzed with 5 ml of a hydrochloric acid solution (2.5N HCl). The mixture was heated with a double boiler for 3 hours. After hydrolysis, the tubes were cooled to room temperature and then neutralized with sodium carbonate (solid). Aliquots (0.1 ml) of the neutralized solution containing the sample were diluted to 1: 10 and 1: 100 respectively in 0.9 ml of distilled water. After dilution, 1 ml of a phenol solution (5%) and 5 mL of a sulfuric acid solution (96%) were added and the contents were well mixed and cooled to 25-30 °C in a water bath. The intensity colour of the samples was measured at 490 nm using an Orion Aquamate 7000 ultraviolet-visible spectrophotometer. The total sugar content was calculated using **equation 1** of the standard calibration curve. The standard D-Glucose curve was:

ISSN: 2961-6611

$$y=0.0104\,x + 0.0108 \text{ with } R^2 = 0.9979 \qquad \textbf{(Equation 1)}$$

where R^2 represents the linear regression and x, *y* are respectively the glucose concentration and absorbance.

2.2.4. Determination of total lipids

Total lipid extraction was performed using C. Gerhardt's SOXTHERM® rapid method based on the use of solvents (polar and non-polar) to extract crude oils from the samples. Since the solvents react differently with the sample, polar and non-polar solvents were used to evaluate the effect of solvent polarity on lipid extraction. The solvents used in this study are: n-heptane as non-polar solvent and diethyl ether as the polar solvent. The physical properties of each solvent are shown in **Table 1**.

Table 1: Physical properties of solvents used for lipid extraction [22]

Solvent	Formula	Physical state	Fusion point (°C)	Boiling Point (°C)	Density (g/ml)
Non-polar solvent					
n-Heptan	C_7H_{16}	liquid	-90.6 °C	98.4 °C	0.68
Polar solvent					
Diethyl ether	$C_4H_{10}O$	liquid	- 116.3 °C	34.6 °C	0.714

About 6 g of dried-ground sample were weighed into a cellulose sewing thimble and placed in a cylindrical glass container containing pumice stone. A volume of 125 ml of solvent were poured into the cylindrical glass container until the sample in the thimble was completely immersed in the solvent. The set was placed in the Soxhlet extractor. The extraction process was carried out through a high temperature extraction phase followed by an evaporation phase during which the level of the solvent was reduced until a clear separation between the solvent and the extraction dice occurs. The lipids were then extracted from by the boiling solvent through reflux and condensation movements. Most of the solvent was distilled in the storage tank for later recovery. At the end of the process, the extraction beakers were lifted automatically from the hotplate. The evaporation process continued slightly without any adverse effects on the sample. Coolant and heating was automatically disabled when extraction was complete. The total lipid content was determined by using **equation 2** from the initial weight of the sample and the weight of the cylindrical glass container before and after the extraction.

$$\textbf{\% Lipid content} = \frac{(W2-W1)}{W3} * 100 \qquad \textbf{(Equation 2)}$$

where *W1* = Weight of the cylindrical container with pumice stone before the extraction process;
W2 = Weight of the cylindrical container containing the lipid extract and pumice stone; *W3* = Weight of the sample.

2.3. Estimation of the stoichiometric methane (Bo) yield of the samples.

The empirical formula ($C_aH_bO_cN_dS_x$) was established based on the elemental composition (C, H, N, S, O) of the samples. According to Angelidaki et al.[23] , when the composition of organic matter

ISSN: 2961-6611

is known, it is possible to evaluate the theoretical yields of methane and ammonia that can be expected from anaerobic digestion. Therefore the maximum methane stoichiometric (B_o) yield of the samples was determined following the **equations 3&4** established by Buswell et al. [24] and adopted by Sialve et al. [25]. The results, however, give only a maximum potential for methane, and will often be far too optimistic because neither the non-degradable materials nor the energy demand of the microbes as well as the inhibitory effects are not considered.

$$C_aH_bO_cN_d + \frac{(4a-b-2c+3d)}{4} H_2O \longrightarrow \frac{(4a+b-2c-3d)}{8} CH_4 + \frac{(4a-b+2c+3d)}{8} CO_2 + dNH_3 \quad \textbf{(Equation 3)}$$

In this equation, the organic matter is stoichiometrically converted to methane, carbon dioxide and ammonia. The specific stoichiometric methane yield expressed in milliliters of CH_4 per gram of volatile solids (VS) can therefore be calculated as follows:

$$Bo = \frac{1}{8}\left(\frac{4a+b-2c-3d}{12a+b+16c+14d}\right) Vm \quad \textbf{(Equation 4)}$$

where *Vm* is the molar volume of methane under normal pressure and temperature conditions.

2.4. Estimation of the theoretical methane yield of the samples.

Organic materials are mainly composed of carbohydrates, proteins and lipids that can be broken down into simpler compounds by microorganisms in an oxygen-free environment with the following process steps: hydrolysis, acidogenesis, acetogenesis and methanogenesis [26], [27]. The process of producing biogas from an organic material depends mainly on the content of the substrates that can be converted into biogas, while their chemical compositions and their biodegradability are the key factors in the production of biogas and methane [28]. Determining the degree of biodegradability and substrate composition optimizes biogas/methane production [29]. Knowledge of the concentration (on a % TS basis) of carbohydrates, proteins and lipids in the substrate made it possible to calculate the maximum theoretical yield (B_T) of the samples using the formula **(equation 5)** established by Prajapati et al[30] :

$$B_T = \frac{1}{100}(A \times Cl + B \times Cp + C \times Cc) \quad \textbf{(Equation 5)}$$

where A, B and C are respectively the specific methane yields of lipids, proteins and carbohydrates and *Cl, Cp, Cc* are the respective concentrations (based on % TS) of the lipids, proteins and carbohydrates of the organic substrate.**Table 2** extracted from Angelidaki et al.[23] compiles the specific methane yields of carbohydrates, lipids and proteins.

ISSN: 2961-6611

Table 2: Theoretical characteristics of typical substrate components

Substrate	Components	Specific yield of methane (l/gVS)
A : Lipids	$C_{57}H_{104}O_6$	1.014
B : Proteins*	$C_5H_7NO_2$	0.496
C : Carbohydrates	$(C_6H_{10}O_5)_n$	0.415

* Nitrogen is converted to NH_3

2.5. Experimental evaluation of biochemical potential of methane (BMP).

2.5.1. Method for determination of the rate of the biodegradation

The biochemical methane potential of the samples collected in Benin was carried out following the protocol developed by Angelidaki et al. [31] with minor modifications. Actually, biochemical methane potential gives the best information on the behaviour of a biogas feedstock in a biogas plant [32] which is an important test for the anaerobic degradability and acceptability of a feedstock. The experiment was conducted in 500mL serum flasks handle hermetically sealed caps with orifices for gas outlet and sampling. The useful volume was maintained at 400 ml and the remaining 100 ml were left for gas storage. The cassava peels used was previously mixed with *akanwu at* 1:1 ratio. Water hyacinth and cassava wastewater have not undergone any pre-treatment. The inoculum was taken directly from the anaerobic reactor in the GEPEA laboratory treating green waste, food waste and primary sludge. The initial concentration of the inoculum was 3.1gVS/L and the ratio of substrate/inoculum was 1 (based on VS content). The volume of the inoculum added was 300mL. Phosphate buffer pH = 7.2 was added to the flasks containing cassava peels then only tap water in those containing water hyacinth and cassava wastewater up to a volume of 400 ml. The carbon to nitrogen ratio was 70 for the cassava peels and 11 for cassava wastewater and water hyacinth.

2.5.2. Lab-scale anaerobic co-digestion of cassava peel with water hyacinth

The C/N ratio is a limiting parameter of biogas production by anaerobic digestion which expresses the relationship between the amount of carbon and nitrogen present in organic materials. The C/N ratio makes it possible to judge the ability of organic matter to decompose more or less quickly. Materials with different C/N ratios differ widely in their biogas yield. The ideal C/N ratio for anaerobic biodigestion is ranged from 20 to 30 [33]. Cassava peels are rich carbohydrates substrate with the low nitrogen content making its C/N ratio high and unconfortable for unique substrate of anaerobic digestion. In order to balance the nutrient required for microbial production and biogas production, the anaerobic co-digestion was led by mixing raw cassava peels as carbon-rich substrate with water hyacinth as nitrogen-rich substrate. The experiment was done in 500 ml batch digesters with an adjusted C/N ratio to 30. The substrate to inoculum ratio was approximately 1.3. The inoculum concentration was 4.7 gVS/L. A volume of 300ml were added in each flask. After feeding the substrate and the inoculum in the vial, only water was added to reach the volume of 400mL.

All tests were done in duplicate and vials containing only inoculum and water were used for control. The pH of each vial was measured at the beginning and at the end of the reaction. After inoculation, the prepared flasks were purged with N_2 and then maintained under stationary conditions at 37± 1°C

ISSN: 2961-6611

for incubation. The volume of biogas produced was measured every 24 hours by a liquid replacement system until the cessation of production. The biogas flow rate produced daily was measured by the displacement of the water in the test tube. Biogas from the headspace of the flask was collected daily using a gas syringe and analyzed using G2801A Model 3000A Micro GC 4-Channel gas chromatography (Agilent Technologies, China). Biogas production from the control bottle was also analyzed simultaneously then subtracted from the total volume of biogas produced in the samples.

3.Results and discussions

3.1. Evaluation of feedstock of cassava waste and water hyacinth

Cassava processing is an activity that generates solid and liquid wastes. The cassava root (3.6 kg) processed in the laboratory generated approximately 0.83 kg (23%) of peels and 0.65 l (18%) of starch water consisting solely of pressing juice. The cassava waste feedstock evaluation in Benin showed that cassava peels account for about 33% of the cassava fresh root weight. As industries do not have a cassava wastewater collection system, it was difficult to quantify the amount of wastewater discharged. The peels quantity obtained are in the range of 20-35% reported by Ekundayo et al [8]. The amount of cassava wastewater obtained in the GEPEA laboratory was close to those found by Nago et al [4] . The water hyacinth is a perennial plant with indeterminate growth that invades the Beninese rivers including rivers *Sô*, *Ouémé* and *Lake Nokoué*. The multiplication of hyacinth is mainly by vegetative release of clones [34] which allows the plant to produce a large number of individuals in a relatively short time interval. The maximum growth of hyacinth is observed at 20-30° C and its maximum density in infestation areas can reach 60kg/m^2 [35].

3.2. Samples characterization.

The results of physico-chemical and biochemical analysis are shown in **Table 3.**

Table 3: Biochemical and elemental composition of samples (represented as mean ± SD, for n ≥ 1).

Parameters*	**Values found in this study**			**Literature review values**		
	Cassava peels (CP)	**Cassava wastewaters (CWW)**	**Water hyacinth (WH)**	**Cassava peels (CP)**	**Cassava wastewaters (CWW)**	**Water hyacinth (WH)**
pH	ND	3.8	ND	5.68 [44]	4.04-5.4 [45]	-
Total solids	ND	3.5±0.65	ND	25-35 [7]	0.4-4.6 [45]	6.12 [22]
Volatile solids	91.7±0.4	76.8± 7.2	84.2 ± 0.7	90-97 [7]	31.6-86 [45]	75.8% [21]
Carbon	41.8±0.2	36.4 ± 0.2	40.5 ± 0.3	33-46 [7]	-	-
Hydrogen	6.0±0.2	5.7 ± 0.02	5.4 ± 0.1	-	-	-
Nitrogen	0.6±0.3	3.2 ± 0.2	3.7 ± 0.2	0.6 [7]	0.001- 0.05[45]	1.5% [21]
Oxygen calculated	43.3±0.4	30.8 ±9.6	36.2 ± 4.3	-	-	-
Ash content	8.3±0.4	23.2 ±7.2	15.8 ± 0.7	-	-	24.2%[21]
Sulfur	< LD	< LD	< LD	-	-	-
Carbohydrates[a]	63.0±4.4	3.63± 0.14	26.5± 4.3	65-85 [7] (starch)	0.04 [11]	-

ISSN: 2961-6611

Protein calculated	3.6 ±2.6	20.3±1.6	23.1±1.8	-	-	12-35 [20]
Lipid[b]	9.6± 0.2	3.0±0.3	26.1± 5.3	-	-	-
Cellulose	14.1	5.2	14	-	-	-
Hemicellulose	40.2	45.3	29	-	-	-
Lignin	13.6	15.6	18.8	-	-	-
C/N ratio	46.7-138.7	11.4±0.9	11.0±0.7	76 [7]	-	-

* All data are given as a percentage of dry matter (DM), total solids (TS) as percentage of fresh matter, C/N and pH are unit less

ND: Not Determined

LD: Limit of Detection

[1] Determined using equation 1

[2]Determined using equation 2

Globally, the results obtained in this study are similar close to those found in the literature even if they are less complete. The analyzed samples contain high biodegradable organic matter proven by the high volatile solids and relatively low lignin content. The acid pH of cassava wastewater observed is mainly due to the presence of cyanogenic glycoside compounds such as linamarin and lotaustralin [36]. In fact, the linamarin presents in each part of the plant gives by hydrolysis, glucose, acetone and hydrocyanic acid consisting of organic matter observed. Cassava peels has showed the highest sugars content compared to cassava wastewater and water hyacinth whereas water hyacinth and cassava wastewater have a relatively high protein content. The complex carbohydrates (hemicellulose and cellulose) content observed by thermogravimetric analysis (TGA) was higher in comparison to the total sugars obtained by chemical analysis. This disparity may be due to the simultaneous degradation of proteins and lipids bonded to carbohydrates either in the form of glycoproteins or glycolipids at high temperature. The difference was even higher in the case of cassava wastewater indicating the presence of fermentation product such as lactic acid, acetic acid mixed to the degradation product of cyanogenic glycoside that are not detectable during the chemical analysis of carbohydrate but which could be degraded during thermogravimetric analysis. Further, the relatively high carbohydrate content of the cassava peels and water hyacinth observed in this study shown that these substrates could also be used as a good source of bioethanol production. This observation is related to Prajapati et al.[30] who reported algae carbohydrates content of 25.30% as good for a bioethanol production. The chemical composition of cassava wastewater varies significantly from one sample to another depending on the extraction process used [10], [36]. The high nitrogen content of the cassava wastewater observed in this study may be linked to the variety of the cassava root and the starch extraction process used. In fact , the composition of the cassava root varies according to the variety, the locality, the age of the harvested plant and the environmental conditions [37]. According to the process , the amount of residual starch in the cassava wastewater varies significantly. This parameter also affects the cassava wastewater composition such as the total solids and the volatils solids.

ISSN: 2961-6611

Overall, the C/N ratios calculated in the different samples make it possible to conclude that this feedstock cannot be used as sole substrate of anaerobic digestion. Calculated C/N values are not included in the optimal range of anaerobic digestion , i.e. 20-30 [33]. The high C/N ratio and the presence of cyanogenic glycosides in cassava peels can induce excess acid production, nitrogen deficiency and the release of cyanide, which is highly toxic to methanogenic bacteria [38]. A high C/N ratio ranged from 48.7 to 76 was also quoted in the literature [6], [44] indicating the nitrogen deficiency of cassava peels which could lead to a decrease in methane production efficiency due to the deactivation of methanogens and the possible failure of the whole process [40]. Kpata-Konan et al [41] stated that cassava wastewater are biorecalcitrant to anaerobic mono-digestion due to their acid pH (pH < 3) and a nitrogen deficiency (0.6 - 0.8 g/L). An inhibitory effect due to high acid production and nitrogen deficiency in cassava waste methanogenesis in fermenters was also reported in the literature [42], [43]. However, the nitrogen deficiency of cassava peels (0.6 ± 0.3% TS) could be offset by the high nitrogen content of both water hyacinth (3.7 ± 0.2% DM) and cassava wastewater (3.2 ± 0.2 % TS) by anaerobic co-digestion. Attention must be paid to the high acidity of the mixture while co-digesting cassava wastewater and cassava peels.

3.3. Estimation of the maximum stoichiometric and theoretical methane yield.

The elemental composition of the different samples made it possible to establish their empirical formula according to the method defined by Murphy et al. [44]. The **Table 4** shows the atomic constituents of the different samples.

Table 4: Atomic constituents of the samples.

Sample	Chemical element	Elemental composition (% DM)	Mass contribution of each element(g/L)	Atomic mass	Ratio of mass contribution by the atomic mass	Number of atoms per mole
CP	Carbon	41.8	418	12	34.83	81
	Hydrogen	6	60	1	60	140
	Nitrogen	0.6	6	14	0.43	1
	Oxygen	43.3	433	16	27	63
CWW	Carbon	36.4	364	12	30.33	13
	Hydrogen	5.7	57	1	57	25
	Nitrogen	3.2	32	14	2.29	1
	Oxygen	30.8	308	16	18.25	8
WH	Carbon	40.5	405	12	33.75	13
	Hydrogen	5.4	54	1	54	20
	Nitrogen	3.7	37	14	2.64	1
	Oxygen	36.2	362	16	22.62	9

ISSN: 2961-6611

The following empirical formulas emerge: $C_{81}H_{140}O_{63}N$; $C_{13}H_{25}O_8N$ and $C_{13}H_{20}O_9N$ respectively for cassava peels (CP), cassava wastewater (CWW) and water hyacinth (WH). By integrating respectively, the number of atoms and the concentration of organic compounds of each sample in the formulas established in **equations 4 & 5**, the values B_O and B_T obtained are shown in the **Table 5**.

Table 5: Results of maximum stoichiometric B_o and theoretical B_T yields of samples.

Samples	Empirical formula	**B_o(ml CH_4 g^{-1}VS)**	**B_T(ml CH_4 g^{-1}VS)**
CP	$C_{81}H_{140}O_{63}N$	440	377
WH	$C_{13}H_{20}O_9N$	428	489
CWW	$C_{13}H_{25}O_{12}N$	362	146

As expected, the samples showed different stoichiometric and theoretical yields of methane. These yields are a function of their respective chemical compositions. Cassava peels showed the highest stoichiometric value. This high value can be attributed its high carbon content (41.8 % TS). In addition, the volatile solids content of cassava peels was higher than cassava wastewater and water hyacinth (91.7% DM vs 76.8% TS and 84.2 % DM respectively). Water hyacinth has the highest theoretical potential (B_T) due to its high lipid content (26.12 ± 5.3% DM). In fact, in terms of the theoretical methane potential, the higher the lipid content of the organic compound, the higher the yield of the methane potential. The high energy content of lipids makes lipid-rich substrates most attractive for anaerobic digestion due to their higher gas production potential than carbohydrates and proteins [45], [46].Indeed the low lipid content of cassava and its residues was also reported [13]

In general, the stoichiometric potential B_o values observed in the present study are relatively higher than the theoretical potential B_T calculated. The B_T values obtained could be explained by the fact that the specific methane yields extracted from Angelidaki et al. [23] to calculate the theoretical potential B_T are specific to lipids, proteins and carbohydrates determined by empirical formulas of the substrates used . It is also important to mention that the organic matter content of a sample may vary according to age, climate or region and this parameter may significantly affect the theoretical potential methane of a substrate. Therefore, methane potential estimation based on empirical formulas developed from the elemental composition is more appropriate. The stoichiometric methanogenic potential values are more or less close to methanogenic potential values expected in practice.

ISSN: 2961-6611

3.4. Biochemical potential of methane.

The evaluation of the biochemical methanogenic potential lasted between 7 and 15 days. The biogas yield measured in ml biogas/gVS_{added} and the methane yield measured in $mlCH_4/gVS_{added}$ are shown in the **table 6**.

Table 6: Result of biochemical potential in methane and biogas potential of samples (represented as mean ± SD, for $n \geq 2$).

Parameters	CP	CWW	WH	Control 1	CP+WH	Control 2
Volatile solid Substrate (g)	0.92	0.92	0.92	0	1.8 (CP =1.38; WH= 0.42)	0
Volatile solid Inoculum (g)	0.92	0.92	0.92	0.92	1.41	1.41
Potash (g)	1	0	0	0	0	0
Phosphate buffer (ml)	98	0	0	0	0	0
Water (ml)	0	71	99	100	98	100
C/N ratio	70	11	11	-	30	-
pH initial	7.5±0.1	6.1±0.5	6.8±0.1	7.0	7.1	7.3
pH final	7.2±0.1	7.31±0.2	6.9±0.1	7.0	7.1±0.1	7.5
Vol Biogas.cum Substrate (ml)	545±75	535±15	285±15	0	685±5	0
Vol Biogas.cum Inoculum(ml)	190	190	190	190	0	0
Vol Biogas.cum Total (ml)	735±75	725±15	475±15	190	685±5	0
$\%CH_4$ average	56±2	55±2	55±1	37	55±1	0
Vol CH_4.cum Substrate (mL)	307±53	296±1	157±11	70	380±6	0
Biogas yield (mLbiogaz /gVS substrate)	592±82	581±17	309±17	207		0
Methane yield ($mLCH_4$ /gVS substrate)	333±58	322±1	171±12	76	380±3 211±3	0

ISSN: 2961-6611

The average methane content was 56 ± 2% (v/v of biogas) in all flasks. The biogas yield values observed of cassava peels and water hyacinth were close to those reported by Cuzin et al.[6] and Almoustapha et al. [47] respectively. Average methane content of 51% was also observed during anaerobic digestion of cassava peels in batch mode reactor under mesophilic conditions [13]. The biogas yield observed of cassava wastewater was slightly higher than that reported by Colin et al.[10] .However, it is important to highlight that the samples used during that study have low total solids and volatils solids content compared to the one experimented in this study.

Basically the methane yield obtained through the biochemical methanogenic potential test are in line with Speece et al. [48] who stated that a BMP measurement should never exceed 350Nm^3/t COD_{added}.

The cumulative production of methane curve as a function of time of all tests is shown in the **figure** below.

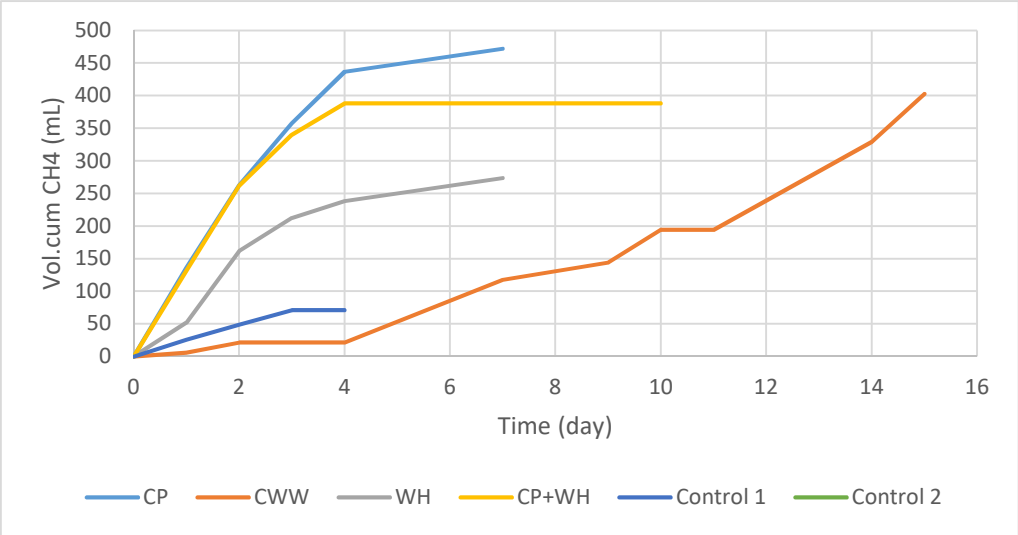

Fig. Evolution of cumulative methane production of cassava peels **(CP) ,** water hyacinth **(WH**) and cassava wastewater **(CWW)** and the co-digestion (**CP+WH**) as a function of time.

The cumulative methane production curves of cassava peels (CP), water hyacinth (WH) and the co-digestion (CP+WH) observed were similar and significantly different from cassava wastewater cumulative methane production. Methane production grew quickly in the first four days due to the initial pH values ranged from 6.8 to 7.5 which is favourable to the good activity of the methanogenic bacteria contained in the inoculum. In addition, the quick methane production is a proof of the high biodegradability of both substrates. The potash has improved the cassava peels anaerobic digestibility and allowed a high methane yield observed. This observation is in line with Ofoefule et al.[49] who obtained the highest cumulative methane yield with cassava peels premixed with *akanwu* potash. In fact, the low biodegradability of lignocellulosic materials under anaerobic conditions preventing their use as sole substrate for anaerobic digestion can be improved by using an alkaline solution such as NaOH, KOH [15]. During the first four days, hydrolytic and fermentative bacteria degrade polymers and monomers and produce mainly acetate

ISSN: 2961-6611

and hydrogen and varying amounts of volatile fatty acids (VFAs) such as propionate and butyrate. Hydrolytic microorganisms excrete hydrolytic enzymes such as cellulase, cellobiase, xylanase, amylase, lipase and protease. Most of the bacteria involved in the degradation process are strict anaerobic bacteria such as *Bactericides, Clostridia and Bifidobacteria* . After that step, volatile fatty acids are converted to acetate and hydrogen by hydrogen producing acetogenic bacteria. At the end of the degradation chain, two groups of methanogenic bacteria consisting of hydrogenotrophic methanogenic bacteria and methanogenic acetoclastic bacteria produce methane from acetate or hydrogen and carbon dioxide. Hydrogenotrophic bacteria use the H_2 produced by the acetogenic bacteria. H_2 absorption by methanogens is very efficient, having an affinity of parts per million, which ensures a very low hydrogen partial pressure. The relationship between acetogenic bacteria and methanogenic hydrogenotrophic bacteria is an excellent example of syntropic mutualism. Bacteria from different trophic groups convert propionate, butyrate and long-chain fatty acids into methane and water. Starting from the day 4, a slight decrease of methane production was observed and peaked on day 7 for cassava peels and water hyacinth and then plateaued until day 10 for the co-digestion (CP+WH). This period corresponds to the conversion of the residual volatile fatty acids into the methane and the gradual depletion of the substrate in the flasks. Despite the fact that the cumulative methane production curves of cassava peels and water hyacinth showed a good production of methane of both substrates, the presence of intact particles in the digestate indicates that pre-treatment of the biomass would improve the anaerobic biodegradation and therefore increase the methane yield.

The methane production of cassava wastewater (CWW) flasks showed a delay until day 4 then increased considerably from the day 4 until the day 15. This delay was linked to initial acidic pH conditions (6.1±0.5) which are not favourable to methanogenic bacteria activities. In fact, little methanogenesis reaction can take place between pH 6-6.5[50]. However, in high acidic condition, two situations can occur, either the anaerobic digestion starts again after the pH has risen, or the micro-organisms could adapt to the pH [51]. In this study, the anaerobic digestion has started again due to the rise of pH (6.1 to 7.3).

The methane yield in co-digestion of cassava peels with water hyacinth was relatively higher compared to the mono digestion of water hyacinth alone. In addition, the co-digestion removed the chemicals such as *akanwu* potash and phosphate buffer used in the treatment of cassava peels alone. Finally, co-digestion improved the nutrient balance of total organic carbon and nitrogen content of the mixture resulting in a stable and maintainable digestion process. These observations are in line with Braun et al.[52] that stated that co-digestion helps to maintain stable and reliable digestion performance and a good quality of digestate fertilizer.

In summary, experimental methanogenic potential values observed were lower than estimated stoichiometric (B_o) values. This difference is related to a certain number of factors such as non-degradable material and energy demand of the microbes. Angelidaki et al.[23] also stated that the practical efficiency obtained in a biogas reactor will always be lower compared to theoretical biogas potential. Indeed, estimating the theoretical potential of specific methane makes it possible to quickly and easily understand the bioenergy production potential of any organic substrate.

ISSN: 2961-6611

4. Large-scale feasibility of the biogas process from cassava waste and water hyacinth in Republic of Benin.

In practice, to initiate a biogas plant, one must ensure the availability and the biodegradability of the substrate to be used but also the socio-economic feasibility aspect of the project. From the point of biomass availability in Republic of Benin, the cassava plant adapts to all climatic conditions and even the most hostile. Its cultivation does not require fertilizer. These characteristics make cassava easily cultivable for all farmers and its availability throughout the year. Cassava production has grown rapidly over the last decade. The average yield per hectare of cassava estimated at 12 tons in 2010 increased to 13 tons in 2014, then to 15 tons and 16 tons in 2015 and 2016 [2]. In parallel, the water hyacinth grows in a very dense way on the rivers *Sô* and *Ouémé*, and the lake *Nokoué* forming a green carpet [53]. Besides, the biochemical methanogenic potential value observed has demonstrated that the co-digestion of cassava peels and water hyacinth could be an interesting way of valorization of these substrates to generate biogas. However, the limits of the process cannot be ignored and must be overcome so that the production of methane as a renewable fuel from cassava waste and water hyacinth becomes sustainable. The major difficulties in the anaerobic treatment of cassava waste are mainly related to their high starch content, a high C/N ratio and the presence of cyanogenic glycosides [6], [41].The co-digestion has allowed to treat effectively two different substrates in the same reactor. The use of water hyacinth has removed the chemicals such as potash *akanwu* and phosphate buffer used in the treatment of cassava peels alone. The co-digestion will therefore reduce the investment cost due to the treatment of these different organic matter at a larger scale. From the point of socio-economic, given that, the limits and possibilities of anaerobic digestion are better known, co-digestion has become a standard technology. Biogas technology by anaerobic digestion is now one of the most viable renewable energy technologies. The level of profit is based on its direct use for cooking or conversion into electricity. However, since 1993, *SONGHAÏ* project has been developing the production of biogas in the country with a digester designed in China of $20m^3$ capacity. The main substrates used are water hyacinth and pork droppings. The biogas produced is mainly used for domestic cooking [54]. After a study of the profitability of the system which turned out to be positive, *SONGHAÏ* was asked to set up similar projects with other substrates such as droppings chicken and/or quail and salad. Since then, many non-governmental organizations and start-ups are actively involved in the recovery of household and municipal organic waste for the production of biogas and/or compost. This is among others, the *ReBin Foundation*, *ACEED-Benin*, *EREP SA-Benin*, the *UAC Startup Valley*…. etc . This shows the feasibility of implementing a biogas project in Republic of Benin through the anaerobic digestion technology and therefore its social acceptability.

5. Conclusions

The full characterization of cassava waste and water hyacinth showed the existent of high content of biodegradable organic matter consisting of lipids, proteins, carbohydrates and a low fraction of non-biodegradable material such as lignin . These observations were confirmed by the theoretical and experimental evaluation of methanogenic potential. Estimating the theoretical methanogenic potential allowed to quickly and easily understand the bioenergy production potential of any organic substrate. However, the experimental values of methanogenic potential obtained were relatively lower in comparison to the theoretical calculated

ISSN: 2961-6611

values. Using of chemical products increased the cassava peels biochemical methanogenic potential. However, the co-digestion of cassava peels with water hyacinth removed the chemical products such as potash *akanwu* and phosphate buffer used in the treatment of cassava peels alone. Moreover, the methane yield of water hyacinth has increased during the co-digestion. Finally, the anaerobic co-digestion could be an alternative of energy recovering at a larger scale. The cost of anaerobic treatment process of cassava peels on an industrial scale could be reduced through the use of water hyacinth as a source of nitrogen. Given to the carbohydrate content of cassava peels and water hyacinth, production of bioethanol could also be a suitable way to recover energy from these organic compound. On the other hand, the high acidity of cassava wastewater does not allow the rapid degradation of organic matter and requires longer retention times. This observation is not economically sustainable to the biogas plant. Hence, other paths of valorization of cassava wastewater must be explored. Aerobic treatment could be the sustainable way of valorization of the cassava wastewater. Despite of its wider land area requirement, the residual sludge could be used in the anaerobic treatment of the cassava peels and water hyacinth. Anaerobic co-digestion on large scale of cassava peels with water hyacinth would be one step ahead to solve environmental problem caused by the proliferation of both cassava industries and water hyacinth in Republic of Benin. The biogas produced could provide cassava industries cost-effective energy and the surplus of biogas could be injected into the natural gas grid to offset the energy deficit of rural communities. The residual digestate could be used as fertilizer to boost Beninese agriculture.

Conflict of interest

The authors declare no conflict of interest.

Acknowledgements

The present research work was fully funded by the Islamic Bank of Development Group through its Merit Scholarship Program and grant of research funds. I would like to thank technician Eric CHEVREL, the research engineers Katell CHAILLOU and Gaeëtan BURNENS from IMT-Atlantique for providing technical assistance.

References

[1] R. J. Hillocks, J. M. Thresh, and A. Bellotti, *Cassava: Biology, Production and Utilization*. CABI, 2002.

[2] FAOSTAT, “Cassava production in the world,” Rome-2016. [Online]. Available: http://www.fao.org/faostat/fr/#data/QC. [Accessed: 26-Sep-2017].

[3] B. G. Soulé, F. Aboudou, S. Gansari, M. Tassou, and J. D. Yallou, “Analyse de la structure et la dynamique de la chaîne de valeur du manioc au Bénin,” *Rapp. D’étude Réalisé Par Lab. D’Analyse Régionale D’Expertise Soc. LARES Cotonou Bénin*, 2013.

[4] Nago et al, “La préparation artisanale du gari au Bénin : aspects technologiques et physico-chimiques = Artisanal gari production in Benin : technological and physico-chemical aspects - éditions ORSTOM,” 1995.

[5] K. Sriroth, K. Piyachomkwan, S. Wanlapatit, and C. G. Oates, “Cassava Starch Technology: The Thai Experience,” *Starch - Stärke*, vol. 52, no. 12, pp. 439–449, Dec. 2000.

[6] N. Cuzin, J. L. Farinet, C. Segretain, and M. Labat, “Methanogenic fermentation of cassava peel using a pilot plug flow digester,” *Bioresour. Technol.*, vol. 41, no. 3, pp. 259–264, Jan. 1992.

[7] A. Kamaraj, N. O. Gopal, P. Venkatachalam, and A. Sampathrajan, “Biofuel production from tapioca starch industry wastewater using a hybrid anaerobic reactor,” *Energy Sustain. Dev.*, vol. 10, no. 3, pp. 73–77, Sep. 2006.

ISSN: 2961-6611

[8] J. A. Ekundayo, *In; Fungal Biotechnology. Eds.: Smith JE, Berry D R, Kristiasen B*. London: Academic Press, 1980.

[9] P. G. Hien, L. T. K. Oanh, N. T. Viet, and G. Lettinga, "Closed wastewater system in the tapioca industry in vietnam," *Water Sci. Technol.*, vol. 39, no. 5, pp. 89–96, Jan. 1999.

[10] X. Colin, J. L. Farinet, O. Rojas, and D. Alazard, "Anaerobic treatment of cassava starch extraction wastewater using a horizontal flow filter with bamboo as support," *Bioresour. Technol.*, vol. 98, no. 8, pp. 1602–1607, 2007.

[11] Okafor N, "An integrated Bio-system for the disposal of Cassava Wastes. In Proceedings: Internet conference on Integrated Bio-systems in Zero Emissions Applications," *http://www.ias.unu.edu/proceedings/icbs.*, 1998.

[12] S. A. Odunfa and S. B. Shasore, "Saccharification of cassava peels waste for microbial protein enrichment," *Eng. Life Sci.*, vol. 7, no. 1, pp. 23–29, 1987.

[13] V. Okudoh, C. Trois, T. Workneh, and S. Schmidt, "The potential of cassava biomass and applicable technologies for sustainable biogas production in South Africa: A review," *Renew. Sustain. Energy Rev.*, vol. 39, pp. 1035–1052, Nov. 2014.

[14] S. O. Jekayinfa and V. Scholz, "Potential Availability of Energetically Usable Crop Residues in Nigeria," *Energy Sources Part Recovery Util. Environ. Eff.*, vol. 31, no. 8, pp. 687–697, Mar. 2009.

[15] G. Bochmann and L. F. R. Montgomery, "4 - Storage and pre-treatment of substrates for biogas production," in *The Biogas Handbook*, A. Wellinger, J. Murphy, and D. Baxter, Eds. Woodhead Publishing, 2013, pp. 85–103.

[16] V. B. Manilal, C. S. Narayanan, and C. Balagopalan, "Anaerobic digestion of cassava starch factory effluent," *World J. Microbiol. Biotechnol.*, vol. 6, no. 2, pp. 149–154, Jun. 1990.

[17] L. Lareo and R. Bressani, "Possible utilization of the water hyacinth in nutrition and industry," *Food Nutr. Bull.*, vol. 4, no. 4, pp. 60–64, 1982.

[18] N. AFNOR, "T 90–105," *Qual. L'eau-Dos. Matières En Suspens. Par Centrifugation Assoc. Fr. Norm. Paris*, 1997.

[19] C. E. Marcato, E. Pinelli, P. Pouech, P. Winterton, and M. Guiresse, "Particle size and metal distributions in anaerobically digested pig slurry," *Bioresour. Technol.*, vol. 99, no. 7, pp. 2340–2348, 2008.

[20] W. Zhong, Z. Zhang, Y. Luo, W. Qiao, M. Xiao, and M. Zhang, "Biogas productivity by co-digesting Taihu blue algae with corn straw as an external carbon source," *Bioresour. Technol.*, vol. 114, pp. 281–286, 2012.

[21] M. Dubois, K. A. Gilles, J. K. Hamilton, P. t Rebers, and F. Smith, "Colorimetric method for determination of sugars and related substances," *Anal. Chem.*, vol. 28, no. 3, pp. 350–356, 1956.

[22] INRS, "Fiche Toxicologique," *INRS Ed INRS*, 2008.

[23] I. Angelidaki and W. Sanders, "Assessment of the anaerobic biodegradability of macropollutants," *Rev. Environ. Sci. Biotechnol.*, vol. 3, no. 2, pp. 117–129, 2004.

[24] A. M. Buswell and H. F. Mueller, "Mechanism of Methane Fermentation," *Ind. Eng. Chem.*, vol. 44, no. 3, pp. 550–552, Mar. 1952.

[25] B. Sialve, N. Bernet, and O. Bernard, "Anaerobic digestion of microalgae as a necessary step to make microalgal biodiesel sustainable.," *Biotechnol. Adv.*, vol. 27, no. 4, pp. 409–416, 2009.

[26] D. Deublein and A. Steinhauser, *Biogas from waste and renewable resources: an introduction*. John Wiley & Sons, 2011.

[27] M. H. Gerardi, *The microbiology of anaerobic digesters*. John Wiley & Sons, 2003.

[28] T. Amon, B. Amon, V. Kryvoruchko, W. Zollitsch, K. Mayer, and L. Gruber, "Biogas production from maize and dairy cattle manure—Influence of biomass composition on the methane yield," *Agric. Ecosyst. Environ.*, vol. 118, no. 1, pp. 173–182, Jan. 2007.

[29] A. R. SAHITO, R. B. Mahar, and K. M. BROHI, "Anaerobic co-digestion of canola straw and buffalo dung:

ISSN: 2961-6611

optimization of methane production in batch experiments," *Mehran Univ. Res. J Eng. Technol. 33 1 49*, vol. 60, 2014.

[30] S. K. Prajapati, A. Malik, and V. K. Vijay, "Comparative evaluation of biomass production and bioenergy generation potential of Chlorella spp. through anaerobic digestion," *Appl. Energy*, vol. 114, pp. 790–797, 2014.

[31] I. Angelidaki *et al.*, "Defining the biomethane potential (BMP) of solid organic wastes and energy crops: a proposed protocol for batch assays," *Water Sci. Technol.*, vol. 59, no. 5, pp. 927–934, Mar. 2009.

[32] B. Drosg, R. Braun, G. Bochmann, and T. Al Saedi, "3 - Analysis and characterisation of biogas feedstocks," in *The Biogas Handbook*, A. Wellinger, J. Murphy, and D. Baxter, Eds. Woodhead Publishing, 2013, pp. 52–84.

[33] U. Marchaim and F. and A. O. of the U. Nations, *Biogas Processes for Sustainable Development*. Food & Agriculture Org., 1992.

[34] A. Malik, "Environmental challenge vis a vis opportunity: the case of water hyacinth," *Environ. Int.*, vol. 33, no. 1, pp. 122–138, 2007.

[35] B. Gopal, *Water hyacinth.* Elsevier Science Publishers, 1987.

[36] A. S. Sánchez, Y. L. Silva, R. A. Kalid, E. Cohim, and E. A. Torres, "Waste bio-refineries for the cassava starch industry: New trends and review of alternatives," *Renew. Sustain. Energy Rev.*, vol. 73, no. Supplement C, pp. 1265–1275, Jun. 2017.

[37] Balagopalan, C.., Padmaja, G, Nanda, S. K., and Moorthy, S. N., *Cassava nutrition and toxicity*, In: Balagopalan, C.; Padmaja, G.; Nanda, S.K.; Moorthy, S.N. Cassava in food, Feed, and Industr. CRC Press.Boca Raton, FL, USA.1988.p. 13-36., 1988.

[38] B. Eikmanns and R. K. Thauer, "Catalysis of an isotopic exchange between CO2 and the carboxyl group of acetate by Methanosarcina barkeri grown on acetate," *Arch. Microbiol.*, vol. 138, no. 4, pp. 365–370, 1984.

[39] B. A. Adelekan and A. I. Bamgboye, "Comparison of biogas productivity of cassava peels mixed in selected ratios with major livestock waste types," *Afr. J. Agric. Res.*, vol. 4, no. 7, pp. 571–577, Jul. 2009.

[40] M. Kayhanian, "Ammonia inhibition in high-solids biogasification: an overview and practical solutions," *Environ. Technol.*, vol. 20, no. 4, pp. 355–365, 1999.

[41] N. E. Kpata-Konan, K. F. Konan, M. K. Kouame, Y. F. Kouame, T. Gnagne, and K. Tano, "Optimisation de la biométhanisation des effluents de manioc issus de la filière de fabrication de l'attiéké (semoule de manioc)," *Int. J. Biol. Chem. Sci.*, vol. 5, no. 6, pp. 2330–2342, Jan. 2011.

[42] R. Wurster, "Experiences with anaerobic digestion of various cassava residues in Indonesia," in *International conference on Biomass. 3*, 1985, pp. 501–505.

[43] C. Segretain and A. Bories, "Fermentative trends and cyanide effects during anaerobic digestion of cassava by-products.," in *Biomass for energy and industry. 4th EC conference. Proceedings of the international conference, Orléans, France, 11-15 May, 1987.*, 1987, pp. 808–813.

[44] J. D. Murphy and T. Thamsiriroj, "5 - Fundamental science and engineering of the anaerobic digestion process for biogas production," in *The Biogas Handbook*, Woodhead Publishing, 2013, pp. 104–130.

[45] Y. Y. Li, H. Sasaki, K. Yamashita, K. Seki, and I. Kamigochi, "High-rate methane fermentation of lipid-rich food wastes by a high-solids co-digestion process," *Water Sci. Technol.*, vol. 45, no. 12, pp. 143–150, 2002.

[46] D. G. Cirne, X. Paloumet, L. Björnsson, M. M. Alves, and B. Mattiasson, "Anaerobic digestion of lipid-rich waste—Effects of lipid concentration," *Renew. Energy*, vol. 32, no. 6, pp. 965–975, May 2007.

[47] O. Almoustapha and J. Millogo-Rasolodimby, "Production de biogaz et de compost à partir de eichhornia crassipes, (mart) solms-laub

ISSN: 2961-6611

(pontederiaceae) pour un développement durable en Afrique sahélienne," *VertigO - Rev. Électronique En Sci. Environ.*, no. Volume 7 Numéro 2, Sep. 2006.

[48] R. E. Speece, "Anaerobic biotechnology for industrial wastewaters," in *Anaerobic biotechnology for industrial wastewaters*, 1996.

[49] A. U. Ofoefule, E. L. Eme, E. O. Uzodinma, and C. N. Ibeto, "Comparative study of the effect of chemical treatments on cassava (Manihot utilissima) peels for biogas production," *Sci. Res. Essays*, vol. 5, no. 24, pp. 3808–3813, 2010.

[50] F. Raposo, C. J. Banks, I. Siegert, S. Heaven, and R. Borja, "Influence of inoculum to substrate ratio on the biochemical methane potential of maize in batch tests," *Process Biochem.*, vol. 41, no. 6, pp. 1444–1450, Jun. 2006.

[51] T.-H. Chen and A. G. Hashimoto, "Effects of pH and substrate:inoculum ratio on batch methane fermentation," *Bioresour. Technol.*, vol. 56, no. 2, pp. 179–186, May 1996.

[52] R. BRAUN and A. WELLINGER, "Potential of Co-digestion," p. 16, 2003.

[53] K. Dagno, R. Lahlali, D. Friel, M. Bajji, and M. Haïssam Jijakli, "Synthèse bibliographique : problématique de la jacinthe d'eau, Eichhornia crassipes, dans les régions tropicales et subtropicales du monde, notamment son éradication par la lutte biologique au moyen des phytopathogènes," *BASE*, Dec. 2007.

[54] A.Vorsters, "Rentabilité d'un biogaz de type chinois au Bénin," *TROPICultura*, vol. 12, no. 1, pp. 27–28, 1994.

ISSN: 2961-6611

Utilization of Waste heat from Domestic Refrigerator for Water heating-an Experimental Analysis

Missaoui Sami[*1], Ben Slama Romdhane [2], Béchir chaouachi[3]

[*1] *University of Tunis, Department of Mechanical Engineering , The Higher National Engineering School of Tunis (ENSIT), Box.1008.Tunis. Tunisia*

[2] *University of Gabes, Department of Chemical-Process Engineering, National Engineering School of Gabes (ENIG), Box.6029.Gabes. Tunisia*

[3] *University of Gabes, Department of Chemical-Process Engineering, National Engineering School of Gabes (ENIG), Box.6029.Gabes. Tunisia*

[1] Missaouisami1988@gmail.com

[2] romdhaneb.Slama@gmail.com

***Abstract*— This article presents the experimental investigation of domestic refrigerator by using waste heat recovery for water heating. The results obtained, with the recovery of the thermal discharges of this refrigerating machine, demonstrated that the water temperature in the tank reached 50°C, and with a continuous use of the domestic refrigerator to maintain proper food storage condition, the temperature will be better. This system will reduce the electricity consumption and rejected less heat to the environment so it is safer in environmental aspects.**

***Keywords*— Waste heat recovery, Domestic Refrigerator, Energetic and Environmental Interest, Experimental analysis.**

I. Introduction

In the world, a large amount of hot water is required for many purposes like cleaning, bathing, washing etc [1]. With this demand of hot water in residential and commercial buildings, the most used method to heat water is the fossil fuels, the natural gas or electricity. These conventional methods for water heating are leading to global warming and ozone layer depletion [2]. With the demand of emission reduction and energy conservation, the domestic refrigerator technology for water heating should be a feasible system to save energy consumption and reduce the greenhouse gases [3]. Therefore, in comparison with traditional water heater, the condenser of domestic refrigerator immersed in water makes a better use of energy. Then, why not to recover waste heat from condenser unit of a domestic refrigerator to heating water and to improve the performance of the system. [4]

II. System Description

The household refrigerator with a water heater tank is based on the same principle of vapor compression cycle but with few modifications. The condenser cooled by the ambient air is change by another one immersed in water to recover the quantity of heat rejected in atmosphere (waste heat). The main objective of this experiment is to utilize these different heat discharges provided by the condenser to heating water (as shown in figure 1).

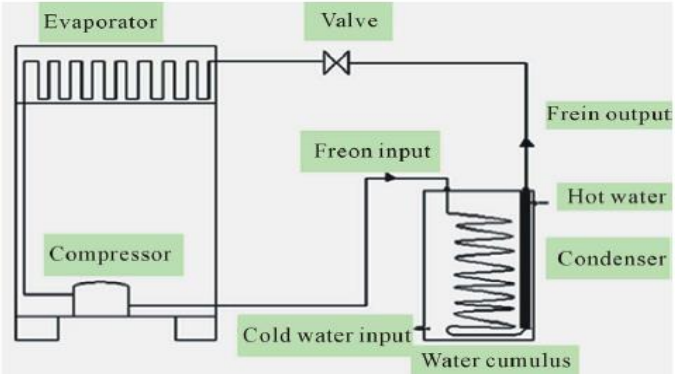

Fig.1: Domestic Refrigerator with Water Heater Tank [3]

III. Experimentation and Measurement

Experimental Setup

As shown in Fig.2, an experimental test has been purposely designed to investigate the different temperature and pressure of household refrigerator with water heating system.

Fig.2: Domestic Refrigerator with Water Heater Tank photograph.

ISSN: 2961-6611

TABLE.1: SPECIFICATIONS OF THE REFRIGERATOR (NEWSTAR, MODEL MP0500).

Refrigerator model : (NewStar MP0500)	***Compressor model :AES30DS***
climate class: ST	***Power supply(V/Hz):220-240 /50***
Rated current: 1.2A	***Displacement: 3.88 cm^3***
Refrigerant gas : R134a	***Motor type: RSIR***
Volume: 46 L	***Cooling capacity: 88w***
Energy consumption:0.52 KWh/24h	***COP:0.98***
Type of water tank: FRIGOBAMBO cooler with a capacity of 30 liters	

IV. RESULT AND DISCUSSION

Figure 3 shows the variation of temperature with time. According to this Fig., The water temperature in the tank is increased significantly (26 to 33°C) with a volume of water is $0{,}024m^3$. This increase is due to the waste heat recovery from the condenser of a domestic refrigerator. With increasing of water temperature, the temperature of evaporator is change (not stable) but not influenced by the rise of water temperature.

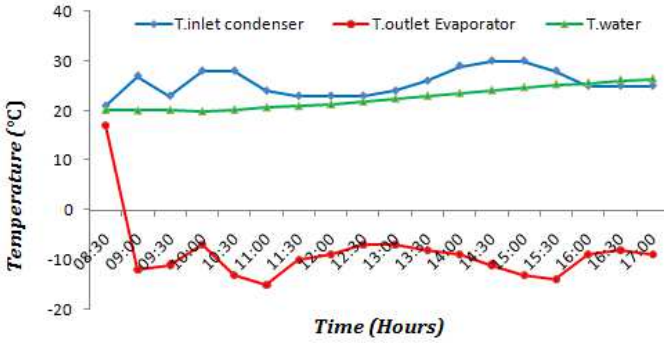

Figure.3.Variation of temperature with time

Figure 4 illustrates the experimental results of temperature with time. In the experimental study, the total amount of hot water in the tank is conserved as no water consumption during heating process. The results obtained after one day of operation shows that the value of water temperature reached is of 50°C with a volume of heated water is $[0{,}024m^3]$, with a continuously use the domestic refrigerator this value may be will be better.

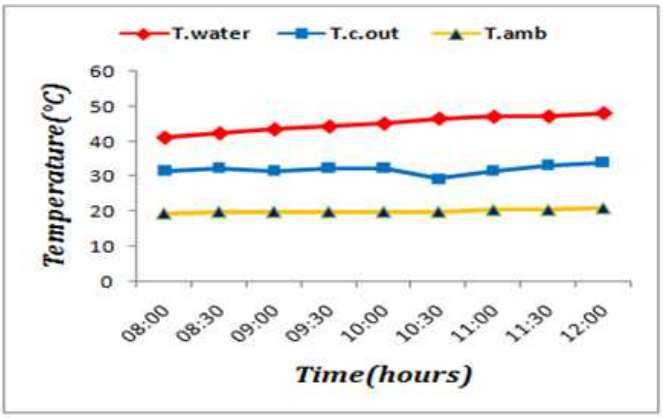

Fig.4.Experimental results of the temperature with time

Figure 5 shows the variation of water temperature and heat gained by the water with time. According to this Fig., the water temperature in the tank increases with time. The heat gained by the water curve is change (variable) with time (with the increase of water temperature in the tank). It can be seen that the temperature inside the water tank increases, the heating capacity of the domestic refrigerator is reduced. This result is in accordance with the literature (Xinhui Zhao et al.)[5]

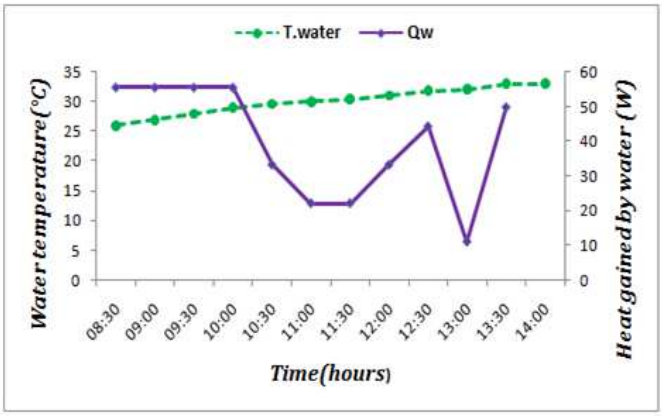

Fig.5. Variation of water temperature and heat gained by the water with time

Figure 6 shows the variation of pressure and mass flow rate of Refrigerant R134a with water temperature.

ISSN: 2961-6611

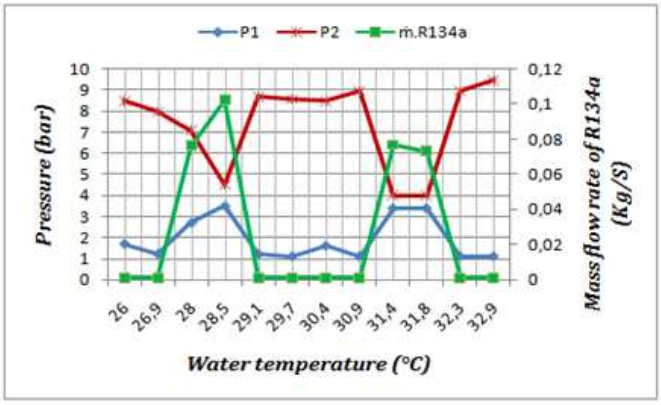

Fig.6: Variation of Pressure and Mass flow rate of Freon R134a vs. Water temperature

❖ Energetic Interest

Refrigerating machines have an energy interest during the valorization of thermal discharges for water heating. For an electrical energy consumption of 1 KWh, refrigerating machines for example a domestic refrigerator provides 3 to 4 KWh of heating energy at their condenser.

With the use of refrigeration machines to heating water, a low power consumption is achieved. So, this valorization technique allows us to reduce the heating bill.

Energy Savings (in KWh)

To calculate the Energy Savings, we are not interested in the price of electric energy but we will evaluate the amount of electrical energy that will be saved from the free energy produced by the condensers of the refrigerating machines that will have been supplied in the atmosphere without used.

To determine it, we have to calculate the coefficient of performance (COP) of our refrigerating machine.

Then, the COP of the domestic refrigerator is defined by the following relation:

$$COP = \frac{\text{Energy produced by the condenser in the form of heat}}{\text{Electric energy consumed by the compressor}}$$

When a refrigerating machine had a coefficient of performance (COP) is 4 (Ben Slama.R [3]), this means that for 1 KWh of electricity consumed, our domestic machine will produce 4 KWh of heating energy.

In terms of electrical energy savings, if the refrigerating machine produces 4 kWh of heating energy during a 1 KWh of electricity consumed by the compressor, the output is 3 KWh of electric energy saved over a total of 4 KWh. Then the energy savings is about 75%.

❖ Environmental Interest

Nowadays, hot water production in residential sectors contributes to the environmental pollution and global warming. The use of the classical method; natural gas, wood and other combustible sources; for heating sanitary water, the planet will be degraded and the sea level will increase due to a decrease in the volume of ice in the sea, and the ozone layer may also be damaged.

All around the world, large emitters of greenhouse gases are the machines that consume electrical energy. Once greenhouse gas emissions begin to increase, the problem of environmental degradation begins to increase. Therefore, with the valorization of the thermal emissions from the refrigerating machines used in heating water, we have guaranteed a zero percentage of fumes released into the atmosphere during the period of heating sanitary water. That means a protection of the layer ozone and a low GWP (Global Warming Potential).

V. Conclusion

The residential and commercial water heating technique requires a high energy consumption; therefore they have a great influence on the environment. The advantage of the valorization of the heat rejection rate from the condenser which have an influence on the economic factors (reduce the cost of energy) and the environmental ones (reduction of the emissions of greenhouse gases). Currently, the application of this type of valorization of thermal discharges is common in industry but given the gradual increase in energy costs and environmental problems this number can only grow.

Acknowledgment

The Authors would like to thank the University of Tunis and the University of Gabes for supporting this research work.

I would also like to thanks to my friends for their guidance, moral boosting, support and encouragement throughout many times.

VI. References

[1] *BEN SLAMA R., "Coupling of a refrigerator to a water heater and heating floor". GRETH Heat set 2010, Opatija, Croatia, October 18-22, 2010.*

[2] *BEN SLAMA R., "Refrigerator coupling to a water-heater and heating floor to save energy and to reduce carbon emissions. 11thInternational Conference on Sustainable Energy technologies (SET-2012). September 2-5, 2012, Vancouver, Canada.*

[3] *BEN SLAMA R., "Refrigerator Coupling to a Water-Heater and Heating Floor to Save Energy and to Reduce Carbon Emission". Computational Water, Energy and Environmental Engineering, 2013, 2, 21-29. Doi: 10.4236/cweee. 2013 (http://www.scirp.org/journal/cweee).*

[4] *BEN SLAMA R., "Valorisation of the Refrigerating Machines Heat : Case of an Air-Conditioner Coupled to Sea Water Still". Int J. of Environnement Engenieering and Natural Resources. Vol 1 , Num 5. 2014. pp 247-253.*

[5] *Xinhui Zhao et al., "Experimental Study on Heating Performance of Air - source Heat Pump with Water Tank for Thermal Energy Storage", Procedia Engineering 205 (2017) 2055–2062.*

ISSN: 2961-6611

Contribution to Characterization of Natural Diatomite

Hazem MERADI[#1], Kotbia LABIOD[#2], Wafia GHABECHE[#3]

[#1,2,3] *Research Center in Industrial Technologies CRTI, P.O. Box 64, Cheraga 16014, Algiers, Algeria*
[1]*meradi213@yahoo.com*
[2]labiodkotbia@yahoo.fr
[3]wafiag@yahoo.fr

***Abstract*— This document gives formatting instructions for authors preparing papers for publication in the Proceedings of an IEEE conference. With the complex examination of raw material from a Sig deposit in Algeria in the region of Mascara area, physical, chemical and mineralogical properties of diatomite have been defined. It has been found that it is a dominantly amorphous material, sedimentary rock of the type silica-diatomite. The raw material consists of approximately 60% SiO_2. Among the physical properties, we find a porosity of 60%, which constitutes a wide range of practical application, in various fields, absorbing, insulating, natural insecticide, and filter water etc. For determination of the chemical contents, properties and origin of the raw material, the following methods have been used, such as, chemical analysis, XRD analysis, optical microscopy (SEM) and thermal analysis.**

***Keywords*— Diatomite, DSC, X-Ray, Kieselguhr, Sig**

I. INTRODUCTION

Natural diatomite was obtained from the Sig area of Mascara in Algeria. Diatomite is a well-known natural product, it carries several name, namely: kieselguhr, diatomaceous earth, diatomite, diatomaceous earth, tripoli, and diatomaceous flour. This is a clear colored rock consisting primarily of silica and impurities (organic compounds, sand, clay, calcium carbonate and magnesium, salts, ...) (Downs et al. 2002). Diatomite used for the manufacture of cements, clay diet, bricks (Peter et al. 2005), adsorbents, filter powders, fillers, and catalysts (Martirosyan et al. 2003; Martinovic et al. 2006). As a siliceous rock made up largely from diatoms, diatomite has a unique combination of physical and chemical properties, making it applicable for the removal of heavy metals and organic pollutants, and as a filtration medium in a number of industrial uses (Lin et al. 2007; Al-Degs et al. 2001). For its high permeability, high porosity and chemical inertness, many studies (Al-Ghouti et al.2003;ERDEM ET AL. 2005; SHAWABKEH ET AL 2003). have been tested as an absorbent product, used to remove dyes. These applications include also filter aid, functional filler, insulation, catalysis support, and carrier application, (Dantas et al. 2001; Martinovic et al. 2006). Most research is focused on the adsorption properties of diatomite. The application of diatomite in the field of wastewater treatment is highly dependent on its origin and further efforts are needed to improve its adsorption capacity (Khelifaoui et al 2014). Porous ceramics supports are, generally needed for membranes. For the development of hight quality supports, it's very important to have pore size distribution, total porosity ratio, surface quality, good mechanical properties and chemical stability (Van Gestel et al. 2002). The use of ceramic membranes has many advantages such as higher thermal and chemical stability, pressure resistance, long lifetime and catalytic properties from their intrinsic nature (Talidi et al. 2011).

The Sig diatomite deposit as presented on Figure 1, is located 5 km south-east of the town of Sig, 50 km from the city of Oran and 40 km from the town of Mascara.

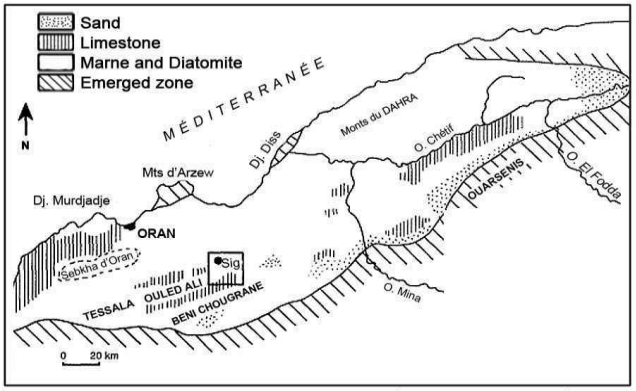

Fig. 1 Geographical localization of the layer of diatomite (Van Gestel,2002)

II. EXPERIMENTAL PROCEDURE

Chemical and phase analyses of the diatomite sample were conducted using X-ray fluorescence (XRF) and X-ray diffraction (XRD) using ULTIMA IV Rugaku powder diffractometer, and employing Cu Kα filtered radiation. The morphology and microstructure of the materials were studied by using PHILIPS XL 30 scanning electron microscopy (SEM) technique. Simultaneous thermal analyser, differential scanning calorimetry and thermogravimetry analysis (DSC-TGA) were carried out using a fully computerized TA Instruments Universal Analysis 4.5A. This analysis is used to investigate physical and chemical processes related to thermal effects

ISSN: 2961-6611

such as phase transitions and mass changes due to evaporation and decomposition of the sample. The tests were carried out under the same experimental conditions, about 10 mg of product were placed in an alumina crucible for simultaneous thermal analysis (TGA-DSC) and heated at a rate of 10°C/min, from room temperature to 1200 °C in a static air environment.

III. MAIN RESULTS

Chemical composition of diatomite sample were conducted using X-ray fluorescence (XRF) and presented in Table 1, shows the predominance of silica and lime with alumina and iron oxide in lower proportion.

Elements	Concentration (%)
Al_2O_3	2,65
SiO_2	60,28
P_2O_5	0,07
SO_3	0,12
K_2O	0,67
CaO	5,50
Fe_2O_3	0,91

TABLE1: Chemical analysis of original diatomite sample.

The X-ray spectrum of the raw diatomite sample presented in Figure 2, shown the existence of calcite, Quartz and Ankerite.

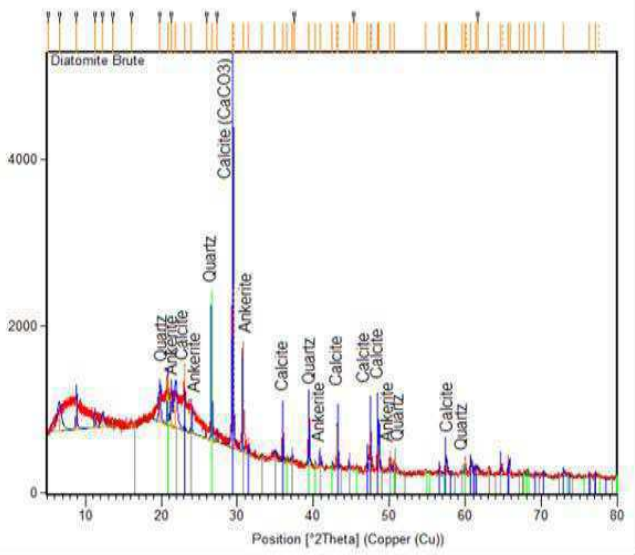

Fig. 2 XRD Patterns of Diatomite original Sample

The morphology of diatomite sample was observed in Figure 3 by PHILIPS XL30 scanning electron microscope. From these results, it is clearly observed that the diatomite has a porous structure in the form of a honeycomb.

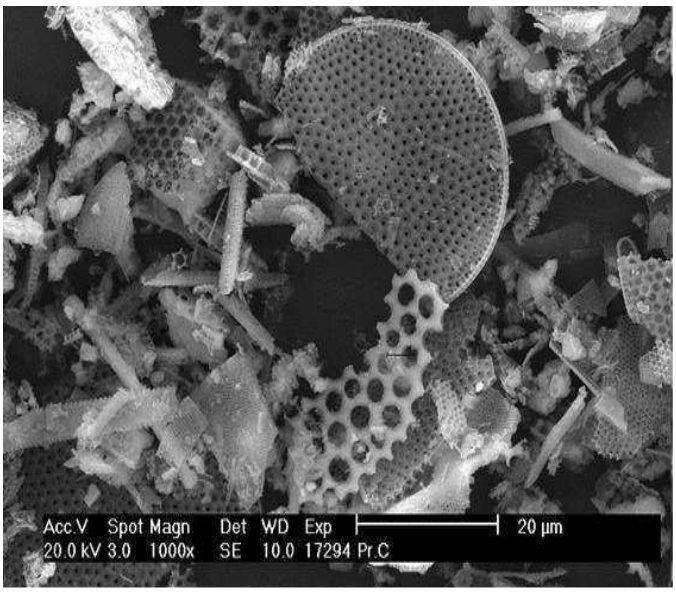

Fig. 3 SEM micrography of the diatomite powder

The results of experiments thermal analysis were performed in a TA Instruments Universal Analysis 4.5A, are shown in Figure 4 with 1000X magnification

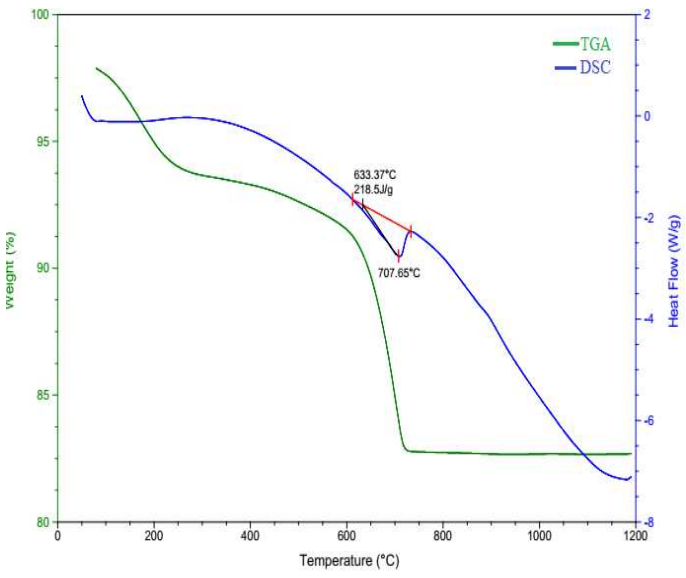

Fig. 4 Simultaneous thermal analysis TGA-DSC for diatomite sample

We see a total weight loss of 17% at 1200 ° C occurring in several steps. The first weight loss is associated with endothermic peak due to evaporation of absorbed moisture. The second weight loss is about 06 % observed at 260 °C and the last mass loss between 633.37°C and 707.65 °C is

ISSN: 2961-6611

divided in two steps. The first mass loss (8 %) is due to burning of residual part and dehydroxylation and the last weight loss (09 %). Thermal reactions associated with weight loss shows two endothermic.

The first endothermic peak is at 84.7 °C and the second peak at 707.65 °C corresponds to α ↔ β quartz transformation.

IV. CONCLUSIONS

The results of characterization of diatomite from a Sig deposit in Algeria show the predominance of silica in chemical analysis obtained by X-ray fluorescence and amorphous material. However, the main quartz and calcite lines are distinguished. During the observation on SEM, it appears clearly a porous microstructure in the shape of honeycomb. Coupled thermogravimetric and differential calorimetry (DSC / TGA) thermal analysis, gave us a good approach to the thermal and mass evolution of the sample according to the temperature. The results show a significant loss of mass for diatomite of the order of 17 %, and the four peak transformation at different temperature.

From the results of the investigation carried out, it can be concluded that the natural diatomite from the Sig deposit may find application for obtaining of ceramic membranes for water filtration.

ACKNOWLEDGMENT

We thank the Research Center in Industrial Technologies CRTI for financial support.

REFERENCES

[1] Bouhameur M(2008) Signification paléoécologique des assemblages de diatomées du Messinien du Dahra sud-occidental (basin du chélif, Algérie, Nord-occidentale, Geoviverssitas, 30 (1), 117-122.

[2] Peter A, Ciullo R.T(2005)The Industrial Minerals Vanderbilt Company, Inc. Norwalk: CT, USA, p. 29

[3] Martirosyan G.G.,Manukyan A.G., Ovsepyan E.B, Kostanyan, K.A(2003). A study of adsorption-structural properties of natural and processed diatomites. Russ. J. Appl. Chem., 76(4), 531-535.

[4] Martinovic S, Vlahovic M, Boljanac T, Pavlovic L(2006) Preparation of filter aids based on diatomites. Int. J. Mineral. Process., 80(2-4), 255-260.

[5] Lin J.X, Zhan S.L, Fang M.H, Qian X.Q(2007) The adsorption of dyes from aqueous solution using diatomite. J. Porous. Mater., 14, 449-455

[6] Al-Degs Y.M, Khrasisheh M.A.M, Tutunji M.F(2001)Sorption of lead ions on diatomite and manganese oxides modified diatomite. Water Res., 35(15), 3724-3728.

[7] Al-Ghouti M.A, Khraisheh M.A.M, Allen S.J, Ahmad M.N(2003) The removal of dyes from textile wastewater: a study of the physical characteristics and adsorption 15 mechanisms of diatomaceous earth. J.Environ. Manage, 69, 229-238.

[8] Erdem E, Qolgecen G, Donat R(2005)The removal of textile dyes by diatomite earth. J. Colloid Interface Sci 282, 314-319.

[9] Shawabkeh R. A, & Tutunji M. F(2003)Experimental study and modeling of basic dye sorption by diatomaceous clay. Applied Clay Science, 24(1-2), 111-120.

[10] Dantas T. D. C, Neto A. D, & Moura M. D. A(2001) Removal of chromium from aqueous solutions by diatomite treated with microemulsion. Water Research, 35(9), 2219-2224.

[11] KHELIFAOUI Nacera (2014) Etude de l''adsorption d'un solvant organique par un matériau alumineux silicate de la ville de Sig ; Mémoire de Master, Université Des Sciences et de la Technologie d'Oran Mohamed Boudiaf USTOMB.

[12] Van Gestel T, Vandecasteele C, Buekenhoudt A, Dotremont C, Luyten J, Leysen R., ... & Maes G (2002) Alumina and titania multilayer membranes for nanofiltration: preparation, characterization and chemical stability. Journal of membrane Science, 207(1), 73-89

[13] Talidi A, Saffaj N, El Kacemi K, Younssi S. A, Albizane A, & Chakir A(2011)Processing and characterization of tubular ceramic support for microfiltration membrane prepared from pyrophyllite clay. Scientific Study & Research. Chemistry & Chemical Engineering, Biotechnology, Food Industry, 12(3),pp. 263 – 268.

ISSN: 2961-6611

Energetic Performance Evaluation of Opening Ratio Using a Parametric Design Tool, Case of School Building in a Hot and Dry Climate

Khaoula LAKHDARI*[1], Leila SRITI*[2]

*LACOMOFA, Université de Mohamed Khider, Biskra, Algérie

[1]lakhdari_khaoula@yahoo.fr

[2]l.sriti@univ-biskra.dz

***Abstract*—this study aims to evaluate the effect of opening ratio of the facade on the total energy consumption of a school building. The goal is to provide architects with simple operational recommendations for the choices they make in designing of the facade. The investigation concerns a middle school located in Biskra, Algeria, which is characterized by a hot and arid climate. In this respect, various opening ratios and different orientations have been tested to achieve optimal lighting with a low level of energy consumption. The parametric study used the Grasshopper program for Rhinoceros which is one of the most popular parametric platforms today. Experimental results are evaluated in terms of monthly and annual energy consumption and optimal values are determined. Simulations indicated that the change in opening ratio and orientation has a significant effect on energy consumption for heating, cooling, and electric lighting and an appropriate choice made at the glass surface of the facade can significantly reduce the total energy requirement of the building.**

***Keywords*— Energy consumption, school building, window-wall ratio, parametric design tool, hot and dry climate.**

I. INTRODUCTION

With the growing global concern for sustainability, the development of high environmental performance of buildings is becoming a topic of interest for research. Maintaining a comfortable and healthy indoor environment with minimal energy consumption is a challenge for architects especially in areas with a hot and arid climate. In these regions, designing naturally lit buildings that are thermally comfortable while consuming as little energy as possible is almost a paradox. However, the design of the facade and especially the appropriate choice of the transparent surface seems to be decisive to meet such a challenge and ensure buildings with "zero energy" [1]. The problem is even more complex in school buildings where it is imperative to ensure both light and thermal comfort in the classroom. Solving this problem requires the development of a multi-criteria approach that integrates climate, formal and functional data.

The main objective of this study is to initiate such an approach that will highlight the impact of the opening ratio and orientation of windows on the energy consumption required for heating, cooling and lighting in classroom.

In Algeria, the realization of schools had to cope with the urgent demand for the lack of infrastructure resulting from escalating demographic and the institutionalization of the right of education. The construction was governed by standard plans largely reproduced to meet the criteria of economy and speed of execution. However, the consequences resulting from this strategy proved to be catastrophic from the point of view of the quality of the spaces produced. Often, the buildings constructed did not provide the minimum required in terms of thermal comfort and level of illumination, which made them highly dependent on the energy for their operation.

Indeed, school buildings by their function and tenure are distinguished by a particular architectural design. Thomas-Releau (1999) [2] states that schools and office buildings require levels of illumination and natural ventilation. These requirements have repercussions on the morphology of such buildings since they often appear with articulated shapes allowing large surfaces of external walls and a maximum of glazed surfaces.

However, window design has a direct impact on energy consumption for heating and cooling because it is responsible for much of the heat loss (or gain) that occurs at the same time on the building envelope. As a general rule, natural lighting performance is better when the window-to-wall ratio increases, at the same time solar heat gains will be increased as this ratio increases [3]. In other words, the higher the opening ratio of the facade, the more heat will be exchanged between the environment and the building, and the building will consume more energy to regulate the indoor environment [4].

According to a study conducted by Inanici and Demirbilek [5] in five cities in Turkey with different climates, it has been shown that optimizing window sizing and reducing energy consumption while ensuring visual comfort , goes through an optimization of the ratio of the length of a building to its width, with an optimal dimensioning of the south window. Muhaisen and Dabboor [6] investigated the impact of the orientation, size and type of window glass on the energy demand for heating and cooling buildings. Wang et al. [7] explored the optimal size of windows and ways to reduce energy consumption of buildings using computer simulation.

In the same context, Alwetaishi [8] carried out a study on the impact of the window ratio of the facade of school buildings in various climatic regions in Saudi Arabia. The results obtained showed that it is more advantageous to have

ISSN: 2961-6611

a larger glazing surface in a humid climate than in a hot and dry climate. Similarly, the East and South orientations are the most unfavorable in terms of undesirable calorific gains, since they cause overheating in all the cases studied. Regarding the ratio between glazed area and façade wall (opening ratio), it seems that the ratio of 10% is recommended both in a hot and dry climate and in a hot and humid climate. This ratio ensured a dry indoor temperature of 37 ° C and 38 ° C respectively in Jeddah and Riyadh. On the other hand, a ratio of 20% is recommended in a temperate climate.

In Amman, a study was conducted by Hassouneh et al. (2010) [9] in a school building to investigate the impact of glazing types. The results suggest that choosing a large area of south, east and west facing windows saves more energy and reduces winter heating costs. On the other hand, a north-facing classroom is better for saving energy in the summer.

II. Methodology

In school buildings classrooms consume most of the energy [10] which is estimated according to Muhaisen (2007) to 70% of the total amount of energy consumption [6]. Our study takes into account the climatic conditions of the city of Biskra; it is interested to study the impact of windows surface on the energy consumption in school buildings according to a parametric approach. Parametric design tools have become a strong trend in contemporary architectural design practice and education [11]. Design parametrically means to design a parametric system based on combination of parameters variations that can provides a design space. [12].

Among several software used to simulate the energy performance of buildings, this study is mainly based on Honeybee and Ladybug which constitute an environmental and climate analysis toolkit for Grasshopper3D. The latter is a "graphical algorithm editor" for Rhino. Honeybee uses a set of integrated software for simulation; DAYISM and RADIANCE for lighting, THERM, EnergyPlus and OPENSTUDIO for building energy, Ladybug imports EnergyPlus climate files (* epw) and provides a variety of interactive 3D graphics / metrics, including: , wind roses, radiation roses, radiation analysis, shadow studies and view analysis. This tool is becoming more and more used by designers, architects and students [13].

The research is structured in two parts: the first part consists in evaluating the thermal and luminous environment in a building taken as a case study (an existing middle school). The second part presents the process of parametric optimization, first, by acting on the orientation of the glass facade along the main directions East, West and North and comparing with the reference orientation which is the South. Then, the third part aims to evaluate different window ratios from 0.1 to 0.9 with a 10% increase in glass area. The Meteonorme software is used to select Biskra climate data [14].

III. Study Case

A. Location and Characteristics of Existing Building

Biskra an Algerian city is located 470 km southeast of Algiers, with latitude of 34.80 N, a longitude of 5.73 N, and an altitude of 86 m above sea level. The city of Biskra is characterized by a hot and arid climate with sunny clear skies most of the year [15]. The analysed case study is a middle school, built in 1995 in the southern part of the city opposite to London Garden. The pedagogical block of the school building is a ground floor plus one floor; bar of rectangular shape oriented along East-West axis in a planar plan (Fig.1). The classrooms are with rectangular shape, 8.75m long, 6.60m wide and 3.40m high. The block consists of 18 rooms 9 rooms in each level. The walls are ordinary with a thickness of 35 cm, single glazed windows are arranged on one side and open to the south with an opening ratio of 23%.

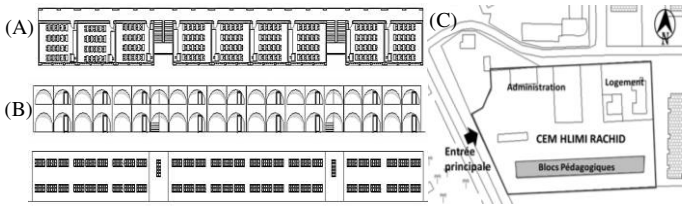

Fig. 1 Presentation of the reference building: (A) plan view, (B) North and South facades) , (C) pedagogical block situation, Source: authors (2019).

B. Material characteristics of the envelope

The construction system uses ordinary materials marketed in the Algerian market (tab.1).

TABLE I
ENVELOPE MATERIALS AND THEIR THERMAL CHARACTERISTICS. SOURCE: KADRI AND MOKHTARI (2011)

Walls / Floors	Materials	λ Conductivity	Thickness (m)
Interior wall	Plaster	0,35	0,015
	Hollow brick	0,5	0,1
	Plaster	0,35	0,015
Floor	Plaster	0,35	0,015
	Hollow brick + compression slab	1,45	0,2
	Mortar	1,4	0,04
	Flooring	2,1	0,06
Roof	Plaster	0,35	0,015
	Hollow brick + compression	1,45	0,2
	Insulation	0,1	0,04
	Slope shape	1,15	0,04
	sealing	0,04	0,03
Glazing	Simple Clear	5,8	0,04

IV. Result

The Rhino / Grasshopper program and Honeybee and Ladybug plug-ins were used to perform simulations tests on the pedagogical block of a middle located in Biskra. The characteristics of this control building are those defined previously. The objective of the simulation is to study the effect of varying the opening ratios of the facade in combination with different orientations on annual and

ISSN: 2961-6611

monthly energy consumption for heating, cooling, and electric lighting in classroom.

A. Evaluation the energy consumption of the classrooms

Comparing the energy needs of the educational block, it appears that the energy consumption required for cooling is the most important. Indeed, the overheating period in Biskra is spread over 7 months, from April to October. During the three months of the Summer-June, July and August, the air conditioning system requires maximum exploitation; the values calculated for energy consumption are between 600 and 1000 KWh for each classroom (Fig. 2). On the other hand, the heating consumes less energy, the use is limited to the three months of the winter season (December, January, February), the maximum values reached are in January is 137 KWh (Fig. 2). For its part, the monthly consumption in electric lighting is remarkable. During all the months of the year, the calculated values are of the order of 100 to 190 KWh. The maximum values are recorded during the winter period when the intensity of the solar rays is the lowest. These values are minimal during the summer period because of the considerable intensity of solar radiation. Figure 3 illustrates the distribution of total annual energy consumption for classrooms: 61% in cooling, 34% in electric lighting and just 5% in heating.

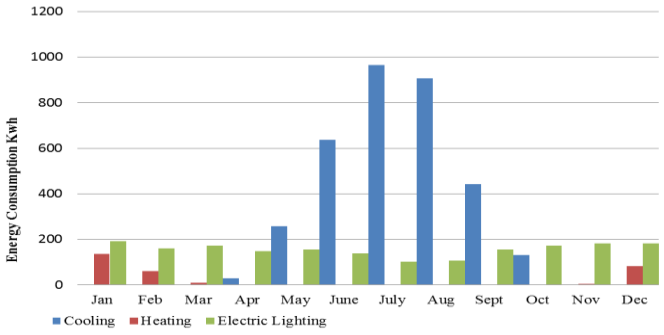

Fig. 2 Total monthly heating, cooling and electrical lighting for a classroom. Source: authors.

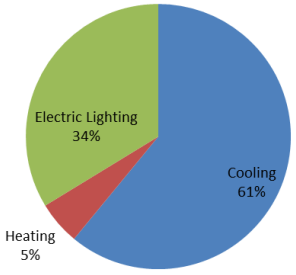

Fig. 3 Figure 3: Percentage of annual heating, cooling and electrical lighting consumption for a classroom. Source: authors.

The distribution of the annual energy consumed in the classrooms was analysed according to their location in the educational block (Fig. 4). Thus, classrooms located on the first floor are more energy-intensive than those located on the ground floor. The values of the annual energy consumption are between 130 and 154 KWh / m2 on the ground floor and between 186 and 210 KWh / m2 on the first floor. This difference is the result of an increase in the area exposed to the outside and therefore an increase in the heat gains (or losses) that occur, especially at the level of the horizontal roof exposed to the sun and hosting a large amount of heat. The same phenomenon can be seen in the classrooms at the east and west ends of the block. These rooms consume more energy than those inside because of the difference in the surface of the walls exposed to the outside.

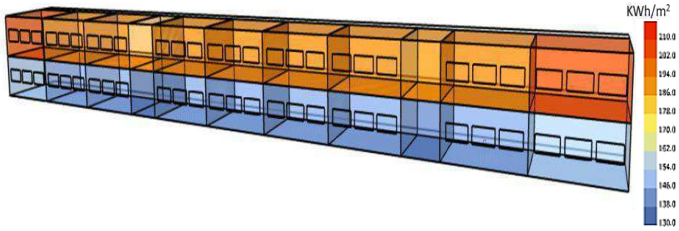

Fig.4 Visualization of annual energy consumption in classrooms according to their location in the building. Source: authors.

B. Impact of changing the orientation

After analysing the energy performance of the control building, the second series of tests are designed to evaluate the impact of the orientation of the glass facade along the main directions on energy consumption in heating, cooling and electrical lighting. The opening ratio is kept constant at 23%. The results obtained are illustrated in the graphs below (Fig. 5).

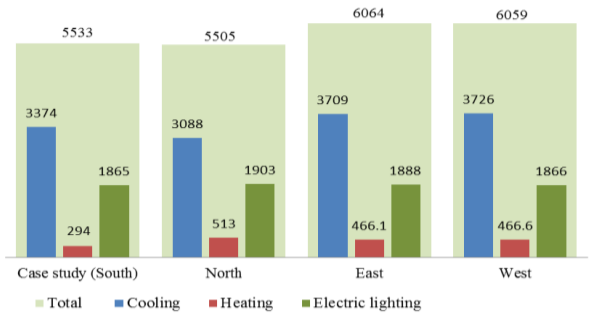

Fig. 5 Annual energy consumption in KWh according to the four orientations in a classroom. Source: authors

The Southern orientation, which represents the orientation of the case study (control building), is the one that records the lowest values in terms of energy consumption for heating and electric lighting. The Northern orientation is optimal in comparison with all other orientations since the total annual energy consumption for this direction is the lowest for cooling (3088KWh). On the other hand, it represents the most energy-consuming case for heating and electric lighting because it is least exposed to sunlight. Finally, the East and West orientations are the most unfavorable, as they record the highest values in energy expenditure for both cooling (more than 3700 KWh) and heating (466 KWh).

C. Impact of changing the window to wall ratio

ISSN: 2961-6611

For this series of tests, it is the opening ratio of the south-facing facade that will be varied to see the impact of the percentage change in glazed area on energy consumption. Thus, by maintaining classroom exposure to the South, the window opening ratio will be gradually increased from 0.1 to 0.9 with an increase in glass area of 10% each time.

The results obtained indicate a proportional relation between the opening ratio and the energy consumption in air conditioning (Fig. 6).

Fig. 6 Impact of changing window to wall ratio on energy consumption of the south facade. Source: authors

Thus, the energy consumption for cooling increases as the opening ratio increases, the difference between the ratios of 0.9 and 0.1 is 1497KWh; it means a percentage of 32% increase in annual energy consumption for cooling needs. An inverse relationship is noted between the opening ratio and the energy consumption in heating. Indeed, as the opening ratio increases, the reduction in energy consumption in heating was reduced; the difference between the ratios of 0.9 and 0.1 is 190 KWh; it means 67% of reduction in annual energy consumption in heating. With regard to, electric lighting a remarkable reduction in consumption of electric lighting occurs when the opening ratio goes from 0.1 to 0.2; but beyond the ratio of 0.5, the increase in the glass area has no effect, since the values are almost identical.

From the results of the parametric study, it seems that for all the ratios proposed, the ratio of 0.2 is the most efficient from the point of view of the total energy consumption. Finally, the analysis showed that a 20% glass surface ratio of the South-facing facade is optimal for the total annual energy consumption for a classroom.

CONCLUSION

This study evaluated the impact of the glass surface of the facade on the energy performance of a school building located in the city of Biskra where a hot and dry climate prevails. Annual and monthly energy consumption has been calculated based on the heating, cooling and electrical lighting requirements of the classrooms. The calculation was done with the Rhino / Grasshopper simulation tool and using the Honeybee and Ladybug plug-ins. The results of a first series of simulations carried out to evaluate the energy performance of a control building have shown that classrooms use 61% of the total annual energy consumption for air conditioning, 34% for electric lighting and just 5% % for heating. In addition, the appropriate choice of aperture area reduces this annual consumption by 16.7%, while the appropriate choice of orientation reduces the annual energy consumption by 9.2% per classroom. The results obtained also confirm the unsuitability of large glass surfaces for the hot and arid climate. The best open ratio is 0.2; this value represents a minimum consumption for the South orientation.

REFERENCES

[1] L. VANHOUTTEGHEM, G. SKARNING, G. C. J. HVIID, C. Anker, *et al.* "Impact of façade window design on energy, daylighting and thermal comfort in nearly zero-energy houses," *Energy and Buildings*, vol. 102, p. 149-156, 2015.

[2] N. THOMAS, J. T. Nigel "Are theories of imagery theories of imagination? An active perception approach to conscious mental content," *Cognitive science*, vol. 23, no 2, p. 207-245, 1999.

[3] X. SU, X. ZHANG, " Environmental performance optimization of window–wall ratio for different window type in hot summer and cold winter zone in China based on life cycle assessment," *Energy and buildings*, vol. 42, no 2, p. 198-202, 2010.

[4] C. E. Ochoa, M. B. C. Aries, E. J. van Loenen, J. L. M. Hensen, "Considerations on design optimization criteria for windows providing low energy consumption and high visual comfort", *Applied Energy*, *95*, 238-245, 2012.

[5] M. N. INANICI, F. N. DEMIRBILEK, "Thermal performance optimization of building aspect ratio and south window size in five cities having different climatic characteristics of Turkey", Building and Environment, 35(1), 41-52, 2000.

[6] A. S. MUHAISEN, H. R. DABBOOR, " Studying the Impact of Orientation, Size, and Glass Material of Windows on Heating and Cooling Energy Demand of the Gaza Strip Buildings", *J. Archit. Plan*, vol. 27, p. 1-15, 2013.

[7] L. WANG, J. GWILLIAM, P. JONES, "Case study of zero energy house design in UK", *Energy and buildings*, 41(11), 1215-1222, 2009.

[8] M. ALWETAISHI, "Impact of glazing to wall ratio in various climatic regions: A case study", *Journal of King Saud University-Engineering Sciences. 2017*

[9] K. HASSOUNEH, L. A. ALSHBOUL, A. AL-SALAYMEH, "Influence of windows on the energy balance of apartment buildings in Amman", *Energy Conversion and Management*, 51(8), 1583-1591, 2010.

[9] O. ALI AL-ARJA, T. S. AWADALLAH, "Energy consumption optimization in schools sector in Jordan", *Architectural Science Review*, vol. 59, no 5, p. 400-412, 2016.

[11] K. LAGIOS, J. NIEMASZ, C. F. REINHART, "Animated building performance simulation (ABPS)–linking Rhinoceros/Grasshopper with Radiance/Daysim", *Proceedings of SimBuild*, vol. 4, no 1, p. 321-327, 2010.

[12] M. QINGSONG, H. FUKUDA, "Parametric office building for daylight and energy analysis in the early design stages", *Procedia-Social and Behavioral Sciences*, vol. 216, p. 818-828, 2016.

[13] M. S. ROUDSARI, M. PAK, A. SMITH, et al. , "Ladybug a parametric environmental plugin for grasshopper to help designers create an environmentally-conscious design", *Proceedings of the 13th international IBPSA conference held,* Lyon, France Aug. 2013.

[14] D. Zekraoui, N. Zemmouri , "The Impact of Window Configuration on the Overall Building Energy Consumption under Specific Climate Conditions", *Energy Procedia*, vol. 115, p. 162-172, 2017.

[15] D. BERKOUK, S. MAZOUZ, "Numerical study of the horizontal shading devices effect on the thermal performance of promotional apartments: Case of El-Alia-Biskra", *Journal of Applied Engineering Science & Technology*, vol. 3, no 1, p. 21-27, 2017.

ISSN: 2961-6611

Multiple Fume Jets in Environmental Cross flows

RADHOUANE Amina[#1], MAHJOUB SAID Nejla[*2], MHIRI Hatem[#3], BOURNOT Philippe[”4]

[#]*National Engineering School of Monastir, Route of Ouardanine, 5000 Monastir, Tunisia*

[1]radhouane_amina@yahoo.fr

[3]hatem.mhiri@enim.rnu.tn

[*] *LGM, ENIM, Preparatory Institute for Engineering Studies, University of Monastir, Tunisia*

[2]mahjoub_nejla@yahoo.fr

[”] *Aix Marseille University, CNRS, IUSTI, Marseille, France*

[4]bournot@unimeca.univ-mrs.fr

Abstract **— One of the main solutions to the higher power demands in the industry is to introduce higher temperature inflows, namely to combustions chambers and turbine engines. As a consequence to such inlet conditions, we may obtain heated exhausts that may contain reactive effluents that are likely to damage the atmosphere seriously by the formation of acid rain and fog.**

To cope with such intricate situations, the discharge of multiple fume jets in a surrounding atmosphere has to be seriously detailed in terms of heat and mass transfer in order to understand properly all the mechanisms induced, their origin, their extent and how to control each of them.

For the matter, a variable number of variably elevated inline jet models are considered experimentally in the present work, in interaction with an oncoming cross flow generated within a laboratory wind tunnel.

A good comprehension of these experimental models will be followed later by numerical simulations, first small scale and then big real scale to find out solutions to real large scale industrial problems.

***Keywords*— multiple jets, cross flow, injection height, injection ratio, vortices.**

I. INTRODUCTION

Jets in cross flow (JICF) constitute a common model frequently found in several applications, in various domains. An efficient control of the different mechanisms it engenders is consequently highly recommended to avoid hazardous behaviors and useless risks on operators and the sheltering environments.

JICF are found in industrial applications such as film cooling of turbine blades and effusion cooling of combustors. In both applications the problem consists of introducing higher pressure ratios and higher temperature rises, to reach better performances of modern gas turbine engines.

JICF are also of particular interest in the medical field in applications like blood injection during hemodialysis through one or more holes at the tip of a catheter, typically positioned at the superior vena cava [1].

Finally and not the least, liquid and gas JICF are observed in environmental applications. In fact, waste waters generally need some chemical treatment and a serious control while being discharged through multiport diffusers into coast waters either because of their contents or of their thermal characteristics. Fume stacks, as well, need similar accurate handling when discharged in the atmosphere at high temperatures and or/containing reactive particles.

The consideration of these configurations among the open literature was carried out either globally by considering multiple, differently arranged, jets in cross flow, or gradually by detailing the single jet model physics and trying afterward to upgrade it to reach more realistic models. The earliest single jet in cross flow-studies available in the literature were carried out by Jordinson et al. in 1958 [2] and Gordier in 1959 [3] while the earliest multiple jets in cross-flow study dates back to 1971 where Ziegler and Wooler [4] generalized an analytical model initially dedicated for a single short and descending normal jet in crossflow. To reach that goal, they first solved the continuity and momentum equations to obtain the jet path. Then, they evaluated the jet velocity field by replacing the jet with a sink-doublet singularity distribution, accounting for the entrainment of mainstream fluid and the blockage effect of the jet. They finally represented the influence of an upstream jet on a downstream jet in a multiple configuration by including a reduced mainstream velocity in the equations of motion. A satisfactory agreement was obtained between theoretical and experimental data relative to the jet centerlines and surface pressure distributions.

Briggs [5] tried to make an overview of the models available in the literature that predicted the rise of the bent-over plumes. The recent models were based upon the conservation equations for buoyancy and momentum or energy, and assumed that the mean horizontal speed of the plume in the bent-over stage essentially equals the ambient wind speed. Earlier models, on the other hand, made diverse assumptions about how the plume grows which gave rise to diverse expressions of the corresponding plume paths and final rise. The third and more recent collection of models that was reported by Briggs [5], made similar assumptions about how the plume grows in the initial stage of bent-over rise due

ISSN: 2961-6611

to self generated turbulence, with the difference of the proportionality statement between the rise and the jet radius.

More realistic multi-source models were considered by Briggs [6] in order to provide a simple enhancement factor for their plume rise. A factor was proposed for bent-over buoyant plumes to correct the single source rise equation. For calm conditions, a crude but simple method was suggested for predicting the height of plume merge and subsequent behavior. Finally, it was suggested that large clusters of buoyant sources might occasionally give rise to concentrated vortices either within the source configuration or just downwind of it.

The above discussed semi empirical of Briggs [6] together with a further one developed by Briggs too [7] were reconsidered by Anfossi et al. [8] in an attempt to develop a new model based on "virtual" stack concept, able to provide estimates of maximum plums height for stacks of different emission conditions. A simplified expression was first compared to Briggs' models for equal heights and emissions. A new model was then confronted with experimental data relative to stacks of different heights with a general satisfactory agreement. Finally, a comparison was carried out with reference to the empirical expression of Montgomery et al.[9] which gave a correction factor for ground level concentrations for multiple sources and analogue ones derived from the models of Briggs [6, 7] and Anfossi et al.[8].

Overcamp [10] tried to investigate the plume rise enhancement and merge process in the case of two to four stacks models. The plumes frequently merge as they rise, and the rise is enhanced when the resultant plume rises higher than the individual plumes would have separately. The study included three major parts, namely a laboratory study on the interaction of line thermal pairs released in various configurations to determine the dynamics of plume merging, a wind tunnel study of plume rise from one to four stacks to measure plume rise enhancement and an analysis of field data to determine if plume rise enhancement is observed for actual power plant plumes.

To complete the above cited work, Overcamp [11] added three further studies that investigated the effect of the number of stacks and of the azimuthal angle between the direction of the wind and the line of stacks on plume rise enhancement. In the first study, observations were made of the merger and motion of thermal pairs: thermal pairs released in one-above-the other configurations merged more rapidly and moved faster than thermal pairs released in a side-by-side configuration. In the second study, plume rise measurements were made in a wind tunnel for plumes from two to four stacks. For a given number of plumes, the rise was higher for smaller azimuthal angles. The third study was an analysis of experimental data that was so large but lacked of observations which made the results inconclusive for cases with two to four plumes. Nevertheless, the ten plume cases showed higher rise and the rise was larger for smaller azimuthal angles.

Finally, Zanetti [12] considered hot pollutants injected into ambient air, which is the case of most industrial pollutants. The pollutants, emitted from smokestacks or chimneys, possess an initial vertical momentum. Both factors (thermal buoyancy and vertical momentum) contributed to increasing the average height of the plume above that of the smokestack. This process terminates when the plume's initial buoyancy is lost by mixing with ambient air.

With regards to the abovementioned references, we see how important the issue of the elevated jets in environmental cross flows is. Since most jets were considered side by side in the open literature, we propose in the present to enrich the documentation on multiple inline jets in environmental cross flows. For the matter, we propose to consider the effect of jets' number and height on their rise and merge, in addition to the subsequent accompanying phenomena and processes like the wake vortices and the final jets' fading

II. Experimental Set Up

The experiments were carried out in a wind tunnel at the university institute of the industrial thermal systems (IUSTI), a joint research unit between the University of Provence (Aix-Marseille) and the Mediterranean University in Marseille, France.

The jets handled in the present paper are emitted from elliptical cross-sections with d and $D = d/sin\ \alpha$ as small and great diameters respectively. In fact, the jets are emitted from 60° inclined discharging nozzles that were razed at different levels from the ground.

The jets are placed three great diameters apart and tandem toward the oncoming cross flow; and are sent according to jet to cross-flow velocity ratio inferior to one (R<1). As illustrated in Fig.1 the leading injection nozzle was placed 20 great diameters apart from the wind tunnel inlet section in order to avoid the transition zone of the mainstream entrance and therefore stay away from the boundary layer influence as illustrated in previous papers in the case of twin inline jet in cross flow [13].

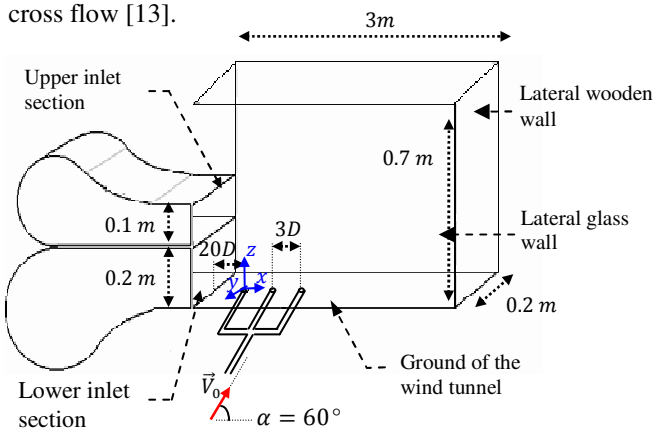

Fig. 1 Experimental setup associated with the Cartesian coordinate system

Measurements were depicted by means of Coupled Charge Device (CCD) images together with a two-component Particle Image Velocimetry (PIV) technique, in the symmetry plan $z = 0$; which allowed a non intrusive, instantaneous and mean bi-dimensional dynamic diagnosis of the resulting flow field for a given injection ratio inferior to one.

ISSN: 2961-6611

III. Results and Discussion

We propose to start our discussion with the description of the established dynamic field due to its close and direct dependence on the thermal field and the induced mass transfer. Whether single or in group, when the jets interact with the surrounding cross flow, they generally result in four main vortical structures: the horseshoe vortices and counter-rotating vortex pair, known as CVP, that are present in the transverse plane, and the leading edge/shear layer vortices and wake/upright vortices that develop in the symmetry plane.

Figure 2 provides streamlines of double and triple inline jets discharged from different levels from the tunnel ground ($h = 1, 2\ and\ 5\ cm$) under an injection ratio inferior to 1 ($R < 1$). Our objective consists of evaluating the impact of these parameters over the jets' progression among the surrounding domain, in terms of rise, bending, merging and fading; all of which are closely implied by the established vortices, and highly affecting on their turn on the induced heat transfers. Generally, as they rise, the jets expand in accordance with the adopted injection ratio, and block more or less consistently the oncoming mainstream, inducing a bow shock ahead of the first injection orifice as already observed by Chen et al. [14] in the case of a triple jet in cross flow configuration. According to the same authors [14], the bow shock produces an adverse pressure gradient and forces the approaching boundary layer to separate with an oblique separation shock. In Fig.2, the bow shock appears as a separation continuous line between the evolving jets and crossflow regions that reaches progressively higher levels as the jets are sent from higher injection nozzles. It also rises higher when more jets are discharged, as indicated by the double sided arrows in Fig.2-II, evaluated three great diameters downstream of the rear jet nozzle). The separation line appears more smoothly curved in the case of twin inline jets even if both twin and triple jet configurations are observed under almost the same injection ratio, inferior to one. Actually in a double jet configuration the leading edge jet is consistently flattened by the oncoming cross flow. Once flattened it merges with the downstream evolving jet, and they keep on rising together before fading.

When a third jet is discharged, it rises and merges farther downstream with the upstream already merged first two jets. The moment the three of them merge, the resulting plume is "straightened", which changes the smooth curved profile of the separation line (Fig. 2-II). The separation line contains consequently quasi-stages relative to the corresponding discharged jets that are more emphasized and apparent when the jets are sent from higher levels from the ground (indicated by arrows in Fig. 2). The second important features to comment on the present streamlines are the wakes of the discharging nozzles, where the streamlines seem to be sent from either a reattachment point or line, particularly when the jets are sent close to the ground (Fig. 2-a). These points or lines take place in the wake regions where wake vortices originate from the downstream cross flow shear layer [15, 16]. The induced vorticity results from the injection of the wall boundary layer where the boundary layer fluid has been "lifted-off" and wrapped around the jets [15].

Fric and Roshko [16] attribute the boundary layer fluid "lifting-off" or "sucking up" to the pressure gradient discussed by Chen et al. [14] which is actually the origin of the vertical momentum and a tornado-like structure, also said wake or upright vortices that will entrain a proportional amount of fluid with reference to the injection ratio [17].

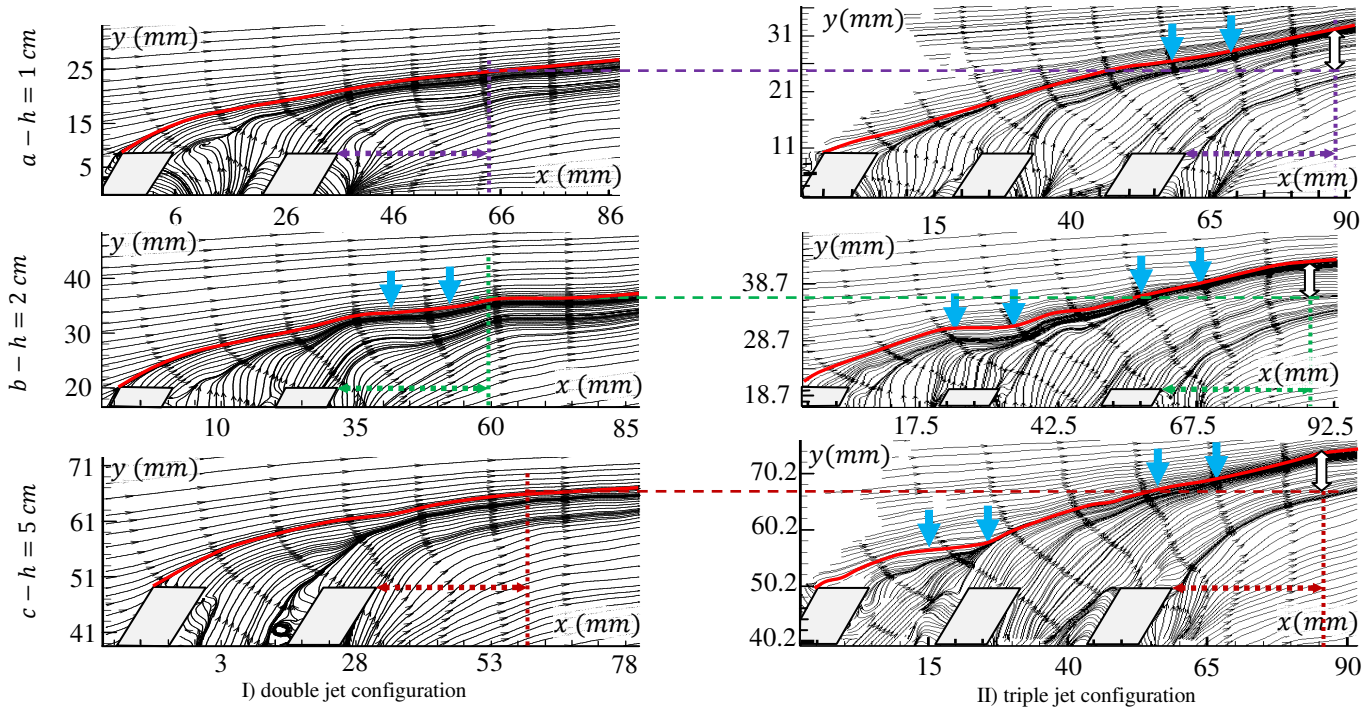

Fig. 2 Streamtraces under variable heights in the twin (I) and triple (II) jets configurations under R<1.

ISSN: 2961-6611

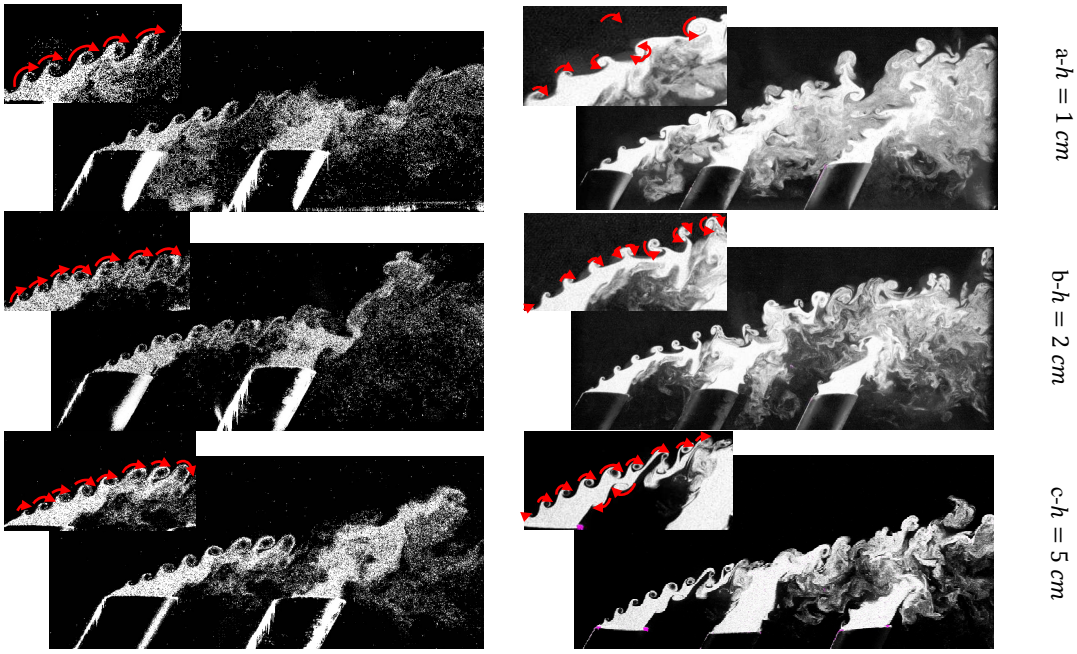

I) double jet configuration II) triple jet configuration

Fig. 3 CCD images of twin (I) and triple (II) jets configurations under a variable height under R<1

Figure 3 presents the different stages of the jets' emission both in double and triple jets' models. It further emphasizes on the vortices developed on the periphery of the rising jets and their wakes. Since the injection ratio is inferior to one, it's obvious to note the clockwise sense of rotations of the vortices. What is more interesting is the merge process that takes place farther from the injection cross-section as the jets are sent farther from the ground. In fact the jets are freed from the attachment to the ground which enables them to cross deeper the domain before bending and merging. When more jets are discharged, the stages already observed on the streamlines of Fig. 2 are found back here as soon as the upstream expanded jets join the downstream just emitted jets.

IV. Conclusions

Experimental consideration was given in the present study to multiple inline inclined and variably elevated jets in cross flow. We mainly observed:

- A change in the separation line (bow shock) shape between the emitted jets and the cross flow: from smoothly curved to staged line, the stages corresponding to the emission of more and higher emitted jets.
- The presence of attachment points or lines that take place in the wake of the jet nozzles when the jets are discharged close to the ground (decreasing h).
- When more jets are emitted the merge process is postponed deeper vertically and streamwise in the domain.

References

[1] J. Froust and D. Rockwell, "Flow structure associated with the multiple jets from a generic catheter tip", *Exp Fluids* vol.42, pp 513-530, 2007. Doi:10.1007/s00348-006-0249-z

[2] R. Jordinson, "Flow in a jet directed normal to the wind". R&M No. 3074, Brit. A R C, 1958.

[3] R.L. Gordier, "Studies on Fluid Jets Discharging Normally into Moving Liquid". St. Anthony Falls Hyd. Lab., Tech. Paper, No. 28, Series B, 1959.

[4] H. Ziegler and P.T. Wooler, "Multiple Jets Exhausted into a Crossflow". *J. Aircraft*, vol. 8(6), pp. 414-420, 1971

[5] G.A. Briggs, "Discussion on chimney plumes in neutral and stable surroundings", *Atmospheric Environment*, vol. 6, pp. 507-510, 1972

[6] G.A. Briggs, "Plume rise from multiple sources". Proc. of Cooling Tower Environment symposium, university of Maryland, pp.161-179, 4-6th March 1974.

[7] G.A. Briggs, "Plume rise predictions. Lectures on air pollution and environemental impact analysis" , pp. 59-111, 1975

[8] D. Anfossi, G. Bonino, F. Bossa and R. Richiardone, "Plume rise from multiple sources: a new model", *Atmospheric Environement*, vol. 12, pp. 1821-1826, 1978.

[9] T.L. Montgomery, W.B. Norris, F.W. Thomas and S B. Carpenter, "A simplified technique used to evaluate atmospheric dispersion of emissions from large plants", *J. Air Poll. Control Ass*. Vol. 23, pp. 388-457, 1973

[10] T.J. Overcamp, " Plume rise from two or more adjacent stacks", Report N° PPRP-67 (PB-83-179036), Power Plant Siting Program, State of Maryland, National Technical Information Service, Springfield, VA, 1982

[11] T.J. Overcamp and T. Ku, "Plume rise from two or more adjacent stacks", *Atmosphenc Enrironment*, vol. 22(4), pp. 625-637, 1988.

[12] P. Zannetti, "Plume rise, Air Pollution Modeling", DOI: 10.1007/978-1-4757-4465-1_5, 1990

[13] A. Radhouane, N. Mahjoub Saïd, H. Mhiri, P. Bournot and G. Le Palec, "Twin inclined jets in crossflow: experimental investigation of different flow regimes and jet elevations", *Environ Fluid Mech* vol.16(1), pp.45-67, 2016.

[14] P. Chen, S. Li, S. Luo and Z. Ni, "Flow visualization on lateral multiple jet interaction with freestream", *J of Flow Control, Measurement and Visulization*. vol.2, pp. 7-11, 2014

[15] Y. Yao, and M. Maidi, "Direct numerical simulation of single and multiple square jets in cross-flow", *Journal of Fluids Engineering*, vol. 133(3), pp:031201(1)- 031201(10), 2011

[16] T.F. Fric and A. Roshko, "Vortical structure in the wake of a transverse jet", *J. Fluid Mech*, vol.279, pp:1-47, 1994

[17] S.H. Smith and M.G. Mungal, "Mixing, structure and scaling of the jet in crossflow". *J Fluid Mech* , vol.357, pp.83–122, 1998

ISSN: 2961-6611

Monte Carlo Simulation and Six Factor Formula Using for Calculation of Effective Multiplication Factor of a Subcritical Reactor

F. Rouihem [b,c*], W. DRIDI [c], F.HOSNI [a,c]

[a] University of Bisha, Faculty of Sciences, Kingdom of Saudi Arabia

[b] *Faculty of Sciences of Tunis, Campus Universitaire El-Manar, 2092 El Manar Tunis, Tunisia*

[c] *Laboratory of Energy and Matter for Development of Nuclear Sciences (LR16CNSTN02), National Center for Nuclear Sciences and Technology (CNSTN), Sidi Thabet Technopark, 2020, Tunisia*

[*]fadi.rouihem@fst.utm.tn

walid.dridi@cnstn.rnrt.tn

faouzi.hosni@cnstn.rnrt.tn

Abstract— **Jordan Subcritical Assembly (JSA) is uranium fueled light water moderated and reflected subcritical reactor. The purpose of our study is to evaluate the effective multiplication factor K_{eff} with the Monte Carlo MCNP code indicating the fuel mapping in the reactor core and to calculate the spatial neutron flux distribution. Many cases have been studied on the subcritical assembly to show how small perturbation affect K_{eff}. Using the six-factor formula, we have estimated the value of K_{eff}, this method is the decomposition of the neutron balance in six factors. These formulas are no longer used in reactor calculation since the introduction of computer science into neutrons but remain useful for understanding physics and evaluation the perturbations effects. The K_{eff} value found by this method is close to that calculated by the MCNP code.**

Keywords: Subcritical Assembly, Effective multiplication factor, Monte Carlo, Six-factor formula.

I. INTRODUCTION

In nuclear reactor, nuclear fission is initiated by bombarding fissile nuclei with neutrons. Then, the fission of a nucleus is always accompanied by the release of neutrons, these can in turn cause the fission of other nuclei and the release of other neutrons, and so on. These cascading fissions is called a chain reaction [1].

In a subcritical reactor, the fuels are chosen so that less than one neutron per fission induces a new fission. Such a reactor cannot maintain the chain reaction by itself. It must be supplied with neutrons by an external source, which minimizes the potential risk of accidents [2].

The rate of this chain reaction is measured by the effective multiplication factor k_{eff}. This factor is the average number of neutrons emitted by fission that generate a new nuclear fission. So, it is essential to determine this factor when modeling or designing the core of this type of reactor.

The fuel system under consideration consists of a mixture of a fissile material by thermal neutrons as uranium 235 and a non-fissile material by thermal neutrons but capturing as uranium 238. For the first, as well as for capturing other materials (moderator, clad), it can be assumed that all absorptions occur in the thermal domain. Calculation must take into account fissions induced by the fast neutron, captures in epithermal resonances and neutron leakage out of the reactor core. The effective multiplication factor is the balance that is established starting from a fission and analyzing the neutron history until the next fission estimated by so-called six factor formula [3] :

$$K_{eff} = \eta_T \times f \times p \times \epsilon \times P_{FNL} \times P_{TNP} \quad (1)$$

II. JORDAN SUBCRITICAL ASSEMBLY (JSA) DESCRIPTION

Jordan sub-critical assembly at the University of Science and Technology (JUST) is fueled by uranium oxide fuel, light water as a moderator and reflector, and a plutonium-beryllium neutron source located under the core at the centerline.

The core of the reactor is composed of 313 uranium oxide (UO2) rods enriched with 3.4 wt% U235 forming a square lattice of 1.91 cm pitch and supported by upper and lower grid plates. Its diameter is 40 cm and its height equal to 55 cm and it is positioned in the center of a water vessel whose diameter and height are 120 cm and 132 cm respectively (Fig.1).

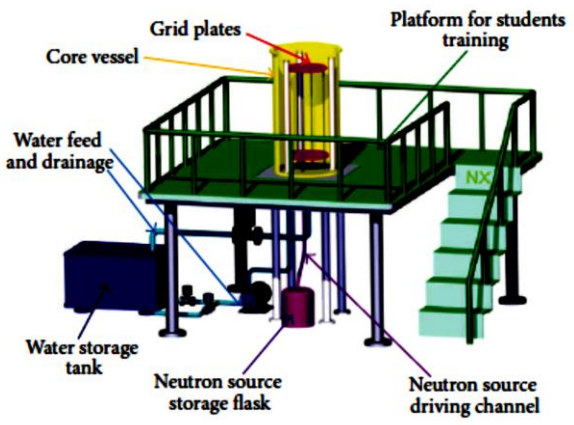

Fig. 1 Layout design of JSA main systems [4]

ISSN: 2961-6611

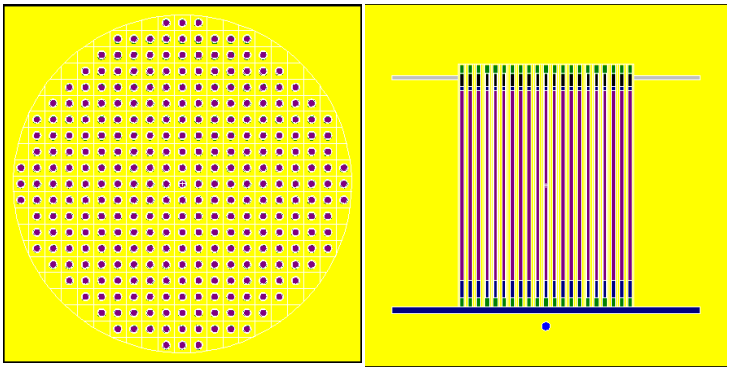

(a) (b)

Fig. 2 (a) MCNP modeling *x-y* view of the JSA reactor at mid-plane (b) MCNP modeling *y-z* view of the JSA reactor at mid-plane showing fuel rods (purple color) surrounded by water (yellow color) and fixed source (light-blue color).

The rod is composed of 43 cylindrical pellets of uranium oxide of 1cm in height and 0.4215 cm in radius, a gap of helium gas between fuel and a zirconium cladding tube, and five insulating granulate made of aluminum trioxide Al_2O_3 : four below the fuel pellets and one above the fuel pellets that is held down by a spring and it is plugged at both ends with upper and lower caps forming a rod of 0.5 cm in radius and 55 cm in height [4]

III. MCNP SIMULATION OF JSA

The assembly simulation was performed by the MCNP 5 code [5] using the ENDF / B-VII.0 cross section data library. This code is based on transport theory and Monte Carlo calculation.

The lattice containing 313 fuel rods cladded with zirconium, the helium gap, the caps, grid plates, the moderator, the reflector and the reactor vessel were explicitly modeled in this work. (Fig.2).

The criticality problem was scheduled to skip 50 cycles and run a total of 550 cycles with nominally 5000 neutrons per cycle totaling 2751391 neutron histories. A combined estimate (collision / absorption / path length) of multiplication factor K_{eff} then was given in output file (Table I).

After few generations the characteristics of the initial source (strength and energy distribution) are lost and the absolute neutron flux depend on the reactor geometry and materiel distribution. The F5 tally was used to calculate neutron flux at the core midplane and it was normalized by neutrons fissions sources and scaled to reactor power [7, 8].

Fig.3 shows the normalized results of Kcode estimation of the radial thermal, epithermal and fast neutron flux.

In Fixed source simulation (NPS), the source was modeled by the SDEF card as a volumetric source and placed under the core at the centerline with a weight equal to 1.1E6 neutrons per seconds. The spectrum of the 239 Pu-Be neutron source was taken from reference [6].

MCNP calculation of neutron flux was also performed with run of 10^6 neutrons source (Fig.4). The F5 detector must be scaled to neutron source strength to depict radial absolute flux for thermal, epithermal, and fast neutron flux.

As expected, the flux has a maximum at the core center and it collapses at approximately 40 cm far away from it and is symmetrical on both sides.

TABLE I
CRITICALITY CALCULATION RESULTS

Effective multiplication factor K_{eff}	0.96295 ± 0.0045
Estimated 68% k-effective confidence interval	0.96250 to 0.96340
Estimated 95% k-effective confidence interval	0.96205 to 0.96385
Estimated 99% k-effective confidence interval	0.96176 to 0.96415
Prompt removal lifetime (seconds)	9.4610E-5 ± 5.3735E-8
Average number of neutrons produced by fission	2.449

.

Thermal neutron flux is the highest at reactor middle plane in kcode calculation and appear at the same amplitude with fast neutron flux in fixed source mode. It manifests two peaks at the core- reflector interfaces (-20 cm and 20cm) due to the reflecting of thermal neutrons back to the core by the light water.

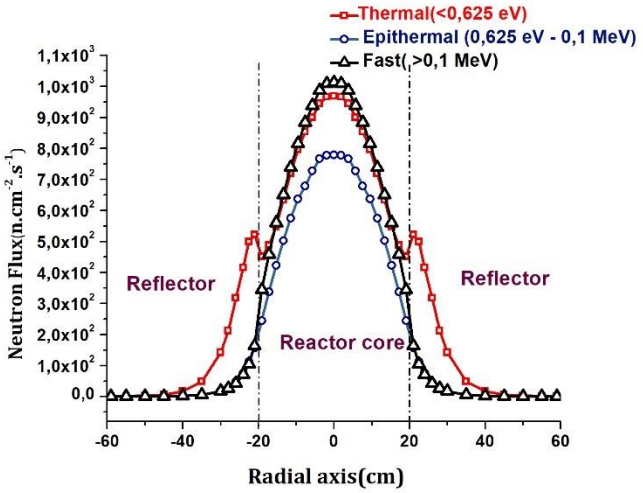

Fig. 3 Kcode estimation of the radial absolute thermal, epithermal and fast neutron flux (n/cm² s)

The Kcode estimation of the total flux is slightly higher than that estimated by fixed source mode. In the first mode, criticality calculations are carried out using the core characteristics (geometry and materials) without considering the source, the solution is close to cosine shape and the flux is expected to be highest at the core center. Besides, in the second mode, calculation depend on the source location and the flux is expected to be highest at the bottom of the core.

IV. EFFECTIVE MULTIPLICATION FACTOR CALCULATION WITH THE SIX-FACTOR FORMULA

ISSN: 2961-6611

A. Thermal fission factor (Reproduction factor) η_T

The value of η_T is the number of fast neutrons produced by thermal fissions per thermal absorption in the fuel, it is defined as the ratio of the number of fission neutrons to the number of thermal neutrons absorbed in the oxide uranium rod.

The JSA reactor is fueled with partially enriched uranium in oxide form and the numerical value of η is given by following equation:

$$\eta_T = \frac{\upsilon_{25} * \Sigma_{f25}}{\Sigma_{a25} + \Sigma_{a28}} = \frac{\upsilon_{25} * \sigma_{f25} * g_{f25}(20°C)}{\sigma_{a25} * g_{a25}(20°C) + \frac{N_{28}}{N_{25}} * \sigma_{a28} * g_{a28}(20°C)} \quad (2)$$

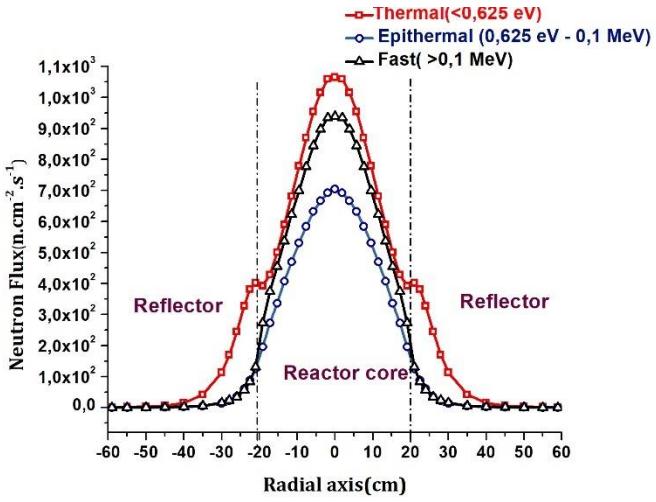

Fig.4 Fixed source estimation of the radial absolute thermal, epithermal and fast neutron flux (n/cm² s)

Where υ_{25} is the average neutrons production of ^{235}U, N_{28} and N_{25} are the atomic number densities of isotopes ^{235}U and ^{238}U, σ_{a25} and σ_{a28} are the thermal absorption microscopic cross sections of ^{235}U and ^{238}U, σ_{f25} is the fission microscopic cross section of ^{235}U and g_{a25}, g_{a28} and g_{f25} are the non- l/v factors.

B. Thermal utilization factor f

The thermal utilization factor is the probability of a thermal neutron being absorbed by fissile material whether causing fission or not in reactor core. It is equal to the ratio of the number of neutrons that are absorbed in fuel to the number absorbed in both fuel and moderator, so that f can be put in the form:

$$f = \frac{\Sigma_{aF}\, V_F}{\Sigma_{aF}\, V_F + \Sigma_{aM}\, V_M \xi} \quad (3)$$

Where Σ_{aF} and Σ_{aM} are the macroscopic absorption cross sections of the fuel and the moderator, V_F and V_M are the fuel and Moderator volumes and $\xi = \frac{\bar{\phi}_{TM}}{\bar{\phi}_{TF}}$ is called the thermal disadvantage factor.

The f factors cannot be calculated analytically, but it is possible to derive an approximate formula by Wigner-Seitz method [9] :

$$\frac{1}{f} = \frac{\Sigma_{aM}\, V_M}{\Sigma_{aF}\, V_F} F + E \quad (4)$$

E and F are called lattice functions, calculated by using the equivalent cylindrical cell parameters a, $b = \frac{\pi}{\sqrt{pitch}}$, L_F and L_M (Fig.5).

Where, a is the fuel rod radius, b is the radius of equivalent cell, L_F and L_M are the diffusion lengths in the fuel and the moderator.

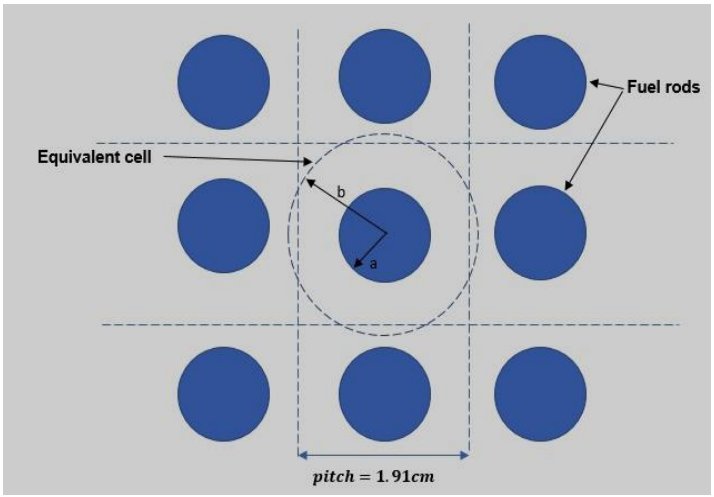

Fig.5 The equivalent cylindrical cell

C. Resonance escape probability p

The probability of escaping absorption in the resonances while neutron slowing down is called the resonance escape probability. Measurement of this factor shows that p can be expressed by the equation [10]:

$$p = \exp\left(-\frac{N_F V_F I}{\xi_M \Sigma_{SM} V_M}\right) \quad (5)$$

Where ,N_F is the atom density of the fuel lump, in units of 10^{24}, V_F and V_M are the volumes of fuels and moderator, respectively, ξ_M is the average increase in lethargy per collision in the moderator, Σ_{SM} is the macroscopic scattering cross-section of the moderator at resonance energies, and I is a parameter known as the resonance integral. Values of I for cylindrical fuel rods are well represented by the following empirical expression:

$$I = A + \frac{C}{\sqrt{a\rho}} \quad (6)$$

Where A and C are measured constants and ρ is the density of the fuel.

D. Fast fission factor ϵ

The fast fission factor is defined as the number of neutrons generated from both thermal and fast fission to the number generated in thermal fission. it has been calculated and measured for large number of heterogeneous reactors.

ISSN: 2961-6611

ϵ increases as the ratio of the metal rod volume to water increases and it is independent of the radius of the fuel rods and at low enrichment the ^{238}U of the fuel it is not sensitive to ^{235}U enrichment. For metal-water volume ratio in equivalent cylindrical cell of 0.1526 it was taken from [9] that ϵ is equal to 1.028.

E. Thermal and fast non-leakage probability

The JSA lattice containing square cells is estimated by a cylindrical lattice containing 313 cylindrical equivalent cells with a geometric radius R_{geo} and a geometric height H_{geo} and compacted with just fuel and moderator.

It is known that the neutron economy is improved when the core of reactor is surrounded by a reflector. At JSA bare reactor, the effective multiplication factor does not exceed 0.89966 but when it is surrounded by a reflector : unfueled region of moderator, it reaches the value of 0.96295.

Under the design of JSA, the reflector is used to surround the core whose the extrapolated radius R_{ext} and extrapolated height H_{ext} [11] are written as:

$$R_{ext} = R_{geo} + \delta = \left(\sqrt{313} \times b\right) + \delta \quad (7)$$

$$H_{ext} = H_{geo} + 2\delta \quad (8)$$

Where δ is the reflector saving factor determined by the following empirical formula:

$$\delta = 7.2 + 0.1(M_T^2 - 40) \quad (9)$$

and M_T^2 is the thermal migration area in the core

The thermal and fast non-leakage probability is the probability that thermal and fast neutrons will not leak out of the reactor [12,13]. It is simplified in the following form:

$$P_L = P_{TNP} \times P_{FNL} \approx \exp\left(-B_g^2 \times M_T^2\right) \quad (10)$$

The geometric buckling B_g^2 is depending on the shape and the size of the core and it has the following expression:

$$B_g^2 = \left(\frac{2.405}{R_{ext}}\right)^2 + \left(\frac{\pi}{H_{ext}}\right)^2 \quad (11)$$

F. The effective multiplication factor calculation

The effective multiplication is expressed by the equation (1).

The comparison between the two calculation methods shows that the six-factor calculation slightly overestimates the MCNP calculation with a relative deviation equal to 1.23%.(Table II)

TABLE II
COMPARISON BETWEEN MCNP AND SIX FACTORS FORMULA CALCULATIONS OF K_{EFF}

η_T	1.8513
f	0.7850
p	0.9482
ϵ	1.028
P_L	0.6881
K_{eff} calculated with the six factors formula	0.97475
K_{eff} calculated with the MCNP5 code	0.96295
Relative deviation	1.23%

V. CONCLUSION

MCNP calculation makes it possible to calculate the effective multiplication factor and the flux and to study the perturbation effects on K_{eff}

The Six-Factor method helps to understand the conduct of the chain reaction, the fuel, clad, moderator and reflector roles in the reactor and to have an idea about the order of the neutron non-leakage probability.

Perturbation calculated by MCNP code and its theoretical analysis by the method of six factor formula constitute a very preferment tool for understanding the physical process taking place in the subcritical reactor and to enhance its constructions by changing its geometry and materials.

Therefore, MCNP code will be used to study the effect of the following perturbations on the core of JSA and its impacts on the six factor :

- Changing oxide-uranium rod density
- Changing Moderator and reflector
- Adding material different than fuel in the center of the core
- Changing the number and the distribution of the fuel rods in the core
- Changing the position of the external source and its nature
- Adding Control rods

REFERENCES

[1] Stacey, W. M. (2018). *Nuclear reactor physics*. John Wiley & Sons.
[2] Shahbunder, H., Pyeon, C. H., Misawa, T., Lim, J. Y., & Shiroya, S. (2010). Subcritical multiplication factor and source efficiency in accelerator-driven system. *Annals of Nuclear Energy*, *37*(9), 1214-1222.
[3] Reuss, P. (2012). *Précis de neutronique*. EDP sciences.
[4] Xoubi, N. (2013). Design, development and installation of Jordan subcritical assembly. *Science and Technology of Nuclear Installations*, *2013*.
[5] MCNP, X., *Monte Carlo Team, MCNP–A General Purpose Monte Carlo N-Particle Transport Code, Version 5*. LA-UR-03 1987, Los Alamos National Laboratory, April 2003, The MCNP5 code
[6] Harvey, Z. R. (2010). Neutron flux and energy characterization of a plutonium-beryllium isotopic neutron source by Monte Carlo simulation with verification by neutron activation analysis.
[7] Vega-Carrillo, H. R., Esparza-Garcia, I. R., & Sanchez, A. (2015). Features of a subcritical nuclear reactor. *Annals of Nuclear Energy*, *75*, 101-106.
[8] Xoubi, N. (2016). Calculation of the power and absolute flux of a source driven subcritical assembly using Monte Carlo MCNP code. *Annals of Nuclear Energy*, *97*, 96-101.
[9] Lamarsh, J.R. and A.J. Baratta, *Introduction to nuclear engineering*. Vol. 3. 2001: Prentice Hall Upper Saddle River, NJ.
[10] Duderstadt, J.J. and L.J. Hamilton, *Nuclear reactor analysis*. Vol. 84. 1976: Wiley New York.
[11] Deutsch, R. W. (1961). Method for analysing low-enrichment, light-water cores. *Journal of Nuclear Energy. Parts A/B. Reactor Science and Technology*, *14*(1-4), 168-179.
[12] Papastefanou, C. (2004). Measurement of neutron flux and albedo of water for thermal neutrons with foils of indium in a subcritical nuclear reactor. *Journal of radioanalytical and nuclear chemistry*, *261*(3), 671-678.
[13] Glasstone, S., *Principles of Nuclear Reactor Engineering: With the Assistance of {Oak Ridge National Laboratory} Staff*. 1956: Macmillan

ISSN: 2961-6611

Exergetic analysis of propylene refrigeration unit using Aspen Plus software

Haifa FITOURI [1], Mohamed-Razek JEDAY [2], Noureddine HAJJAJI [3]

Unité de Recherche Energétique et Environnement Ecole Nationale d'Ingénieurs de Gabes, Universite de Gabes cité erriyadh Zrig, 6029 Gabes, Tunisie

[1]haifahaifa02@gmail.com

[3]hajjaji.nour @gmail.com

[2]raz.jday @yahoo.fr

***Abstract*— This work is a contribution on exergetic life cycle analysis of liquefied Petroleum Gas (LPG) production. The refrigeration unit of the plant will be studied in order to analyse inefficiencies in production chain. The data for the exergetic calculation is provided by a simulation of the unit in Aspen Plus ™.**

The refrigeration unit contain 4 sections: compression, condensation, expansion and evaporation. The refrigerant used is propylene. As a result, two thirds of exergy destruction is in the compression and condensation section. This is due mainly to pressure and temperature differences.

***Keywords*— Exergetic Life Cycle Analysis, Exergy, LPG, Aspen Plus, Propylene.**

I. INTRODUCTION

The increase in energy prices has generalised an undisputed awareness of all the industries of the world including the oil industry. Faced with these problems, industries have naturally taken an interest in this position, which plays a very important role in the cost of the finished product. Thus, it gradually emerged that, in industrial units, the function of the objective to be maximized was not only the short-term profile or the increase in the amount of work, but also to make the equipment fully functional with maximum efficiency. The objective of this work is to thermodynamically evaluate a propylene refrigeration unit belonging to the LPG production plant .For these several methods are proposed to study the sources of energy degradation. The exergy analysis, a thermodynamic approach that has been developed over the last decade, is one of the methods that can detect and evaluate the energy degradations in the various equipment of an installation. It is based on the simultaneous establishment of the first and second principles. The exergy analysis makes it possible to pose a real " diagnosis " concerning the " thermodynamic health " of the considered system by detecting all the imperfections corresponding to the following sequence: irreversibility → energy degradation → loss of exergy. A simulation of the refrigeration unit is done in advance using ASPEN PLUS software. The main objective of this simulation is to provide the data necessary for the exergetic study in question which are not accessible on the site.

II. Process Description

The refrigeration unit is essentially equipped with two twin-stage screw compressors GB-1301-A / B, which aspirate the propylene vapors at 0.06 barg and compress them to 17barg. The vapors discharged by the compressors are condensed in the aerocondenser EC-1306 at the temperature of 46°.In addition, it is composed of a propylene cooler EA-1309, two expansion valves LV-3989 and LV-3986, an economizer FA-1310 and an evaporator EA-1304. For illustration, see Fig. 1.

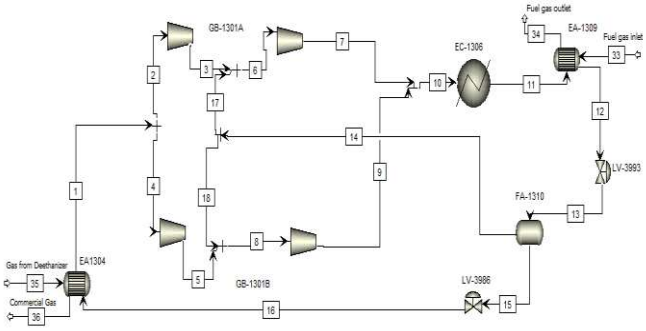

Fig. 1 Aspen plus simulation flowsheet of the refrigeration unit.

III. Process Simulation

Before applying the exergetic analysis, the propylene refrigeration unit was modelled in Aspen Plus™ process simulation software developed by Aspen Tech. The simulation provided the properties of the stream (T, P, enthalpy, entropy, etc.) at different locations.

A. Simulation data

To calculate the exergy balance we have to estimate the enthalpy and the entropy of each stream of the refrigeration unit at its current temperature and pressure, as well as those of reference (T_0=298K and P_0 =1atm) .The thermodynamic properties were calculated using the Peng-Robinson equation of state. The Peng-Robinson model is selected for natural gas systems in the petroleum industry [1]. Operational data required for simulation are clustered in table I.

ISSN: 2961-6611

B. Results and discussion

The results obtained from the simulation are grouped in Tables III and.IV.

TABLE I
CHARACTERISTICS OF VARIOUS DEVICES
OF THE REFRIGERATION UNIT

Devices	Characteristics
GB1301A1 GB1301B1	discharge pressure=3,5 barg, Isentropic efficiency=0,57
GB1301A2, GB1301B2	discharge pressure=17barg, Isentropic efficiency=0,95
EC 1306	propylene outlet temperature=46°C
EA1309	propylene outlet temperature=11°C
Lv3993	propylene outlet pressure=5bar
Lv3986	propylene outlet pressure=1,003bar
FA 1310	adiabatic
EA1304	propylene outlet temperature =-46,8°C

The mass flow rate of propylene circulating in the refrigeration circuit is 12490 kg / h

TABLE II
CHARACTERISTICS OF INLET GAS

Gas	Characteristics
Fuel gas inlet	Inlet pressure= 31bar Mole fraction N_2 = 0,021 CO_2 = 0,007 CH_4 = 0,822 C_2H_6 =0,122 C_3H_8 =0,028
Gas from deethanizer	Inlet pressure= 31bar Mole fraction N_2 = 0,019 CO_2 = 0,007 CH_4 = 0,779 C_2H_6 =0,146 C_3H_8 =0,049

TABLE III
EXERGY RELATED TO
THE FLOW OF THE REFRIGERATION UNIT.

Flow	Mass Flow(Kg/h)	Exergy(KW)
1	12490	58,32639
2	7244,227	33,82944
3	7244,227	142,5636
4	5245,773	24,49696
5	5245,773	103,2348
6	7928,459	156,0333
7	7928,459	363,8678
8	7723,17	152,4982
9	7723,17	348,2778
10	15651,63	711,9965
11	15651,63	596,1573
12	15651,63	586,8431
13	15651,63	556,3921
14	12490	81,70051
15	12490	473,2725
16	3161,629	432,4453
17	684,2312	17,6814
18	2477,398	64,01911
33	32967	3986,225
34	32967	3986,572
35	37850	4496,856
36	37850	4816,962

TABLE IV
EQUIPMENTS POWER

Equipments	Power (KW)
GB-1301A	413,834
GB-1301B	347,047
EC1306	10,21

IV. EXERGY ANALYSIS

Exergy analysis is performed to evaluate the energetic performance of the system based on both the first and the second laws of thermodynamics. The exergy is defined as the maximum amount of work which can be produced by a system or a flow of matter or energy as it comes to equilibrium with a reference environment. It measures the potential of the system or flow to cause change as a consequence of not being in stable equilibrium relative to the reference environment. [2] Rather exergy is consumed or destroyed, due to irreversibilities in any real process.

The exergy consumption is proportional to the entropy created due to irreversibilities associated with the process.

ISSN: 2961-6611

For exergy analysis, the reference state must be specified, in terms of its temperature, pressure and chemical composition. Exergy is calculated using the following general equation which relates enthalpy H, entropy S and temperature T [3]:

$$EX = (H - H_0) - T_0 (S - S_0) \quad (1)$$

Where the subscript 0 indicates the temperature, pressure, composition, etc. of the environment.

Three forms of the exergy transfer are distinguished in this paper: with work, with the heat interaction and with the matter.

The exergy associated with the work exchange is:

$$EX_W = W \quad (2)$$

The exergy associated with the heat interaction is given by Eq (3):[4]

$$EX_Q = Q\left(1 - \frac{T_0}{T}\right) \quad (3)$$

Where T_0 is the reference temperature, T is the temperature at which the heat transfer takes place and Q is the heat transferred.

The exergy associated with the matter is

$$EX_i = \overline{M}\,(H - T_0\, S) \quad (4)$$

In this expression M is the mass flow rate of material flow M. While H and S respectively represent the specific enthalpy and entropy corresponding to material flows (i) at temperature T.

The balance sheet corresponding to the system is then written in the following form:

$$Ex_l = \sum_i Ex_i - \sum_j Ex_j + \sum_k Ex_{Q_k} + \sum_l Ex_{w_l} \quad (5)$$

$Ex_{l,}$: Exergy lost by the system.
Ex_i : Exergetic content of the material flow (i) entering the system.
Ex_j : Exergetic content of the flow of material (j) leaving the system.
Ex_{QK}: Thermal exergy associated with the amount of heat Q_k at temperature T_K
Ex_{wl} Pure energy corresponding to noble energies (potential, kinetic...)

The exergetic analysis of the propylene refrigeration unit is presented in Table below which shows the exergy loss values of each equipment in the unit.

TABLE IV

EQUIPMENT EXERGY LOSSES

Equipments	Ex_l (KW)	Ex_l(%)
GB-1301A	97,26534	23,08632449
GB-1301B	72,52956	17,21518639
EC-1306	115,8392	27,49490579
EA-1309	8,9672	2,128401432
Lv-3993	30,451	7,227668839
FA- 1310	1,41909	0,33682679
Lv-3986	40,8272	9,690502158
EA-1304	54,01291	12,82018412

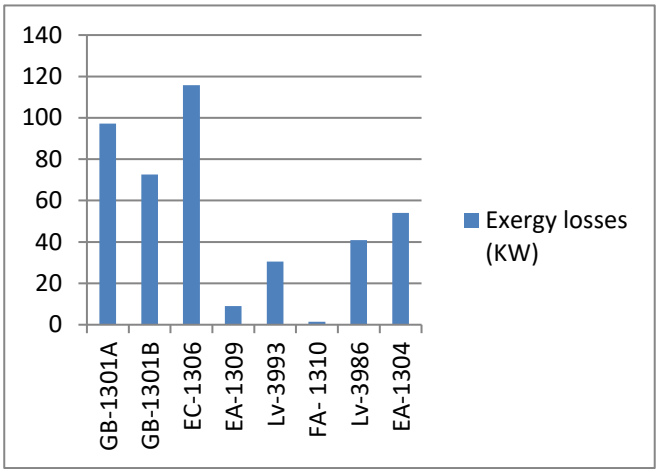

Fig. 2 Total exergy losses in different equipments of refrigeration unit

The distribution of exergetic loss by section is given by the following figure

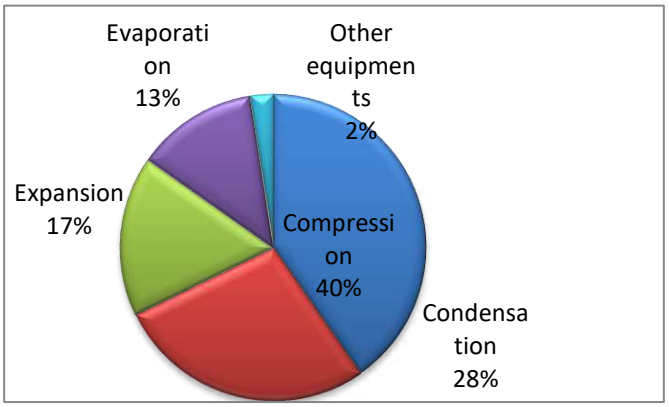

Fig. 3 Exergy losses by section

The results thus obtained show that more than two thirds of the exergy losses of the refrigeration cycle come from the compression and condensation stages. In addition, about 17% and 13% of energy degradation come from the expansion and evaporation section, the remaining 2% is spread over the rest of the equipment.

Note that the difference in the losses of the two compressors is due to the difference between the processed loads. On the other hand, the degradation of energy in these two equipments is mainly due to pressure and temperature differences.

Indeed, we have a compression ratio of about 4.87 in the first two stages and 3.73 in the other two.

Note that these compressions are accompanied by a temperature increase that can reach 170°C in each compressor. It should be noted that the loss identified at the level of the aerocondenser represents more than that associated with the evaporator. This is explained by the fact that the quantity of heat extracted from propylene at the aerocondenser is

ISSN: 2961-6611

released into the atmosphere, while that exchanged at the evaporator is recovered by propylene.

V. CONCLUSIONS

The present research addresses an exergetic analysis of propylene refrigeration unit. The exergetic analysis involves a simulation of the unit using the aspen Plus software.

The main findings of this research can be summarized in these points:

- More than two thirds of the exergy losses of the refrigeration cycle come from the compression and condensation stages.
- The aerocondenser is the main source of thermodynamic imperfections of the propylene refrigeration unit

As a result of this work, we propose to conduct studies further to reduce energy consumption in the unit, by applying the thermal pinch method that will detect inefficiencies in energy use and identify cost-effective energy saving projects in unit.

REFERENCES

[1] S. M. J. S. Lopez-echeverry, S. Reif-acherman, and E. Araujo-lopez, "Fluid Phase Equilibria Peng-Robinson equation of state : 40 years through cubics," Fluid Phase Equilib., vol. 447, pp. 39–71, 2017.

[2] M. A. Rosen and I. Dincer, "Exergy as the confluence of energy , environment and sustainable development," vol. 1, no. 1, pp. 3–13, 2001.S. Zhang, C. Zhu, J. K. O. Sin, and P. K. T. Mok, "A novel ultrathin elevated channel low-temperature poly-Si TFT," IEEE Electron Device Lett., vol. 20, pp. 569–571, Nov. 1999.

[3] R. Rivero, "Application of the exergy concept in the petroleum refining and petrochemical industry," vol. 43, pp. 1199–1220, 2002.

[4] J.J., KOTAS "The exergy method of the thermal plant analysis", Ed. Bull Worths, London (Angleterre) (1985).

ISSN: 2961-6611

Optimization by simulation of thin film solar cell based on $Cu_2ZnSn(S,Se)_4$

Abdelkader Benmir

Laboratory of Electrical Engineering (LAGE)

Electrical engineering department, Kasdi Merbah University Ouargla

Ouargla, Algeria

ge.benmira@gmail.com

***Abstract*— The aim of this work is to make an optimization by simulation of Thin film solar cell based on $Cu_2ZnSn(S,Se)_4$. It is found that, the increase of thickness of the window layer reduces the conversion efficiency of the cell. However, the doping concentration of the buffer layer must have a value at least equal to 10^{16} cm^{-3}. On the other hand, the doping concentration of the absorber layer must be less than or equal to 10^{15} cm^{-3}. In addition, the cell's performance is little variable as long as the defects density of the absorber layer does not exceed 10^{15} cm^{-3}. But as soon as it exceeds this value, a significant decrease is observed. The maximum efficiency that can be achieved with these optimal values is of the order of 13%.**

***Keywords*— Thin film solar cell; $Cu_2ZnSn(S,Se)_4$; Optimization; Simulation; CZTSSe**

I. INTRODUCTION

An intense research effort has been undertaken to develop thin film solar cells absorbers with abundant, inexpensive and non-toxic elements capable to produce high efficiency devices, economically competitive with conventional energy sources, and support the next-generation in terawatt scale of these solar cells [1]. Copper zinc tin sulfo-selenide $Cu_2ZnSn(S,Se)_4$ (CZTSSe) is an excellent absorber and a serious candidate for thin-film solar cells owing to its tunable direct bandgap of 1.0–1.5 eV with a large optical absorption coefficient (>10^4 cm^{-1}) and p-type conductivity [2]. According to Shockley-Queisser limit, the theoretical conversion efficiency of single-junction CZTSSe solar cells is 32.2 % [3]. These cells are based on a p/n junction which is formed between the p-type absorber and the n-type window. The n-type window consists of a TCO layer and a buffer layer. So far, the highest reported efficiency of SLG/ Mo/CZTSSe/CdS/ZnO:Al thin-film solar cell is 12.6% [4]. In parallel with experimental work, and with the remarkable development of computer tools, the modeling of solar cells [5] has become an indispensable tool for optimizing the design of all types of efficient solar cells. Numerical simulation helps to limit the risk and to avoid the cost of a series of real tests. It will predict the quantitative impact of variations in material properties on device performance and suggest ways to change the deposition process and to improve the performance. The goal of this work is to optimize by simulation the thickness of the ZnO window layer and the doping of the CdS buffer layer as well as the doping and the defects density of the CZTSSe absorber layer. Following a mathematical model, the simulation is done using the MATLAB programming language.

II. SIMULATION MODEL

A. Structure and optical properties of the cell

The cell structure considered in this study consists of the following materials: ZnO(n) Window / CdS(n) Buffer / CZTSSe(p) Absorber. The solar flux $F(\lambda)$ at $x = 0$ is given by:

$$F(\lambda) = F_0(\lambda).e^{-\alpha_{ZnO}(\lambda).w_{ZnO}} \quad (1)$$

Where: $F_0(\lambda)$ is the incident solar flux. $\alpha_{ZnO}(\lambda)$ and w_{ZnO} are the absorption coefficient and the thickness of ZnO(n) layer respectively. The analytical expressions of the absorption coefficient $\alpha(\lambda)$ for the two materials CdS and CZTSSe can be found in [6] and [7] respectively.

B. Calculation of the photocurrent density, J_{ph}

In all regions, the resolution of the continuity equation combined with Poisson's equation and the current density equation allow us to calculate the current density in each region. Taking into account the phenomenon of generation presented by the rate $G(\lambda,x)$ given by [8] :

$$G(\lambda, x) = \alpha(\lambda)F(\lambda)\big(1 - R(\lambda)\big).e^{-\alpha(\lambda)x} \quad (2)$$

Where, $R(\lambda)$ is the fraction of the photons reflected from the front surface. Taking also into account the recombination rates for the electrons in the p-neutral region of CZTSSe presented by $U_n = n - n_0 / \tau_n$ and for the holes in the n-neutral region of CdS presented by $U_p = p - p_0 / \tau_p$ [8]. Where, n is the electron concentration in the p-CZTSSe layer and p is that of the holes in the n-CdS layer. n_0 and p_0 are the equilibrium electron and hole concentrations, respectively. τ_n and τ_p are the lifetimes for electron and hole respectively given by [8]. The total photocurrent density J_{ph} is obtained by integrating the current density $J_{ph}(\lambda)$ on the whole range of the solar spectrum [8]:

$$J_{ph} = \int J_{ph}(\lambda)d\lambda = \int \big(J_p(\lambda) + J_n(\lambda) + J_{zce}(\lambda)\big)d\lambda \quad (3)$$

Where $J_p(\lambda)$, $J_n(\lambda)$ and $J_{zce}(\lambda)$ are the photocurrent density in the neutral zone N (CdS), in the neutral zone P (CZTSSe) and in the space charge region respectively.

C. Solar cell characteristics

The current-voltage (J-V) characteristic of the cell is given by the following equation [8]:

ISSN: 2961-6611

$$J = J_{ph} - J_0\left(e^{\frac{V+R_sJ}{QU_t}} - 1\right) - \frac{V+R_sJ}{R_{sh}} \quad (4)$$

Where: the saturation current density J_0 is extrapolated according to (5) [9] :

$$J_0 = J_{00}.e^{\frac{-E_g}{Q.K.T}} \quad (5)$$

Where: J_{00} is a constant which depend to temperature.

The diode ideality factor Q and J_{00} are extracted from the reference [10].

The numerical solution of (4) for $V = 0$ and $J = 0$ gives respectively the solution as short-circuit current density $J = J_{sc}$ and open circuit voltage $V = V_{oc}$.

From the plot of the JV characteristic, the maximum power, P_m can be calculated by:

$$P_m = (J.V)_{\max} \quad (6)$$

And therefore, we can easily deduce the fill factor and the conversion efficiency which are respectively given by [8]:

$$FF = \frac{P_m}{J_{sc}V_{co}} \quad (7)$$

$$\eta = \frac{P_m}{P_i} \quad (8)$$

Where: $P_i = 100$ mW-cm^{-2} is the incident power in standard conditions $AM1.5G$ [11].

III. Simulation Parameters

The result of our bibliographic research has inspired us the variation ranges of parameters, where:

For the ZnO layer: The thickness, W_{ZnO} varies from 100 to 600 *nm* [12]. For the CdS(n) layer: The doping, N_d varies from 10^{14} to 10^{20} cm^{-3} [13]. Whereas, for the CZTSSe(p) layer, The doping, N_a varies from 10^{14} to 10^{20} cm^{-3} [14] and the Defect density, N_t varies from 10^{12} to 10^{18} cm^{-3} [15].

The Material and device parameters used in the simulation are shown in Table. I.

TABLE I
DATA VALUES USED IN SIMULATION

Material	**CdS**	**CZTSSe [Ref]**
Layer thickness w(nm)	50	2500 [16]
Electron Affinity, χ (eV)	4.2	4.1 [16]
Relative permittivity, ε_r	10	13.6 [16]
Electron mobility, μ_n (cm^2/V.s)	100	100 [16]
Hole mobility, μ_p (cm^2/V.s)	25	25 [16]
Donor concentration (cm^{-3}) N_d	1×10^{17}	[17]
Acceptor concentration (cm^{-3}) N_a	-	1×10^{15} [16]
Band gap Energy E_g (eV)	2.42	1.5 [10]
CB[a] Effective density of states, N_C (cm^{-3})	2.2×10^{18}	2.2×10^{18} [16]
VB[a] Effective density of states, N_V (cm^{-3})	1.8×10^{19}	1.8×10^{19} [16]
Hole recombination velocity at CdS front surface, S_p (cm/s)	10^7	[14]
Electron recombination velocity at CZTSSe back surface, S_n (cm/s)	-	10^7 [14]
Defects density, N_t (cm^{-3})	1×10^{17}	1.35×10^{15} [17]
Electron capture cross section, σ_e (cm^2)	10^{-17}	10^{-14} [17]
Hole capture cross section, σ_h (cm^2)	10^{-13}	10^{-14} [17]
General device properties		
Reflectivity, R		0.1 [16]
Series resistance, R_s (Ω-cm^2)		0.72 [10]
Shunt conductance, G_{sh} (Ω^{-1}-cm^{-2})		1610 [10]
Diode ideality factor Q		1.45 [10]
Cell temperature, T (K)		300
[a] *CB* and *VB* represent the conduction and valence bands, respectively		

IV. Results and Discussion

A. Thickness effect of ZnO Window layer

Fig. 1 shows the effect of the thickness W_{ZnO} of the ZnO window layer on the cell performance for: $N_d = 10^{17}$ cm^{-3}, $N_a = 10^{15}$ cm^{-3} and $N_t = 1.35\times10^{15}$ cm^{-3}.

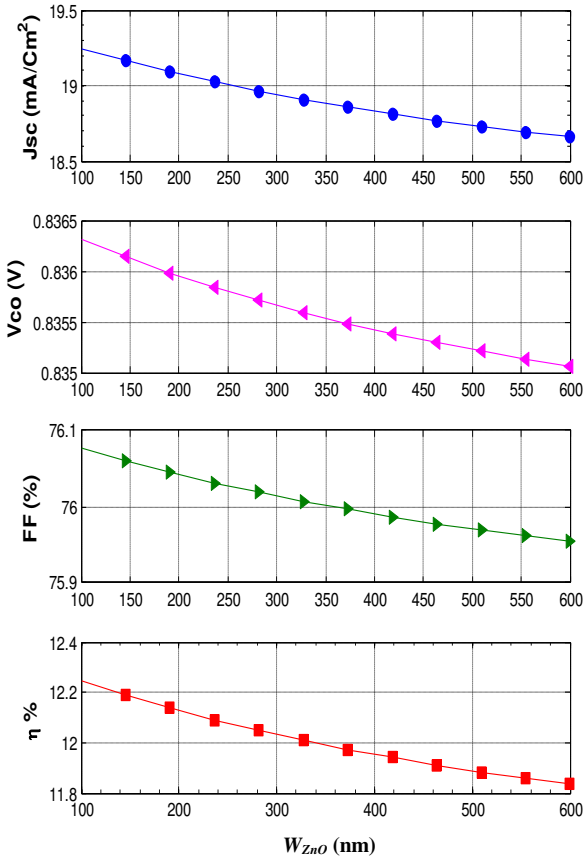

Fig. 1. Cell performance as a function of the window layer thickness

In accordance with (1) and (2), if W_{ZnO} increases, the solar flux $F(\lambda)$ at $x = 0$ and the generation rate $G(\lambda,x)$ decrease. Which decreases the number of electron-hole pairs generated and therefore the decrease in the short-circuit current density J_{sc} . Hence, the decrease in the conversion efficiency η shown in Fig. 1. But, V_{oc} and FF are almost not affected by W_{ZnO}.

ISSN 1737-9334

B. Doping effect of CdS buffer layer

Fig. 2 shows the effect of the doping N_d of the CdS buffer layer on the cell performance for: W_{ZnO} = 200 nm, $N_a = 10^{15}$ cm^{-3} and $N_t = 1.35\times10^{15}$ cm^{-3}.

We know using the electrical neutrality equation ($N_d.w_1 = N_a.w_2$) that it is the concentration of doping which controls the distribution of the PN junction into zones (Space charge zone E ≠ 0 where the current is of drift type and the neutral zone E = 0 where the current is of diffusion type) on both sides of a PN junction. That is to say, the width of the space charge region on one side of a PN junction increases with increasing of doping concentration on the other side of this junction and vice versa.

So, if N_d increases the space charge zone spreads on the side of CZTSSe absorber layer. Which increases the electric field in this layer and hence, the increase in the collection of charge carriers. Subsequently, a rise in the short circuit current density J_{sc} and the conversion efficiency η.

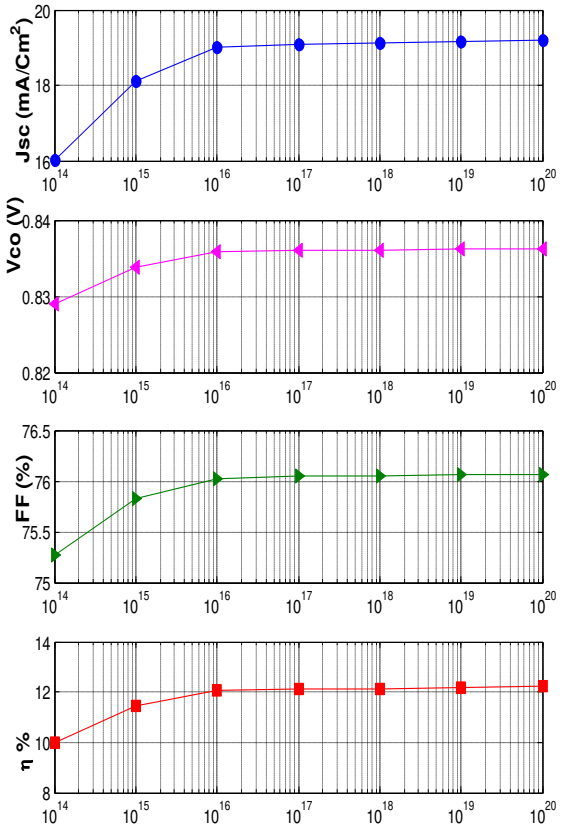

Fig. 2. Cell performance as a function of the buffer layer doping

Therefore, from Fig. 2, the optimal values of the doping concentration of CdS buffer layer are all values where $N_d \geq 10^{16}$ cm^{-3}.

C. Doping effect of CZTSSe absorber layer

Fig. 3 shows the effect of the doping N_a of the CZTSSe absorber layer on the cell performance for: W_{ZnO} = 200 nm, $N_d = 10^{16}$ cm^{-3} and $N_t = 1.35\times10^{15}$ cm^{-3}.

As in the previous case, if N_a increases, the space charge zone is reduced on the side of the CZTSSe absorber layer.

This decreases the electric field in this layer and therefore the decrease of the collection of charge carriers. Hence, the decrease in the short circuit current density Jsc and the conversion efficiency η.

Therefore, from Fig. 3, the optimal values of the doping concentration of CZTSSe absorber layer are all values where $N_a \leq 10^{15}$ cm^{-3}.

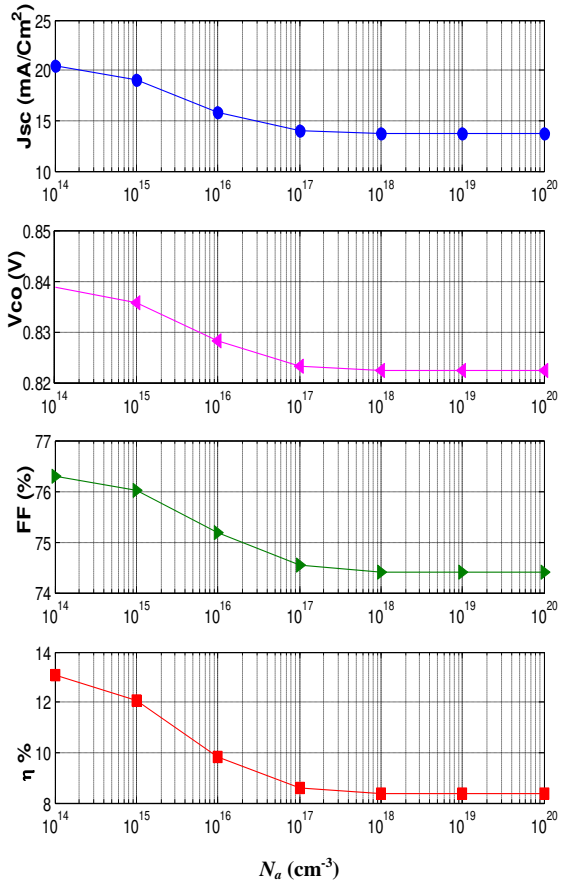

Fig. 3. Cell performance as a function of the absorber layer doping

D. Defects density effect of CZTSSe absorber layer

Fig. 4 shows the effect of the defects density N_t of the CZTSSe absorber layer on the cell performance for: W_{ZnO} = 200 nm, $N_d = 10^{16}$ cm^{-3} and $N_a = 10^{15}$ cm^{-3}.

We know from equation ($\tau_n=(\sigma_n.v_{th}.N_t)^{-1}$) where $v_{th}\approx10^7$cm/s is the thermal velocity that the lifetime τ_n of electrons in the P layer is inversely proportional to the defects density N_t. So, if N_t increases τ_n decreases. This leads, according to equation ($L_n=(D^2_n.\tau_n)^{1/2}$), to decrease the diffusion length of electrons L_n, and therefore the increase of electron recombination rate. Hence the decrease in the performance of the cell as it is shown in Fig. 4.

ISSN: 2961-6611

It is also clear in Fig. 4 that the performances of solar cell based on CZTSSe absorber are not very variable as long as their defects density does not exceed 10^{15} cm^{-3}. But as soon as it exceeds this value, a significant decrease is observed. Therefore, the optimal values of the defects density of CZTSSe absorber layer are all values where $N_t \leq 10^{15}$ cm^{-3}. Results similar to these are found by the references [20, 22].

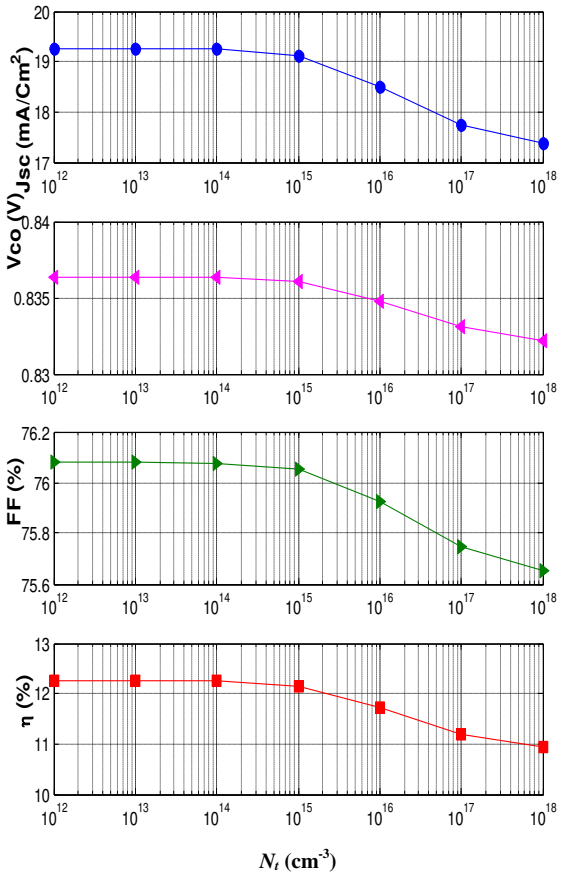

Fig. 4. Cell performance as a function of the absorber layer defect density N_t

V. Conclusion

In this work, we made a simulation of a solar cell based on $Cu_2ZnSn(SSe)_4$. The calculation program that we have developed allows us to optimize by simulation the thickness of the ZnO window layer and the doping concentration of CdS buffer layer as well as the doping concentration and the defects density of CZTSSe absorber layer.

The obtained results showed that:

The increase of the thickness of ZnO window layer reduces the conversion efficiency η of the cell. However, the doping concentration of CdS buffer layer must have a value at least equal to 10^{16} cm^{-3}. On the other hand, the doping concentration of CZTSSe absorber layer must be less than or equal to 10^{15} cm^{-3}. In addition, the cell's performance is little variable as long as the defects density of CZTSSe absorber layer does not exceed 10^{15} cm^{-3}. But as soon as it exceeds this value, a significant decrease is observed. The maximum efficiency that can be achieved with these optimal values is of the order of 13%. All these optimization results give helpful indication for feasible fabrication process.

References

[1] D. B. Mitzi et al., "A High-Efficiency Solution-Deposited Thin-Film Photovoltaic Device," Adv. Mater., vol. 20, pp. 3657–3662, 2008.

[2] D. B. Mitzi, O. Gunawan, T. K. Todorov, K. Wang, S. Guha, "The path towards a high- performance solution-processed kesterite solar cell," Sol. Energy Mater. Sol. Cells, vol. 95, pp. 1421-1436, 2011.

[3] W. Shockley, H. J. Queisser, "Detailed balance limit of efficiency of p-n junction solar cells," J. Appl. Phys. vol. 32, pp. 510-519, 1961.

[4] M. A. Green, Y. Hishikawa, E. D. Dunlop, D. H. Levi, J. Hohl-Ebinger, A. W. Y. Ho-Baillie, "Solar cell efficiency tables (version 51)," Prog Photovolt Res Appl. vol. 26, pp. 3‑12, 2018.

[5] M. Burgelman, J. Verschraegen, S. Degrave, P. Nollet, "Modeling thin-film devices," Prog Photovoltaics Res Appl, vol. 12, pp. 143-153, 2004.

[6] M. Jayachandran, M. J. Chockalingam, K. R. Murali, A. S. Lakshmanan,"$CuInSe_2$ for photovoltaics: a critical assessment," Materials Chemistry and Physics, vol. 34, pp. 1-13, 1993.

[7] J. J. Scragg, Copper Zinc Tin Sulfide Thin Films for Photovoltaics Synthesis and Characterisation by Electrochemical Methods, Ed. Berlin, Germany: Springer-Verlag, 2011.

[8] S. M. Sze, Physics of semiconductor Devices, 2nd ed., Ed. USA: John Wiley & Sons, 1981.

[9] J. Krustok, R. Josepson, M. Danilson, D. Meissner, "Temperature dependence of $Cu_2ZnSn(Se_xS_{1-x})_4$ monograin solar cells," Solar Energy 84 379–383 (2010).

[10] W. Wang et al. , "Device characteristics of CZTSSe thin-film solar cells with 12.6% efficiency, " Advanced Energy Materials. Vol. 4, 1301465 (2014) 1-5.

[11] S. J Fonash, Solar Cell Device Physics, 2nd ed., Ed. USA:Elsevier, 2010.

[12] S. R. Kodigala, Thin Film Solar Cells from Earth Abundant Materials, Growth and Characterization of $Cu_2ZnSn(SSe)_4$ Thin Films and Their Solar Cells, Ed. London:Elsevier, 2014.

[13] A. Morales-Acevedo, N. Hernández-Como, G. Casados-Cruz, "A method for improving their efficiency, " Materials Science and Engineering B, vol. 177, pp. 1430–1435, 2012.

[14] M. Patel, A. Ray, "Enhancement of output performance of Cu_2ZnSnS_4 thin film solar cells— A numerical simulation approach and comparison to experiments, " Physica B, vol. 407, pp. 4391–4397, 2012.

[15] M. Djinkwi Wanda, S. Ouédraogo, F. Tchoffo, F. Zougmoré and J. M. B. Ndjaka, "Numerical Investigations and Analysis of Cu_2ZnSnS_4 Based Solar Cells by SCAPS-1D, " International Journal of Photoenergy, vol. 2016, Article ID 2152018, 9 pages, 2016.

[16] O. K. Simya, A. Mahaboobbatcha, K. Balachander, "A comparative study on the performance of Kesterite based thin film solar cells using SCAPS simulation program, " Superlattices and Microstructures, vol. 82, pp. 248–261, 2015.

[17] A. Kanevce, I. Repins, S. Wei, "Impact of bulk properties and local secondary phases on the $Cu_2(Zn,Sn)Se_4$ solar cells open-circuit voltage, "Solar Energy Materials & Solar Cells, vol. 133, pp. 119–125, 2015.

ISSN: 2961-6611

PROPERTIES AND POTENTIALITIES OF THE SEWAGE SLUDGE LIKE RENEWABLE ENERGY SOURCE IN CEMENT MANUFACTURE

Ouassyla Belarbi[1, 2], Mokhtaria Rezig[1], Sofiane Nekrouf[1], Reda Marouf[2],

[1] *Department du Genie des Procédés, Université Dr Moulay Tahar Saida Algérie*

[2] *Laboratory of Materials, Applications and Environment, Mustapha Stambouli University, Mascara 29000, Algeria*

[1]ouasbelarbi@yahoo.fr

Abstract— **The sewage sludge potentiality to decrease the energy demand in cement manufacture was the subject of this study. The initial idea is to replace the ordinary Portland cement clinker by mud of various origins which the technical landfill centers represent the end of its life cycle. This study enabled us to examine the effect of mud of different natures: urban and industrial like source of silica and waste lime like source of lime; in the temperature reduction to obtain a profit of energy.**

From a mixture of sewage sludge urban or industrial, we can synthesize belitic cement at 1200°C.

This study also explored the possibility of produce belitic cement at low temperature (1100°C). In this work, the raw mixture (limestone and clay) of belitic cement was substituted by another mixture made up of waste lime of the industrial gases industry ENGI, of urban sewage sludge and industrial muds resulting from the Company Paper mill and Boarding from Saida GIPEC. The results showed that: a mixture (GIPEC sludge, ENGI residue.) with CaO /SiO_2 =1.73 gives belitic cement without free lime. The X-ray Diffraction analysis shows the presence of the most active phase βC_2S. The 50% substitution of the Ordinary Portland cement by urban mud produces a belitic clinker at 1200°C where the majority of lime was combined. The X-rays diffraction analysis showed that the strongly reactive phase of the belite (βC_2S) was stabilized as well as the crystallization of C_3S.

Keywords— **belite, mud, energy, cement, lime, sludge.**

I. INTRODUCTION

The daily life and several activities (industry, transportation, resource exploitation, agriculture, etc.) lead to massive waste and sludge production, generally derived from liquid effluent treatment processes commonly called sewage sludge. Sewage sludge are solid matrices, often heterogeneous and variable, which makes the characterizations and treatments quite complex. Also, further sludge use or its disposal would be associated with high costs of transportation, combustion or drying, and the sludge to be destroyed would take up too much space in landfills. This is a problem.

In Algeria, the industry has a major responsibility for the global pollution of the country, especially the cement industry [1].

However, it is also recognized that the production industry remains a key driver of economic growth, but reducing pollution and the rational use of resources and energy are imperatives for sustainable development and make frequently unit costs of products lower.

The cement industry is a big heat and electricity consumer. Global energy requirements for cement manufacturing are estimated at about 6 109 GJ / yr for fuels and 200 TWh / yr for electricity [2].

This industry is also a strong emitter of greenhouse gases (carbon dioxide - CO_2), coming from the heat energy needs, but also from the cement manufacturing process. The issue of climate change encourages us to look for all means of reducing CO_2 emissions: the improvement of specific energy consumption must be coupled with a new approach to replace traditionally manufactured products (clinker) with products with similar characteristics [3-4].

In fact during the decarbonation, a quantity of 520 kg of CO_2 per ton of clinker is emitted. The only way to reduce CO_2 emissions is to use already decarbonated products [5-7].

They are generally used as a partial substitute for clinker because they have the ability to develop mechanical resistance similar to clinker.

They are beginning to be used as a partial substitute for mixed raw materials when their ability to replace clinker is low [8-9].

This paper presents the possibility to energetically promote sludge from urban wastewater treatment plants and industrial effluents in the cement industry. It includes tests carried out to obtain belitic clinker at low temperature and it presents the results obtained during the evaluation of Portland clinkers produced by substitution of the Portland raw material by the collected sludge.

II. MATERIALS AND METHODS

A. *Materials*

ISSN: 2961-6611

The urban sewage sludge was collected from the water treatment plant of Saida city, Algeria. The industrial sewage sludge was collected from the effluent treatment plant of GIPEC paper mill group in Saida city, Algeria. The samples initially were dried in oven at 105°C for 24 h, finely crushed and properly stored for further studies. These samples were noted as U-SS and GIPEC-SS, respectively. The chemical composition was determined.

The lime milk rejected by the plant of manufacturing of acetylene of the National Industrial Gases Company (The Linde Group), located in Sidi Bel Abbes was collected from the cesspool.

After fast settling of the lime milk, the residue was dried in oven at 105°C for 24 h and finely crushed noted ENGI-R .

The natural raw materials: clay and limestone are from the cement plant of Saida. The raw meal is removed from the storage tank feeding the oven of the Saida cement manufactory.

B. Characterization

The chemical analysis of raw materials was performed with X-fluorescence XRF 9900. The loss on ignition (LOI) was determined by chemical analysis according standard norm [10]. The trace elements of the urban sewage sludge and the GIPEC sewage sludge were detected by Perkin Elmer A Analyst 700 atomic absorption spectrophotometer (air-acetylene oxidizing flame, slit width 0.5 nm). X-ray analyses were performed using Bruker D8 Advance diffractometer employing copper Kα radiation (λ= 0.154 nm) operating at 40 kV and 40 mA with a fixed slit. The chemical composition of synthesized clinkers was determined by volumetric dosages in accordance with Algerian Standard Specifications [11]. The residual free lime content is determined by the (glycerine–alcohol) method, according to the European standard [12]

C. Synthesis experiment

6 g of mixture was prepared with different low CaO / SiO_2 ratios = 1.73, 1.87 and 2. The reference mix (M0) was prepared from natural raw materials: limestone as CaO source and clay as SiO_2 source, quarried from the quarries of Saida cement plant, Algeria. The two other mixtures were prepared from alternative raw materials. The second mix (M1), the clay was totally replaced by urban sewage sludge and the limestone was replaced by ENGI residue. The third mix (M2) was composed of the industrial sewage sludge from GIPEC and ENGI residue.

The raw materials are finely crushed separately at 90 µm mesh sieve. After homogenization, the mixture was introduced into an alumina crucible and placed in a muffle furnace with a heating rate of 20°C/min. The sample was maintained at the desired burning temperature during 30 min, then quickly cooled by applying air flow and crushed.

III. RESULTS AND DISCUSSIONS

A. Characterization of raw materials

Table 1 illustrates the percentage oxide composition of the raw materials used. The chemical compositions of alternative raw materials are shown in Table 2. The results indicated that the high value of Loss on ignition (LOI) reported to the sewage sludge is due to important amount of water and carbonates which contained the materials. The silica, alumina and lime are the major oxides of the samples. The iron and magnesium oxides exist as minority elements. The ENGI residue is composed mainly lime

Table 3 illustrates the trace elements determined in the urban sewage sludge and GIPEC sewage sludge samples. The results indicate significant amounts of Zinc (568 and 224.6 mg/Kg), Lead (137 and 45.79 mg/Kg) and Copper (131 and 53.54 mg/Kg) in both sludge respectively. The trace elements content of the alternative raw materials shows highest Zinc and Lead concentrations in urban sewage sludge. Nickel is highest in GIPEC residue

The XRD patterns of alternative raw materials: urban sewage, GIPEC sewage and ENGI residue were shown in figure 1. The X-ray diffraction pattern of urban sewage sludge indicates that it contains some mineral phases concerning montmorillonite (M), illite (I), quartz (Q), calcite (C) and dolomite (D) (Figure 1). In the same figure, the GIPEC sewage sludge is seen to be composed of calcite, Quartz and Kaolinite (K). Also, it is clear from the figure that hydrated lime (HL) is the main phase composing ENGI residue powder.

TABLE I
OXIDE COMPOSITION OF THE RAW MATERIALS (%)

Raw material	**Chemical composition (wt %)**					
	CaO	**SiO_2**	**Al_2O_3**	**Fe_2O_3**	**MgO**	**LOI**
limestone	48.99	5.22	2.55	0.90	1.02	40.50
Clay	6.92	51.82	16.14	7.31	1.95	11.07

TABLE 2
OXIDE COMPOSITIONS OF THE ALTERNATIVE RAW MATERIALS (%)

Alternative raw material	**Chemical composition (wt %)**					
	CaO	**SiO_2**	**Al_2O_3**	**Fe_2O_3**	**MgO**	**LOI**
U- SS	14.05	21.69	3.43	1.41	3.67	60.76
GIPEC-SS	22.17	13.25	7.4	1.06	1.14	55.34
ENGI-R	71.08	1.82	1.44	0.56	0.85	24.49

TABLE 3
TRACE ELEMENTS OF THE ALTERNATIVE RAW MATERIALS (MG/KG)

Alternative raw material	**Element (mg/Kg)**					
	Cu	**Zn**	**Cd**	**Cr**	**Ni**	**Pb**
U-SS	131	568	1	37	24	137
GIPEC-SS	53.54	224.6	<6	<40	28.27	45.79

ISSN: 2961-6611

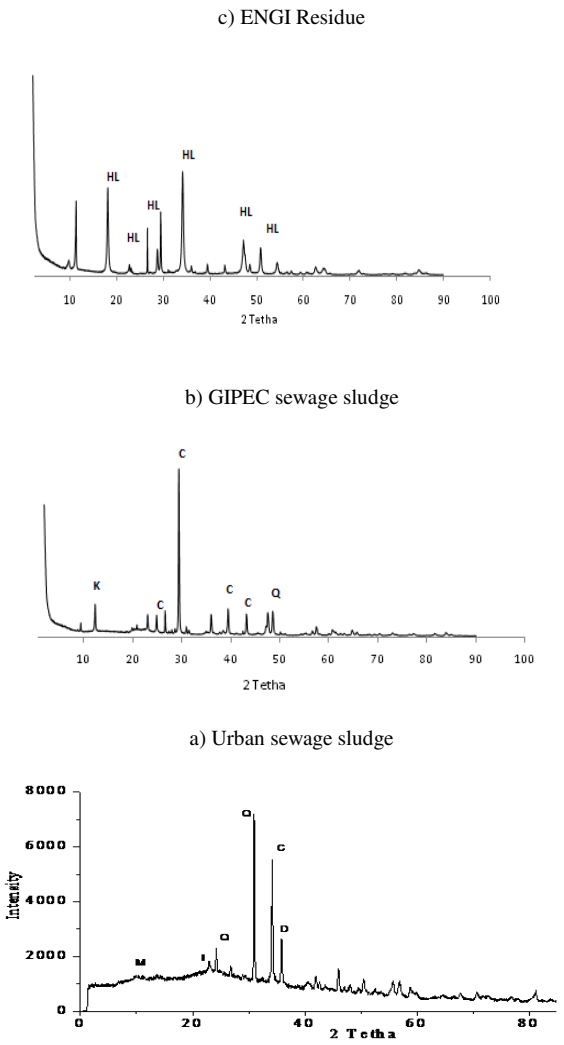

Fig. 1 The X-ray diffraction patterns of the sewage sludge (M=Montmorillonite, Q=Quartz, Ha=Halloysite F=Feldspar He=Hematite, I=Ilite, K=Kaolinite, C=Calcite, HL=Hydrated lime).

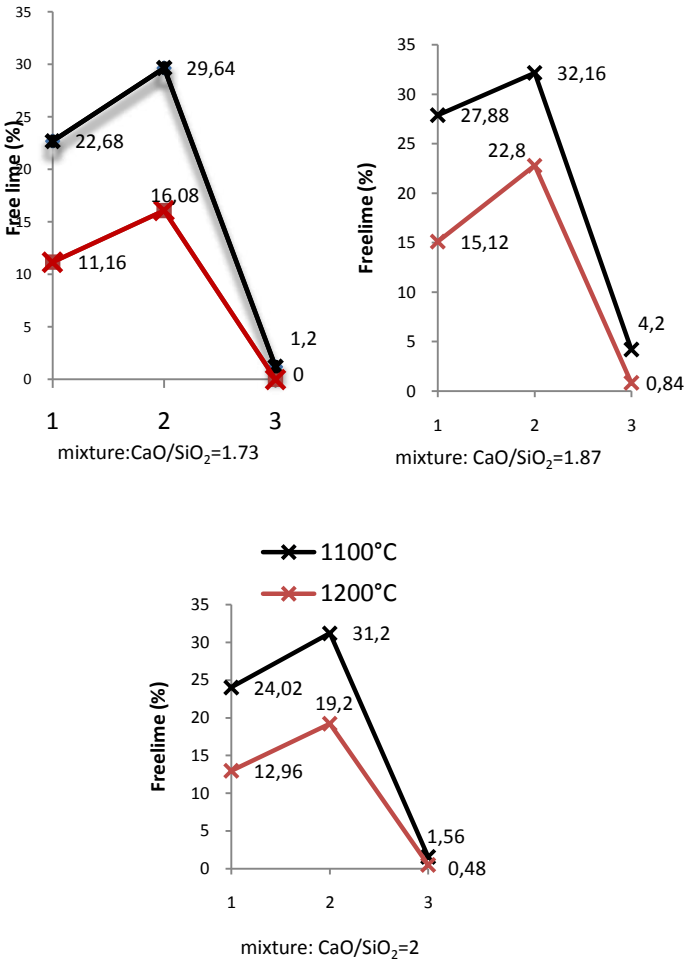

Fig. 2 Variation in free lime content. versus mixture composition (1=M0, 2=M1, 3=M2)

B. Clinkers

The results obtained from the burnability tests of the mixes are illustrated in Figure 2. The results show that burning at 1200 °C leads to lower free lime contents in the clinkers.

For CaO/SiO_2=1.73, the liquid solid reaction is more complete.

The mixtures prepared from alternative raw materials exclusively favors lime combination with the different oxides As the quantity of lime in the mix increases, the combination of this one with other oxides present is not complete.

The free lime quantity in the clinkers prepared from GIPEC sewage sludge and ENGI lime residue is lower than in the clinkers prepared from natural raw materials and the other alternative raw materials (Fig. 2). This result indicates that the calcium element present in GIPEC residue can precipitate the clinker minerals.

Figure 3 illustrates the concentration of the clinker phases resulted at 1200°C as estimated from Bogue equations.

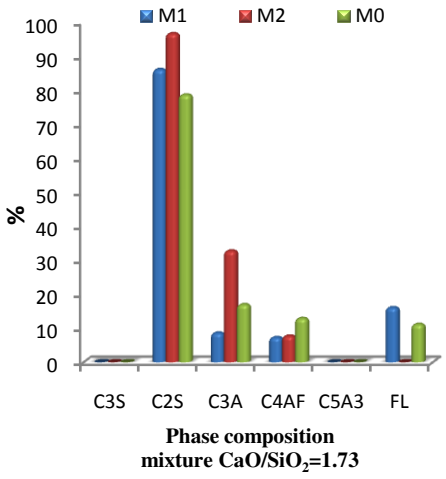

°

ISSN: 2961-6611

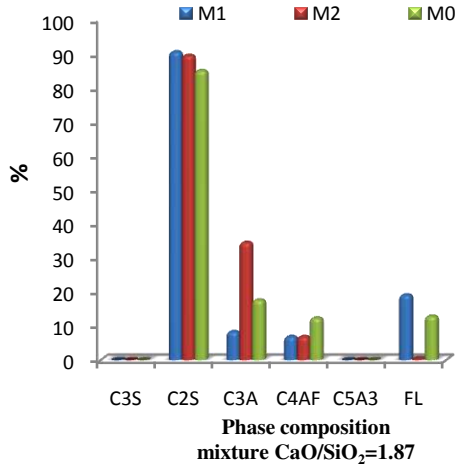

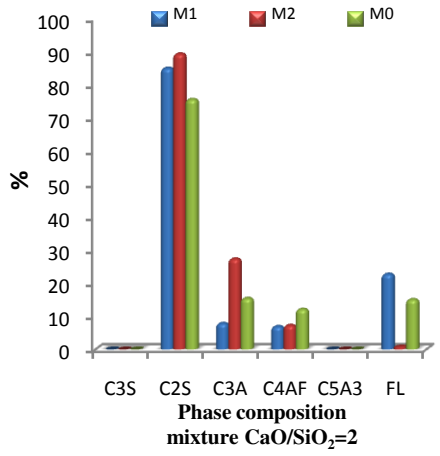

Fig. 3: Phase composition of clinkers synthesized at 1200°C

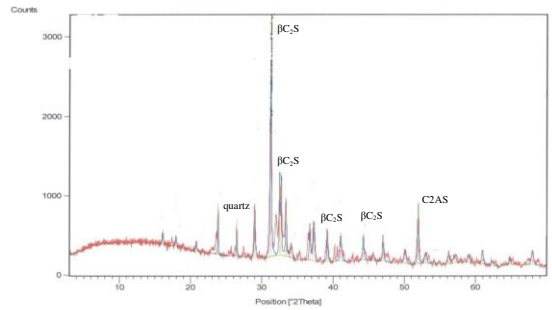

Fig. 4: Phase composition of clinkers synthesized at 1200°C

Belite phase is the predominant in all clinkers. The belite value of clinker synthetized form M2 mixture with ratio CaO/SiO_2 = 1.73 is 96.72 %. The X-ray diffractogram of this clinker is illustrated in Figure 4. Active belite βC_2S characteristic peak is seen at an angle of 31

IV. Conclusions

The ENGI residue can be a source of lime. GIPEC mud lime is about twice higher than silica. But also this mud is rich in heavy metals especially zinc. The silica content in urban sewage sludge is highest. Urban sewage sludge is rich in lead. The loss on the ignition is considerable in sewage sludge. From a mixture of waste sludge urban or industrial, cement belitic can synthesized at 1200°c.

These alternative raw materials contain a very high organic matter count which by combustion generates an energy which can contribute to the combination of various oxides present in the mixture believed at low temperatures. the formation of c_2s was clearly supported by the use of the sewage sludge. the rate of c_2s in the clinkers obtained starting from the mixtures of sludge varies between 85% and 96%.cao/sio_2 ratio of 1.73 in the raw mixture composed of waste mud makes it possible to obtain a clinker rich in belite of 96.72%.sludge gives different results according to their origin. This can be with the metal elements present or also with the grains shape of mud

Acknowledgment

The authors would like to thank, the personal of Cement manufactory of Saida, Algeria,

They offered us continue help to achieve almost analyses needed in this work.

References

[1] S. Boughrara, M. Chedri, K. Louhab , Evaluation of environmental impact of cement production in Algeria using life cycle assessment International Letters of Chemistry, Physics and Astronomy ISSN: 2299-3843, Vol. 45, pp 79-84 doi:10.18052/www.scipress.com/ILCPA.45.79 2015 SciPress Ltd., Switzerland

[2] Guidelines on Co-Processing of Waste Materials in Cement Production. Eurpean cement association, Cembureau, Brussels, Belgium. 2004

[3] convention de Stockholm sur les polluants organiques persistants , le brulage de déchets dangereux dans les fours à ciment , directives sur les meilleures techniques disponibles et les meilleurs pratiques environnementales , en liaison avec l'article 5 et l'annexe C, Genève – suisse Mai 2007

[4] Technical Guidelines for the Environmentally Sound Management of Wastes Consisting of, Containing or Contaminated with Persistent Organic Pollutants (POPs), Conférence des Parties à la Convention de Bâle, Dixième réunion Cartagena (Colombie), 17-21 octobre 2011

[5] - Charles Hoi King Lam, John Patrick Barford, Gordon McKay, Utilization of Incineration Waste Ash Residues in Portland Cement Clinker, chemical engineering transactions Volume 21, 2010.

[6] -Chen I.A. and Juenger M.C.G., Incorporation of waste materials into Portland cement clinker synthesized from natural raw materials, Journal of Materials Science, 1-11. 2009.

[7] Guerrero, A.; Goñi, S.; Campillo, I.; Moragues, A. Belite cement clinker from coal fly ash of high Ca content. Optimization of synthesis parameters. Environ. Sci. Tech. 38, 2004

ISSN: 2961-6611

[8] Rodrigues, F.A. Low-temperature synthesis of cements from rice hull ash. Cem. Concr. Res., 33, 2003.
[9] Iacobescu, R.I.; Koumpouri, D.; Pontikes, Y,; Saban, R.; Angelopoulos, G. Utilization of EAF metallurgical slag in green belite cement. U.P.B. Sci. Bull; Series B, 1, 73, 2011
[10] NF-2-1-010-1984.
[11] Algerian norm NA: 5044 V 2005, 231, 442/2000.
[12] Algerian norm NA: 17058

ISSN: 2961-6611

ISSN: 2961-6611

Assessment of wind power potential in Ouargla region using Weibull Distribution

Halima Boutelli [#1], Ahmed Djafour [*2], Mohammed Bilal Danoune [#3]

[#] *Electrical engineering Department, kasdi Merbah University*
LAGE Laboratory, Faculty of Applied Sciences, Kasdi Merbah Ouargla University, Ouargla 30000, Algeria
[1]halimaboutelli1992@gmail.com
[3]danoune.mohammed.bilal@gmail.com
[2]djafour.ah@univ-ouargla.dz

***Abstract*— in this work, we aim to statistically analyse wind speed data using Weibull distribution function in order to determine the characteristics of the wind potential in Ouargla region. For this purpose, Weibull parameters were calculated using five methods: moment's method, the empirical method of Lysen, power density, the variability of wind and energy pattern factor method. These methods are used to calculate the wind power density, in addition, the estimated wind power density using mentioned methods have been validated with actual measurements. The results show that, the Moments method is the most efficient method in assessing wind power density compared to other methods. A set of simulation results obtained during this study is presented. These results show that the atmosphere is not stable throughout the year, this confirms the existence of seasonal winds Power increases considerably after extrapolation to 50 m, giving estimated energy of 953.77 KWh per year. m².**

***Keywords*— Weibull parameters; Statistical analysis; Ouargla; wind potential; power density**

I. INTRODUCTION

These last years, the world has experienced a rapid increase in energy demand, in addition to economic and demographic growth and improved living standards, this growing demand for energy has led to the inability to meet energy needs. In the other hand, utilization of fossil fuels as a main source of energy deteriorate environment. Number of researchers considering renewable energy sources (solar, wind, biomass .... etc.) are the optimal alternative to fossil energy, renewable energy has remarkably developed and become more economically competitive [1]. Wind energy is considered a more sustainable and more environmentally friendly source of energy [2], [3]. Moreover, wind energy does not consume water, which makes it more attractive than thermal plants that require intensive use of fresh water for cooling, especially in hot or arid areas .At the level of our country, Algeria has a diversity of renewable energy sources (solar, wind) and this in an area of 2 381 741 km². Algerian has completed several projects related to wind energy, for example in the wilaya of Adrar, it has created a large station of a wind farm [4].In this work we want to look for ways to invest in this energy in our country Algeria, and use it in the best way, we wanted by virtue of our presence in Ouargla region to take advantage of these energy circumstances. But before starting any project, we must study whether the site you want to establish the project is suitable or not?

II. WEIBULL DISTRIBUTION FUNCTION

The Weibull distribution used for the statistical analysis of the data, it is better known and preferable to represent the distribution of the wind speed [6]. The Weibull distribution function is based on two parameters of modelling (k) shape parameter and scale parameter (c) [5]. The Weibull probability density is given by.

$$f(v) = \frac{k}{c}(\frac{v}{c})^{k-1} exp(-\frac{v}{v})^{k} \quad (1)$$

III. DETERMINATION OF WEIBULL PARAMETERS

In fact, every location has different parameters (k) and (c) to describing the distribution of wind speed for a candidate site, thus, (k) and (c) need to be determined. Several methods were used in literature to determine (k) and (c). In this section, five methods have been compared to determine the parameters of Weibull distribution function (k) and (c) for our region of study (Ouargla).

A. MOMENT METHOD

In 1977, Justus and Mikhail [8] introduced this method. This method is based on the standard deviation and the means of wind speeds for determining the two parameters k and c the shape parameter (c) can be calculated iteratively using Eq(2) .[9],[10],[11].

$$v_m = c\Gamma(1+\frac{1}{k}) \quad (2)$$

$$\sigma = c[\Gamma\left(1+\frac{2}{k}\right) - \Gamma^2\left(1+\frac{1}{k}\right)]^{1/2} \quad (3)$$

The scale parameter is calculated using Eq. (4).

$$\mathrm{c} = (\frac{1}{\mathrm{n}}\sum_{\mathrm{i}=1}^{\mathrm{n}} \mathrm{v_i^k})^{1/\mathrm{k}} \quad (4)$$

B. Empirical method of Lysen

Based on the empirical method introduced by Lysen, shape parameter (k) is calculated by Eq. (5) and the scale parameter(c) is computed as Eq. (6) [8].

$$\mathrm{k} = (\frac{v_m}{\sigma})^{-1.086} \quad (5)$$

$$\mathrm{c} = \mathrm{v_m}(0.568 + \frac{0.433}{\mathrm{k}})^{-1/\mathrm{k}} \quad (6)$$

C. VARIABILITY OF WIND METHOD

Previous studies have revealed the existence of a general trend between parameter k values and mean wind speed [7].

ISSN: 2961-6611

Mathematical results can be expressed for average, high (90%) and low (10%) variability sites by the following relation.

$$k = \begin{Bmatrix} 5{v_m}^{0.5} & (low) \\ 0.94{v_m}^{0.5} & (average) \\ 3{v_m}^{0.5} & (high) \end{Bmatrix} \quad (7)$$

Then, the mean wind speed Vm is related to k and c as follow:

$$V_m = c\Gamma(1 + k^{-1}) \quad (8)$$

D. ENERGY PATTERN FACTOR METHOD

Mathematically, EPFM is given by Eq. (9). This is a dynamic method based on the fact that energy can be efficiently extracted from the wind [7], [12], [13].

$$EPFM = \frac{\text{the average power of the wind}}{\text{the power of the average wind}} \quad (9)$$

The primary step in this method is to compute energy patterns factor Epf, which is given by the following relationship.

$$E_{pf} = \left(\frac{1}{n}\sum_{i=1}^{n} v_i^3\right) / \left(\frac{1}{n}\sum_{i=1}^{n} v_i\right)^3 \quad (10)$$

Can be determined the shape parameter by Eq. (11) and the scale parameter by Eq. (4)

$$k = 1 + \frac{3.69}{(E_{pf})^2} \quad (11)$$

E. POWER DENSITY METHOD

This new and more accurate method to determine the scale and shape parameters, the parameter (k) can be calculated by iterating of numerical method Eq.(12) [7],[16].

$$E_{pf} = \frac{\overline{v^3}}{\bar{v}^3} = \frac{\Gamma(1+\frac{3}{k})}{\Gamma^3(1+\frac{1}{k})} \quad (12)$$

The scale parameter(c) is calculated by the following Eq. (13)

$$c = \frac{v_m}{\Gamma(1+\frac{1}{K})} \quad (13)$$

IV. EVALUATION OF THE AVERAGE WIND POWER DENSITY

The power density of the wind gives the strength of the wind available at a particular site. Wind Power Density (WPD) is a principal factor in determining wind potential and makes it possible to quantify the energy produced during a time T by the wind turbines. WPD is calculated by two approaches

The first approach, the power density for the real time series wind speed data for a site can be calculated using the following Eq. [14], [15].

$$P = 0.5\rho\overline{v^3}(\text{W/m}^2) \quad (14)$$

With, V: is wind speed (m/s),ρ is density of surrounding air (kg/m^3).

The second approach, the WPD is calculated by using Weibull probability density function and can be estimated by the following Eq.

$$\frac{p}{A} = 1/2\rho c^3\Gamma\left(1+\frac{3}{k}\right)(\text{W/m}^2) \quad (15)$$

It is possible to calculate the available wind energy at a given location using the Weibull distribution, the annual wind energy, expressed in kWh/m². This calculation can yield by the following relation [17].

$$E = 3.56\, c^3\Gamma(1 + {}^3/_k)(\text{Kwh/m}^2\text{/an}) \quad (16)$$

V. RESULTS AND DISCUSSION

For this study, we chose the Ouargla region. Ouargla is a city in the south-east of Algeria. It is characterized by a Saharan climate. The site is geographically located at 31.93° is latitude and 5.4° longitude. We obtained the data used in this study from the meteorological service in Ouargla region. The measurements of wind speed were taken every day for ten years (2006-2015) at 10m height. In this study the wind power density was estimated using five methods, theses lasts have been compared with measured data values, to determine the most accurate method. In order to achieve this goal we have used statistical analyses (RMSE, Chi-Square and MAPE).The results obtained in this study can be summarized as follows.

A. ESTIMATION THE WEIBULL PARAMETERS IN OUARGLA REGION

In this study, Weibull parameters are estimated by five methods, Moments method(MOM), the Empirical method of Lysen(EML), power density method(PDM), the variability of wind method (VWM)and Energy Pattern Factor method(EPFM) as presented in TableI.

The moment's method and empirical method of Lysen estimated monthly shape parameter varies from 1.2766 to 2.5749. The monthly scale parameter varies from 2.5810 to 5.1501 by the moment's method and but by the empirical method of Lysen, it varies from 2.5825 to 5.1528. Power density method and Energy Pattern Factor Method estimated monthly shape parameter varies from 1.3388 to 2.5339. Monthly scale parameter varies from 2.6054 to 5.1512 by the Power density method and it varies from 2.6469 to 5.1583 in the year. Variability of wind method estimated monthly shape parameter varies from 1.6242to 2.0145 and monthly scale parameter varies from 2.6723 to 5.1480 in the year.

It was observed in all methods used for Weibull parameter estimations that the lowest value for two parameters (k and c) in December and the highest in March.

B. ESTIMATION THE WIND POWER DENSITY FROM WEIBULL DISTRIBUTION PARAMETERS

1) Monthly power density: The monthly wind power density is estimated by using air density and Weibull parameters in (14.15). Measured monthly WPD and estimated monthly WPD using Weibull parameters from MOM, EML, PDM, VWM and EPFM at different heights are shown in the figure (1-2).The results obtained show the monthly power density values varied between (29.82-245.64) (w / m²) at 10m height, and for the 50m height the monthly power density values varied between 48.25-398.27), this is according to moments method and empirical method. For the Power density method and Energy Pattern Factor method, the monthly power density values varied between (27.35-259.54) and (44.34-420.64) at 10m-50m height respectively. And for Variability of wind method the monthly power density values varied between (20.39-107.01) (33.05-152.66) at the 10m-50m height respectively.

ISSN: 2961-6611

TABLE I
Estimate Weibull parameters by five methods at Ouargla region

Month	V(m/s)	Moments Method		Empirical method of lysen		Power density method		Variability of wind method		Energy Pattern Factor method	
		K (-)	C (m/s)	K (-)	C (m/s)	K (-)	C (m/s)	K (-)	C (m/s)	K (-)	C (m/s)
Jan	2.88	1.3470	3.1446	1.3470	3.1468	1.3740	3.1554	1.7834	3.2423	1.3740	3.1841
Feb	3.67	1.9629	4.1494	1.9629	4.1519	1.9947	4.1508	1.8029	4.1371	1.9947	4.2330
March	4.56	2.5749	5.1501	2.0686	5.1528	2.5339	5.1512	2.0077	5.1480	2.1399	5.1883
Apr	4.50	2.2563	5.0823	2.2563	5.0842	2.2631	5.0822	1.9944	5.0793	2.2631	5.1041
May	4.27	1.1553	4.4998	1.1553	4.5004	1.0428	4.3492	1.9439	4.8227	1.0428	4.3180
June	4.59	1.0025	4.5974	1.0025	4.5930	1.0183	4.6272	2.0145	5.1829	1.0183	4.6166
Jul	3.80	2.3106	4.2924	2.3106	4.2937	2.3810	4.2905	1.8331	4.2799	2.3810	4.3064
August	3.83	2.1922	4.3274	2.1922	4.3292	2.2744	4.3265	1.8402	4.3138	2.2744	4.3522
Sept	4.12	2.0686	4.6479	2.5749	4.6485	2.1399	4.6499	1.9096	4.6517	2.5339	4.6424
Oct	3.12	1.8223	3.5183	1.8223	3.5208	1.8709	3.5220	1.6622	3.4989	1.8709	3.5525
Nov	2.82	1.4880	3.1277	1.4880	3.1303	1.4891	3.1280	1.7652	3.1750	1.4891	3.2371
Dec	2.39	1.2766	2.5810	1.2766	2.5825	1.3388	2.6054	1.6242	2.6723	1.3388	2.6469

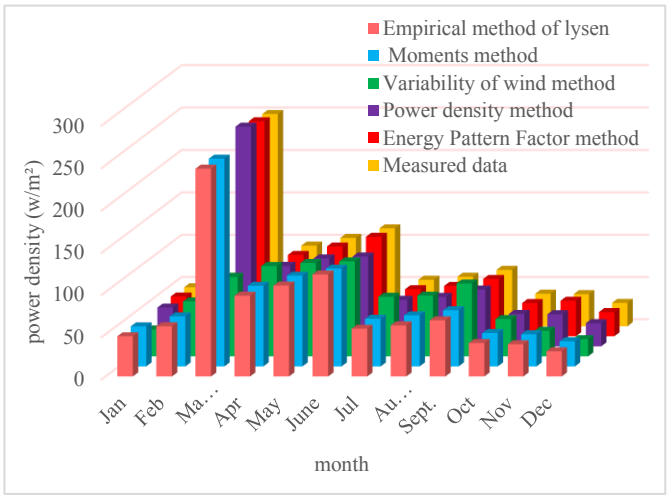

Fig.1 Estimate the Monthly Power Density (W/m²) by the five methods at 10m.

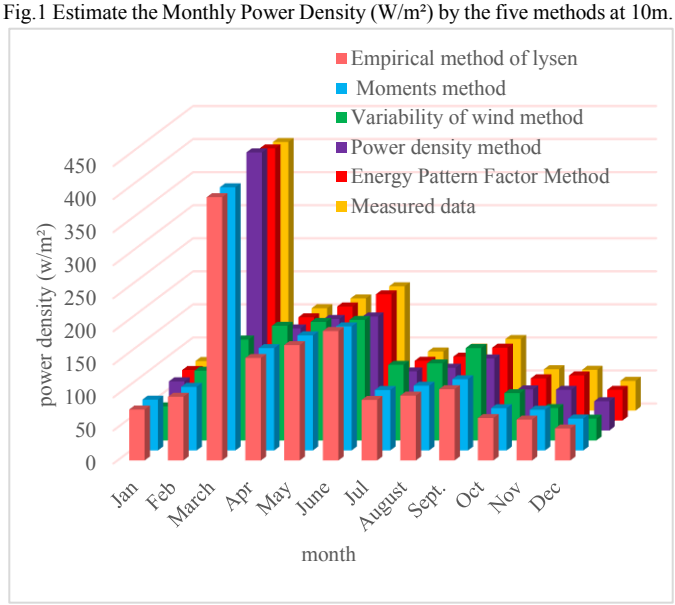

Fig.2 Estimate the Monthly Power Density (W/m²) by the five methods at 50m.

The results obtained show the power density shows a large month-to-month variation. The minimum power densities occur in December (29.82, 48.33) W/m² at 10m-50m heights and we recorded the highest value in March (250.63, 500) W/m² at 10m-50m heights respectively (figure 1-2). It is interesting that highest power density values occur in the spring months of March, April and May.The results indicate that Ouargla site has a seasonal wind potential, as the wind blows at a relatively high speed in spring and summer.

2) Seasonal Power Density: The maximum seasonal average power density of (80.25, 130.069) W/ m² is recorded in the spring for heights (10, 50) successively, while the minimum values of (58.36, 94.59) W/m² are recorded in the winter for heights (10, 50) successively (Table II). Thus, the higher power density at the Ouargla site in two seasons (spring - summer) and low in winter and autumn.

TABLE III
Estimate Seasonal power density at (10 m, 50 m) altitude

Season	Vm (m/s)	Power Density(w/m²)	
		10m	50m
Winter	3.6017	58.364	94.591
Spring	4.3005	80.255	130.069
Summer	4.2843	81.581	132.218
Autumn	3.2335	60.976	98.824

The analysis of the results also shows that:

♦ the change from the 10 m height to the 50 m height makes it possible to increase the WPD available on site by a factor of approximately 1.6 to 2.

♦ the atmosphere is not stable throughout the year on the Ouargla site and the existence of seasonal winds, this confirms that there is a potential for significant winds in this site.

♦ it is noted that the power increases considerably after the extrapolation to 50 m, which gives an estimated energy of 953.77 KWh for each m².

♦ We find that the months in the centre of the year, which are part of spring and summer, are the windiest months, and this

ISSN: 2961-6611

assures us the greatest power and energy is in coastal months of the year.

C . STATISTICAL ANALYSIS

There are several statistical test tools, such as the RMSE, the Chi square test (X^2) and the Mean Absolute Percent Error (MAPE) test. In this work, we have used the previous tools to test the accuracy of the used methods to find the most efficient method for determining the density of wind energy, (Table III) shows more about obtained results. It is observed that the wind variability method has the highest percentage of error. In contrary, the Moments method shows a more efficient and lower error percentage. it is the better method to estimate the WPD.

TABLE IIIII
Statistical analysis for five methods at 10m, 50 m altitude

Method	Statistical Analysis					
	10m			50m		
	RSME	MAPE	X^2	RSME	MAPE	X^2
MOM	1.94	0.46	0.12	3.14	0.27	0.33
EML	2.41	0.96	0.19	3.91	1.56	0.52
PDM	3.77	0.17	0.48	6.14	0.28	1.27
VWM	46.44	9.28	73.2	92.27	15.05	75.2
EPFM	2.06	1.72	0.14	3.35	2.80	0.38

D. THE ANNUAL ENERGY DENSITY

Figure 3 shows the wind energy density in the Ouargla region for 10 years at different heights. It is remarkable that (figure 3) an aerogenerator on this site can produce 588.62 KWh annually at 10 m for each m². Given the nature of the Saharan soil in this region, and the effect of the roughness of the surface, we note that the power increases considerably after the extrapolation to 50 m, so that the average energy estimated (417.59, 660.08) kWh for each m² this at the heights 10m 50 m successively. After gathering knowledge about the densities of the average powers in this site, we propose the setting of small wind turbines can be chosen to produce electricity in a hybrid way with a photovoltaic system, for example.

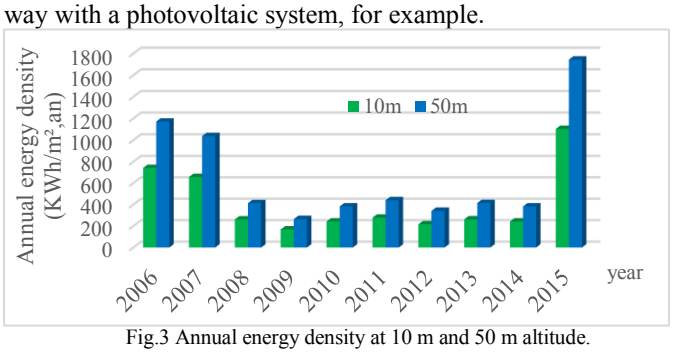

Fig.3 Annual energy density at 10 m and 50 m altitude.

VI. CONCLUSION

This study allowed us to evaluate the potential energy of the wind in the region of Ouargla. The average monthly wind speed at the Ouargla site was relatively varied between (3- 4.5 m / s), The Weibull parameters were calculated by five methods: Moments method, the Empirical method of Lysen, power density, the variability of wind and Energy Pattern Factor method, where it was found in a period the shape parameter (k) varied between (1.2766 to 2.5749) with respect to the parameter (c) it varies between 2.5810 to 5.1501.the wind power has been estimated at different heights according to the Weibull distribution. We find that the months in the centre of the year, which are part of spring and summer, are the months more windy, and this assures us the greatest power and energy that the coastal months of the year. This confirms the existence of seasonal winds. Therefore we consider that small wind power plants can be a hybrid power generation choice eg (PV-E) as a solution to avoid energy shortage throughout the year or this level of power density may be adequate for nonconnected electrical and mechanical applications, such as battery charging and water pumping.

REFERENCES

[1] A.Allouhi et al*" Evaluation of wind energy potential in Morocco's coastal regions"* Renewable and Sustainable Energy Reviews, vol.72 pp311–324, 2017.

[2] Abbasi SA, Abbasi T*"Impact of wind-energy generation on climate: a rising spectre"* Renewable and Sustainable Energy Reviews, March. 2018.

[3] Mahela OP, Shaik AG*" Comprehensive overview of grid interfaced wind energy generation systems*" Renew Sustain Energy Rev vol.57,pp 260–281,Dec.2016.

[4] Ayad A. Ani et al*" Weibull Parameters and Wind Power Assessment for Three Locations in Iraq"* Iraqi Journal of Science 2014, Vol.55, paper729-740,2014.

[5] Isaac YF Lun, Lam, Joseph C*" A study of Weibull parameters using long-term wind observations"*Renewable Energy, vol.20, pp145-153, Aug1999.

[6] Bagiorgas HS et al*" Wind power potential assessment for seven buoys data collection stations in Aegean Sea using Weibull distribution function"* J Renew Sustain Energy 2012,N°1:0131,19-1–16.

[7] Muhammad Shoaib et al*" Evaluation of wind power potential in Baburband (Pakistan) using Weibull distribution function"* Renewable and Sustainable Energy Reviews (2016).

[8] C.G. Justus,et al*"Methods for estimating wind speed frequency distributions"* J. journal of Applied Meterology.vol.17,pp350–353,Nov.1977.

[9] F. George*"A comparison of shape and scale estimators of the two-parameter Weibull distribution"*J. Journal of Modern Applied Statistical Methods,vol.13,pp23–35,May.2014.

[10] T. Arslan,et al*" Comparative study of numerical methods for determining Weibull parameters for wind energy potential* Renewable and Sustainable Energy Reviews,vol.40 pp820–825,Aug.2014.

[11] P.A.C. Rocha, et al*"Comparison of seven numerical methods for determining Weibull parameters for wind energy generation in the northeast region of Brazil"* Appl. Energy,vol.89, pp395–400,Sep.2012.

[12] P.K. Chaurasiya et al*" Study of different parameters estimation methods of Weibull distribution to determine wind power density using ground based Doppler SODAR"*Alexandria Engineering Journal, August .2017.

[13] J.L. Nsouandélé et al*" Estimation statistique des données du vent à partir de la distribution de Weibull en vue d'une prédiction de la production de l'énergie électrique d'origine éolienne sur le Mont Tinguelin à Garoua dans le Nord Cameroun"* Revue des Energies Renouvelables ,Vol. 19, Paper 291 – 301, 2016

[14] S.H. Pishgar-Komleh,et al *" Wind speed and power density analysis based on Weibull and Rayleigh distributions (a case study: Firouzkooh county of Iran)"* Renewable and Sustainable Energy Reviews , vol .42,pp 313–322,Oct.2015.

[15] *Saïd Diaf, Estimation de la production éolienne d'électricité dans la région d'Adrar, Revue des Energies Renouvelables in Bou Ismail Tipaza –Alegria, paper161 – 172,2010.*

[16] Halima Boutelli et al *" Etude et analyse de potentiel du vent dans la région Ouargla- Biskra par la distribution de Weibull"* International Seminar on New and Renewable Energies, in Ghardaïa -Algeria , Oct. 2018.

[17] Benali Oussama" *Evaluation de potentiel énergétique éolien dans la région sud-est du Sahara algérienne* " M. Eng. thesis, univ -Kasdi Merbah,ouargla, Algeria ,June.2015.

ISSN: 2961-6611

Design and Performance of mixed flow turbine used as butane turbo expander for a combined power – refrigeration system

Hamel Mohammed[#1], Benlefki Abdelkrim[*2]

[#]*Faculté de génie mécanique, Université des Sciences et de la Technologie M. B. Oran, ALGERIA*

[1] hamel_moh78@yahoo.fr

[*] *Centre Universitaire El Wancharissi, Tissemsilt, ALGERIA*

[2] abdelkrim.benlefki@gmail.com

***Abstract*— Power production and refrigeration are two problems of human communities which contribute in environmental degradation. Clean power can be produced by means of solar energy using organic Rankin cycle where refrigeration systems are power consumption and must be associated to clean energy source to conserve environment. In this paper a combined cycle for power production and refrigeration is presented. The system produces 30 Kw of power by a mixed flow turbine and 50 Kw of cold using solar energy and butane us working fluid. A CFD model is used to test the performance of the mixed flow turbine for a wide range of working conditions.**

***Keywords* — Power; solar energy; mixed flow turbine; ejector; butane; CFD.**

I. INTRODUCTION

Ozone depletion and global warming are major environmental concerns with serious implications for the future development of refrigeration-based industries and power production. The challenge is to use the renewable energy sources in power plant to eliminate pollutant emissions and non-toxic working fluid in refrigeration plant to conserve the ozone layer.

Organic Rankin cycles (ORC) are one of the available solutions for converting low grade heat source into electrical power. The benefit of ORC systems is the recovery of useful energy, often as electrical output, from low-energy sources such as the low-pressure steam associated with steam-driven turbines used for electricity generation [1–5].

Ejector refrigeration systems, which were very popular in the early 1930s, are also receiving renewed interest since they can be activated by low temperature thermal energy from renewable sources or thermal wastes thus reducing the use of fossil fuels or improving the efficiency of their usage. An ejector is a simple apparatus using the low pressure created by the accelerated stream of a primary (or motive) fluid to aspirate and compress a secondary (or suction) fluid [6].

Some researcher proposed ejector-refrigeration cycle and Rankine cycle (ORC) based combine power and ejector-refrigeration cycles to utilize the low temperature heat. In this type of combined cycles, the ejector refrigeration cycle and the power cycle share the same heat source.

The cycles could be divided into two kinds according to the configuration. In the first type, the ejector and power turbine are arranged in parallel. It was first proposed by Oliveira et al. [7 and 8].

The other type is that the ejector and the power turbine are arranged in series. The vapor form the power system acts as the primary flow and there is no generator in the refrigeration cycle. Dai et al. [9] proposed this kind of cycle, in which the high temperature and pressure organic gas expands in the turbine. Then the exhaust gas enters the ejector as primary flow (Fig. 1). This cycle is considered in this study, where a mixed flow turbine is designed and tested numerically.

II. CYCLE DESCRIPTION

In the combined cycle (Fig. 1), the liquid flow from the exit of the pump (state 1) is heated to super heat gas (state 2). Then the vapor enters the turbine and expands. The turbine exhaust gas (state 3) enters the ejector. In the ejector, the exhaust gas induces a low pressure region at the exit of the ejector nozzle and accelerates to the supersonic condition as it passes through the converging– diverging nozzle of the ejector. Then the secondary flow is entrained into the ejector from the evaporator (state 7) as secondary flow. Subsequently, these two streams are mixed in the mixing section. The mixed flow then undergoes a transverse shock and a pressure rise. And then it is compressed to state 4. In condenser, the compressed gas is cooled to saturated liquid (state 5). A part of the saturated liquid is pumped to high pressure in the pump. The other part of the saturated liquid expands in the valve (state 8) and then evaporates to saturated vapor (state 7). The solar energy with cylindro-parabolic concentrator can be used as high temperature heat source.

ISSN: 2961-6611

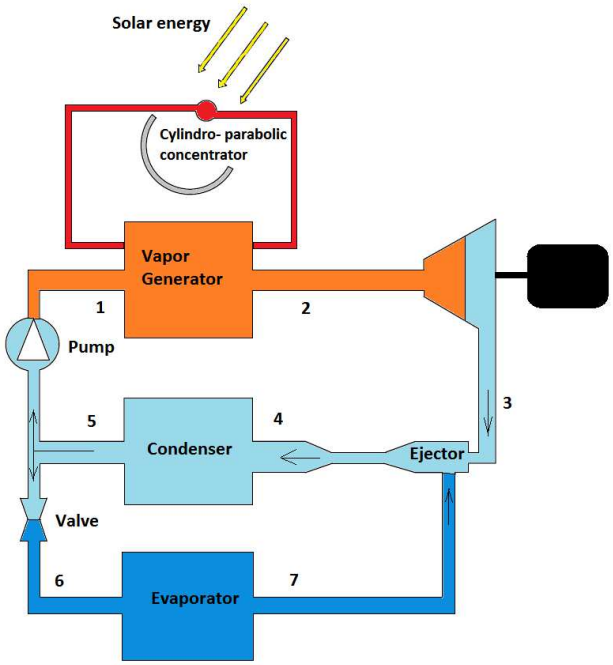

Fig. 1 Schematic diagram of the combined power and ejector-refrigeration cycle

III. WORKING FLUID

The only fluids of substitution without additional inconvenience both regarding the ozone layer and the greenhouse effect are non-halogenated fluids like ammonia (R717), propane (R290), butane (R600), isobutane (R600a), carbon dioxide (R744) and water (R818).

The main concern regarding the adoption of hydrocarbons as a refrigerant is their flammability. It should be remembered that millions of tonnes of hydrocarbons are used safely every year worldwide for cooking, heating, vehicle fuelling and aerosol propellants. In these industries, procedures and standards have been developed and adopted to ensure the safe use of the product.

Figure 2 shows the changes in saturated vapor pressure and temperature for R134a, R22, R12, and mixtures of propane (R290)- butane R600, As shown in this figure, the saturated vapor pressure curves for various proportions of mixtures are close to the refrigerant vapor pressure curve R134a and R12, and the R290 curve is very close to the R22 curve. This indicates that these mixtures may have similar properties and could be used as a substitute for R134a and R22 refrigeration system. The butane curve indicate that w it can be used when a law-grade energy sources is considered with the generation temperature ranging from 70 C to 95 C and low compression ratios.

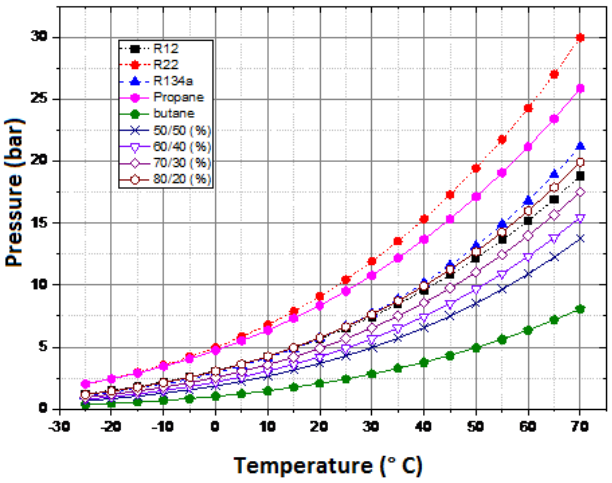

Fig. 2 Pressure and saturation temperature of Propane-Butane mixtures

IV. RADIAL TURBINE

Radial inflow turbines have established their place in industrial applications, especially in the field of small turbomachinery because of their simplicity, reliability, low manufacturing cost, relatively high performance, easy installation and maintenance and fast response.

When a law power output is required, where the radial gas turbine has many advantages, both economically and aerodynamically, over the axial turbine. Where small sizes are concerned the relatively large clearances at the rotor tips have a smaller effect on turbine performance than in the axial flow machine. From the economic point of view the simpler fabrication of the radial rotor and nozzle assembly compared with the blade assembly for the axial turbine renders the turbine at a particular advantage when the machine is used as an accessory, for example, in turbochargers or starters. Furthermore, since it is essentially a low specific speed machine, it can cope with large overall pressure ratios in a single stage and this has advantages as an expander in liquid gas plant. Among the works that give a detailed approach to optimal sizing of a radial turbine one can quote that of Benson [10], and that of Ebaid et al. [11]

To be continued….

REFERENCES

[1] Capata, R.; Toro, C. Feasibility analysis of a small-scale ORC energy recovery system for vehicular application. Energy Convers. Manag. 2014, 86, 1078–1090.
[2] Hyunjin, K.; Jeseung, Y. Design of a Scroll Expander for an ORC Applicable to a Passenger Car for Fuel Consumption Improvement; Department of Mechanical Engineering, University of Incheon: Incheon, Korea, 2013.
[3] Johnson, I.; Choate, W.T. Waste Heat Recovery: Technology and Opportunities in U.S. Industry; BCS, Incorporated, US Department of Energy: Washington, DC, USA, 2008.
[4] Qiu, G.; Liu, H.; Riffat, S. Expanders for micro-CHP systems with organic Rankine cycle. Appl. Therm. Eng. 2011, 31, 3301–3307.
[5] Rettig, A.; Lagler, M.; Lamare, T.; Li, S.; Mahadea, V.; McCallion, S.; Chernushevich, J. Application of Organic Rankine Cycles (ORC). In

ISSN: 2961-6611

Proceedings of the World Engineer's Convention, Geneva, Switzerland, 4–8 September 2011.

[6] Nicolas Galanis*, Mikhail Sorin; Ejector design and performance prediction; International Journal of Thermal Sciences 104 (2016) 315e329.

[7] Oliveira A, Afonso C, Matos J, Riffat S, Nguyen M, Doherty P. A combined heat and power system for buildings driven by solar energy and gas. Appl Therm Eng 2002;22:587–93.

[8] Wang J, Dai Y, Sun Z. A theoretical study on a novel combined power and ejector refrigeration cycle. Int J Refrig 2009;32:1186–94.

[9] Dai Y, Wang J, Gao L. Exergy analysis, parametric analysis and optimization for a novel combined power and ejector refrigeration cycle. Appl Therm Eng 2009;29:1983–90.

[10] R. S. Benson, "Computer aided design of radial gas turbines: a method for determining the overall rotor dimensions," *Computers and Fluids*, vol. 5, pp. 219-240, 1977.

[11] M. S. Y. Ebaid and Q. Z. Al-Hamdan, "Optimization techniques for designing an inward flow radial turbine rotor," Proceedings of the Institution of Mechanical Engineers Part a-Journal of Power and Energy, vol. 218, pp. 655-668, Dec 2004.

ISSN: 2961-6611

Simulation of Electricity Production by a Solar Tower Power Plant with Thermal Storage System in Algeria

IKHLEF Khaoula[#1], LARBI Salah[#2]

[#]*Ecole Nationale Polytechnique d'Alger (ENP), Laboratoire de Génie Mécanique et Développement (LGMD)*
10, Avenue Hassen Badi, BP182, El Harrach, Alger, Algérie
[1]khaoula.ikhlef@g.enp.edu.dz
[2]salah.larbi@enp.edu.dz

Abstract— **Concentrating solar tower power plant with thermal storage system has received particular attention among researchers, power-producing companies and policymakers according to its bulk electricity generation ability by overcoming the intermittency of solar energy. The parabolic trough collector and solar tower are the two dominant CSP systems which are either operational or in the construction stage.**
The aim of this paper is to study the production of electricity by a solar tower power plant with thermal storage system (type PS10). The power plant capacity is 150MWe and it is located in Hassi R'mel (south region of Algeria). The purpose is to highlight the importance of developing concentrating solar thermal technologies in Algeria.
Concentrating solar thermal technologies belong to an engineering field, which can significantly contribute to the delivery of clean, stainable energy worldwide.

Keywords—**Solar Tower Power Plant, Thermal Storage System, Simulation, System Advisor Model.**

Abbreviations

CCGT	Combined Cycle Gas Turbine
CDSEP	Crescent Dunes Solar Energy Project
CF	Capacity Factor
CRS	Central Receiver Systems
CSP	Concentrating Solar Power
DNI	Direct Normal Irradiation
DSG	Direct Steam Generation
HTF	Heat Transfer Fluid
ISEGS	Ivanpah Solar Electric Generating System
LFR	Linear Fresnel reflector
PD	Parabolic Dish
PTC	Parabolic Trough Collector
SAM	System Advisor Model
SM	Solar Multiple
SPT	Solar Power Tower

I. Introduction

In order to take up the global challenges of clean energy, climate change and sustainable development, it is necessary to boost the development of environmentally friendly energy technologies. In this context, concentrating solar power plants (CSP) are increasingly relevant because of the need to reduce carbon dioxide emissions in electricity production and heat generation required to reach the goal of limiting climate change to 2°C above the pre-industrial levels.

CSP power plants are gaining in popularity with advances in technology. There is a type of concentrating solar thermal technologies available nowadays, being solar thermal collectors the major component of solar power systems. As previously stated, these collectors receive the incoming radiation and concentrate solar rays to heat a fluid, which then directly or indirectly drives a turbine and converted mechanical energy into electricity through a generator. The concentration of sunlight allows the fluid to reach working temperatures high enough to ensure affordable efficiency in turning the heat into electricity, while limiting heat losses in the receiver. The four main commercial CSP technologies are distinguished by the way they focus the sun's rays and the technology used to receive the solar energy (Fig. 1): parabolic trough collector (PTC), solar power tower (SPT), linear Fresnel reflector (LFR) and parabolic dish (PD). The basic principles of concentrated CSP systems are covered in previous reference works such as [1], [2], [3], [4] and [5].

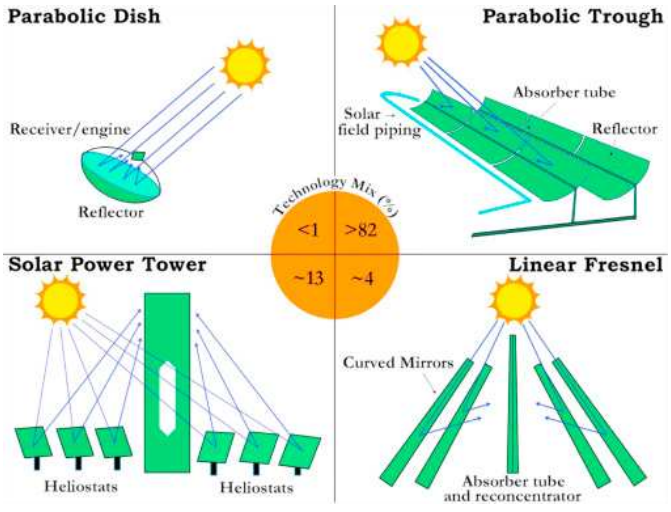

Fig. 1 Categories of CSP technologies.

ISSN: 2961-6611

In the SPT plants (see Fig. 2), also called central receiver systems (CRS) or power tower, a large number of computer-assisted mirrors (heliostats) track the sun individually over two axes. Heliostats are less expensive than trough mirrors because they used standard flare glass, instead of glass that is manufactured at specific curves. They concentrate the solar radiation onto a single receiver at the top of a central tower where the solar heat drives a thermodynamic cycle and generates electricity. SPT plants can achieve higher temperatures than PTC and LFR systems because they have higher concentration factors. The SPT can use water-steam (DSG), synthetic oil or molten salt as the primary heat transfer fluid [6].

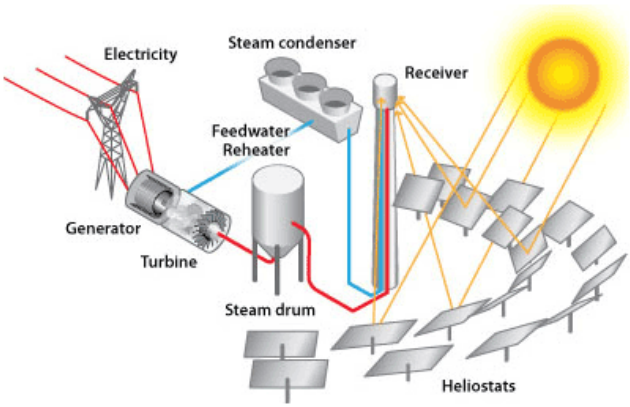

Fig. 2 Schematic of a Solar Tower Power Plant.

The number of existing CSP SPT plants of significant size is very limited, and the time they have been operational is also minimal. Additionally, not all the data needed are publicly available. Hence, the full potential of the SPT technology is not shown by the surveys of plants. In the list of the SPT plants of [7], there are only 34 CSP SPT plants worldwide. Only 3 above 20 MW of capacity are operational, ISEGS of 377 MW capacity since 2014, Crescent Dunes Solar Energy Project (Tonopah) of 110 MW capacity since 2015, and Khi Solar One of 50MW capacity since 2016. The 377 MW ISEGS plant only producing 703,039 MWh/year (2016), the output of a medium to small scale CCGT plant, has the best data set covering 3 years.

Recently, there has been a particular interest to solar tower power technology, as is evident from the fact that there are several companies involved in planning, designing and building utility size power plants. This is an important step towards the ultimate goal of developing commercially viable plants. There are numerous examples of case studies of applying innovative solutions to solar power [8].

II. Results and Discussions

The solar power tower simulation is performed using the System Advisor Model (SAM) simulator. The meteorological data of the selected site are taken by METEONORM 7 software with period data (1991-2010) for numerical simulation. Some important design parameters used in the simulation are given by tables, I, II and III.

TABLE I
HELIOSTAT FIELD

Total heliostat reflective area	Heliostats number	Mirror washing
1269055 m^2	8790	0.70L/m^2 and 63 washes per year

TABLE II
POWER CYCLE

Solar multiple	Capacity	Cycle	Condenser type
2	**150 MWe**	**Rankine**	**Air-cooled**
HTF type	HTF temperature		HTF mass flow rate
Salt (60% $NaNO_3$, 40% KNO_3)	**Hot: 574°C Cold: 290°C**		**850.9 kg/s**

TABLE III
THERMAL STORAGE

Type	Full load hours	Tank volume	Hot tank heater capacity
Two tank	6	11087 m^3	30MWe

Figures 3, 4 and 5 illustrate the meteorological data of Hassi R'Mel site.

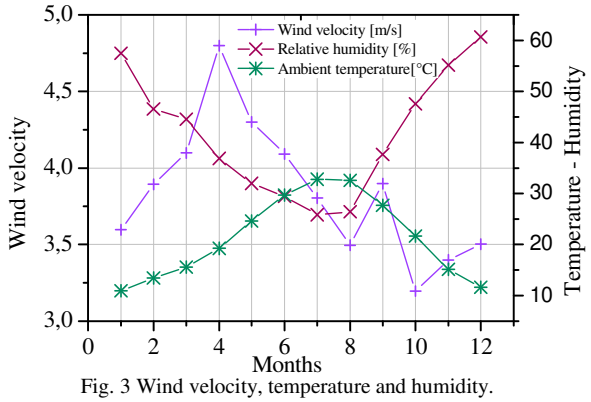

Fig. 3 Wind velocity, temperature and humidity.

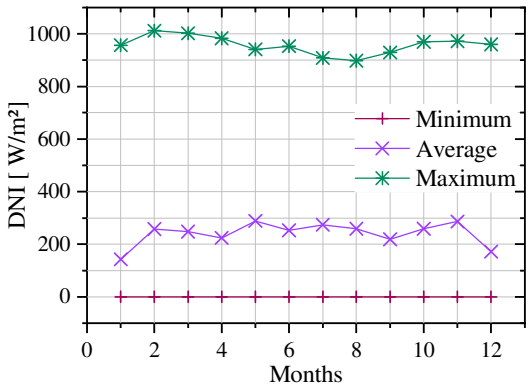

Fig. 4 Direct normal irradiation.

ISSN: 2961-6611

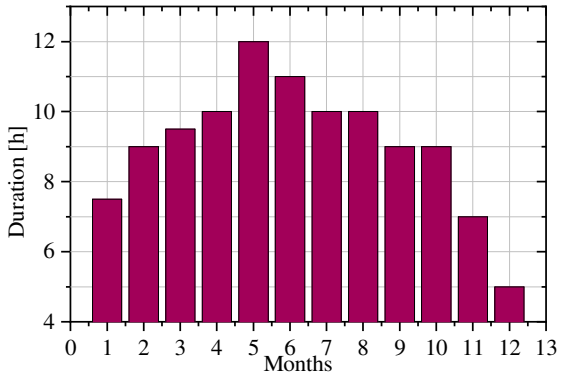

Fig. 5 Hours of sunshine.

The hours of sunshine are the hours whose DNI is greater than 300W/m² the threshold of deliverability of the plant.

Figure 6 illustrates the changes in the monthly averages of the production capacity of the power plant. Notice that the production varies proportionally to the DNI. Thus, the decrease in the production capacity from the incident radiation to the net power produced is caused by the optical, thermal and parasitic losses generated in the installation.

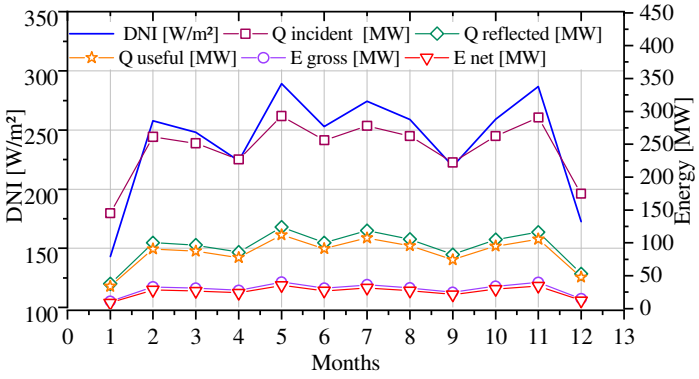

Fig. 6 Average monthly production capacity of the solar power plant.

The net hourly production capacity of the different months is given by figure 7.

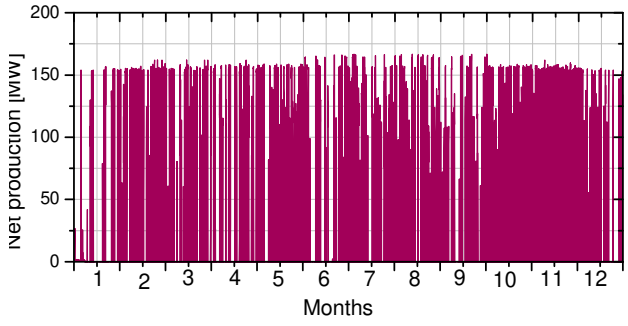

Fig. 7 Hourly production capacity of the solar power plant.

According to this figure, the best production is reached in the summer period, which records values that exceed 150 MW, where the plant works in an overcapacity.

Figures 8 and 9 show the monthly average daily production of the plant with a storage system that actually starts from a DNI greater than 300W/m² for the two typical days in May and January.

For the typical day of May, the energy incident, absorbed and reflected by the solar field follow the same shape as the DNI. The other energies (useful, gross and net) follow the variation of the DNI until 18h where they continue to be generated despite the disappearance of the DNI (null DNI). This generation of energy is provided by the storage tanks.

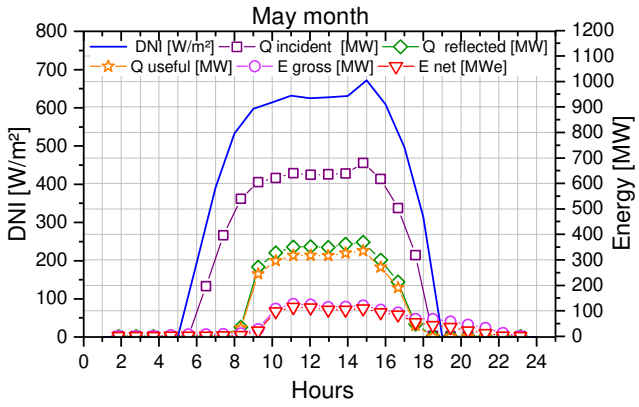

Fig. 8 Monthly average daily production of the power plant (21May).

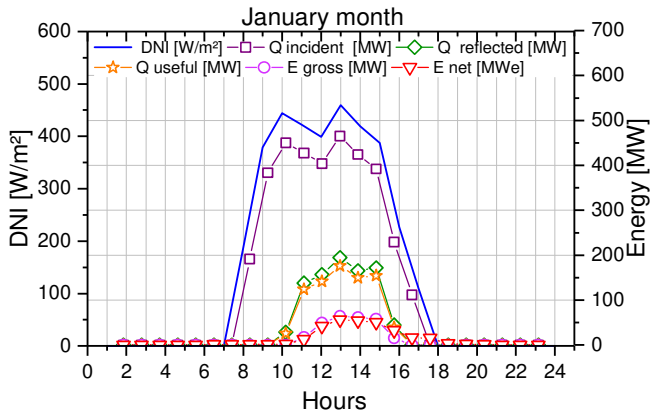

Fig. 9Monthly average daily production of the power plant (21January).

For the typical day of January, all energies follow the same shape as the DNI. The production of electricity starts when the DNI exceeds 300W/m². The power plant operates approximately one-third of its capacity.

ISSN: 2961-6611

A. *Validation*

To validate the results of our simulations, the Crescent Dunes Solar Energy Project is chosen. The project has a capacity of 125MWe [9] and 1.1 GW-hours of energy storage [10]. The site is located closely to Tonopah at approximately 310km from northwest of Las Vegas [11, 12]. It is the first utility-scale CSP plant with a solar tower and advanced molten salt energy storage technology from Solar Reserve. Results comparison between theoretical and experimental data are illustrated on table IV.

TABLE IV
RESULTS COMPARISON

	CDSEP [13]	Our simulation
Capacity	125MWe	150MWe
Storage system	10h	6h
Total collector area	1200000 m^2	1269055 m^2
Site resource	2685 kWh/m^2/yr	2828 kWh/m^2/yr
CF	more than 50%	57,9%
Annual net output	196 GWh (2018)	223,11GWh

III. CONCLUSIONS

The CSP STP plant technology is still far from the standards of conventional power plants in the power industry, where the actual costs and performances are usually close to the planned values. More experience must be gathered to proper develop a technology that appears to be still in its infancy. The different alternatives that are presently under study at different stages of development may only progress slowly, benefiting from real world experiences requiring time rather than simulations or laboratory experiments. This paper illustrates a simulation of a solar power tower with a capacity of 150MWe with heat storage system and the importance of installing such power plant in Algeria.

The main conclusions are presented as follows:

1) The parameters that have a great influence on the energy produced are the DNI and the duration of sunshine.

2) Thermal energy storage system plays a positive role in annual electricity generation and system capacity factor.

3) The results of this study were compared with those of the CDSEP power plant. Good agreement is observed between theoretical results and experimental data.

To make these technologies competitive with conventional fossil-based technologies, a reduction in the cost of production must be sought in the years to come.

This objective will be achieved on one hand, thanks to the technological innovations brought by the research and development work on solar sectors and their components (mirrors, panels, receivers, fluids and storage) and on the other hand by the massive construction of these power plants around the world.

REFERENCES

[1] Romero-Alvarez, M. and Zarza, E., Concentrating solar thermal power. Handbook of energy efficiency and renewable energy, 2007:21-1.

[2] Müller-Steinhagen, H. and Trieb, F., Concentrating solar power. A review of the technology. Ingenia Inform QR Acad Eng, 2004, 18:43-50.

[3] Zhang, H.L., Baeyens, J., Degrève, J. and Cacères, G., Concentrated solar power plants: Review and design methodology. Renewable and Sustainable Energy Reviews, 2013, 22:466-481.

[4] Barlev, D., Vidu, R. and Stroeve, P., Innovation in concentrated solar power. Solar Energy Materials and Solar Cells, 2011, 95(10):2703-2725.

[5] Winter, C.J., Sizmann, R.L. and Vant-Hull, L.L. eds., 2012. Solar power plants: fundamentals, technology, systems, economics. Springer Science & Business Media.

[6] Mehos, Turchi, Vidal, et al, Concentrating Solar Power Gen3 Demonstration Roadmap, NREL/TP-5500-67464, January 2017.

[7] National Renewable Energy Laboratory (NREL), Power Tower Projects, www.nrel.gov/csp/solarpaces/power_tower.cfm, Retrieved November 9, 2017.

[8] Joseph Perkins, Solar Power in the News, http://pointfocus.com/.

[9] Grupo COBRA, Crescent Dunes Solar Thermal Power Plant, Retrieved 15 January 2016.

[10] CleanTechnica, Crescent Dunes 24-Hour Solar Tower Is Online, 22 February 2016. Retrieved 15 June 2016.

[11] Loan Programs Office (LPO), Dept. of Energy (DOE), Energy Department Finalizes $737 Million Loan Guarantee to Tonopah Solar Energy for Nevada Project, 28 September 2011. Retrieved 2 July 2014.

[12] Loan Programs Office (LPO), Dept. of Energy (DOE), Crescent Dunes: Project under construction, 1 September 2015. Retrieved 17 January 2016.

[13] Albert Parker, The Failure of Solar Tower Thermal Energy Storage, Published on May 3, 2018.

ISSN 1737-9334

Geometry effect on the improvement of the performance of a thermoelectric generator under a pulsed heat source

Sonia Besbes [#1], Ghada Ben Abdallah [#2], Habib Ben Aissia [#3], Jacques Jay [*4]

[#] *Laboratory of Metrology and Energy Systems (LRMSE), National School of Engineers of Monastir, Road Ouerdanine, 5000 Monastir, Tunisia*

[1]soniabesbes767@gmail.com

[2]benabdallahghada@hotmail.fr

[3]habib.enim2017@gmail.com

[*]*Thermal Center of Lyon (CETHIL), INSA Lyon, 20 Av. A. Einstein, 69621 Villeurbanne Cedex, France*

[4]*jacques.jay@insa-lyon.fr*

Abstract— **This paper presents a transient simulation based on the coupling of electric conduction and heat transfer in order to quantify the conversion efficiency enhancement of thermoelectric generators (TEGs) under periodic heating. TEG allows the conversion of thermal energy into electrical energy when a temperature difference is applied to it. The effect of leg geometry on the device performance has been discussed. For this purpose, TEGs with various leg geometries (rectangular (∏-TEG) and trapezoidal (T-TEG)) were modeled and 3D finite-element analyses were carried out. It is found that geometric shape and dimensions of the TEG legs enhance significantly the thermoelectric (TE) performance of the device. However, it is observed that for a given value of leg length (L), the output power in the case of T-TEG is higher than that of ∏-TEG. Hence, this result can facilitate the prediction of TEG performance.**

Keywords— **Thermoelectric generator; TEG ; Output Power; Leg gometry; Leg dimension.**

I. INTRODUCTION

Thermoelectric (TE) devices have recently emerged as a promising alternative among other renewable energy technologies due to their particular advantages. Thermoelectric power generators (TEGs) can recycle a portion of the waste heat into useful electricity, this has led to a growing interest in TEGs [1]. The improvement of the performance of TEGs can be realized through two pathways [2]. One is interested in improving the efficiency of thermoelectric materials while the other concerned the geometric configuration of legs of the TE element. However, the design of TEGs made from commercially available TE materials seems to be more rational since the cost of manufacturing new advanced materials is very high. Therefore, geometric optimization of TEGs is an easy and practical solution to improve TEG performance and lower the cost as well. In this regard, much research works derived that the maximum output power of a TEG only depends on a certain optimal ratio of leg length to area regardless of their respective values [3]-[6]. Fabián et al. [7] developed a novel design of a thermoelectric module having asymmetrical legs with truncated square pyramid shape, as compared to conventional one with a constant square cross section, their results prove that geometrical configuration of the device legs can improve significantly the thermoelectric performance of the device. Ravita et al. [8] analyzed the variation of thermoelectric leg configuration to improve the power output and efficiency of the thermoelectric generator system. Their results show that when the shape parameter (ratio of hot area to cold area) is increased from 1 (rectangular TEG) to 2 (trapezoidal TEG), then the power output was decreased by 1.3% under a given operating condition. Erturun et al. [9] investigated the effect of various TE leg geometries (rectangular, trapezoidal, octagonal and cylindrical prism) on the performance of the output power. They reported that the power outputs are slightly affected by geometrical configurations due to the same Seebeck coefficients, temperature gradients and heights of the TE leg. Brito et al. [10] explored the impacts of TEM leg length on its power output and found that an optimal TE leg length lies in a compromise of resulted varying internal resistance and the Seebeck voltage. In recent years, few works have focused on the behavior of TEGs under transient operating conditions [11-13]. Thus, there is still a great deal of opportunity for fundamental exploration of module design under a periodic heat source. In the present study, 3D simulation of the performance of the TEGs under periodic heat source has been carried out. The effect of leg geometry on the device performance has been discussed by defining two types of TEG elements: rectangular (∏-TEG) and trapezoidal (T-TEG).

II. MODULES GEOMETRIES

Two types of thermoelement leg geometries were considered. First, a 16-leg module with p- and n-type

ISSN: 2961-6611

rectangular TEG (∏ -TEG) with dimensions of 3.2 mm x 3.2 mm x 1.7 mm was modeled. The legs were spaced with 2.8 mm distance between each other. Another module is modeled with trapezoidal leg geometries (T-TEG). Leg geometries were modeled with equal cross-sectional areas. For the trapezoidal model, cross sectional area at the mid-height was considered. The thicknesses of ceramic substrates and copper blocks (1 mm) and the dimensions of the copper blocks (9.2 mm x 3.2 mm) remained the same for the both models. The geometric configuration of ∏-TEG and T-TEG composed of a pair of TE materials is shown in Fig. 1. A bismuth telluride (Bi_2Te_3) based alloys are the most commonly preferred leg materials for relatively small temperature gradient applications. The material properties of TE elements are listed in Table I. The contact resistances are neglected because they are small compared to the target resistances.

TABLE I
MATERIALS PROPERTIES

Components	S (V/K)	σ (S/m)	K (W/mK)
p-type	2.5e-4[a]	0.5e5[b]	1.736[b]
n-type	-2.5e-4[a]	0.5e5[b]	1.359[b]
Copper	1.0e-6	6.0 e7	400
Alumina	-	-	24
Solder	-	6.9 e6	28

[a] Ref.[14] ; [b] Ref.[15]

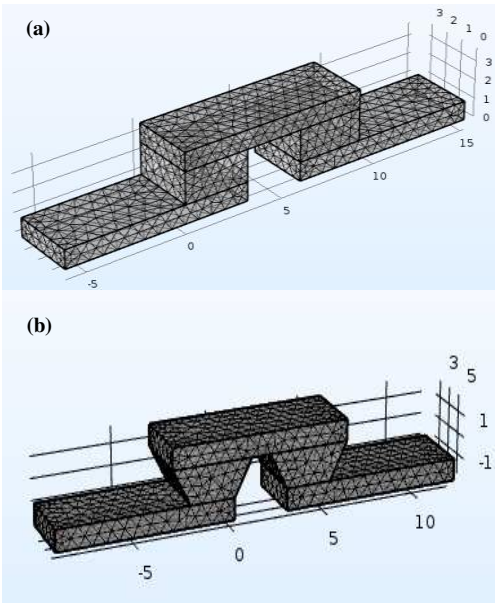

Fig.1 Finite element model mesh; (a) ∏-TEG and (b) T-TEG

III. ANALYTICAL EXPRESSIONS

The magnitude of the open-circuit voltage, V_{oc}, is determined by the Seebeck coefficient, S, and the temperature difference and it is expressed as:

$$V_{oc} = S\,(T_h - T_c) = S\,\Delta T \quad (1)$$

In the absence of heat loss, the efficiency of TEG is defined as the ratio between the output power P delivered by the load resistance R_L and the thermal power absorbed on the hot side Q, that is:

$$\eta = \frac{P}{Q} \quad (2)$$

The output power supplied to the load is defined as follows:

$$P = S\,I\,\Delta T - Ri\,I^2 = R_L I^2 \quad (3)$$

where, R_L and Ri, represent the load resistance and the internal resistance, respectively. In Eq.(3) the output power can be optimized by acting on the load resistance, which is connected to the output current I given by:

$$I = \frac{S\,\Delta T}{Ri+R_L} \quad (4)$$

then we can rewrite Eq.(3) as follows:

$$P = R_L \frac{(S\,\Delta T)^2}{(Ri+R_L)^2} \propto (\Delta T)^2 \quad (5)$$

The absorbed thermal power Q, is the sum of the heat flow, the Seebeck effect and the Joule effect:

$$Q = (S_p - S_n)\,I\,T_h + k\,\Delta T - \frac{RI^2}{2} \quad (6)$$

The input heat power (q) per unit area (A) is given by:

$$q = \frac{Q}{A} \quad (7)$$

The total Seebeck coefficient, S, the total internal electrical resistance, R_i ,and the total thermal conductance, K, of the TEG can be expressed respectively as:

$$S = N(S_p - S_n) \quad (8)$$

$$R_i = N\left(\frac{1}{\sigma_p} + \frac{1}{\sigma_n}\right)\frac{L}{A} \quad (9)$$

$$K = N(k_p + k_n)\frac{A}{L} \quad (10)$$

here, σ and k are the electric and thermal conductivity of each p and n semiconductor material respectively. While L is the length and N is the number of pairs of TE elements.

IV. NUMERICAL SIMULATIONS

Thermoelectric behavior of the unsteady-state governing equations which couple heat transfer and current density continuity is described by the following equations [16]:

Conservation of heat energy:

$$\varrho C_p \frac{\delta T}{\delta t} + \nabla . q = Q_j \quad (11)$$

Conservation of electrical current:

$$\nabla . J = \frac{\delta \rho_c}{\delta t} \quad (12)$$

where ρ, density; C_p, heat capacity; T, temperature; t, time; q, heat flux; Q_j, Joule heat source; J, flux of the electric current and ρ_c, charge density. These equations are coupled by the set of thermoelectric constitutive equations:

$$q = -K\nabla T + P'J \quad (13)$$

$$J = -\sigma(\nabla V + S\nabla T) \quad (14)$$

here S and P' are the Seebeck and Peltier coefficients, respectively. Where P' takes into account the Peltier effect as a result of the heat absorbed or realized when an electric current crosses the junction and it is expressed as:

$$P' = S\,T \quad (15)$$

Some other quantities of relevance are the electric field, E, and the Joule heat source, Q_j:

$$E = -\nabla V \quad (16)$$

$$Q_j = J\,E \quad (17)$$

ISSN: 2961-6611

From Eqs. (13-17), we can rewrite Eqs. (11) and (12) as:

$$\rho C_p \frac{\delta T}{\delta t} + \nabla\left(-K \nabla T + S T\left(-\sigma \nabla V - \sigma S \nabla T\right)\right) = -\sigma(\nabla V + S\nabla T)(-\nabla V) \quad (18)$$

$$-\sigma(\nabla^2 V + S\nabla^2 T) = \frac{\delta \rho_c}{\delta t} \quad (19)$$

Finite element simulations on 3D geometries of the rectangular (∏-TEG) and trapezoidal (T-TEG) TEGs using COMSOL Multiphysics has been carried out. The input heat flux is applied to the hot side, the temperature of which is T_h. The temperature of the cold side is held at the desired constant uniform temperature (T_C). One side of the thermo-element leg pair is electrically grounded to provide a voltage reference, while the other leg is supplied with a variable voltage. Once, the circuit is closed by an external load resistance a direct current flowing through the device. This is the process that the TE generator converts thermal energy into electrical energy directly through the temperature difference at the ends of the TE elements.

V. RESULTS AND DISCUSSION

In this study, we are interested to evaluate the effect of leg geometric shape and dimensions on the performance of TEG under periodic heat flux. The cold side temperature is fixed at 303 K (ΔT = 80 K). The time average of the rectangular pulsed heat flux which is equivalent to the heat flux under a constant heat source is maintained at 0.05 W/mm^2 for a time period of 1000 s and 10 % duty cycle (Fig. 2). Indeed, the duty cycle is the proportion of time during which the device is operated, it represents the ratio between operating time and period time.

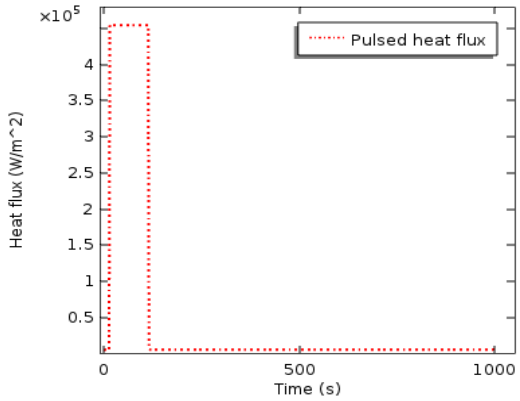

Fig. 2. Heat flux pulses for <q> = 0.05 W/mm^2

Therefore, the output power of a TEG can be optimized by balancing the internal and external resistances. As shown in Fig.3, the output power for ∏-TEG and T-TEG with TE legs of 1.7 mm in height, first increases when the load resistance is increased to attain its parabolic peak value and then decreases with further increase in R_L. The load resistance corresponding to the peak output power is the internal resistance of the device. It can be observed that the output power for the T-TEG is higher than that for the ∏-TEG, indeed the maximum power increase is 0.44 W. The maximum output power of 4.12 W for the T-TEG corresponds to its parabolic peak where it is 3.68 W for the ∏-TEG.

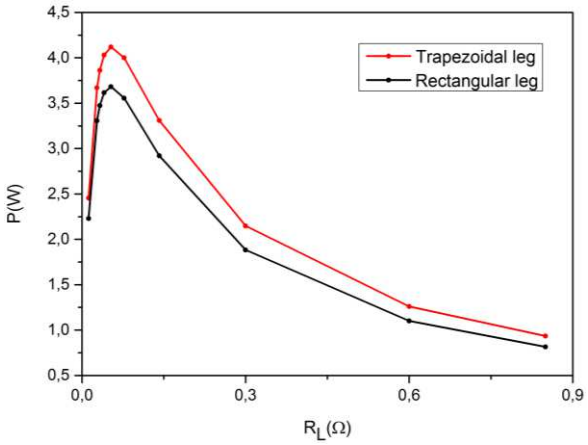

Fig. 3. Output power versus load resistance for <q> = 0.05 W/mm^2

Fig.4 shows the variation of the output voltage with the electric current for the case of ∏-TEG and T-TEG. It can be observed that, for the T-TEG, the induced voltage decreases with the increase of the output current and it is higher than that in the case of ∏-TEG. The output voltage is maximal when the circuit is open; no current is drawn by the load. Indeed, for the T-TEG, the open circuit voltage V_{OC} achieves 0.33 V which is better than 0.31 V attained in the case of ∏-TEG. Once the load is applied, the V_{OC} decreases linearly. When the TEG terminals are shorted together, short-circuit current I_{SC} = 6.2 A is obtained from the T-TEG, and it is greater than I_{SC} = 5.9 A for ∏-TEG. The absolute value of U–I slope corresponds to the internal resistance of the device.

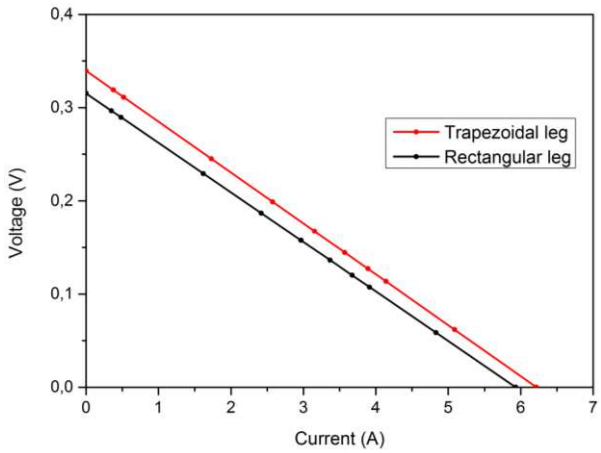

Fig. 4. Current-voltage characteristics for <q> = 0.05 W/mm^2

Fig. 5 shows the output power vs. time for a pulsed heat flux of 0.05W/mm^2. The instant output power achieved in the case of T-TEG is higher than the output power of ∏-TEG. In Fig.5 the difference between the two geometric configurations is the improvement over the case of rectangular TEG.

ISSN: 2961-6611

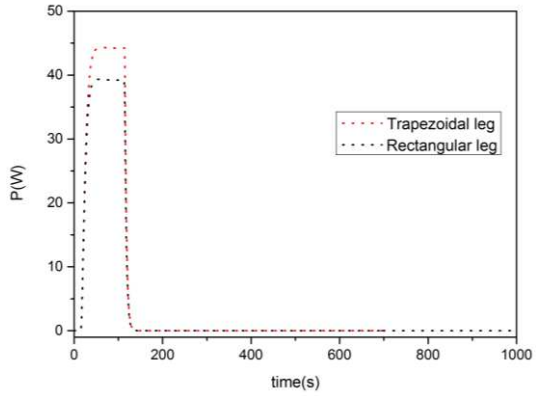

Fig. 5. Output power for <q> = 0.05 W/mm^2

Looking at Fig. 6 (a), it can be seen that with increasing leg length in the range of 1.7 to 4 mm, the output power for ∏-TEG and T-TEG increases from 3.68 W to 7.6 W and from 4.12 W to 7.88 W for ∏-TEG and T-TEG, respectively. It can be observed, for a given value of L, that the output power for T-TEG is higher than that for ∏-TEG. This enhancement can be explained in context of Fig. 6 (b) where the hot side temperature which increases linearly with leg length, is higher in the case of T-TEG than that of ∏-TEG. This increases the temperature difference between the hot side and the cold side and therefore enhances the output power according to Eq. (5).

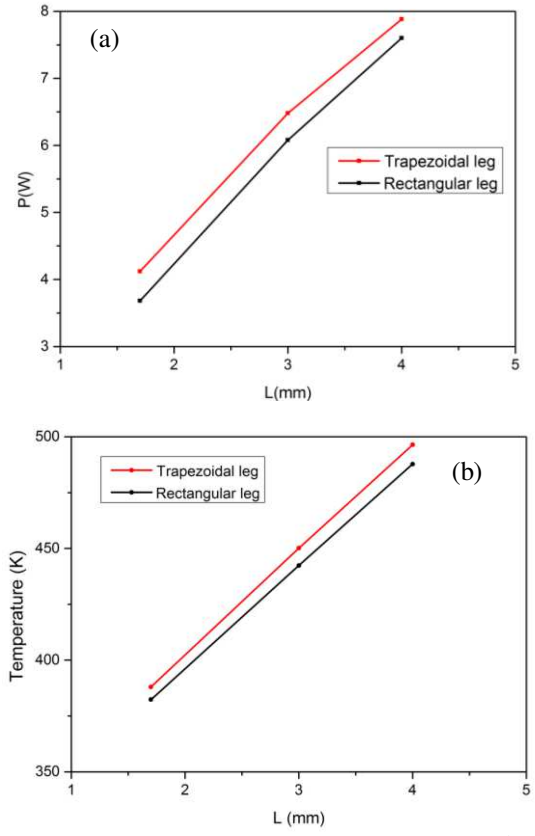

Fig. 6. (a) Output power and (b) Temperature for <q> = 0.05 W/mm^2

VI. Conclusions

The output power versus load resistance, the current and the voltage under periodic heating were studied for two geometric configurations of TEGs (rectangular (∏-TEG) and trapezoidal (T-TEG)). Therefore, the maximum output power was achieved at a load resistance corresponding to the internal resistance of the device and for T-TEG. The effect of leg dimensions on the output power of ∏-TEG and T-TEG was evaluated for three leg heights of 1.7, 3 and 4 mm. The results showed an improvement of thermoelectric performance of T-TEG for the three heights considered which is due to the increase of the temperature difference between the hot side and the cold side. Hence, this result can facilitate the design and conception of TEGs.

References

[1] J. Chen, C. Wu, “Analysis on the performance of a thermoelectric generator,” J. Energy Resour. Technol., vol. 122 (2), p. 61, 2000.
[2] L. E. Bell, “Cooling, heating, generating power, and recovering waste heat with thermoelectric systems,” Science, vol. 321 (5895), pp. 1457–61, 2008.
[3] D. M. Rowe, G. Min, “Design theory of thermoelectric modules for electrical power generation,” IEE Proc. Sci. Meas. Technol., vol. 143, pp.3521–4356, 1996.
[4] L. H. Fan, G. B. Zhang, R. F. Wang, K. Jiao, “ A comprehensive and time-efficient model for determination of thermoelectric generator length and cross-section area,” Energy Conversion and Management, vol. 122, pp.85–94, 2016.
[5] He Hailong, Y. Wu, W. Liu, M. Rong, Z. Fang, X. Tang, “Comprehensive modeling for geometric optimization of a thermoelectric generator module,” Energy Conversion and Management, vol. 183, pp. 645–659, 2019.
[6] L. Fan , G. Zhang, R. Wang, K. Jiao, “A comprehensive and time-efficient model for determination of thermoelectric generator length and cross-section area,” Energy Conversion and Management, vol. 122, pp. 85–94, 2016.
[7] A. Fabián-Mijangos , G. Min, J. Alvarez-Quintana, “Enhanced performance thermoelectric module having asymmetrical legs,” Energy Conversion and Management, vol. 148, 2017.
[8] R. Lamba, S.C. Kaushik, “ Thermodynamic analysis of thermoelectric generator including influence of Thomson effect and leg geometry configuration,” Energy Conversion and Management, vol. 144, pp. 388–398, 2017.
[9] U. Erturun, K. Erermis , K. Mossi, “Effect of various leg geometries on thermo-mechanical and power generation performance of thermoelectric devices,” Applied Thermal Engineering, vol. 73, pp. 1372-1381, 2014.
[10] Brito, “Analysis of the effect of module thickness reduction on thermoelectric generator output,” J. Electron Mater, vol. 45(3), pp. 1711–29, 2016.
[11] A. Montecucco, J. R. Buckle, A. R. Knox,“ Solution to the 1D unsteady heat conduction equation with internal Joule heat generation for thermoelectric devices,” Appl. Therm. Eng., vol. 35, pp. 177-84, 2012.
[12] L. Chen, J. Lee, “ Effect of pulsed heat power on the thermal and electrical performances of a thermoelectric generator,”Appl. Energy, vol. 150, pp. 138-149, 2015.
[13] X. D. Jia, Yu. J. Wang, Y. W. Gao, “Numerical simulation of thermoelectric performance of linear-shaped thermoelectric generators under transient heat supply, ”Energy, doi:10.1016/j. energy. 2017. 04. 072.
[14] D. M Rowe, CRC handbook of thermoelectric, Boca Raton (FL) CRC Press, 1995.
[15] H. J. Goldsmid, Introduction to thermoelectricity, New York Springer, 2010.
[16] Comsol Release 5.3 Documentation, COMSOL Inc., 2017.

ISSN: 2961-6611

ISSN: 2961-6611

EFFECT of ORGANOCLAY on the THERMAL and DIELECTRICPROPERTIES of POLYPROPYLENE NANOCOMPOSITES

L. Ben Ammar, S. TAKTAK and S. Fakhfakh
LaMaCop, faculty of sciences of Sfax,
University of Sfax, BP 1171, C.P 3000 Sfax, Tunisia

latifabenammar@gmail.com

Abstract :In this work, thermal and dielectric properties of polypropylene (PP) and PP based nanocomposites, filled with 2% and 6% by weight of Cloisite 20A natural montmorillonite clay platelets was studied. Thermal properties were examined using differential scanning calorimetry (DSC). The dielectric permittivity ε' and loss factor ε'' of PP and PP nanocomposites (PNCs), was investigated using broadband dielectric spectroscopy from 10^{-1} to 10^{6} Hz and at high temperatures between 90 and 120 °C. The nanocomposites show increased of the dielectric permittivity and loss factor compared with unfilled PP, attributed to the appearance of two thermally activated relaxation processes in this frequency range : a low-frequency relaxation that can be attributed to an interfacial process MWS and a high frequency relaxation that is related to and ac-relaxation related to crystalline or para crystalline domain . In order to probe matrix/oraganoclay interface properties, dielectric strength of the interfacial polarization Δε is calculated by fitting the dielectric permittivity through the known Havriliak–Negami model. Calculation of the activation energy for the different processes revealed that both relaxation were suitably fitted with the Arrhenius law

Keywords— **polypropylene , nanocomposites , oraganooclay, thermal and dielectric**

I. INTRODUCTION

Polymer nanocomposites with better dielectric and electrical insulation properties are steadily appear as excellent functional materials for dielectric and electrical insulation application and the term "nanodielectrics" for such material is progressively becoming popular. Although , for several decades , the technology of addition of additives, agents and fillers are often used for improving dielectric properties has been in existence [1-3]. However , nanosized fillers with large specific surface area may form large interfacial zones in the nanocomposite, it is supposed that the interface may be the key and dominate the electrical properties of the nanocomposite.

polymeric insulating materials such as polypropylene (PP), with considerable high breakdown strength and relatively low dielectric losses [4, 5], has manifested itself as the dominant dielectric materials for power capacitors. Meanwhile, PP has drawn more and more attention to the application of power cable and cable accessories since it is easy-processing and more environmentally friendly [6,7] . In recent studies it has reported that loading PP with small quantities of nanoclays can enhance the dielectric properties of the composites , such as space charge accumulation , electrical conductivity , dielectric strength and partial discharge [8,9].considerably little work has been carried out examining the dielectric behaviour of polymer nanocomposites involving nanoclays. Therefore, many aspects in terms of insulation are not well known and should be extensively investigated.

In fact in our previous work , the space charge and conductivity evolution in the PP filled with different concentrations natural clay were reported. We exhibit that the interfaces between nanoparticles and surrounding medium play major role in controlling the carrier transport through PNCs [10].

In this paper, thermal and dielectric properties of Polypropylene (PP) and PP containing different amounts of nanoparticles of organoclay (2% and 6% by weight) were studied . Differential scanning calorimeter (DSC) was used to detect the melting and crystallization behavior of the samples. Next, the dielectric permittivity ε' and loss factor ε" of PP and Polymer nancomposites (PNCs) was investigated using a Novocontrol dielectric spectrometer in the frequency range 10^{-1} to 10^{6} Hz

ISSN: 2961-6611

at high temperatures 90, 95, 100,105, 110,115 and 120 °C.

II. Materials and Methods

A. Materials

All the samples were supplied from the project VAMAS (The Versailles Project on Advanced Materials and Standards) [11]. They are unfilled base PP and its PNCs containing 2 and 6wt% of clay nanofillers (Southern Clay Products Cloisite 20A), which are called PP0%, PP 2%, and PP6 %. Cloisite 20A (montmorillonite: MMT) is a natural clay phyllosilicate belonging to the smectite family. Its chemical composition is $[Si_4\ O_{10}\ Al^{3+}{}_{(2-x)}\ Mg^{2+}{}_x(OH)_2]$ and is intercalated with di-methyl dihydrogenated tallow. The polymer matrix (PP0%) is a thermoplastic semi-crystalline belonging to the family of polyolefin polymer. Its chemical formula is of the form - [CH2-CHB]n-, where in B is a methyl group.

B. Experimental Methods

Perklin-Elmer 4000 DSC was used to determine the effect of the nanoclay reinforcement on the thermal properties of the samples; the measurements were performed on 10–12 mg samples under nitrogen atmosphere.

Dielectric relaxation spectroscopy experiments were carried out using a Novocontrol alpha-N in the 10^{-1} to 10^6 Hz frequency domain at temperatures of 90, 95, 100, 105, 110°,115° and 120 °C. The temperature was controlled using a Novotherm system with a stability of 0.5◦ C.

The complex dielectric permittivity is given by Eq 1:

$$\varepsilon^*(\omega) = \varepsilon'(\omega) - i\varepsilon''(\omega) \qquad \text{Eq(1)}$$

where ε'(ω) represents the real part, ε"(ω) represents the imaginary part, and ω = 2πf represents the angular frequency.

The experimental dielectric data can be fitted into the Havrilialk-Negami equation as shown below [12,13]:

$$\varepsilon^*(\omega) = -j\left(\frac{\sigma_{dc}}{\varepsilon_0\omega}\right)^N + \sum_{i=1}^{n}\left(\varepsilon_{i\infty} + \frac{\Delta\varepsilon_i}{\left[1+(j\omega\tau_i)^{\alpha_i}\right]}\right) \qquad \text{Eq(2)}$$

where i is the number of the relaxation process, $\Delta\varepsilon = \varepsilon_s - \varepsilon_\infty$ the dielectric relaxation strength, εs is the real permittivity at $\omega \to 0$ and ε∞ is the real permittivity at $\omega \to \infty$, τ is the relaxation time, α and β are HN shape parameters (0 < α, β < 1). The term $j\left(\frac{\sigma_{dc}}{\varepsilon_0\omega}\right)^N$ is the dc conductivity term where ε0 is the permittivity of free space, σdc is the dc conductivity and N is a fractional exponent.

III. Results and Discussion

A. Thermal Properties

DSC is a technique used to study thermal properties of material , Fig. 1.(a and b) shows DSC curves of PP/clay nanocomposites and pure PP, and Table 1 lists the data of thermal properties of PP/clay nanocomposites. It can been seen in Fig. 1.(a and b) and Table 1 that the melting temperature (Tm) of neat PP is 162.75 °C and increases slightly to 163.33 °C by adding 6% of nanoclay to PP matrix. However, the Tc increases also lightly with content of nanoclays (Fig. 1b.). Therefore, the glass temperature Tg, for neat PP is located at -8 °C and increases significantly with nanoclays rate.

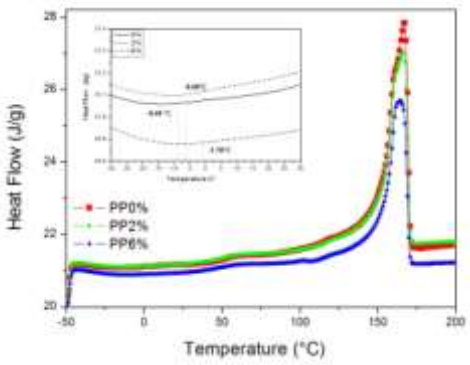

(a)

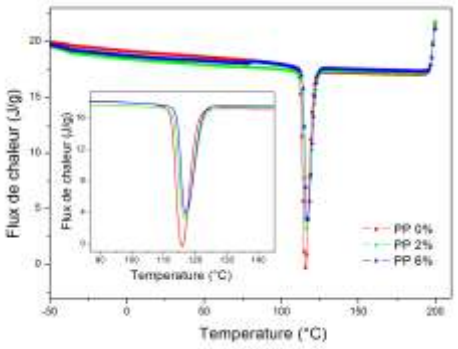

(b)

Fig. 1 DSC cooling (a) and melting (b) thermograms of PP0%, PP2% and PP6%. The inset in (a) is an enlarged view around Tg.

Sample	T_g (°C)	T_m (°C)	T_C (°C)	ΔH_m	χ_c
PP0%	-8.48	162.72	116.16	87.48	41.85
PP2%	-6.68	163.25	116.92	86.96	42.45
PP6%	-1.78	163.33	117.25	90.74	46.18

TABLE 1 DSC RESULTS OF PP0%, PP2% AND PP6%.

From Table 1, it can be noticed that the crystallinity degree χc of PP0% increases when the nanoclay particles are added. The rise in PP crystallinity suggests that the added clay in the polymer matrix has a nucleation effect [14]. On the other hand; the increase in glass transition temperature of PNCs over base polymer might suggest that a reduction in polymer chain mobility

ISSN: 2961-6611

occurs in the interaction zone contributing to the reduction in polymer chain relaxation.

B. Dielectric Spectroscopy

1) Different relaxation processes: Polyepropylene (PP) is classified as a nonpolar polymer with low dielectric permittivity. In general, this type of material exhibits no notable or significant ionic, interfacial, or dipolar polarization, being characterized by low flat dielectric losses. Fig. 2(a) and 2 (b) show respectively real (ε') and imaginary (ε") parts of the permittivity for the unfilled PP vs. frequency at different temperatures. As expected , no relaxation process is seen neither in the imaginary or the real part. The slight decrease in the (ε') values upon temperature increasing can be attributed to changes in the local density due to onset of melting as well as due to water evaporation at elevated temperatures [15].

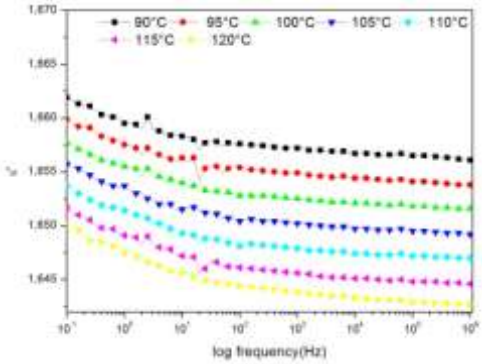

(a)

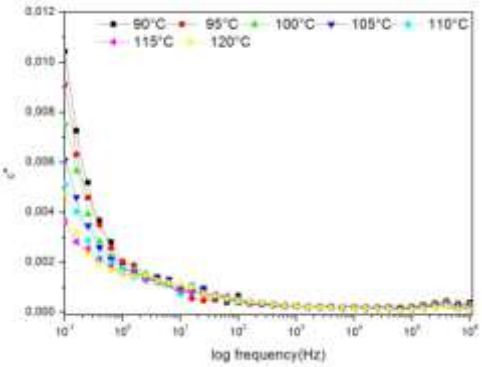

(b)

Fig. 2 Relative permittivity ε' (a) and dielectric loss ε" (b) versus frequency at various temperatures observed for the neat PP blend.

Fig. 3a and 3b , Fig. 4a and 4b shows the temperature and frequency dependence of the real (ε') and imaginary (ε") parts of the dielectric permittivity for PNC PP2% and PP6% respectively.

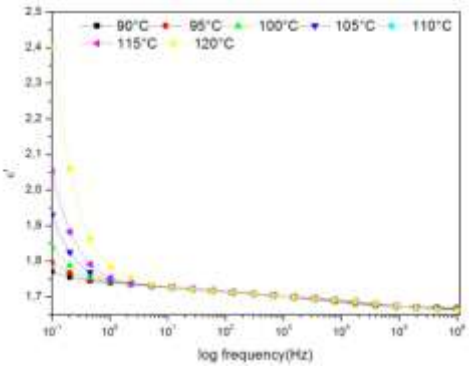

(a)

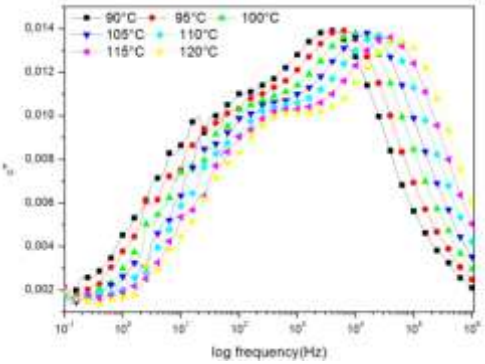

(b)

Fig. 3 Relative permittivity ε' (a) and dielectric loss ε"(b) for PP2% nanocomposites versus frequency at different temperatures.

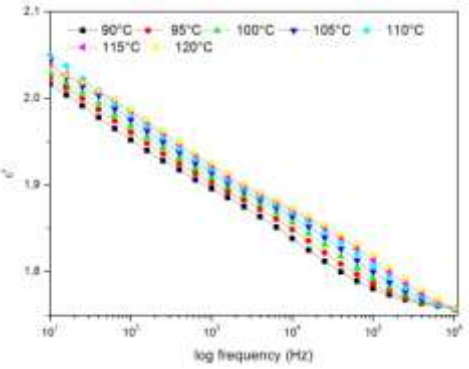

(a)

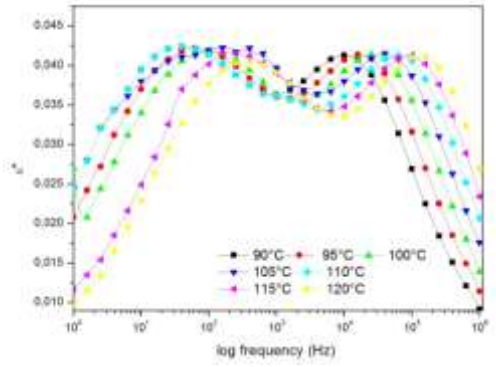

(b)

ISSN: 2961-6611

Fig. 4 Relative permittivity ε' (a) and dielectric loss ε"(b) for PP2% nanocomposites versus frequency at different temperatures.

It is clearly seen that the nanoparticles load has a significant influence on the nanocomposite's properties. In fact, ε' values increase with the concentration of nanoclay. This can be explained by the multiplication of permanent dipoles' number, which will be aligned with the applied field direction, within the material.

Comparing with the host polymer PP , It is clear that the inclusion of nanoparticles of clay exhibited the apparition of two peak of dielectric relaxation. Additionally, we note that the intensity of this peak increase with increasing of nanoparticles. For both nanocomposites PP2% and PP6% , It can be seen that the relative permittivity ε' shows two sharp decreases (Fig. 3a and 4a), corresponding to the two peaks in the dielectric losses ε" (Fig. 3b. and 4b).

The first relaxation was detected at low frequency, and it is attributable to the Maxwell-Wagner-Sillars (MWS) relaxation, which is due to charge trapping at the interface between the nanofiller particles and the polymer[16].The relaxation of MWS type is generally located at a lower frequency than observed here (less than 10 Hz) but it has been proposed that the nanoscale dimension of the interfaces present in these materials causes the shift of the loss factor peaks to higher frequencies [17,18]. Regarding the second peak, it is known that PP exhibits several relaxation processes, such as the α-relaxation linked to the glass transition, and α-relaxation related to crystalline or paracrystalline domains (indeed, PP is a semicrystalline polymer). These processes can be observed only through dynamic mechanical experiments [19] .

2) Havriliak and Negami analysis: In order to exploit the experimental results, the data have been adjusted analytically using empirical laws, with the objective of examining the mechanism of the different observable relaxations on the dielectric measurements. The dielectric permittivity data for each sample were collected and evaluated by the WinFit impedance analysis, which is a standard software package for the analytic evaluation of the dielectric spectra, using the well-known Havriliak–Negami (HN) function [13] given by equation (2)

So as, to carry out the deconvolution due to the overlapping processes, we fit the imaginary part of the dielectric permittivity basing on the HN function (Eq. 2). As an example of such fits, Fig. 5. reveals a separation of overlapping relaxation regions via the deconvolution of the imaginary part of the dielectric permittivity at 100 °C for the PNCs PP6%

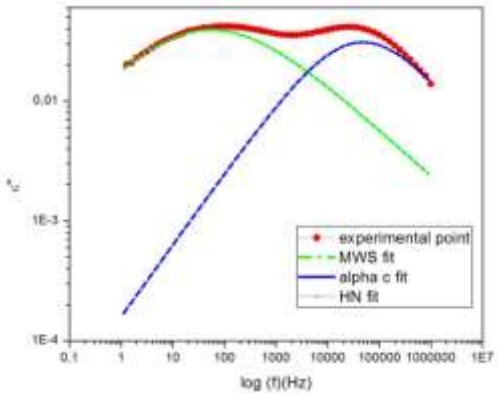

Fig.5 Imaginary part of dielectric permittivity versus frequency for the PP6% nanocomposite at 100°C.

The experimental data related to the dielectric loss ε" for both polymer nanocomposites were fitted into the Havrilialk- Negami function , and the optimum dielectric parameters as the parameters Δε, τ, α and β, for the αc and MWS relaxation, for PP2% and PP6% are shown in Table 2 and Table 3 respectively .

MWS				
Temperature(°C)	τ (10^{-2})(s)	$\Delta\varepsilon$(10^{-2})	α	β
90	1,33	4,45	0.78	0.29
95	1,6	5,46	0.58	0.38
100	0.854	4,36	0.71	0.42
105	0.314	4,41	0.56	0.7
110	0.143	4,19	0.52	0.86
115	0.0784	4,10	0.52	0,94
120	0.0945	4,65	0.51	0.7

α_C				
Temperature(°C)	τ (10^{-5}) (s)	$\Delta\varepsilon$ (10^{-2})	α	β
90	3.09	3.43	0.78	0.29
95	2.04	3.48	0.58	0.38
100	1.24	4.23	0.71	0.42
105	0.755	4.34	0.56	0.7
110	0.495	4,46	0.52	0.86
115	0.329	4,5	0.52	0,98
120	0.208	3.9	0.51	0.7

TABLE 2: OPTIMUM FIT PARAMETERS FOR MWS AND α_C RELAXATIONS OF PP2%

ISSN: 2961-6611

MWS				
Temperature(°C)	τ (10^{-2})(s)	Δε	α	β
90	1,471	0.252	0.47	0.63
95	0.7.33	0.257	0.45	0.62
100	0.4	0.253	0.43	0.74
105	0.27	0.257	0.47	0.29
110	0.17	0.240	0,95	0.171
115	0.0857	0.226	0.43	0,98
120	0.0569	0.217	0.43	0,93

α_C				
Temperature(°C)	τ (10^{-6})(s)	Δε	α	β
90	8.84	0.101	0.65	0,99
95	6.88	0.009	0.71	0.84
100	4.2	0.102	0.68	0.86
105	2.8	0.104	0.44	0,98
110	1.91	0.109	0.68	0,98
115	1.18	0.120	0.64	0,95
120	1.08	0.122	0.67	0.84

TABLE 3: OPTIMUM FIT PARAMETERS FOR MWS AND α_C RELAXATIONS OF PP6%

As we can see in both table ; The symmetrical shape parameter alpha and the parameter beta describing the asymmetry of the relaxation are both strictly lower than 1. Thus, both relaxation are not attributed to a simple process of Debye type; it is rather a Havriliak and Negami behavior.

As observed from Fig. 3b and 4b ,the peaks of the relaxation processes presented in both nanocomposites PP2% and PP6% were shifted to higher frequencies as the temperature was increased. The increase in the characteristic frequency means shorter relaxation time ($\tau = 1/f_{max}$) (see tables 2 and 3). This is compatible with an increase in the mobility of charge carriers [16]. Additionally, this change shows that the relaxation processes exhibited thermal activation behavior.

On the other hand , In order to have an idea about nanoparticles/matrix interfacial adhesion [20]. The dielectric relaxation strength of MWS polarization PP2% and PP6% $\Delta\varepsilon_{MWS}$ is calculated by fitting the dielectric permittivity through the HN model (Eq. 2). The obtained values are summarizes in Table 2 and 3. As it can be seen, MWS relaxation strength $\Delta\varepsilon_{MWS}$ increase with the reinforcement content. This can result from the increase of the number of polarized dipoles trapped in the nanoparticles /matrix interfaces.

3)Arrhenius analysis: It is informative to examine the temperature dependence of the two relaxation times for both nanocomposites PP2% and PP6%. The characteristic relaxation time τ_{max} of αc relaxation and MWS relaxation, obtained from the maximum of ε″ (Fig.3b , Fig.4b) for both nanocomposites PP2% and PP6%, was determined and plotted versus the inverse of the temperature in Fig.6.(a,b) and Fig.7.(a,b) respectively. The temperature dependence of the loss peak position of αc and MWS relaxation, effect follows an Arrhenius type behavior, which can be expressed via the equation :

$$\tau(T) = \tau_0 \exp\left(\frac{-E_a}{K_\beta T}\right) \qquad \text{Eq(3)}$$

where τ represents the relaxation time , Ea represents the activation energy, and Kβ represents the Boltzmann constant.

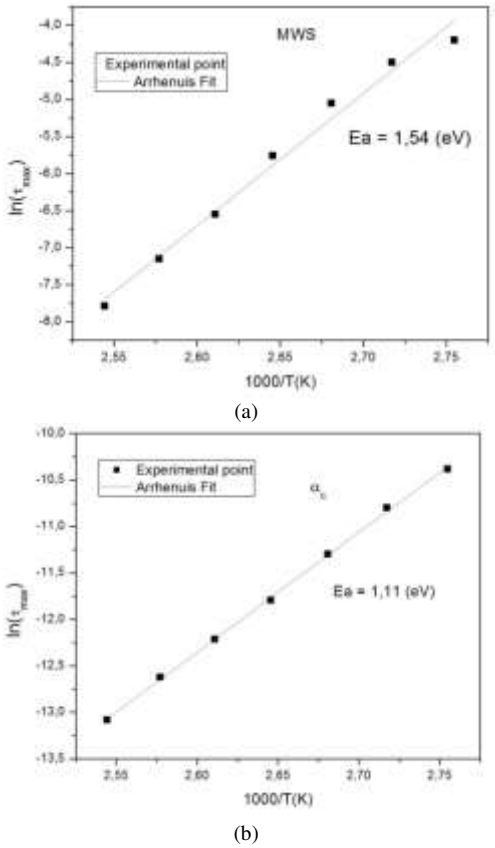

Fig. 6 Arrhenius diagram for the position of MWS(a) and αc relaxation (b) of PP2%

ISSN: 2961-6611

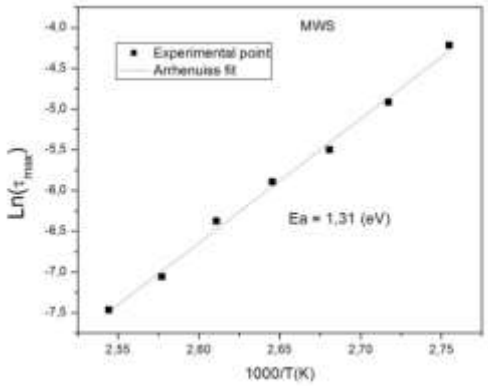

(a)

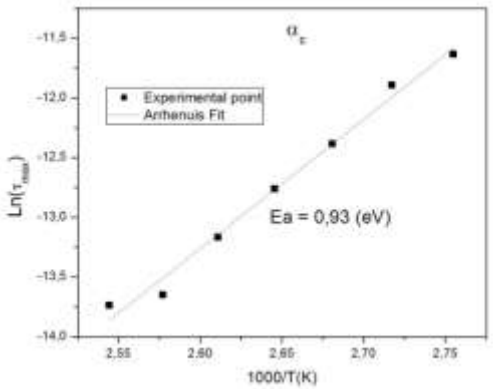

(b)

Fig. 7 Arrhenius diagram for the position of MWS (a) and αc relaxation (b) of PP6%

The activation energy values for different samples are summarized in Table 4.

Sample	Ea MWS (eV)	Ea αc (eV)
PP2%	1.55	1.11
PP6%	1.3	0.93

TABLE 4. ACTIVATION ENERGIES E_A (EA) FOR PP2% AND PP6%

We note that for both relaxation , PP2% has the greatest value of activation energy ; this due of the fact that the activation energy decreases as the number of free charge increases and the ability of the material to be polarized is favored [21].

V. CONCLUSION

Thermal and dielectric properties of polypropylene and PP /organo clay nanocomposites have been investigated . DSC results showed that the crystallinity of PNCs increases with the nanoclay concentration. No relaxation processes were observed in the neat PP, while The presence of nanoparticules of clay increases the dielectric permittivity at low frequencies. Two thermally activated dielectric relaxation processes are observed and attributed to interfacial polarization (MWS polarization) and αc-relaxation related to crystalline or para crystalline domain. The interface properties were investigated by the calculation of the strength parameter $\Delta\varepsilon_{MWS}$. It was found that $\Delta\varepsilon_{MWS}$ increases with nanoparticles of clay amounts as a result of the increase of the number of polarized dipoles trapped in the interfaces.

The further studies would be carried out in the area of some other dielectric properties such as the measurement of resistivity and the evaluation of insulation aging, together with the research in mechanical properties

ACKNOWLEDGEMENTS

The authors thank Pr M. Abou-Dakka from National Research Council Canada for providing samples and for discussions on the effect of nanoclay concentration level.

REFERENCES

[1] F. Carmona, "Conducting Filled Polymers, "*Physica A*, 461-469 ,1989.

[2]. Y. Bai, Z. Y. Cheng, V. Bharti, H. S. Xu and Q.M. Zhang, "High dielectric-constant ceramic powder polymer composites," *Appl. Phys. Letters*, 3804-3806 ,2000,

[3].M. M. Ueki and M. Zanin, "Influence of additives on the dielectric strength of High-densityPolyehtylene, "*IEEE Trans. Dielectr. Electr. Insul*, 876-881,1999.

[4] E. Ildstad, T.Haave, "Conduction and partial discharge activity in HVDC cable insulation of lapped polypropylene films". *IEEE Int. Conf. on Solid Dielectrics, Eindhoven*, 137–140, 2001.

[5] C.L.Wu, M.Q. Zhang, M.Z.Rong, et al, "Tensile performance improvement of low nanoparticles filled-polypropylene composites", Compos. Sci. Technol, 1327–1340,2002.

[6] P.Maiti, And M. Okamoto, et al "Influence of crystallization on intercalation, morphology, and mechanical properties of polypropylene/clay nanocomposites", *Macromolecules*, 2042–2049, 2002.

[7] W.Cao, Z. Li, G. Sheng, et al "Insulating property of polypropylene nanocomposites filled with nano-MgO of different concentration", *IEEE Trans. Dielectr. Electr. Insul*, 1430–1437,2017.

[8] M. Abou-Dakka, Y. Chen, "Effect of Reverse Polarity on Space Charge Evolution in Polypropylene with Different Concentration of Natural and Synthetic Nano Clay", *In Proceedings of the IEEE Conference on Electrical Insulation and Dielectric Phenomena, Shenzhen*, 671–675, 2013.

[9] A.Bulinski,.S.S.Bamji , M. Abou Dakka and Y,Chen, "Dielctric properties of polypropylene containing synthetic and natural organoclay. *In IEEE International Symposium on electrical Insulation IEEE*, 2010.

.

[10] L. Ben Ammar, S. Fakhfakh, O, Jbara, S. Rondot, "Effect of nanoclayconcentration level on the electrical properties of polypropylene underelectron irradiation in a SEM", *Journal of Microscopy*,.1–13, 2016.

[11] http://www.scprod.com/product bulletins/PB%20Cloisite% 2020A.pdf

[12]. S. Havriliak, S. Negami, "A complex plane analysis of α-dispersions in some polymersystems," *Polym. Sci. C.*, 14, 99,1966.

[13] S. Havriliak, S. Negami, "A complex plane representation of dielectric and mechanical relaxation processes in some polymers," *Polymer 8*, 161-210, 1967.

ISSN: 2961-6611

[14] Y. Li, C. Han and J. Bian, “Crystallization and morphology studies of biodegradable poly(e-caprolactone)/silica nanocomposites”, *Polymer Composites*, 131–140, 2013

[15] V. Tomer, G. Polizos, C. A. Randall, and E. Manias, “Polyethylene nanocomposite dielectrics: implications of nanofiller orientation on high field properties and energy storage,” *Journal of Applied Physics*,1-11 , 2011.

[16] L.Ben Ammar, S. Fakhfakh, O. Jbara, S. Rondot, and al.,"Study of temperature effects on the electrical behavior of polypropylene-clay nanocomposites submitted to electron beam irradiation in a SEM", *Micron*, 39 – 48, 2017.

[17] S. George, K. T. Varughese, and S. Thomas, “Dielectric properties of isotactic polypropylene/nitrile rubber blends: Effects of blend ratio, filler addition, and dynamic vulcanization”, *Journal of Applied Polymer Science*, 255-270, 1999.

[18] T. Umemura, T. Suziki, and T. Kashiwazaki, “Impurity effect of the dielectric properties of isotactic polypropylene”, *IEEE Dielectrics and Electrical Insulation Society*, 300-305, 1982

[19] M. Amhid, D. Mary, G. Teyssedre, C. Laurent , G. C. Montanari, D. Kaempfer et al., "Effect of Filler Concentration on Dielectric Behaviour and on Charge Trapping in PP/clay Nanocomposites", *The 17th Annual Meeting of the IEEE Lasers and Electro-Optics Society*, 2004.

[20] A. Ladhar, M. Arous, H. Kaddami, Z. Ayadi, A. Kallel, "Correlation between the dielectric and the mechanical behavior of cellulose nanocomposites extracted from the rachis of the date palm tree," *Materials Science and engineering*, 2017

[21] H, Douiri , N, Ghorbel, M,Raihane, et al " Effect of Clay on the Dielectric Properties of Novel Fluorinated Methacrylate Nanocomposites," *polymer composites* , 2018

ISSN: 2961-6611

Production of High quality of TiO_2 -NTs for solar cells application

Djedjiga. Hatem [1], Henia. Fraoucene [1], Mohammed Said Belkaid [1], Florence. Vacandio [2], Marcel. Pasquinelli [3#]First-T1. Laboratory of Advanced Technologies of Genie Electrics (LATAGE), Faculty of Electrical and Computer Engineering Mouloud Mammeri University (UMMTO), BP 17 RP 15000, Tizi-Ouzou, Algeria

2. Laboratory MADIREL (UMR 7246), University of Provence, St Jérôme Center, Traverse Susini, 13397 Marseille Cedex 20, France

3. Institute of Microelectronic Materials Nanosciences of Provence (IM2NP), Optoelectronics and photovoltaics (OPTO-PV) team, University of Provence, St Jérôme Center, Traverse Susini, 13397 Marseille Cedex 20, France
Address Including Country Name

[1]djedjiga.hatem@ummto.dz

[2]belkaidms@yahoo.fr

Abstract— **One-dimensional titanium dioxide (TiO_2) nanotubes (TiO_2NTs) have attracted great interest over the past few years to be used in optoelectronic applications . The present paper gives an overview of the formation process via electrochemical anodizing method in fluorinated electrolyte of a titanium self ordered nanotubes . This article gives the essentials factors affecting the growth of TiO_2 nanotubes and its morphological parameters such as applied voltage, electrolyte type, anodizing time and fluoride concentration.**

Keywords— **TiO2 nanotubes, electrochemical anodizing, solar cells application, thin films.**

I. INTRODUCTION

In recent years, nanostructured materials have acquired great intent because of their many properties that make it an active component in several applications such as: photocatalysis [1], photovoltaics [2, 3], biological coatings [4], sensors and micro-battery [5, 6]. Studies have indicated that for photovoltaic applications, highly ordered Titanium dioxide (TiO_2) nanotubes (NTs) are required. Their great importance is due to their one-dimensional (1D) nature, ease of handling, and simple preparation.

The concept of a vector electron transfer through an electrode based on TiO_2 NTs allows faster charge transfert. The nanotubular structure of TiO_2 is a direct path for the electron passing from the active layer to the electrode unlike the porous network in which the path taken by the electron is random and longer. The advantage that nanotubes have over the porous layer was demonstrated by Jennings et al. The electron diffusion length in solar cell based on nanotubular structure is close to 100 µm, which is much higher than conventional solar cells. All photogenerated charges are collected which induces a very low rate of recombination rate [7]

The geometrical parameters of the TiO_2 NTs such as the length and the diameter of the tubes making it possible to improve the optical properties. In addition, the increase in number of reaction sites provides a larger specific surface area for photon absorption in solar cells. The anodizing approach can build highly ordered titanium dioxyde nanotubes (TiO_2 NTs) with controllable geometrical parameters by varying the anodization parameters. Assefpour-Dezfuly. in 1984 [8] and Zwilling et al. in 1999 [9], were the first reported the formation of TiO_2 porous films by anodization of Ti foil in chromic acid (CA) (0.5 mol l^{-1} Cr_2O_3) solution with and without hydrofluoric acid (HF) ($9.5*10^{-2}$ mol 1^{-l}). A decade later, Grimes et al. [10] first reported formation of uniform titania nanotubes arrays via anodic oxidation of Ti foil in an hydrofluoric (HF) electrolyte. Recently, Schmuki group [11, 12] also reported the formation of long nanotubes during anodization of Ti in neutral fluoride solutions.

.

II. PARAMETERS INFLUENCING THE FORMATION OF TITANIUM DIOXIDE NANOTUBES

To form a defined TiO_2 nanotubes, electrochemical anodization was carried at room temperature . A two-electrode cell was used with a platinum plate as the counter electrode, separated from the working electrode (titanium foil) by 1.5 cm. Immediately after anodization, the samples were rinsed in ultrapure water to remove residual electrolyte for 10 minutes and then dried in an oven at 50 °C for 10 minutes. We have studied three factors affecting the morphology of TiO_2 NTs resulting from the anodization process, which are : the applied voltage, the anodizing time and the electrolyte type.

A. The effect of applied voltage

ISSN: 2961-6611

To investigate the influence of the applied voltage on the morphological parameters of TiO_2 nanotubes produced by anodizing of titanium foil, electrochemical anodization was carried at room temperature in ethylene glycol ($HOCH_2CH_2OH$, Sigma-Aldrich) solution containing 0.3 wt% Ammonium fluorides (NH_4F, Sigma-Aldrich) and 2wt % ultrapure water for three (03) hours at different anodization voltage (20,30, 40 and 60V). Figure1 shows top surface morphology of the TiO NTs prépared with various anodization voltage Through the SEM images of these films, we can clearly observe that the increase in anodization voltage leads to an increase in the diameter and in the wall thickness of the produced tubes. An average inner diameter of about 52 nm and 106 nm are obtained at 20V and 60V respectively. The applied potential determines the electric field strength across the oxide, which in turn affects the migration of the ions and ultimately determines the size of the NTs. Geometric characteristics of TiO_2 NTs produced at different anodization voltages are summarized in Table 1.Cummings et al [7] demonstrated the existence of a linear relationship between the applied potential and the diameter of the NTs is generally observed up to 60 V . This relation is described by the following equation

$$d\,[nm] = k \times V \quad (1)$$

where k equals 2×fg; fg being the growth factor for anodic oxides and typically between 2 and 2.5 nmV^{-1} for TiO_2 films .

B. The effect of aodization time

The anodization time is certainly a key parameter for the growth of TiO2 NTs. The tube lengths increase with time until a balance between the formation and dissolution of TiO2 occurs. After this point, the NTs length becomes independent of anodizing time [13]. In this part of our work we synthesized TiO2 NTs from anodization of Ti foil by varying the anodization time. Anodization experiments were carried out in ethylene glycol (HOCH2CH2OH, Sigma-Aldrich) solution containing 0.3 wt% Ammonium fluorides (NH4F, Sigma-Aldrich) and 2wt % ultrapure water solution at 60 V for different anodization time (1h, 2h, 3h and 4h) . By varying the anodization time respectively 1h, 2h, 3h and 4h the SEM images presented in Figure 2 show that only nonoporous TiO_2 films are obtained for the anodization time of 1 hour, The top morphology chanched abviously with increasing the reaction time and separated nanotubes are formed in the films anodized for 2 h and 3 h the thickness of walls is mainly changed with increasing anodisation time from 2h to 4h. This results confirmed that we can controll the morphologies parameters and the sizes of TiO NTs with adjusting the anodization time.

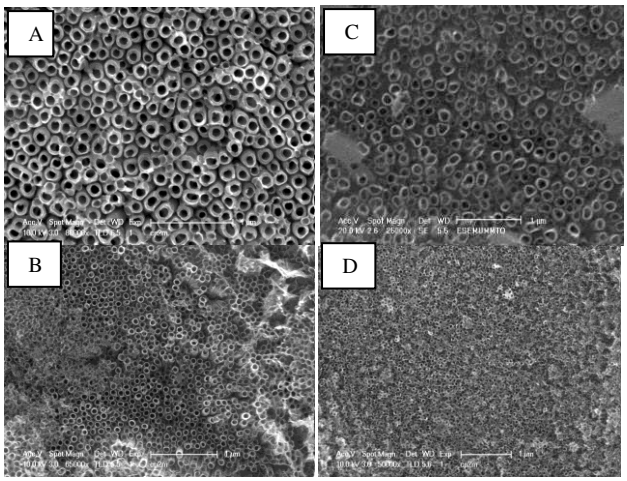

Fig. 1 SEM images of the TiO NTs prepared with 0.3% of NH4F for 3hours and atvarious anodization voltage, A: 60V, B: 40V, C:30V and D:20V

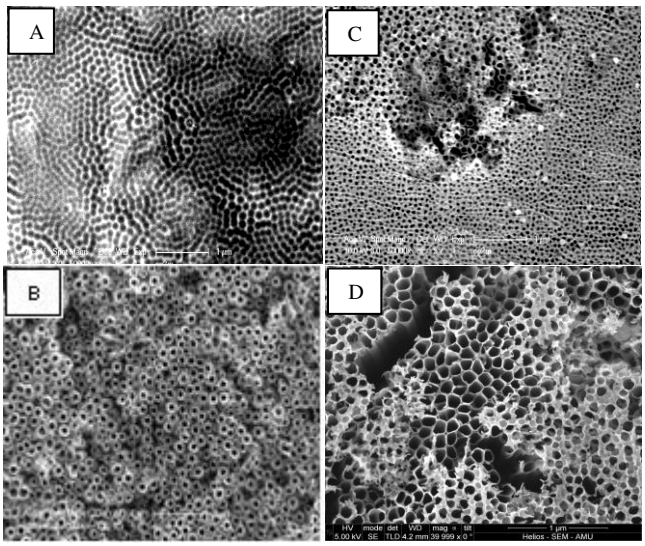

Fig. 2 SEM images of anodized samples at 60V in EG during: A) 1 h, B) 2 h, C) 3 h and D) 4 h

ISSN: 2961-6611

TABLE I
GEOMETRICAL CHARACTERISTICS OF NT TIO2 PRODUCED AT DIFFERENT ANODIZATION VOLTAGES

Voltage (V)	D_{int} (nm)	D_{ext} (nm)	w (nm)	x (nm)	L (µm)	φ (%)	P	n * 10^{23} (pores/cm²)	R	A_i*10^{-6} (cm²/cm²)
20	52	68	8	16	118	0,24	84	12,48	1 735,30	0,88
40	79	117	19	8	119	0,43	125	4,21	1 017,09	01,46
60	106	196	45	19	122	0,53	215	01,50	622,45	02,31

with: (Dint) is the inner diameter and (Dext) is the externe diameter, (w) the thickness of the walls, (x) the space between the nanotubes , (L) the length of nanotubes , (p) the periodicity, (φ) The fraction of the solid semiconductor covering the surface of TiO2, (n) the pore density, (Ai) the total surface area of a tube and (R) the aspect ratio

TABLE III
CHARACTERISTICS OF TiO_2 NTS DEPENDING ON ANODIZATION TIME

Time (h)	D_{int} (nm)	D_{ext} (nm)	w (nm)	x(nm)	φ (%)	P	n * 10^{23} (pores/cm²)
01	80	-	-	48	-	128	-
02	92	164	35	24	0,46	186	02,14
03	106	196	45	19	0,53	215	01,50
04	125	161	10	0,5	0,23	145	02,23

C. The effect of electrolyte type

Electrolytes containing F^- such as organic (or neutral) and aqueous electrolytes have been used for the synthesis of TiO_2 NTs. Four types of electrolytes were adopted to investigate the morphological properties of TiO_2 NTs based on organic and aqueous solutions: The prepared organic glycerol solution containing 1.3 wt% NH_4F and 2 wt% H_2O, and the second organic electrolyte is the Ethylene Glycol + 0,3wt% NH_4F +2wt% H_2O. For the aqueous solution we have used; the first solution based on Ammonium Sulfate (1M $(NH_4)_2SO_4$) and the second based on the Sodium Sulfate (1M Na_2SO_4) with two different fluoride concentration of 0.5 wt% and 1 wt%. For all experiences, the anodization time was varyed from 1 to 2 hour. Through SEM images presented in Figure 3 and Figure 4, the synthesis of TiO_2 nanotubes took place in the two organic solutions where the nanotubes are characterized by various morphological parameters summarized in Table 3 . The nanotubes formed in the ethylene glycol (EG) are characterized by a regular, orderly and uniform morphology with smooth and very thick walls (45nm) comparing with the tubes obtained in glycerol having small grains along the tube. This difference is due to the properties of ethylene glycol in terms of viscosity and the kinetics of the species present in the solution, EG is selected from the best organic solutions used to synthesize TiO_2 nanotubes.

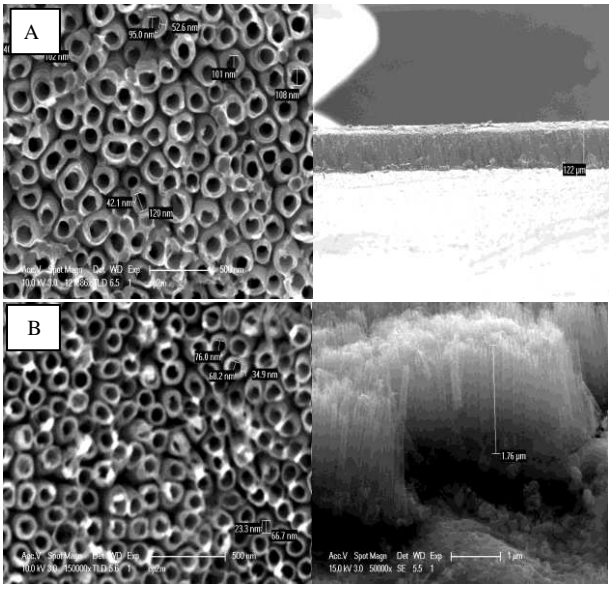

Fig. 3 SEM images of surfacic and transversal of samples anodized at 60V for 3h in A/ Ethylene glycol et B/ Glycerol

ISSN: 2961-6611

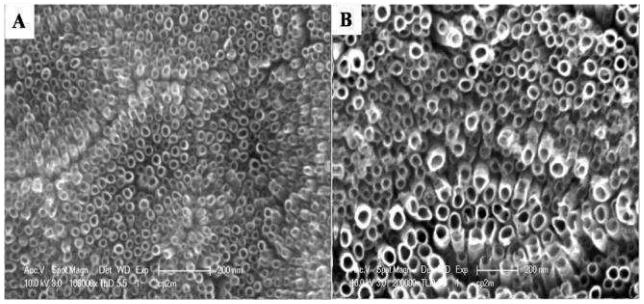

Fig. 4 SEM images of TiO_2 NTs synthesized at 20V in Glycérol+1.3wt% NH_4F + 2wt% H_2O during: 1h (A) and 2h (B).

Figure 5 and figure 6 show that when working in aqueous media the fluorine concentration is far aggressive and a high chemical dissolution of TiO_2 is caused. The nanotubular structure obtained is completely destroyed with very low ordering degree of TiO_2 in contrast the growth process in organic electrolyte which is much slower and low aggressive. . By reducing the acidity of the electrolyte and the use of aqueous solutions containing fluorinated salts rather than HF aqueous solutions, the chemical solubility of TiO_2 can be reduced. These results show that it is extremely important to select the appropriate solution for growth of the TiO2 NTs if we want to produce a high quality and ordered TiO NTs.

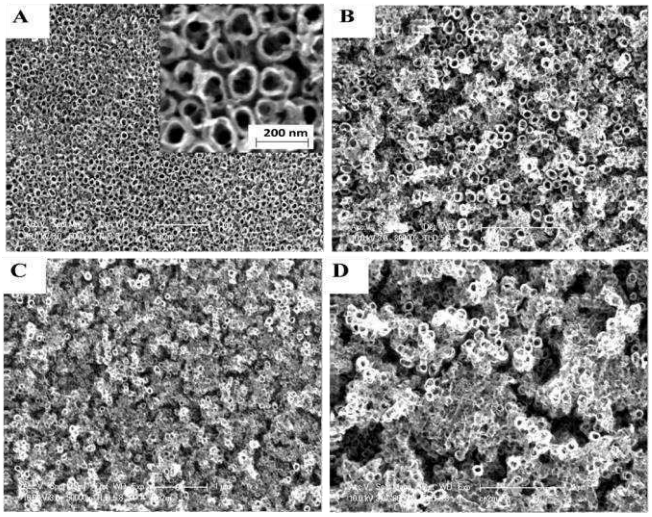

Fig. 5 SEM images of TiO_2 NTs synthesized at 20V in 1M $(NH_4)_2SO_4$ containing: 0.5wt%NH_4F (A and B) and 1wt%NH_4F (C and D) during 1h (A and C) and 2h (B and D).

TABLE IIIII
CHARACTERISTIC OF TiO_2NTS DEPENDING ON THE ORGANIC ELECTROLYTE TYPE

Electrolyte Type	D_{int} (nm)	D_{ext} (nm)	w (nm)	x (nm)	L (µm)	φ (%)	P	n * 10^{23} (pores/cm^2)	R	Ai*10^{-6} (cm^2/cm^2)
Glycerol	76	144	34	18	01.76	0.51	162	02.78	12.22	0.025
Ethylene Glycol	106	196	45	19	122	0,53	215	01,50	622,45	2,31

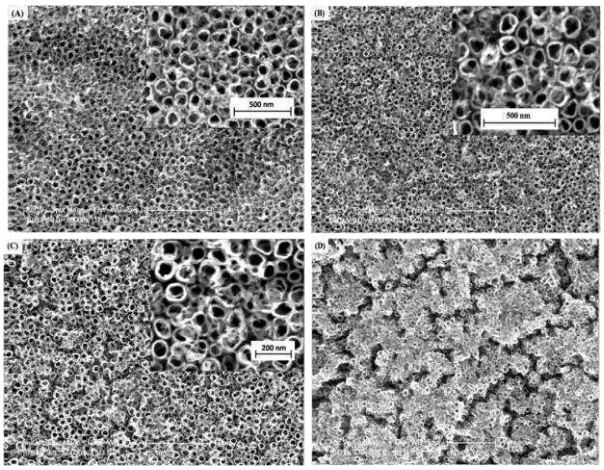

Fig. 6 SEM images of TiO_2 NTs synthesized at 20V in 1M Na_2SO_4 containing: 0.5wt% NH_4F (A and B) and 1wt% NH_4F (C and D) during 1h (A and C) and 2h (B and D).

III. CONCLUSION

In this paper, the synthesis of TiO_2 NTs by electrochemical anodization is analyzed in detail from the experimental results. The formation of TiO_2 NTs arrays is a direct consequence of the competition between the electrochemical oxidation of Ti and the chemical etching (chemical dissolution) of TiO_2 by the electric field assisted fluorinated ions.With controlling anodization parameters of Ti foil, we can obtain different TiO_2 structures such as a compact oxide, a disordered porous layer and highly self-organized nanotubular layer.. The resulting TiO_2 NTs layers and the different morphological parameters of the TiO_2 NTs lead to different properties with the possibility of integrating them into solar cells applications.

ISSN: 2961-6611

REFERENCES

[1] J. Kong, C. Song, W. Zhang, Y. Xiong, M. Wan, and Y. Wang, Enhanced visible-light-active photocatalytic performances on Ag nanoparticles sensitized TiO2 nanotube arrays, Superlattices and Microstructures, 109, 579–587, 2017.

[2] S. Ananthakumar, J. Ramkumar, and S. M. Babu, Semiconductor nanoparticles sensitized TiO2 nanotubes for high efficiency solar cell devices, *Renewable and Sustainable Energy Reviews*, 57, 1307-1321, 2016.

[3] S. V. A. Tran, T. T. Truong, T. A. P. Phan, T. N. Nguyen, T. Van Huynh, A. Agresti, and S. N. Le, Application of nitrogen-doped TiO2 nano-tubes in dye-sensitized solar cells. *Applied Surface Science*, 399, 515–522, 2017.

[4] D. Khudhair, H. A. Hamedani, J. Gaburro, S. Shafei, S. Nahavandi, H. Garmestani, and A. Bhatti, Enhancement of electro-chemical properties of TiO2 nanotubes for biological inter-facing, Materials Science and Engineering: C, 77, 111-120, 2017

[5] V. Galstyan, E. Comini, G. Faglia, and G. Sberveglieri, TiO2 Nanotubes: Recent Advances in Synthesis and Gas Sensing Properties, *Sensors*, 13, 14813–14838, 2013

[6] S. Yuan, S. Chen, Z. Hu, G. Jiang, Y. Zhang, Y. Yang, P. Xiong, X. Zhu, and J. Xiong, Reduced graphene oxide and carbon/elongated TiO2 nanotubes composites as anodes for Li-ion batteries, *Nano-Structures and Nano-Objects*, 12, 27–32, 2017.

[7] F. R. Cummings, L. J. Le Roux, M. K. Mathe and D. Knoesen, Structure induced optical properties of anodized TiO_2nanotubes, *Materials Chemistry and Physics*, 124, 234-242, 2010.

[8] M. Assefpour-Dezfuly, C. Vlachos, and E. H. Andrews, Oxide morphology and adhesive bonding on titanium surfaces, Journal of materials science, 19, 3626-3639, 1984.

[9] V. Zwilling, M. Aucouturier, and E. Darque-Ceretti, Anodic oxidation of titanium and TA6V alloy in chromic media. An electrochemical approach, *Electrochimica Acta*, *45*, 921-929, 1999

[10] D. Gong, C. A. Grimes, O. K. Varghese, W. Hu, R. S. Singh, Z. Chen, and E. C. Dickey, Titanium oxide nanotube arrays prepared by anodic oxidation, *Journal of Materials Research,* 16, 3331-3334, 2001.

[11] J. M. Macák, H. Tsuchiya, and P. Schmuki, High-aspect-ratio TiO2 nanotubes by anodization of titanium, Angewandte Chemie International Edition, 44, 2100-2102, 2005.

[12] J. M. Macak, H. Tsuchiya, L. Taveira, S. Aldabergerova, and P. Schmuki, Smooth anodic TiO2 nanotubes, Angewandte Chemie International Edition, 44, 7463-7465, 2005.

[13] G. K. Mor, O. K. Varghese, M. Paulose, K. Shankar, and C. A. Grimes, A review on highly ordered, vertically oriented TiO2 nanotube arrays: Fabrication, material properties, and solar energy applications, Solar Energy Materials and Solar Cells, 90, 2011–2075, 2006..

ISSN: 2961-6611

Investigation of Steam Ejector Design and Performance Optimization

Doniazed Sioud[#1], Raoudha Garma[#2], Mahmoud bourouis[*3], Ahmed Bellagi[#4]

[#]*U.R. Thermique & Thermodynamique des Procédés Industriels*

Ecole Nationale d'Ingénieurs de Monastir-ENIM, University of Monastir, Monastir, Tunisia

[*]*Department of Mechanical Engineering, Universitat Rovira i Virgili, Av. Països Catalans No. 26, 43007 Tarragona, Spain*

[1]siouddoniazed@gmail.com

[2]raoudhagarma83@gmail.com

[3]mahmoud.bourouis@urv.cat

[4]Ahmedbellagi@rnu.tn

***Abstract*— In this paper, a computer simulation model of steam ejector is used to enhance the performances of absorption chiller. The 1D model is developed based on thermodynamic equations governing perfect gas flow correlations is used in the current study to improve the ejector: design and performance. Actual study specifies the constant-pressure ejector flow model at critical operating mode for steam as working fluid. The effect of design parameters, particularly the primary nozzle area ratio and the ejector area ratio, and operating conditions of primary, secondary and back pressure are used to evaluate the ejector operating zone according to entrainment ratio calculations. Besides that, the effect of pressure exiting nozzle and the area ratio on ejector performance: pressures and Mach number behavior inside the ejector are discussed and optimized.**

***Keywords*—Ejector; Performance, Design, Steam, Operating conditions and optimization.**

I. INTRODUCTION

Steam ejectors are used in vapour compression refrigeration and absorption chillers technology to enhance machines performances [1-4]. Ejectors are classified based on the state of the working fluid (gas-liquid ejector, gas-gas ejector) or based on geometry (constant area ejector [5] or constant pressure ejector as described below). Experimental works and a computational Fluid Dynamics (CFD) model are conducted to predict the ejector performances by studying the effect of the primary nozzle and the mixing chamber diameters [6] on the entrainment ratio. Different ejector geometries are tested under different working conditions. A 1D analysis is presented [7] to evaluate ejector performance. The entrainment ratio at working conditions is investigated in order to validate analytically the experimental results of a steam ejector. Results show that the model predicts fairly the entrainment ratio of the ejector and the performances of many studied refrigerator machines. Experimental and theoretical studies [8] are investigated to study ejector working with various flow to establish its design and then optimize the chiller prototype. Experimental works are performed to study the effect of ejector geometries on the performances of a cooling system [9], Results showed the difficulty to reach the optimum of using one ejector under various operating conditions. A 3D ejector model [10] is developed using AutoCAD, meshed and simulated using Ansys CFX. for predefined inputs and boundary conditions, pressure, temperature, Mach number and velocity contours are analysed Parametric analysis was carried out to identify the convergence. A steam ejector [11] is investigated. Two theoretical approaches are discussed: ejector design for a fixed duty and performance ejector prediction for known geometry. Semi-empirical correlations are proposed for the design and performance prediction of steam ejectors. Investigations are carried out to design and optimize an ejector using ammonia [12] in order to find out the optimum operation conditions. A maximum entrainment ratio is found under various boundary conditions and for each value. An optimum area ratio is then concluded for each case. The purpose of the present work is to analyse theoretically the design under various operating conditions of steam ejector. Optimum operating conditions as function of thermodynamic and geometric parameters governing the ejector are discussed in order to optimize its performances and to evaluate its off design conditions.

II. EJECTOR DESCRIPTION

A typical ejector configuration is shown in Fig.1. A steam ejector is composed from four elements, a primary nozzle, a suction chamber, a mixing chamber (convergent-duct-constant section) and a subsonic diffuser. Where Secondary mass flow rate m2 is entrained by primary flow rate m1, defining ω the entrainment ratio.

In the primary nozzle (convergent–divergent)the high pressure of the primary fluid P1expands and accelerates, creating a vacuum at the nozzle exit position (i) with very low pressure Pi in order to entrain the secondary flow inside the mixing chamber. At the exit of the mixing chamber j, the combined two streams are assumed to be completely mixed at a uniform pressure (Pj=Pi). Due to the existence of a high pressure area, the mixed stream undergoes normal shock

ISSN: 2961-6611

wave within the constant section area Ak, so the pressure rises to Pk, and a compression effect is created. At the exit of the diffuser the pressure is compressed to the back pressure P3.

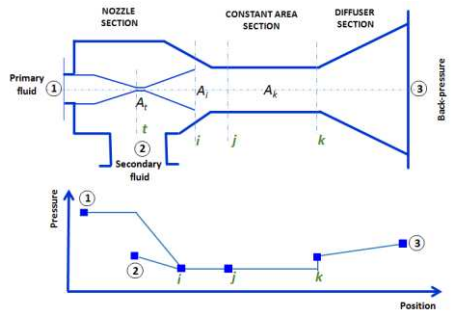

Fig. 1. Schematic Presentation of an Ejector.

III. EJECTOR SOLUTION PROCEDURE

Mathematical 1-D model of the ejector is developed based on mass, momentum and energy balances, in order to carry out the ejector entrainment ratio ω=m2/m1 and ejector area ratio AkAt=Ak/At. In this work a new algorithm chart is developed based on iterations to calculate to optimize and design the ejector.

First knowing the nozzle area ratio AiAt=Ai/At, the Mach number M1i in the outlet of the primary nozzle can be found, and then the pressure exiting the nozzle Pi is calculated. Also knowing the secondary pressure P2, Mach number M2i is calculated. Hence the critical mach numbers M1i* and M2i* are calculated. As it is an ejector with constant pressure, the mixing pressure before the shock wave is known (Pi=Pj). Also for a given back pressure P3 the pressure Pk and the Mach number Mk after the shockwave ,Mj are evaluated by solving a system of three equations (6–7-8)and three unknown value. Then Mj* (9)is deduced and ω is concluded from the expression of Mj (10). Once ω is deduced, it is injected in the equation expressing the area ratio AkAt and a new Pk and AkAt are calculated. If Pk from equation (6) is different of Pk from (11) so iteration should be redone until reaching unidentical Pk between equation (6) and (11). Ones this condition is reached so ω is calculated from (10) and AkAt from (11).

IV. RESULTS AND DISCUSSION

A. Effect of Nozzle design on Ejector Performances

Fig. 2 depicts the evolution of the entrainment ration with pressure at exit primary nozzle Pi for constant primary and secondary flow properties (T1=120, P1=1.98bar) and (T2=10°C, P2=12.3mbar) where each pressure is a saturation pressure. For four fixed values of back pressure P3 (30, 32, 34, 36mbar), curves of entrainment ratio have the same shape, it increases until reaching a maximum and later decreases with increasing Pi. For each of the four curves, calculations of ω is stopped with Pi=12mbar≈P2 which presents the limit of the nozzle exit pressure. Otherwise the ejector will be shocked by the value of Pi and the secondary flow could not be entrained into the mixing chamber.

Whereas Pi it is directly related to the primary pressure and nozzle area ratio as shows Fig. 3. So higher is the Primary flow, higher is nozzle area ratio but higher is Pi lower is AiAt. Thus the nozzle area ratio gives Pi which gives ω. As results ω reach a visible maximum for an optimum Pi related to primary pressure and primary nozzle area ratio (the throat exit and diameter of the nozzle). Therefore optimizing the entrainment ratio leads to know exactly the adequate nozzle geometry.

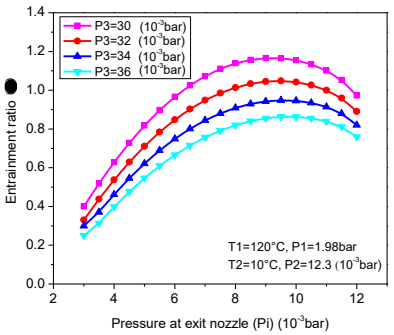

Fig. 2. Effect of pressure at exit nozzle (Pi) on entrainment ratio.

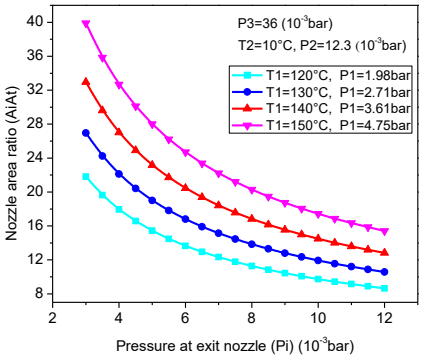

Fig. 3. Effect of Pressure at Exit Nozzle (Pi) on Nozzle Area Ratio.

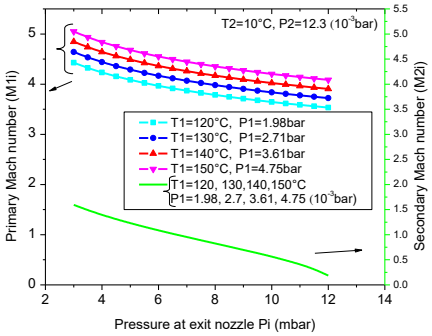

Fig. 4. Effect of Pressure at Exit Nozzle (Pi) on Primary and Secondary Mach Number.

ISSN: 2961-6611

Fig. 4 shows the influence of nozzle exit pressure on the Mach numbers of both primary and secondary flow. First the primary Mach number is more important for important primary pressures also it decreases with increasing Pi. But evaluation the secondary Mach number show that it is first independent to the primary flow: all curves are identical for all the studied primary pressure, second the secondary Mach number decreases until reaching a value almost equal to zero when Pi=P2 which mean that the velocity of the secondary flow is zero leading to stagnant and non moving flow. So as referring to Fig. 2, the ejector is in off design condition and the flow is no more entrainment at Pi=P2mainly because the state of the secondary flow at this specific pressure become a non moving flow with velocity equal to zero (M2i=0).

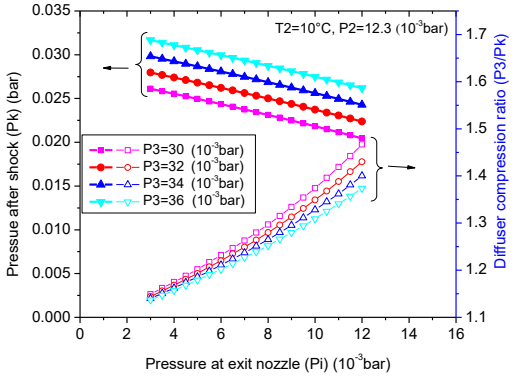

Fig. 5. Effect of Pressure at Exit Nozzle (Pi) on Pressure After Shock and on Diffuser Compression Ratio.

Referring to Fig. 2, curves of the entrainment ratio have a starting point and an ending point, above an explanation of the ending point is achieved. Although, basic on figure 5 the starting point of entrainment ratio curves could be explained: Thus four value of back pressure P3 are studied. For each curve, the pressure after shock Pk increases with increasing P3. Also in the starting point Pk is very near to P3, i.e. for P3 = 30mbar, Pk = 26mbar, for P3 = 32mbar, Pk = 28mbar, for P3=34mbar, Pk = 30 mbar and for P3 = 36 mbar, Pk = 33mbar. While Pk is the last evaluated pressure in the ejector process (just before the back pressure), that is why a diffuser compression ratio reported by P3/Pk is evaluated. Curves show that at the starting point this ratio is almost equal to one (unit) which mean that if this point is reached, no compression exist which is a contradiction with the concept of ejector specially the diffuser, because a diffuser is placed to increase the pressure of the flow after the mixing chamber. So calculation at the starting point is limited by Pk = P3. Otherwise the flow exiting the ejector will be shocked by the flow at the back pressure.

B. Effect of Ejector Design (Area Ratio) on Ejector Performances

Fig. 6 presents the relationship between the pressure at exit the nozzle and the ejector area ratio. For fixed primary and secondary conditions, curves of ejector area ratio have an optimum value corresponding to its maximum. The optimum values decrease with increase of back pressure.

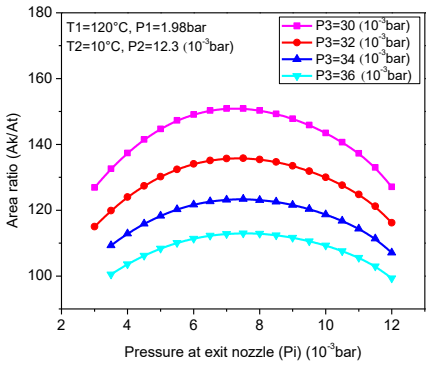

Fig. 6. Effect of Pressure at Exit Nozzle (Pi) on Ejector Area Ratio

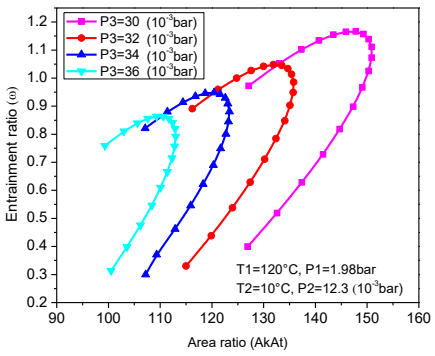

Fig. 7. Effect of Ejector Area Ratio on Entrainment Ratio.

Fig. 7 shows that for every back pressure there are n optimum value of entrainment ratio. For constant primary and secondary operating condition, the optimum values of the entrainment ratio decrease with increasing of the back pressure. While it is possible to have the same entrainment ratio for different value of area ratio and back pressure , i.e to get ω = 0.4, the area ratio of the ejector should be 107,110,120, 125 for back pressure 36, 34, 32, 30 mbar respectively.

Fig. 8 shows the evolution of ejector area ratio with the back pressure, secondary pressure 8, 12, 17, 23 mbar and for primary pressure is constant and equal to 1.98bar. It can be seen that area ratio AkAt increases with increasing the secondary pressure and decrease with increasing the back pressure.

Fig. 9 presents the evolution of ejector area ratio with the primary pressure, secondary pressure 8, 12, 17, 23 mbar and for constant back pressure equal to 36mbar. It can be seen that area ratio AkAt increases with increasing the secondary pressure and the primary pressure.

ISSN: 2961-6611

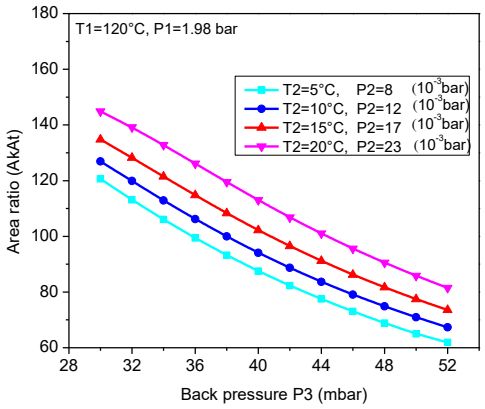

Fig. 8. Effect of back Pressure on Ejector Area Ratio.

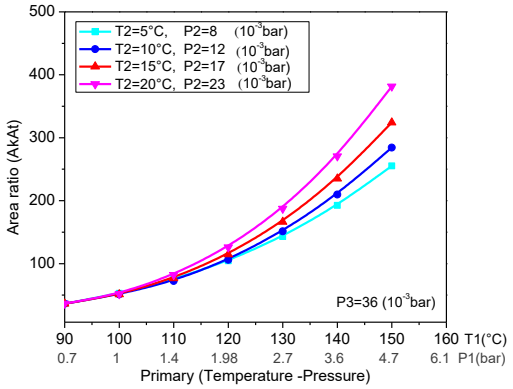

Fig. 9. Primary Pressure on Ejector Area Ratio.

V. Conclusion

In this paper, a theoretical investigation is carried to evaluate the performance and limits of design of steam ejector. A simplified ejector 1D–model, taking account of the irreversibility in nozzle, diffuser and mixing chamber is used and a specific chart algorithm is applied to solve it. The model is first validated based on data from literature and then performance of the ejector for varying operating conditions and ejector geometry was studied via the behavior of parameters inside the ejector. It was found that

For constant primary and secondary flow properties (P1,T1, T2, P2), the entrainment ratio increases with increasing pressure at nozzle exit Pi reaches a maximum, and then decreases, when the back pressure P3 is constant. Two borders (starting and ending points) was found limiting the design of the ejector: the ending point is limited when Pi ≈ P2 which chock the secondary flow and disable it to entrained into the mixing chamber. Also Pi related to primary pressure and primary nozzle area ratio. Thus the limit on it is characterized by the nozzle geometry design.

Also secondary Mach number is independent of the primary flow and decreases until reaching a value almost equal to zero when Pi = P2, the velocity of the secondary flow is zero for stagnant and non moving flow at Pi = P2.The starting point (on curbe ω = f(Pi)) is related to the pressure after shock Pk. Based on a diffuser compression ratio reported by P3/Pk. A starting point about 1 is reached and no compression process undergoes the diffuser of the ejector. The nozzle design at the starting point is limited by Pk = P3.

Ejector area ratio has maximum corresponding to an optimum Pi value. While The optimum values decrease with increase of back pressure. For every back pressure there are an optimum value of entrainment ratio that decrease with increasing of the back pressure, for constant primary and secondary operating condition, Area ratio AkAt increases with increasing the secondary pressure and decrease with increasing the back pressure, for constant primary and secondary operating condition.

Acknowledgment

Acknowledgements Doniazed Sioud gratefully acknowledges the Tunisian Ministry of Higher Education and Scientific Research for funding her internships at Rovira i Virgili University of Tarragona (Spain).

References

[1] Xiangjie Chen, Siddig Omer, MarkWorall, Saffa Riffat. (2013).“*Recent developments in ejector refrigeration technologies*”. Renewable and Sustainable Energy Reviews, vol.19, pp. 629-651.

[2] M. Elakhdar, E. Nehdi. (2011). *“Simulation of an ejector used in refrigeration systems”*. Int. J. refrigeration, vol. 34, pp.1657-1667.

[3] D. Sioud, R. Garma, and A. Bellagi, “*Thermodynamic Analysis of a Solar Combined Ejector Absorption Cooling System*”, Journal of Engineering
Vol. 2018, Article ID 7090524, 12 pages https://doi.org/10.1155/2018/7090524

[4] D. Sioud, M. Bourouis and A. Bellagi, “Investigation of an ejector powered double-effect absorption/recompression refrigeration cycle”, International Journal of Refrigeration, Vol. 99, pp. 453-468 March 2019.

[5] Sriveerakul, S. Aphornratana , K. Chunnanond. (2007).*“Performance prediction of steam ejector using computational fluid dynamics: Part 1. Validation of the CFD results*”.International Journal of Thermal Sciences, vol. 46, pp.812–822.

[6] Satha Aphornatana. (June 1996). “*Theoretical study of a steam-Ejector Refrigerator*”. International Energy Journal, vol. 18 no.1, pp.61-73.

[7] A. Milazzo, A. Rocchetti, Ian W. Eames,.“Theoretical and experimental activity on Ejector Refrigeration”. Energy Procedia vol. 45, pp. 1245- 1254, 2014.

[8] Da Wen Sun. “Variable geometry ejectors and their applications in ejector refrigeration systems”. Energy, vol. 21, pp. 919-929, 1996).

[9] C. Moorthy, V Srinivas, V. Prasad, T Vanaja, *“Computational analysis of a cd nozzle with ‘sed’ for a Rocket air ejector in space applications*”. International Journal of Mechanical and Production Engineering Research and Development (IJMPERD) Vol. 7, Issue 1,pp. 53-60, Feb 2017.

[10] H. El-Dessouky, H. Ettouney, I. Alatiqi, G. Al-Nuwaibit. (2002). “*Evaluation of steam jet ejectors*”. Chemical Engineering and Processing, vol.41, n°6,pp. 551–561.

[11] E.D. Rogdakis, G.K .Alexis, “*investigation of ejector design at optimum operating condition*”, Energy conversion & management, vol. 41, pp. 1841-1849, 2000 .

[12] S. A. Klein, F. Alvarado. Engineering equation solver. Middleton, WI: F–chart software, 2003.

ISSN: 2961-6611

Numerical Investigation of Void Fraction and Flow Patterns Distribution for various Bubble Pump Heating Models

R. Garma#1, D. Sioud#2, Y. Stiriba*3, M. Bourouis*4, A. Bellagi#5

National Engineering School of Monastir, Unit of Thermic and Thermodynamics of the Industrial Processes, Ibn El Jazzar street, 5019 Monastir, Tunisia

[1]raoudhagarma83@gmail.com

[2]siouddoniazed@gmail.com

[5]a.bellagi@enim.rnu.tn

**Department of Mechanical Engineering, UniversitatRoviraiVirgili, Av. PaïsosCatalans No. 26, 43007 Tarragona, Spain*

[4]mahmoud.bourouis@urv.cat

[3]youssef.stiriba@urv.cat

Abstract— **Bubble pumps are used for the circulation of the liquid in the diffusion absorption machine and have considerable effect on its performances. In this paper, numerical simulation of the heating repartition effect on the boiling flow in this component was conducted with the commercial CFD (Computational Fluid Dynamics) package Ansys-Fluent 12.0. The Eulerian multiphase flow framework model was used to model the phases' interactions. User-Defined Functions (UDFs) are provided to compute the wall heat transfer and to calculate the inter-phase heat and mass transfer. The heat flux from the wall is divided into three parts according to a wall heat partitioning model based on three mechanisms including convective heat for heating the bulk liquid, evaporative heat for generating vapor and quench heat for heating the liquid in the nucleation sites. The rate of vapor formation is obtained by adding the mass exchange at the bubble surface and the bubble formation due to heat supplied at the wall. Total and partial heating of the tube are treated to approach to two different configurations of the bubble pump encountered in praxis. The simulations in this paper are conducted with pure water as working fluid. The vertical void fraction distribution is determined in order to localize the onset of vapor generation and to predict the flow patterns throughout the tube length.**

Keywords— **Bubble pump, Heating, Boiling flow, Void fraction, Flow pattern, CFD, Simulation, DAR**

I. INTRODUCTION

Several advantageous characteristics such as the absence of mechanical moving part, causing vibration and noise, and specially the possibility to operate with waste heat or solar energy, attracted the attention of researchers to experimental and numerical investigations of diffusion absorption refrigerators (DARs) invented by Platen and Munters [1] in the 1920s. In these absorption systems, the bubble pump is an essential component. Therefore, significant attention has been devoted to this device to improve its performance, which would contribute to the performance of the whole system. The thermally driven bubble pump is a simple vertical tube which can be powered by heat from any source (electricity, burner, waste heat, solar energy). When the liquid solution is heated up, vapor bubbles are generated causing pressure difference between the bottom and the top of the tube. As result, natural circulation of the liquid solution is occurring through the tube and so boiling flow takes place inside the bubble pump. Zohar et al.[2] developed and analyzed by computer simulation a detailed thermodynamicmodel for three generator and bubble pump configurations of a DAR to study their effect on the system performance. A mathematical model for the forced convective boiling of refrigerant-absorbent mixtures in vertical tubular generator is proposed by Pasupathy et al. [3]. A parametric analysis has been performed to study the effect of various factors on the performance of the generator. Two-fluid model is employed by Ma et al. [4] to describe the two-phase flow and heat transfer processes in a two-phase closed thermosyphon. Numerically predicted flow patterns and distribution of parameters under different conditions show a good agreement with experimental results. Taieb et al. [5,6] tested the pumping capacity of bubble pumps by using Behringer correlation (cited in Ref. [7]). Uniformly heated bubble pump configuration was numerically investigated by Garma et al. [8,9] using the commercial CFD package Ansys-Fluent. It was found that the onset boiling point is reduced and the void fraction at tube's outlet is increased when the wall heat input is increased. An experimental investigation of an air-cooled diffusion-absorption machine operating with a binary light hydrocarbon mixture is presented by Ben Ezzine et al. [10]. A new concept of generator consisting in a separated boiler and bubble pump instead of the usual combined generator is tested. The experimental results show that the bubble pump

ISSN: 2961-6611

exiting temperature as well as those of the major components of the machine is very sensitive to the heat input to the bubble pump. Experimental study and theoretical thermodynamic simulations of the same absorption refrigerator prototype with methylamine-water-helium were carried out by Mazzouz et al. [11]. The test showed that all machine's components are very sensitive to the behaviour of the bubble pump. The performance of three different indirectly heated solar powered bubble pumps/generators were investigated and discussed by Jacob et al. [12,13,14,15].

Research effort has been also focused on predicting the flow regime transition using the void fraction profile. Radovich and Moissis [16] considered that the bubbly to slug flow transition is due to the collisions between small bubbles and supposed the transition to occur when the maximum packing of these small bubbles is reached. They suggested that this is the case when the void fraction is around 0.3. This same value was proposed by Taitel et al. [17] and Mishima et al. [18]. On the other side, Brauner et al. [19] and Barnea [20] claimed that the slug to churn transition takes place when the gas void fraction in the liquid slug reaches 0.52 corresponding to the maximum cubic lattice packing fraction. Transition from intermittent (slug or churn) flow to annular flow pattern can be observed when the vapor flow rate becomes sufficiently high. Wallis [21] suggested a transition void fraction of 0.8 after comparing void fraction data with theoretical prediction for intermitting and annular flow.

In the present paper, a CFD analysis of a bubble pump using the commercial package ANSYS-FLUENT is worked out. Full and partial length heating tube are considered in order to compare both configurations of thermally driven pump. Void fraction profiles for different heat fluxes are predicted and the evolution of flow patterns throughout the tube length is discussed.

II. CFD MODELLING

Mathematical model utilized in this paper was developed and then applied in CFD codes to be finally implemented in ANSYS-FLUENT via user-defined functions (UDFs) in conjunction with the Eulerian multiphase model in which the conservation equations are written for each phase, liquid and vapor [8,9].

The commercial CFD code ANSYS-FLUENT 12.0 [22] is used to perform the simulations. The interfacial forces models and the wall boiling model described previously were implemented in the code through User-Defined Functions (UDFs). The stainless-steel made vertical tube is 1m in length and 10 mm in diameter. Wall thickness is fixed to 2 mm. The sub-cooled water enters the system at the bottom, and then boils due to the constant heat flux supplied from the pipe walls.

A. *Mesh geometry*

The geometry used for problem formulation was two-dimensional axi-symmetric. Quadrilateral computational mesh is recommend for Eulerian multiphase model [23]. We started first to find the best computational meshes, Figure 1 shows the adopted grid consisting uniform rectangular cells.

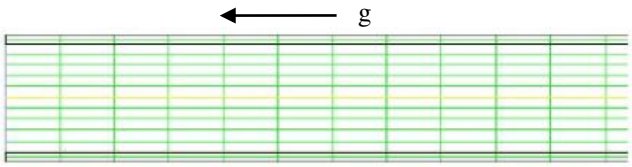

Fig. 1 Mesh geometry.

B. *Initial and Boundary conditions*

Bubble pump saturation temperature is fixed to 425.15 K corresponding to the operating pressure of the machine. Fixed sub-cooling temperature (T_{sub} = 5K) and fully-developed profile of velocity are applied at the inlet (no vapor at the inlet α_{in}= 0). No-slip conditions on the tube wall. Liquid-vapor mixture leaves the tube at the saturation temperature. Heat Flux are specified at the external wall. The effect of the heat distribution is investigated for various heating rates ranging between 628 and 1728 W. At the interface wall-liquid, the UDFs was used to specify heat flux and heat transfer coefficient. Symmetry is used at the centreline axis.

C. *Solution techniques*

Unsteady state calculations with a time step of 0.1s were performed for all cases. SIMPLE algorithm was applied for the calculations of the pressure velocity-coupling with first order upwind calculation scheme for the discretization of momentum, energy and volume fraction equations.

III. NUMERICAL MODEL VALIDATION

To examine the validity of the mathematical model, using ANSYS-FLUENT, the numerical predictions are compared [24, 25, 26] with the experimental data of Bartolomei and Chanturiya [27]. The predictions of axial distribution of average void fraction along the tube length [25] show an excellent agreement with experiments, figure 2.

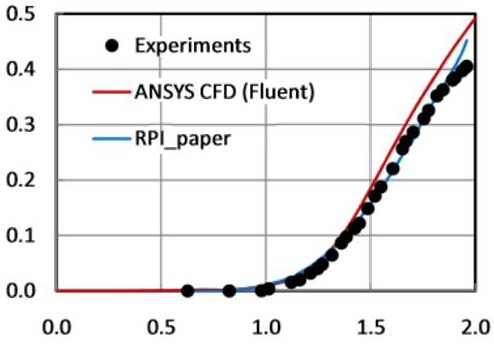

Fig. 2：Model validation: Void fraction along tube length [27]

Braz Filho [24] proved that ANSYS-FLUENT code results are in reasonable agreement with the experimental data for void fraction and in excellent agreement for inner wall temperature evolution versus the fluid enthalpy, figure 3.

ISSN: 2961-6611

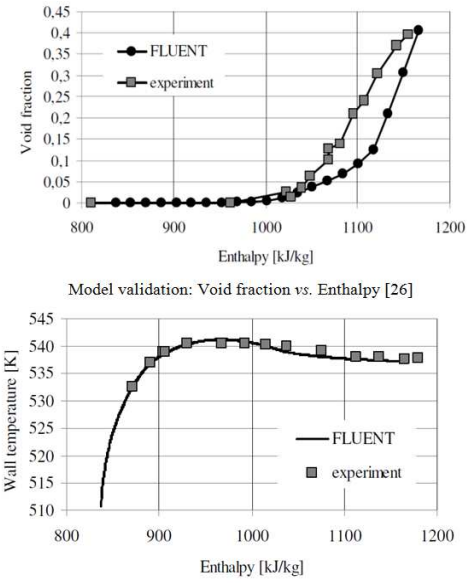

Fig. 3Model validation: Void fraction and wall temperature vs. Enthalpy

IV. Bubble pump heating models

For the purposes of the present study, two bubble pump models are treated - uniformly and partially heated tube as it is previously mentioned - to show the heat distribution effect on the boiling flow characterization. Heat flux is supplied to the bubble pump wall according to the following configurations:

- **Test 1**: Uniformly heated pump, full-length heating pipe, as depicted in Figure 4.
- **Test 2**: The heat flux is supplied in the lower 1/3 of the tube length (30 cm), partial-length heating pipe, as indicated in figure 5.

The boiling flow characteristics of bubble pump including void fraction evolution and flow pattern arrangement throughout the tube are investigated for various heat inputs from 628 (minimum heat flow rate for starting boiling) to 1728 W (beyond this limit: transition to annular flow not interesting for the bubble pump applications).

A. Effect of heating configuration on void fraction profiles

Figures 6 and 7 depict the effect of the heat inputs on the void fraction profiles along the bubble pump for various heat inputs from 628 to 1728 W respectively for test 1 (Uniformly heated tube) and test 2 (partially heated tube).
One can see in the two cases that the higher the heat is, the lower is the start up of boiling and the higher is the void fraction. In fact, when the heat input is increased from 628 W to 1728 W, the onset boiling length is reduced from 96 to 15 cm for uniformly heated pipe and from 5 to 1.5 cm for the partially heated one. Here, one can obviously remark how greatly this parameter is sensitive to the heating repartition. Actually, for the same heat input, 628 W, boiling starts at 96 cm in the first heating model (test1) and at 15 cm in the second one (test2) which can be explained by the higher heat density in the bottom of the tube; which have a great impact on the performances of the bubble pump, flow regimerepartition, liquidvapour velocities arrangement and temperature profiles [28].

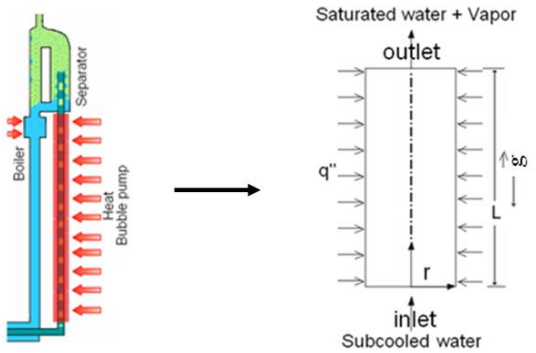

Fig. 4Test1: Uniformly heated bubble pump.

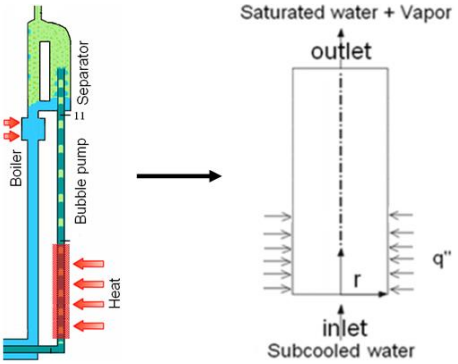

Fig. 5Test2: Partially heated bubble pump

V. Results and discussion

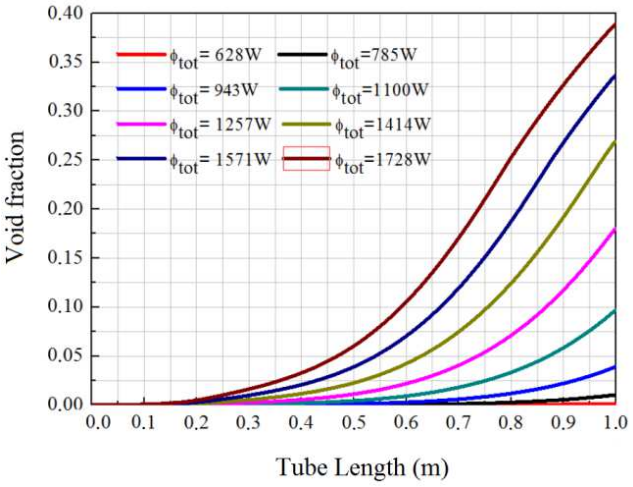

Fig. 6Void fraction evolution of the uniformly heated pump (test1) for different heat fluxes

On the other hand, the void fraction at the tube outlet is increased from 0.001 to 0.39 and from 0.22 to 0.58 respectively for the totally heated tube and the partially heated tube. One also can observe, as illustrated in figure 8, that for the first heating model the void fraction increases

ISSN: 2961-6611

slightly over the whole tube length [8, 9], attains a value of 0.016 at z = 30 cm and a maximum of 0.39 at the tube outlet for Φ_{tot} = 1728 W.

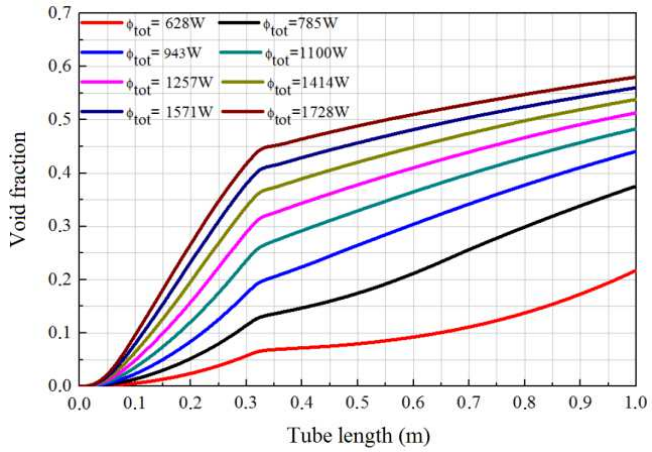

Fig. 7Void fraction evolution of the partially heated pump (test2) for different heat fluxes

This behavior is completely different from that of the second heating model. In fact, for this case (test 2) the void fraction rises sharply, reaches a value in the order of 0.42 at the outlet of the heated zone (z =30 cm) and then increases slightly over the remaining length of the tube to attain a maximum of 0.58 at the outlet. The same remark can be observed for the other heat inputs as shown in figure 9.

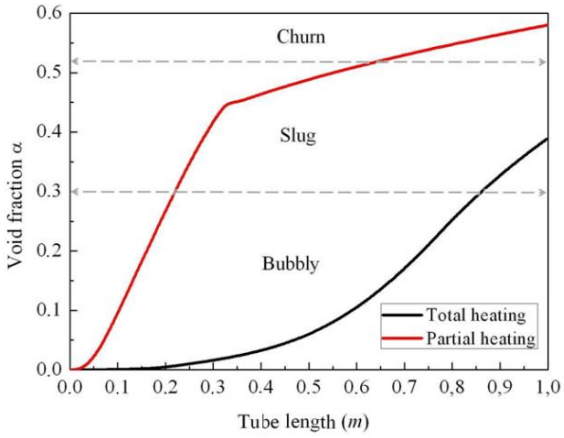

Fig. 8Void fraction distribution for Φ=1728W

B. Identification of different flow regimes in the bubble pump

In this section the void fraction is used to predict the flow regime repartition in the thermally driven bubble pumps. As it was previously reported, the critical void fraction for bubbly-to-slug, slug-to-churn and churn-to-annular transition are respectively 0.3, 0.52, and 0.8. Figures 9 and 10 show the flow patterns limit for different heating distribution and heat fluxes. Specially, the heating repartition effect can be remarked.

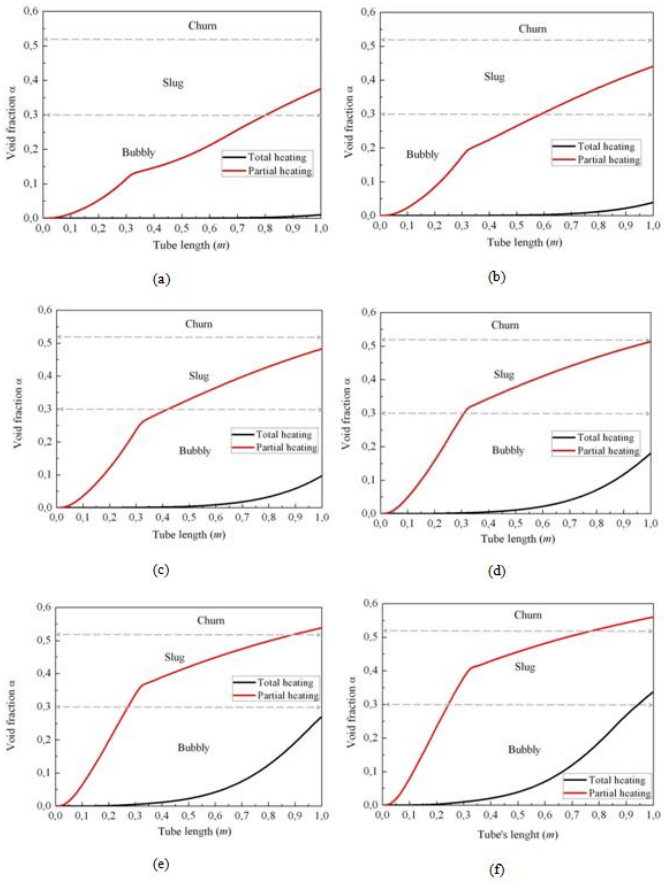

Fig. 9Void fraction distribution for test1 and test 2 (a): Φ=785W, (b): Φ=943W, (c): Φ=1100W, (d): Φ=1257W, (e): Φ=1414W, (f): Φ=1571W

TablesIrecapitulate the length of the zone occupied by different flow regimes along the bubble pump for each heating configuration and various tested heating power.

One can remark that as we reduce the heating power, the slug zone length is reduced to disappear completely at low heat input for partially heated tube (test2). In fact, it is reduced from 69 cm to 20 cm when the heat input reduced from 1257 to 785W before totally disappearing for 628W. Nevertheless, the bubbly flow regime occupies the hall tube length for all previous heat input ranging from 785 to 1257W when the pump is uniformly heated (test1).

the same table show that increasing heat input from 1414W to 1728W decreases the slug zone length from 63cm to 43cm in favour of the churn flow zone which increases from 10 to 35cm in case of the partial heating configuration. As regards the uniformly heated configuration, the slug flow zone length varies from 0 to 14 cm to occupy part the bubbly flow zone for the same variation of heat input to the bubble pump, namely from 1414 to 1728W.

VI. Conclusion

Numerical simulation of the heating distribution effect on the boiling flow of water in vertical tube was carried out with the commercial CFD package ANSYS-FLUENT. User defined Functions (UDFs) are employed to model the boiling phenomena. Void fraction distributions are calculated, discussed and then flow patterns throughout the tube length

ISSN: 2961-6611

are predicted. It was found that the void fraction is higher when heating partially the wall. Flow regimes repartitions are identified referring to the void fraction variation along the tube. It was found that the void fraction at the tube outlet is higher for the partially heated tube then the totally heated tube. Moreover, when the heating power, is increased for the partially heated tube, the slug flow zone length first increases and then decreases in favor of the churn flow regime.

TABLE II
ZONE REGIME LENGTH FOR FULL AND PARTIAL LENGTH HEATED TUBEAT VARIOUS HEAT INPUT

Heating at **628W**	Zone regime length (m)		
	Bubbly	Slug	Churn
Test 1	**1**	**0**	**0**
Test 2	**1**	**0**	**0**
Heating at **785W**	Zone regime length (m)		
	Bubbly	Slug	Churn
Test 1	**1**	**0**	**0**
Test 2	**0.80**	**0.20**	**0**
Heating at **943W**	Zone regime length (m)		
	Bubbly	Slug	Churn
Test 1	**1**	**0**	**0**
Test 2	**0.59**	**0.41**	**0**
Heating at **1100W**	Zone regime length (m)		
	Bubbly	Slug	Churn
Test 1	**1**	**0**	**0**
Test 2	**0.42**	**0.58**	**0**
Heating at**1257W**	Zone regime length (m)		
	Bubbly	Slug	Churn
Test 1	**1**	**0**	**0**
Test 2	**0.31**	**0.69**	**0**
Heating at **1414W**	Zone regime length (m)		
	Bubbly	Slug	Churn
Test 1	**1**	**0**	**0**
Test 2	**0.27**	**0.63**	**0.1**
Heating at **1571W**	Zone regime length (m)		
	Bubbly	Slug	Churn
Test 1	**0.94**	**0.06**	**0**
Test 2	**0.244**	**0.536**	**0.22**
Heating at **1728W**	Zone regime length (m)		
	Bubbly	Slug	Churn
Test 1	**0.86**	**0.14**	**0**
Test 2	**0.22**	**0.43**	**0.35**

VII. REFERENCES

[1] B.C. Von Platen, C.G. Munters, US Patent 1, 685,764, 1928.
[2] A. Zohar, M. Jelinek, A. Levy, I. Borde, The influence of the generator and bubble pump configuration on the performance of diffusion absorption refrigeration (DAR) system, International journal of refrigeration, 31 (2008) 962–969.
[3] B. Pasupathy, A. Mani, Numerical Studies on Vertical Tubular Generator in Vapour Absorption Refrigeration System, International Refrigeration and Air Conditioning Conference at Purdue, July 12-15, 2010.
[4] Zh. Ma, A. Turan, and Sh. Guo, Practical Numerical Simulations of Two-Phase Flow and Heat Transfer Phenomena in a Thermosyphon for Design and Development, ICCS, Part I, LNCS 5544, (2009) 665–674, Springer-Verlag Berlin Heidelberg.
[5] Ahmed Taieb, Khalifa Mejbri, Ahmed Bellagi, Theoretical analysis of a diffusion-absorption refrigerator, International journal o f hydrogen energy 41 (2016) 14293-14301.
[6] Ahmed Taieb, Khalifa Mejbri, Ahmed Bellagi, Detailed thermodynamic analysis of a diffusion-absorption refrigeration cycle, Energy 115 (2016) 418-434.
[7] Almen GC. Gas absorption Refrigerator technology. ABS reftec; 2003. http://www.absreftec.com/index.html [accessed 13.09.12].
[8] R. Garma, Y. Stiriba, M. Bourouis, and A. Bellagi, Numerical Investigation of Nucleate Boiling Flow in Vertical Tubes, 2nd International Symposium on Energy CIE'12, March 26-28 (2012) Tozeur, Tunisia. Comm039.
[9] R. Garma , M. Bourouis , A. Bellagi, Numerical Investigation of Nucleate Boiling Flow in Water Based Bubble Bumps International Journal of Fluid Mechanics & Thermal Sciences; 1(2015): 36-41.
[10] N. Ben Ezzine, R. Garma, M. Bourouis, A. Bellagi, Experimental Studies on Bubble Pump Operated Diffusion Absorption Machine Based on Light Hydrocarbons for Solar Cooling, Renewable Energy, 35 (2010) 464-470.
[11] S. Mazouz, N. Ben Ezzine, R. Garma, M. Bourouis, A. Bellagi, Experimental Investigation and Theoretical Model of a Diffusion Solar Absorption Machine, International Sorption Heat Pump Conference, September 23-26 (2008) Seoul, Korea, Comm AB-072.
[12] U. Jacob, and U. Eicke, Solar cooling with diffusion absorption principal, Proceeding of the 7th World Renewable Energy Congress, WREN, U.K., (2002)1-5
[13] U. Jacob, U. Eicker, D. Schneider, A.H. Taki, and M.J, Cook, Development of an optimized solar driving diffusion-absorption cooling machine, Proceeding of the ISES Solar Xorld Congress, June 16-19, ISES, Goteborg (2003) 1-6.
[14] U. Jacob, U. Eicker, D. Schneider, A.H. Taki, and M.J, Cook, Development of a solar powered diffusion absorption cooling machine, Proceeding of the 1st International Conference Solar Air-Conditioning, October 6-7, Staffelstein, Germany (2005) 111-115.
[15] U. Jacob, U. Eicker, D. Schneider, A.H. Taki, and M.J, Cook, Simulation and experimental investigation into diffusion absorption cooling machines for air-conditioning application, Applied Thermal Engineering. 28 (2008) 1138–1150.
[16] N. A. Radovicich and R. Moissis, The transition from two-phase bubble flow to slug flow, MIT Report No. 7 (1962) 7633-22.
[17] Y. Taitel, D. Bornea, and A. E. Dukler, Modelling flow pattern transitions for steady upward gas-liquid flow in vertical tubes, AIChE J. 26 (1980) 345-354.
[18] K. Mishima, and M. Ishii, Flow regime transition criteria for upward two-phase flow invertical tubes, Int. J. Heat and Mass Transfer 27 (1984) 723-737.
[19] N. Brauner, and D. Barnea, Slug/churn transition in upward vertical flow, Chem. Eng. Sci. 41 (1986) 159-163.
[20] D. Barnea, A unified model for predicting flow-pattern transitions for the whole range of pipe inclinations, Int. J. Multiphase Flow 13 (1987) 1-12.
[21] G. B. Wallis, One-Dimensional Two-Phase Flow, (1969) McGraw-Hill, New York
[22] ANSYS FLUENT Theory Guide. Release 12.0. ANSYS, Inc. April 2009.
[23] F.A. Braz Filho, A.D. Caldeira and E.M. Borges, Validation of a multidimensional computational fluid dynamics model for subcooled flow boiling analysis, International Nuclear Atlantic Conference - INAC 2011 Belo Horizonte, MG, Brazil, October 24-28 (2011) ASSOCIAÇÃO BRASILEIRA DE ENERGIA NUCLEAR - ABEN.
[24] G. Eggenspieler, Multiphase Models in ANSYS CFD, 2011 ANSYS, Inc. May 14 2012. http://www.ansys.com/staticassets/ANSYS/Conference/Confidence/San%20Jose/Downloads/mutliphase-summary-3.pdf
[25] Fluent Tutorial: Modeling Nucleate Boiling Using FLUENT.
[26] G. G. Bartolomei and V. M. Chanturiya, Experimental Study of True Void Fraction When Boiling Subcooled Water in Vertical Tubes, Thermal Engineering 14 (1967) 123-128.
[27] R. Garma, Y. Stiriba, M. Bourouis, A. Bellagi, Numerical Investigations of the Heating Distribution Effect on the Boiling Flow in the Bubble Pumps, International Journal Of Hydrogen Energy, 39 (2014) 15256–15260.
[28] R. Garma, Youssef stiriba, M. Bourouis, and A. Bellagi. 2012. Numerical Investigation of Nucleate Boiling Flow in Vertical Tubes, 2nd International Colloque of Energy, CIE'12, March 26-28 (2012)

ISSN: 2961-6611

Thermodynamic Analysis of Ejector Position in an Absorption Refrigeration Machine

Doniazed Sioud[#1], Jouda hattab[#2], Raoudha Garma[#2], Mahmoud bourouis[*4], Ahmed Bellagi[#5]

[#]*U.R. Thermique & Thermodynamique des Procédés Industriels*

Ecole Nationale d'Ingénieurs de Monastir-ENIM, University of Monastir, Monastir, Tunisia

[*]*Department of Mechanical Engineering, Universitat Rovira i Virgili, Av. Països Catalans No. 26, 43007 Tarragona, Spain*

[1]siouddoniazed@gmail.com

[2]raoudhagarma83@gmail.com

[3]mahmoud.bourouis@urv.cat

[4]Ahmedbellagi@rnu.tn

Abstract— **In this work a hybrid ejector single-effect lithium-bromide water cycle is theoretically investigated. The system is a conventional single-effect cycle activated by an external steam-ejector loop. A mathematical model of the whole system is developed. Simulations are carried out to study the effect of the major parameters of the hybrid cycle on its performances, and in comparison with the conventional cycle. The ejector performance is also investigated. Results show that the entrainment ratio rises with steam pressure and condenser temperature, while it decreases with increasing generator temperature. The effect of the evaporator temperature on ejector performance is negligible. It is shown also that the hybrid cycle exhibits better performances than the corresponding basic cycle. However, the performance improvement is limited to a specific range of the operating parameters. Outside this range, the hybrid system behaves similar to a conventional cycle. Inside this range, the COP increases, reaches a maximum then decreases and rejoin the behaviour of the basic cycle. The maximum COP, which can be as large as that of a conventional double-effect cycle, about 1, is obtained at lower temperatures than in the case of single-effect cycles.**

Keywords—**absorption refrigeration, ejector, lithium bromide, simulation.**

I. INTRODUCTION

Cooling and air conditioning are essential for small scale and industrial process applications. While compressor refrigerator cycles worked with fluids presenting carbon dioxide emission. Absorption cycles using water-lithium bromide are alternative. But, they have a low coefficient of performance. That's why new hybrid and combined configurations where the integration of new component, such as ejector, in the basic absorption cycles, to enhance to performances, were studied.

Various configuration integrating ejector were studied; Combined cycle was investigated, in which the ejector is at the absorber inlet [1-4], COP of this cycle was higher by about 2–4% than conventional cycle. Principally, investigations indicate that COP of the combined configuration are greater or equal to that of single effect cycles at low generator temperatures.

Also, another configuration was studied, where the ejector is located in the condenser inlet of the single effect absorption cycle, theoretical study [5,6], confirm that the coefficient of performances was higher than single effect cycle. Experimental study [7] show that the combined cycle is 30-60% higher as compared to the COP of the basic absorption and almost reaches the COP of double-effect absorption systems .Besides modified configuration by adding a flash tank between ejector and evaporator was designed [8-9].

Also ejector double effect absorption systems was investigated [10-11], so COP of the proposed a new ejector refrigeration cycle, increases with the temperature of the heat source until the temperature of the heat source was higher than 150 °C the new cycle worked as a double effect cycle.

Novel configuration was studied where the ejector was coupled to vapour generator, [12,13] to enhance the concentration process by compressing the vapour produced from the lithium bromide solution in order to re-heat the solution from which it came. Results showed that COP of the new cycle can increase specially with the heat source temperature.

In this paper, an hybrid ejector single effect cycle is investigated and specially the whole cycle and the ejector were modeled. The entrainment ratio as ejector performances is carried out for different generator, condenser and ejector temperature. Also a comparison with the basic single effect absorption cycle and the evolution of the coefficient of performances are studied.

II. SYSTEM DESCRIPTION

Fig. 1 (a) and (b) present a schematic diagram of a conventional single effect system and an hybrid ejector-single effect system.

A conventional single effect absorption cycle is composed of evaporator, absorber, condenser and generator, expansion solution valve pump, solution heat exchanger and refrigerant expansion valve, presented in fig. 1 (a). While a steam-ejector-generator loop is coupled to the conventional single effect via the solution generator, as presented in fig. 1 (b). The steam-

ISSN: 2961-6611

ejector loop is composed of a steam ejector, a steam generator vapor, a water pump and an expansion valve.

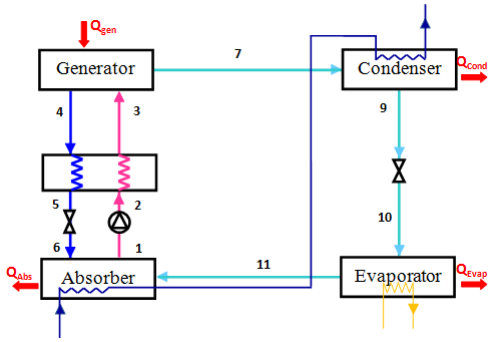

(a)

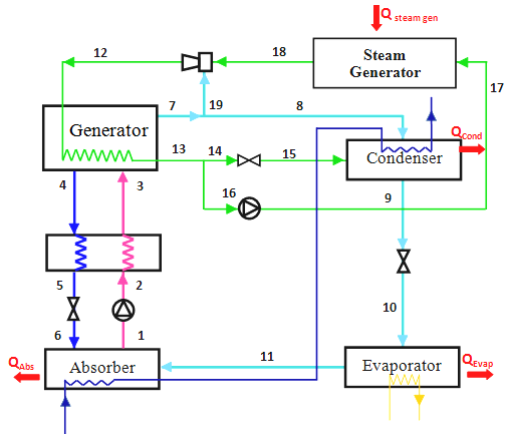

(b)

Fig. 1 Single effect absorption system: (a) Conventional, (b) hybrid

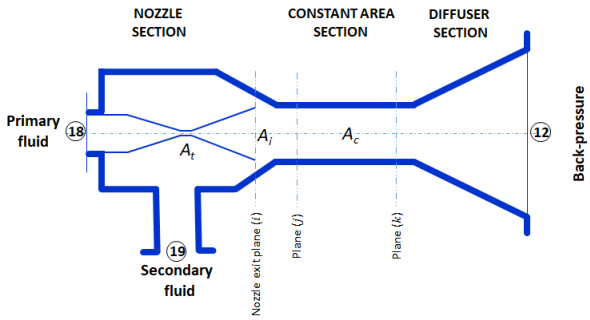

Fig. 2 Ejector schematics

The steam-ejector-generator loop is used to enhance the cycle performance by enhancing the concentration process. The steam ejector is the main key of the enhancement process. A high pressure flow (18) coming from the steam generator enters the primary nozzle of the ejector, its pressure drops at the exit of the nozzle point (i), as shown in fig. 2, and its velocity becomes very high so it entrain a secondary flow, the vapor (19) as part of the total vapor (7) produced from the solution generator, the two streams are mixed in the mixing chamber and then, compressed in the ejector, to exit at backpressure (12). This flow condenses in the solution generator and exceeds condensation heat until become liquid saturated (13). The condensation heat is used to concentrate the saline solution by producing vapor from the diluted solution entering the solution generator (3). Part of the flow (3) undergoes to the condenser and another part (19) is pumped to the steam generator.

III. Results and Discussion

A computer program has been developed using the software Engineering Equation Solver (EES) [14] to thermodynamically analysis the proposed hybrid single effect absorption refrigeration system. In the program, the thermo-physical properties of LiBr-H2O are used as internal functions from the EES database where the temperature reaches 500°K for all composition range.

- The evaporator temperature equal to 4°C,
- Condenser temperature equal to 30°C,
- Absorber temperature equal to Tc-2°C because it is cooled via water cooling tower,
- Effectiveness heat exchanger equal to 0.8,
- Flow rate leaving the absorber equal to 2Kg/s.

A. *Ejector performances*

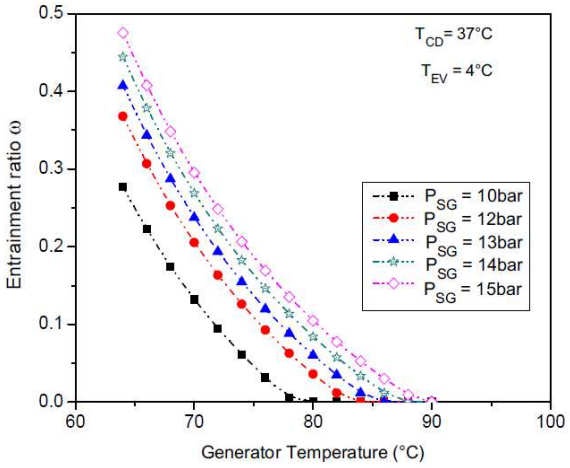

Fig. 3 ω vs. T_G for various primary pressure P_{SG}

Fig.3 indicates that the entrainment ratio depend on the steam generator pressure, while deceases with increasing the generator temperature. The steam pressure is the primary pressure; fig.3 shows that the primary pressure affects the entrainment ratio. The entrainment ratio reaches zero respectively at generator temperature of 80, 83, 85, 87, 90°C for steam pressure of 10, 12, 13, 14, 15bar. Ones the entrainment ratio is zero, the flow is no more entrained inside the ejector, so the ejector is off design and its geometry should be changed.

Fig. 4 shows that the entrainment ratio increases with the condenser temperature and decreases with increasing the generator temperature, when the pressure at generator is set at

ISSN: 2961-6611

15bar. When the generator temperature becomes equal to 90°C, the entrainment ratio becomes equal to zero. The entrainment ratio vary from 0.2 to 0.4, from0.12 to 0.2, from 0.7to 0.1 and from 0.03 to 0.05 when the temperature in the generator is 70, 75, 80 and 85°C respectively.

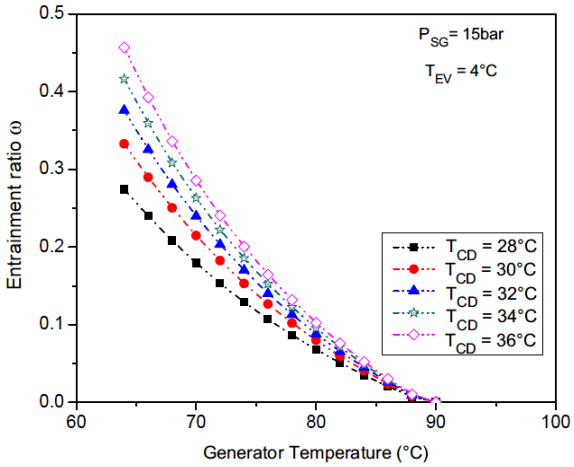

Fig. 4 ω vs. T_G for various condenser temperature T_{CD}

Fig. 5 shows that the entrainment ratio is practically identical for every generator temperature. The entrainment ratio is about 0.3, 0.18, 0.1 and 0.05 for generator temperature 70, 75, 0, 85°C respectively.

In the hybrid cycle the evaporator temperature practically don't has effect on the ejector inlet and outlet parameters so that's why the entrainment ratio is almost same for all the evaporator temperature.

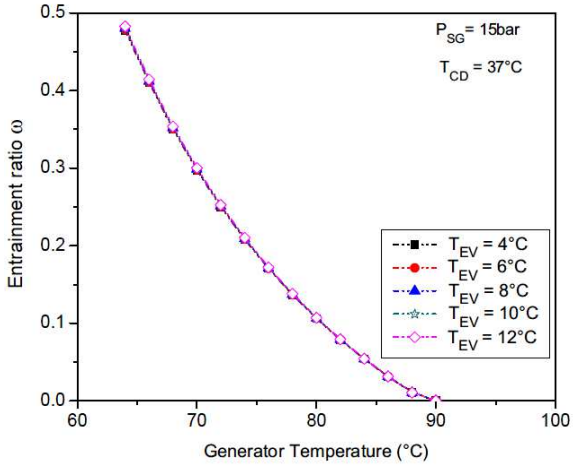

Fig. 5 ω vs. T_G for various evaporator temperature T_{Ev}

B. *Hybrid and basic cycle performances*

In the studied cycle, first a basic comparison was done between the basic single effect cycle and the hybrid ejector single effect absorption. Thus the effect of generator temperature, condensation and evaporation temperature is studied.

The coefficient of performances is more important for the hybrid cycle until the temperature in the generator become equal to a 90, as shown in fig. 6. After 90°C, the COP of the hybrid cycle reaches the same COP of the basic cycle because the entrainment ratio with these parameters is zero as shown in fig.5 (a). The COP of the hybrid cycle reaches a maximum of performances is 0.88 for 78°C while the basic cycle reaches 0.8 at 90°C. Thus the ejector in the hybrid cycle improves the cycle performances at low generator temperature.

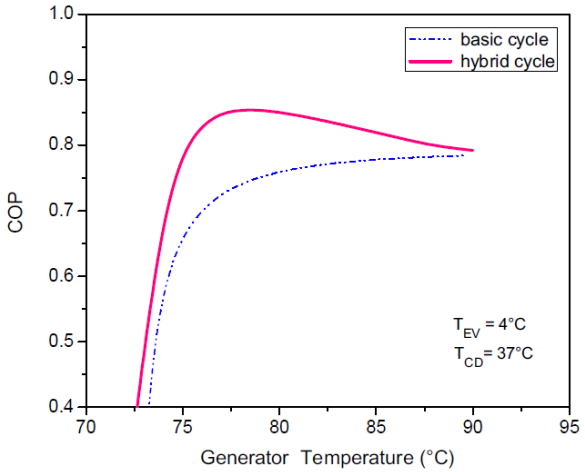

Fig. 6 COP of hybrid and conventional cycle vs. machine generator temperature, T_G (P_{18}=15bar)

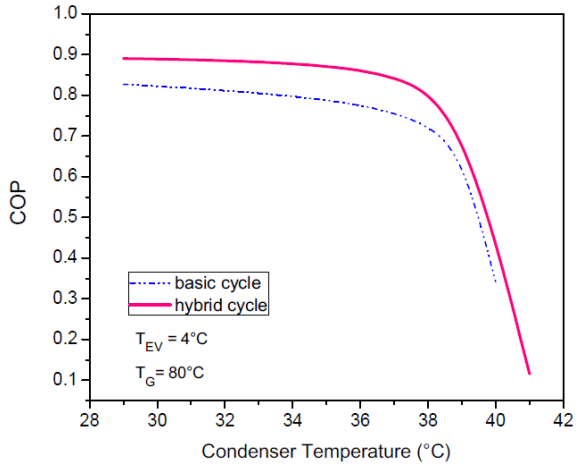

Fig. 7 COP of hybrid and conventional cycle vs. condenser temperature T_{CD}

Fig.7 shows that the coefficient of performance of both hybrid and basic cycle decrease with the condenser temperature. Also, it is shown that the COP of the hybrid cycle is higher than the basic cycle. The hybrid cycle coefficient of performance reaches 0.9 when the evaporator and generator temperatures are at 4 and 80°C.

The coefficient of hybrid and basic cycles increases with increasing the evaporator temperature, as shown in Fig.8. Also, when the condenser temperature is at 37°C and the generator temperature is 80°C, the COP of hybrid cycle is 13% higher than that of basic single effect cycle.

ISSN: 2961-6611

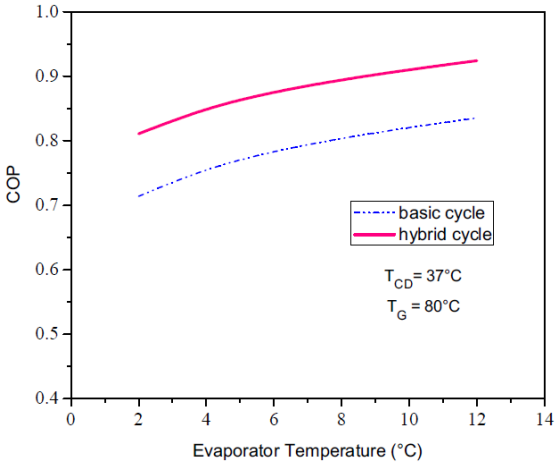

Fig.8 COP of hybrid and conventional cycle vs. evaporator temperature, T_{EV}

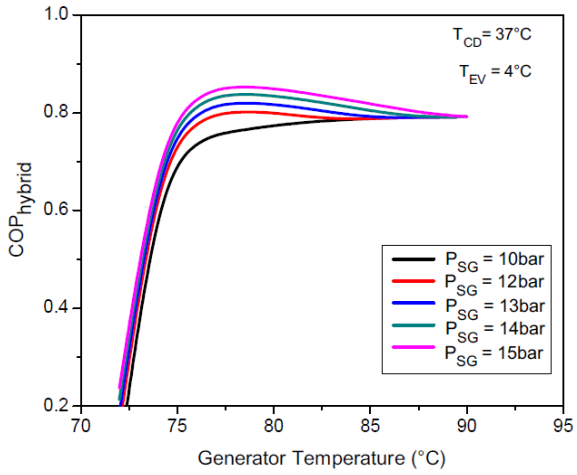

Fig. 9 COP_{hybrid} vs. T_G for various steam-generator temperatures, T_{SG}

Fig. 9 shows: The higher the steam-generator pressure (and consequently temperature), the larger the machine-generator temperature range where the cycle performance is improved, and the higher the maximum COP that could be reached inside this interval. On the opposite, when the steam generator pressure P_{SG} is decreased to 10 bar, practically no improvement more of the cycle performance is observed under the prevailing conditions.

IV. Conclusions

In this study an hybrid cycle composed of steam-ejector loop coupled with single effect absorption refrigeration cycle working with water lithium-bromide. Mathematical model of the hybrid cycle and the ejector were detailed. Results show that entrainment ratio of the ejector depend on steam pressure and condenser temperature. While, it is slightly depend on the evaporator temperature. Comparing the basic cycle performances to the hybrid cycle performance, it was found that the COP of the hybrid one is higher than the basic one when the temperature of the generator is less than 90°C.

It was concluded that the COP of the new cycle is higher for lower generator temperature, until 90°C when the entrainment ratio become equal to zero, the hybrid COP reaches COP's of the basic cycle.

The COP of the hybrid cycle increases with the steam pressure and increases with the generator temperature until 90°C, which refers to entrainment ratio equal to zero.

Acknowledgment

Acknowledgements Doniazed Sioud gratefully acknowledges the Tunisian Ministry of Higher Education and Scientific Research for funding her internships at Rovira i Virgili University of Tarragona (Spain)

References

[1] L. Shi, J. Yin, X. Wang, M. S. Zhu, "Study on a new ejection-absorption heat transformer, Applied Energy, vol. 68, n°2, pp. 161-171, 2001.

[2] A. Sözen, M. Özalp, "Performance improvement of absorption refrigeration system using triple-pressure-level", Appl. Therm. Eng, vol. 23,n°13, pp. 1577-1593, 2003.

[3] C. Vereda,R. Ventas, A. Lecuona, "Study of an ejector-absorption refrigeration cycle with an adaptable ejector nozzle for different working conditions". Applied Energy, vol. 97, pp. 305-312, 2012.

[4] L. G. Farshi, A.H. Mosaffa, C.A.I Ferreira, M.A. Rosen, "Thermodynamic analysis and comparison of combined ejector–absorption and single effect absorption refrigeration systems", Applied Energy, vol. 133, pp. 335–346., 2014.

[5] D.W. Sun, I.W. Eames, S. Aphornratana, "Evaluation of a novel combined ejector-absorption refrigeration cycle I: computer simulation". Int. J. Refrigeration vol. 19, n°3, pp. 172-180,1996..

[6] D. Sioud, R. Garma, and A. Bellagi, "*Thermodynamic Analysis of a Solar Combined Ejector Absorption Cooling System*", Journal of Engineering
Vol. 2018, Article ID 7090524, 12 pages https://doi.org/10.1155/2018/7090524

[7] S. Aphornratana, I.W. Eames, "Experimental Investigation of a Combined Ejector-Absorption Refrigerator". Int. J. Energy. Res., vol. 22, n°3, pp. 195-207, 1998.

[8] R. Sirwan, M.A. Alghoul, K. Sopian, Y. Ali, J. Abdulateef, "Evaluation of adding flash tank to solar combined ejector–absorption refrigeration system". Solar Energy, vol. 91, pp.283- 296, 2013.

[9] A. M. Abed, M.A. Alghoul, R. Sirawn,R., A. N. Shamani,K. Sopian, "Performance enhancement of ejector-absorption cooling cycle by re-arrangement of solution streamlines and adding RHE", Applied Thermal Engineering, vol. 77,pp. 65-75, 2015.

[10] D.Hong, G. Chen, L. Tang, Y. He., "A novel ejector-absorption combined refrigeration cycle". Int. J. Refrigeration,vol. 34, n°7, pp. 1596–1603, 2011.

[11] L.G. Farshi, S.M.S. Mahmoudi, M.A. Rosen, M. Yari, " Use of low grade heat sources in combined ejector–double effect absorption refrigeration systems". J Power and Energy, vol.226, n°5, pp.607–622, 2012.

[12] I.W. Eames, S. Wu, "Experimental proof-of-concept testing of an innovative heat-powered vapour recompression-absorption refrigerator cycle", Appl. Therm. Eng, vol. 20, n°8, pp. 721-736, 2000.

[13] D. Sioud, M. Bourouis and A. Bellagi, "Investigation of an ejector powered double-effect absorption/recompression refrigeration cycle", International Journal of Refrigeration, Vol. 99, pp. 453-468 March 2019.

[14] S.A. Klein.,F. Alvarado, Engineering equation solver, Version 7.441. Middleton, WI: F–chart software, 2003.

ISSN: 2961-6611

Environmental Assessment Method Applicability Evaluation Methodology

Mohamed Amine Zainine [1, 2, a], Taoufik Mezni [1, b], Mohamed Ali Dakhlaoui[1,2,c], Amenallah Guizani [3, d]

[1]*Université de Tunis, Ecole Nationale Supérieure d'Ingénieurs de Tunis, U.R. MSSDT 99/UR/11-46*
5, Av. Taha HUSSEIN, 1008, Tunis, Tunisie.
[2]*Université de Tunis el Manar, Ecole Nationale d'Ingénieurs de Tunis (ENIT)*
B.P. 37, 1002, Tunis-Belvédère, Tunisie
[3]*Research and Technology Center of Energy (CRTEn)*
B.P. 95, 2050, Hammam Lif, Tunisia
[a]zainine.amine@hotmail.com
[b]mezni.taoufik@planet.tn
[c]dakhlawimedali@yahoo.fr
[d]amenallah.guizani@crten.rnrt.tn

***ABSTRACT* — Environmental impact assessment tools suffer from an applicability issue which could impede their use and development. The main purpose of this article is to present a methodology to evaluate building environmental assessment tool applicability and to propose solutions for their best implementation or to pave the way for. First, the criteria of evaluation had been chosen based on review of flows and obstacles encountered by various building environmental assessment tools. Then, the evaluation methodology was applied to the Tunisian case. It came out that, given the lack of building environmental regulations and adequate subsidy mechanisms, the success and development of an official building environmental assessment method in Tunisia could be questioned.**

***Keywords* — building – environmental assessment – applicability – Tunisia**

I. INTRODUCTION

Buildings environmental assessment has gained increasing importance around the world. Many countries have developed or are developing methods and laws related to buildings environmental assessment [1, 2, 3, 4]. The best known methods are, for example, BREEAM [1, 5], LEED [6, 7] and HQE [1, 8].

Several studies have shown that building environmental assessment had a beneficial effect on the energetic, environmental, economic and social sectors [9, 10, 11, 12, 13]. However, building environmental assessment methods available in numerous countries suffer from an applicability issue which may be related to matters addressed by the method or other factors, such as the institutional, legislative or economic framework [14, 15, 16, 17, 18, 19, 20, 21]. Therefore, before implementing a building environmental assessment method, it is essential to identify any problems that might impede or constrain the application of this method. For this purpose, a methodology for evaluating building environmental assessment tool applicability will be presented and solutions for their best implementation or to pave the way for will be proposed.

First, the evaluation criteria will be identified and weighting method will be exposed. Then, the developed methodology will be applied to the Tunisian case and compared to results obtained by a deep analysis.

II. FEEDBACK FROM VARIOUS EXISTING BUILDING ENVIRONMENTAL ASSESSMENT METHODS AND IDENTIFICATION OF APPLICABILITY EVALUATION CRITERIA

From available methods feedback, some weak points, mentioned below, have been reported. The major disadvantages encountered during the application of existing building environmental assessment methods are both their subjective nature making the obtained results user dependent and the long building evaluation process [14, 20]. In order to eradicate these problems, designers are constantly improving their building environmental assessment tools. The new version of BREEAM In-Use International, for example, is available via an online interface and therefore saves time over the building evaluation period. In order to standardize the buildings environmental assessment practices between the different users of the repository, a technical guide is provided with this latter. This expands the benchmark between certified buildings [15].

Another defect mentioned in several studies on the building environmental assessment methods is their results presentation. Sometimes, presented results do not allow the user to situate the building according to its performance level or to know which target is below the required level of performance. Therefore, the assessment method would not be able to orient the user towards the optimal solution and could even lose credibility as to the displayed results [14, 20]. In this context, Cole indicates that the separation between qualitative and quantitative targets when presenting the results would allow a better user interpretation [14]. Haapio and Viitaniemi add that a poor results presentation combined

ISSN: 2961-6611

with measurement uncertainties and the dependence of certain methods on the evaluated building types could lead the user to an evaluation error [20]. Sometimes, some evaluation criteria are not applicable and therefore become penalizing for some buildings. This observation has obliged some methods to adapt and/or modify their rating system such as GBTool or BREEAM [14, 15].

Cole argues that one premise of voluntary assessments is that if the market is provided with improved information and mechanisms, an informed client group can and will provide leadership in environmental responsibility and others will follow suit to remain competitive [14]. It is therefore clear that a good communication system is essential to ensure an increased use of building environmental assessment methods.

Recent studies have shown that the availability of building environmental regulation would promote and consolidate the use of building environmental assessment methods [16, 17, 18]. Gabe confirms that voluntary tools such as LEED are used more for advertising purposes than for optimizing environmental performance [17]. Arts reports that the 2011 regulations introduced in Scotland and later in England and Wales contributed to the consolidation and updating of the building environmental assessment methods [18].

A study conducted by Ballu and Toulouse showed that the main factor that hindered the use of energy-efficient products was the initial investment cost [19]. Therefore, in order to encourage consumers to use these products and therefore to comply with possible environmental regulations, it is necessary to set up financing mechanisms through subsidies. These subsidies will have a beneficial effect on the use of building environmental assessment methods if they cover both the equipment and study costs. However, even if it does not cover study costs, they would still have a positive effect on the use of building environmental assessment methods if a building environmental regulation was implemented.

Haapio and Viitaniemi support the idea that building environmental assessment methods should line up with a standardized rating system and database [20]. Indeed, when analyzing several building environmental assessment methods, they found it difficult, if not impossible, to compare the results given by different methods.

Ciaran reports that public participation in building environmental assessment is of great importance. It enables citizens to contribute to government decision-making through the reporting to decision-makers and provides an educational function that enables citizens to better understand their governmental system. [21] As a result, it could facilitate successful implementation of projects or programs and enhance the application and use of building environmental assessment methods.

The development of environmental assessment methods is in some way due to the existence of a specialized institutional framework. Indeed, the availability of an organization promoting and monitoring the implementation of a building environmental regulations or supporting high environmental value project would promote the use of building environmental assessment methods through communication, grants or training. In addition, specialized staff would support the various stakeholders through training and speed up the processing time. The agency 'ADEME', for example, has contributed to the success of several programs and is an important pillar in the development and promotion of buildings environmental assessment methods such as 'HQE' [8].

Moreover, implemented environmental programs play an important role in the development of environmental assessment methods. Some methods such as 'HQE' have been created under an environmental program.

Finally, six applicability evaluation criteria have been identified from the above analysis. Table 1 present this criteria and provide a description for each one.

TABLE 1
APPLICABILITY EVALUATION CRITERIA

Criteria	Description (sub-criteria)
Tools	- Results presentation (separation between qualitative and quantitative targets). - Line up with standardized rating system and database. - Minimize measurement uncertainties. - Avoid subjective nature. - Applicability of evaluation criteria and independence on the evaluated building.
Institutional framework	- Development of the institutional framework. - Experts in building environmental assessment availability.
Legislative framework	- Availability of legislative framework.
Subsidies	- Availability of funding mechanisms.
Communication systems	- Information about notation system and advantage. - Availability of communication mechanisms: advertisement, conference, sponsoring… - Public participation in building environmental assessment.
Environmental programs	- Implementation of environmental programs.

Weighting of each criteria is made based on its degree of importance. This weighting is presented in tables 2 and 3.

TABLE 2
APPLICABILITY EVALUATION CRITERIA WEIGHTING

Criteria	Nature		Weighting
	Mandatory	Optional	
Tools	X		30
Institutional framework	X		25
Legislative framework	X		20
Subsidies	X		15
Communication systems		X	5
Environmental programs		X	5

ISSN: 2961-6611

The criteria weighting was made according to different scenario results. From this different scenario, we were able to identify mandatory and optional criteria and to classify the evaluation criteria from the most important to the less important.

For example, if in a given country, an environmental impact assessment tool and an institutional and legislative frameworks are available and verify all the sub-criteria described in table 1, but institutional framework don't verify the sub-criteria, it's obvious that the implementation of this environmental tool would be difficult. From this point of view, we can confirm that institutional framework criteria is more important than institutional or legislative frameworks criteria.

TABLE 3
APPLICABILITY EVALUATION CRITERIA AND SUB-CRITERIA WEIGHTING

Criteria	Sub-criteria	Weighting	
		Sub-criteria	Criteria
Tools	Results presentation (separation between qualitative and quantitative targets). *(Maximum score) – (Maximum score) x (Percentage of criteria containing qualitative and quantitative targets)	8	30
	Line up with standardized rating system and database. *(Maximum score) x (Percentage of criteria similar to criteria of standardized rating system)	5	
	Minimize measurement uncertainties. *<2% = 2 ; <5% = 1 ; >5% = 0	2	
	Avoid subjective nature. *(Maximum score) x (Percentage of non-subjective criteria)	5	
	Applicability of evaluation criteria and independence on the evaluated building. *All criteria are applicable = 10 ; one non applicable criteria = 5 ; more than one non applicable criteria = 0	10	
Institutional framework	Development of the institutional framework. * nonexistent institutional framework = 0 ; existent institutional framework but not well organized = 12 ; excellent institutional framework = 15	15	25
	Experts in building environmental assessment availability. *No expert = 0 ; insufficient number of expert = 5; sufficient number of expert = 10	10	
Legislative framework	Availability of legislative framework. *Not available = 0 ; Available but not well developed = 10 ; Good legislative framework = 20	20	20
Subsidies	Availability of funding mechanisms. *Not available = 0 ; <20% = 10 ; >20% = 15	15	15
Communication systems	Information about notation system and advantage. *No information = 0 ; medium information = 1 ; sufficient information = 2	2	5
	Availability of communication mechanisms: advertisement, conference, sponsoring… *Not available = 0 ; available =1	1	
	Public participation in building environmental assessment. *No participation = 0 ; medium participation = 1 ; high participation = 2	2	
Environmental programs	Implementation of environmental programs. *No program = 0 ; few program related to environmental program (renewable energy) = 2 ; environmental program availability = 5	5	5

* Weighting method

The same analysis has been made for a scenario where tool, institutional framework and subsidies criteria verify the sub-criteria but legislative framework don't. From this analysis, we find that legislative framework criteria are more important than subsidies criteria. This is due to the fact that legislative framework would make the application of a given environmental impact assessment tool mandatory while subsidies will only support the application of such tool.

Furthermore, communication systems and environmental programs criteria would only support the application of a given environmental tool. Also, they are somehow linked to criteria such as legislative or institutional framework. For example, if a building environmental assessment law is published, it will be a kind of communication systems for building environmental assessment tool. Then, we could

ISSN: 2961-6611

classify communication systems and environmental programs criteria as optional criteria.

Eventually, building environmental assessment tool applicability evaluation is made as follow:

- Low applicability level: each mandatory criteria should have a minimum score of 80%.
- Medium applicability level: each mandatory criteria should have a minimum score of 80% and each optional criteria should have a minimum score of 50%.
- High applicability level: each mandatory criteria should have a minimum score of 90% and each optional criteria should have a minimum score of 90%.

III. TUNISIAN CASE: SITUATIONAL ANALYSIS AND WAYS TO IMPROVE THE APPLICABILITY OF AN OFFICIAL BUILDING ENVIRONMENTAL ASSESSMENT METHOD

In order to appreciate the applicability of an official buildings environmental assessment method in Tunisia, an overview of the current Tunisian situation in terms of laws, programs, tools and institutional frameworks that can motivate and/or facilitate the application of an official building environmental assessment method, is essential.

Environmental protection has a prominent place in Tunisian politics. The active participation of Tunisia in international conferences and programs for the environment and the adoption of conventions and protocols relating thereto (Kyoto Protocol) confirm this fact [23].

Since 1989, in order to implement environmental upgrading programs, Tunisia has developed an important institutional framework. The themes covered are wastewater management (ONAS), waste management (ANGED), coastal protection (APAL), environmental prevention and pollution control (ANPE), environmental management (OTEDD) and environmental technologies (CITET) [24, 25]. Similarly, in order to reduce the energy consumption at the national level, the National Agency for Energy Management (ANME) was created in 1985.

Therefore, it appears that Tunisian institutional framework is well developed. However, improvements should be done at the organizational level and in the training of experts in building environmental assessment. A lead agency could be created by the merger of the ANPE and the ANME. Given the close link between energy and environmental analysis, the merger would allow the simultaneous treatment of both themes (energetic and environmental). Thus, administrative tasks will be facilitated, the processing time minimized and the future application of a building environmental regulation that encompasses both energy and environmental aspects of the building will be supervised by one organization instead of two (ANPE and ANME). Such mergers have already taken place in several countries such as France where the French Environment and Energy Management Agency (ADEME) is formed from the merger of several organizations, such as the Agency for Air Quality (AQA), the French Agency for Energy Management (AFME) and the National Agency for the Recovery and Disposal of Waste (ANRED) [26].

In addition to this institutional framework, and as specified in section 2, it is necessary to establish funding mechanisms through subsidies. Two funds have been set up in Tunisia: the Depollution Fund (FODEP) for financial support to environmental programs implementation [25] and the National Energy Management Fund (FNME) to support energy management action through the granting of subsidies [27]. Regarding the mechanisms for granting these subsidies, mechanisms similar to those used for granting subsidies for thermal insulation as PROMO-ISOL or for the use of renewable energy as PROSOL TUNISIA could be implemented [28, 29]. Given the success of the latters in terms of simplifying administrative formalities and encouraging investment, the application of such mechanisms for a building environmental program could be a good choice.

Moreover, the availability of specialized legislation is essential for the promotion and development of these methods. These laws should be developed in collaboration with civil society to ensure the smooth implementation of future projects or programs and to boost the use and application of building environmental assessment methods (as specified in Section 2) [21]. In this context, it appears that Tunisia has promoted energy efficiency and renewable energies at the expense of the building environmental aspect. No law relating to building environmental aspect was promulgated. In contrast, several laws relating to building energy aspect exist: the law of 2 August 2004 amended by the law of 9 February 2009 to pave the way for the self-generation of electricity from renewable energies [29] and the decrees of 23 July 2008 and 1 June 2009 fixing the minimum energy-saving technical specifications, respectively, for construction and extension projects of office buildings and similar and for construction and extension projects of residential buildings [30, 31]. Therefore, it is essential that Tunisia develops adequate environmental regulations and this should be done in collaboration with civil society for the reasons mentioned above.

Concerning implemented programs, once again, it appears that Tunisia has promoted energy efficiency and renewable energies in disregard of the building environmental aspect. Several programs related to energy efficiency and renewable energy have been set up such as the triennial (2005-2007) and quadrennial (2008-2011) energy management programs, the presidential program (2009- 2014) and the Tunisian solar plan (2010-2016) [29]. These programs give concrete expression to the national policy of energy management and of renewable energy promotion followed by the Tunisian State. In contrast, few environmental programs have been established. The Environment-Energy Program (PEE), launched in January 2009 and aiming to align Tunisian companies with national and international environmental requirements and to improve their competitiveness, would be the only program implemented to date that supports companies in the implementation of ISO 14001, ISO 50001 and the Tunisian 'Ecolabel' (for tourist accommodation

ISSN: 2961-6611

service) [32, 33]. Nevertheless, other projects in collaboration with other countries or international organizations have been undertaken. A twinning project between France, Germany, Portugal and Tunisia has served as a support for the Tunisian administration for the development and promotion of eco-construction [34]. Since 2003, Tunisia has launched an environmental program in collaboration with GIZ [24]. The main themes of this program are communication and environmental education, competence decentralization, technology transfer and environmental prevention. One of the consequences of this program is the development of regional plans for environment and sustainable development. These plans, through their participatory character, would boost the communication on the environmental theme [35].

In addition, as specified in Section 2, a good communication system boosts the use of building environmental assessment methods. Therefore, it is essential to have a good communication system not only to promote the use of these methods but also to gain feedback from the various stakeholders, which will be useful to develop and update these methods. The twinning project between France, Germany, Portugal and Tunisia, mentioned above, contains a rather interesting communication component, defining the communication strategy for eco-construction development [34]. This strategy could be a good communication strategy for an official building environmental assessment method.

Furthermore, in order to avoid making the same mistakes, the tool or method that will be used for building environmental assessment should take into account feedback from other internationally available tools, such as BREEAM, LEED and HQE. Also, this tool should be in line with a standardized database and scoring system (or as close as possible to those methods where appropriate). Then, the tool that will be made available to design offices should present clear results to direct the user towards the optimal solution and to avoid leading him towards an evaluation error. The evaluation criteria must be carefully chosen according to building type and regional conditions. Among other things, it is necessary to rely on a tool with no subjective character, in order to make the obtained results user-independent. In order to standardize the buildings environmental assessment practices between different users of the tool, a technical guide could be provided.

In Tunisia, several building design and/or simulation tools are available such as CLIP and CHEOPS for simple design buildings and EQUEST for more complex buildings [36, 37]. Concerning environmental assessment tools, in 2013, a new label called ‘ECO-BAT’ has been developed by the ANME in partnership with ADEME and with the assistance of the design offices ALCOR and ECOTECH [38]. This label is still not implemented but seems to include targets corresponding to the Tunisian priority stakes while retaining its ease of use.

Finally, it appears that Tunisia nowadays has a fairly mature thermal regulation. This finding comes from the success of the building energy management programs initiated by the Tunisian government and the availability of adequate tools, laws and institutional frameworks. However, institutional and legislative framework and communication with professionals and general public need to be improved. After consulting the ANME, this latter confirms the difficulty of checking the conformity of buildings with thermal regulations, which takes sometimes quite a long time, due to the lack of human resources. Other professionals and individuals assert the difficult access to information [39], hence the need to improve the means of communication. Also, a recent study demonstrated the need to update the Tunisian thermal regulations [22].

In contrast, although Tunisia has an important environmental institutional framework, environmental programs remain focused on sanitation, waste management, coastal protection and discharges monitoring due to economic activities. Unfortunately, the building sector is not given proper consideration yet. Nevertheless, some projects such as the twinning program between France, Germany, Portugal and Tunisia, cited above, are encouraging and demonstrate the beginning of interest for the building sector. Moreover, the unavailability of building environmental regulation and adequate subsidy mechanisms is a sufficient reason to question the success and the development of an official building environmental assessment method in Tunisia. The ‘ECO-BAT’ label, even though it is an important step in the transition from building energy evaluation to building environmental assessment, could unfortunately not evolve without supporting laws and financial mechanisms.

Using the applicability evaluation methodology presented in section 2, results exposed in table 4 have been obtained.

TABLE 4
RESULTS OF THE EVALUATION OF BUILDING ENVIRONMENTAL ASSESSMENT TOOL APPLICABILITY IN TUNISIA

Criteria	Sub-criteria	Weighting	
		Sub-criteria	Criteria
Tools: ECO-BAT	Results presentation (separation between qualitative and quantitative targets).	8/8	23/30
	Line up with standardized rating system and database.	1/5	
	Minimize measurement uncertainties	1/2	
	Avoid subjective nature.	3/5	
	Applicability of evaluation criteria and independence on the evaluated building.	10/10	
Institutional framework	Development of the institutional framework.	12/15	17/25
	Experts in building environmental assessment availability.	5/10	

ISSN: 2961-6611

Legislative framework	Availability of legislative framework.	0/20	0/20
Subsidies	Availability of funding mechanisms.	0/15	0/15
Communication systems	Information about notation system and advantage.	1/2	3/5
	Availability of communication mechanisms: advertisement, conference, sponsoring…	1/1	
	Public participation in building environmental assessment.	1/2	
Environmental programs	Implementation of environmental programs.	2/5	2/5

As each mandatory criteria didn't reach a minimum of 80%, we could say that the environmental assessment tool (ECO-BAT) is not applicable at the moment.

At this step of the study, it's clear that there is a good agreement between results obtained by the applicability evaluation method and results obtained by the above deep analysis of the Tunisian case.

IV. Conclusion

The main objective of this study was to present an environmental assessment method applicability evaluation methodology.

For this purpose, the defaults faced by the various building environmental assessment method available internationally and barriers that have hindered their use or development were analyzed. Based on this analysis, the evaluation criteria have been identified and weighting method has been exposed. Then, the developed methodology has been applied to the Tunisian case and compared to results obtained by a deep analysis. A good agreement between results obtained by the applicability evaluation method and results obtained by the above deep analysis of the Tunisian case has been found.

It came out that the environmental assessment tool (ECO-BAT) is not applicable at the moment. Indeed, given the unavailability of building environmental regulation and adequate subsidy mechanisms, the success and development of an official building environmental assessment method in Tunisia could be questioned. Even if the 'ECO-BAT' label constitutes an important step in the transition from building energy evaluation to building environmental assessment, it could unfortunately not evolve without supporting laws and financial mechanisms. Among other things, the institutional framework and communication systems would not constitute major obstacles to the applicability of an environmental assessment method. It has been shown that the Tunisian institutional framework is only suffering from a lack of organization and of specialized staff. Solutions have been proposed, such as the merger of ANME and ANPE. Concerning the communication systems, programs in collaboration with others countries and international organizations would provide a good basis for the implementation of an efficient communication system.

Acknowledgments

The authors would like to thank Mr. Bruno PEUPORTIER, Professor at the "Ecole des Mines de Paris" for his participation in the reviewing of this article and for his valuable comments. They also would like to thank the National Agency for Energy Management (ANME) and the National Agency of Environment Protection (ANPE) for their collaboration. Eventually, they thank Ms. Meriem JRADI, former translator at the United Nations, for her helpful linguistic contribution.

This research did not receive any specific grant from funding agencies in the public, commercial, or not-for-profit sectors.

Références

[1] Hildegund Mötzl, Maria Fellner, Environmental and health related criteria for buildings, Final Report. IBO Österreichisches Institut für Baubiologie und –ökologie GmbH., P: 24, 25, 28, 29, 30, (2011).

[2] Alberto Fonseca, Luis Enrique Sánchez, José Claudio Junqueira Ribeiro, Reforming EIA systems: A critical review of proposals in Brazil, Environmental Impact Assessment Review, 62 (2017) 90–97, doi: 10.1016/j.eiar.2016.10.002

[3] Hikmat H. Ali, Saba F. Al Nsairat, Developing a green building assessment tool for developing countries – Case of Jordan, Building and Environment, 44 (2009) 1053–1064, doi:10.1016/j.buildenv.2008.07.015

[4] Erkki Seinre, Jarek Kurnitski, Hendrik Voll, Building sustainability objective assessment in Estonian context and a comparative evaluation with LEED and BREEAM, Building and Environment, 82 (2014) 110-120, doi: 10.1016/j.buildenv.2014.08.005

[5] http://www.breeam.org/, Last accessed on October 5, 2017.

[6] Green Building Information Gateway, http://www.gbig.org/collections/14544, last accessed on October 10, 2017.

[7] U.S. Green Building Council, 2015, "Green Building Facts", via http://www.usgbc.org/articles/green-building-facts, last accessed on October 10, 2017.

[8] Y. Moch, W. Persello, Bâtiment et démarche HQE, ADEME, 2007.

[9] Nigar Zeynalova, The applicability of BREEAM energy category for achieving energy efficiency in context of Zero energy buildings, Research Essay, AAR4817 ZEB Theory, 2011.

[10] Vanclay F., International principles for social impact assessment. Impact Assess Proj Apprais, 21(1), (2003) 5-11.

[11] Gagnon C, Hirsch P, Howitt R., Can SIA empower communities?, Environ Impact Assess. Rev., 13 (1993) 229–53.

[12] Gagnon C., Social impact assessment in Quebec: issues and perspectives for sustainable community development, Impact Assess., 13 (1995) 273–88.

[13] Akari Abdallah, L'économie verte pour la Tunisie 'verte', les journées de l'entreprise, 2012.

[14] Raymond J. Cole, Building environmental assessment methods: clarifying intentions, Building Research & Information, 27:4-5, (1999) 230-246

[15] BREEAM In-Use international 2015 : les évolutions par rapport à la version 2013, Sinteo, 1 avril 2015, via http://idee.sinteo.fr/?p=1114, Last accessed on August 25, 2017.

[16] Urmila Jha-Thakur, Thomas B. Fischer, 25years of the UK EIA System: Strengths, weaknesses, opportunities and threats. Environmental Impact Assessment Review, 61 (2016) 19-26, Doi: 10.1016/j.eiar.2016.06.005

[17] Jeremy Gabe, Creating an efficient market for green buildings: what can we learn from the first 450 users of the LEED assessment tool?, SB10 Innovation and Transformation, New Zealand Sustainable

ISSN: 2961-6611

Building Conference, 26-28 May 2010, Te Papa, Wellington, New Zealand.

[18] Arts, J., Runhaar, H.A.C., Fischer, T.B., Jha-Thakur, U., Laerhoven, F.V., Driessen, P.P.J., Onyango, V., The effectiveness of EIA as an instrument for environmental governance reflecting on 25 years of EIA practice in the Netherlands and the UK. Journal of Environmental Assessment Policy and Management, Volume 14, Issue 04, (2012) Doi: 10.1142/S1464333212500251

[19] Matthieu Ballu, Edouard Toulouse, Energy savings in practice: potential and delivery of EU Eco design measures, Cool products for a cool planet campaign, 2010.

[20] Appu Haapio, Pertti Viitaniemi, A critical review of building environmental assessment tools, Environmental Impact Assessment Review, 28 (2008) 469 – 482.

[21] Ciaran O'Faircheallaigh, Public participation and environmental impact assessment: Purposes, implications, and lessons for public policy making, Environmental Impact Assessment Review, 30 (2010) 19–27.

[22] M. A. Zainine et al., Energetic and Economic Impact of Using Bioclimatic Design Technics and of Solar Water Preheating System Integration on Tertiary Building, International Journal of Renewable Energy Research, Vol.6, No.3, (2016) pp. 787-794

[23] La Tunisie et l'environnement, Ministère des Affaires Étrangères, République Tunisienne, via http://www.diplomatie.gov.tn/index.php?id=396, Last accessed on September 20, 2017.

[24] Programme pour l'Environnement Une approche systémique payante, Deutsche Gesellschaft für Internationale Zusammenarbeit (GIZ) GmbH, 2013.

[25] La politique environnementale, portail du gouvernement tunisien via http://www.tunisie.gov.tn/index.php?option=com_content&task=view&id=1519&Itemid=530&lang=french, Last accessed on September 17, 2017.

[26] Loi n° 90-1130 du 19 décembre 1990 portant création de l'Agence de l'environnement et de la maîtrise de l'énergie

[27] Nejib Osman, Tunisie : une politique nationale d'efficacité énergétique, L'efficacité Energétique à travers le monde Sur le chemin de la transition, Les Cahiers de Global Chance N°32, 2012.

[28] Baccouche Abdelkader, Programme national de Promotion du solaire thermique en Tunisie : PROSOL, ENERSOL-WSEF 2014: Les opportunités d'utilisation du solaire thermique au niveau des procédés industriels, 2014.

[29] Mounir Bahri, Programme d'Efficacité Energétique en Tunisie, ANME, 2009.

[30] Journal Officiel de la République Tunisienne N° 62, 1er août 2008

[31] Journal Officiel de la République Tunisienne N° 45, 5 juin 2009

[32] Programme environnement énergie, via http://www.pr-e-e.org/index.php/presentation/presentation-pee/description, Last accessed on September 22, 2017.

[33] Ecolabel tunisien pour les services d'hébergement touristique, Institut national de la normalisation et de la propriété industrielle.

[34] Raoudha Jebari Larbi, Le développement et la promotion de l'éco-construction, Projet de jumelage entre la France, l'Allemagne, le Portugal et la Tunisie, 2014.

[35] Plan régional d'environnement et de développement durable (PREDD) du Gouvernorat de Médenine, Deutsche Gesellschaft für Internationale Zusammenarbeit (GIZ) GmbH, 2014

[36] Règlementation thermique et énergétique des bâtiments neufs en Tunisie via http://www.enerbat.nat.tn/site/logiciel_simplifier.php, Last accessed on September 15, 2017.

[37] Elaboration d'un plan d'action visant le renforcement de l'application de la règlementation thermique des bâtiments en Tunisie, Deutsche Gesellschaft für Internationale Zusammenarbeit (GIZ), Rapport préliminaire, 2012.

[38] Elaboration des référentiels de notation des cibles du label ECO-BAT, rapport final, ANME, 2013.

[39] Jouhaina Ben Boubaker Gherib, Sandrine Berger-Douce, L'engagement environnemental des PME : Une analyse comparative France Tunisie, conférence de l'AIMS, 2008.

ISSN: 2961-6611

Linear-Quadratic-Gaussian (LQG) Controller for Three thank Hydraulic system

Mounir BEKAIK[#1], Abdelghani REDJATI[*2]

[#1.2]*Annaba University, Laboratory of LASA*

Algeria

[1]mounir.bekaik@gmail.com

[2]redjati@yahoo.fr

Abstract— We present in this work a new technique of stabilization for a family of nonlinear systems. Our choice relates to three-tank hydraulic systems. The basic idea is to build a LQG control low based on the results of the quadratic linear control LQ as well as the famous observer Kalman filter. In our case the complexity comes from the fact that the system is highly nonlinear as well as the presence of defects. In order to reduce this complexity, we have represented the nonlinear system as a set of several linear sub-models through a new technique based on two algorithms C-Means and N4Sid. By using the Takgi Sugeno Model, the control is obtained by combining the stabilizing control laws of linear subsystems.

Keywords— LQG, Multi-model, Takagi-Suegno, Fuzzy.

.

I. INTRODUCTION

. Optimal control problems [2] are encountered in everyday life: how to get to a destination as quickly as possible, how to minimize consumption. For a given dynamic system whose equations are known, the optimal control problem [7] is then to find the control that minimizes a given criterion. The LQG control [7] has the advantage of applying to systems whose condition is not fully measured. Developed at the beginning of the second half of the 20th century, it emerged as the first general method for the control of multivariable systems [1], [3]. Since the 20th century, many publications have been published testifying to the success of the LQG order.

The main contribution of our work is to propose a Gaussian quadratic linear control for an hydraulic system which is a highly nonlinear system. The development of these new results is based on the Multi-model approach [4].

This controller is developed from a multi-model representation of the Takagi-Sugeno [9] form of the system. For each linear model on the system reference path, an optimal multivariable LQG control law [11], [8] is established minimizing a quadratic criterion depending on the different control objectives such as uncertain additive noise. The control applied to the system is then obtained by interpolating the control laws of the different linear subsystems.

Takagi-Sugeno approximation [10] that relies on a bank of piecewise linear models to capture the possible input-output response behavior has been developed. Using a divide and conquer strategy, local linear models set is described and the global output is obtained by the integration of locale ones. Our approach is based on the fuzzy C-Means (FCM) [5], [6] . This algorithm is used to find operators regimes which are associated to dynamical linear local models. The clusters are formed according to the distance between data points and the cluster centers are formed for each cluster through N4sid identification approach. The N4SID algorithm [12] allows modeling a system from the measured input and output data. it leads to determining the order of the system by applying the dominant singular value technique.

One of the main advantages of the N4SID is that it is non-iterative and does not require the involvement of non-linear optimization methods. This allows it to overcome the problems exposed when applying iterative techniques that suffer from the absence of a guarantee of convergence and minimization of the criteria mentioned and from the sensitivity to the estimation of the initial state.

These features make the implementation of such method provide a system state representation that facilitates the implementation of the LQG control.

This paper is organized as follows. Section 2 is devoted to the Fuzzy approach and Takagi-sugeno representation. In Section 3 we present our main result in Section 4 which introduces the TS fuzzy system subject to define multi-model LQG controller. An application of the results is made on a hydraulic system Section 5. In the end, a conclusion will be quoted in Section 6.

2 FUZZY IDENTIFICATION APPROACH :

2.1 Fuzzy C-Means algorithm:

The first step consists to dividing data elements into classes or clusters using FCM algorithm. This algorithm is used for analysis based on distance between various input data points. The clusters are formed according to the distance between data points and the cluster centers are formed for each cluster. In fact, FCM is a data clustering technique in which a data set is grouped into n clusters with every data point in the dataset related to every cluster and it will have a high degree of belonging (connection) to that cluster and

ISSN: 2961-6611

another data point that lies far away from the center of a cluster which will have allow degree of belonging to that cluster.

Algorithmic steps for Fuzzy C-Means.

We are to fixe *c* where *c* is ($2 \le c \le n$) and then select a value for parameter "m" and there after initialize the partition

1- We calculate the center for each cluster

$$v_{ij} = \frac{\sum_{K=1}^{K} (u_{ik})^m x_{kj}}{\sum_{n=1}^{N} (u_{ij})^m} \quad (1)$$

2- The distance matrix $D_{[c,n]}$ is given by:

$$D_{ij} = \left(\sum_{j=1}^{m} (x_{kj} - v_{ij})^2 \right)^{1/2} \quad (2)$$

3- Update the partition matrix for the

$$r^{th} \text{ step } u_{ij}^{r-1} = \frac{1}{\sum_{j=1}^{c} \left[d_{ik}^r / d_{ik}^r \right]^{\frac{2}{m-1}}} \quad (3)$$

If

$$\left\| U^{it+1} - U^{it} \right\| < \zeta \ , \quad (4)$$

then we are to stop otherwise. We have to return to step 2 by updating the cluster centers iteratively and also the membership grades for the data point.

The second step consists to define for each cluster a local model using Subspace identification approach N4SID .This algorithm is based on the estimation of the state sequence matrix to estimate the matrices of the system and Kalman gain. One of the major advantages of N4SID is that it is non-iterative and does not involve non-linear optimization methods. This allows it to overcome the problems presented by the application of iterative techniques that suffer from the unsecured convergence and the minimization of the target criterion as well as the sensitivity to the estimation of the initial state . These features make the implementation of such a method attractive and provide a system state representation facilitating the implementation of the LQG command.

2.2- Fuzzy Takagi-Sugeno presentation:

A nonlinear dynamic system can be described in a simple way by a Takagi-Sugeno fuzzy model, which uses series of locally linearized models from the nonlinear system. So any TS fuzzy model of a nonlinear system is structured as an interpolation of linear systems. The i-th rule is expressed as

If Z_1 is F_i^1 and $z_p(t)$ is F_i^p Then:

$$\dot{x}(t) = A_i x(t) + B_i u(t)$$
$$y(t) = C_i x(t) \quad (5)$$

F_i^j are fuzzy sets. $x(t) \in R^n$ is the reference state, $u(t) \in R^m$ is the control, $y(t) \in R^q$ is the reference output, $A_i \in R^{n*n}$ $B_i \in R^{n*m}$, $C_i \in R^{q*n}$ and $z_1(t) \ldots z_p(t)$ is a known vector of premise variables. Given a pair of ($y(t)$, $u(t)$) the fuzzy system inference is given by:

$$\dot{x}(t) = \frac{\sum_{i=1}^{r} w_i(z(t))(A_i x(t) + B_i u(t))}{\sum_{i=1}^{r} w_i(z(t))} \quad (6)$$

$$y(t) = \frac{\sum_{i=1}^{r} w_i(z(t)) C_i x(t)}{\sum_{i=1}^{r} w_i(z(t))} \quad (7)$$

With: $z(t) = \left[z_1(t) \quad z_2(t) \quad \cdots \quad z_p(t) \right]$, (8)

$w_1(z(t)) = F_i^j(z_j(t)) \quad i = 1, 2, \ldots, r$

where $w_i(z(t))$ are normalized rule firing strengths, and $\forall t \ge 0$ we have:

$$\sum_{i=1}^{r} w_i(z(t)) \succ 0$$
$$w_i(z(t)) \ge 0 \quad (9)$$

Consider :

$$h_i(z(t)) = \frac{w_i(z(t))}{\sum_{i=1}^{r} w_i(z(t))} \quad (10)$$

T-S fuzzy model can be inferred as:

$$\dot{x}(t) = \sum_{i=1}^{r} h_i(z(t))(A_i x(t) + B_i u(t)) \quad (11)$$
$$y(t) = \sum_{i=1}^{r} h_i(z(t)) C_i x(t)$$

The rule firing strengths $\sum_{i=1}^{r} h_i(z(t)) \ge 0$, verify :

$$\sum_{i=1}^{r} h_i(z(t)) = 1 \quad (12)$$

ISSN: 2961-6611

An approach to obtain T-S fuzzy model that has been used in this work is local approximation in fuzzy partition spaces. In fact, in this method, nonlinear terms have been approximated by chosen linear terms. This procedure leads to reduction of the number of model rules. The number of model rules is directly related to complexity of analysis and design LMI conditions or Riccati equation solution. This is because the number of rules for the overall control system is basically the combination of the model rules and control rules

3. MULTIMODEL LQG CONTROL DESIGN

Consider the system (13) such that the output and the state are disturbed by noise

$$\dot{x}(t) = A\,x(t) + B\,u(t) + w_1(t)$$
$$z(t) = C\,x(t) + w_2(t) \qquad (13)$$

with: *dim x(t) = n x 1, dim u(t): l x 1,* where *l* is the number of actuators, *dim z(t) = m x 1*

$w_1(t)$ and $w_2(t)$ are two vectors of Gaussian white noise where *dim* $w_1(t)$ *:n x l* and *dim* $w_2(t)$ *:m x l.*

with $w(t) = \begin{bmatrix} w_1(t) \\ w_2(t) \end{bmatrix}$, where the noises $w_1(t)$ and $w_2(t)$ are independent and stationary, we obtain:

$$E\{w(t)w^T(\tau)\} = \begin{pmatrix} v_1 & 0 \\ 0 & v_2 \end{pmatrix}\delta(t-\tau) \qquad (14)$$

The matrix $v=\begin{pmatrix} v_1 & 0 \\ 0 & v_2 \end{pmatrix}$ is a constant variance covariance matrix, where the matrices v_1 and v_2 are positive definite symmetric.

The LQG regulator consists of two parts: an optimal state-feedback gain and a Kalman state estimator.

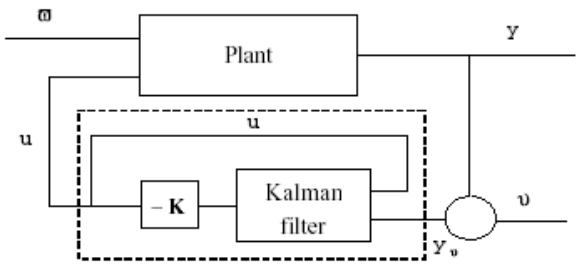

Figure 1: LQG controller

The feedback gain matrix is sought to minimize a quadratic performance criterion *J* expressed as:

$$J_{LQG} = E\{\int_0^\infty [x^T(t)Q\,x(t) + u^T(t)R\,u(t)]dt\} \qquad (15)$$

The weighting matrices Q and R are positive definite matrices.

The gain of the feedback $u(t) = -Kx(t)$ that minimizes the cost function J is:

$$K = R^{-1}B^T P \qquad (16)$$

is usually called the LQ-optimal gain, where the matrix *P* is obtained by solving an algebraic Riccati equation:

$$P\,A + A^T P + Q - P\,B\,R^{-1}B^T P = 0 \qquad (17)$$

The next step is to derive a state estimator $x(t)$ generated by Kalman filter. The gain L of the observer is given by

$$L = \tilde{Q}C^T V_2^{-1} \qquad (18)$$

Where Q is the solution of the following Riccati equation

$$A\,\tilde{Q} + \tilde{Q}A^T + V1 - \tilde{Q}C^T V_2^{-1}\,C\,\tilde{Q} = 0. \qquad (19)$$

Through TS representation, the fuzzy LQG controller is given by:

$$u(t) = \sum_{i=1}^{r} h_i(z(t))u_i(t) \qquad (20)$$

Where $u_i(t)$ is the LQG controller for each subsystem.

4. Application and simulation:

The nonlinear controlled system consists of three cylinders T1, T2 and T3 with the cross-sectional area A which are interconnected in series by two connecting pipes. The liquid (distilled water) leaving T2 is collected in a reservoir from which pumps 1 and 2 supplies the tanks T1 and T2. All three tanks are equipped with piezo-resistive pressure transducer for measuring the level of the liquid. A digital controller controls the flow rate Q1 and Q2 such that the levels in the tanks T1 and T2 can be preassigned independently. The level in tank T3 is always a response which is uncontrollable. The connecting pipes and the tanks are additionally equipped with manually adjustable valves and outlets for the purpose of simulating clogs as well as leaks.

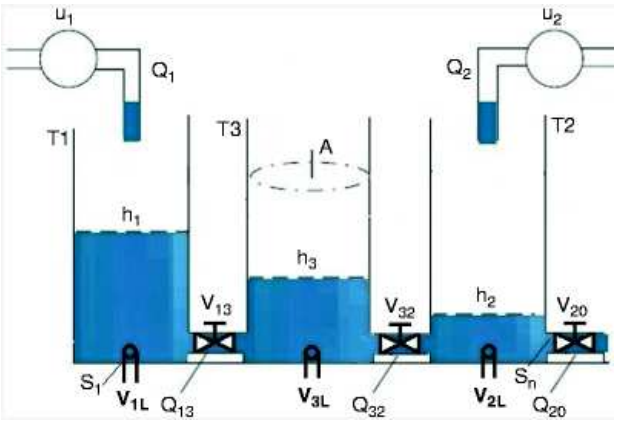

Figure 2 : Three thank hydraulic system

ISSN: 2961-6611

The flow rates q_1 and q_2 are defined through the rotational flow. The interconnection rates Q_{13} et Q_{32} depend of levels on the tanks. The flow rate Q_{20} is the output of the system. The input vector is given by:

$$U = [Q_1 \quad Q_2]^T \tag{21}$$

Then, the output vector is given by:

$$Y = [h_1 \quad h_2 \quad h_3]^T \tag{22}$$

The selected nonlinear system composed of three tank system, have a measurement data of inputs and outputs. Due to its high nonlinearity, and inaccessibility of some its outputs and states for measurements, the system is often perceived as a challenging engineering problem. In order to control the levels in the tanks, the following steps are also made: The first step consists to find the local linear models for TS fuzzy model through Fuzzy C-means and N4sid approach.

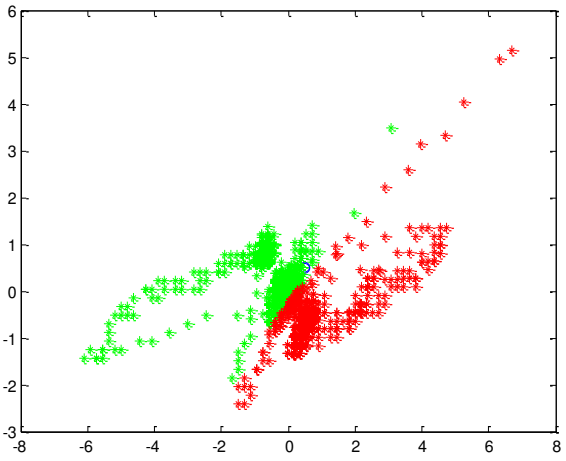

Figure 3: fuzzy C-means decomposition.

According to Fig. 3, Fuzzy C-means is a suitable method for approximation of this system, with this approximation the nonlinear and linear parts of the system. Due to the decomposition to two regions, we can utilize a LQG controller for each local linear model.

Then, the second step consists in the design of a LQG controller, which stabilizes the nonlinear fuzzy system.

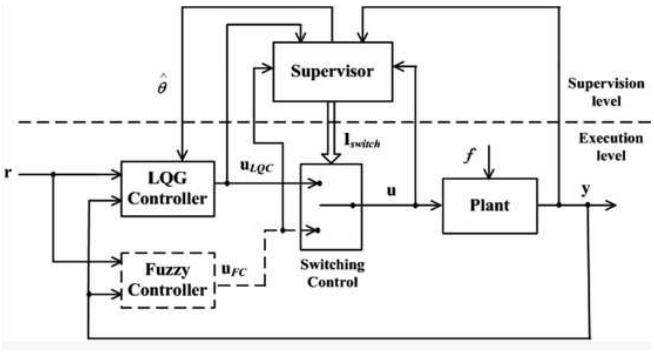

Figure 4: Fuzzy LQG controller

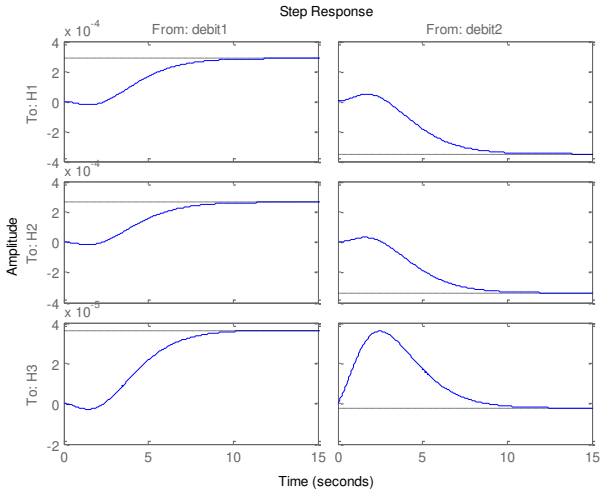

Figure 5 : Time response of the system with the fuzzy LQG Controller

According to Fig 5 the LQG control provides very good performance in terms of good reference tracking, estimated response time less than 10 s and there is also no static error. LQG controller keeps this stability with different variance of the flow rates.

5. Conclusion:

In this work, we proposed Gaussian linear quadratic control for a three tank hydraulic system. To handle the problem caused by nonlinear data, we choose Fuzzy c-means algorithm and N4SID identification approach to define local linear models. The Fuzzy LQG control is based on TS presentation of the system. The simulations show the effectiveness of our approach, the fuzzy LQG control ensures the stabilization of the system. One topic for future research may be in the use of the subspace identification approach to define local linear models. We can use an extended Kalman filter to define LQG control and compare it with a multi-model adaptive control.

6. Bibliography:

[1] A. Boulkroune, M. Saad and M. Farza, « *Adaptive fuzzy controller for* Multivariable nonlinear state time-varying delay systems subject to input nonlinearities ». Fuzzy Sets and Systems, In Press 2010.

[2] D. Subbaram Naidu, « *Optimal Control Systems* ». CRC Press, 2003

ISSN: 2961-6611

[3] E. Ostertag, « *Commande et Estimation Multivariables* », TechnoSup, Ellipses, Paris, 2006.

[4] G. Li and F. Zhao. « Flexibility control and simulation with multi-model and LQG/LTR design for PWR core load following operation». Annals of Nuclear Energy, Volume 56, June 2013.

[5] J. Abonyi , R. Babuska and F. Szeifert, « *Modified Gath-Geva fuzzy clustering for* identification of Takagi-Sugeno fuzzy models ». IEEE Transactions on Systems, Man and Cybernetics, Part B: Cybernetics, 32(5):612–621.2002.

[6] V. S. Rao and Dr. S. Vidyavathi, «Comparative Investigations and Performance Analysis of FCM and MFPCM Algorithms on Iris data », Indian Journal of Computer Science nd Engineering.

[7] B. Cardenas and M. Molinas, « Optimal LQG Controller for Variable Speed Wind Turbine based on Genetic Algorithms », Energy Procedia, vol. 20, pp. 207–216, 2012.

[8] S. Nourdin, H. Camblong, I. Vechiu and G.Tapia, « Comparison of wind turbine LQG controllers using individual pitch control to alleviate fatigue loads », IEEE conference on control & automation, pp. 1591-1596, 2010.

[9] T. Johansen, Shorten and R Murray-Smith, « On *the interpretation and* Identification of dynamic Takagi-Sugeno fuzzy models ». IEEE Transactions on Fuzzy Systems, 8(3):297–313.2000.

[10] T. Takagi and M. Sugeno, « Fuzzy identification of systems and its application to *modeling and control* ». IEEE Transactions on Systems, Man and Cybernetics, 15:166–172.1985.

[11] X. Yang and O. Marjanovic, « LQG Control with Extended Kalman Filter for Power Systems with Unknown Time-Delays ». preprints of the 18th ifac world congress, Milano (Italy) August 28 - September 2, 2011.

[12] P. Van Overschee, and B. De Moor, N4SID: « Subspace algorithms for identification of combined Deterministicstochastic Systems », Automatica, , Vol. 30, pp. 75-93,1994.

ISSN: 2961-6611

OPTIMIZIATION OF THERMAL PERFORMANCE OF AIR FLAT PLATE SOLAR COLLECTOR

Marwa Ammar[#1], Ameni Mokni[#2], Hatem Mhiri[#3] ,Philippe Bournot[# 4]

[123#] *Laboratory of thermal and thermodynamic of industrial processes, National School of Engineers of Monastir, road of Ouardanine, 5000 Monastir, Tunisia*

[4#] *IUSTI, UMR CNRS 6595, 5 Rue Enrico Fermi, Technopôle de Château-Gombert, 13013 Marseille, France*
1 ammarmriwa@gmail.com

***Abstract*— The objective of our work is to propose a solution to optimize the performance of a flat solar collector as this type of collector presents the problem of low performance. In a first part our numerical model realized with the software gambit and exported towards Fluent was well validated by referring to an experimental study. The effects of the most active geometrical parameters of fins on the efficiency of the solar air collectors as well as on the processes of heat transfer and fluid flow within the collector were discussed in detail. Numerical analyses on different models of flat plate solar collectors with various heat transfer enhancement strategies were shown.**

***Keywords*— Solar energy; Solar air collector; Rectangular fins; Thermal efficiency; Pressure drop; Effective efficiency; Serpentine flow; Numerical analysis.**

I. INTRODUCTION

Global renewable energy reserve can be considered inexhaustible. Solar energy is considered to be the energy of the future. The thermal conversion of solar energy heater is undoubtedly the most mature. Flat plate solar collectors (FPSCs) remain commonly used devices for converting solar radiation into useful heat to cover the human need for a variety of thermal applications. Solar heat has long been used in many activities, such as drying clothes, fish, and other agricultural products (cocoa, coffee, rubber, pepper, tobacco, pepper, tea, bananas, anchovies and seaweed). [1] Ahmad Fudholi. View their numberless environmental and economic benefits; flat plate solar collectors (FPSCs) represent an interesting topic to study. Two types of flat plate collector exist; solar water heaters and solar air heaters which have lower thermal efficiency than solar water collectors, which is due to the low thermodynamic air properties and the presence of a viscous sub-layer in the vicinity of the hot wall, S.B.Bopche et al [2].

Many studies on solar collector have been reported on flat plate solar collector particularly focusing on improving thermal efficiency; it was found that the heat transfer coefficient can be enhanced by generating the turbulence in the flowing fluid which is possible with the help of artificial roughness.

C.Foued et al.[3] have experimentally developed a solar collector with five semi-cylindrical shapes attached to the absorber. They found that the most important thermal efficiency found was in the order of 51.5% corresponding to a finned collector with a solar heat flux of 480 W / m² a flow rate of 0.016 Kg/s angle of inclination of the collector of 45°.

A.Aben et al. [4] tested delta-winglets in solar collector: useful heat quantities were increased by a factor of about 1.65 compared to the case of the classic solar collector.

A. Kumar [5] studied experimentally effect of multi v-shaped rib with gap roughness on one broad wall. For (Nu), the maximum enhancement of the order of 6.74 times of the corresponding value of the smooth duct has been obtained, however the friction factor (f) has also been seen to increase by 6.37 times of that of t:he smooth.

S.Youcef et al. [6] have experimentally the influence of increasing the number of baffle rows on thermal efficiency. An increase in efficiency of the order of 2% on average at each addition of a row.

ISSN: 2961-6611

N.Moummi et al.[7] have developed an experimental study of the collector with rectangular fins which occupied 80% of the height of the air channel. In the presence of the fins in the air channel the improvement of the coefficient of forced convection transfer is 50%.

Several experimental studies have been conducted to investigate rectangular fins, thermal performance of an air duct, in general, improves as a result of providing the fins, but this improvement is also accompanied by an improvement of pressure drop. Hence a thermo hydraulic analysis should be done for various cases studied

The main idea of the present study is the creation of an air collector with higher thermo hydraulic efficiency.

II. ANALYSIS AND MODELLING

A. SOLUTION DOMAIN:

The three-dimensional computation model of the solar air collector has 1,6 m length an 0.8 m width. The transparent cover is in alveolar polycarbonate sheets 10 mm thick and the gap between the cover and the absorber-plate was 25 mm. The collector is formed by a black-painted aluminium sheet 0.4 mm thick used as an absorber plate and by a wooden plate as the back side of the collector duct. N.Moummi.[7]. Second model was the same collector with rectangle fins having 50mm of width and 20mm of height and attached to the lower wall of the duct, the total number of fins added was 1056 fins.

The developed numerical model is solved using the commercial software of Fluent6.3.26. The results were obtained for a heat flux of 900 W/m2.

B. VALIDATION OF NUMERICAL MODEL:

The first part of our numerical simulation aims to validate our numerical model, so first configuration is chosen. Present numerical results of the collector efficiency in a smooth duct were compared with those experimental of N. Moummi [7], in figures blown.

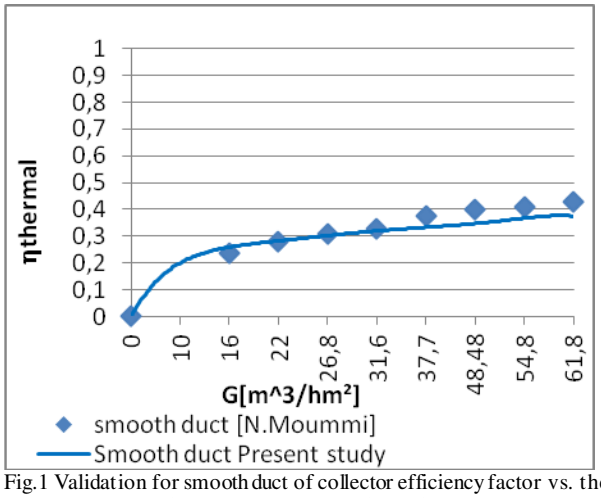

Fig.1 Validation for smooth duct of collector efficiency factor vs. the air volume flow rate at constant flux of 900 w/m².

Numerical results of solar collector's thermal efficiency are found to be in excellent agreement with experimental values of N.Moummi [7]. The model is then modelled correctly.

III. RESULTS AND DISCUSSION

Once we have proved the good agreement between our numerical results and experimental results, we opt to ameliorate the performance of solar collector.

The previous curve shows the influence of the inlet volume flow rate on the thermal performance of the collector; more than volume flow rate increases more than thermal efficiency increases. Hence, the solar collector efficiency's relies heavily on volume flow rate.

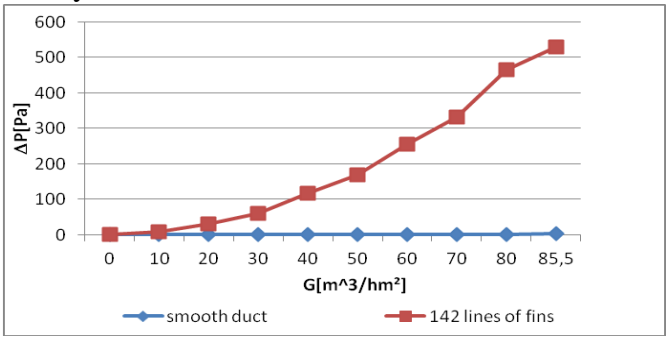

Fig.2 Variation of pressure drop with air volume flow rate for smooth and finned duct.

Variations of pressure drop according to the air volume flow rate of smooth and roughened duct are illustrated in Figure 2. The curves show that increasing the volume flow rate of air causes a

ISSN: 2961-6611

significant increase in friction losses. Also, addition of fins on the lower wall increases the pressure drop.

Hence it is clear that the well thermal efficiency enhancement was accompanied with an important increase of pressure drop. The presence of 142 lines of fins of 5cm of width and 20 mm height, is associated with a very important pressure drop and increased weight and cost of the collector.

The objective of our numerical study is to predict a lightweight solar air collector with low pressure drop, which has driven us to minimize the number of fins.

Hence, a thermo hydraulic analysis will take place in our present study by evaluating the effective efficiency reported by Cortes [8] as follow;

$$\eta_{eff=}(Q_u - (\Delta P * G)/C)/(A_c * I)$$

The following part mainly discusses the influence of the fins number in the air duct;

Four fins:

The collector is equipped with four fins, attached on the lower wall of the air channel, of 0.6m (l'/l=0.75) of width and 0.02m (e'/e=0.8) of height, which divide the cavity into five several chambers and form a serpentine flow channel.

Eight Fins:

Eight fins are attached to the lower wall of the air duct and divide the channel into nine chambers.

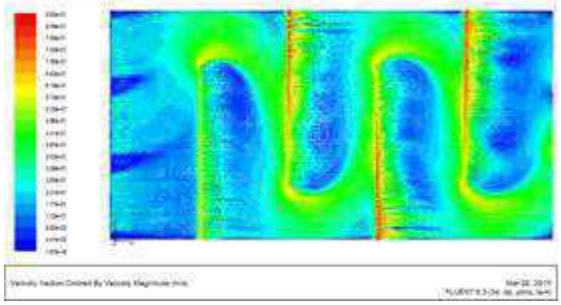

Fig.3 Vectors of velocity in the air channel with four fins

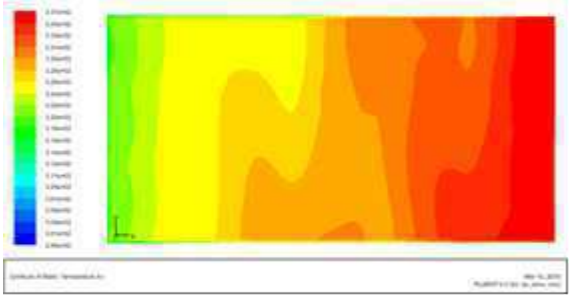

Fig.4Contour of temperature on absorber plate
With four fins

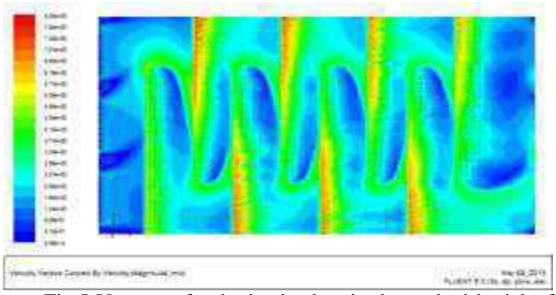

Fig.5 Vectors of velocity in the air channel with eight fins

Fig.6 Contour of temperature on absorber plate with eight fins

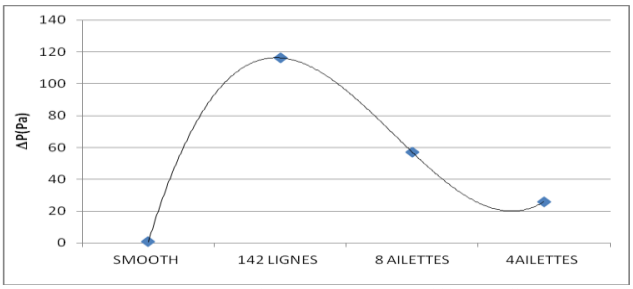

Fig.7 Variations of pressure drop at different fins
Numbers for G=40[m^3/hm²].

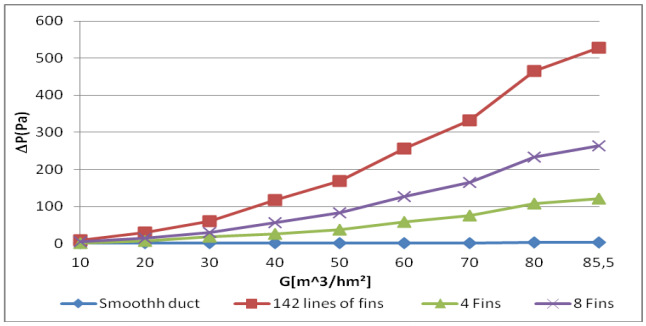

Fig.8Variation of pressure drop with air volume flow rate for smooth duct and various number of fins.

ISSN: 2961-6611

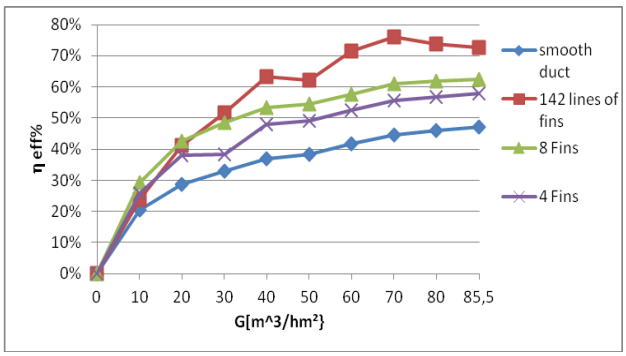

Fig.9 Variation of effective efficiency of smooth duct and various numbers of fins according to air volume flow rate

The performance evaluation index of the SAC mainly includes the treatment capacity, the temperature rise between the inlet and outlet, the pressure drop and the heat collecting efficiency.

Figures 3 and 5, show the vectors of velocity in the air duct for four fins and eight fins. It is observed that the air gets into the cavity from the entrance and goes along the serpentine passage before coming out from the exit. The air's residence time in the channel was prolonged thanks to the arrangement of fins in the duct, the residence time of the serpentine flow increase more than the fins number increase. A significant flow separation and reattachment which results in flow loss to some extent is shown in the air channel. The dead zones reduce as the number of fins increases.

The flow pattern in the collector influences the temperature distribution significantly. The temperature distribution on the absorber plate is shown in Fig.4 and Fig.6 for both cases at solar intensity of 900w/m². It indicates that the high temperature zone exactly corresponds to the vortex zone while the low temperature zone corresponds to the direct flow zone.

Fig. 7 reflects the influence of the number of fins on the pressure drop with fixed volume flow rate of 40[m^3/hm²]. Pressure drop is the higher for the 142 lines of fins for all volume flow rates studied, then for the eight fins and the lower pressure drop was found corresponding to the four fins.

Evolution of pressure drop versus flow rate for smooth and various fins arrangement is illustrated in figure 8.

Figure 9 shows the variation of effective efficiency with the volume flow rate without fins and with various numbers of fins.

For volume flow rate of 85.5m^3/hm² the effective efficiency of solar collector without fins is 47% while for collector having 4 fins is 57.7% and for eight fins is 62.5%.

IV. CONCLUSIONS

In this paper, an air flat plate solar collector is numerically analysed. To summarize we can conclude that;

-Solar collector efficiency's relies heavily on volume flow rate.

-Pressure drop in the air duct relies also heavily on volume flow rate.

-The addition of fins causes a significant flow separation and reattachment which results in flow loss to some extent.

-Number of fins has a remarkable effect on pressure drop.

-The addition of four fins in the air channel has the advantages of simple structure, convenient installation and easy maintenance, and low pressure drop.

References

[1] Ahmad Fudholi, Kamaruzzaman Sopian A review of solar air flat plate collector for drying application, Renewable and Sustainable Energy Reviews 102 (2019) 333–345, https://doi.org/10.1016/j.rser.2018.12.032

[2] Santosh B. Bopche a,*, Madhukar S. Tandale, Experimental investigations on heat transfer and frictional characteristics of a turbulator roughened solar air heater duct, International Journal of Heat and Mass Transfer 52 (2009) 2834–2848, doi:10.1016/j.ijheatmasstransfer.2008.09.039.

[3] Foued Chabane, Noureddine Moummi,Said Benramache, Experimental study of heat transfer and thermal performance with longitudinal fins of solar air heater, Journal of Advanced Research (2014)

[4] A. Abene, V. Dubois, M. Le Ray, A.OuaguedA. Abene, V. Dubois, M. Le Ray, A. Ouagued, Study of a solar air flat plate collector: use of obstacles and application for the drying of grape, Journal of Food Engineering 65 (2004) 15–22, doi:10.1016/j.jfoodeng.2003.11.002.

[5] Anil Kumar, R.P. Saini, J.S. Saini, Development of correlations for Nusselt number and friction factor for solar air heater with roughened duct having

[6] S. Youcef-Ali, J.Y. Desmons, Numerical and experimental study of a solar equipped with offset rectangular plate fin absorber plate, Renewable Energy 31 (2006) 2063–2075, doi:10.1016/j.renene.2005.10.008

[7] N. Moummi, S. Youcef-Ali, A. Moummi, J.Y. Desmons, Energy analysis of a solar air collector

withrows of fins, Renewable Energy 29 (2004) 2053–2064, doi:10.1016/j.renene.2003.11.006.) 5, 183 192,http://dx.doi.org/10.1016/j.jare.2013.03.001

[8] S.K. Saini a, R.P. Saini, Development of correlations for Nusselt number and friction factor for solar air heater with roughened duct having arc-shaped wire as artificial roughness, Solar Energy 82 (2008) 1118–1130, doi:10.1016/j.solener.2008.05.010997.

ISSN: 2961-6611

ISSN: 2961-6611

Comparison of the use of Solar building's system Between the north and the south of Algeria

Nor REBAH
LPMR, university of Souk Ahras, Algeria
Emaill: nahrnor@yahoo.fr

Abstract*— Seen the evolution of the energy situation in the world, the lower oil prices, Algeria has become aware that the use of renewable energy is becoming very important and urgent, as the solar potential it possesses, making them very favorable conditions for the execution of the new directive taken by the authorities of the country concerning the design of the houses which must imperatively be in accordance with a thermal regulation, which is ever realized in Algeria also in the field of space heating and domestic hot water. For these reasons we wanted in this study show the interest of the use of systems powered by solar energy in individual homes, The results we obtained after comparison of the use of the solar systems between two cities, shows that we can overcome the problem of total reliance on fossil energy, the use of RES (renewable energy sources) can cover more than 50% of the space heating and hot water in the north and more 90% in the south

***Keywords*—Solar energy, Solar system, space heating, domestic hot water, Algerian sites**

I. INTRODUCTION

It has been seen a remarkable advances in the field of solar heating and cooling systems over the world, and refreshing interest in environmental issues, a major impetus was provided by the Report of the world Commission on the Environment and Development (the Brundtland Report); the Rio Summit in 1992 sought to accelerate the impetus. The potential of global solar heating and cooling continues to grow. The solar thermal capacity in operation worldwide equaled 171 gigawatts thermal corresponding to 244 million square meters at the end of 2008 [1] The largest country using solar systems are the USA, Germany, Turkey; and China, which alone has more than half of global capacity with 101 GW_{th}, solar system for domestic hot water is common all over the world with significant market, with the space heating who show a rapidly development. In Algeria the building sector is responsible for more than 50% of the final energy consumption, with 82% from the total household consumption represents space heating followed by water heating at 6% [2].
The aim of this study is to promote the use of renewable sources, the agreement made with Germany and England [3] implied that Algerian officials must increase the use of renewable energy sources and not rely on fossil fuels is the primary objective of the new policy and prepare the ground for people to accept change is the first concerns met.

II. DESIGN OF THE BUILDING

There is no secret that the current problem of declining prices of a barrel of oil in the world this year, 2015, had serious consequences for the Algerian economy, which has pushed even Algerian responsible to consider, the use of renewable energy as a substitute to fossil fuels, especially in the area of housing, whether for space heating and domestic hot water or the conversion of renewable energies in electricity, with the incorporation of the national program of solar energy in building the Algerian government proceeded with the adoption of a legal framework, creating a multitude of organizations working in this sector and the launch of major projects in which the objective is represented in

ISSN: 2961-6611

reducing the use of fossil energy to more than 70% by 2020 [4].

For our simulation we took a standard model of house that represents most of the housing in Algeria; Figure 1 shows a local area of 85 m² with two bedrooms, a living room and bathroom.

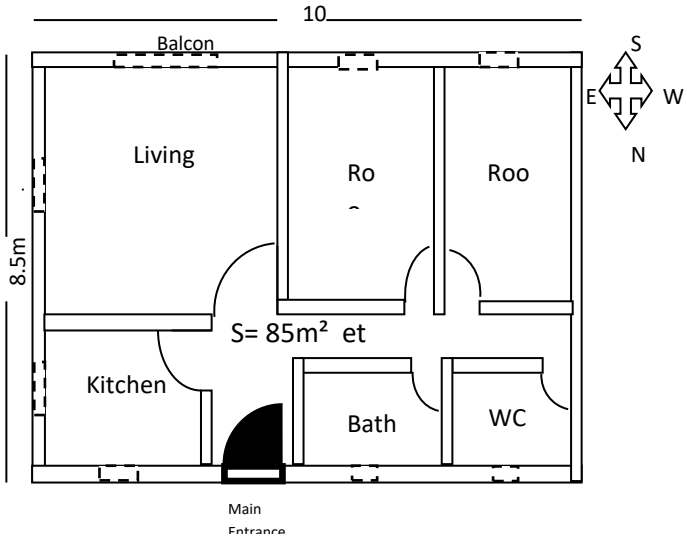

Figure 1 the schema of the standard house

We chose two cities the first in the north of the country and the second in the south of it; it is the capital Algiers which has a mediterranean climate. Algirs is known for its sweet summers. Winters are mild and humid; snow is rare but not impossible. The rains are abundant and can be torrential. It is generally warm especially July to September, and the other Tamanrasset which is the most populous city in the Algerian Sahara it has a hot desert climate (Köppen climate classification BWh) typical of the Hoggar mountains located in the Sahara with long, hot summers and short and moderately warm winters. The high altitude (1400 m) moderates much the average maximum temperatures encountered throughout the year and is responsible for slightly more precipitation that around at low altitude.

Table 1 presents the total area of the Structural Elements of the building in the oven hand orientations, the heat transfer coefficient of Each element, as well as the average heat transfer coefficient of the building [5]

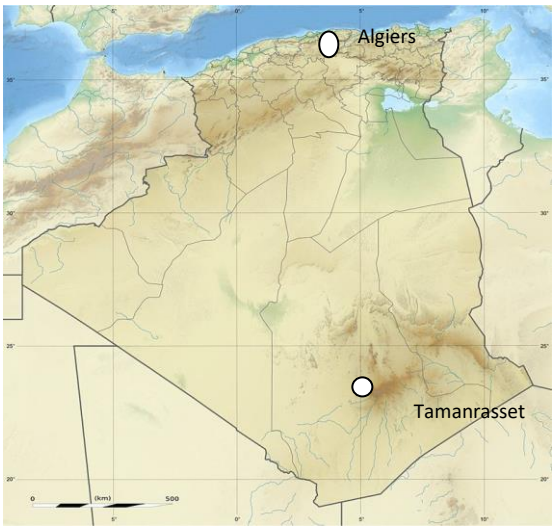

Figure 2: location of cities

Element/Orientation	South	Nord	West	East
Uew (W/m²K)	0.45	0.45	0.45	0.45
Ucw (W/m²K)	0.41	0.41	0.41	0.41
Uw (W/m²K)	2.8	2.8	-	2.8
Ufd (W/m²K)		4.5		
Urt (W/m²K)	0.37			
Uf (W/m²K)	0.74			

Table 1: coefficient heat transfer element of the structure of the house

Typical houses in the tow selected sites are equipped with typical solar system for space heating and domestic hot water, technical characteristic are shown in the table 2

ISSN: 2961-6611

Collector type	Tube on Copper with foils on Copper
Paint	A = 0.96 ± 0.04 E= 0.04 ±0.03
Glazing	Double sheet clear tempered glass
Collector inclination	45°
Area	10m²
Storage capacity	0.70 m3
CL	6w/m²K
CE	0.85

Table 2: The technical characteristics of the solar heating system

III. Building loads

Climate data from selected cities is simulated using the Matlab logitiel in the laboratory MRPL Souk Ahras, The thermal loads which we need were made every month of heating season from November to April we calculated the annual energy saving from space heating and hot water production six months heating period was used for the thermal load with an internal temperature of 21° the monthly space heating needs of each site were presented in the figure 3

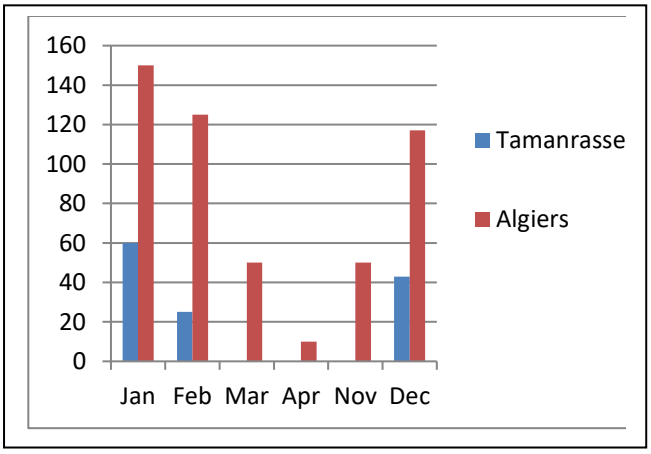

Figure 3: Monthly space heating necessity for each site

For the needs of domestic hot water were calculated for a volume of 40 l / day throughout the year by person, are showing in the figure 4

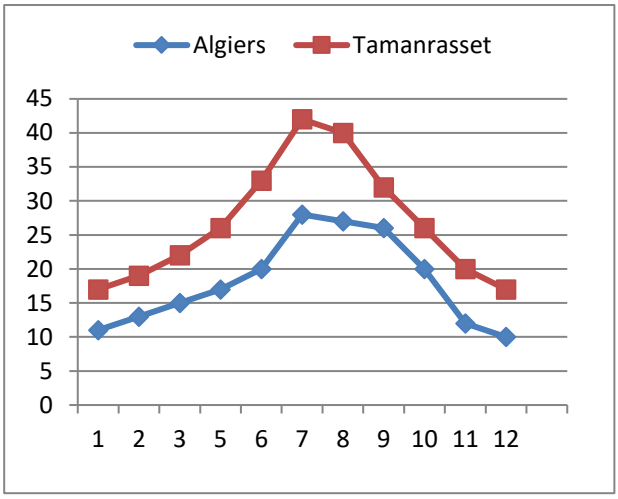

Figure 4 : The hot water demand

For the air temperature of each city, the calculation is demonstrated in the following figure

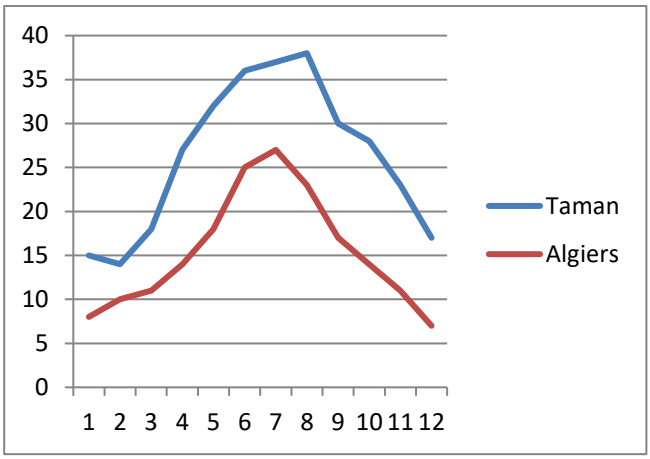

Figure 5:Air temperature °c

IV. Results

The proper sizing of the components of a solar energy system is a complex problem, which includes both predictable (collector and other components' performance characteristics) and unpredictable (weather data) components.

Several methods exist, among it the f- chart method, described in Klein and Beckman (1979) is integrated to our program simulation to estimate the long term performance of solar heating systems, for designing process heat and power systems, for which the thermodynamic cycle efficiency is independent of

ISSN: 2961-6611

the heat supply temperature. This method is also useful for calculation of load covered by systems of each installation site [6].

The influence of the total area of the solar collectors was studied in order to identify the system with the optimal energy performance. According to the simulation results, the examined system was able to cover more than 55% and as much as 98% of the total thermal needs in the chosen sites. In general, the surface of the collector positively affects the performance and the efficiency of the solar system.

V. Conclusion

It is known that energy consumption has been soaring, especially in emerging countries despite the fact that oil prices are high and the amount emissions of CO2, which is the main source of global warming, has significantly grown, with the ever increasing energy consumption, in modern society. With the intention of saving fossil fuels and reducing CO2 emissions, many countries have been searching for renewable and clean energy sources such as solar energy, like Algeria. So; the use of renewable energies in Algeria has become a very important step in emergency especially with oil prices falling and exhaustion, which impacted negatively on the economy of the country, which shook our leaders and encourage them to review the country's energy policy based on renewable energies especially in the dwelling areas, the objectives needed were:

1- All new buildings must be nearly zero energy buildings

2- All buildings (or the most of them) introduce minimum energy use requirements for all HVAC technical building systems.

3- Make the use of solar heating systems and accessible and within reach of people

The use of a solar thermal system for space and water heating enables the minimization of energy costs as well as that of the subsequent air emissions. In all cases, the system analyzed is proved to be able to cover more than 55% of the total load and as much as 98% while exhibition a discounted payback period of less than 12.

Those results comply well with other studies that have been carried out in Greece [26], Germany [27], Spain [28], and other non-European countries with climates ranging from subtropical [29] humid continental [30], as the use of RES in order to cover at least a part of a dwellings thermal needs which have been studied long before the new directives in Algeria According to the economic aspect, our study shows that the use of the solar system for space heating and hot water can save more than 60% of amount on the bill for electricity and natural gas of consumers.

VI. References

[1] To Environmental Impact Assessment (The atural and Built Environment Series) John Glasson and all ,Book, 2005

[2] Algerian portal renewable energy, CDER 2012

[3] Algerian portal renewable energy, ‘Un accord Algéro-allemand en vue, CDER 2013

[4] National Agency of investment Development, ANDI 2008

[5] G. Martinopoulos, G. Tsalikis Active solar heating systems for energy efficient buildings in Greece: A technical economic and environmental evaluation.Energy and building ,2014

[6] Upper bounds for thermally driven cooling cycles optimization derived from the f–φ̄ chart method S Colle, H Vidal - Solar Energy, 2004 .

[7] A. Argiriou, N. Klitsikas, C.A. Balaras, D.N. Asimakopoulos, Active solar space heating of residential buildings in northern Hellas—a case study, Energy and Buildings 26 1997

[8] V. Badescu, M.D. Staicovici, Renewable energy for passive house heating: Model of the active solar heating system, Energy and Buildings 38 February 2006

ISSN: 2961-6611

[9] J.D. Marcos, M. Izquierdo, D. Parra, Solar space heating and cooling for Spanish housing: potential energy savings and emissions reduction, Solar Energy 85 November 2011.

[10] T.T. Chow, K.F. Fong, A.L.S. Chan, Z. Lin, Potential application of a centralized solar water heating system for a high-rise residential building in Hong Kong, Applied Energy 83 January 2006.

[11] M. Leckner, R. Zmeureanu, Life cycle cost and energy analysis of a Net Zero Energy House with solar combi-system, Applied Energy 88 January 2011

.

ISSN: 2961-6611

Numerical simulation of air-water two phase flow in horizontal confined channel

Hella Adouni[#1], Yoldoss Chouari[#2], Wassim Kriaa[#3], Hatem Mhiri[#4], Philippe Bournot[*5]

[#]*UTTPI, National Engineering School of Monastir, Monastir, Tunisia*

[1]hella.adouni2@gmail.com

[*]*IUSTI, UMR CNRS 6595,5 rue Enrico Fermi, Technopole de Château-Gombert*

[5]philippebournot@yahoo.fr

***Abstract*— The flows frequently encountered in sewerage networks are characterized by the presence of pressurized air above the treated water. The interaction between air and water generates transitions in the flow regime that can be accompanied by phases of air entrapment. These trapped air pockets have destructive effects on the sanitation infrastructure and can lead to serious accidents, including manhole overflows initiating flooding, leaks, geyser phenomena, violent expulsion of the manhole cover, etc. Hence the importance of understanding two-phase flows in sanitation networks. The objective of our work is to develop a numerical model capable of simulating two-phase flows in confined channels and then studying the effect of air velocity on flow dynamics. The geometric modeling of the study area was carried out using the "Gambit" software. The numerical simulation of the air/water flow in the considered channel is developed on the Fluent software. To predict the air/water interface, the VOF (Volume Of Fluid) model has been adapted. The turbulence model chosen is the K-epsilon RNG. A comparison between the velocity profiles and the experimental results obtained was carried out in order to validate the model. Several meshes were tested. The results showed that to gain in computation time and accuracy, the mesh chosen is the one consisting of 1,314,000 cells, from which the results no longer vary. This study was carried out for different water levels and air velocities. Thus, the model developed perfectly fits our case study and allows us to accurately predict the behavior of a two-phase flow in a confined channel.**

***Keywords*— two phase flow, air-water internal flow, air velocity effect, interfacial behaviour, VOF**

I. INTRODUCTION

Two-phase flows in pipes, also called internal flows, are generally characterized by an interface that constitutes the place where energy is transmitted between the two phases. This type of flow is found in sewerage networks where it is essential to understand the mechanisms of these exchanges, quantify them precisely and monitor their evolution in order to avoid the hydraulic failures they can generate such as manhole overflows initiating flooding, the phenomenon of water hammer, pipe breakage, leaks, geyser phenomena, violent expulsion of the manhole cover, etc **[1, 2]**.

This is a topical research subject since accidents that occur due to misunderstanding of the internal flow are serious. The studies carried out on urban sewerage networks exploit practically 3 sections that start from pipe's initial size dimensioning, passing through the internal behaviour of the flow up to the evacuation of pollutants in the ejection points (sea, river...). This paper focuses on understanding the air/water interaction that is the driving force behind the transition from gravity flow to forced flow.

In this context, Hamam and McCorquodale **[3]** conducted experimental tests on a two-phase gravity and confined flow that suddenly turns into a forced flow. The size of the pipe, its shape, speed, flow rate, Froude number, relative depth of flow, slope of the pipe, aeration arrangement... are among the factors that cause this transition. Their tests highlighted the high pressures that generally occurs with transient flows and described the transition to a forced flow in three steps, which are the formation of a surge, the formation of instabilities, and the transition to a forced flow. This transition to forced flow is accompanied by phases of air entrapment that have been the subject of several studies **[4] [5]** due to their significant effect on the pipes. Initial and boundary conditions are among the factors that stimulate the creation of air pockets in wastewater systems. The results of Hamam and McCorquodale **[3]** showed that when the ratio between water velocity phase and air velocity reaches a certain limit V = 6.46 m/s given by Kelvin_Hemholtz, a large air pocket is formed. The air pockets will be expelled at the evacuation points generating pressure peaks similar to "waterhammer", thus disrupting the water flow. In this perspective, the results given by Li and McCorquodale **[6]** showed that these pressure peaks are caused either by the change in flow conditions (sudden closure of a valve) or by the evacuation of air bubbles during rapid pipe filling. Air enters the pipes and can be trapped during rapid filling **[7]**. This filling causes the compression or evacuation of air pockets, resulting in significant pressure variations. Insufficient ventilation is also one of the factors that stimulate air pockets creation. Zhou et al. **[8]** reported that flow conditions are becoming more complex when it comes to lack of aeration. Indeed, an unsuitable ventilation system leads to the creation of large air bubbles in the flow **[9]**. When the capacity of the air flow fails to move the air bubbles in the channel, they will accumulate forming a large bubble that will generate pressure on the water leading to the blockage of the pipe in some cases **[10]**. This usually happens for large slope variations **[11]**. Thus, in order to avoid the accumulation of air pockets, it is

ISSN: 2961-6611

essential to know the regime of these flows and particularly the boundary conditions that make the transition from one regime to another [12].

However, after a literature review, it was found that there is a considerable lack of literature regarding the effect of air velocity on water in a horizontal confined channel. However, it is an essential parameter for understanding and controlling the behaviour of internal flow. In addition, compared to the extensive studies available on two-phase flows in small diameters (D < 50 cm), little researches has been conducted on two-phase horizontal flows in large diameters although the actual size of pipes in engineering systems may be relatively large, compared to that used in an experimental environment [13].

II. Results and Discussions

A. Numerical method

Gambit and Fluent, two commercially licensed software packages, were used to perform 3D simulations in fluid mechanics ranging from mesh construction with Gambit to solving Navier Stokes equations and post processing with Fluent. The specification of the mesh size depends on the complexity of the geometry. Since the geometry considered is rectangular, a hexahedral mesh grid was chosen. The domain is subdivided with a uniform mesh size. The number of meshes at the four walls at the inlet, as well as at the interface, is increased to ensure high resolution and accuracy during flow transitions. All numerical simulations were performed using the second order upwind scheme. The "PISO" method was used to calculate the Pressure/Speed coupling. For all cases studied in this paper, a transient simulation with a time step of 0.0001was identified. The dimensions considered in this work correspond to those of the hydraulic canal of the laboratory located at the IUSTI of the University of Aix Marseille; rectangular and confined canal 5m length, 0.075m wide and 0.15m deep (Fig.1) where the experimental part was carried out.

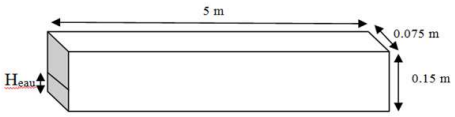

Fig. 1 Domain geometry

In this work, we plan to carry out 10 numerical simulations studying the behavior of a two-phase air/water flow within a horizontal channel confined under variations in air velocity as listed in Table 1.

B. Validation of the air-water flow model

1) Mesh sensitivity analysis

In order to study the sensitivity of the results to the mesh size, three different mesh sizes were checked for a water level H_L= 0.032m: M1=930 000 cells; M2=1 314 000 cells; M3=1 800 000 cells.

The respective water and air velocities of mesh sensitivity test were: V_{water} = 0.47 m/s and V_{air} = 3.2 m/s. The simulation of the different meshes is performed using the standard k-Ɛ turbulence model. As seen in Fig. 2, there is no significant difference between the results of the simulations performed using the 1,314,000 cells and the 1,800,000 cells. Thus, to save calculation time, the mesh size chosen is that consisting of 1,314,000 cells.

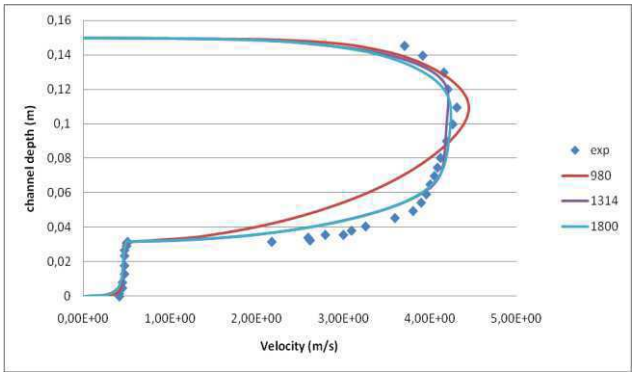

Fig. 2 Mesh sensitivity analysis

2) Turbulence model validation :

In order to choose the best turbulence model, simulations were performed with the first order models K-ε Standard, K-ε RNG and K- ε Realisable. The K-ε RNG model is considered sufficient to predict flow quantities as shown in Fig. 3.

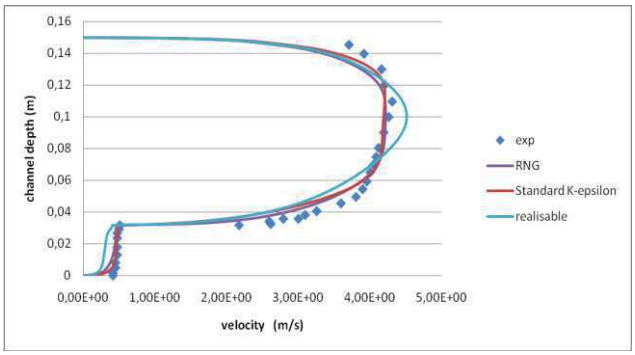

Fig. 3 Turbulence model validation

3) The effect of air velocity on the water level:

Ten cases of air-water volumes fractions have been investigated as shown in Table. 1 .In all cases, the liquid superficial velocity was constant at V_{water} = 0.16 m/s and introduced from the bottom region with H_L = 0.055m.

Table 1 The superficial velocities for the simulation cases

ISSN 1737-9334

Air-Water cases	Water superficial velocity (m/s)	Air superficial velocity (m/s)
Case 1	0.16	0.5
Case 2		1
Case 3		2
Case 4		1.5
Case 5		3
Case 6		5
Case 7		6
Case 8		7
Case 9		8
Case 10		9

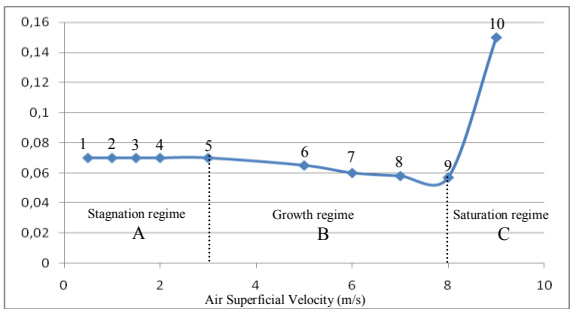

Fig. 4 The effect of the superficial air velocity on the water level

Three regimes could be distinguished from Fig. 4:

A. A stagnation region under V^{S}_{air} = 3m/s, in which a stratified smooth flow is observed. The air is at the top of the channel and the water is at the bottom. Liquid level H_L is independent from the superficial air velocity.

B. Above V^{S}_{air} = 3m/s, a growth regime is observed. Periodic 2D waves with small amplitude appears at the interface, and the water level is getting slightly lower as proved by Ramin Dabirian [14], and Akhmad Zidni Hudaya [15]. In this regime, the interfacial behaviour is dependent to gas flow rate. As Vg increases, it creates drag forces that reduces the liquid level and increases the area occupied by the air phase as shown in velocity profiles in Fig. 5. It is also noticed that the maximum water velocity is near the interface whereas the maximum air velocity is shifted closer to the upper side of the channel.

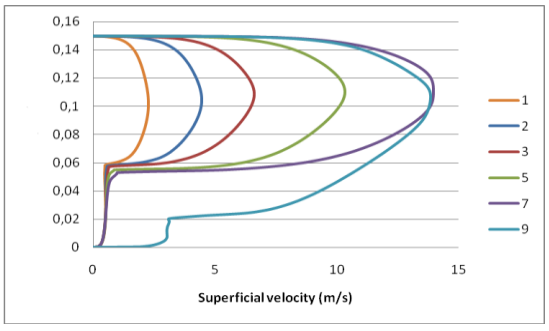

Fig 5 Longitudinal velocity profiles for x = 1.5m

C. A saturation regime starts from V^{S}_{air} = 9m/s. As the gas passes over the wave, an upward wave force is raising the wave until it reaches the top wall of the channel. In fact, the shear stress along the flow direction tends to increase with the increasing of Vg leading to a sudden increase of the liquid level that touches the top wall and block the gas phase. This interfacial behaviour forms into the slug shape. The speed of this slug creation and its location from the inlet is dependant to the gas velocity. Indeed, as Vg increases the slug is closer to the inlet and faster as shown in Fig. 6 and Fig. 7. This result proves the one found by Xiaoyan Liu [16].

Vg = 9m/s

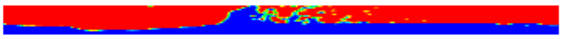

Fig. 6 Slug created at 0.46 s at 1.2m from the inlet

Vg = 11 m/s

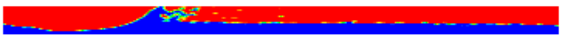

Fig. 7 Slug created at 0.22 s at 0.8m from the inlet

III. Conclusions

Consideration was given in the present study to the effect of air velocity on a two phased flow into a confined horizontal channel with big diameter. Behavior of the flow was effectively predicted by the 3D VOF model with K-Ɛ RNG turbulence model.

The conclusions reached from this study are recapitulated in the following key notes:

- Under constant water velocity, the flow goes through three regimes according to gas velocity raise;
- Liquid level decreases as the gas level increases;
- The higher the gas velocity, the faster the wave formation is and the closer to the inlet.

References

[1] Pozos-Estrada, O., et al. “Failure of a drainage tunnel caused by an entrapped air pocket.” Urban Water J., 2015
[2] Vasconcelos, J. G., and Leite, G. M. “Pressure surges following sudden air pocket entrapment in storm-water tunnels.” J. Hydraul. Eng., 2012
[3] Hamam, M. A., and McCorquodale, J. A, “Transient conditions in the transition from gravity to surcharged sewer flow”, 1982
[4] Zhou, F., Hicks, F., and Steffler, P, “Analysis of effect of air pocket on hydraulic failure of urban drainage infrastructure.” 2004
[5] Vasconcelos, J. G., Klaver, P. R., and Lautenbach, D. J, “Flow regime transition simulation incorporating entrapped air pocket effects.” 2015
[6] Li, J., and McCorquodale, A, “Modeling mixed flow in storm sewers.” J. Hydraul. Eng.,1999.
[7] Lauchlan, C. S., Escarameia, M., May, R. W. P., Burrows, R., and Gahan, C. “Air in pipelines: A literature review”, HR Wallingford, Oxfordshire, U.K, 2005
[8] Zhou, F., Hicks, F. E., and Steffler, P. M. (2002a). “Observations of air-water interaction in a rapidly filling horizontal pipe.” J. Hydraul. Eng., 2002
[9] Vasconcelos, J. G., and Wright, S. J. “Mechanisms for air pocket entrapment in stormwater storage tunnels.” Proc., World Environmental and Water Resources Congress 2006
[10] Granata, F., de Marinis, G., and Gargano, R. “Air-water flows in circular drop manholes.” Urban Water J., 2015
[11] Lubbers, C. L., and Clemens, F. H. L. R. (2005b). “Capacity reduction caused by air intake at wastewater pumping stations.” Proc., 3rd Int. Conf. on

ISSN: 2961-6611

Water and Wastewater Pumping Stations, P. May, ed., BHR Group, U.K., 2005
[12] Christophe Conan, « étude expérimentale et modélisation des écoulements liquide-liquide en conduite horizontale », 2007
[13] Ran Kong, Qingzi Zhu, Seungjin Kim, and Chris Hoxie, "Characterization of Horizontal Air-Water Two-Phase Flow in Different Pipe Sizes", 2018
[14] Ramin Ramin Dabirian "CFD simulation of turbulent flow structure in stratified Gas/Liquid Flow and Validation with Experimental data", 2015
[15] Akhmad Zidni Hudaya, Hadiyan Yusuf Kuntoro, Okto Dinaryanto, Deendarlianto, and Indarto. "Experimental investigation on the interfacial characteristics of stratified air-water two-phase flow in a horizontal pipe", 2016
[16] Xiaoyan Liu, Wei Chen, Lijun Liu, and Dianwei Liu. "The numerical simulation of oil-water two phase flow in horizontal pipeline based on the VOF model", 2013

ISSN: 2961-6611

Impact of the hot thermal environment on the ambient temperatures of hospital rooms.

Dr. Yasmina BESBAS[#1], Phd. Soumaya BESBAS[#2]

[#]*Department of Architecture, Mohamed Khider University*
BP 145 RP,Biskra, 07000, Algeria

[1] besbasyasmina2@gmail.com

[2] s.besbas@univ-Biskra.Dz

***Abstract*— As part of a hot climate impact study on ambient temperature variations in hospitalization rooms, we selected a recently completed hospital facility for in situ quantitative evaluation and TRNsys simulation. The measurements taken during the overheating period were validated by the simulation, so that both results are very high compared to the values indicated in the standards.**

***Keywords*— Hot climate, ambient temperature, in situ measurements, simulation, standards.**

I. INTRODUCTION

The hot and arid climate is most dominated in the southern foot of Algeria. Where, rainfall is less than 1500mm per year and temperatures are very high during the day.

In a warm climate, it is difficult to adapt and live in comfortable conditions. In the construction industry, this climate causes many problems for buildings, especially in summer. The commonplace solutions of that time, such as air conditioners and refrigeration techniques inserted enormously and randomly, helped to exacerbate the problem more and more.

Firstly, hot and hard climatic conditions, and on the other hand artificial and exaggerated freshness, are two situations that are not preferable, especially for people who are sensitive to excessive variations in ambient temperature, such as: patients. According to a previous study [1], this sensitive category prefers to have a natural environment for physiological and pathological reasons. Passive solutions, hybrid systems, and old buildings are the best and most favourable choices for this particular case according to recent research comparing a new hospital with an old one [2].

In this perspective, the present study was carried out in summer in the most occupied places by the patients: the rooms of hospitalization, within the new maternity of the city of Biskra. This study aims to study the impact of the hot environment on the ambient temperatures of this hospital.

II. METHODOLOGY

The methodology of approach that we adopted in this study is a coupling of an in situ quantitative evaluation method with validation of results by TRNsys logieciel.

The quantitative approach was based on in situ measurements in the inpatient rooms using the Testo 480, placing it in the center of the chamber and the probe should be moved slightly to about 60 cm. above the ground (speed: about 1.5 m / s) until the displayed values stabilize.

Fig. 1 Measuring device Testo 480

The simulation was done in order to validate the results of the in situ measurements, after choosing the same climatic conditions by working on the same period in both methods.

A. Case study

Our in situ experiment took place in the service of the new materiality of Biskra city. A new building characterized by a typical simple plan with rooms distributed on the north / south axis; it has a very low height concrete structure (only ground floor), walls built of hollow brick with air blades for thermal insulation. Rooms of 21,35m² with a single window for each room characterized by a single glazing and external solar protection (shaded area = 75%) [3].

Fig. 2 Graphic presentation of the maternity ward

ISSN: 2961-6611

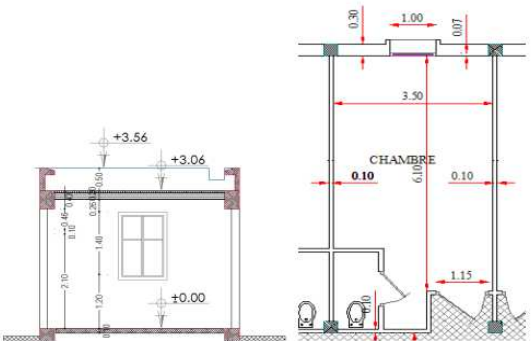

Fig. 3 Plan and section of the room of hospitalization of the materiality

B. *Period and climatology*

Using the design-month concept inspired by the design-day [4] concept, we determined the resulting overheating period through a series of average temperature calculations for the period between 2000 and 2015. As a result, In situ measurements were taken for 12 days in July, where daily average temperatures increase above 35 C°.

III. RESULTS

A. *In situ measurements*

The experiment was carried out in July 2016 in the hospital sector of the new maternity hospital in Biskra. The measures were distributed over four different periods during the day, which stretch from morning to evening and are separated by an interval of two hours:

From 9:00 to 11:00 from 13:00 to 15:00 from 16:00 to 18:00, 20:00 to 22:00

This is repeated four days a week (three weeks in total). Each time we take the measurements of four different rooms between East and West (48 rooms in total).

Fig. 4 taking of measurements

The graphs below show a comparison between the ambient temperature measurements of the East and West chambers and the values of the average outside temperature.

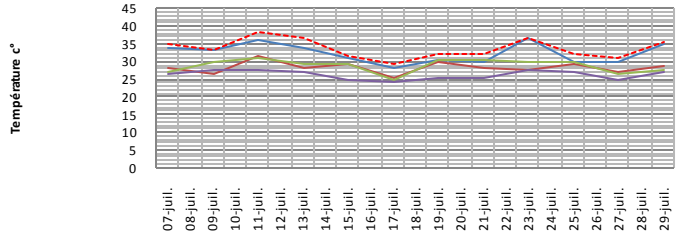

	07-juil	09-juil	11-juil	13-juil	15-juil	17-juil	19-juil	21-juil	23-juil	25-juil	27-juil	29-juil
9h-11h	33,9	32,9	35,85	33,8	30,75	27,95	30,1	29,5	36,6	29,85	29,45	34,85
13h-15h	28,1	26,55	31,8	28,25	29,25	25,3	29,85	28,55	27,55	29,55	27,35	29,05
16h-18h	26,9	29,75	31	29,2	29,25	24,55	30,3	30,25	29,75	29,75	26,25	27,3
20h-22h	26,4	27,65	27,65	26,9	24,75	24,15	25,35	25,55	27,65	26,95	24,65	27,2
Tex	35	33,5	38,5	37	32	29,5	32,5	32,5	37	32,5	31	35,5

Fig. 5 Variations of ambient temperatures in the East rooms as a function of the average outside temperature.

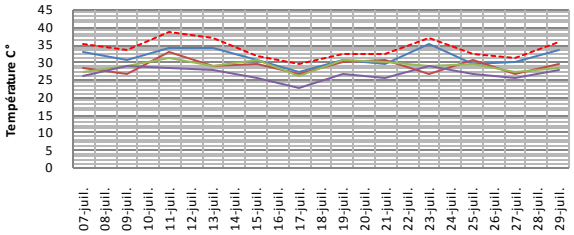

	07-juil.	09-juil.	11-juil.	13-juil.	15-juil.	17-juil.	19-juil.	21-juil.	23-juil.	25-juil.	27-juil.	29-juil.
9h-11h	32,85	30,8	33,85	33,85	30,55	27,15	30,35	29,35	35,25	29,25	30	33,35
13h-15h	28,15	26,45	33	28,55	29,45	26,3	29,7	30,6	26,4	30,75	26,3	29,15
16h-18h	27,15	29,05	31,1	28,85	30,25	26	30,3	30,2	29,05	29,25	26,85	28
20h-22h	26	28,95	28,65	27,55	25,55	22,65	26,45	25,55	28,95	26,7	25,25	27,9
Tex	35	33,5	38,5	37	32	29,5	32,5	32,5	37	32,5	31	35,5

Fig. 6 Variations of ambient temperatures in western chambers as a function of average outdoor temperature.

B. *Simulation*

Using a dynamic thermal simulation software such as TRNsys, we can model the thermal behavior of the building over a defined period of time by a calculation made according to a time and according to the weather, occupation, location and orientation [5].

Several parameters are taken into consideration in the simulation of TRNsys. In parallel, it gives us a variety of output choices by allowing a deep and precise study of the thermal behavior of buildings.

In fact, we performed the simulations by choosing the same approved period for in situ measurements. The climate file that we used in the software contains the same outdoor temperature values that are often very high throughout the day with humidity remaining frequently constant within the basal limits; and a constant air speed.

The following figures show the modeling of the maternity building with 8 zones (8 rooms, 4 East and 4 West):

ISSN: 2961-6611

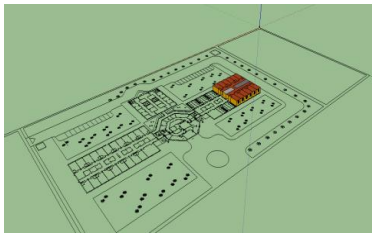

Fig. 7 General (outdoor) view of the maternity model on SketchUp

Fig. 8 Modeling rooms (zones) of the maternity ward

The graphs below show the the simulation results of ambient temperatures in maternity hospital rooms as a function of changes in outdoor temperature.

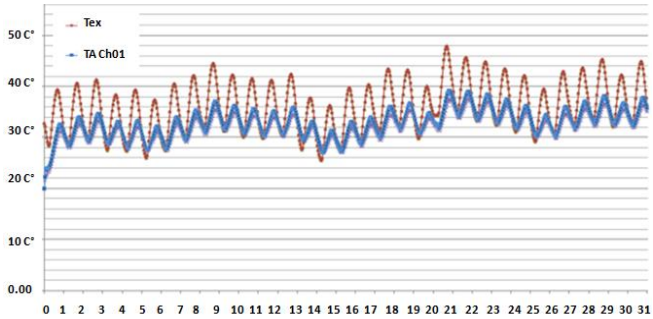

Fig. 9 Variations of the ambient temperature compared to the outside temperature of the month of July in room 01 (east orientation).

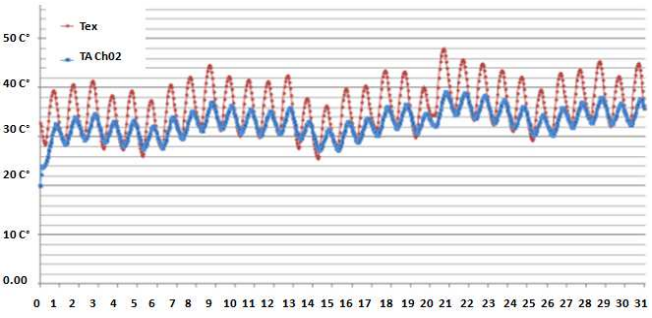

Fig. 10 Variations of the ambient temperature compared to the outside temperature of the month of July in room 02 (West orientation).

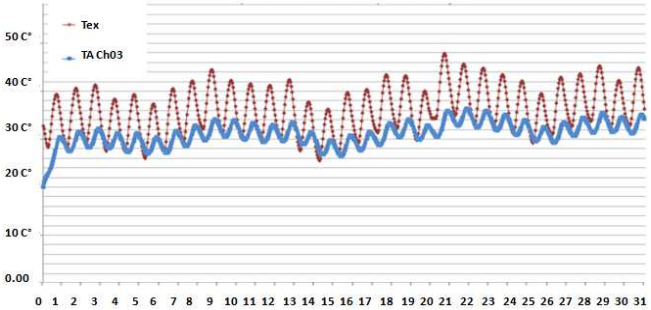

Fig. 11 Variations of the ambient temperature compared to the outside temperature of the month of July in room 03 (orientation East).

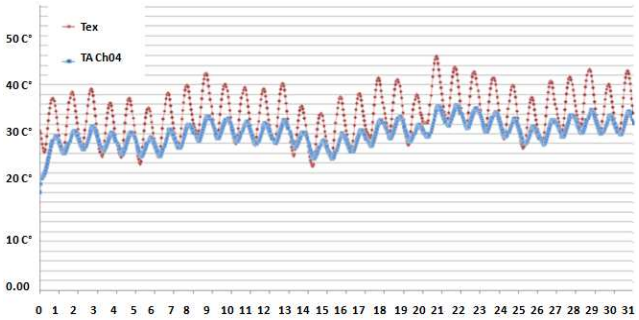

Fig. 12 Variations of the ambient temperature compared to the outside temperature of the month of July in room 04 (West orientation).

IV. DISCUSSION

Depending on the physical measurements taken, the temperature values are often high and reached 36 and 37 C°. The most extreme temperatures (the highest) were recorded in the morning from 9:00 to 11:00, this is certainly due to the total absence of air conditioning. The afternoon period, when the air conditioners are put into operation, the situation gradually changes until the difference between the extreme values is 5 C°. In this period the maximum value is between 29.85 and 29.55 C°; values still high compared to the values indicated in the standards. Noting that the ISO 7730 standard [6] indicates that for standard hospitalization areas (internal medicine, pediatrics, etc.) the recommended operational temperatures in summer are between 23 and 26 C°.For the same sector, the European standard NBN EN 13779 [7], recommends a temperature range of 20-26 C°.

From 4:00 pm to 6:00 pm, the temperature will rise to considerably higher values, which will fluctuate around 31 and 29.75 C°. During the night, the ambient temperatures stabilize somewhat at 27 to 24.65 C° as shown in Fig. 5.

This analysis may be valid for both orientations, only that the temperature values within the western chambers move between 29 and 33 C° during the morning period from 9:00 to 11:00 as shown in Fig. 6.

Fig.9 and 11 shows the variations of the ambient temperature in the rooms 01 and 03 having two facades (east and south facade), their results are almost similar, or the curve extends in the two graphs from the 1st day to the 31st day with irregular changes taking highs and lows within 28.1 C° and

ISSN: 2961-6611

39.5 C°. The variation of the temperature is very variable and generally nonlinear, but it remains all the same monotonous. Almost the same result was found at the time of the measurements which proved to us that the ambient temperature of the rooms never drops below 25 C° throughout the period of overheating.

At a certain moment, precisely the 13th and 14th days, we noted that the graph of the outside temperature takes values lower than those of the ambient temperature. This is quite similar to the human body, when the heat input is greater than the heat loss, the indoor temperature rises and this will be difficult to resume low values; while the outside temperature decreases at this time [8].

Although the chamber 02 is oriented West, the simulation results shown in Fig. 10 have shown that there is not a big difference between the results of the two orientations and that's exactly what we got by the measures.

As shown in Fig. 12, the curve frequencies of the ambient temperatures in the chamber 04 are almost regular, with a trajectory similar to that of the chamber 03, but sometimes the values are close to the values of the chamber 02, especially in peaks where the temperature reaches 39 C° for the maximum value and 28 C° for the minimum.

V. CONCLUSIONS

The simulation method relies on taking the values of the temperature every hour, while taking in situ measurements back and forth between the East and West chambers is a very complicated task; which made us distribute the moments of measurements over different periods of time.

Indeed, the results of the temperature measurements in the maternity rooms are very close to the results of the simulation. These results showed us that the values of the ambient temperature observed and simulated in the East and West chambers of the material are very high compared to the values indicated in the norms and therefore, we can confirm that the outside hot temperatures influence on the interior environment of the new construction despite the use of air conditioning. This can definitely affect the comfort of patients.

ACKNOWLEDGMENT

The authors would like to thank all those who contributed to this research; and particularly grateful for the assistance given by all the medical team in Maternity of Biskra.

REFERENCES

[1] Y. Besbas, N. Zemmouri, “Beyond thermal comfort in the hospital rooms. Investigation of thermal summer comfort in patients rooms: case of Biskra hospitals.” Journal of Applied Engineering Science & Technology, Vol. 4(1), 13-20, May. 2018.

[2] Y. Besbas, N. Zemmouri, “Investigation sur le confort thermique dans les chambres des malades. Étude comparative entre l'hôpital ancien et l'hôpital neuf à Biskra.” In Proceeding of Engineering and Technology, CIER- 2017, Vol.30 pp.87-92, Dec. 2017.

[3] Y. Besbas, “Caracterisation du confort thermique estival dans les chambres des malades. Cas des hopitaux de Biskra” Doctoral. thesis, Mohamed Khider University, Biskra, Algeria, February. 2019.

[4] S. Khelil, “Biomimicry, towards a living Architecture in hot and arid regions” magister dissertation, Mohamed Khider University, Biskra, Algeria, 2015.

[5] Delmas, m. D. (2014) Technique et logiciel- la simulation thermique dynamique.. [Online]. Available: http://dauchezpayet.fr/wp-content/uploads/la-std-par-dauchezpayet.pdf .

[6] OLESEN, B., & PARSONS, K. “Introduction to thermal comfort standards and to the proposed new version of en ISO 7730.” Energy and buildings, Vol. 34 (6), p 537-548, 2002.

[7] NBN EN 13779 . Ventilation dans les bâtiments non résidentiels – spécification des performances pour les systèmes de ventilation et de climatisation. AFNOR Std. 2004.

[8] M. RABOUILLE, “Recherche de la performance en simulation thermique dynamique: application à la réhabilitation des bâtiments” Doctoral. thesis, Grenoble Alpes University, Grenoble, France, 2014.

ISSN: 2961-6611

Overhead Transmission Line Design Learning software Using MATLAB Part –I Electrical Line Design

Salem Kurdi
Power system department, Higher Institute of Science and Technology Tiji
Tripoli, Libya
kusalem@gmail.com

***Abstract*—this paper presents a learning computer program for three phase's overhead transmission line design using MATALB. This program can be used as a self-learning tool to understand the course material offered in class in order to enhance students understanding to the subject of the first introductory course in the field of electrical power engineering. This program is also equipped with an additional feature to compute the line sequence impedances and the line sequence capacitances. Using this program the students will then be able to compute the line sequence parameters for both the single circuit as well as the double circuit tower configuration, with and without ground wire.**

The program has been also provided with a built in data base library to most of the available power line conductors. Therefore the power engineering students will then be able to grasp the transmission line course contents in more depth and to use the program as a self-learning tool for line design and line modeling performance.

***Keywords*: Line inductance, capacitance, transposition, sequence impedances and sequence capacitances,**

INTRODUCTION

Visualization of the solution of complex problems reinforces the basic principles learned via the traditional methods. The reinforcement is greater if the students from the beginning are exposed to such facilities. Such as graphical representation of solving equations that describe the physical system. This in turn will reinforce and accelerate the students learning and understanding to the field concept [1]. The effect of changing system parameters, topology, boundary and initial conditions provides a dramatic reinforcement to the mathematical description and to the analytical system knowledge a power student acquires in the classroom.

This paper will present a transmission line program using MATLAB which will help students to understand the material given in class for the core course taken during their undergraduate program.

The developed program is a user friendly, highly interactive during both the data entry phase and during the execution phase where the user can visualize the input data and see it on the screen. He or she can check, change, modify or completely erase the data so easily. The program solution can also be visualized.

A number of applications will be presented in a sequential order to present the usefulness of the program. Following this methodology the program can be very useful in class and as well as at home for better, faster and user friendly tool.

The subject of transmission line design is extensive as is the detailed modeling, since the overhead transmission line is a major component in power system. Therefore, the availability of a well developed and easy computer program for students, instructors and line designers is very essential.

SUBJECT BACKGROUND AND THE NEED FOR TRANSMISSION LINE PROGRAM

The new undergraduate students registering for the first time in the first electrical power engineering course is very much interested primarily to understand the transmission line principles such as; the line inductances per unit length , the line capacitance per unit length and the line resistance per unit length. Once all these line parameters are taken in class and understood then the line impedance, line admittance can be calculated based on a given and know system frequency. To model such a line in a particular study the line length must be also know. Since the line model varies with the line length. Different line models are available. Therefore students should be aware of such line models. The appropriate line model selection will depend on many factors such as; line length; steady state or transient condition, normal or faulted situation.

The three phase transmission line theory is given to undergraduate students as a core course. In this course the students will be exposed to the basic theoretical background with some line modeling details.

The line basic components such as; line inductance and line capacitance can be easily computed for a given line conductors and given tower configuration. Most of the time the homework assignments given to students during the course are devoted to a single circuit tower configuration without ground wire and assuming the line is completely transposed [3]

In some cases the undergraduate students will be given the appropriate techniques and the short cut approach without going in deep details in the analysis on how to deal with double circuit tower configuration and how to take into consideration the influence of ground wire. During the course work the undergraduate students are given in class enough background to be used to compute the positive sequence inductance and positive sequence capacitance assuming the line is completely transposed. Under such condition the effect

ISSN: 2961-6611

of ground wires are usually neglected [2,3,4] Very often during the lecture a brief discussion concerning the transposition concept is covered. The majority of students in class may or may not be familiar with the deep understanding of the need for line transposition and what are the real impacts on line performance in case the line is not transposed. What will be the effect on line impedance and line capacitance? When the line should be transposed? The students may raise many other questions such as what are the meanings of line sequence impedance, line sequence capacitances. Why do we need to get such sequence impedances? What do we mean by transmission line unbalance ……..etc?.
The answers to all these questions and others can be shown and explained with typical applications as will be described below.

APPLICATION#1

The first application will be devoted to develop user confidentiality session between the students and the program. The students will be asked to do the following assignments:
Turn the computer on and do call the transmission line program. The student is expecting to see a display on the screen with four options: these four options are:

- Electrical Design
- Mechanical design
- Thermal limit and line loading capability
- Environmental effects

A decision has to be made by the student to choose either a single circuit tower or double circuit tower
Let us now assume that the student selects the single circuit option; a new display will be shown on the screen as indicated in fig.1

This screen shows a large number of information that will guide the students step by step to insert the input data. The information required to be inserted on the screen are in itself very useful and are designed in a way to help the student to be well guided to accomplish his goal very successfully such as:

- Choice of the type of the line parameters to be calculated first for example; line inductance, line capacitance or line impedance:
- Choice of the type of units to be used in the calculation ; metric or English
- For a single conductor, the student must click on single conductor option and for the bundle conductor the student must click on the bundle conductor and then he should insert the number of the bundle conductors;2,3,4.…etc . The spacing between sub-conductors must be also specified.
- Tower configuration; the student should also insert the positions of the three phase conductor on tower. Therefore the three phase conductors should be inserted and specified as an (x,y) coordinates .

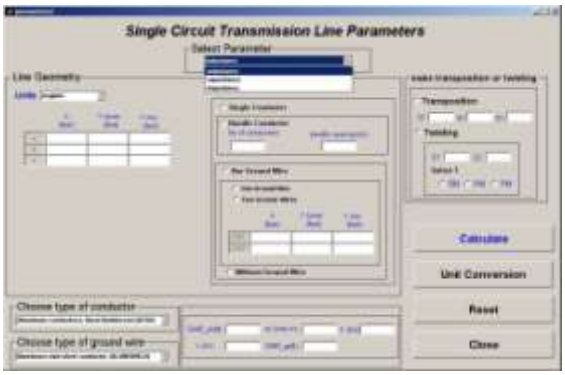

Fig.1 A single circuit tower line input data parameters.

The student should also have been selected the conductor name from the beginning; and from the stored and the available data base library in the program an automatic display for all the data needed for the inductance, capacitance and impedance calculation will be shown on the screen such as: Conductor geometric mean radius, conductor radius, conductor resistance….etc

If the circuit has a ground wire, then the name of the ground wire should have been also selected with the same procedure similar to the phase conductor. The location of the ground conductor should have been decided and an automatic fill in information will be displayed at the appropriate space provided for the ground wire, such as; ground wire resistance, ground wire geometric mean radius and ground wire radius.
Let us now be very specific and let us assume that the following home work assignment is given to the student as:

APPLICATION# 2

A 400kv three phase single circuit completely transposed line , is composed of a single conductor per phase ACSR 1,272,000cmil, 45/7 Bittern conductor per phase with the tower configuration as shown in fig.2 Use the developed program and compute the following : The line inductance L , The line Capacitance C , The line Impedance Z

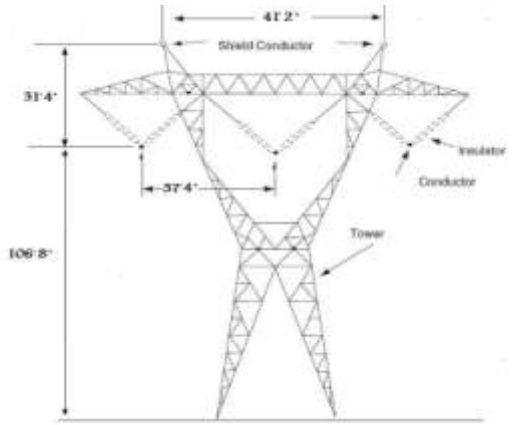

Fig.2 A 400 kv single circuit tower configuration.

ISSN: 2961-6611

The required input data to the program are:

Conductor name: Bittern, CSA 1,272,000 ACSR
Single conductor /phase, line completely transposed
Let us go back to the screen display of fig.1 and select the conductor name as given above
Let us also insert the tower configuration shown in fig.2 and let us select also the completely transposed line option as normally mentioned in the course. No ground wire information is provided therefore; no ground wire exists. Let the English units; inches and feet are selected for this calculation
Let us calculate first the Line inductance by clicking on the inductance option

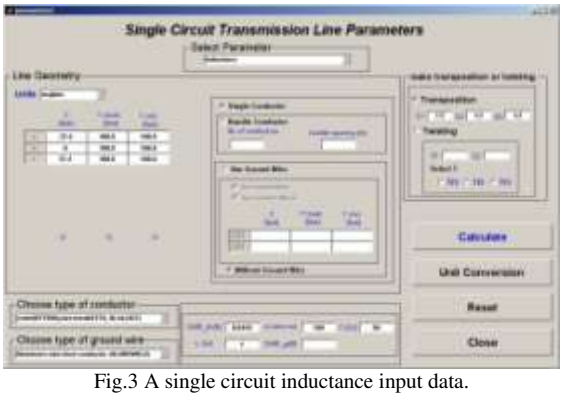

Fig.3 A single circuit inductance input data.

The solution to this application will be shown on the screen as indicated in fig.4

The students can now compare the computed values with the value obtained using the formula that he took in class: where
L = 0.2 x ln (GMD/GMR) mH/km
OR L = 0.3219 x ln (GMD/GMR) mH/mi

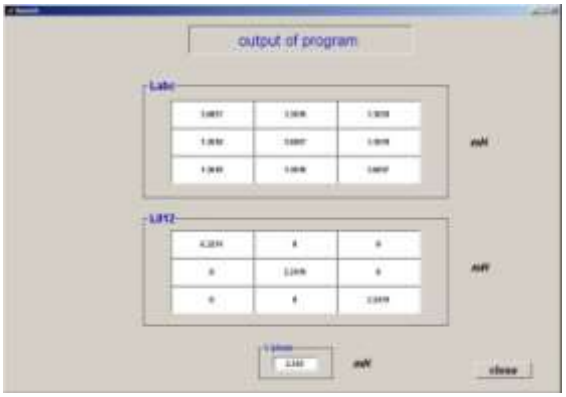

Fig.4 A single circuit inductance results.

GMD = (D_{ab} x D_{bc} x D_{ca})$^{(1/3)}$ where D_{ab} is the distance between phase a and phase b and D_{bc} is the distance between phase b and phase c and D_{ca} is the distance between phase c and phase a and the **GMR** can be taken from the input data display shown in fig.3. The student can now go back and run the program again by choosing the capacitance option calculation. The solution output is displayed on the screen as shown in fig.5
The student can now check and compare this computer solution output with what he learned in class where:
C= 0.0556 / ln (GMD/r) μ F/km
OR C= .0895 / ln (GMD/r) μ F/mi

GMD is the same value used in the inductance calculation.

Fig.5 A single circuit capacitance results.

Let us continue with the same example and let us compute the line impedance Z
The student can now go back to the same input data screen and click the impedance option .using the mouse. The computer output results are displayed on the screen as shown in fig.6

The student can now check this value with what he also learned in class Z= R+j(ωL) where ω = 2Π f L

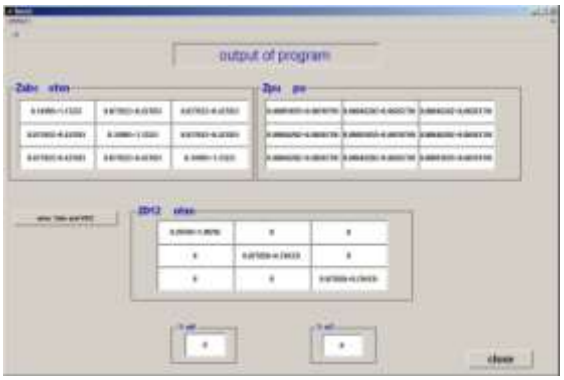

Fig.6 A single circuit impedance results.

APPLICATION#3

Let us replace the single conductor used in the previous application by 2 sub-conductors per phased (ACSR 636,000 CMIL ROOK) conductors which have the total cross sectional area of aluminum as one Bittern conductors. Assume the line spacing is the same as in the previous. Therefore the bundle conductor option will be activated.
These home work objectives are:

ISSN: 2961-6611

- To teach students the benefits of using bundle conductors in overhead transmission line. The program can be used in this case to compute both line inductance as well as line capacitance.
- The second objective of the program is to check the influence of line length on the line equivalent circuit. We teach students in class that if the transmission line length is up to 50mi Then the effect of capacitance is neglected and only the series impedance will be considered [2,3]
- If the line length is greater than 50mi and up to 150mi then the medium model representation is used and in case of long line which is greater than 150mi then the long line representation is used.

This exercise will be used to accomplish the above objectives. The student should go to the same input data screen as described earlier and select from the conductor type the one with the conductor name ROCK. He should then click the mouse and insert 2 as the number of sub-conductors per phase and insert the space between the bundle conductors and repeat the same calculation for L, C and Z. The relevant circuit model will then be displayed on the screen

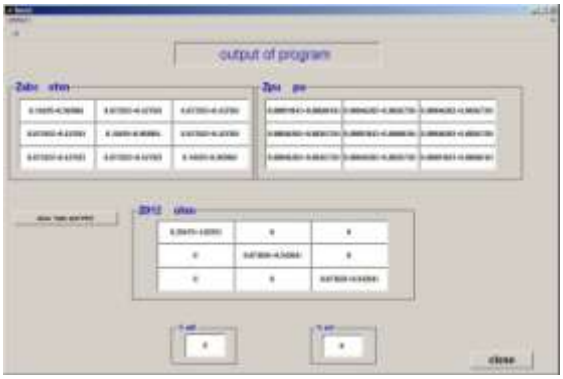

Fig.7 impedance results with bundle conductors.

The student can now run the program by changing the line length to 80 mi. Figure. 8 show the impact of choosing the medium line length on the impedance calculation module where the medium line representation T and Π models will be displayed accordingly. Figures.9, and 10 shows the medium line representation T and Π models

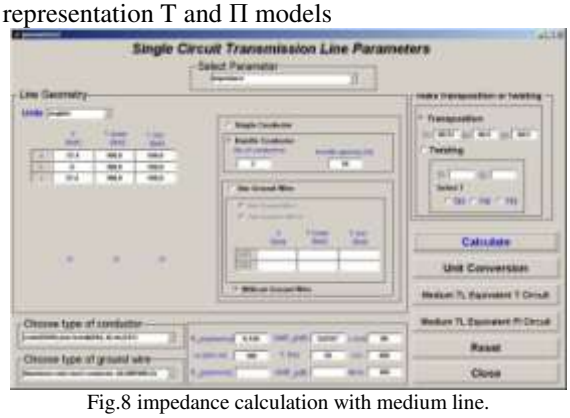

Fig.8 impedance calculation with medium line.

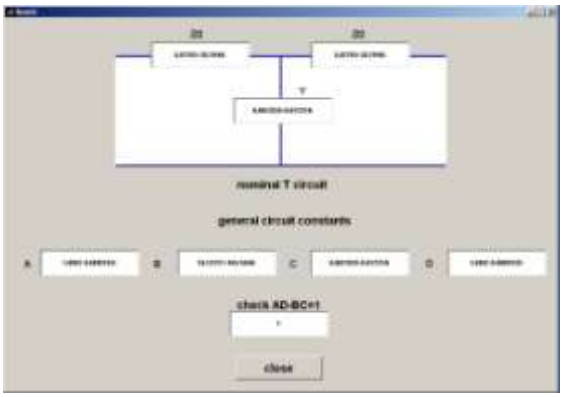

Fig.9 medium line T model.

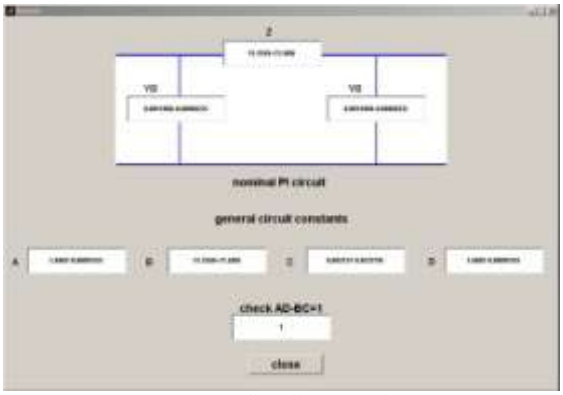

Fig.10 medium line Π model.

LINE SEQUENCE IMPEDANCES AND SEQUENCE CAPACITANCES CALCULATION

This section will introduce the students to application of the developed program to the course material which is normally given to graduate students .The developed program computes the transmission line impedance matrix and capacitance matrix for three phase transmission line single circuit and double circuit tower configuration with and without ground wire and taking into account the following option:

- Line not transposed
- Partially transposed line
- Completely transposed line
- Twisted line
- The sequence impedance and the sequence capacitances can be obtained for every option of the above mentioned cases.
- The electrostatic and the electromagnetic balance factors are also computed for each transposition cycle option

With this program the student will be able to understand the covered material given in class. At the same time the students will be able to understand and to practice different transposition cycles easily. They will understand and grasp the material given in class much faster. The impact of transposition on the impedance and capacitance matrix elements will be computed and assessed. The impact of transposition on the sequence matrix elements will be seen and evaluated. We do feel very strongly that explaining such

ISSN: 2961-6611

transposition cycle options for the transmission line cannot be handled and understood easily by solving examples on the blackboard. Therefore having a computer program which has such features will help explaining this subject and reinforce the classroom lectures. The following applications will demonstrate this idea.

APPLICATION#4

After the student became familiar with the use of the program he will be able to compute the line impedance matrix and the line capacitance matrix for two types of tower configuration; a single circuit tower and double circuit tower configurations, with and without ground wires. The following cases are easy to solve using the program :

1. A single tower configuration calculation
   - Computing the line impedance matrix without ground wire
   - The line impedance matrix With ground wire
   - Assuming the line partially transposed
   - The line completely transposed
   - The line sequence impedance with line not transposed
   - The line sequence impedance with the line partially transposed
   - The line sequence impedance with the line completely transposed
2. Repeating all of the above for double circuit tower configuration

CONCLUSION

The developed program in this paper presents many valuable features which can support the instructors in class in order to explain and teach the course material related to the three phase transmission line theory and design very effectively. A number of selected topics from the course material which are normally given in class are programmed and presented to enhance and modify the existing classical lecturing approach in class to more active one and using this program the classroom then becomes similar to a laboratory. This developed program will help the instructors to present the class material easily and it well help the students also to easily understand the class lectures effectively.

Both undergraduate students and graduate students will be able to learn and to compute the following: Transmission line parameters; line inductance and line capacitance, line impedance, the effect of line transposition, line twisting on the computed line parameters. and other line features can now be computed and assessed . The student's interaction with the instructors during the class lectures and simulation will make the classroom more live.

Using this program the instructor will be able to present many examples in class provided a computer is available which will be difficult or impossible to be presented in class without having such facilities due to lecture time constrain. The instructor will then be able to assign and defer the longer homework problems for students to be done at home or through mini projects during the course

REFERENCES

1. Jomaa B. and others ;"Interactive Computer Programs For Electrical Power Engineering Students Part IV: Interactive Calculation of Transmission Line Seq. Impedance and Seq. Capacitance" Proceedings of the Second Libyan Arab International Conference on Electrical and Electronic Engineering March 1989
2. Glover and Sarma ; Power system analysis and design. Second Edition McGraw Hill
3. Grainger J , Stevenson W: Power System Analysis; McGraw Hill international 1994
4. Saadat Hadi, Power System Analysis. McGraw Hill international 1999
5. Bayless , Transmission and Distribution Electrical Engineering Reference book
6. Burgen Arthur, Power system Analysis, Prentice Halt Series in Electrical and Computer Engineering
7. Anderson Paul , Analysis of Faulted Power System; , Iowa State University press , Ames Iowa 1970
8. Electric Power Research Institute; Transmission Line Reference book 345Kv and above / Second Edition

ISSN: 2961-6611

Assessment of mass, energy, exergy and environmental analysis of a rotary kiln for clinker production in cement industry

Ghada Ghoudi[1], Fourat Maghrebi[2], Mourad Magherbi[12]

UR11ES80, APPLIED THERMODYNAMICS

(1) Chemical and Process Engineering Department, Engineers National School of Gabes, Gabes University, Omar Ibn El Khattab Street, 6029 Gabès, Tunisia

(2) High Institute of Applied Sciences and Technology of Gabes, Gabes University, Omar Ibn El Khattab Street, 6029 Gabes, Tunisia

ghadaghoudi@hotmail.fr; fourat.maghrebi@gmail.com; magherbim@yahoo.fr

Abstract: This study focuses on energy, exergy and the evaluation of atmospheric emissions from a rotary kiln (dry) in a cement plant in operation in Tunis. Using the first and second laws of thermodynamics, the energy and exergy destruction and emissions allocations are analyzed for the rotary kiln of a Tunisian cemetery factory. The atmospheric emissions method was used to calculate the annual emissions from the cement kiln. It is found that the Carbon dioxide CO2 accounts for approximately 99% of total air pollutant emissions.

Key words: Rotary kiln, Mass balance, emission factor, exergetic efficiency, energetic efficiency.

I. Introduction

For many years the cement industry is a big consumer of energy. Countries' energy consumption has been investigated using exergetic analysis [1] in order to understand the efficiency and the capacity of amelioration of the degraded energy, which is manifested as form of heat and atmospheric emissions (gas and dust). The main objective of this work is to evaluate the energy, exergy efficiencies and the atmospheric emissions related to a rotary kiln in the clinker production process.

In the United States of America and for 27 years (1970-1997) Worrell et al. [1] attributed the energy survey in industry. For the preheating process, the CO2 emission intensity per 1000 kg of cement is 5.4 kg of CO2.

Engin and Ari [2] presented an investigation concerning a rotary kiln in a cement plant in Turkey. The authors noted the existence of a large loss of energy in the manufacturing process and that it is possible to recover 4 MW of energy with some modifications. In their study, Kabir and El-Nafaty [3] used a blanket surrounding the surface of the oven. They found that this method can provide energy savings of about 42.9 MWh/year. Atmaca et al. [4] studied a cyclone insulation that affects a total heat loss of 22.7 MW to 17.3 MW.

In this study, using the actual operating data of a Tunisian cement plant, a rotating kiln in operation was analyzed with the evaluation of balance equations of energy, exergy and mass.

II. Methodology

A. Process description

The raw materials used in the manufacture of cement are extracted from quarries (open pit) from limestone and clay. They are then transported by dumper to the crushing hall. The previously crushed raw materials are pre-homogenized, dried and then ground mechanically. Other minerals are usually added to correct the chemical composition of the mixture. This first grinding produces a fine powder; it is the "raw cement" or farine. The raw material is poured into a heat exchanger in which the hot gases escaping from the oven circulate in the opposite direction. The material progresses to the entrance of the latter where the temperature is around 800 ° C. This preheating thus makes it possible to start the decarbonation process. The raw material then enters a rotary calcination furnace which is generally fed with petroleum coke or ground coal. This method of cooking allows the material to be progressively conveyed against the current of the hot gases thanks to a slow rotation of 1 at 3 rpm . The interior of the furnaces is generally covered with refractory bricks, which makes it possible to reach a temperature of 1450°C and to trigger a physicochemical phenomenon called "clinkerization" As soon as you leave the oven, the incandescent granules must be cooled rapidly. Thus, several types of cement can be created according to the added products, called "adjuvants". In general, a small amount of plaster (3 to 5%) and gypsum are added to the clinker to regulate the setting characteristics of the cement.

B. Energy and Exergy analysis

The following assumptions have been made: (i) the process occurs in a steady state, (ii) the stack gases are ideal gases, (iii) the kinetic and potential energy

ISSN: 2961-6611

variations are negligible, (iV) the temperature of the system is kept constant.

The thermodynamic properties of each stream with well-defined compositions and temperatures were extracted by aspen simulation plus, but the result can be confirmed with the calculation as well, so both methods are used.

The mass balance equation is expressed as follows with a general steady-state:

$$\sum_i \dot{m}_{in} = \sum_i \dot{m}_{out} \quad (1)$$

Where $\dot{m}$ is the mass flow rate, the subscript out for outlet and in stands for inlet.

It is generally more practical to define the mass / energy data per kg of clinker produced per unit of time.

The mass balance of the rotary kiln is summarized in Fig. 1.

	Inputs: kg/kg-clinker		Outputs: kg/kg-clinker	
1.6	farine	Rotary kiln	clinker	1
1.5	Secondary air		Hot gases	2.3
2.3	Primary air		dust	0.6
0.15	coke			

Fig.1. Mass balance of the rotary kiln

Energy balance can be expressed as:

$$\dot{Q}_{net,in} - \dot{W}_{net,out} = \sum \dot{m}_{out} h_{out} - \sum \dot{m}_{in} h_{in} \quad (2)$$

Where W is the rate of work, Q is the heat transfer rate and h is the enthalpy.

Energy efficiency is defined as the ratio of the output energy amount and the input energy:

$$\eta_I = \frac{\sum \dot{E}_{out}}{\sum \dot{E}_{in}} \quad (3)$$

The total exergy of a material stream can be expressed as the summation of its chemical exergy (Exch) and the physical exergy (Exph) [5]:

$$Ex = Ex^{ph} + Ex^{ch} \quad (4)$$

$$Ex^{ph} = \dot{m}\,[(h - h_0) - T_0(S - S_0)] \quad (5)$$

Where T_0 is the reference temperature (K), m is the mass flow rate (kg/h), $(S - S_0)$ is the entropy change from reference point (kJ/kgK) and $(h - h_0)$ is the enthalpy change from reference point (kJ/kg).

From the first law of thermodynamics, the enthalpy change is given as:

$$(h - h_0) = C_p(T - T_0) \quad (6)$$

The entropy change is obtained by combining the first and second laws of thermodynamics. It's given by:

(i) For ideal gases

$$(S - S_0) = \left[C_p \log\left(\frac{T}{T_0}\right) - R \log\left(\frac{P}{P_0}\right)\right] \quad (7)$$

(ii) For solid and liquid (8)

$$(S - S_0) = \left[C_p \log\left(\frac{T}{T_0}\right) - V(P - P_0)\right] \quad (8)$$

In the Eq. (8), V is the specific volume (m3/kg) and $(P - P_0)$ is the pressure change from reference point. The dead state properties are denoted by the subscript 0. The chemical exergy is determined using the equation (9) [6]:

$$Ex^{chi} = D\left[\sum X_i \xi_{io} + RT_0 \sum_i X_i (\log X_i)\right] \quad (9)$$

In the Eq. (9), D, Xi and ξ_{io} are respectively the molar flow of material flow (kmol/s), the molar fraction of component (i) and standard chemical exergy of component (i) (KJ/Kmol);

The exergy efficiency η is calculated using:

$$\eta = \frac{\sum Ex_{out}}{\sum Ex_{in}} \quad (10)$$

C. Inventory of atmospheric emissions

According to the literature review, there are several methods to make an inventory of emissions. In our case we chose the product-oriented method.

- Process Emission Factors

The estimation of the emissions of the process is carried out with reference to European emission factors according to the following formula [7]:

$$E_1 = E_S = P_r * FE_s \quad (11)$$

(Pr) is the annual production in tons per year (T/year).

(Fes) is the substance emission factor s (g/ton).

- Fuels Emission Factors

The emissions estimation related to the fuel is carried out by referring to French emission factors according to the following formula:

$$E_2 = E_s = \sum Q_f\, PCI_f FE_{s,f} \quad (12)$$

(Es) is the emission of the substances (ton/year).

(Qf) is the amount of fuel consumed (ton/year).

(PCIf) is the lower calorific value of the fuel (f) (MJ/Kg).

($FEs_{,f}$): emission factor of the substance (s) of the fuel (f) (g/GJ).

- Estimation des émissions atmosphériques

The estimated atmospheric emission (E) for a given industry sector is equal to the sum of process emissions (E1) and fuel emissions (E2)

$$E = E_1 + E_2 \quad (13)$$

III. Results and discussions

A. Energy and Exergy analysis

Total energy output (Σ Ėout) involves the energy of constituents and hot gas leaving the component and heat loss of outer surface of the rotary kiln. The energy input by the input materials, the electrical energy and the energy obtained from the combustion process are the total energy input (in). It is found that 25% of the input energy is lost during the formation of the clinker and in the form of heat on the surface of the rotary kiln. The total amounts of energy entering and leaving the system were calculated and found equal respectively to 86.935 MW and 65.319 MW. The energy efficiency of the furnace is equal to 65.8%. The sum of physical and chemical exergy is equal to 107.65MW. The total exergy for the output is a summation of physical exergy, chemical output exergy and heat transfer exergy and clinker training through the furnace. This is equal to 64.15MW.

ISSN: 2961-6611

The main input energy is provided by the combustion process. The combustion process has the greatest influence on the combustion process.

Table1. Energy and Exergy values of rotary kiln

Input material	Content	ṁ (kg/h)	cp kJ/kgK	T0 (K)	Tin (K)	Δh (kJ/kg)	Δs (kJ/kgK)	Σ ṁ h (kW)	Σ ṁ ψ (kW)	Exchi (kW)	EXph (kW)
Farine	CaO	42673,05	0,6	298	1050	451,2	0,756	5348,356	2670,479	8,409558	2677,876
	SiO2	12792,15	0,69	298	1050	518,88	0,8694	1843,775	920,6127	1176,879	923,1626
	Al2O3	3124,8	2,01	298	1050	1511,52	2,5326	1311,999	655,0924	172,4888	656,9069
	Fe2O3	2050,65	4,16	298	1050	3128,32	5,2416	1781,969	889,7524	70,74747	892,2169
	MgO	585,9	0,37	298	1105	298,59	0,4662	48,59552	22,61047	80,85258	25,98506
	K2O	390,6	4,31	298	1105	3478,17	5,4306	377,3814	175,5876	46,87166	201,7939
	CO2	35056,35	1,259	298	1105	1016,013	1,58634	9893,808	4603,379	10741,58	5290,429
	Na2O	195,3	4,36	298	1105	3518,52	5,4936	190,8797	88,81228	35,93485	102,0674
	SO3	390,6	0,6	298	1105	484,2	0,756	52,5357	24,44375	53,9068	28,09195
Total	-	97650						20849,3	10050,77	12387,67	10798,53
Coke kiln	C2	4655	0,03	298	330	0,96	0,00306	1,241333	1,178996	2082,651	0,062337
	Ash	1428	1,3	298	330	41,6	0,132587	16,50133	15,67267	0	0,828666
	O2	266	0,92	298	330	29,44	0,093831	2,175289	2,06605	44,62885	0,109239
	H2	252	14,32	298	330	458,24	1,460497	32,0768	30,46596	671,0725	1,610837
	H2O	196	4,18	298	330	133,76	0,426318	7,282489	6,916776	58,4107	0,365713
	N2	112	1,04	298	330	33,28	0,10607	1,035378	0,983383	21,46403	0,051995
	S2	91	5,64	298	330	180,48	0,575224	4,562133	4,333032	15,2674	0,229102
Total	-	7000.00						64,87476	61,61687	2893,494	3,257889
Combustion	-	7000	3.45	298	1270	3359.98	1,6675	58333,33	966,2236		57367,11
Primary Air kiln	N2	14430,8	1,041	298	298	0	0	0	0	2840,431	0
	O2	3866,03	0,93	298	298	0	0	0	0	666,1559	0
	Ar	222,612	4,97	298	298	0	0	0	0	30,72574	0
	CO2	7,32765	0,85	298	298	0	0	0	0	0,916393	0
	H2O	5,6395	4,18	298	298	0	0	0	0	1,716371	0
	Other	16,733	1,007	298	298	0	0	0	0	3,185572	0
Total	-	18551						0	0	3543,131	0
Secondary air	N2	65829,79	1,15	298	413	132,25	0,3749	2418,33	2042,921	12957,33	375,409
	O2	17635,85	1,07	298	413	123,05	0,34882	602,8032	509,2271	3038,836	93,57602
	Ar	1015,5	4,97	298	413	571,55	1,62022	161,2247	136,197	140,1631	25,02769
	CO2	33,42688	1,21	298	413	139,15	0,39446	1,292042	1,091472	4,180354	0,20057
	H2O	25,726	2,4	298	413	276	0,7824	1,972327	1,666153	7,829652	0,306174
	Other	76,33175	1,18	298	413	135,7	0,38468	2,877283	2,430629	14,53178	0,446654
Total	-	84625						3188,5	2693,534	16162,87	494,9661

ISSN: 2961-6611

Table2. Continued Energy and Exergy values of rotary kiln

Material	Content	ṁ (kg/h)	cp kJ/kgK	T0 (K)	Tin (K)	Δh (kJ/kg)	Δs (kJ/kgK)	Σ ṁ h (kW)	EXchi (kW)	Σ ṁ ψ (kW)	EXph (KW)
Hot clinker	4CaO	1875	0,62	298	1550	776,24	1,044638	404,2917	505,3689	162,1365	242,1551
	Al2O3	1375	2,17	298	1550	2716,84	3,656233	1037,682	103,8077	416,1504	621,5315
	Fe2O3	2812,5	4,43	298	1550	5546,36	7,464107	4333,094	132,7085	1737,737	2595,356
	2CaO	7231,3	0,6	298,0	1550	776,24	1,044638	1559,218	1949,034	625,3065	933,9117
	SiO2	7500	0,7	298	1550	876,4	1,17943	1825,833	943,704	732,2295	1093,604
	3CaO	3125	0,62	298	1550	776,24	1,044638	673,8194	842,2798	270,2275	403,5919
	Al2O3	3250	2,17	298	1550	2716,84	3,656233	2452,703	245,3637	983,6282	1469,075
	3CaO	22500	0,62	298	1550	776,24	1,044638	4851,5	6064,414	1945,638	2905,862
	SiO2	10625	0,7	298	1550	876,4	1,17943	2586,597	1336,915	1037,325	1549,272
	K2O	287,5	4,78	298	1550	5984,56	8,053822	477,9336	47,18469	191,6698	286,2638
	SO3	1168,75	0,89	298	1550	1114,28	1,499561	361,7541	1166,281	145,0773	216,6768
	MgO	706,25	0,39	298	1550	488,28	0,657111	95,79104	133,298	38,4159	57,37515
	Na2O	43,75	4,71	298	1550	5896,92	7,935879	71,66396	11,0099	28,74001	42,92395
total		62500	-	-	-			20731.88	13481,37	4956,156	7402,149
Hot gases	N2	12638,76	1,08	298	1300	1082,16	1,5876	3799,21	2258,69	1660,96	17966,54
	CO2	105222,2	1,09	298	1300	1092,18	1,6023	31922,67	11969,45	13956,13	2366,881
	H2O	7370,418	2,05	298	1300	2054,1	3,0135	4205,438	2048,193	1838,557	625,6732
	O2	3954,538	1,01	298	1300	1012,02	1,4847	1111,687	618,6913	486,0134	941,0309
	CO	1208,696	4,97	298	1300	4979,94	7,3059	1672,009	152,1649	730,9784	109,5921
	SO2	985,35	0,71	298	1300	711,42	1,0437	194,7216	77,07627	85,12948	24147,97
Total		131380						42905.74	17124.26	18757.77	46157.68
Dust kiln	4CaO	502,056	0,71	298	710	292,52	0,61628	40,79484	25,61203	15,18281	12,32631
	Al2O3	195,244	2,6	298	710	1071,2	2,2568	58,09594	36,4741	21,62184	10,73789
	Fe2O3	334,704	5,3	298	710	2183,6	4,6004	203,0166	127,4589	75,55764	11,50447
	2CaO	1854,818	0,71	298	710	292,52	0,61628	150,7143	94,62222	56,09205	910,7795
	SiO2	1004,112	0,92	298	710	379,04	0,79856	105,7218	66,37484	39,347	92,03637
	3CaO	794,922	0,71	298	710	292,52	0,61628	64,59183	40,55238	24,03945	26,02225
	Al2O3	474,164	2,6	298	710	1071,2	2,2568	141,0901	88,57995	52,51019	26,07677
	3CaO	4685,856	0,71	298	710	292,52	0,61628	380,7518	239,0456	141,7062	153,3938
	SiO2	1673,52	0,92	298	710	379,04	0,79856	176,2031	110,6247	65,57833	153,3935
	Ash	2426,604	1,3	298	710	535,6	1,1284	361,0248	226,6605	134,3643	0
Total	-	13946	-	-	-	-	-	1682,005	1056,005	625,9998	1396,271

Summarizing these tables, we can extract the following table concerning the energetic and exergetic efficiency of the kiln.

Table3. Energy efficiency and exergy efficiency of the kiln.

	Input energy (MW)	Output energy(MW)	Energetic efficiency	Input exergy (MW)	Output exergy (MW)	Exergetic efficiency
kiln	86.436	56.875	0.658	107.652	64.151	0.59

ISSN: 2961-6611

B. Emissions from the cement industry

The flue gases and most of the particles are emitted by the large chimney; the other filters only remove dust. Energy emissions are the atmospheric emissions associated with the combustion of the fuel used by the rotary kiln. For an annual consumption of 61320 tons/year of petroleum coke and 191135 tons/year of natural gas, the calculation of energy emissions resulting from combustion is carried out according to the expressions of Eqs. (11) and (12). For an annual clinker production in the order of 814164.8 tons/year, with a known process emission factor, the calculation of process emissions is calculated according to equation (11). The fuel and process emissions are summarized in the following table.

Table4. Cement Industry Contribution to Air Pollution

	E SO2	E NOx	ECO	E CO2	ECOV	ETSP
Natural gas	0	635.18	180.12	54037.68	37.92	0
Pet coke	2569.2	323.4	26.94	172480.89	5.38	0
Process	0	0	0	427436.52	0	73.27
Total emissions	2569.2	985.32	207.06	653955.09	43.3	73.27

It was noted that the CO2 gas is the main pollutant compared to other pollutants. The calcination process and the fuel combustion process are responsible for emissions of particulates and gases of nitrogen oxides (NOx), carbon monoxide (CO), sulfur, carbon dioxide (CO2)) and other pollutants. The carbon dioxide CO2 represents the major air pollutants with a percentage of 99%. Dry cement [8] revealed that about 0.59 tons of CO2 is emitted per ton of cement. However, the estimated value obtained for this study is about 0.90 ton of CO2 per ton of clinker produced. This value represents approximately 1.53 times the one obtained by the previous study [8]. In recent years, several studies have been conducted to reduce CO2 emissions, considered as the main greenhouse gas. The settlement approaches proposed in recent decades include the use of alternative fuels and energy sources, the substitution of raw materials, the use of energy-efficient equipment and the replacement of old facilities. Better furnace insulation and optimization of clinker cooling are part of the process upgrade [9]. Using the best available technology can help increase energy efficiency and reduce pollutant emissions. Increasing energy consumption increases pollutant emissions.

IV. Conclusion

This work, which concerns the simulation of a rotary kiln in a Tunisian cement factory, leads to evaluate the exergy, the energy efficiency and the pollutant emissions from this equipment. Results show that, the exergetic and energetic efficiency of the rotary kiln are respectively equal to 0.59 and 0.65. The degraded exergy in the furnace is found to be equal 43.5 MW. The CO_2 emissions accounted for more than 99%. Results reveal that, approximately 0.9 tons of CO_2 were emitted per ton of produced clinker.

The thermodynamic parameters must be optimized to improve its exergetic efficiency. The Carbon mitigation and capture strategies need to be used to reduce CO_2 emissions in the cement industry.

References

[1] Worrell E, Martin N, Price L. Potentials for energy effi ciency improvement in the US cement industry. Energy 2000; 25:1189–1214.

[2] Engin T, Ari V. Energy auditing and recovery for dry type cement rotary kiln systems – a case study. Energy Conversion and Management 2004; 46:4:551–562.

[3] Kabir A, El-Nafaty UA. Energy audit and conservation opportunities for pyroprocessing unit of a typical dry process cement plant. Energy 2010; 35:1237–1243.

[4] Atmaca A, Kanoglu M, Gadalla M. Thermodynamic analysis of a pyroprocessing unit of a cement plant: a case study. Int J Exergy 2012; 11:2:152-172.

[5] Cengel YA and Boles MA. Thermodynamics: an engineering approach. 5th ed. New York, USA:McGraw Hill,2006.

[6] Gurturk M and Oztop HF. Energy and exergy analysis of a rotary kiln used for plaster production.Appl Therm Eng 2014; 67: 554–565.

[7]Fontelle,J.P.,Andre,J.M.,Bastide,A,R.,Chang,J.P. ,Deflorenne.,2012.National inventories of air emissions in France : organisation and methology-OMINEA,February 2011.

[8] Oni AO, Fadare DA and Adeboye LA Thermoeconomic and environmental analyses of a dry process cement manufacturing in Nigeria. Energy 2017; 135: 128–137.

[9] Vatopoulos K and Tzimas E. Assessment of CO2 capture technologies in cement manufacturing process. J Clean Prod 2012; 32: 251–261.

ISSN: 2961-6611

Dry Anaerobic Co-digestion of Vegetable Wastes and Cow Manure Mixtures for Enhanced Biogas Production

Najoua Mlaik*[1], Fathi Aloui1, Sami Sayadi[1] and Sonia Khoufi[1]
1-*Laboratory of Environmental Bioprocesses, Centre of Biotechnology of Sfax, P. B "1177", 3018 Sfax, Tunisia.*
*Author to whom correspondence should be addressed
e-mail: mnajwa212@yahoo.fr; Phone/Fax: +216 74 874 452

Abstract—
Anaerobic digestion is an environmentally sustainable technology for converting a variety of feedstock's (waste sources), including manure, organic fraction of municipal solid waste (OFMSW) and agricultural residue, to energy in the form of methane. In this study, dry mesophilic co-digestion of vegetable wastes (VW) and caw manure (CM) was investigated. The effect of substrate to inoculum ratio (S/I ratio: 0.5 and 1) on the biochemical methane potential (BMP) of these substrates during mono-digestion and co-digestion were investigated. Methane yields about 31 and 168.3 mL/g VS were obtained during mono-digestion of VW and CW at S/I of 0.5, respectively. The low methane yield of VW can be explained by the low C/N ratio. A methane yield of 284 mL CH_4/g VS was obtained from VW and CM mixture at S/I of 0.5 and TS of 20%. These results indicated the highest efficiency of co-digestion compared to mono-digestion. The kinetics of biogas production was modeled with the modified Gompertz model. A higher correlation between this model and the experimental data was observed (R^2 of 0.99 for S/I equal to 0.5).
The optimal conditions obtained from preliminary experiments of VW and CM co-digestion were studied at laboratory-scale digester of 10 L (Leach Bed Reactor). Results showed a low cumulative biogas yield of 445 mL/g VS, which is due to high level of ammonia and alkalinity
Keywords: **Vegetable wastes, cow manure, co-digestion, S/I ratio, biochemical methane potential**

I. Introduction

As global energy demand is dramatically increasing, the renewable energy produced from biomass is an alternative method to energy production based on fossil fuels, which has negative environmental effects such as air pollution [1,2] . Anaerobic digestion (AD) is an attractive method for treatment of organic biomass to recovery renewable energy and to stabilization of organic matters. Therefore, agricultural and organic fractions of municipal solid wastes (MSWs) as well as animal manure are suitable raw materials for energy production because of their high content of biodegradable organic matter [3,4]. Because biomass materials generally contains high amounts of water (50–98% by weight), energy extraction using thermal treatment methods, such as incineration or thermal gasification is less optimal since evaporation consumes a large fraction of the energy released. Thus, anaerobic digestion is often the most suitable method for the energy extraction from wet and easily degradable biomass materials [5-7]. Anaerobic digestion of organic waste can be proceeded on single materials (mono-digestion) or on mixes of multiple materials (co-digestion). Nevertheless, low methane yield and high incidence of process instability have been commonly reported in mono-AD [8]. Co-digestion, a strategy mainly implemented to enhance biogas production, balance nutrients, and control acidogenesis in the anaerobic digestion process, has better performance compared to mono-AD.
Several studies reported that co-digestion could be beneficial since it lead to the dilution of toxic chemical compounds, improvement of nutrients balance and synergistic effect of microorganisms [9].
Thus, the objective of this study was to evaluate the co-DA of vegetable waste (VW) and cow manure (CM) mixture. The effect of S/I ratio on methane yield of VW and CM mixture was also investigated.

II. Materials and Methods

A. Substrates and Inoculum

Vegetable wastes (VW) and dry Cow Manure (CM) were used as a substrates in this study. The VW was obtained from the vegetable markets of Sfax city, whereas CM was collected from local farms. The waste samples were first shredded in a blender to reduce its particle size then mixed and stored at 4°C until use.
Inoculum was collected from a laboratory anaerobic digester treating the organic fraction of municipal solid waste (OFMSW).

B. Biochemical Methane Potential

Two runs of dry AD batch tests were conducted at different substrate to inoculum (S/I) ratios: S/I=0.5 and S/I=1 (VS based). In the first run, mono-fermentation of VW and CM were investigated at TS equal to 20%. Co-digestion tests of VW and CM were conducted in the second run of tests, where the total mass of mixture was fixed to 100 g with a TS of 20%. 250 mL glass bottles were used as an anaerobic batch reactors

ISSN: 2961-6611

and then placed in an incubator at 37 °C. Batch containing only inoculum without any addition of feedstock was used as a control. All tests were conducted in duplicates. The air in the headspace of each reactor was flushed with nitrogen and then the bottles were incubated at 37 °C to keep reactors at a fixed mesophilic condition. Methane production was monitored by measuring the volume of alkaline solution (NaOH 10%) displaced from the measure bottle and collected in graduated cylinder.

C. Lab-Scale Dry Anaerobic Digestion

A discontinuous co-digestion of VW+CM mixture was conducted on double-walled glass Leach bed reactor with a total volume of 10 L under optimized S/I ratio. The total amount of VW was 0.7 kg along with 0.1 kg CM were added in the reactor. 3.5 kg of anaerobic sludge was loaded. The temperature of the reactor was kept constant at 37 °C by water jacket and the leachate was recycled using a pump.

D. Data Analysis

The modified Gompertz equation has been commonly used and identified as a good empirical non-linear regression model in the simulation of biogas accumulation [10,11]. The maximum methane production rate (R_{max}) and lag phase (λ) were determined by fitting the modified Gompertz model (Eq. (1)) [12] to the experimental cumulative methane production curves.

$$M=P.\exp\left\{-\exp\left[\frac{R_{max}\,e}{p}(\lambda-t)+1\right]\right\} \quad Eq\ (1)$$

where M is the cumulative methane expressed in mL CH_4/ g VS; P is the maximum methane potential (mL/g VS); t is the time (day); R_{max} is the maximum methane production rate (mL CH_4/ g VS. d) and λ the lag phase (day). P, R_{max} and λ were determined using Mathematica.

The correlation index (R^2) was quantified to indicate the accuracy of the models.

E. Analytical Methods

Standards methods were used for measurement of Total solids (TSs) and volatile solids (VSs) [13]. pH was measured by a pH-meter. Soluble COD was estimated as described by Knechtel [14]. Total nitrogen Kjeldahl (TNK) was determined using Kjeldahl-N method. The identification and quantification of volatile fatty acids (VFAs) as acetate, propionate, butyrate and isobutyrate, were carried out by HPLC. Samples were acidified with 1 M H_2SO_4, centrifuged for 15 min at 12 000 rpm, filtered through 0.45 µm filter (MILLIPORE) and finally injected (20 µl). The assays were performed on a Shimadzu CTO-10 AS apparatus composed of a Hiplex H column (300 mm x 7.7mm) connected to UV detector (210 nm). The mobile phase was H_2SO_4 (0.017 M) at a flow rate of 0.6 mL/min, and the column temperature was maintained at 50 °C. Total Organic Carbon (TOC) based on a high-temperature combustion method and Inorganic Carbon (IC) were measured in dissolved matter using Shimadzu TOC-VCSN Total Organic Carbon Analyzer with Shimadzu ASI-V auto sampler.

III. Results and Discussion

A. Physico-Chemical Characterization of Agriculture Wastes

The characteristics of the vegetable wastes and cow manure are shown in Table 1. VW has an acid pH (5.2), which could be explained by the high VFA concentration (2 g/L), while CM is characterized by an alkaline pH. VW has a low TOC and TNK compared to CM. In addition to its low C/N ratio, VW was characterized by high moisture content. Therefore, their mixture could complement each other to achieve a suitable nutrient content for anaerobic co-digestion.

TABLE I
CHARACTERISTICS OF THE SUBSTRATES USED IN THE BATCH TEST

	Vegetable Waste	Cow Manure
pH	5.29 ± 0.03	8.7 ± 0.02
TS (g/kg)	166.82 ± 1.4	736.83 ± 2.62
VS (g/kg)	147.57 ± 0.86	470.37 ± 4.33
SCOD (mg/g)	286.45 ± 15.67	321.7± 23.07
TOC (g/Kg)*	401 ± 4.24	371.1 ± 11.17
TNK (g/Kg)	5.6 ± 0.12	15 ± 0.78
VFA (g/L)	2.22 ± 0.25	0.96 ± 0.34

*Dry matter

B. Biomethane Potential of Batch Digestion Experiments

As shown in Figure 1, the methane yields of the two mono-substrate (VW,CM) increased quickly and then decreased. At the end of AD, VW as single substrate achieved a methane yield of 31 and 46 mL/g VS for S/I equal to 0.5 and 1, respectively (Fig. 1a). The low methane yield could be explained by the insufficient buffering capacity of VW due to the imbalanced of acidogenesis and methanogenesis, thereby disrupting the performance of the AD [15]. This result confirm that vegetable waste alone was not suitable for AD. However, methane yields of 168.3 and 132.8 mL/g VS were obtained during mono-fermentation of CM at S/I ratios of 0.5 and 1, respectively (Fig. 1b).

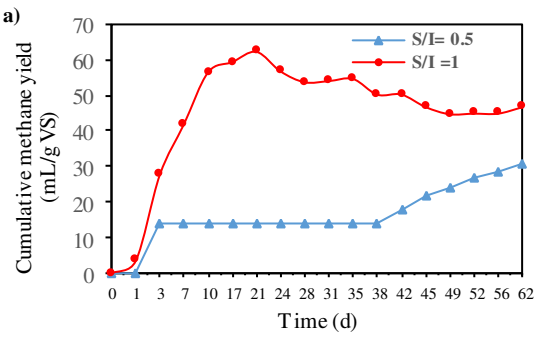

ISSN: 2961-6611

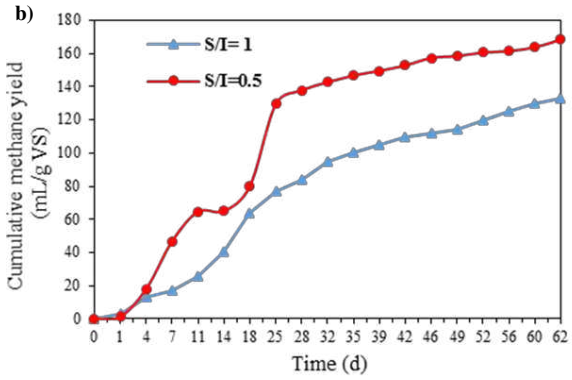

Fig. 1 Cumulative methane yield as function of digestion time for mono-substrate (a) vegetable wastes and (b) cow manure at different S/I ratios

The daily methane production and the methane yield of VW+CM mixture at different S/I ratio are summarized in Figure 2. The first methane peak was reached at the 4th day for the both S/I ratios (0.5 and 1). After that, the biogas production for the two S/I ratio was different, while the biogas production for S/I of 0.5 tended to rise, however, the biogas production for S/I of 1 started plummeting (Fig. 2 a). During the co-digestion of VW+CM mixture at S/I equal to 1, the low methane production might be caused by the high concentration of the VW, as VW could promote fast acidification of medium, which is unfavourable for methanogenesis [16,17]. For S/I of 0.5, the daily methane production showed several methane peaks and the most important one of 342 mL/d was obtained at day 11. This result was possibly due to the suitable ratio providing appropriate conditions to promote cow manure degradation. VW+CM mixture gives the best methane yield of 284 mL/g VS at S/I of 0.5 (Fig. 2b). Methane during co-digestion of VW and CM was significantly higher in comparaison to mono-digestion of VW (10.9 folder) and CM (0.5 folder), at S/I ratio of 0.5

Statistical analysis demonstrate that methane yield of S/I of 0.5 was significantly higher than that at S/I equal to 1 (e.g. *P-value* =0.027 for CM+VW mixture). It can be concluded that S/I of 1 lead to inhibition of micro-organisms explained by overloading phenomena. Similarly, Li et al., [18] found that methane yield was decreased as S/I ratio was increased during co-digestion of kitchen waste and cow manure mixture.

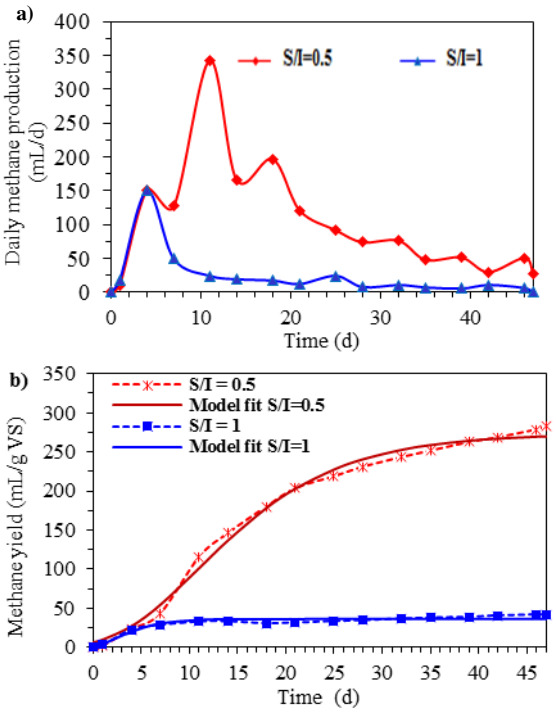

Fig 2. Daily biogas production (a) and methane yield and their models (b) of the anaerobic co-digestion of vegetable waste and cow manure at different S/I ratios

In order to compare the effect of S/I on methane yield, empirical non-linear regression models (Eq. (1)) were fitted to the data and the constants estimated are summarized in Table 2. The R^2 results and Fig 2b demonstrate that all experimental data showed a good fit with Gompertz model. As shown in table 2, R_{max} rise from 5.6 to 12.1 mL/g VS.d for S/I of 1 and 0.5, respectively, which corresponded with the delay in the establishment of the exponential methanogenesis phase. Besides, the rate of methane yield at S/I of 0.5 was 7.5-fold faster than that at S/I of 1.

TABLE II
Model parameters estimated from the co-digestion of VW and CM at different S/I ratio

S/I ratio	λ (d)	R_{max} (mL/gVS.d)	P (mL/gVS)	R^2
0.5	2.66	12.13	273.49	0.99
1	0.43	5.65	36.19	0.96

λ: Lag phase time (d), R_{max}: Maximum methane production rate (mL/g VS.d), P: Estimated ultimate cumulative methane yield (mL/g VS)

C. Reactor Performance

Figure 3 illustrates the variation of daily biogas production from VW and CM mixture and methane content during co-digestion. Digestion process can be divided into three separate time periods. During early time (period I: From 0- 4 days) biogas production increases consistently from initial

ISSN: 2961-6611

day to a peak value of about 8.9 L/d. At intermediate period (period II, From 5-19 days), biogas production decrease with a presence of a small peak of about 2.4 L. at later times, the biogas production decreased again with a much lower rate and becomes constant at a value of about 380 mL after 28 days of digestion.

During the first period the CH_4 content was below 50% which indicate the imbalance of AD. Thus in this period, hydrolysis of easily biodegradable compounds (i.e. sugars and carbohydrates) and acetogenesis stage are faster than methanogenesis step. In the second stage, methanogens activity was improved and resulted an increase of methane content. At the third stage, the decrease of biogas production could be explained by the inhibition of methanogens activity. Therefore, the pH and total alkalinity of leachate were of 8.5 and 5.7 g/L at the end of DA, contributing to instability of the anaerobic digestion process. On the other hand, an accumulation of ammonia was also noticed with a concentration of 2.7 g/kg for a digestate at the end of AD. The ammonia increment of 29 % could resulted in a failure of AD and a decrease of biogas production [19].

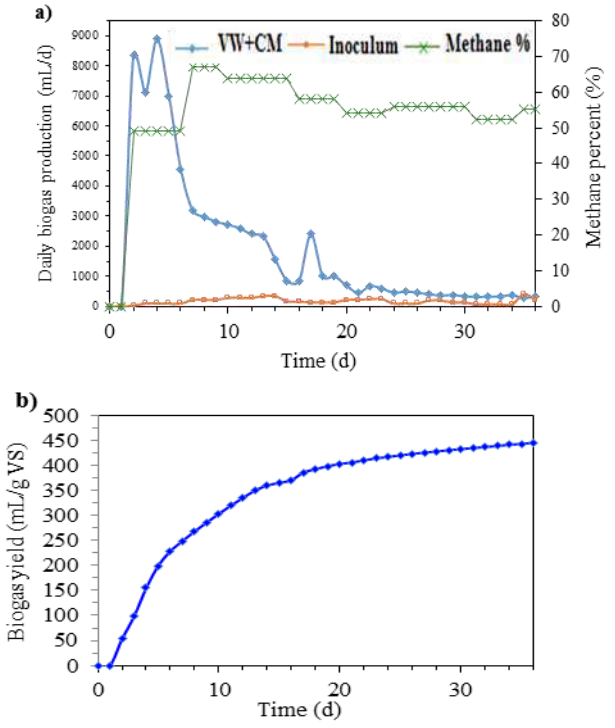

Fig. 3. Daily biogas production (a) and methane yield (b) of the anaerobic co-digestion of vegetable wastes and cow manure on leach bed reactor.

IV. Conclusions

In this study, the impact of co-digestion versus mono-digestion of vegetable wastes and cow manure was investigated at different S/I ratio. Result showed that co-digestion of VW+CM improved methane yield of about 10.6 fold compared to mono-digestion of VW at S/I ratio equal to 0.5. Adding to this, the later ratio leads to methane yield higher than that of S/I equal to1. Estimated parameters from regression models confirms that S/I ratio of 0.5 improve the methane production of VW+CM mixture. However, co-digestion of VW+CM mixture under optimized S/I ratio conducted in bed leach reactor showed a low biogas yield of 445 mL/g VS This could be explained by the high levels of total alkalinity and ammonia at the end of AD process.

Acknowledgment

This research was supported by ERANETMED project (01 DH 17060) BIOGASMENA: Demonstration of biogas technology for rural communities in the Mena region.

References

[1] T.G. Poulsen, L. Adelard. “Improving biogas quality and methane yield via co-digestion of agricultural and urban biomass wastes,” *Waste Manage.* 54, pp. 118-125, 2016.

[2] C. Mao, Y. Feng, X. Wang, G. Ren, Review on research achievements of biogas from anaerobic digestion. *Renew. Sustain. Energy Rev.* 45, 540–555, 2015.

[3] M. Hoogwijk, A. Faaij, R. van den Broeka, G. Berndes, D. Gielen, W. Turkenburg, Exploration of the ranges of the global potential of biomass for energy. *Biomass Bioenergy* 25, p.p 119–133, 2003.

[4] K. Koch, B. Helmreich, J.E. Drewes, Co-digestion of food waste in municipal wastewater treatment plants: effect of different mixtures on methane yield and hydrolysis rate constant. *Appl. Energy* 137, p.p 250–255, 2015.

[5] D. Li, S. Liu, L. Mi, Z. Li, Y. Yuan, Z. Yan, X. Liu, Effects of feedstock ratio and organic loading rate on the anaerobic mesophilic co-digestion of rice straw and pig manure. *Bioresour. Technol.* 187, p.p. 120–127, 2015.

[6] Z. Yong, Y. Dong, X. Zhang, T. Tan, Anaerobic co-digestion of food waste and straw for biogas production. *Renew. Energy* 78, p.p. 527–530, 2015.

[7] I.S. Zarkadas, A.S. Sofikiti, E.A. Voudrias, G.A. Pilidis, Thermophilic anaerobic digestion of pasteurised food wastes and dairy cattle manure in batch and large volume laboratory digesters: focussing on mixing ratios. *Renew. Energy* 80, p.p. 432–440, 2015.

[8] B. Xiao, W. Zhang, H. Yi, Y. Qin, J. Wu, J. Liu, Y-Y Li, Biogas production by two-stage thermophilic anaerobic co-digestion of food waste and paper waste: Effect of paper waste ratio. *Renew. Energy*

[9] V. Razaviarani, I.D. Buchanan, Reactor performance and microbial community dynamics during anaerobic co-digestion of municipal wastewater sludge with restaurant grease waste at steady state and overloading stages. *Bioresour. Technol.* 172, p.p. 232–240. 2014

[10] C. Li, P. Champagne, B.C. Anderson, Evaluating and modeling biogas production from municipal fat, oil and grease and synthetic kitchen waste in anaerobic co-digestions. *Bioresour. Technol.* 102, p.p. 9471–9480. 2011.

[11] H.M., Lo, T.A. Kurniawan, M.E.T. Sillanpää, et al., Modeling biogas production from organic fraction of MSW co-digested with MSWI ashes in anaerobic bioreactors. *Bioresour. Technol.* 101, p.p. 6329–6335, 2010.

[12] C. Li, P. Champagne, B.C., Anderson, Effects of ultrasonic and thermochemical pre-treatments on methane production from fat, oil and grease (FOG) and synthetic kitchen waste (KW) in anaerobic co-digestion. *Bioresour. Technol.* 130, p.p. 187-197, 2013.

[13] APHA, Standard Methods for the Examination of Water and Wastewater, 18th ed., American Public Health Association, Washington, DC, USA, 1992.

[14] R.J. Knechtel A more economical method for the determination of chemical oxygen demand. *J. Water Pollut. Control.*, pp. 25–29, 1978.

ISSN: 2961-6611

[15] D.I. Masse, R. Rajagopal, G. Singh, Technical and operational feasibility of psychrophilic anaerobic digestion biotechnology for processing ammonia-rich waste. *Appl. Energy* 120, 49–55. 2014.
[16] R. Ganesh, M. Torrijos, P. Sousbie, A. Lugardon, J.P. Steyer, J.P. Delgenes, Effect of increasing proportions of lignocellulosic cosubstrate on the single-phase and two-phase digestion of readily biodegradable substrate. *Biomass and Bioenerg*. 80, p.p. 243-251, 2015.
[17] S. Pavi, L.E. Kramer, L.P. Gomes, L.A. Miranda, Biogas production from co-digestion of organic fraction of municipal solid waste and fruit and vegetable waste. *Bioresour. Technol.* 228, p.p. 362-367, 2017.
[18] S. Pavi, L.E. Kramer, L.P. Gomes, L.A. Miranda, Biogas production from co-digestion of organic fraction of municipal solid waste and fruit and vegetable waste. *Bioresour. Technol.* 228, p.p. 362-367, 2017.
[19] X. Meng, D. Yu, Y. Wei, Y. Zhang, Q. Zhang, Z. Wang, J. Liu, Y. Wang, Endogenous ternary pH buffer system with ammonia-carbonates-VFAs in high solid anaerobic digestion of swine manure: An alternative for alleviating ammonia inhibition? *Process Biochem.* 69, p.p. 144–152, 2018.

ISSN: 2961-6611

Modelling of Photovoltaic Water Pumping System Using the Multi-model Approach

*Nawel Mensia#1, Mourad Talbi*2, Mongi Bouaicha#3.*

Laboratoire Photovoltaïque, Centre de Recherches et de Technologies de l'Energie de Borj Cedria

[1]Mensia_nawel@hotmail.com, [3]mongi.bouaicha@crten.rnrt.tn

Laboratoire des Semi-Conducteurs, Nanostructures et Technologie Avancée

[2]talbi1969@yahoo.fr

Centre de Recherches et de Technologies de l'Energie de Borj Cedria

Abstract— **In this work, we develop and simulate an accurate model of a gird connected photovoltaic system composed by a photovoltaic generator, a buck converter and a motor-driven pump. The modeling method reposes on the multi-model approach and elaborate a flexible and reliable model. This can be used to develop easily an intelligent controller to effectively attain Maximum Power Point Tracking (MPPT) in Photovoltaic (PV) system. The simulation result of the obtained model proves the success of this model to represent closely the system behavior under different climatic conditions of temperature and illumination.**

Keywords— **Multi-model approach, Photovoltaic pumping system, Convex polytopic transformation, vertex matrices, extreme values of temperature and illumination.**

I. INTRODUCTION

Traditional energy sources are not able to meet the growing demand for energy worldwide. Therefore, alternative energy sources like biomass, sunlight and wind, come into mentality. In this context, photovoltaic energy presents a source of attractive energy; it is non-polluting, sustainable and renewable. Today, photovoltaic energy is increasingly used in various terrestrial applications such as lightning, water pumping and telecommunication [1], [2]. Though, its exploitation is less than conventional energy sources due to the high cost and the low efficiency of photovoltaic systems. Consequentially, it is necessary to have flexible and reliable models, in order to perform an intelligent command to getting its performance as maximum as possible.

The Photovoltaic System performance is greatly depending on temperature and solar radiation (intermittent production). The rational employment of solar energy imposes the determination of the maximum operating Photovoltaic Generators (PVG) and estimation of the produced energy. Knowledge that goes through the modeling of photovoltaic systems. In literature, many techniques have been proposed for modeling and simulating (PVG) based on a diode model. Although, a great number of this techniques are based on the adjustment of the curve I(V) at the points of the experimental curve, which requires the graphic extraction of curve slope at determined points or require an experimental analysis of photovoltaic device. These techniques have drawbacks, for the experimental curves I(V) are not permanently accessible in manufacturers' data sheets, and devices for measurement of experimental data are not usually available as well. Others modeling techniques based on the modification of the electronic characteristic of a diode model of photovoltaic cell [3]. Some others have proposed techniques of modeling tools based on the adjustment of the curve P(V). Although, this latter is based only on the characteristic I(V) and the peak power of the resulting model is not always peak power of the real device. Furthermore, there are few modeling studies based on artificial intelligence such as multi-model approach [4]. The main advantage of the multi-model approach lies in the ability to provide an accurate model for the nonlinear and complex systems. This advantage is exploited in this work to establish a perfect model of a gird connected photovoltaic system. The latter system is presented by several simple models easy to manipulate, without use of an order reduction technique which causes an information loss, and without require of the functioning point identification.

This paper is organized as follow: in section 2, we present the photovoltaic pumping system to be study. In section 3 we give its model state. The elaboration of the multi-model representation of the system is detailed in section 4. In section 5, we give the simulation results and interpretations.

II. PRESENTATION OF THE STUDY PHOTOVOLTAIC PUMPING SYSTEM

A photovoltaic pumping system is generally composed by a photovoltaic generator, a motor-driven pump and a water tank to ensure the continuity of the supply when solar energy is not sufficient. Two types of systems can be used. In the first type, the Photovoltaic Generator (PVG) is directly coupled to the motor-driving pump. In the second type the PVG can be coupled either to an AC motor-driven pump through a DC-DC converter connected to a DC-AC converter [5], or to a DC motor-driven pump through a DC-DC converter. The latter type is the subject of our interest, indeed we will modeling the photovoltaic system consists of a PV generator coupled to a DC permanent magnet motor through a buck convertor which equivalent circuit diagram is the following:

ISSN: 2961-6611

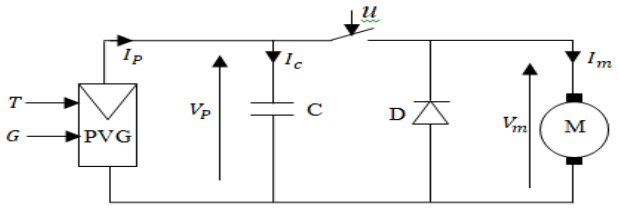

Fig. 1 Electrical diagram of water pumping photovoltaic system.

It's consisted by the following components:

- Photovoltaic Generator (PVG)

The PVG consist of N_p arrays connected in parallel. Each array is composed of n_p panels associated in series, and each panel is formed of n_c cells related in series. Therefore, the array is composed by $N_s = n_p \times n_c$ cells. So, if the cell current is I_{pvc} and its voltage is V_{pvc} then the PVG current and voltage are successively: $I_p = N_p I_{pvc}$ and $V_p = N_s V_{pvc}$.

- Buck converter

The chopper is controlled by the switched control variable u and its input is connected to the capacitor C, which allows transforming the current source I_p to a voltage source V_p.

- Diode

The diode ensures continuity of the current in the motor at the moment of disconnecting power to avoid peak overvoltage.

- Motor-driven pump

We consider a DC permanent magnet motor with Constant flux, where the armature reaction and the switching phenomenon are assumed to be negligible.

III. STATE MODEL OF THE PHOTOVOLTAIC PUMPING

The electrical behavior of a PV cell can be described with good accuracy by the single diode equivalent circuit [6]. The ideal equivalent circuit is a current source in parallel with a single-diode which governed by the following equation:

$$I_{pvc} = I_{phc} - I_{sd}\left(e^{\frac{qV_{pvc}}{KnT_c}} - 1\right) \quad (1)$$

where :

I_{pvc}: PV cell current;

I_{phc}: light current;

I_{sd}: diode reverse saturation current;

V_{pvc}: PV cell voltage;

q= 1.6. 10^{-19} C : electron charge,

K = 1.38. 10^{-23}J/K : Boltzmann's constant,

n : ideal factor,

T_c : the actual cell temperature.

From the last equation, we can deduce the expression of the PVG output current I_P according to its voltage V_P:

$$I_p = N_p I_{phc} - N_p I_{sd}\left(e^{\frac{qV_P}{N_S KT_c n}} - 1\right) \quad (2)$$

If we consider: $I_{ph} = N_p I_{phc}$ and $I_S = N_p I_{sd}$ then we can write the following:

$$I_p = I_{ph} - I_S\left(e^{\frac{qV_P}{N_S KT_c n}} - 1\right) \quad (3)$$

The motor-pump functioning is described by the following equations:

$$V_m = k_e\Omega + L\frac{dI_m}{dt} + RI_m \quad (4)$$

$$J\frac{d\Omega}{dt} = k_b I_m - f\Omega \quad (5)$$

where:

k_e: counter-electromotive force constant

Ω: angular velocity

L: electric inductance

R: electric resistance

f: motor viscous friction constant

k_b: torque equation constant

J: total inertia moment

The current I_c and the voltage V_m are expressed according the switched control variable u as following:

$$I_c = I_P - u.I_m \quad (6)$$

$$V_m = u.V_p \quad (7)$$

Combining the above equations gives:

$$\begin{cases} \frac{dV_P}{dt} = \frac{1}{C}I_P - \frac{1}{C}I_m.u \\ \frac{dI_m}{dt} = \frac{1}{L}V_P.u - \frac{R}{L}I_m - \frac{k_e}{L}\Omega \\ \frac{d\omega}{dt} = \frac{k_b}{J}I_m - \frac{f}{J}\Omega \end{cases} \quad (8)$$

If we considered the state vector $x = \begin{bmatrix} x_1 \\ x_2 \\ x_3 \end{bmatrix}$

where:

$x_1 = V_p$; $x_2 = I_m$ and $x_3 = \Omega$. Then the model state of the water pumping photovoltaic system presented in figure (1) can be written as following:

$$\begin{cases} \dot{x}_1 = \frac{1}{C}I_p - \frac{1}{C}x_2 u \\ \dot{x}_2 = \frac{1}{L}x_1.u - \frac{R}{L}x_2 - \frac{k_e}{L}x_3 \\ \dot{x}_3 = \frac{k_b}{J}x_2 - \frac{f}{J}x_3 \end{cases} \quad (9)$$

we suppose that $\alpha(x_1) = \frac{I_p}{C}$, then system of equations (9) can be written as follow:

$$\begin{cases} \dot{x}_1 = \alpha(x_1) - \frac{1}{C}x_2.u \\ \dot{x}_2 = \frac{1}{L}x_1.u - \frac{R}{L}x_2 - \frac{k_e}{L}x_3 \\ \dot{x}_3 = \frac{k_b}{J}x_2 - \frac{f}{J}x_3 \end{cases} \quad (10)$$

where $\alpha(x_1)$ varies depending on the temperature and illumination.

The system non-linearity comes from the exponential function which describes the internal diode behavior in the expression of I_p. This function prevents to isolate V_p by a reliable linearization. Consequently, the dependency between I_p and V_p constitutes a major obstacle for the command synthesis. To solve this problem, we will use in this paper, a transformation procedure of system in order to writing the model state in multi-model form .That makes it possible to calculate easily a robust control for the system, under different climatic conditions of temperature and illumination.

ISSN: 2961-6611

IV. MULTI-MODEL REPRESENTATION OF THE PHOTOVOLTAIC PUMPING SYSTEM

A. *Multi-model principle*

A multi-model is a system representation composed by a set of simple models easy to manipulate, each of which is valid in a well-defined feature space corresponding to a part of global system's behavior [7]. One degree of validity is associated to each of these models forming a base of model. An activation function which tends to 1 in the feature space and tends to zero outside, specifies the validity degree which estimates the model contribution in the global functioning of the system. The global system's behavior can then be described by the combination of all models of the base. In literature, we can mention three approaches which are largely used for obtaining a multi-model representation: by identification, by linearization and by non-linear sectors transformation [8]. In this paper, we will be interested in the last approach. It is a convex polytopic transformation of scalar functions origin of nonlinearity.

B. multi-model elaboration

In order to represent a pumping system in a multi-model form, we will first transform the non-linear model state (10) into a quasi-Linear model with Variable Parameters (quasi-LPV) having the following form:

$$\dot{x} = A\big(\rho(x,u)\big)x + B\big(\rho(x,u)\big)u \qquad (11)$$

It deserves mentioning that the parameters vector $\rho(x,u)$ will be different in the matrices A and B. However, for simplicity, a single notation will be used in those two matrices.

Since the state variable x_1 can vary depending the temperature and illumination between a non-zero minimum and a maximum values, therefore we can reformulate the system of equation (10) as follow:

$$\begin{cases} \dot{x}_1 = \alpha(x_1).\left(\frac{x_1}{x_1}\right) - \frac{1}{C}x_2.u \\ \dot{x}_2 = \frac{1}{L}x_1.u - \frac{R}{L}x_2 - \frac{k_e}{L}x_3 \\ \dot{x}_3 = \frac{k_b}{J}x_2 - \frac{f}{J}x_3 \end{cases} \qquad (12)$$

This makes it possible to establish the following quasi-LPV form of the photovoltaic pumping system:

$$\begin{bmatrix}\dot{x}_1\\ \dot{x}_2\\ \dot{x}_3\end{bmatrix} = \begin{bmatrix}\alpha(x_1)/x_1 & 0 & 0\\ 0 & -R/L & -k_e/L\\ 0 & k_b/J & -f/J\end{bmatrix}\begin{bmatrix}x_1\\ x_2\\ x_3\end{bmatrix} + \begin{bmatrix}-x_2/C\\ x_1/L\\ 0\end{bmatrix}u \qquad (13)$$

Thereafter, we define the set of non-constant variables in matrices A and B as the set of premises V_z [9]:
$V_z = \{z_1(x),\ z_2(x),\ z_3(x)\}$,
where: $z_1(x) = \alpha(x_1)/x_1$; $z_2(x) = -x_2/C$; $z_3(x) = x_1/L$.

Each of these premises can be bounded by two extreme values depending on temperature and illumination:
$\underline{z_1} < z_1(x) < \overline{z_1}$; $\underline{z_2} < z_2(x) < \overline{z_2}$; $\underline{z_3} < z_3(x) < \overline{z_3}$

Then, we apply to these bounded premises a polytopic transformation based on the following lemma [10].

Lemma: Any nonlinear function: $g(x): R \to R$ satisfying $\underline{g} < g(x) < \overline{g}; \forall x$ can be written as:

$$g(x) = G_1(x)\underline{g} + G_2(x)\overline{g}\ ; \quad \text{where:}$$
$$G_1(x) = \frac{\overline{g}-g(x)}{\overline{g}-\underline{g}}; \qquad G_2(x) = \frac{g(x)-\underline{g}}{\overline{g}-\underline{g}};$$

and the functions $G_i(x)$ satisfy the convex sum property i.e. $G_1(x) + G_2(x) = 1$, and $0 < G_i(x) < 1, \forall x$.

After premises transformation, we obtain:

$$z_i(x) = F_{i1}(z_i(x))\overline{z_i} + F_{i2}(z_i(x))\underline{z_i}; \quad i \in \{1,2,3\} \qquad (14)$$

where:

$$F_{i1}(z_i(x)) = \overline{z_i}\ \frac{z_i(x)-\underline{z_i}}{\overline{z_i}-\underline{z_i}};\ F_{i2}(z_i(x)) = \underline{z_i}\ \frac{\overline{z_i}-z_i(x)}{\overline{z_i}-\underline{z_i}} \qquad (15)$$

$$F_{i1}(z_i(x)) + F_{i2}(z_i(x)) = 1 \qquad (16)$$

We will denote by F_{ij} instead of $F_{ij}(z_i(x))$, $j \in \{1,2\}$.

Our aim consists in evaluating the matrixes A and B from the polytope vertex matrixes which defined from the partitions of the premises that configure in these matrixes.

Considering:

$$A(z_1(x)) = \begin{bmatrix}z_1(x) & 0 & 0\\ 0 & 0 & 0\\ 0 & 0 & 0\end{bmatrix}, A_0 = \begin{bmatrix}0 & 0 & 0\\ 0 & -R/L & -k_e/L\\ 0 & k_b/J & -f/J\end{bmatrix}.$$

Then the matrix $A\big(\rho(x,u)\big)$ can be expressed as follow:

$$A\big(\rho(x,u)\big) = A(z_1(x)) + A_0 \qquad (17)$$

when $z_1(x)$ is replaced by its expression of equations (14) and (15), we can obtain the next equation:

$$A(z_1(x)) = F_{11}.\begin{bmatrix}\overline{z_1} & 0 & 0\\ 0 & 0 & 0\\ 0 & 0 & 0\end{bmatrix} + F_{12}.\begin{bmatrix}\underline{z_1} & 0 & 0\\ 0 & 0 & 0\\ 0 & 0 & 0\end{bmatrix} \qquad (18)$$

The next step is to multiply the members of equation (18) by the unit term: $(F_{21} + F_{22})(F_{31} + F_{32})$, which gives the equation (19).

$$A\big(z_1(x)\big) = \mu_1A_1 + \mu_2A_1 + \mu_3A_1 + \mu_4A_1 + \mu_5A_2 + \mu_6A_2 + \mu_7A_2 + \mu_8A_2 \qquad (19)$$

where:

$\mu_1 = F_{21}F_{31}F_{11}$; $\mu_2 = F_{21}F_{32}F_{11}$; $\mu_3 = F_{22}F_{31}F_{11}$;
$\mu_4 = F_{22}F_{32}F_{11}$; $\mu_5 = F_{21}F_{31}F_{12}$;
$\mu_6 = F_{21}F_{32}F_{12}$; $\mu_7 = F_{22}F_{31}F_{12}$; $\mu_8 = F_{22}F_{32}F_{12}$;

$A_1 = \begin{bmatrix}\overline{z_1} & 0 & 0\\ 0 & 0 & 0\\ 0 & 0 & 0\end{bmatrix}$ and $A_2 = \begin{bmatrix}\underline{z_1} & 0 & 0\\ 0 & 0 & 0\\ 0 & 0 & 0\end{bmatrix}$.

Consequently, matrix $A(z_1(x))$ is written as a function of two vertex matrixes A_1 and A_2.

We proceed in the same way for B in order to express it according to the premises z_2 and z_3.

We have :

$$B\big(\rho(x,u)\big) = B(z_2(x), z_3(x)) = \begin{bmatrix}z_2(x)\\ z_3(x)\\ 0\end{bmatrix} \qquad (20)$$

first, $B\big(\rho(x,u)\big)$ is decomposed with respect to $z_2(x)$, then with respect to $z_3(x)$:

$$B(z_2(x), z_3(x)) = F_{21}.F_{31}\begin{bmatrix}\overline{z_2}\\ \overline{z_3}\\ 0\end{bmatrix} + F_{22}.F_{31}\begin{bmatrix}\underline{z_2}\\ \overline{z_3}\\ 0\end{bmatrix} + F_{21}.F_{32}\begin{bmatrix}\overline{z_2}\\ \underline{z_3}\\ 0\end{bmatrix} + F_{22}.F_{32}\begin{bmatrix}\underline{z_2}\\ \underline{z_3}\\ 0\end{bmatrix} \qquad (21)$$

ISSN: 2961-6611

After that we multiply the members of the equation (21) by the unit quantity $(F_{11} + F_{12})$. So we find the subsequent expression of $B(\rho(x,u))$:

$$B(\rho(x,u)) = \mu_1 B_1 + \mu_2 B_3 + \mu_3 B_2 + \mu_4 B_4 + \mu_5 B_1 + \mu_6 B_3 + \mu_7 B_2 + \mu_8 B_4 \quad (22)$$

with : $B_1 = \begin{bmatrix} \overline{Z_2} \\ \overline{Z_3} \\ 0 \end{bmatrix}, B_2 = \begin{bmatrix} Z_2 \\ \overline{Z_3} \\ 0 \end{bmatrix}, B_3 = \begin{bmatrix} \overline{Z_2} \\ Z_3 \\ \overline{0} \end{bmatrix}, B_4 = \begin{bmatrix} Z_2 \\ Z_3 \\ \overline{0} \end{bmatrix}$.

therefore, matrix $B(\rho(x,u))$ is then written as a function of four vertex matrixes B_1, B_2, B_3 and B_4.

Finally the state model of the photovoltaic pumping system can be reformulating according the vertex matrices as following:

$$\dot{x} = (A_{0+}\vartheta_1 A_1 + \vartheta_2 A_2)x + (\vartheta_3 B_1 + \vartheta_4 B_2 + \vartheta_5 B_3 + \vartheta_6 B_4)u \quad (23)$$

where:

$\vartheta_1 = \mu_1 + \mu_2 + \mu_3 + \mu_4$; $\vartheta_2 = \mu_5 + \mu_6 + \mu_7 + \mu_8$;
$\vartheta_3 = \mu_1 + \mu_5$; $\vartheta_4 = \mu_3 + \mu_7$; $\vartheta_5 = \mu_2 + \mu_6$; $\vartheta_6 = \mu_4 + \mu_8$.

It is deserve mentioning that each vertex of the polytope defines a linear subsystem, and that the nonlinearity of the global system is rejected in the weighting functions ϑ_i.

V. SIMULATION RESULT

In order to show the reliability of the developed model, we will consider a photovoltaic pumping system which has the following characteristics:

- PVG : PV module : SPM (P) 240-260W;

$I_{SC} = 8.3A$;$V_{mp} = 31.58V$; $I_{mp} = 7.6A$; $V_{oc} = 36.6V$;
$\beta_0 = \frac{-0.34\%}{℃}$; $\alpha_0 = \frac{0.05\%}{℃}$; $N_S = 60$; NOCT $= 45 \mp 2°C$.

- Motor-pump DC : It is characterized by a nominal functioning point: $u_n = 24V$; $I_n = 12A$; $\omega_n = \frac{2000tr}{mn}$.

Its parameters are: $R = 1.072$; $L = 0.05H$; $f = 8814.10^{-7} N.m.\frac{s}{rd}$;
$k_e = 0.5$; $k_b = 0.1$; $J = 476.10^{-6} Kg.m^2$; $C = 4.7mF$.

Concerning the experimental conditions, we choose the maximum and minimum values of temperature and irradiance as follow:

$G_{max} = \frac{1200W}{m^2}$; $G_{min} = \frac{400W}{m^2}$; $T_{max} = 60℃$; $T_{min} = 0℃$.

The extreme values of the PVG voltage V_p and the current I_p are calculated according to the temperature and irradiance by the following formulas [11], [12]**:**

$$V_p = V_{mp}\left[1 + 0.0539Ln\left(\frac{G}{G_0}\right)\right] + \beta_0(T_C - T_{C0}) \quad (24)$$

$$I_p = I_{ph} - I_S\left(e^{\frac{qV_P}{N_S KT_c n}} - 1\right) \quad (25)$$

where : $T_C = T_a + \left[\frac{NOCT-20}{800}\right].G$

with:

T_C: Temperature of the PV module;
T_a: is the ambient temperature;
T_{C0}: Temperature of the PV module at STC;
NOCT: Nominal Operating cell Temperature;
V_{mp}: The maximum PVG voltage under standard conditions;
α_0 : Coefficient of current according the temperature;
β_0 : Coefficient of voltage according the temperature;
$T_0 = 298°k$; $G_0 = 1000Watt/m^2$.

The ideality factor n depends on PV cell technology and can be chosen in [13]

I_{ph} is expressed according temperature and irradiance by the following equation [14]:

$$I_{ph} = \frac{G}{G_0}(I_{SC} + \alpha_0(T_C - T_{C0})) \quad (26)$$

and I_S is given by the equation (27).

$$I_S = I_{S0}\left(T_C/T_{C0}\right)^3 e^{\frac{qEg}{N_S nK}\left(\frac{1}{T_{C0}} - \frac{1}{T_C}\right)} \quad (27)$$

where *Eg* is the bang-gap energy of the semiconductor used in the cell, and I_{S0} is given by:

$$I_{S0} = \frac{I_{SC}}{e^{\frac{qV_{OC}}{N_S nKT_{C0}}} - 1} \quad (28)$$

After calculating the weighting functions ϑ_i and the vertex matrices relating to the model developed according to the preceding parameters, this latter is simulated in Matlab environment. The result is given in the following figure, which illustrate the evolution of system's PVG voltage and that of model PVG voltage for different temperature and irradiance pairs chosen arbitrarily, and for two values of command randomly selected.

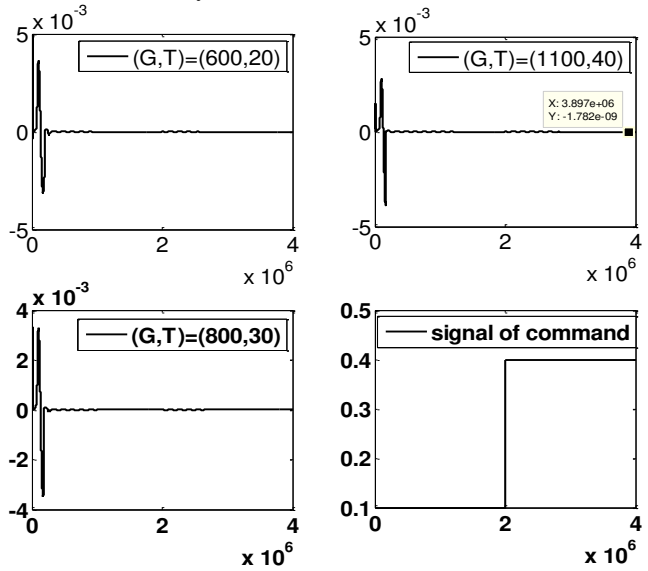

Fig. 2 Evolution of the system's PVG voltage and that of the model's PVG voltage, for two different values of command and different couples of temperature and irradiance

We note that the error between voltage generate by the system's PVG and that generate by the model's PVG under diverse climatic conditions of temperature and illumination, and for different command decreases up to 10^{-9}. This result leads to a model able to imitate with a great precision the PVG voltage of the system.

To test the model aptitude to replicate the behavior of all system state variables, we have simulated the angular velocity Ω of the system and that of the model. As well as the motor current I_m of the system and that of the model. The simulation result is given respectively in figures 3 and 4:

ISSN: 2961-6611

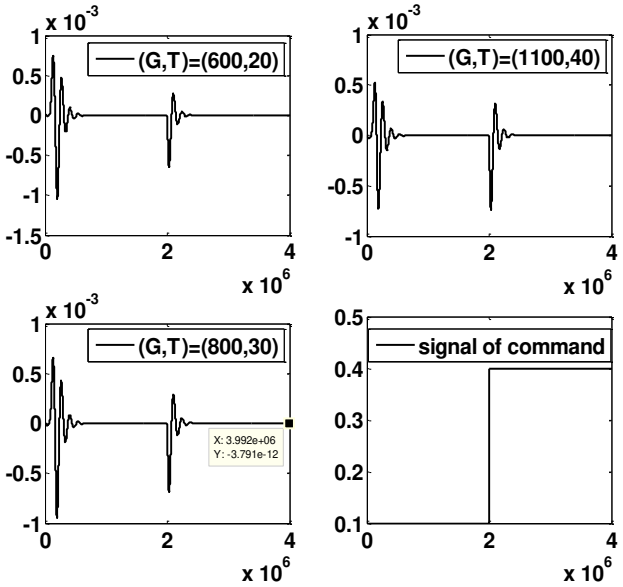

Fig 3 Evolution of the angular velocity Ω of the system and that of the model. for two different values of command and different couples of temperature and irradiance.

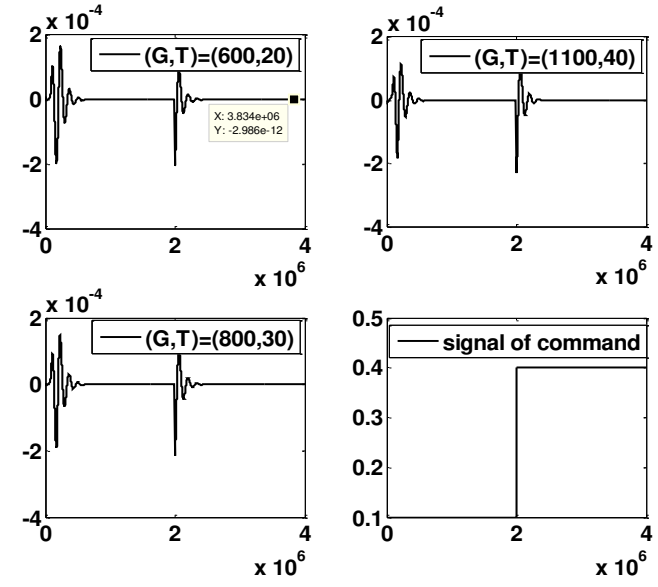

Fig 4 Evolution of motor current I_m of the system and that of the model, for two different values of command and different couples of temperature and irradiance

We notice according to the simulation results given in figures 3 and 4, that the modeling error reaches 10^{-12} .These results demonstrates the model success to reproduce with high precision the conduct of the system state variables. That attests again the high quality of the elaborate model.

VI. CONCLUSION

The performance of a Photovoltaic pumping system highly depends on the weather conditions, such as temperature and illumination, so does the performance of the PV generator degrade with increasing temperature and decreasing illumination. To provide water continuously throughout the year, a PV pumping system must be led by intelligent control which depends heavily on the quality of the system model. The model must guarantee a correct description of the expected variation in the system. This objective is reached by the model structure proposed in this paper. Indeed, we have developed an accurate model that represents the behavior of the system under different climatic conditions of temperature and illumination. The multi-model approach is used to represent the system by a set of simple models, which calculates according the extreme values of temperature and illumination. The modeling begins with the establishment of the quasi-LPV form, then the identification of the premise variables, next the premise decomposition and finally the development of matrices and weighting functions. The simulation results of the method proved the good quality of the established model. In perspective, this work will be continued with a practical implementation of the model by an Arduino board for increasing the efficiency of the system to extract the maximum energy.

VII. REFERENCES

[1] J. Patel and G. Sharma, ‘‘Modeling and Simulation of Solar Photovoltaic Module using Matlab/Simulink,’’ International Journal of Research in Engineering and Technology, Vol. 02, Issue. 03, Mars. 2013.

[2] M. Abdulkadir, A. S. Samosir, and A. H. M. Yatim “Modeling and Simulation of a Solar Photovoltaic System, ItsDynamics and Transient Characteristics in LABVIEW,” International Journal of Power Electronics and Drive System (IJPEDS) Vol. 3, pp. 185-192, Nov. 2013.

[3] T. Hongmei, F. M. Davida, E. Kevin, M. Eduard, and J. Peter, « A cell- to – module –to-array detailed model for photovoltaic panels,” Solar Energy, vol. 86, pp 2695-2706, September. 2012.

[4] KK. Ravinder, SL. Shimib, S. Chatterjib, and A. Fahim, “Modellign of solar pv module and maximum power point tracking using ANFIS,” Renew. Sustain. Energy rev, vol. 33, pp 602-612. May 2014.

[5] S. M. Ait-Cheikh: “Etude, Investigation et conception d’algorithmes de commande appliqués aux systèmes photovoltaïque,’’ PhD thesis, Ecole Nationale Polytechnique, 2007.

[6] S. Petibon, “Nouvelles architectures distribuées de gestion et de conversion de l’énergie pour les applications photovoltaïques, ” Ph.D. thesis, Toulouse university, 2009.

[7] R.M. Smith, T .A. “ Johansen Multiple multimodel approachs to modelling and control,” Edition, Taylor and francis, 1997.

[8] N. Elfelly, “ Approche neuronale de la représentation et de la commande multimodèle de processus complexe,’’ Ph.D. thesis, Ecole Doctorale Science pour l’Ingénieur Université Lille. 2010.

[9] M. N. Anca, “ Analyse et synthèse de multimodèle pour le diagnostic. Application à une station d'épuration,” Ph.D. thesis, National Polytechnic Institute of Lorraine.2010.

[10] K. Tanaka, H. O. Wang “Fuzzy Control Systems Design and Analysis: A Linear Matrix Inequality Approach,” A Wiley-Interscience Publication, September. 2001.

[11] M. Belhaj, T. Benouaz, A. Cheknane and S.M.A. Bekkouche, “Estimation de la puissance maximale produite par un générateur photovoltaique,’’ Revue des Energies Renouvelables, vol 13. N° 2, pp 256-257, Nov. 2010.

[12] H Bellia, Y. Ramdani, F. Moulay. ‘‘A detailed modeling of photovoltaic module using MATLAB’’, NRIAG Journal of Astronomy and Geophysics, vol 3, pp 53-61, June. 2014.

[13] S.B. Bogdan, Z.M. Salameh, ‘‘Methodology for optimally sizing the combination of a battery bank and PV array in a wind/PV hybrid system ’’, IEEE Transactions on Energy Conversion, vol 11. N° 2, pp 367–375, 1996.

[14] Huan-Liang Tsai., Ci-Siang Tu., Yi-Jie Su., ‘‘ Development of generalized photovoltaic model using MATLAB/Simulink ’’. in Proc. World Congress on Engineering and Computer Science, San Francisco, USA, October.2008.

ISSN: 2961-6611